JOURNAL OF APPLIED PHYSICS

Vol 31, No. 7 July, 1960

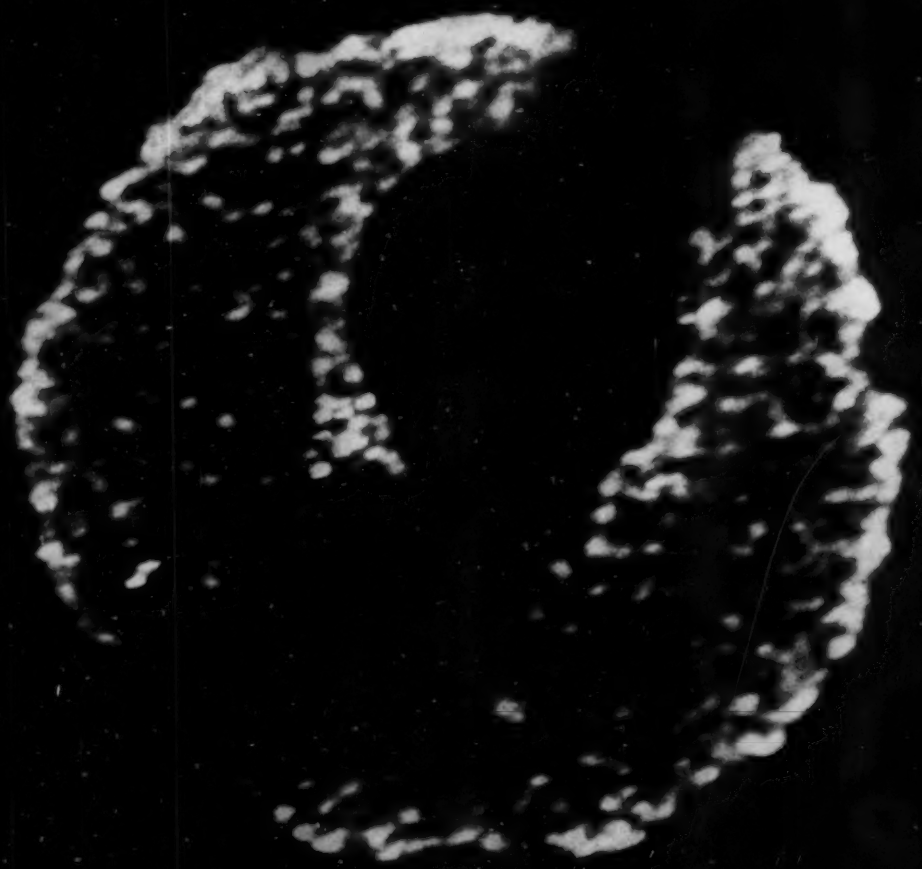

Visible Light from a Junction.
See Page 1153.

HARSHAW MANUFACTURES A COMPLETE LINE OF SCINTILLATION AND OPTICAL CRYSTALS

SCINTILLATION *Mounted* NaI(T1) *Crystals*

Crystal detectors designed for the most sophisticated counting problems. Our physics and engineering group are available to assist you in your special detector problems.

More detailed information is contained in our 32-page book, "Harshaw Scintillation Phosphors." We invite you to write for your free copy!

STANDARD LINE
(Hermetically Sealed Crystal Assemblies)

- The accepted standard of the industry
- Proven through years of service in research, medical and industrial applications
- unparalleled performance
- dependability
- consistent good quality.

INTEGRAL LINE
(Crystal photo multiplier tube combination assembly)

- Improved resolution
- Ready to use plug-in unit
- Permanently light sealed
- Capsule design facilitates decontamination
- Close dimensional tolerances
- Harshaw guaranteed

***Large Crystal* MATCHED WINDOW LINE**
(Designed primarily for crystals 4" dia. and larger)

- "Small crystal" performance achieved through improved optical design
- Low mass containers
- Available in standard aluminum or complete low background assemblies
- Convenient mounting flange
- Ready to use

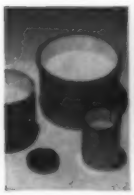

Every Harshaw crystal is a product of our experience in crystal growing technology since 1933

Other Phosphors Available from The Harshaw Chemical Company

ROUGH CUT THALLIUM ACITVATED SODIUM IODIDE CRYSTAL BLANKS • EUROPIUM ACTIVATED-LITHIUM IODIDE (NORMAL) • EUROPIUM ACTIVATED LITHIUM IODIDE (96% Li^6 ENRICHED) • THALLIUM ACTIVATED CESIUM IODIDE • THALLIUM ACTIVATED POTASSIUM IODIDE • ANTHRACENE • PLASTIC PHOSPHORS

OPTICAL *Crystals*

For Infrared and Ultra Violet Transmitting Optics

"HARSHAW QUALITY" INHERENT IN EACH HARSHAW-GROWN CRYSTAL GUARANTEES THE MOST EFFICIENT OPTICAL TRANSMISSION POSSIBLE THROUGH:

1) Negligible light scattering in crystals, permitting higher sensitivity and improved resolution
2) Freedom from absorptions caused by trace impurities in crystal optics
3) Minimum strain

"HARSHAW QUALITY" meets the demand for uniformity of optical properties such as dispersion and refractive index.

Prices, specifications, or other information will be sent in answer to your inquiry.

The following infrared and ultra violet transmitting crystals are available; others are in the process of development:

SODIUM CHLORIDE • SODIUM CHLORIDE MONOCHROMATOR PLATES POTASSIUM BROMIDE • POTASSIUM BROMIDE PELLET POWDER • (through 200 on 325 mesh) • POTASSIUM CHLORIDE • OPTICAL SILVER CHLORIDE • THALLIUM BROMIDE IODIDE • LITHIUM FLUORIDE • LITHIUM FLUORIDE MONOCHROMATOR PLATES • CALCIUM FLUORIDE • BARIUM FLUORIDE • CESIUM BROMIDE • CESIUM IODIDE

Additional information on the physical and optical properties of the above crystals is available in our 36-page booklet "Synthetic Optical Crystals". Send for your free copy.

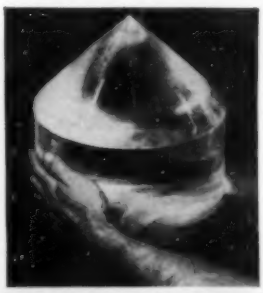

HARSHAW

THE HARSHAW CHEMICAL CO.
Crystal Division • Cleveland 6, Ohio

JOURNAL OF APPLIED PHYSICS

Vol. 31, No. 7 JULY, 1960

In This Issue

Diagrams Representing States of Operation of a General Thermocouple . . . . . A. H. Boerdijk 1141
Time Discrimination in Solid-State Infrared Quantum Counters . . . . . J. V. Jelley 1145
Power Flow and Stored Energy in Thin Electron Beams . . . . . W. W. Rigrod 1147
Uniform Silicon *p-n* Junctions. I. Broad Area Breakdown . . . . . R. L. Batdorf, A. G. Chynoweth, G. C. Dacey, and P. W. Foy 1153
Uniform Silicon *p-n* Junctions. II. Ionization Rates for Electrons . . . . . A. G. Chynoweth 1161
Propagation Mechanism of Germanium Dendrites . . . . . D. R. Hamilton and R. G. Seidensticker 1165
Monte Carlo Calculation of Molecular Flow Rates through a Cylindrical Elbow and Pipes of Other Shapes . . . . . D. H. Davis 1169
Transport Equation for the Spectral Density of a Multiple-Scattered Electromagnetic Field . . . . . Dimitri S. Bugnolo 1176
Small Angle Scattering Investigation of Ludox Mixtures . . . . . Robert H. Bragg, Irene Corvin, and John W. Buttrey 1183
Charged-Particle Orbits in Varying Magnetic Fields . . . . . E. I. Gordon 1187
On the Kinetics and Mechanism of the Precipitation of Lithium from Germanium . . . . . J. R. Carter, Jr., and R. A. Swalin 1191
Beam Refrigeration by Means of Large Magnetic Fields . . . . . Robert Adler and Glen Wade 1201
Growth of Atomically Flat Surfaces on Germanium Dendrites . . . . . R. L. Longini, A. I. Bennett, and W. J. Smith 1204
Parametric Diode Figure of Merit and Optimization . . . . . K. E. Mortenson 1207
Use of the Omegatron in the Determination of Parameters Affecting Limiting Pressures in Vacuum Devices . . . . . David Lichtman 1213
Low-Temperature Transport Properties of Commercial Metals and Alloys. IV. Reactor Grade Be, Mo, and W . . . . . Robert L. Powell, James L. Harden, and Edward F. Gibson 1221
Ultra-High-Speed Photographs Refuting "Cohesion in Plasma" . . . . W. C. Davis and A. W. Campbell 1225
Magnetization of a Dilute Suspension of a Multidomain Ferromagnetic . . . C. P. Bean and I. S. Jacobs 1228
Thermionic Properties of UC . . . . . George A. Haas and John T. Jensen, Jr. 1231
Criteria for the Choice of a Superconducting Bolometer . . . . . Bogoljub Lalevic 1234
Response of a Loaded Idealized Piezoelectric Plate to an Electric Signal . . . . . Leo Levi 1237
Electrostatic Acceleration of Microparticles to Hypervelocities . . . . . H. Shelton, C. D. Hendricks, Jr., and R. F. Wuerker 1243
Impact Crater Formation in Rock . . . . . William C. Maurer and John S. Rinehart 1247
Equation of State for Nineteen Metallic Elements from Shock-Wave Measurements to Two Megabars . . . . . R. G. McQueen and S. P. Marsh 1253
Resistance to Potential Flow through a Cubical Array of Spheres . . . . . Robert E. Meredith and Charles W. Tobias 1270
Photographic Verification of Ultrasonic Plane Wave Scattering by Cylinders . . . . . Harmon D. Nine and Norman W. Schubring 1274
Gamma Irradiation of Silicon. I. Levels in *n*-Type Material Containing Oxygen . . . . . E. Sonder and L. C. Templeton 1279
Electron Microscopic Study of Thin Films of the Aluminum-Copper Eutectic Prepared by a Melting Method . . . . . Noboru Takahashi 1287
Microwave Properties of Nonstoichiometric Polycrystalline Yttrium Iron Garnet . . . . . P. E. Seiden, C. F. Kooi and J. M. Katz 1291

Letters to the Editor:

Technique for Calculating X-Ray Intensities in the Electron Probe Microanalyzer . . . . . L. S. Birks 1297
Classification of Wire Explosions . . . . . William G. Chace and Morton A. Levine 1298
On the Observation of Macroscopic Spirals on Gallium Arsenide Surfaces . . . . . Warren J. Little and Kathryn A. McCarthy 1298
Microscopic Study of Neutron-Irradiated Germanium . . . . B. B. Meckel, E. G. K. Schwarz, and R. A. Swalin 1299
Electron Damage in Mica . . . . . T. J. Seed 1300
Heat Treatment Effects in Indium Arsenide . . . . . J. T. Edmond and C. Hilsum 1300
Saturation of Photocurrent with Light Intensity . . . . . Richard H. Bube 1301
Damaged Layers and Crystalline Perfection in the {111} Surfaces of *III–V* Intermetallic Compounds . . . . . E. P. Warekois, M. C. Lavine, and H. C. Gatos 1302
Direct Observation of Superdislocations in a Superlattice . . . M. J. Marcinkowski, R. M. Fisher, and N. Brown 1303
Fine Structure of Bloch Walls . . . . . S. Shtrikman and D. Treves 1304
Experimental Test of the First Kelvin Relation . . . . . F. J. Donahoe and L. R. Testardi 1304
Errata: Books Reviewed 1305

Books Reviewed 1305
Books Received 1308

JOURNAL OF APPLIED PHYSICS

A journal of general physics and its applications to other sciences and to industry

Published by the

American Institute of Physics

GOVERNING BOARD

Members

Ralph A. Sawyer, *Chairman*
James G. Baker
R. H. Bolt
W. R. Brode
Harvey Brooks
Dirk Brouwer
J. W. Buchta
Vernet E. Eaton
J. H. Elliott
Herbert A. Erf
S. A. Goudsmit
W. W. Havens, Jr.
Winston E. Kock
R. Bruce Lindsay
H. V. Neher
C. J. Overbeck
G. E. Pake
Ray Pepinsky
F. W. Sears
Frederick Seitz
John Strong
George E. Uhlenbeck
M. E. Warga
Victor F. Weisskopf
W. R. Willets

ADMINISTRATION

Elmer Hutchisson
Director

Wallace Waterfall
Secretary and Treasurer

Henry A. Barton
Administrative Consultant

W. C. Kelly
Director of Education

Eugene H. Kone
Director of Public Relations

Hugh C. Wolfe
Director of Publications

Kathryn Setze
Assistant Treasurer

Norma Frankel
Publications Editor

Alice Mastropietro
Circulation Manager

Edward Tober
Manager, Production and Distribution

Theodore Vorburger
Advertising Manager

Emily Wolf
Manager, Special Services

Editor
James A. Krumhansl

Assistant Editor
Ethel McMillan

Editorial Board

J. H. Crawford
Arthur Kantrowitz
A. F. Kip
J. E. Goldman
J. L. Tuck
C. A. Wert
Herman A. Haus
C. Lester Hogan
R. S. Rivlin

THE JOURNAL OF APPLIED PHYSICS is devoted to general physics and its applications to other sciences, to engineering, and to industry. Previous to 1937, this journal was called PHYSICS.

The JOURNAL OF APPLIED PHYSICS welcomes articles of two distinct kinds: (1) Descriptions of new results in experimental or theoretical physics which are of general interest to physicists. The author should explain his contribution in such a way that a physicist or engineer in another field of specialization can appreciate its objectives and essential features. (2) Critical reviews of particular areas of physics or surveys of extensive investigations at a single laboratory. Authors contemplating writing such should correspond with the Editor before they begin writing.

The JOURNAL OF APPLIED PHYSICS welcomes Letters to the Editor which are short [approximately four (4) typewritten pages] communications without abstracts. Timeliness, briefness, and degree of current importance of the subject matter will be of primary concern in the publication of Letters. Letters should not be looked upon as partial publication or announcement of more comprehensive work, but rather self-contained presentations in themselves.

Manuscripts should be submitted to the Editor, James A. Krumhansl, Rockefeller Hall, Cornell University, Ithaca, New York. Authors should read the "Information for Contributors," facing page 1 of the January issue, before writing articles or letters. The *Style Manual* of the American Institute of Physics is also helpful to writers preparing manuscripts for journals published by the American Institute of Physics. It can be obtained for $1.00 from the American Institute of Physics, 335 East 45 Street, New York 17, New York.

Corrected proofs and all correspondence concerning papers in the process of publication should be addressed to the Publication Manager, American Institute of Physics, 335 East 45 Street, New York 17, New York.

Subscriptions, renewals, and orders for back numbers should be addressed to the American Institute of Physics, 335 East 45 Street, New York 17, New York.

Subscription Price	U.S. and Canada	Elsewhere
To members of member organizations of the American Institute of Physics and Affiliated Societies ..	$12.00	$13.00
To all others	14.00	16.00

Back Number Prices

Yearly back number rate when complete year is available: $17.00.
Single copies: $1.75 each (exception: March, 1958—$3.00 each).

Changes of address should be sent to the American Institute of Physics.

Advertising rates supplied on request. Orders, advertising copy, and cuts should be sent to the American Institute of Physics.

The Journal of Applied Physics is published monthly at Prince and Lemon Streets, Lancaster, Pennsylvania.
Second-class postage paid at Lancaster, Pa.

DESIGN WITH ARNOLD 6T CORES... SAME-DAY SHIPMENT OF STANDARD DELTAMAX CORE SIZES

Arnold 6T tape cores (aluminum-cased and hermetically-sealed) offer you three very important design advantages. *One:* Maximum compactness, comparable to or exceeding that previously offered only by plastic-cased cores. *Two:* Maximum built-in protection against environmental hazards. *Three:* Require no supplementary insulation prior to winding and can be vacuum impregnated after winding.

Now we've added a fourth vital advantage: Maximum availability. An initial stock of approximately 20,000 Deltamax 1, 2 and 4-mil tape cores in the proposed EIA standard sizes (See AIEE Publication No. 430) is ready on warehouse shelves for your convenience. From this revolving stock, you can get immediate shipment (*the same day order is received*) on cores in quantities from prototype lots to regular production requirements.

Use Arnold 6T cores in your designs for improved performance and reduced cost. They're guaranteed against 1000-volt breakdown . . . guaranteed to meet military test specifications for resistance to vibration and shock . . . guaranteed also to meet military specifications for operating temperatures. The 6T hermetic casing method is extra rigid to protect against strains.

Let us supply *your* requirements. Full data (Bulletin TC-101A and Supplements) on request. • Write *The Arnold Engineering Company, Main Office and Plant, Marengo, Ill.*

ADDRESS DEPT. J-7

ARNOLD
SPECIALISTS in MAGNETIC MATERIALS

BRANCH OFFICES and REPRESENTATIVES in PRINCIPAL CITIES • *Find them FAST in the YELLOW PAGES*

1539

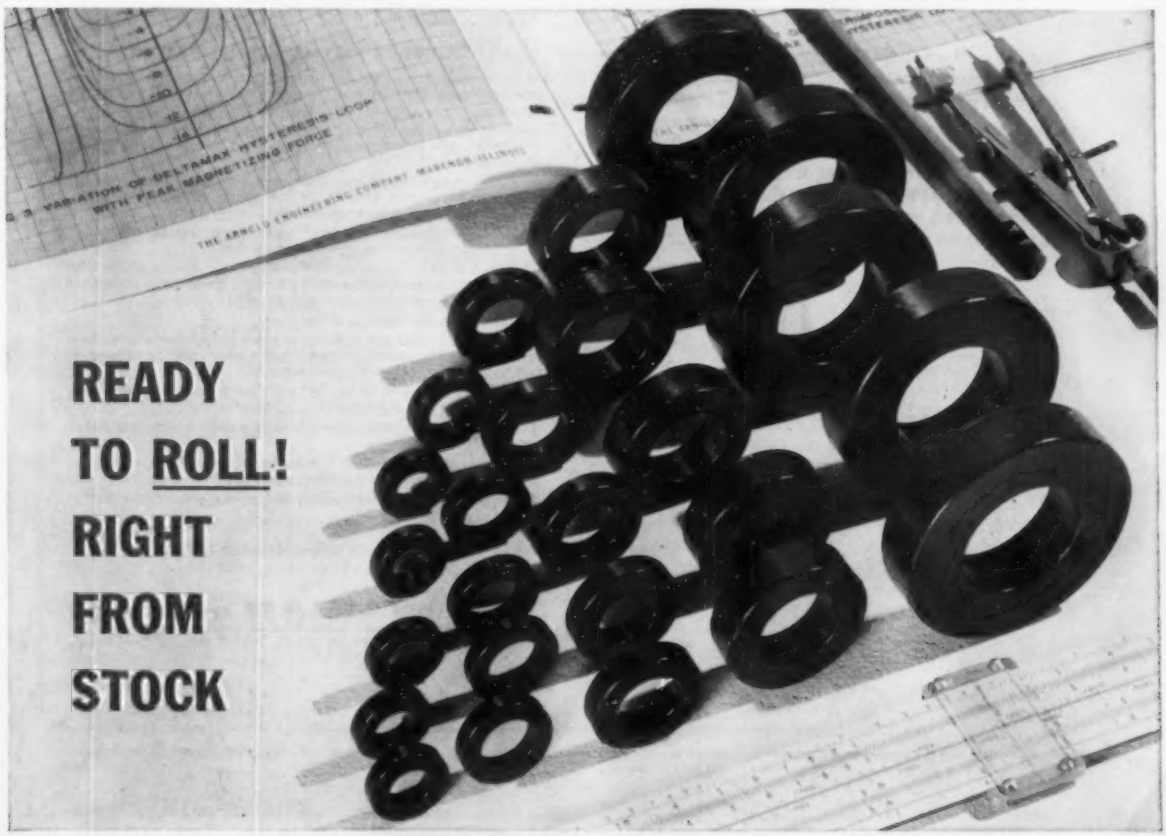

NEW NMR FLUXMETER

(Nuclear Magnetic Resonance)

FROM VARIAN

VARIAN MODEL F-8 NUCLEAR FLUXMETER WITH 50-FOOT EXTENSION CABLE REPRESENTED BETWEEN MAIN UNIT AND FIELD PROBE.
6-FOOT EXTENSION CABLE IS STANDARD EQUIPMENT.

The Varian Model F-8 Nuclear Fluxmeter provides precise *measurement* and/or *control* of magnets used in laboratory and industrial applications.

As a control device, the F-8 Fluxmeter holds fields stable against residual slow drift or external stray magnetic interferences not sensed by straight current regulation. Furthermore, the F-8 is capable of providing such control at extended distances from the magnet by mere addition of an accessory cable.

The frequency-determining (hence field-determining) circuitry of the F-8 Fluxmeter is buffered completely from the crossed-coil probe by several stages of amplification. Thus, for example, the varying probe position encountered during field plotting cannot inadvertently reduce accuracy.

CHARACTERISTICS AND ADDITIONAL FEATURES

- Wide frequency range and two probe samples (H^1 and H^2) permit field coverage from 1,000 gauss to an upper limit of 52,000 gauss.
- Accuracy—a function of signal-to-noise ratio, inherent sample line-width, and inhomogeneity of the field being measured — is as follows:

  ±0.05 gauss with 1 gauss external field gradient across ¼" diameter proton sample of 0.5 gauss natural line-width, using external frequency counter.

  ±0.2% with vernier and calibration curve (furnished).
  ±5% on convenient, direct-reading dial.

  Absolute accuracy is also limited by the accuracy of the NBS accepted determination for the gyromagnetic ratio of protons in water (approximately 1 part in 10^5).
- Standard probe cable is 6 feet long.
- F-8 may be used for NMR class-room experiments and demonstrations; absorption or dispersion signal may be chosen at will by one-knob balance adjustment on main unit.
- Plug-in jacks at rear of chassis permit external frequency measurement and crystal lock-in of transmitter.
- Control output suitable for direct use with Varian Regulated Magnet Power Supplies.
- Samples can be supplied in a choice of natural line widths for best match to available field homogeneity.
- Sweep amplitude and transmitter power are adjustable for optimum performance.

For full specifications, write the **Instrument Division,**

VARIAN associates
PALO ALTO 36, CALIFORNIA

NMR & EPR SPECTROMETERS, MAGNETS, FLUXMETERS, GRAPHIC RECORDERS, MAGNETOMETERS, MICROWAVE TUBES, MICROWAVE SYSTEM COMPONENTS, HIGH VACUUM EQUIPMENT, LINEAR ACCELERATORS, RESEARCH AND DEVELOPMENT SERVICES

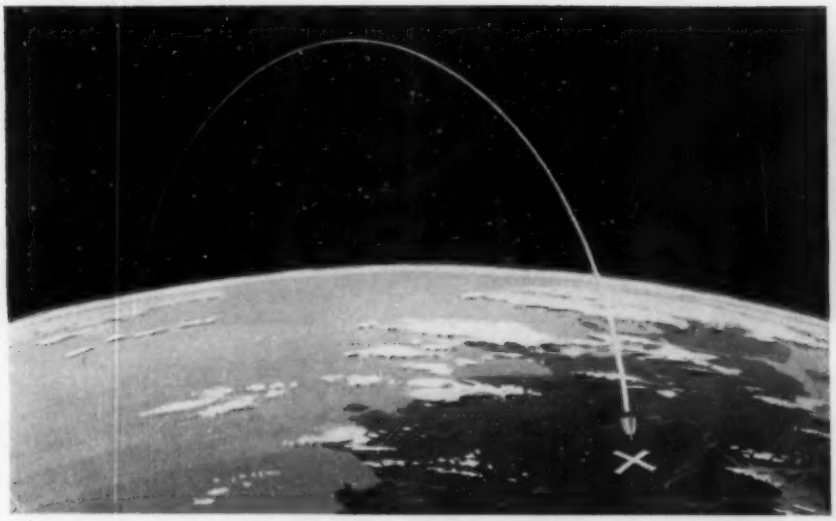

ASSIGNMENT: HIT A TARGET 6000 MILES AWAY

Can you guide a 110-ton Air Force Titan missile far up into the sky, to bring its nuclear warhead down with pinpoint accuracy on a target one-fourth the way around the globe—a target you not only can't see but which continually moves with the spinning earth?

This was the problem in missile guidance the Air Force presented to Bell Telephone Laboratories and its manufacturing partner, Western Electric. The answer was the development of a command guidance system which steers the Titan with a high degree of accuracy.

Unlike self-contained systems which demand complex equipment in the missile itself, Bell Laboratories Command Guidance System keeps its master control equipment on the ground where it can be used over and over again. Thus a minimum of equipment is carried in the missile, and the ground station has full control of the missile during its guided flight. Techniques drawn from the communications art render the system immune to radio jamming.

Bell Laboratories scientists and engineers designed the transmission and switching systems for the world's most versatile telephone network, developed much of our nation's radar, and pioneered in missile systems. From their vast storehouse of knowledge and experience comes the guidance system for the Titan.

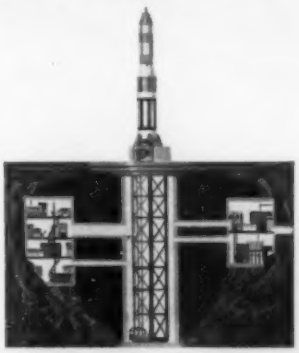

BELL TELEPHONE LABORATORIES

World center of communications research and development

The Big Contribution of

VAC

in X-ray

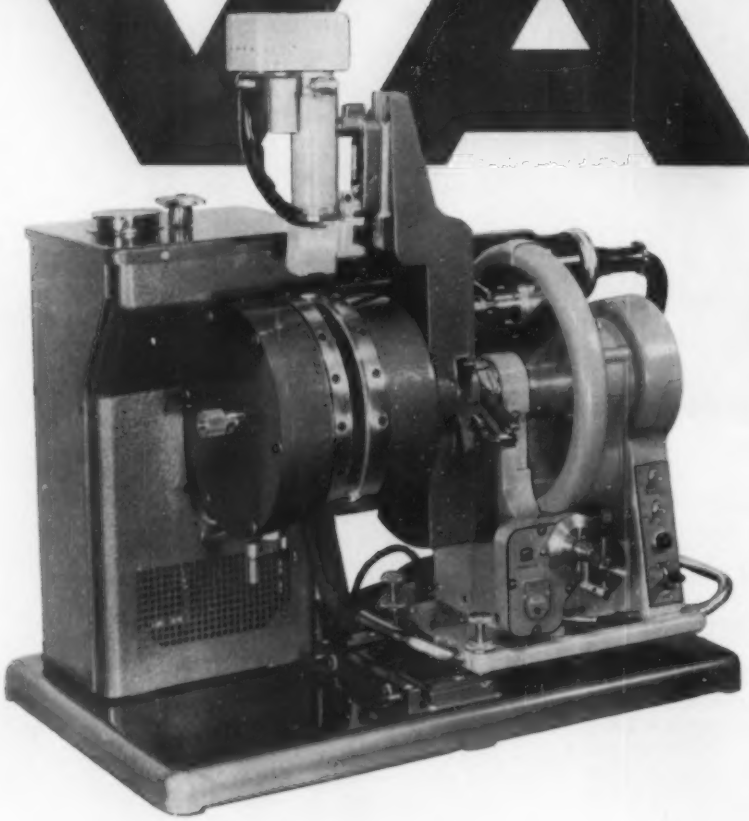

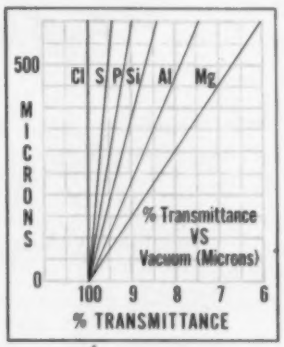

In X-ray spectrographic analysis, evacuation of the radiation path results in significantly higher counting rates than those obtained in air or even helium — particularly for the lighter elements magnesium (12) through sulphur (17).

The true value of the Norelco Vacuum Spectrograph lies in the fact that its satisfactory use as a routine laboratory and industrial tool, requires no expert supervision to obtain optimum performance. It can be readily integrated into existing laboratory or industrial conditions to provide dependable data. It is versatile, durable and ideally suited for routine as well as diverse applications.

The graph here illustrated reveals that the percentage of quanta transmittance varies minutely with increases in vacuum below 100 microns, (0.1 mm. Hg.). In terms of efficiency, this degree of vacuum is obtained in *less than one minute* with the Norelco vacuum apparatus — and within this time period, offers ideal conditions for reproducible results which are well within the range of required statistical accuracy.

Write today for more information on this truly versatile addition to your X-ray laboratory.

UUM

Spectrographic Analysis

The Vacuum Spectrograph is universal in the sense that it may be used to provide either evacuated or gas-filled atmospheres.

Two crystals, mounted on a holder in the X-ray path, permit optional choice of either crystal without breaking vacuum — effectively extending the analytical range to all detectable elements.

Two detectors, scintillation and proportional, may be used alternatively or sequentially with either crystal.

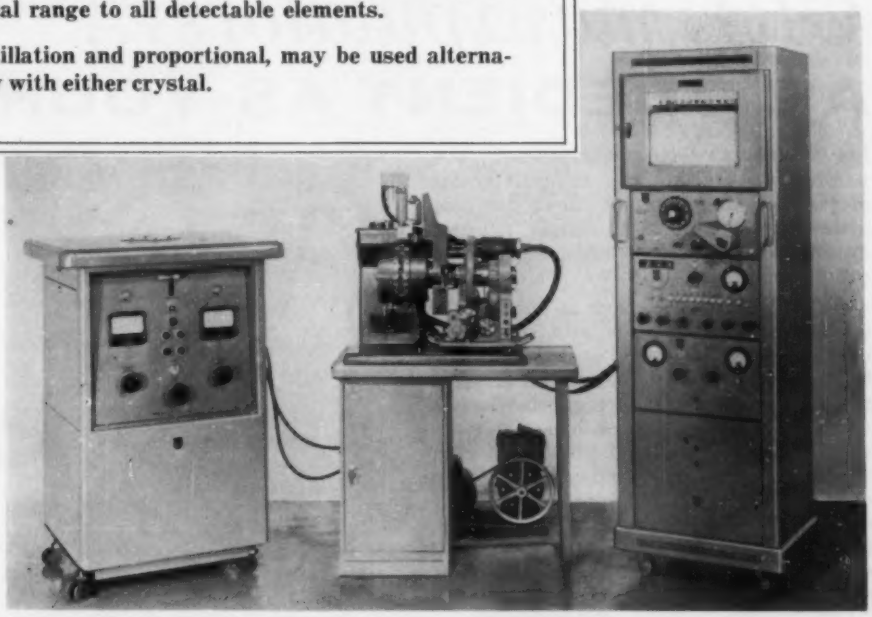

PHILIPS ELECTRONIC INSTRUMENTS Norelco

PHILIPS ELECTRONIC INSTRUMENTS

A Division of Philips Electronics and Pharmaceutical Industries Corp.

750 SOUTH FULTON AVENUE, MOUNT VERNON, N.Y.

In Canada: Research & Control Instruments • Philips Electronics Industries Ltd. • 116 Vanderhoof Ave. • Leaside, Toronto 17, Ont.

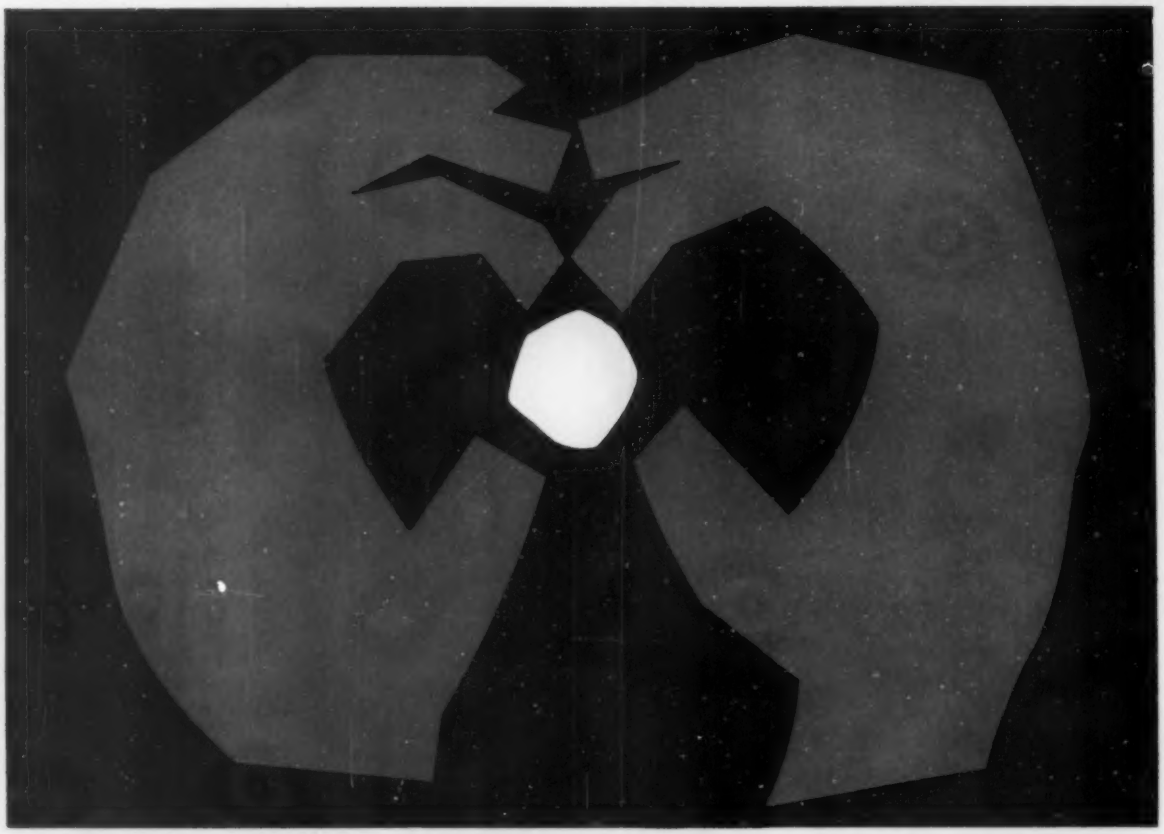

CRL manipulators...

AS OBEDIENT AS YOUR HAND!

Slave ends of CRL Manipulators obey perfectly—duplicate the natural motions of the operators' hands—make operation of the system amazingly simple. An operator becomes perfectly adept with practically no training.

Simplicity of operation is only one of several reasons research and production organizations all over the world specify CRL Manipulators. The system is versatile. Accessories such as special-purpose tongs, load hooks, motion locks, and protective booting allow adaption to a great variety of purposes. A continuous program of improvement . . . uncompromising workmanship . . . and standardized, interchangeable parts provide more reasons why you should consider CRL Manipulators for handling hazardous materials.

Central Research Laboratories will be glad to advise you on the handling of radioactive materials, explosives, hazardous chemicals, biological materials—in the layout of hot cells—in other research areas, too. For complete information, write CRL today.

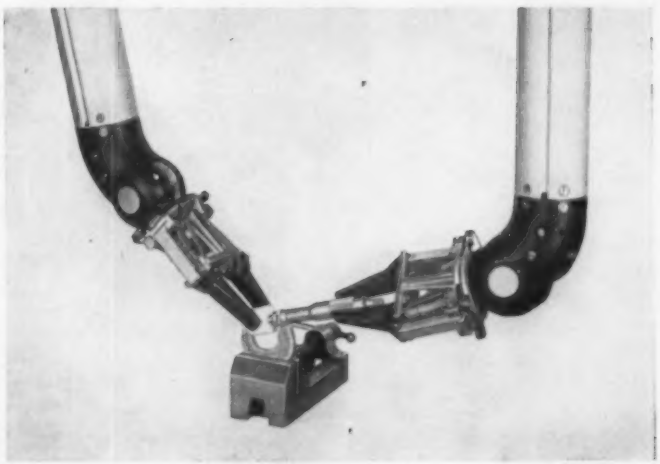

Central Research Manipulators from basic Argonne National Laboratory design

Central Research
laboratories, inc.
Red Wing, Minnesota, Dept. 301

Kodak reports on:

sooty things with a lot of physics in them . . . color lore that might have bored Goethe to death . . . what to do with wiggle-bearing paper . . . increasing the peak value of informational sensitivity

Adjustable boundary for the infrared

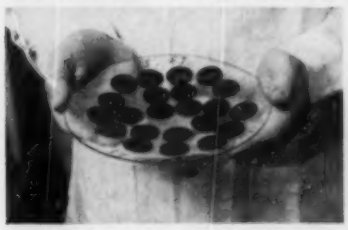

These sooty things have a lot of physics in them. The physics is of the old-fashioned type, not very clear, but not nearly so opaque as the little wonders themselves look when held to the light. Yet they transmit to 30μ in the very far infrared. Their utility lies in the easy adjustability of the spectral position of the transition from opacity to clarity. The opacity is achieved not by absorption and not by interference but by marvelously selective and effective scattering. What interference there is, in fact, operates on the side of clarity by beating down Fresnel reflection losses.

These *Kodak Far Infrared Filters* have turned into a hotter item than we dared hope when we first taught ourselves how to take silver chloride and convert its surface to silver sulfide in a manner as tunable as a fiddle string. Now the infrared trade—military and analytical—has grown to where it needs cut-on filters worse than it needed them ever before. And we are ready—even with a warning that these filters require precautions to protect them from harsh military environments and that silver chloride in the presence of water vapor still corrodes metal just as it always has. Of course, they can be mounted in plastic. The corrosion we can forestall if, at the expense of inserting a few absorption bands, we can be permitted to overcoat with polystyrene.

The pitch for the business is made by a collection of mimeographed sheets entitled "Kodak Far Infrared Filters," obtainable from Eastman Kodak Company, Special Products Sales, Rochester 4, N. Y. Here are given sizes, prices, and the code for specifying the cut-on wavelength wherever wanted from 1 to 5μ.

Gelatin responsibly dyed

A rich legacy of heuristic nonsense has been accumulating for generations in the next region of the electromagnetic spectrum over from the infrared, where the eye reigns supreme as the receptor and has qualified every seeing, thinking man to hold opinions. Even the mighty Johann Wolfgang Goethe, author not only of "Faust" but also of "Die Farbenlehre," put in his *zweipfennig* worth.

Amid rampant intellectuality, it has behooved us to tread lightly and confine our thinking to such *farbenlehre* as will fit us the better to flood the earth with color photography, myriad-colored Tenite plastics, color-locked Chromspun fibers, and Eastman textile dyes. Plus another field of dye art, tiny in economic comparison and disproportionately demanding in technical patience but important to those who, whatever their theories or purposes, wish to modify spectral distribution or overall intensity of light in systematic, quantitative, reproducible, simple, and inexpensive fashion. We refer to the celebrated little marvel of precision dye chemistry, the *Kodak Wratten Filter* of uniform gelatin, with or without glass mounting.

The reason we refer to it is that the new 20th edition of "Kodak Wratten Filters for Scientific and Technical Use," containing 81 pages of curves, data, and other useful information, is now obtainable from well-stocked photographic stores for 75¢ or from Eastman Kodak Company, Sales Service Division, Rochester 4, N.Y.

Back from the brink

When visitors come shuffling through your laboratory, it makes a terrific impression to show you are equipped for:

- Infrared absorption spectroscopy
- Ultraviolet absorption spectroscopy
- Visible absorption spectroscopy
- X-ray diffraction
- Nuclear magnetic resonance spectroscopy
- Fluorescence spectroscopy
- Raman spectroscopy
- Mass spectroscopy
- Gas chromatography
- Miscellaneous analytical methods like polarography
- Miscellaneous physical testing methods

Aside from creating an impression, these procedures generate strips of paper bearing wiggles. That there would be produced many such useful strips of wiggles to keep and compare had justified the acquisition of the instrumentation. The truer this has proved, the worse you may need help. We ourselves did. Fortunately, as we approached the brink of madness in coping with the sheer volume of spectrophotometric curves generated at the research laboratories of our division, Tennessee Eastman Company, we were able to call on our subsidiary, Recordak Corporation.

The Recordak people are experts at working out systems that combine micro-

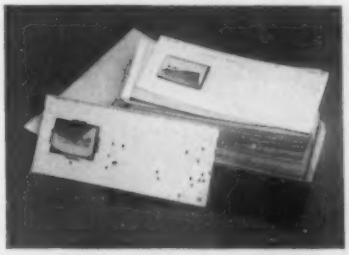

Neat, like this.

filming with punched cards. They say they would be willing to help you, too. They suggest you write them at 415 Madison Avenue, New York 17, N. Y., for a copy of "The Use of Aperture Cards for the Consolidation of Spectrophotometric Data."

Nice sharp pictures

We must not lose our sense of proportion. We must recognize that some people take so little technical interest in photography that they have never even heard of *Kodak Tri-X Pan Film.* Others who do use it have noticed that since that "Improved Type" has appeared on the carton, results have somehow improved. Most of these folk will be content with a bland assertion that the recently added notation signifies a major advance in reduction of graininess and improvement in picture sharpness. A single congenial luncheon table could probably accommodate all who would press us to explain that what we have really done is to increase the peak value of the informational sensitivity *I* of *Kodak Tri-X Pan Film* from .0016 to .0036

where $I = \frac{g}{a_s} \cdot \frac{1}{\sigma_s(D)}$

g = gradient of the linearized characteristic curve

a_s = area of the spread function

$\sigma_s(D)$ = standard deviation of the granularity trace for a scanning aperture having the size of the spread function

If you want to talk like that you should first consult Journal of the Optical Society of America, 48, *926, but if you just want very sharp pictures from very fast film, ask the Kodak dealer for Kodak Tri-X Pan Film, Improved Type.*

Price quoted is subject to change without notice.

Kodak
TRADE MARK

This is another advertisement where Eastman Kodak Company probes at random for mutual interests and occasionally a little revenue from those whose work has something to do with science

ENGINEERS • SCIENTISTS

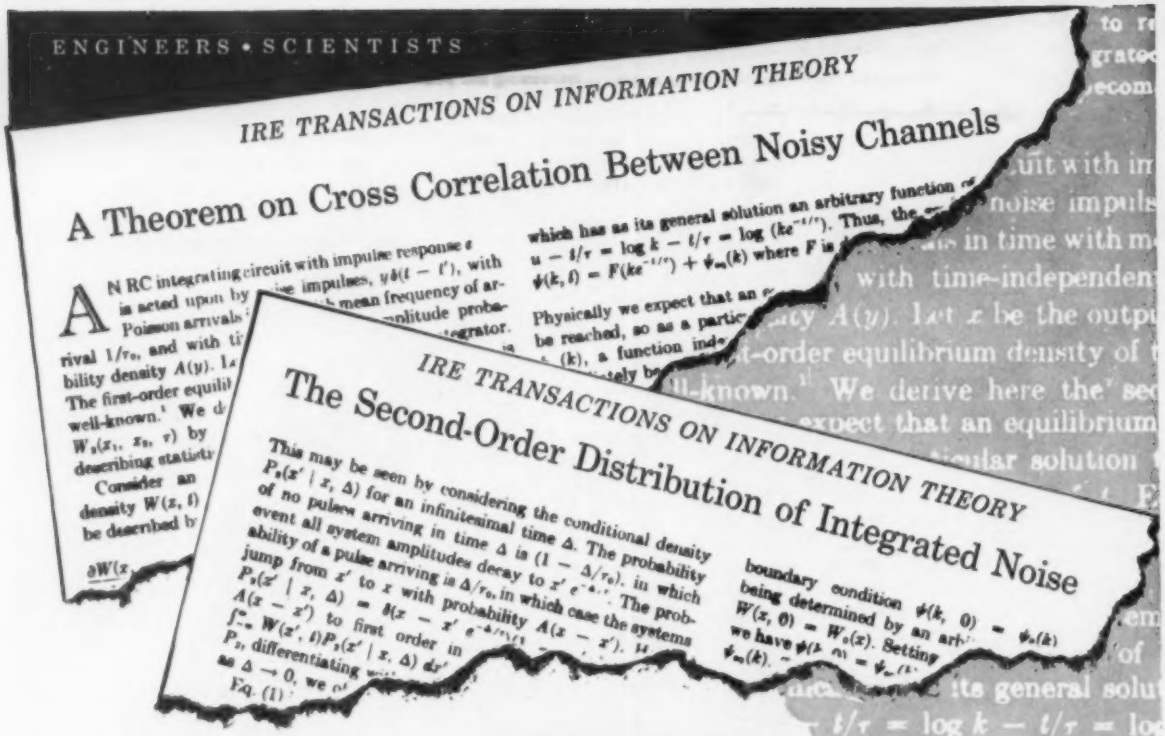
IRE TRANSACTIONS ON INFORMATION THEORY
A Theorem on Cross Correlation Between Noisy Channels
IRE TRANSACTIONS ON INFORMATION THEORY
The Second-Order Distribution of Integrated Noise

SYLVANIA'S ARL Applied Research Laboratory

Is engaged in diversified, active programs that afford broad individual participation

The Applied Research Laboratory is directing its growing capability toward theoretical and experimental investigations that will lead to major state-of-the-art advances in the field of military and commercial electronic systems. The opportunity for individual recognition in this challenging technological area is typified by the titles of the two recent technical papers, by ARL staff members, which are depicted here.

If you possess superior qualifications (an advanced degree is desirable) and would like to join this highly professional group, you are invited to inquire about career positions in these areas:

- RADIO PHYSICS ▪ ELECTROMAGNETIC PROPAGATION
- HYPERSONIC GAS DYNAMICS ▪ MICROELECTRONICS
- MATHEMATICAL ANALYSIS & OPERATIONS RESEARCH
- INFORMATION & COMMUNICATION THEORY

For further information about research work in the above areas, and other technical publications by ARL engineers, you are invited to write to:

Dr. L. S. Sheingold, Director, Applied Research Laboratory

Waltham Laboratories / SYLVANIA ELECTRONIC SYSTEMS

A Division of SYLVANIA

Subsidiary of GENERAL TELEPHONE & ELECTRONICS

100 First Avenue—Room 7-B—Waltham 54, Massachusetts

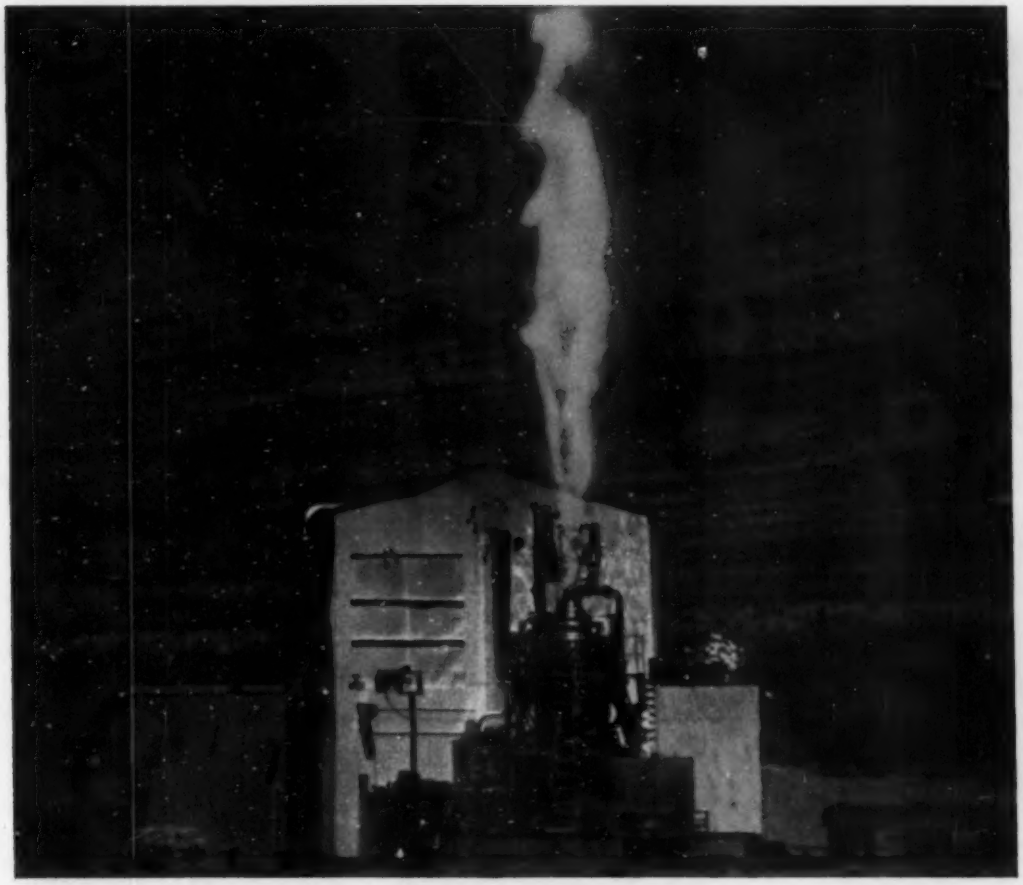

Space Propulsion for the future . . .

from the **KIWI** *family of Nuclear Reactors*

Los Alamos Scientific Laboratory has the major responsibility for research, development and testing in the AEC-NASA Rover program . . . another of the many investigations at Los Alamos into peacetime uses of nuclear energy.

PHOTO: First field test of a KIWI nuclear propulsion reactor.

los alamos
scientific laboratory
OF THE UNIVERSITY OF CALIFORNIA
LOS ALAMOS, NEW MEXICO

For employment information write:
Personnel Director
Division 60-68

PRINCIPLES OF MECHANICS OF SOLIDS AND FLUIDS, Volume I — Particle and Rigid-Body Mechanics

By HSUAN YEH, University of Pennsylvania; and JOEL I. ABRAMS, Yale University. *McGraw-Hill Series in Engineering Sciences.* Ready in August.

The first volume of a two-volume series designed for a two-year sequence, the first half being suited for a full year sophomore or junior course. This text departs from tradition not only in combining fluids but also in integrating them. The mechanics of particles and rigid bodies are treated in a mature manner.

DIGITAL COMPUTER AND CONTROL ENGINEERING

By ROBERT S. LEDLEY, George Washington University. *McGraw-Hill Electrical and Electronic Engineering Series.* Now Available.

Contents of this book include: (1) an introduction to programming, and to advanced automatic programming techniques, (2) an explanation of numerical analysis and data handling techniques, (3) the mathematics of computer circuit logic, (4) how this logic is applied to design the operational sections of the computers, and (5) techniques of electronic design.

TRAVELING WAVE ENGINEERING

By RICHARD K. MOORE, University of New Mexico. *McGraw-Hill Electrical and Electronic Engineering Series.* Ready in September.

This book can be associated with the school of "modern" thinking in curriculum planning in E.E. The first textbook in English which treats the analogies between many different types of waves. Included are several new approaches to transmission lines, and also new approaches with respect to acoustic waves. Many problems and references are provided.

QUANTUM THEORY OF ATOMIC STRUCTURE, Volume I

By JOHN C. SLATER, Massachusetts Institute of Technology. *McGraw-Hill International Series in Pure and Applied Physics.* Ready in July.

This first volume designed for graduate level work presents a broad and general treatment of the entire quantum theory of atoms, molecules, and solids. Much detailed tabular material relating to multiplet structure in the transition elements, which is not available elsewhere, is presented.

INFORMATION AND DECISION PROCESSES

Edited by ROBERT E. MACHOL, Purdue University. Ready in July.

In April of 1959 a Symposium on Information and Decision Processes was held at Purdue University. This book is an outgrowth of that conference, in that each speaker has contributed a chapter. In addition, two of the outstanding papers from the 1958 Purdue Conference on the same subject are included.

Send for Copies on Approval

McGRAW-HILL BOOK COMPANY, INC.

330 WEST 42nd STREET NEW YORK 36, N.Y.

MODEL 415 features include capability of detecting current of approximately 1×10^{-14} ampere, a 1% mirror scale panel meter.

new high-speed research micro-microammeter

Model 415 offers high speed of response, accuracy, and zero suppression.

The new Model 415 incorporates advanced high-speed circuitry developed by Keithley Instruments for rocket and satellite experimentation — where measurements of Lyman-Alpha night glow and upper air density require fast response.

A speed response of less than 600 milliseconds to 90% of final value at 10^{-12} ampere is possible where external circuit capacity is 50 picofarads ($\mu\mu$f). Critical damping of the circuit, with any input capacity, is maintained on all ranges through one infrequent adjustment. There is no possibility of oscillation or poor response, on any range.

Accuracy is ±2% of full scale on 10^{-3} through 10^{-8} ampere ranges, and ±3% of full scale on 3×10^{-9} through 10^{-12} ampere ranges.

The 415 also provides zero suppression up to 100 full scales, permitting full scale display of one per cent variations of a signal. Once suppressed to zero, such variations may be observed on any of the next four more sensitive ranges without resetting the suppression.

Excelling other Keithley 400 Series Micro-micro-ammeters in speed of response, the 415 is ideal for current measurements in ion chambers, photomultipliers, gas chromatography, mass spectrometry.

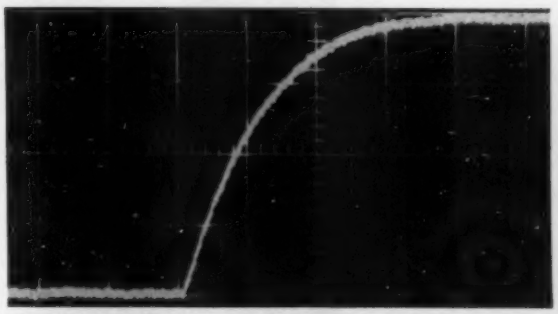

AN OSCILLOGRAM demonstrating response to a current step of 10^{-12} ampere. Input capacity is 35 picofarads ($\mu\mu$f). One major horizontal division equals 200 milliseconds.

BRIEF SPECIFICATIONS

RANGES: 10^{-12}, 3×10^{-12}, 10^{-11}, 3×10^{-11}, etc. to 10^{-3} ampere f.s.

ACCURACY: ±2% f.s. 10^{-3} thru 10^{-8} ampere ranges; ±3% f.s. 3×10^{-9} thru 10^{-12} ampere ranges.

ZERO DRIFT: Less than 2% of f.s. per day after warmup.

INPUT: Grid current less than 5×10^{-14} ampere.

OUTPUT: 1 v f.s. at up to 5 ma. Noise less than 20 mv.

RISE TIME: Typical values given in sec. to 90% of final values.

Range amps f.s.	C_{in} = 50 $\mu\mu$f seconds	C_{in} = 150 $\mu\mu$f seconds	C_{in} = 1500 $\mu\mu$f seconds
10^{-12}	.600	.800	2.5
3×10^{-12}	.200	.300	1.0
10^{-11}	.060	.080	.250
3×10^{-11}	.020	.030	.100
10^{-10}	.006	.010	.030
3×10^{-10}	.002	.003	.010
10^{-9}	.001	.001	.003
3×10^{-9} and above	.001	.001	.001

PRICE: Model 415, $750.00

For complete details, write:

KEITHLEY INSTRUMENTS, INC.
12415 EUCLID AVENUE
CLEVELAND 6, OHIO

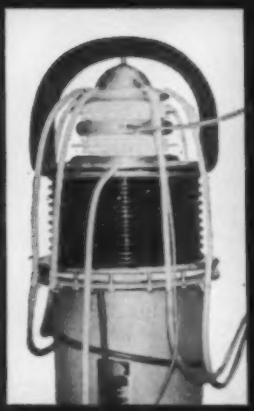

600,000 amperes help harness H-power

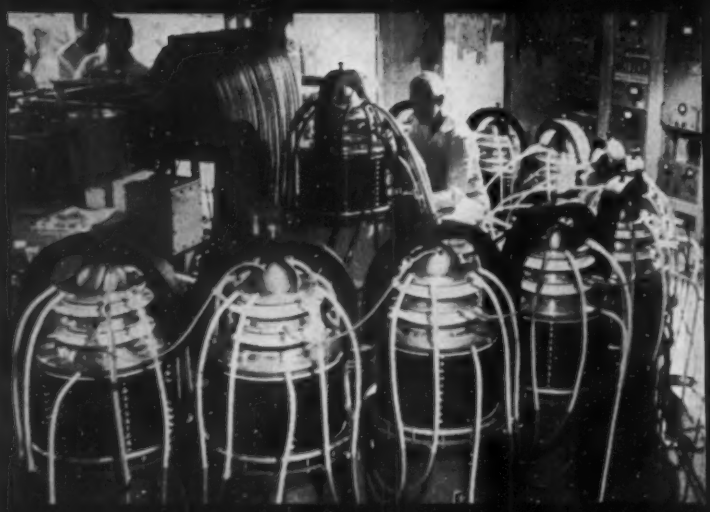

At the historic Geneva Atoms-For-Peace Conference, Los Alamos scientists unveiled **Scylla**—a fusion device used to heat a plasma of ionized heavy hydrogen particles millions of degrees by blasting it with a 600,000-ampere thunderbolt.

Surrounding the heart of this thermonuclear machine is a bank of low-inductance, energy-storage capacitors...each rated at 100,000 volts, each capable of a 20,000 megawatt peak surge.

This unique installation, like others of its type, is the result of long experience in capacitor specialization. If adherence to rigid specifications is a 'must' on your project—call us in to help with creative engineering. We invite inquiries for a single energy-storage capacitor or a complete energy-storage system including capacitors, racks, interconnecting lines, protective devices and charging power supply.

For further technical information, write for Bulletin No. 191 to Cornell-Dubilier Electric Corporation, New Bedford, Mass.

CDE

CORNELL-DUBILIER ELECTRIC CORPORATION

AFFILIATED WITH FEDERAL PACIFIC ELECTRIC COMPANY

Physicists...

S

I

RESEARCH AND DEVELOPMENT IN SEMICONDUCTORS

Pacific Semiconductors, Inc. recently has made a number of notable accomplishments in the field of semiconductors, including a range of high frequency power transistors, micro miniaturized diodes and transistors. For example, the PSI high frequency transistor line ranges from the largest (100 watts at 5 mc) to the smallest silicon mesa transistors available.

These accomplishments have created important new opportunities at PSI. In addition, PSI is broadening its range of activities to include such new fields as solid state circuits.

The nature of the semiconductor field has created an unusual need and opportunity for physicists at PSI. We are seeking highly competent scientists who have an interest in solid state research and development.

Experience in the field is highly desirable. However, if you lack such experience but believe you have unusual ability and a desire for stimulating and challenging work, we would like to hear from you.

SURFACE RESEARCH Basic research on semiconductor surfaces with the ultimate objective of increasing the state of understanding of semiconductor surface phenomena. Whatever theoretical and experimental approaches are required in order to accomplish this goal will be employed. An important part of this objective will be the correlation of surface film composition and structure with the physical model of the surface. A surface design theory of fundamental value might reasonably be expected to be an important outgrowth of this endeavor.

SOLID STATE DIFFUSION Investigation and improvement of solid state diffusion processes. This includes fundamental work on diffusion mechanisms and the growth and control of oxide layers at the surface. Some or all of the following experience is highly desirable: High furnace temperature operation, gaseous purge systems, light interference measurement techniques.

DEVICE PHYSICS Balanced experimental and theoretical research on new processes and new devices of advanced types. Read and understand semiconductor literature. Work with chemists, metallurgists and electronic engineers. Supervise experiments involving advanced laboratory measurement techniques, including infrared, X-ray and electrical. Diffusion, surfaces, crystal imperfections, device theory, process theory.

SEMICONDUCTOR MATERIALS — INTERMETALLIC COMPOUNDS Physical chemists or physicists to work in preparation and purification of semiconductor elements and intermetallic compounds. The work also may include the study of decomposition reactions of silanes and halides of silicon to form single crystal deposits of pure silicon. Interest in infrared absorption studies desirable.

These are only a few of the many fine opportunities available at PSI. If you have an M.S. or Ph.D. degree in physics or a B.S. degree and equivalent experience in semiconductor physics, write today in confidence to:

DR. J. W. PETERSON, *Director, Research and Development*

or MR. LARRY LONG, *Head, Technical Staff Placement*

PSI®

Pacific Semiconductors, Inc.

10451 WEST JEFFERSON BOULEVARD • CULVER CITY, CALIFORNIA

SOVIET PHYSICS—CRYSTALLOGRAPHY

A cover-to-cover translation of the USSR Academy of Sciences journal Kristallografiya

Experimental and theoretical papers on crystal structure, lattice theory, diffraction studies, and the effects of external influences (including radiation damage) on crystalline structure.

Also publishes studies employing X-ray, electron and neutron diffraction of all materials of interest to the crystallographer, metallurgist, solid-state physicist, and chemist.

Six issues per year

Subscription rates:

Regular $25.00 U.S., Can.; $27.00 elsewhere
Special* $10.00 U.S., Can.; $12.00 elsewhere

* Discounts to libraries of non-profit academic institutions.

Orders and inquiries should be sent to:

American Institute of Physics
335 East 45 Street, New York 17, N.Y.

Subscription prices subject to annual variation depending on size of Russian originals.

New from RCA . . . X-Ray Vacuum Spectrometer

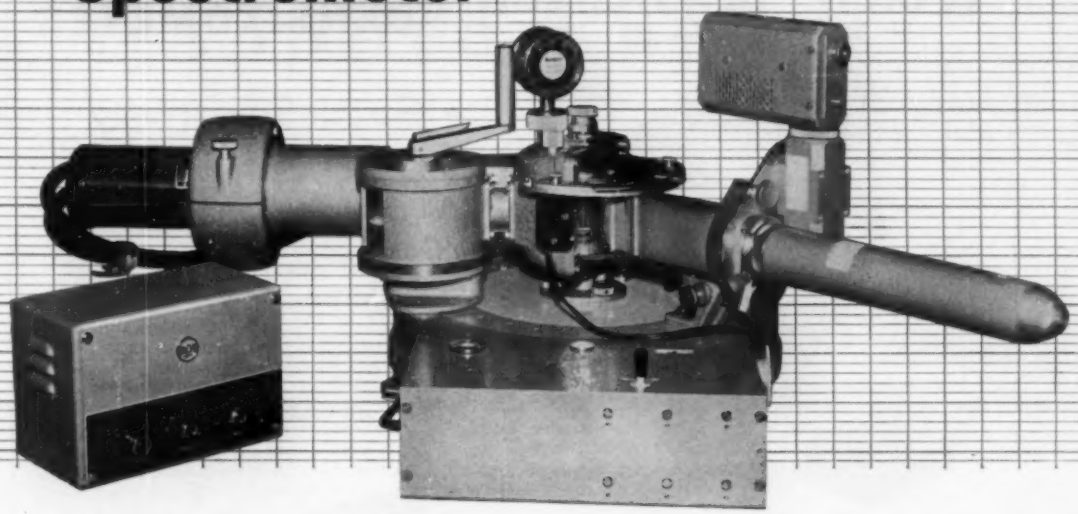

for analysis of the lighter elements

Especially suited to the X-ray spectro-chemical analysis of elements below atomic number 22, RCA's new Vacuum Spectrometer permits the use of three samples at one time. Samples—powders or solids—can be moved in and out of the vacuum path without breaking vacuum. The need for helium is eliminated, but air or helium can be used when desired. A flange connects the sample chamber directly to the X-ray tube, making higher intensities possible, and eliminating the need for a second beryllium window. From a cold start the recommended vacuum of 0.1mm or 100 microns can be reached in less than two minutes. Designed primarily for the analysis of lighter elements, the Vacuum Spectrometer can be used to advantage with heavy elements to give higher intensities.

The Vacuum Spectrometer is one of a wide range of attachments and accessories available for RCA X-Ray Diffraction and Spectroscopy equipment which contribute to its extreme flexibility of application. Installations already made in some of the nation's leading research laboratories are demonstrating the efficiency, technical excellence and versatility of these instruments.

Installation supervision and contract service for RCA Electron Microscopes and X-Ray Diffraction and Spectroscopy Equipment are available through the RCA Service Company.

For details on the new Vacuum Spectrometer or RCA's full line of X-Ray Diffraction and Spectroscopy equipment, write to RCA, Dept. J-65, Building 15-1, Camden, New Jersey.

Vacuum Spectrometer and a Diffractometer mounted on Crystalloflex IV and connected to Electronic Circuit Panel

RCA

The Most Trusted Name in Electronics

RADIO CORPORATION OF AMERICA

A Versatile Instrument for the Measurement of Reflectance and Transmittance

Welch DENSICHRON® ELECTRONIC DENSITOMETER

- *Good Sensitivity*
- *High Stability*

NO. 3830A DENSICHRON AND PROBE

REFLECTION UNIT NO. 3832A

—SPECIAL FEATURES—

Patented Magnetic Modulation

Simple to Use

Convenient Small Size—5″ x 7¼″ x 13″

Light in Weight—only 11½ pounds

NO. 3830A. DENSICHRON WITH BLUE PROBE, including amplifier with logarithmic-scale meter, metal probe support, five different measuring apertures, a cone with ¼ inch aperture and a set of instructions. The amplifier operates on 115 volts, 60 cycle, A.C. only, except on special order.
Each $250.00

NO. 3830B. WITH RED PROBE. Each $265.00

NO. 3832A. REFLECTION UNIT. When coupled to the Densichron amplifier this unit becomes a convenient reflectance meter. It has a self-contained light source, filter wheel and phototube, and includes optics for both small and large spot work, a calibrated gray scale, and three Carrara working standards.
Each $160.00

WRITE FOR OUR DENSICHRON CATALOG

W. M. WELCH SCIENTIFIC COMPANY

DIVISION OF W. M. WELCH MANUFACTURING COMPANY

ESTABLISHED 1880

1515 Sedgwick Street, Dept. C-1 Chicago 10, Illinois U. S. A.

Manufacturers of Scientific Instruments and Laboratory Apparatus

Journal
of
Applied Physics

Volume 31, Number 7 July, 1960

Diagrams Representing States of Operation of a General Thermocouple

A. H. Boerdijk
N. V. Philips' Gloeilampenfabrieken, Eindhoven, Netherlands
(Received February 1, 1960)

The state of operation of a thermocouple of which (a) the bars have an arbitrary shape; (b) the properties of the materials are arbitrary functions of temperature; and (c) the composition is, under certain restrictions, inhomogeneous and anisotropic depends on three independent parameters: the current I and the temperatures T_1, T_2 of the junctions. If T_2 is kept constant, operating characteristics, such as curves of constant output power or efficiency, can be plotted in an I, (T_2-T_1) diagram. The existence of regions of generation of electricity and of cooling is proved. These regions are investigated. Possible generalization and reduction of the diagram are discussed. As an illustrative example, the cooling region of a general couple with temperature independent properties is dealt with.

1. NOTATION, DEFINITIONS

We will consider a couple consisting of two bars, a and b (Fig. 1). At one side the bars are connected to an external electrical circuit by leads 3 and 4. At the other side the bars are joined by lead 5. We suppose that all leads are of the same material, which perfectly conducts heat and electricity, and that leads 3 and 4 have equal temperatures. Part of these leads will be referred to as "junction 2." Lead 5 will be referred to as "junction 1." Symbols relating to junctions will be distinguished by subscripts 1 and 2 and symbols relating to bars by subscripts a and b. The couple is thought to be surrounded by a perfect insulator for heat and electricity which restricts external electrical current to leads 3 and 4 and external heat exchange to junctions 1 and 2.

Each bar has an arbitrary shape. Denoting by O_1 and O_2 the surfaces in contact with junctions 1 and 2, respectively, and by O_3 the remaining part of the surface of the bar, we use a position coordinate u satisfying the following conditions: $\nabla^2 u=0$ inside the bar and on its surface, $u=0$ on O_1, $u=1$ on O_2, ∇u on O_3 is tangent to O_3. We define a characteristic length l by

$$l=\int_{O_1} |\nabla u|\, dO_1. \tag{1}$$

Each of the bars is inhomogeneous with the restriction that the composition is a function of u only. The material of each bar may be anisotropic, with the restriction that at any point the direction of ∇u is a symmetry axis of the angular distribution of the properties. In this case the values of the properties occurring in the equations are those measured in the direction of ∇u. Thermal expansion is neglected.

We denote by λ the thermal conductivity (for zero electrical current), T the absolute temperature, σ the (isothermal) electrical conductivity, τ the Thomson coefficient, equal to $T(\partial S/\partial T)_u$, S the absolute Seebeck coefficient ("thermoelectric power"), Π the absolute Peltier coefficient, equal to $-TS$, I the electrical current, W_e the electrical output power, W_1, W_2 the thermal output powers at junctions 1 and 2, respectively, and V the voltage W_e/I. Efficiencies for generation of heat and cold from electricity and for generation of electricity from heat or cold are denoted, respectively, by

$$\varphi_e=-W_e/W_2, \quad \varphi_e'=W_e/W_1,$$
$$\varphi_k=-W_2/W_e, \quad \varphi_c=W_1/W_e, \tag{2}$$

for the case $T_2 \gtrless T_1$.

2. BASIC EQUATIONS

It has been shown[1] that application of thermodynamics of irreversible processes to the thermocouple

[1] A. H. Boerdijk, J. Appl. Phys. **30**, 1080 (1959).

Copyright © 1960 by the American Institute of Physics.

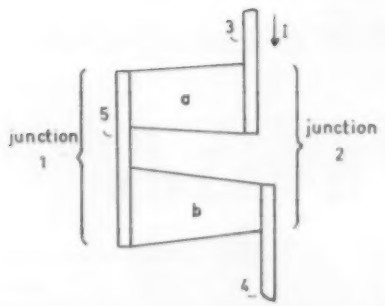

FIG. 1. Thermocouple consisting of bars a and b with junctions 1 and 2, and electrical leads 3, 4, and 5.

defined in Sec. 1 leads to

$$W_e=-I\int_{T_1}^{T_2}\eta\,d\theta - I^2\int_0^1\{(1/\sigma_a J_a)du_a+(1/\sigma_b J_b)du_b\}, \quad (3)$$

$$W_1=-I\eta_1T_1+\lambda_{1a}J_a(dT/du_a)_1+\lambda_{1b}J_b(dT/du_b)_1, \quad (4)$$

$$W_2=I\eta_2T_2-\lambda_{2a}J_a(dT/du_a)_2-\lambda_{2b}J_b(dT/du_b)_2, \quad (5)$$

where $\eta=S_b-S_a$ (for $T_a=T_b$). Unless explicitly stated otherwise, η is assumed to be positive for the interval T_2 to T_1. The temperature distribution is determined by

$$\lambda\frac{d^2T}{du^2}+\frac{\partial\lambda}{\partial T}\left(\frac{dT}{du}\right)^2+\left\{\frac{\partial\lambda}{\partial u}+\tau\frac{I}{l}\right\}\frac{dT}{du}-\frac{I}{l}\frac{\partial\Pi}{\partial u}+\frac{I^2}{\sigma l^2}=0, \quad (6)$$

for bar a, and for bar b by the corresponding equation with replacement of I by $-I$, with the boundary conditions $u=0$, $T=T_1$ and $u=1$, $T=T_2$.

3. GENERAL DIAGRAM

3.1. Operating Characteristics

The quantities W_e, W_1, W_2, V, φ_e, φ_e', φ_k, and φ_c are functions of T_1, T_2, and I. The complete set of states of operation of the couple can be described in a three-dimensional representation. Because of the relations (2) and the relations $W_e+W_1+W_2=0$, $V=W_e/I$, the eight quantities are known once we have found any two of the quantities W_e, W_1, W_2 as a function of T_1, T_2, and I.

In a practical design problem, often either T_1 or T_2 can be taken constant. We will consider the case in which T_2 is constant ($T_2\geqslant T_1$). We have two independent variables: I and $\Delta=T_2-T_1$. In the diagram obtained by plotting I, Δ in rectangular coordinates, we have eight sets of operating characteristics, i.e., the curves for which W_e, W_1, W_2, V, φ_e, φ_e', φ_k, or φ_c, respectively, are constant. We will investigate interesting regions of this diagram.

3.2. Origin and Immediate Neighborhood

In the origin O ($I=0$, $\Delta=0$) we have $T=T_2$ in every point of the couple, and therefore

$$R_0=\int_0^1\{(1/\sigma_a J_a)du_a+(1/\sigma_b J_b)du_b\}, \quad (7)$$

$$\Lambda_0=l_a\left\{\int_0^1\lambda_a^{-1}du_a\right\}^{-1}+l_b\left\{\int_0^1\lambda_b^{-1}du_b\right\}^{-1}, \quad (8)$$

where R_0 and Λ_0 are, respectively, the total electrical resistance and the total thermal conductance.

Next we consider values of I and Δ which are so small that in every point of the couple all material properties occurring in (6) can be described with sufficient accuracy by their values at T_2, and for each bar for arbitrary u,

$$\left|I\int_0^u\tau(\lambda l)^{-1}dx\right|\ll 1. \quad (9)$$

In this region (6) can be solved by elementary methods. We obtain from (3)–(5)

$$W_e=IV=-\eta_0I\Delta-R_0I^2, \quad (10)$$

$$W_1=-\eta_0T_2I+\Lambda_0\Delta+\eta_0I\Delta+\alpha R_0I^2, \quad (11)$$

$$W_2=\eta_0T_2I-\Lambda_0\Delta+(1-\alpha)R_0I^2, \quad (12)$$

where, for $T=T_2$,

$$\eta_0=F_b-F_a,\quad F=\left\{\int_0^1\lambda^{-1}du\right\}^{-1}\int_0^1 S\lambda^{-1}du, \quad (13)$$

$$\alpha R_0=G_a+G_b,$$
$$G=\left\{l\int_0^1\lambda^{-1}du\right\}^{-1}\int_0^1\left\{\int_0^x\sigma^{-1}du\right\}\lambda^{-1}dx. \quad (14)$$

The existence of interesting regions in the diagram can be proved from its properties in the neighborhood of O. In the following part of this subsection we omit all insignificant terms from the equations.

The region E of generation of electricity is characterized by $W_e>0$. From (10) we find for this region and its boundaries, respectively,

$$0>I>-(\eta_0/R_0)\Delta, \quad (15)$$

$$I=0, \quad (16)$$

$$I=-(\eta_0/R_0)\Delta. \quad (17)$$

Two interesting curves e_{12}, e_{23} in this region are defined by $\partial\varphi_e/\partial I=0$ and $\partial W_e/\partial I=0$, respectively, from which we find, respectively,

$$I=-\{(1+p)^{\frac{1}{2}}-1\}p^{-1}(\eta_0/R_0)\Delta, \quad (18)$$

$$I=-\tfrac{1}{2}(\eta_0/R_0)\Delta, \quad (19)$$

in which $p=\eta_0^2 T_2/\Lambda_0 R_0$. Since for a given value of $\Delta>0$, the right-hand side of (18) is less negative than that of (19), these curves divide the region E into three parts E_1, E_2, E_3, bounded by (16), (18), by (18), (19), and by (19), (17), respectively.

The cooling region C is characterized by $W_1<0$. From (11) we find for this region and its boundaries, respectively,

$$I>p^{-1}(\eta_0/R_0)\Delta, \tag{20}$$

$$I=p^{-1}(\eta_0/R_0)\Delta, \tag{21}$$

$$\Delta=0. \tag{22}$$

Two interesting curves c_{12} and c_{23} in this region are defined by $\partial\varphi_c/\partial I=0$ and $W_2=\eta_0 T_2 I$, respectively, from which we find, respectively,

$$I=\{(1+p)^{\frac{1}{2}}+1\}p^{-1}(\eta_0/R_0)\Delta, \tag{23}$$

$$I=\Lambda_0^{\frac{1}{2}}\{(1-\alpha)R_0\}^{-1}\Delta^{\frac{1}{2}}. \tag{24}$$

These curves divide region C into three parts: C_1, C_2, and C_3, bounded by (21), (23), by (23), (24) and by (24), (22), respectively.

3.3. Remaining Part of the Diagram

In the general case W_c, W_1 and W_2 can be developed in a MacLaurin series in I and Δ. It will be clear that (10)–(12) represent the terms of lower order in this series. The temperature dependence of the properties of the materials may give rise to higher-order terms, but cannot change the terms occurring in (10)–(12). It follows that the regions and subregions we found cannot be zero or infinitesimally small.

First considering region E in more detail, it follows from the second law of thermodynamics that the locus $V=0$ cannot intersect the axis $\Delta=0$ at a second point. It cannot intersect the axis $I=0$ at a second point either, unless the first integral in (3) is zero for some value of Δ. For practical cases we may as well exclude this case. Under this restriction, the curves e_{12} and e_{23} cannot intersect $V=0$ or $I=0$. Redefining E_2 as the subregion between these curves, it does not matter whether e_{12} and e_{23} cross each other. It follows that generally we have a situation as illustrated in Fig. 2. The significance of the subregions becomes clear if we consider the changes in the state of operation if I is slowly decreased from zero at a constant value of Δ. In the subregion E_1 both the efficiency φ_c and the output power W_c increase, in the subregion E_2 output power and efficiency vary in opposite ways, and in subregion E_3 both decrease. Subregion E_2 should be chosen for economical operation.

Next considering region C in more detail, it follows from the second law of thermodynamics that the locus $W_1=0$ cannot intersect the axis $I=0$ at a second point. It cannot intersect or even touch $\Delta=T_2$ either. There are three possibilities left. The first is that the locus ends at a point in the region $I>0$, $0<\Delta<T_2$. This may be caused by physical destruction of the couple due to overloading. The second possibility is that the locus $W_1=0$ has an asymptote parallel to $\Delta=0$ for some value of Δ. We found a relatively simple model with such an asymptote, so this case cannot be excluded. On the other hand, we had to suppose λ and σ to be such strange discontinuous functions of T that it seems highly improbable that such a case will ever arise in practice. We may conclude that generally we have the third possibility, which consists in the locus intersecting $\Delta=0$ at a second point A. It follows that the most simple shape of the locus $W_1=0$ is that illustrated in Fig. 2. The locus will have a vertical tangent in a point B between O and A, where Δ reaches its maximal value Δ_m and the temperature of junction 1 reaches its minimal value $T_2-\Delta_m$. On the axis $\Delta=0$ between O and A, the output power W_1 reaches its minimal value $W_{1\,\min}$ at a point D.

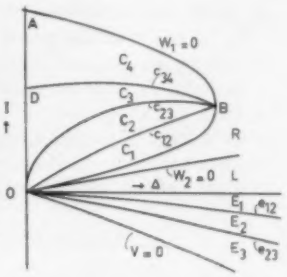

FIG. 2. Diagram for general thermocouple with coordinates I (current) and Δ (temperature difference of junctions), showing region E of generation of electricity with subregions E_1, E_2, E_3, and cooling region C with subregions C_1, C_2, C_3, and C_4.

As follows from its definition, curve c_{12} contains point B. We conjecture that curve c_{23} also contains B. A third interesting curve c_{34} is defined by $\partial W_1/\partial I=0$. From this definition it follows that it contains points B and D. It determines a subregion C_4 "to the north" of C_3. It follows that the most simple situation we can expect is the one illustrated in Fig. 2. The subregions are discussed in more detail in Sec. 4.

Outside regions E and C we have $W_c<0$ and $W_1>0$. We distinguish regions $L(W_2<0)$ and $R(W_2>0)$ separated by the locus $W_2=0$. In the former, the couple behaves as a heat leak and in the latter as an electrical resistance.

3.4. Generalization, Reduction

Changing the definitions (2) in a suitable way, we could extend the diagram to the region $\Delta<0$, or, which amounts almost to the same thing, we could take T_1 constant and T_2 as an independent variable. More generally, we could keep a suitable function of T_1 and T_2 constant and take another suitable function of T_1 and T_2 as an independent variable. Such generalizations can be considered as transformations of the diagram dealt with.

If, instead of using one couple, we use a number of identical couples or a single couple with the same composition and different dimensions, all output powers change by the same factor. Therefore, not the output powers per se but their proportions are important. It follows that the diagram can be generalized by indicat-

ing those proportions only. We could take for instance $-W_{1\min}$ as a standard power and reduce all powers by division by it. The current can be reduced by division by its value I_D in D. So we obtain a diagram which can be used for all couples of similar composition. It is advantageous to reduce Δ by division by Δ_m, since the diagram obtained can be used for couples which are quite similar but have slightly different values of Δ_m.

4. ILLUSTRATIVE EXAMPLE

We will consider the cooling region of a diagram for a general couple of which λ, σ, and S are independent of T. Equations (10)–(12) will be valid for any value of I and Δ. We find

$$W_{1\min} = -\eta_0^2 T_2^2/4\alpha R_0, \tag{25}$$

$$I_D = \eta_0 T_2/2\alpha R_0, \tag{26}$$

$$\Delta_m = \{p+2\alpha-2(\alpha p+\alpha^2)^{\frac{1}{2}}\}p^{-1}T_2 = gT_2. \tag{27}$$

By reduction according to Sec. 3.4, we obtain from (10)–(12), respectively,

$$w_e = i\cdot v = -2gi\delta-\alpha^{-1}i^2, \tag{28}$$

$$w_1 = -2i+2gi\delta+(1-g)^2\delta+i^2, \tag{29}$$

$$w_2 = 2i-(1-g)^2\delta+(\alpha^{-1}-1)i^2, \tag{30}$$

where reduced quantities are denoted by lower case letters. Couples of this type are characterized by two parameters, g and α. The curves c_{12}, c_{23}, and c_{34} have, respectively, equations

$$i = \alpha^{-1}(1-g)\delta[1-g+\{(1-g)^2+4g\alpha-4g^2\alpha(1-\alpha)\delta\}^{\frac{1}{2}}] \times[2(\alpha^{-1}-\alpha^{-1}g\delta+g\delta)]^{-1}, \tag{31}$$

$$i = (1-g)(\alpha^{-1}-1)^{-1}\delta^{\frac{1}{2}}, \tag{32}$$

$$i = 1-g\delta. \tag{33}$$

Figure 3 shows for the case $g=0.2$, $\alpha=0.5$ the region C with its boundaries $\delta=0$, $w_1=0$, the curves c_{12}, c_{23}, and c_{34}, the subregions C_1, C_2, C_3, and C_4 with some curves for which w_1 or φ_c are constant, and the regions R and L with some curves for which w_1 is constant. Lines for which v is constant are parallel to c_{34}.

The significance of the subregions becomes clear by studying the changes in the state of operation if i is slowly increased at constant δ. We find on the axis $i=0$ the so-called heat-leak power w_1. A small current will lower the heat-leak power. We pass $w_2=0$, leaving

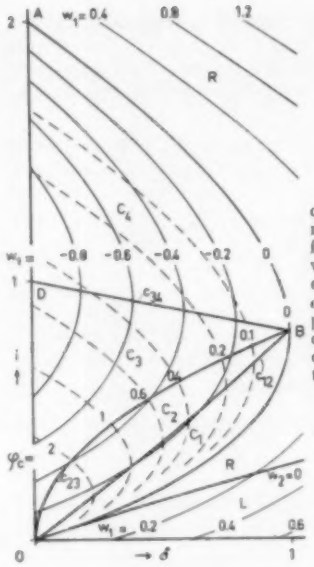

FIG. 3. Diagram showing cooling region C with subregions C_1, C_2, C_3, and C_4, for general thermocouple with temperature-independent properties ($g=0.2$, $\alpha=0.5$); w_1 is reduced output power, φ_c efficiency for cold production, i reduced current, δ reduced temperature difference of junctions.

region L, entering region R, but w_1 remains positive until we enter subregion C_1, where cold is produced at junction 1. The cold output power $-w_1$ and the efficiency φ_c increase in subregion C_1. On c_{12}, φ_c is maximal. In subregion C_2, φ_c decreases but $-w_1$ continues to increase. In subregion C_3 the temperature $T=f(u)$ has a maximum for $0<u<1$ in at least one of the bars, indicating that the same output power can be obtained with a shorter couple at a higher efficiency. On c_{34} the cold output power is maximal. In subregion C_4 both efficiency and cold output power decrease. After passing the locus $w_1=0$ again we return to region R.

In the design of a couple for cooling or heat pumping, we have to distinguish two cases. If the state of operation is stationary, the workpoint has to be chosen in the wing-shaped subregion C_2. It has to be on c_{12} if the cost of the couple can be neglected, and on c_{23} if the cost of electric energy can be neglected. Generally, a compromise has to be found. If the operating conditions are dynamic, for instance, if a substance has to be cooled over a given temperature range, it may not be possible to avoid subregion C_2 because it is difficult to change the dimensions of the couple during operation. The fastest cooling is obtained along c_{34}, the most efficient cooling along c_{12} (O excluded).

Time Discrimination in Solid-State Infrared Quantum Counters

J. V. JELLEY*
Harvard College Observatory and the Gordon McKay Laboratory of Applied Physics, Harvard University, Cambridge, Massachusetts
(Received June 3, 1959; and in final form received November 30, 1959)

The paper discusses various considerations in the practical realization of the infrared solid-state quantum counter recently proposed by Bloembergen. It is suggested that a high degree of discrimination between the quantum to be counted, and the optical pumping flux, could be attained by a time-sequence switching system; it is estimated that an isolation of ~160 db might be required. The proposal demands that at least one of the levels in the crystal have a long lifetime, and a simple expression is derived for the overall efficiency of the detector in this case. An additional gain in efficiency and isolation would result if "double pumping" were used, with detection in the ultraviolet. In conclusion a suggested layout of components is presented incorporating the switching scheme discussed herein.

IN Bloembergen's[1] recent proposal for a sensitive solid-state infrared quantum counter, one of the difficulties likely to be encountered is break-through from the optical pumping band to the optical detection channel, in spite of discrimination in frequency, polarization and direction of propagation.

It would seem, however, that a far more significant isolation could be achieved by time discrimination, in which the pumping source and detector are pulsed and quenched alternately, as frequently adopted in the nuclear physics field. The scheme proposed here is that if it is possible to obtain a suitable material with sufficiently long relaxation times, the infrared quanta may be stored in level E_2, Fig. 1, pumped up to level E_3 later, and finally counted via the transition E_3-E_4 later still. With this suggestion the three processes may be separated in time, with the result that a high degree of isolation may be obtained between the pumping and counting channels. It should be mentioned that in spite of the switching process the detector remains continuously sensitive to the infrared radiation. This idea of storage, of course, would mean that coincidence experiments would not be possible, e.g., observing infrared quanta in association with optical or other infrared quanta; this, however, is of little consequence since at present the efficiencies of all infrared detectors are so low that work of this type is in any case impossible.

The degree of isolation required for optimum sensitivity will depend on the pumping flux required in a specific arrangement, and this in turn on the transition probabilities and relaxation periods of the energy levels involved. However, the present state of the art suggest that the strongest available sources will be necessary. In such a case, the required isolation may be estimated as follows: If we consider a line width of, say, 5 A (typical for an interference filter), centered at a wavelength of 4000 A for the pump, then, for an effective color temperature of, say, 10 000°K (obtainable in discharge tubes), the pumping flux calculated from Planck's equation would amount to 3.3×10^{18} photons sec^{-1}, if the light emitted from a source of area 0.1 cm^2 within 1 sr is concentrated on the crystal. On the detector channel, we will consider a cooled photomultiplier having a dark-current of, say, 10 photoelectrons sec^{-1}. For a signal/noise ratio of unity and a typical photocathode quantum efficiency of ~10%, the sensitivity limit would be ~100 photons sec^{-1}. In this case, therefore, the overall isolation required between the pumping and detection channels would be $\sim3\times10^{16}$, i.e., ~160 db.

The proposal requires that the level E_3 have a spontaneous decay-time τ_3, comparable or long compared with the pumping period t_p. If the counting period is of duration t_c, the average counting efficiency of the

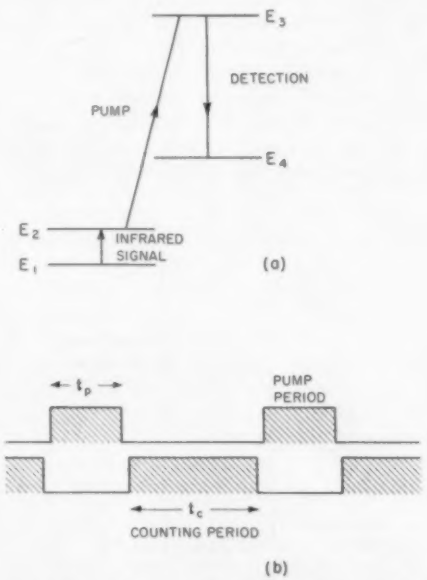

FIG. 1. (a) Bloembergen's notation for the single-pump infrared quantum counter; (b) the proposed pumping and counting sequence for a counter with time discrimination.

* On leave of absence from the Atomic Energy Research Establishment, Harwell, England.

[1] N. Bloembergen, Phys. Rev. Letters 2, 84 (1959).

system would be diminished by a factor of $\sim t_c/(t_p+t_c)$ on that in which there is no time discrimination.

From the point of view of pumping efficiency, it is advantageous that the relaxation time τ_2 of the level E_2 also be long. In the particular case when τ_2 and τ_3 are both much greater than t_p and t_c, the pumping efficiency will contain two factors. One arises from the fact that the pump operates only for a proportion of the total time, so that if the mean flux from the pumping source is I_p, the effective flux will be $I_p'=I_p[t_p/(t_p+t_c)]$. The other factor, which originates from competition between absorption and stimulated emission between the pumping levels E_2 and E_3, will be proportional to $\frac{1}{2}I_p'\tau_2/(1+I_p'\tau_2)$. Clearly, for high pumping fluxes this factor has a maximum value of 0.5 when saturation occurs. The overall efficiency of the system will then be proportional to

$$\frac{1}{2}\cdot\frac{I_p\tau_2[t_p/(t_p+t_c)]}{1+I_p\tau_2[t_p/(t_p+t_c)]}\cdot\left(\frac{t_c}{t_p+t_c}\right),$$

so that, for large I_p, the maximum efficiency is obtained when $t_p=t_c$. If I_p is below the level which produces saturation, the maximum efficiency occurs when t_p and t_c are different from each other.

In the more general case, when τ_2 and τ_3 are comparable to t_p and t_c, the expression would be more complicated, involving exponentials, and having a form similar to those found in radioactivity when parent and daughter products are present, having comparable half lives.

Since one of the limitations to the overall efficiency will be set by the performance of the cathodes of existing photomultipliers in the optical region, i.e., $\sim 10\%$, it is possible, at least in principle, to move the detection-channel into the ultra-violet, in which spectral region photocathode efficiencies approaching unity may be obtained; a Geiger counter might well be a serious competitor to the photomultiplier. To achieve this we invoke the idea of double or multiple pumping, already discussed for masers, see Fig. 2.

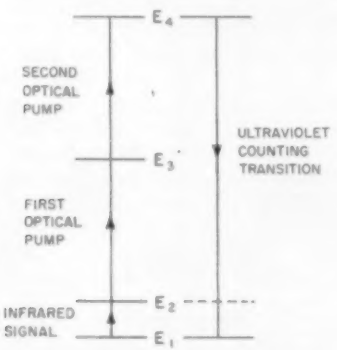

FIG. 2. Possible level-scheme for infrared counter using "double-pumping," with detection in the ultra-violet.

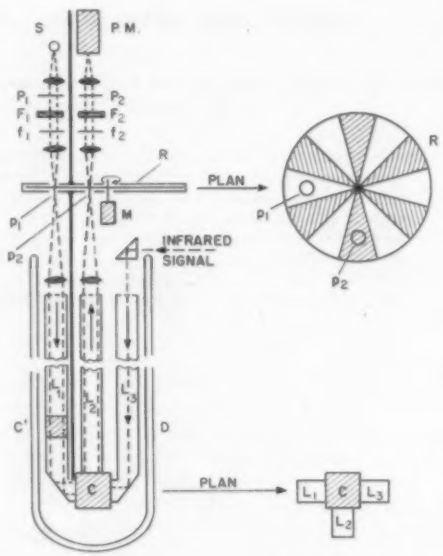

FIG. 3. A proposed layout of components for a single-pump counter, with a rotating shutter for providing time discrimination between the pumping source and the detection channel.

An additional advantage of counting in the ultra-violet is that a more emphatic wavelength discrimination is available if the counting system is insensitive to the visible band.

On the technical aspects, it is quite feasible to switch the pump (e.g., a high-pressure discharge tube) and suppress the photomultiplier electronically, in times of ~ 0.1 μsec. However, if a relaxation period of ~ 100 μsec or longer were available for the transition E_2E_4, it would seem preferable to use a small rotating-disk light chopper, since short-period phosphorescent effects in the source, filters and lenses could be thereby eliminated. A suggested layout of the various components is indicated in Fig. 3, for the case of a system using a single optical pumping channel. The additional crystal C' is of the same material as that of the active crystal C, introducing prefiltering as already proposed.[2]

In conclusion, the author wishes to thank Professor Bloembergen for stimulating discussions which assisted in developing the proposal.

[2] N. Bloembergen, Bull. Am. Phys. Soc. 4, 3, 165 (1959).

JOURNAL OF APPLIED PHYSICS VOLUME 31, NUMBER 7 JULY, 1960

Power Flow and Stored Energy in Thin Electron Beams

W. W. RIGROD
Bell Telephone Laboratories, Incorporated, Murray Hill, New Jersey
(Received December 17, 1959; and in final form March 15, 1960)

The kinetic and electromagnetic components of ac power and stored energy are evaluated for space-charge waves along thin drifting beams of simple geometry. It is found that: (a) when a modulated beam is decelerated, it radiates power into the surrounding space; (b) when both fast and slow waves are excited by a common source, the real kinetic power varies periodically with distance, exchanging energy with the electromagnetic field; and (c) when a finite-area beam is current modulated with zero ac velocity, the total power need not be zero.

The energy transport velocity of a space-charge wave is shown to equal its group velocity, when the time-average stored energy is properly evaluated. A small portion of the stored kinetic energy propagates, together with the field energy, as an electromechanical wave along the beam. The larger part of the kinetic energy, which can be positive or negative, is transported by the motion of the beam itself.

I. INTRODUCTION

IN calculations of ac power flow along electron beams at low signal or noise levels, two assumptions are commonly made. One is that the electromagnetic power flow may be neglected, in the absence of a slow wave circuit, as it is very small compared with the kinetic power.[1,2] The other is that the finite beam area can be adequately represented by a plasma frequency reduction factor, having the same value for the fast and slow waves of a given mode.[3,4] For some types of beam modulation, neither assumption is justifiable. For example, when the fast and slow space-charge waves are excited with nearly equal amplitudes, the electromagnetic power is comparable to the *net* kinetic power, and the total power is very sensitive to the difference between the reduction factors for the two waves.

In this paper, the time-average ac power and stored energy of space-charge waves along thin drifting beams of simple geometry are evaluated, without either of the above assumptions. It is shown that: (a) when a modulated beam is decelerated, it radiates power into the surrounding space; (b) when both fast and slow waves are excited by a common source, the real kinetic power varies periodically with distance, exchanging energy with the electromagnetic field; and (c) when a beam is current modulated with zero velocity modulation, the kinetic power is zero, but the total power need not be zero.

The Chu kinetic power theorem[1] successfully accounts for the power flow out of longitudinal electron beams. It is supplemented here by showing that the energy transport velocity of a space-charge wave (in a thin beam) equals its group velocity. This identity is obtained when the nonlinear force and continuity equations are introduced into the Poynting theorem, as proposed by Louisell, Pierce, and Walker.[2,5] By contrast, when the linearized beam equations are used to split Maxwell's equations into dc and ac parts,[3] the energy conservation equation does not furnish a complete description of the ac stored energy.

II. ENERGY CONSERVATION IN LONGITUDINAL BEAMS

Chu's small signal power theorem for longitudinal beams[1] can be derived in two different ways. The linearized ac current and fields can be introduced directly into Maxwell's equations, leading to the complex Poynting equation for ac power and energy. Alternatively, Maxwell's equations can be expressed in terms of the *total* fields and currents in a modulated beam, and the dc and ac power and energy terms separated in the Poynting equation so derived. Although both procedures lead to the same power conservation theorem, only the latter method accounts fully for the ac stored energy, as will be shown at the conclusion of this paper.

In this section, expressions for the time-average ac power and stored energy will be derived by the latter method, and analyzed in detail for thin longitudinal-flow electron beams in the following two sections. These computations will demonstrate the inadequacy of the complex Poynting theorem derived from the linearized ac field equations.

As discussed elsewhere,[6,7] the slow-wave, small-signal restrictions mean that the contributions of the ac magnetic field to the electric field, and to the force acting on electrons, are relatively negligible. The ac electric field can therefore be derived from a scalar potential, as in electrostatics:

$$\text{curl}E=0. \tag{1}$$

In all other respects, however, the ac magnetic field may not be neglected, as it is essential to electro-

[1] L. J. Chu, IRE-AIEE Conference on Electron Devices, Durham, New Hampshire, June, 1951.
[2] W. H. Louisell and J. R. Pierce, Proc. I.R.E. **43**, 425 (1955).
[3] H. A. Haus and F. N. H. Robinson, Proc. I.R.E. **43**, 981 (1955).
[4] S. Bloom and R. W. Peter, R C A Rev. **15**, 95 (1954).
[5] L. R. Walker, J. Appl. Phys. **26**, 1031 (1955).
[6] W. W. Rigrod, Proc. I.R.E. **46**, 358 (1958).
[7] W. W. Rigrod, Bell Syst. Tech. J. **38**, 121 (1959).

magnetic wave propagation:

$$\text{curl}H = J + \epsilon \partial E/\partial t. \tag{2}$$

These two field equations are appropriate for both slow-wave ac quantities and for steady-state (dc) fields. With E, H, and J defined as the total (dc plus ac) vectors for the electric field, magnetic field, and current density in the modulated electron beam, and ϵ the dielectric constant of free space (all in MKS units), the two field equations may be combined to form the Poynting equation,

$$\text{div}(E \times H) + E \cdot J + \epsilon E \cdot \delta E/\delta t = 0. \tag{3}$$

Tonks[8] has shown how the driving term $E \cdot J$ may be evaluated for a longitudinal electron beam, using the nonlinear force and continuity equations (in Eulerian variables):

$$-\eta E = (\partial u/\partial t) + \tfrac{1}{2}(\partial u^2/\partial z), \tag{4}$$

and

$$\partial \rho/\partial t = -\partial J/\partial z, \tag{5}$$

where $J = \rho u$, with ρ the total space-charge density, u the beam velocity at a fixed location, and η the charge mass ratio of the electron, a positive quantity. From these two beam equations, we readily obtain

$$E \cdot J = (\partial p_k/\partial z) + (\partial w_k/\partial t) \tag{6}$$

where

$$w_k = -\rho u^2/2\eta \tag{7}$$

and

$$p_k = -\rho u^3/2\eta. \tag{8}$$

These are the fundamental definitions of kinetic-energy and kinetic-power densities, respectively, in an electron beam. The Poynting theorem then assumes the form

$$\text{div}(p_e + p_k) + (\partial/\partial t)(w_e + w_k) = 0 \tag{9}$$

in which the densities of stored energy and power flow in the electromagnetic field are given, respectively, by

$$w_e = \tfrac{1}{2}\epsilon E \cdot E \tag{10}$$

and

$$p_e = E \times H. \tag{11}$$

The energy stored in the magnetic field is negligible, owing to the slow-wave assumption (1).

Louisell and Pierce[3] have proposed that the small-signal expansions of w_k and p_k would be consistent with each other and with the linearized force and continuity equations, provided w_k is defined as in Eq. (7), and p_k is defined in terms of current density,

$$p_k = -Ju^2/2\eta. \tag{12}$$

By expanding (8) up to second-order perturbation terms in ρ and u, moreover, and utilizing the exact (nonlinear) beam equations (4) and (5), Walker[5] has shown that the small-signal expansion of Eq. (12) yields the correct value of the total ac power. We proceed, therefore, to expand w_k as defined by (7), and p_k by (12), in terms of small signal variables.

With J replaced by $(-J_0 + J)$, ρ by $(\rho_0 + \rho)$, and u by $(u_0 + v)$, i.e., using the symbols J, ρ, and v to denote the small-signal ac amplitudes, and those with the subscript 0 for the time-average quantities, we obtain the following expressions for the time-average kinetic-energy and kinetic-power densities:

$$\bar{w}_k = -(2\eta)^{-1} \text{Re}[\rho_0 u_0^2 + \tfrac{1}{2}\rho_0 vv^* + u_0 \rho^* v], \tag{13}$$

$$\bar{p}_k = -(2\eta)^{-1} \text{Re}[-J_0 u_0^2 - \tfrac{1}{2}J_0 vv^* + u_0 J^* v]. \tag{14}$$

Similarly, the time-average densities of field energy and power are given by

$$\bar{w}_e = \tfrac{1}{2}\epsilon E_0^2 + \tfrac{1}{4}\epsilon EE^*, \tag{15}$$

$$\bar{p}_e = E_0 \times H_0 + \tfrac{1}{2}\,\text{Re}(E \times H^*). \tag{16}$$

We shall be concerned only with longitudinal beams flowing parallel to enclosing metal walls. Integrating the Poynting equation (3) over the cross section S of beam and surrounding space, we obtain the equation for conservation of total time-average power,

$$\frac{\partial}{\partial z}\left\{-I_0 V_0 + \frac{I_0}{2\eta}(u_0^2 + \tfrac{1}{2}vv^*) + \text{Re}\int_S \left[\tfrac{1}{2}(E \times H^*)_z - \frac{J^* u_0 v}{2\eta}\right] dS\right\} = 0, \tag{17}$$

where I_0 is the total time-average beam current, and V_0 the time-average beam voltage.

The force equation for the modulated beam is

$$-\eta(E_0 + E) = \frac{\partial v}{\partial t} + \frac{1}{2}\frac{\partial}{\partial z}(u_0^2 + 2u_0 v + v^2) \tag{18}$$

and its time-average part is

$$-\eta E_0 = \eta \frac{\partial V_0}{\partial z} = \frac{1}{2}\frac{\partial}{\partial z}(u_0^2 + \tfrac{1}{2}vv^*). \tag{19}$$

This equation, which states that the time-average velocity u_0 of a modulated beam is less than it was without modulation, is originally due to L. A. MacColl.[9] It appears, too, in the work of Boot, Self, and Harvie,[10] treating the deceleration of charged particles by a field gradient, in schemes for the rf containment of plasmas or focusing of beams.

As the time average of the continuity equation (5) shows that I_0 is invariant with distance, Eq. (19) can be written in the form of a conservation statement for

[5] L. Tonks, Phys. Rev. **54**, 863 (1938).

[9] J. R. Pierce, Bell Syst. Tech. J. **30**, 626 (1951).

[10] H. Boot, S. Self, and R. Shersby-Harvie, J. Electronics and Control **4**, 434 (1958).

dc power,

$$\frac{\partial}{\partial z}\left[I_0V_0-\frac{I_0}{2\eta}(u_0^2+\tfrac{1}{2}vv^*)\right]=0. \tag{20}$$

On combining this with (17), we obtain Chu's kinetic power theorem for longitudinal beams,

$$\frac{\partial}{\partial z}\,\mathrm{Re}\int_S\left[\tfrac{1}{2}(E\times H)_z-\frac{J^*u_0v}{2\eta}\right]dS=0. \tag{21}$$

Similarly, we obtain for the total time-average stored energy per unit length of drift region

$$\bar{W}=\mathrm{Re}\int_S\left[\tfrac{1}{2}\epsilon(E_0^2+\tfrac{1}{2}EE^*)-\frac{1}{2\eta}(\rho_0u_0^2+\tfrac{1}{2}\rho_0vv^*+u_0\rho^*v)\right]dS. \tag{22}$$

The dc potential energy density is $\frac{1}{2}\epsilon E_0^2$, and the dc kinetic energy density $-\rho_0u_0^2/2\eta$. [We note from (19) that the latter quantity differs in a modulated beam from $-\rho_0V_0$, the work done by the accelerating field on the dc charge density.] The sum of the remaining terms in (22) is the time-average ac stored energy,

$$\bar{W}_{AC}=\mathrm{Re}\int_S\left[\tfrac{1}{4}\epsilon EE^*-\frac{\rho_0vv^*}{4\eta}-\frac{u_0v\rho^*}{2\eta}\right]dS. \tag{23}$$

III. SMALL SIGNAL POWER FLOW IN THIN BEAMS

To study power-flow relations in beams of finite area, it is expedient to adopt the most transparent beam models of this class, the zero thickness or "thin" beams of two types: (1) the flat (sheet) beam of infinite width, and (2) the cylindrical (pencil) beam. In such beams there is no displacement current and no transverse field variation. Thus the electromagnetic energy of space-charge waves lies wholly outside of the beam, and can be readily computed. In addition, such beams can support only a single pair of space-charge waves, when transverse field periodicity parallel to the conducting boundaries is excluded. For mathematical convenience, each of these thin-beam prototypes will be assigned a nominal thickness or radius in order to describe them in terms of a volume rather than a surface, space-charge density.

For waves propagating as $\exp j(\omega t-\beta z)$ along z directed beams, the ac velocity v, current density J, and field E are interrelated by the linearized force and continuity equations as follows:

$$v=j\eta E/(\omega-\beta u_0), \tag{24}$$

$$J=-j\omega\epsilon\omega_p^2E/(\omega-\beta u_0)^2, \tag{25}$$

where ω_p is the angular plasma frequency, defined by

$$\omega_p^2=-\eta\rho_0/\epsilon. \tag{26}$$

The weakening of the field E in the beam owing to transverse fields in the space outside of the beam is expressed by means of the space-charge reduction factors p_1 and p_2 for the slow and fast waves, respectively:

$$\beta_1=(u_0)^{-1}[\omega+p_1\omega_p]=\beta_e+p_1\beta_p, \tag{27}$$

$$\beta_2=(u_0)^{-1}[\omega-p_2\omega_p]=\beta_e-p_2\beta_p. \tag{28}$$

As p is usually a monotonically increasing function of β (*not* β_e), p_1 is greater than p_2 when the two waves are excited at the same frequency. With these relations, the total convection current i and the ac velocity for each wave can be written as

$$i=-j\omega\epsilon AE/p^2 \tag{29}$$

$$v_{1,2}=\mp j\eta E/\omega_p\cdot p, \tag{30}$$

where A is the beam area, and the upper sign corresponds to the slow wave (subscript 1).

The thin-sheet beam (Fig. 1) has a nominal thickness $2b$ in the y direction, and is located midway between two infinite conducting planes at $y=\pm a$. Because of field symmetry about the $y=0$ plane, only the positive y half-space need be considered. As shown in Appendix A, the time-average electromagnetic power flow, per unit width of this drift region, can be written as

$$\bar{P}_e=\tfrac{1}{2}\,\mathrm{Re}\,i^*\cdot F_e\cdot V, \tag{31}$$

where i is the total convection current in the beam, $V=-jE/\beta$ is the ac voltage in the beam, and F_e is a dimensionless function of $\beta(a-b)$, the beam-wall spacing in electronic wavelengths. F_e ranges from unity for zero spacing to one-half for infinite separation (beam in free space).

For the thin cylindrical beam of nominal radius b, drifting in a concentric tube of radius a (Fig. 2), a similar expression applies

$$\bar{P}_e=\tfrac{1}{2}\,\mathrm{Re}\,i^*\cdot F_c\cdot V, \tag{32}$$

where i and V have the same meanings as for the sheet beam, and F_c is a dimensionless function of βa and βb, given in Appendix B.

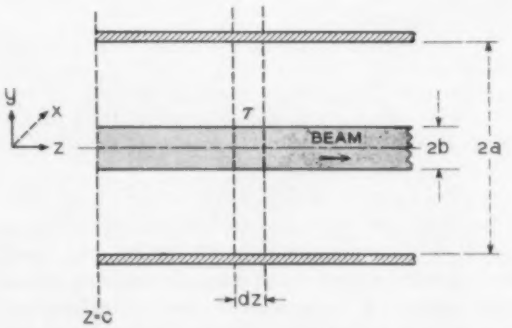

FIG. 1. Thin sheet beam of nominal thickness $2b$, flowing parallel to conducting plates at $y=\pm a$.

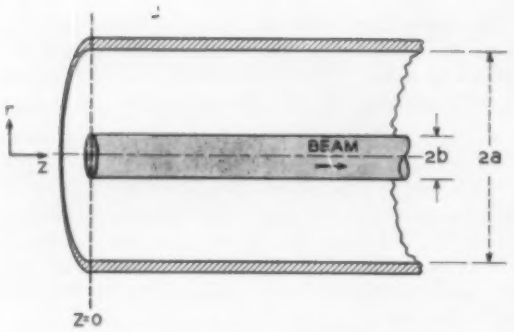

FIG. 2. Thin cylindrical beam of nominal radius b in a concentric drift tube of radius a.

The time-average ac kinetic power flow in either form of beam, according to Chu's kinetic power theorem (21), is given by

$$\bar{P}_k = \tfrac{1}{2}\,\mathrm{Re}\; i^* U, \tag{33}$$

where

$$U = -u_0 x/\eta \tag{34}$$

is the kinetic voltage. Thus the total time-average power flow in both cases is

$$\bar{P}_k + \bar{P}_e = \tfrac{1}{2}\,\mathrm{Re}\; i^*(U + FV), \tag{35}$$

where F is the appropriate geometric function for each type of thin beam. This formulation emphasizes the role of the convection current as the source of the external field. (In the case of a one-dimensional beam, there is no electromagnetic power flow, and $FV = 0$.)

Using the small signal relations (29) and (30) we obtain for the ratio of electromagnetic to kinetic power flow in a single wave

$$P_e/P_k = FV/U = \mp p\beta_p F/\beta. \tag{36}$$

This ratio increases when β increases, or u_0 decreases. Thus the electromagnetic power flow, which is always positive, increases whenever a modulated thin beam is decelerated, i.e., the beam radiates power into the surrounding space.

In approximate treatments of thin electron beams, the total *kinetic* power is found to be conserved in an acceleration.[4] This inexact result is traceable to two false premises: that the space-charge reduction factors of the fast and slow waves are equal, and that they do not change with beam velocity.

When a beam is velocity or current modulated, both a fast and slow wave are excited with nearly equal amplitude. The net kinetic power can be very small, and we might expect electromagnetic power to play a significant role in the total power flow. In the presence of two such waves, the complex amplitudes of the field and kinetic power are given by the following expressions:

$$P_e \cong \frac{F}{2}[i_1^* V_1 + i_2^* V_2 + i_2^* V_1 \epsilon^{-i\theta} + i_1^* V_2 \epsilon^{i\theta}], \tag{37}$$

$$P_k = \tfrac{1}{2}[i_1^* U_1 + i_2^* U_2 + i_2^* U_1 \epsilon^{-i\theta} + i_1^* U_2 \epsilon^{i\theta}], \tag{38}$$

where

$$\theta = (\beta_1 - \beta_2)z = (p_1 + p_2)\beta_p z. \tag{39}$$

The electromagnetic and kinetic power components are seen to vary periodically with drift angle θ. As the total power is always constant, from (21), this means that power is exchanged periodically between the beam and surrounding space.

To see whether this periodic energy exchange is due to the coupling of fast and slow waves by the external fields, we expand (35) for the total time-average power in terms of the currents and voltages in the two waves,[11]

$$\sum(\bar{P}_k + \bar{P}_e) = \tfrac{1}{2}\,\mathrm{Re}[(i_1^* + i_2^*)(U_1 + F_1 V_1 + U_2 + F_2 V_2)]. \tag{40}$$

This expansion is no more than a compact way of computing the kinetic power and the integrals of the longitudinal Poynting vectors in the presence of the two waves. As β, p, and F of the two waves differ very slightly when $\omega_p \ll \omega$, they can be replaced with their values at $\beta = \beta_e$. Using the small signal relations (29) and (30), we express i and U of each wave in terms of the space-charge potential V in the beam, to obtain for the cross-power term:

$$\tfrac{1}{2}\,\mathrm{Re}[i_1^*(U_2 + FV_2) + i_2^*(U_1 + FV_1)] \cong \frac{A\omega\epsilon\beta}{p^2}\left[2F - \frac{\beta(p_1 - p_2)}{p^2\beta_p}\right] V_1 V_2^* \cos\theta. \tag{41}$$

In a first-order Taylor series approximation, the difference in reduction factors is given by

$$p_1^2 - p_2^2 = (\beta_1 - \beta_2)\frac{\partial p^2}{\partial \beta} = (p_1 + p_2)\beta_p \frac{\partial p^2}{\partial \beta}. \tag{42}$$

In the Appendix, it is shown that for each type of thin beam,

$$\partial p^2/\partial\beta = 2p^2 F/\beta. \tag{43}$$

Combining (42) and (43), we find that the cross-power term (41) is zero. The total time-average power can thus be written:

$$\sum(\bar{P}_k + \bar{P}_e) = \tfrac{1}{2}\,\mathrm{Re}[i_1^*(U_1 + FV_1) + i_2^*(U_2 + FV_2)]. \tag{44}$$

The power flow in each wave is conserved separately, showing that the fast and slow waves are not coupled.

In addition to the periodic energy exchange between beam and surrounding space, there is one more signifi-

[11] Following a suggestion of J. R. Pierce.

cant difference between the power flow along thin beams and that along the one-dimensional model. In the latter, the total power flow at any cross-section plane consists only of kinetic power,

$$\bar{P}_{1\,\mathrm{dim}}=\bar{P}_k=\tfrac{1}{2}\,\mathrm{Re}\,i^*U. \tag{45}$$

The total power excited by either velocity modulation ($i=0$) or by current modulation ($U=0$) is zero.

In the case of the thin beam, we have according to (35),

$$\bar{P}=\tfrac{1}{2}\,\mathrm{Re}\,i^*(U+FV).$$

When $i=0$, as in velocity modulation, the total power is zero. However, if current modulation is accompanied by $U=0$, the kinetic power is zero, but the electromagnetic power and thus the total power can be different from zero.

IV. ENERGY TRANSPORT VELOCITY OF SPACE-CHARGE WAVES

In any wave motion along a lossless medium with normal dispersion, the energy transport velocity (defined as the ratio of time-average power flow to the stored energy per unit length of line) must equal the group velocity.[12] This requirement should, we expect, apply to space-charge waves along drifting electron beams, and thus serve as a criterion of the self-consistency of an energy conservation equation. We shall use it to test the validity of the stored energy expression (23).

The group velocities of space-charge waves along finite area beams are readily computed from the expressions for their phase constants (27) and (28):

$$v_{g1}=\left(\frac{\partial\beta_1}{\partial\omega}\right)^{-1}=u_0\left[1-\beta_p\frac{\partial p_1}{\partial\beta_1}\right], \tag{46}$$

$$v_{g2}=\left(\frac{\partial\beta_2}{\partial\omega}\right)^{-1}=u_0\left[1+\beta_p\frac{\partial p_2}{\partial\beta_2}\right]. \tag{47}$$

The first term of the stored energy expression (23) represents the field energy. It has been evaluated in the Appendix for both the thin sheet and cylindrical beams as

$$\bar{W}_e=A\epsilon EE^*/4p^2 \qquad \text{(A11, B10)}$$

where A is the beam area in each case. Thus the total time-average ac energy per unit length of drift region can be written

$$\bar{W}_{AC}=\frac{A\epsilon EE^*}{4p^2}-\frac{A}{4\eta}(\rho_0 v v^*+2u_0\rho^* v). \tag{48}$$

Using (26) and (30), we find that the second term equals the first,

$$-\frac{A\rho_0 v v^*}{4\eta}=\frac{A\epsilon EE^*}{4p^2}, \tag{49}$$

and the third term can be reduced to the form

$$-\frac{Au_0\rho^* v}{2\eta}=\mp\frac{A\beta\epsilon EE^*}{2\beta_p p^2}. \tag{50}$$

Thus the total ac stored energy is given by

$$\bar{W}_{AC}=\mp\frac{A\epsilon EE^*}{2\beta_p p^2}(\beta\mp p\beta_p)=\mp\frac{A\omega\epsilon EE^*}{2p^2\omega_p}. \tag{51}$$

The time-average kinetic power can be written as

$$\bar{P}_k=\mp\frac{A\omega\epsilon EE^*}{2\beta_p p^2}=u_0\cdot\bar{W}_{AC}. \tag{52}$$

From (36), the total time-average power is

$$\bar{P}_e+\bar{P}_k=\bar{P}_k[1\mp(p\beta_p F/\beta)] \tag{53}$$

which reduces with the aid of (43) to

$$\bar{P}_e+\bar{P}_k=\bar{P}_k[1\mp\beta_p(\partial p/\partial\beta)]=v_g\cdot\bar{W}_{AC}, \tag{54}$$

that is, the energy transport velocity equals the group velocity.

The second two terms of (48) represent the stored ac kinetic energy per unit length of beam:

$$\bar{W}_k=-\frac{A\rho_0 v v^*}{4\eta}-\frac{Au_0\rho^* v}{2\eta}. \tag{55}$$

The first term is positive and equal to the stored field energy as shown by (49), and oscillates in time-space quadrature with it (v being 90° out of phase with E). It follows that the stored field energy and this part of the kinetic energy are transported along the beam by an electromechanical wave propagation process, analogous to the propagation of oscillating electric and magnetic energy in an electromagnetic wave.

The second kinetic energy term is negative for a slow wave, and positive for a fast wave. It would be zero if $u_0=0$, as in a stationary plasma. It can be interpreted, therefore, as stored kinetic energy which is transported by the motion of the beam itself. In a passive stationary transmission line, it would be analogous to the nonpropagating stored energy associated with modes beyond cutoff, such as occur in the vicinity of shunt reactances and in coupled cavities.

To derive Chu's kinetic power theorem (21) and the expression (23) for ac stored energy, we have used the nonlinear beam equations to evaluate EJ in the Poynting theorem (3), and have separated ac from dc terms only in the final expressions for power and energy.[2,5] Another method[3] is sometimes used to derive the power conservation equation (21), which leads to a

[12] J. A. Stratton, *Electromagnetic Theory* (McGraw-Hill Book Company, New York, 1941), p. 333.

different expression for the stored energy. In this approach, Maxwell's equations are split into dc and ac parts at the fundamental frequency. The ac equations are combined to form the complex Poynting theorem,

$$\operatorname{div}(E\times H^*)-j2\omega(\tfrac{1}{2}\epsilon EE^*-\tfrac{1}{2}\mu HH^*)+EJ^*=0 \quad (56)$$

where the magnetic stored energy $\frac{1}{2}\mu HH^*$ is zero for slow waves. The ac driving term EJ^* is then evaluated by means of the linearized beam equations to obtain

$$\operatorname{div}\left[E\times H^*-\frac{u_0 v J^*}{\eta}\right]-j2\omega\left[\tfrac{1}{2}\epsilon EE^*+\frac{\rho_0 v v^*}{2\eta}\right]=0 \quad (57)$$

or

$$\operatorname{div}(p_e+p_k)-j2\omega(w_e-w_k)=0. \quad (58)$$

The ac kinetic energy so derived is only that small portion of the total kinetic energy (55) which is propagated along the beam by periodic transformations into field energy. This method, therefore, is inadequate to account for all of the ac stored energy.

ACKNOWLEDGMENTS

The writer wishes to thank Dr. J. R. Pierce and Dr. P. K. Tien for their valuable suggestions and criticism.

APPENDIX

A. Field Power and Energy of Thin Sheet Beam

In the space between beam and upper conducting plane ($b\leq y\leq a$), the field is given by

$$E_z=\frac{E\sinh\beta(a-y)}{\sinh\beta(a-b)}, \quad (A1)$$

$$H_x=\frac{\omega\epsilon}{\beta}E_y=\frac{j\omega\epsilon}{\beta^2}\frac{\partial E_z}{\partial y}, \quad (A2)$$

where E is the longitudinal field in the beam.

The reduction factor p is obtained from the boundary-value equation at the beam surface, together with Eq. (29) for the convection current, in which $A=b$:

$$-\frac{j\omega\epsilon b}{p^2}=\left(\frac{H_x}{E_z}\right)_{b+}=\frac{j\omega\epsilon}{\beta^2}\left(\frac{\partial E_z/\partial y}{E_z}\right)_{b+}. \quad (A3)$$

This yields

$$p^2=\beta b\tanh\beta(a-b). \quad (A4)$$

The longitudinal power flow in the electromagnetic field, per unit width of drift region, is

$$\bar{P}_e=\tfrac{1}{2}\operatorname{Re}\int_b^a E_y H_x^* dy=\frac{A\omega\epsilon EE^* F_e}{2\beta p^2}, \quad (A5)$$

where

$$F_e=\frac{1}{2}\left[1+\frac{2\beta(a-b)}{\sinh 2\beta(a-b)}\right]. \quad (A6)$$

With the aid of (29), this expression for electromagnetic power can be rewritten in terms of the convection current i and a scalar potential V in the beam:

$$\bar{P}_e=\tfrac{1}{2}\operatorname{Re} i^*\cdot F_e\cdot V \quad (A7)$$

where

$$E=j\beta V. \quad (A8)$$

Differentiation of the expression for p^2 yields

$$\partial p^2/\partial\beta=2p^2F_e/\beta \quad (A9)$$

or

$$\partial p/\partial\beta=pF_e/\beta. \quad (A10)$$

The time-average stored field energy in a single space-charge wave, per unit width and length of the positive y half-space, is

$$\bar{W}_e=\frac{\epsilon}{4}\int_b^a (E_y E_y^*+E_z E_z^*)dy=\frac{A\epsilon EE^*}{4p^2}. \quad (A11)$$

B. Field Power and Energy of Thin Cylindrical Beam

In the space between beam and concentric conducting tube ($b\leq r\leq a$), the axisymmetrical field is given by

$$E_z=E\left[\frac{I_{0a}K_{0r}-K_{0a}I_{0r}}{I_{0a}K_{0b}-K_{0a}I_{0b}}\right], \quad (B1)$$

$$H_\varphi=\frac{\omega\epsilon}{\beta}E_r=\frac{j\omega\epsilon}{\beta^2}\frac{\partial E_z}{\partial r}. \quad (B2)$$

Here I_0, K_0 are the zeroth-order modified Bessel functions of the first and second kind, respectively. The argument of each function is given by β times the radius, specified by the second subscript. Polar cylindrical coordinates (r,φ,z) are used.

The boundary-value equation at the beam surface,

$$-\frac{j\omega\epsilon b}{2p^2}=\left(\frac{H_\varphi}{E_z}\right)_{b+}=\frac{j\omega\epsilon}{\beta^2}\left(\frac{\partial E_z/\partial r}{E_z}\right)_{b+}, \quad (B3)$$

yields

$$p^2=\frac{\beta b}{2}\left[\frac{I_{0a}K_{0b}-K_{0a}I_{0b}}{I_{0a}K_{1b}+K_{0a}I_{1b}}\right] \quad (B4)$$

where I_1, K_1 are the first-order modified Bessel functions of the first and second kind, respectively.

The longitudinal power flow in the space outside of the beam, for a single space-charge wave, is readily obtained in a form similar to that for the thin sheet beam:

$$\bar{P}_e=\operatorname{Re}\int_b^a E_r H_\varphi^*\pi r dr=\frac{A\omega\epsilon EE^*\cdot F_c}{2\beta p^2}, \quad (B5)$$

where $A=\pi b^2$ is the beam area, and

$$F_c=1+p^2-\frac{1}{4p^2}[(\beta b)^2-(I_{0a}K_{1b}+K_{0a}I_{1b})^{-2}]. \quad (B6)$$

In terms of the convection current and ac voltage in the beam, the electromagnetic power flow is given by

$$\bar{P}_e=\tfrac{1}{2}\,\mathrm{Re}\,\tilde{\imath}^*\cdot F_e\cdot V. \tag{B7}$$

It is readily confirmed that, just as for the sheet beam, the above expressions for $\bar{p}^2$ and F_e satisfy the relation

$$\partial\bar{p}/\partial\beta=\bar{p}F_e/\beta. \tag{B8}$$

The time-average stored field energy in a single wave, per unit length of drift region, is given by

$$\bar{W}_e=\tfrac{1}{2}\pi\epsilon\int_b^a (E_rE_r^*+E_zE_z^*)r\,dr \tag{B9}$$

which readily reduces to

$$\bar{W}_e=A\epsilon EE^*/4\bar{p}^2. \tag{B10}$$

It should be noted that, for both types of thin beams treated here, the expressions for $\bar{p}^2$ are restricted to small fixed values of βb, the beam thickness in electronic wavelengths. It has been necessary to introduce a nominal beam thickness because $\bar{p}$ relates to the plasma frequency ω_p, which depends on the finite volume space-charge density ρ_0. Although neglect of the field variations across each beam has made the expressions for $\bar{p}^2$ somewhat artificial, it has not made the beam models unrealistic for power balance computations.

JOURNAL OF APPLIED PHYSICS VOLUME 31, NUMBER 7 JULY, 1960

Uniform Silicon p-n Junctions. I. Broad Area Breakdown

R. L. Batdorf, A. G. Chynoweth, G. C. Dacey, and P. W. Foy
Bell Telephone Laboratories, Inc., Murray Hill, New Jersey

(Received January 5, 1960; and in final form February 19, 1960)

Small area silicon p-n junctions have been made which are free from exposed edges and dislocations passing through the space-charge region. It is believed that the space-charge regions of these junctions more closely resemble plane parallel geometries than any studied similarly hitherto. The avalanche breakdown phenomena in these uniform junctions are shown to be drastically different from those occuring in junctions that contain many dislocations. A comparison is made between the uniform junctions and one that is similar except that it possesses two breakdown-inducing sites, probably dislocations. In the latter junction the reverse characteristic shows two slightly separated rapid increases in current which coincide, biaswise, with the formation of two isolated light-emitting microplasmas, the occurrence of characteristic microplasma noise, and two singularities in the charge-multiplication characteristics. The uniform junctions show no such phenomena at intermediate voltages, breakdown occurring at a voltage roughly twice that at which the microplasmas form and which was previously thought typical for the given material resistivity. The light emission pattern accompanying breakdown in the uniform junctions appears more diffuse (giving rise to the term—macroplasma) than in nonuniform junctions where it normally appears as an array of intense local spots (microplasmas). It is concluded that microplasmas are not a necessary accompaniment of avalanche breakdown in silicon, but that they tend to occur where there are field or lattice inhomogeneities.

INTRODUCTION

Chynoweth and McKay[1] have shown that at avalanche breakdown in reverse-biased silicon p-n junctions, the breakdown current does not pass uniformly through the junction over the whole junction area. Instead, the current funnels through the junction at many very small spots. The locations of these spots can be seen (in shallow diffused junctions) since they emit visible radiation arising from recombinations of energetic electrons and holes. The mechanism of formation of these local breakdown spots has been considered by Rose[2] who gave to them the name—microplasmas. These microplasmas are frequently unstable, giving rise to a characteristic form of noise.[2–5] Chynoweth and Pearson[6] showed that these local avalanche breakdowns, or microplasmas, showed a strong tendency to form at points where edge dislocations passed through the space-charge region. Senitzky and Moll[7] subsequently showed that if a gross field inhomogeneity was intentionally built into the junction, the breakdown could be initiated at this inhomogeneity and that higher breakdown currents were carried simply by an expansion of this breakdown area rather than by the formation of additional breakdown sites.

These various investigations suggested that attempts should be made to study avalanche breakdown in junctions as free as possible from field inhomogeneities and dislocations. This paper describes the breakdown behavior of such junctions which, furthermore, by virtue of a special geometry, were also free from edge effects. (Chynoweth and Pearson[6] have previously shown that

[1] A. G. Chynoweth and K. G. McKay, Phys. Rev. **102**, 369 (1956).
[2] D. J. Rose, Phys. Rev. **105**, 413 (1957).
[3] K. G. McKay, Phys. Rev. **94**, 877 (1954).
[4] A. G. Chynoweth and K. G. McKay, J. Appl. Phys. **30**, 1811 (1959).
[5] K. S. Champlin, J. Appl. Phys. **30**, 1039 (1959).
[6] A. G. Chynoweth and G. L. Pearson, J. Appl. Phys. **29**, 1103 (1958).
[7] B. Senitzky and J. L. Moll, Phys. Rev. **110**, 612 (1958), and private communication.

if there are no dislocations in the junction, the next most favored sites for breakdown are around the periphery of the junction.) It is found that in these dislocation- and edge-free junctions the breakdown occurs not by way of microplasmas, but in a much more uniform manner over the whole junction area in what might be called a macroplasma. A detailed study of various avalanche breakdown phenomena in these uniform junctions forms the main topic of this paper. In the following paper the electron ionization rate as a function of field strength is determined from the multiplication data and discussed in detail.

EXPERIMENTAL

The present experiments have been done with a special junction geometry that avoids surface breakdown. Furthermore, as the junctions had small areas and were made in relatively low-dislocation density material, many junctions were obtained which were free from dislocations. The junction geometry, which is shown in Fig. 1, was obtained as follows: The junctions were made on p-type silicon of about 0.2- to 0.3-ohm-cm resistivity. Small areas, which were later to be the active junction areas, were masked by the oxide masking process[8] and the remainder of the surface was diffused with a phosphorus donor diffusion with the surface concentration controlled so as to produce not an n-type layer, but merely a net π-type (lightly p-doped) layer. The oxide mask was then removed with hydrofluoric acid and the entire surface phosphorus diffused again, this time with a heavy concentration of phosphorus in a short cycle so as to produce a thin n-type (n^+ close to the surface owing to the high phosphorus concentration) skin over the whole surface. Two concentric mesas were then etched producing the geometry shown in cross section in Fig. 1. The use of the inner mesa lengthened the surface path between the n^+- and p-type regions. Typically, the diameter of the active junction area was about 0.010 in. It should be noted that the active junction area was where the n- and p-type regions met. Elsewhere the breakdown voltage would be higher because of the π-type guard ring. In this way spurious breakdown around the edges of the active junction was prevented. The p-n junctions were 1000 to 2000 A below the crystal surface so that when these junctions were biased into avalanche breakdown, the accompanying light emission was easily seen.

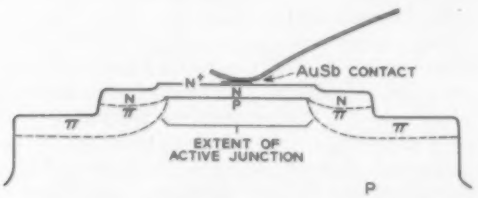

FIG. 1. The geometry of the edge-free junctions used in the present studies.

The experiments consisted primarily in compiling information on: (i) the visible light emission patterns, (ii) the reverse bias characteristics, (iii) capacitance vs bias behavior, (iv) the multiplication characteristics, (v) the integrated light emission vs bias, and (vi) the occurrence of microplasma noise. Throughout most of this paper results will be given for two junction samples; the properties of one are typical of the seven uniform junctions studied while the other junction (which was prepared at the same time and in the same way) exhibits some very informative anomalies. The two samples will be referred to as the smooth and the bumpy junctions.

RESULTS

(i) Light Emission Patterns

Figure 2 shows two photographs of the visible light emission patterns of smooth junctions in avalanche breakdown. The only differences between the two units are that they were made in separate diffusion runs and that different methods were used for making contact to the n^+-type layer. In Fig. 2(a) contact was made by a wire to a small antimony-doped gold-alloyed island whereas in Fig. 2(b) contact was made via an annular ring instead of to an island. Both units had identical breakdown voltages.

The appearances of the light patterns in Fig. 2 [especially Fig. 2(b)] are both quite different from the patterns observed previously in large area junctions.[1] The latter generally consist of random arrays of highly localized intense light spots whereas in the present junctions, though there is a tendency for the light to appear in spots [e.g., Fig. 2(a)], the spots are very much more diffuse and much weaker. In Fig. 2(b) the light emission pattern is particularly uniform, probably as a result of more perfect diffusion during fabrication. It should be noted that the breakdown voltages of these new junctions were 44 v, putting them well out of range of internal field emission breakdown mechanisms (previous work has shown that silicon junctions breaking down at less than about 6 v do so mainly by internal field emission and that this too is accompanied by a quite uniform light emission pattern[9]).

Figure 3 shows the light emission pattern of the bumpy junction, a junction which showed some interesting anomalies in its electrical properties. It will be noted that there are two bright local spots of light near the periphery of the junction while the immediate neighborhood of these spots is dark. Away from this region, however, the light from the rest of the junction appears similar to that for the smooth junction of Fig. 2(a) and noticeably much fainter and more diffuse

[8] C. J. Frosch and L. Derick, J. Electrochem. Soc. **104**, 547 (1957).

[9] A. G. Chynoweth and K. G. McKay, Phys. Rev. **106**, 418 (1957).

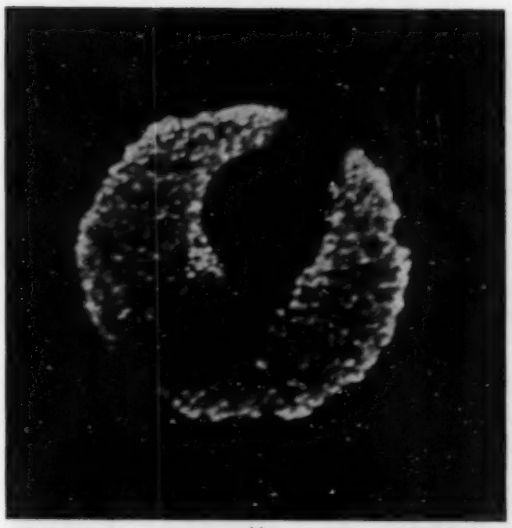

(a)

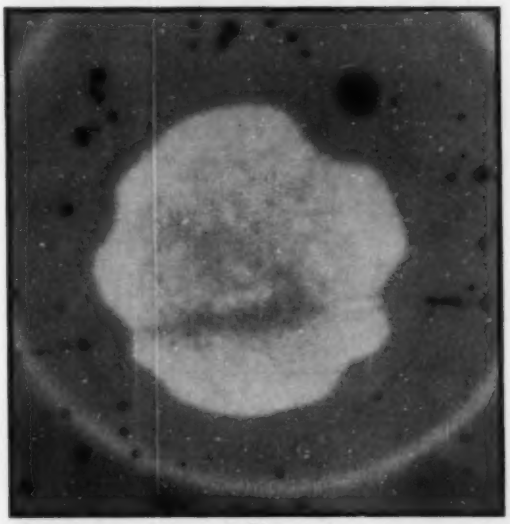

(b)

FIG. 2. Visible light emission pattern from smooth junctions at avalanche breakdown. The junctions used for (a) and (b) were from different batches and had different methods of making electrical connections to the n-type layer.

than the light from the two bright spots. The two light spots appear similar to those representing microplasmas in earlier junctions[4] and in the following sections, conclusive evidence will be presented to show that these two light spots do indeed represent microplasmas.

From previous work it is known that microplasmas, such as those in Fig. 3, tend to occur at imperfections such as dislocations passing through the junction.[6] It is tentatively concluded, therefore, that the junctions represented by Fig. 2 are relatively free from defects which strongly promote the formation of microplasmas, and that the space-charge regions of these junctions have a closer resemblence to plane parallel geometry than has hitherto been obtained. The absence should be noted, also, of the high concentration of light around the junction periphery which is usually present in junctions whose edges are exposed.[1,6]

There still remains, however, a tendency towards a spotty distribution of the light emission suggesting that even in these "smoother" junctions there can persist a *slight* tendency towards microplasma formation. Further evidence will be presented which supports this interpretation, but it should be emphasized here that this slight residual tendency towards microplasma formation will not detract from the main conclusion to be drawn, which is: junctions such as those in Figs. 2(a) and 2(b) are free from defects that cause the formation of the microplasmas which figured in earlier avalanche breakdown studies and as a consequence, the breakdown properties of these new junctions are radically different.

(ii) Reverse Characteristics

Figures 4 and 5 show the room-temperature reverse characteristics for a typical smooth junction and the bumpy junction, respectively. The smooth junction has a smooth though somewhat soft characteristic and it breaks down at about 44 v, (as did all the other junctions to within ± 1 v). Prepared in a similar way and using similar base material, the bumpy junction has the same breakdown voltage, at 44 v. But there are some very noticeable anomalies at intermediate biases. The reverse characteristic enters sharply into what appears to be a breakdown at 22.5 v. This breakdown characteristic enters a load-line form, from 23 to 24 v, whose slope is about 3×10^4 ohm. Centered between 24.5 and 25 v there is another rapid increase in current before the characteristic enters another load-line form. The heights of the first and second bumps in the reverse

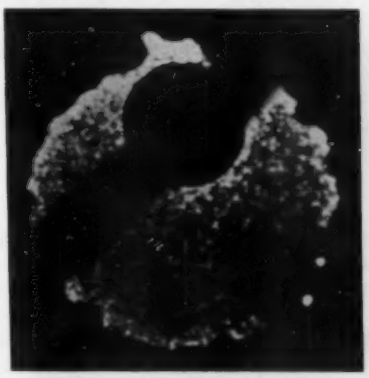

FIG. 3. Visible light emission pattern from the bumpy junction at avalanche breakdown.

characteristic are roughly 30 and 25 μa, respectively. These magnitudes are roughly as expected for the formation of microplasmas.[3] The final load line represents a load of about 2×10^4 ohm. As only one bumpy junction was available, it cannot be concluded for certain whether the relatively low current at reverse biases less than 20 v was typical of bumpy junctions, though there seems no good reason why it should be.

(iii) Capacitance Measurements

For the smooth junctions, the capacitance C closely followed a law of the form, $C^nV=$constant, with $n=3$, for all biases V, up to a bias close to breakdown. Thus, these junctions can be regarded as linear impurity gradient junctions with, consequently, parabolic field distributions. The capacitative behavior of the bumpy

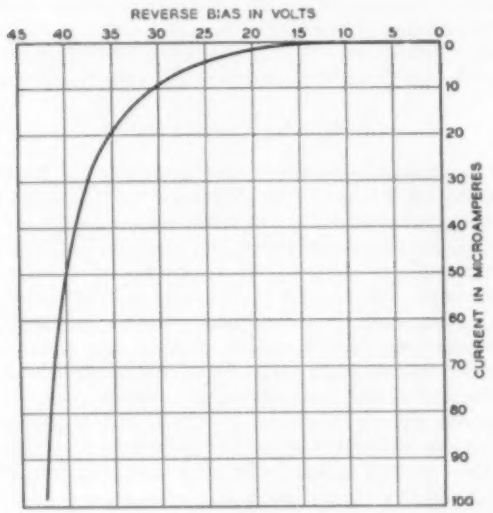

FIG. 4. Reverse characteristic of a smooth junction.

junction was similar up to the onset of the breakdown, described above, at which point the junction became too "lossy" to enable meaningful capacitance measurements to be made. From the capacitance measurements, the width constant of the smooth junction (the width of the space-charge region for a total potential drop of 1 v) was 3.2×10^{-5} cm.

(iv) Multiplication Characteristics

The method of obtaining the multiplication curve has been described previously.[10] The multiplication curves obtained for the smooth junctions were virtually identical and that shown in Fig. 6 is a typical example. In Fig. 6, M increases smoothly to a sharp peak at a bias close to 44 v. This peak was found to be insensitive to

[10] A. G. Chynoweth and K. G. McKay, Phys. Rev. **108**, 29 (1957).

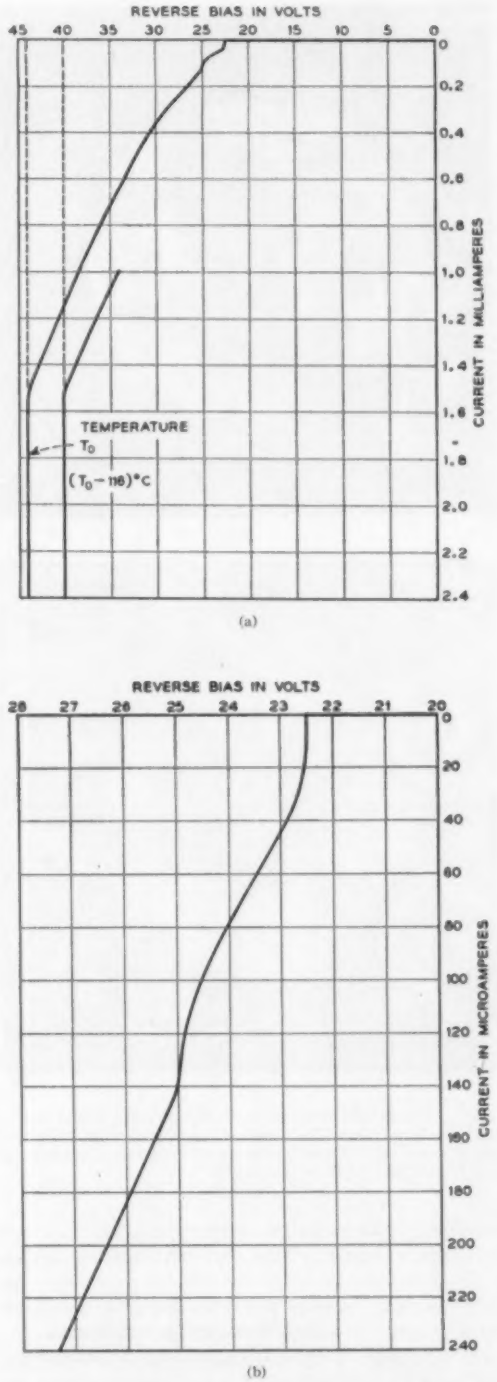

FIG. 5. Reverse characteristic of the bumpy junction: (a) showing the whole curve, (b) showing that portion of the curve corresponding to the formation of two microplasmas.

the circuit load as long as the latter was small. There are two possible causes of such a peak: (i) it can result from a falling dynamic impedance of the junction compared with that of the bulk of the crystal, or (ii) as Senitzky and Moll[7] have shown, it can arise if breakdown brings on the formation of microplasmas. When the microplasma is on all the time (at biases slightly greater than required for microplasma instability) it is current saturated and deliberately injecting a few more carriers does not lead to an enhanced current; hence the measured M drops. It is not known for certain which (if either) of these two hypotheses is responsible for the peak at 44 v though if it is the second hypothesis, this would support the conclusion that there is a slight tendency towards microplasma formation close to 44 v.

The multiplication curve for the bumpy junction is shown in Fig. 7. This curve was taken in the same way as for the smooth junction, using unfiltered tungsten

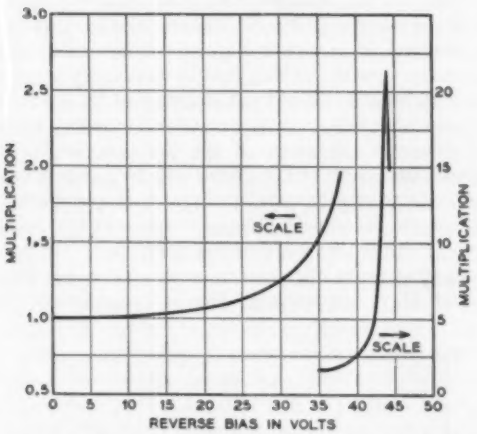

FIG. 6. Multiplication characteristic for a smooth junction.

light for injecting the carriers. The multiplication curves for the two junctions superimpose on each other almost exactly up to a reverse bias of about 35 v and, as did the smooth junction, the bumpy junction shows a multiplication peak at a bias of about 44 v. However, there are two noticeable bumps on the multiplication curve for the bumpy junction at biases of about 21 and 24 v. To within experimental error, these multiplication peaks coincide, biaswise, with the two rapid increases in current in the reverse characteristic which were ascribed to the formation of microplasmas. The discussion given in the previous paragraph regarding the observation of a *peak* in the multiplication characteristic again applies here. (The multiplication and reverse characteristics were taken several weeks apart and it seems that during this time there was a small drift from 21- to 22.5-v bias for one of the bumps. This drift, which may have been caused by channel formation

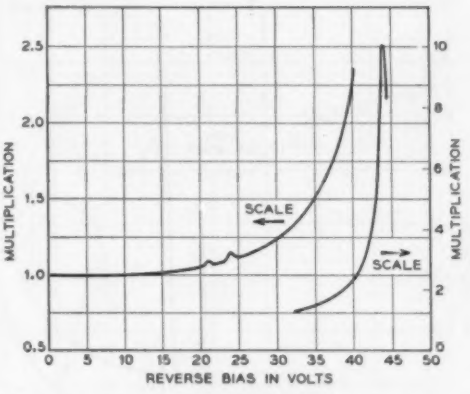

FIG. 7. Multiplication characteristic for the bumpy junction at high light intensity.

or diffusion processes, is irrelevant for the purposes of this paper.)

As seen from Fig. 8, the multiplication characteristic for the smooth junction was essentially independent of the light intensity; the injection rates for the two curves differed by more than three orders of magnitude. For the bumpy junction, however, the magnitudes of the multiplication bumps are enormously enhanced at the lower light intensity while the background multiplication curves do not superimpose (Fig. 9). Again, this can be explained by the fact that the current through the microplasma can reach a saturation value.

(v) Integrated Light Emission vs Current and Bias

To determine the total light emission as a function of current and bias, the units were mounted directly in front of a cooled photomultiplier with an $S1$ spectral response and the number of photons incident per second were counted using conventional counting techniques. It is not known if there is any shift in the spectral distribution of the light with bias at the smaller currents

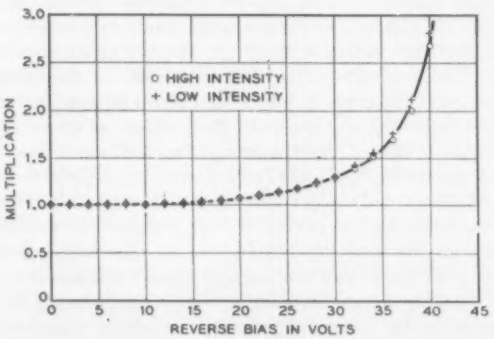

FIG. 8. Multiplication characteristics for a smooth junction for light intensities differing by three orders of magnitude.

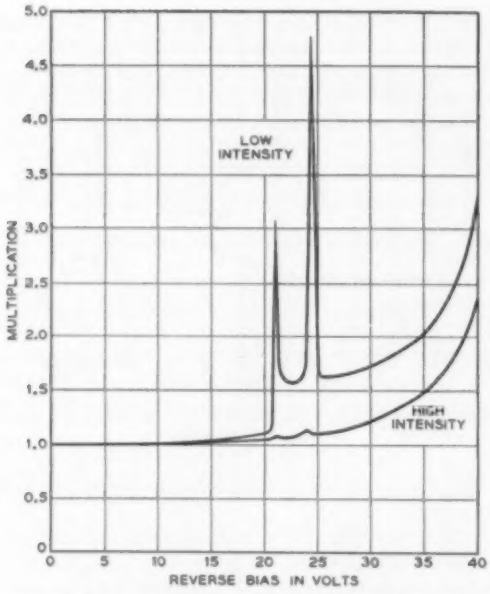

FIG. 9. Multiplication characteristics for the bumpy junction for light intensities differing by three orders of magnitude.

so that the data presented in Figs. 10–12 should be interpreted with this caution in mind. Figure 10 shows the light intensity L vs the current I for the smooth junction, over most of the range the results can be expressed by $L \propto I^n$, with n close to $\frac{3}{4}$. At the highest currents the measured light intensity increases less rapidly with current, an effect which may have been partly explained by pulse pile-up in the counting equipment. However, some curious structure is evident in the curve for currents between 80 μa and 1 ma. For the smooth junction this current range corresponded to a bias range of from 39 to 40 v. Thus, the structure occurs only when fairly close to full breakdown.

The light intensity vs current for the bumpy junction is shown in Fig. 11 and there are some differences to be noted between it and Fig. 10. From the reverse characteristics, interpolation shows that the lowest measurable light intensities occur at the onset of breakdown of the first microplasma so that the whole of the linear portion of the curve in Fig. 11 can be taken to represent light from the microplasmas that appear at about 21- and 24-v bias. Over this range the light varies close to linearly with the total current, which is in agreement with earlier findings.[4] The structure shown in Fig. 11 is remarkably similar to that of Fig. 10 only it occurs not close to the final breakdown, but in the narrow bias range in which the two microplasmas are formed (as can readily be determined by cross-interpolating between the light-current and voltage-current characteristics). Over this bias range the light intensity varies with the bias as shown in Fig. 12. There is no doubt that the two humps in the light vs current or bias for the bumpy junction correspond to the occurrence of the two microplasmas and, in Fig. 12, it will be seen that there is even some similarity in the shapes of the humps. It is easy to imagine a base line, as suggested by the dotted lines of the figures, and starting from this base line, the light intensity shows an initial rapid increase with current, then a leveling off, followed by a second rise to a final peak before falling back towards the base line.

In view of the definite correlations between the humps in Figs. 11 and 12 and the formation of microplasmas, and the similarities between the humps in Figs. 10 and 11, it again appears that there is a tendency towards microplasma formation close to 44 v in the smooth junction.

(vi) Microplasma Noise

A search was made for the characteristic noise that accompanies microplasma formation using the method described elsewhere.[4] For the smooth junction there was no evidence of any such noise throughout the whole bias range—the upper bias limit to this survey occurred well into breakdown and was determined by either the excessive shot noise at high breakdown currents, by the low dynamic impedance of the junction, or by the limited bandwidth of the circuit (10 Mc). These combined effects may have masked any microplasma noise occurring in the smooth junctions when well into breakdown. For the bumpy junction there were two very strong displays of microplasma noise centered at about 20 and 23 v, respectively. This is unambiguous evi-

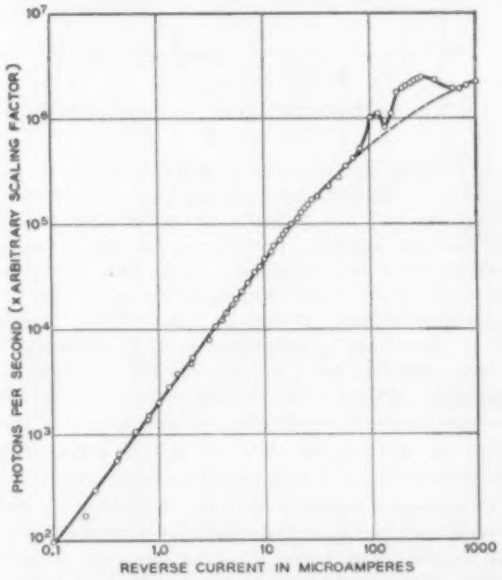

FIG. 10. Light emission intensity vs reverse current for a smooth junction.

dence of microplasma formation at these voltages, which, from Fig. 12, are seen to coincide, roughly, with the onset of the first upswing of light output for the two microplasmas, respectively, as the bias is increased. Throughout most of the remaining bias range over which the light output bumps are prominent, the microplasmas were in the stable rather than the noisy state.

DISCUSSION

There is abundant evidence in the foregoing that the reverse bias behaviors of the smooth and bumpy junctions are very similar except as regards the phenomena occurring in the bumpy junction associated with the formation of the two microplasmas between 20- and 25-v bias. The junctions possess similar bulk breakdown voltages, basic multiplication characteristics that superimpose satisfactorily, and generally similar light emission patterns.

That the two anomalies in the properties of the bumpy junction are caused by microplasma formation is also very clear. We have (i) the light emission patterns revealing two intense spots of light, qualitatively very similar to those seen in the earlier work[1,4] in which, as in the present work, they were definitely correlated with the occurrence of the characteristic microplasma noise, (ii) these two intense light spots forming at the same biases at which sudden increases in the reverse current take place, and the magnitudes of these current increases being roughly as expected for microplasma formation,[3,4,7] and (iii) along the first region, at least, of rapidly increasing current through the microplasma, the light intensity varying linearly with the current[4] (assuming no spectral shift taking place). In addition, there is a considerably enhanced multiplication accompanying microplasma formation. This enhanced multiplication is saturated by relatively low light intensities as is to be expected if the light need only inject a relatively small number of carriers to keep the microplasmas in more or less sustained operation.[7] Finally, there is

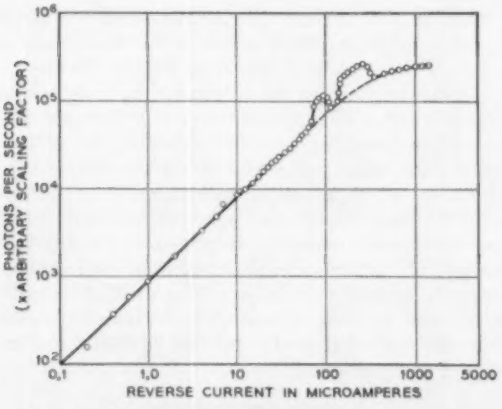

FIG. 11. Light emission intensity vs reverse current for the bumpy junction.

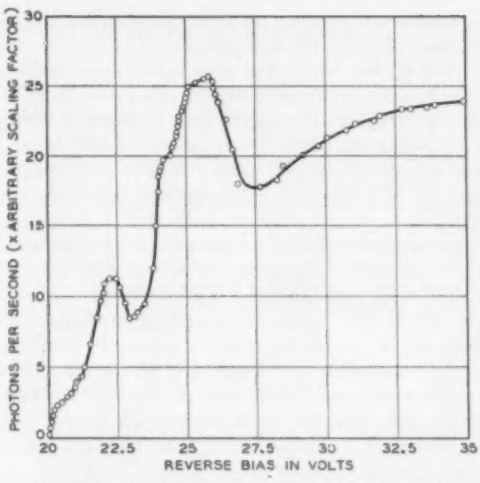

FIG. 12. Light emission intensity vs reverse bias for the bumpy junction in the region of microplasma formation.

the evidence of the load lines. Senitzky and Moll[7] have considered two sources of this load impedance; thermal effects and the spreading resistance associated with a microplasma, assuming that the cross-sectional area of the microplasma remains constant (diameter equal to about 500 A) as the current is increased. The impedance due to heating in the microplasma is given by

$$\Delta V/\Delta I=(\Delta V/V)\cdot(V/\Delta I)=\beta' V\cdot(\Delta T/\Delta I),$$

where β' is the temperature coefficient of the breakdown voltage V and the change in temperature ΔT, caused by a change ΔI in the current has been given by Rose[2] as about 10^5 °C/amp. Thus, for $V\simeq 20$ v, and[3] $\beta'=7\times10^{-4}$/°C, we have $(\Delta V/\Delta I)\simeq 1400$ ohms. This is considerably smaller than the value determined experimentally, namely, about 3×10^4 ohms. If the experimental value is taken, therefore, to represent mainly spreading resistance, it predicts a diameter for the microplasma of 500 A (the bulk material having a resistivity of about 0.3 ohm-cm) which is in excellent agreement with earlier estimates.[2]

It should be noted that the thin n-type layer on the surface of these junctions cannot be the controlling spreading resistance. In particular the macroplasma glow pattern does not arise through microplasma formation being, in general, thwarted by the resistance of the surface layer. These conclusions are drawn from Fig. 3 where it is clear that the current passing through the microplasmas has to pass by regions of the junction which are emitting a glow pattern. However, it is also obvious that the large current through the microplasmas causes a sufficient potential drop in their immediate neighborhood to inhibit breakdown there (the dark area surrounding the microplasmas).

The natures of the crystal imperfections responsible for the two microplasmas in the bumpy junction are

not known at present; obvious possibilities are dislocations, or impurity segregations. *It is obvious, however, that if there were many more microplasma-inducing defects present, (as is generally the case where no special efforts to eliminate the defects have been made) the apparent breakdown voltage of the junction would be in the range between 20 and 25 v rather than at the breakdown voltage of 44 v observed in the junctions free from these defects.* It is illuminating to note that a breakdown voltage of about 25 v, the measured width constant of 3×10^{-5} cm, and the material resistivity of 0.3 ohm-cm, are all in very good agreement with the curves that were given by McKay empirically relating the breakdown voltage to the resistivity and to the width constant.[3] Thus, it is plausible to interpret the 44-v breakdown in these junctions rather than those at 20 to 25 v as being closer to the value for an undistorted silicon *p-n* junction, and that the lower breakdown voltages usually observed are brought about by defects in the junction structure which strongly promote microplasma formation. In particular, it is believed that the smooth junctions more closely approximate the idealized situation of a space charge region with plane parallel geometry and with uniform energy gap than any junctions hitherto investigated by the authors.

[The light emission pattern of Fig. 2(a) suggests that there still persists a slight tendency towards microplasma formation at the 44-v breakdown, even in the smooth junctions. This interpretation is supported by the results of the measurements of the light intensity vs the current. On the other hand, however, the junctions which gave light emission patterns such as that of Fig. 2(b) had the *same* breakdown voltage, yet showed no evidence whatever of any fine spottiness in their light emission patterns, thereby supporting the conculsion that the 44-v breakdown is close to the true value for these silicon junctions.]

The details of the light intensity vs current and bias curves are puzzling at this stage. It has been proposed that the linear dependence of the light intensity on the current for microplasma emission[4] can be explained by an increasing duty cycle while the microplasma is in the unstable condition and by a cross-sectional area that is proportional to the current in the stable phase, the current density being assumed constant. However, it is clear from Fig. 11 that over a brief range of current the light intensity increases at a very rapid rate after which it returns to a roughly linear increase before eventually entering a "negative" region where the intensity actually drops as the current increases. This behavior is somehow related to the occurrence of the microplasmas in the bumpy junction while Fig. 10 shows that similar behavior may be occurring in the smooth junction close to breakdown. It would seem that the short rapid increase of light with current requires a corresponding increase in current *density* through the microplasma but what could bring this about is not obvious. Rough estimates show that at the currents involved there is little likelihood of pinch effects. The fact that the light output increases rapidly for a very small increase in *current* shows that the rapid increase is not caused by the initiation of secondary effects such as internal field emission or internal photoelectric effects. There remains the possibility that these anomalies arise in microplasmas when the injected charge densities become comparable with the existing space charge densities, so causing considerable distortions in the field distribution in the junction. Rough estimates of charge densities show that this condition may have been reached at currents greater than about 100 μa. The four-thirds power dependence of the light intensity on the current for the smooth junction is also unexplained at present though it may arise from a spectral shift in the emitted light as the reverse bias is increased, or if there is a substantial "leakage" current that does not produce light emission. The latter would be in line with the observation that the reverse current for low reverse bias is usually much greater in the smooth junctions then in the single bumpy junction studied. Further work is needed to understand these various effects.

CONCLUSIONS

The relatively uniform light emission patterns, the higher breakdown voltages, the smooth multiplication curves and the absence of pronounced microplasma phenomena for the "smooth" junctions all seem to show that the space-charge regions of these junctions resemble the ideal plane parallel geometry more closely than those of any other junctions similarly investigated before. When some microplasmas are present, as in the reported "bumpy" junction, they occur at the breakdown voltages previously thought appropriate for the resistivity of the base material, they are accompanied by the characteristic microplasma noise, they give rise to large irregularities in the multiplication characteristics and sudden increases of current in the reverse characteristics, and they exhibit spreading resistances which are consistent with microplasmas of about 500-A diameter.

Thus, it is concluded that microplasmas are not a necessary accompaniment of avalanche breakdown in silicon. If a junction is free from field or lattice inhomogeneities, such as are introduced by dislocations, there may be no microplasmas formed. If there are such local inhomogeneities, however, they make breakdown locally much easier, so giving rise to the current concentrations which are called microplasmas. In particular, it has been found that in silicon junctions made from 0.3-ohm-cm material, the presence of a sufficient number of inhomogeneities, probably dislocations, lowers the breakdown voltage to about half of its value for uniform junctions. Almost all earlier data pertaining to breakdown voltages will apply to junctions containing very many dislocations.

ACKNOWLEDGMENTS

The authors are grateful to Mrs. C. Markham for assistance in making the uniform junctions.

Uniform Silicon p-n Junctions. II. Ionization Rates for Electrons

A. G. CHYNOWETH
Bell Telephone Laboratories, Incorporated, Murray Hill, New Jersey
(Received January 5, 1960; and in final form February 19, 1960)

Charge multiplication as a function of reverse bias has been studied in a number of uniform silicon p-n junctions (junctions free from defects which promote local avalanche breakdown sites). From the multiplication characteristics new data have been derived for the field dependence of the ionization rate (α) for electrons. As previously found in junctions containing dislocations, α obeys the empirical relation $\alpha=\alpha_\infty \exp(-b/E)$, where α_∞ and b are constants and E is the field. Thus, this law is not simply a consequence of distortions to the junction introduced by dislocations or other microplasma-inducing defects.

The ionization rates and breakdown voltages for the uniform junctions can be made consistent with older data (for nonuniform junctions) if the junction fields, as determined from capacitance measurements, in the new junctions are multiplied by 0.65. The most obvious interpretation of this experimental fact is that breakdown is made relatively easier at defects because the field is actually higher by a factor of 1.55. Possible causes of such an enhancement are discussed together with alternative hypotheses for the different ionization rates.

INTRODUCTION

CHARGE multiplication in reverse-biased p-n junctions has been studied extensively. McKay and McAfee[1] first demonstrated its occurrence in germanium and silicon p-n junctions, and later their measurements were refined by McKay[2] for silicon. McKay was able to deduce the field dependence of the ionization rate of carriers accelerated by the field in the reverse-biased junction using the charge-injection technique. In this a certain number of carriers are injected by a light pulse or an α particle at one side of the space-charge region, and the charge that sweeps across the junction is measured as a function of the reverse bias. The ratio of the collected charge at any desired bias to the injected charge (the latter being the collected charge at sufficiently low reverse bias) is called the multiplication factor M. If M is known as a function of the bias, it is possible to deduce the ionization rate α as a function of field E. McKay and McAfee showed[1] that the multiplication characteristics were fairly similar whether electrons were injected into the junction from the p-type side or holes from the n-type side. They therefore assumed, as a first approximation, that the ionization rates of electrons and holes were equal. McKay was able to use only a narrow range of fields E, for any one junction so that his final curve of α vs E was obtained from the overlapping of results obtained from many junctions covering different field ranges. Surprisingly, none of the α vs E curves for individual junctions lay along the composite curve but, rather, cut across it quite sharply in a direction corresponding generally to a much less rapid increase of α with E.

Subsequently, Chynoweth[3], using more refined techniques, measured M vs bias for individual junctions over much wider ranges of field. His analysis showed quite conclusively that the ionization rates for electrons and holes, α and β, respectively, followed laws of the form: $\alpha=a\exp(-b/E)$, where a and b are constants. Because of the scatter in McKay's data,[2] it is not possible to say for certain whether they fitted the same law.

Wolff[4] made a theoretical study of the avalanche process based on solving the Boltzmann transport equation. He concluded that McKay's composite curve was in tolerable agreement with his theory, which assumed that the carrier velocity distribution was maintained spherically symmetric by elastic collisions with phonons. However, the α vs E dependence determined by Chynoweth is more suggestive of a carrier motion more or less along the direction of the field. Chynoweth and Pearson[5] showed that dislocations acted as preferred sites for avalanche breakdown in silicon, and they suggested that a tendency toward such a linear motion might be promoted by the lattice distortions produced by a dislocation.

In view of the different breakdown properties of uniform silicon junctions described in the previous paper[6] (hereafter referred to as I), it is now clear that the ionization-rate data previously obtained by both McKay[2] and Chynoweth[3] do apply basically to junctions in which breakdown is made easier by the presence of defects. It was therefore of interest to determine the field dependence of the ionization rate in these new uniform junctions and to compare it with the older data. In particular, it was hoped that such studies would resolve the disagreement between the experimental data and Wolff's theory.

METHOD AND RESULTS

To obtain $\alpha(E)$ and $\beta(E)$ separately (the ionization rates for electrons and holes, respectively) requires complementary multiplication data from n^+p and p^+n junctions, followed by involved evaluation of integrals which take into account the parabolic field distribution.[3]

[1] K. G. McKay and K. B. McAfee, Phys. Rev. **91**, 1079 (1953).
[2] K. G. McKay, Phys. Rev. **94**, 877 (1954).
[3] A. G. Chynoweth, Phys. Rev. **109**, 1537 (1958).
[4] P. A. Wolff, Phys. Rev. **95**, 1415 (1954).
[5] A. G. Chynoweth and G. L. Pearson, J. Appl. Phys. **29**, 1103 (1958).
[6] R. L. Batdorf, A. G. Chynoweth, G. C. Dacey, and P. W. Foy, J. Appl. Phys. **31**, 1153 (1960) this issue.

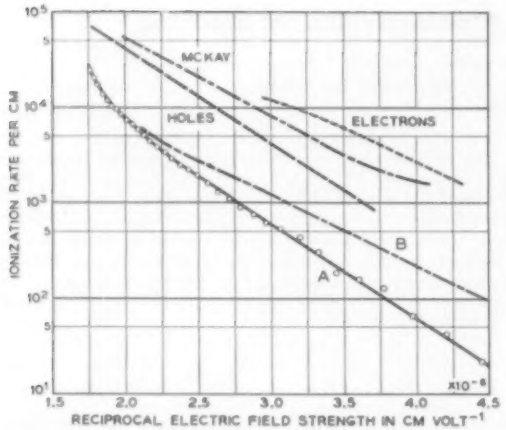

FIG. 1. The logarithm of the ionization rate for electrons in silicon plotted against the reciprocal of the electric field strength. The curves labeled "electrons" and "holes" are taken from footnote reference 3, while McKay's curve is taken from footnote reference 2. The curves *A* and *B* are from the present studies and refer to multiplication determinations using sloping and level base lines, respectively (see text).

It has been shown previously,[3] however, that remarkably similar results are obtained by (i) assuming that the ionization rates α and β are equal; and (ii) approximating the parabolic field distribution by a uniform field, of magnitude equal to the maximum of the parabolic field and acting over an effective width of the junction less than its actual width. In particular, these approximations have been found to have no noticeable effect on the *form* of the α vs E curve, but only on the absolute values for α.

It can be shown[2] that

$$1-\frac{1}{M}=\int_0^W \alpha(E)dx,$$

where W is the width of the junction. On letting the effective width of the junction be mW, with $0<m<1$, we have

$$1-M^{-1}=mW\cdot\alpha(E_M),$$

where E_M is the actual maximum field in the parabolic distribution. From the earlier data of Chynoweth, a reasonably good fit between the approximate square-field calculation and the more exact parabolic-field calculation was obtained by setting $m=0.32$. This value was used in the present work, although it is not known how appropriate it is for the uniform junctions. Curve *A* in Fig. 1 shows the field dependence of α plotted as $\ln\alpha$ vs E^{-1} as deduced from multiplication characteristics of the sort described in I for smooth junctions. The curve represents the average data provided by multiplication runs on four separate junctions—the breakdown voltages of the four junctions were equal, ± 1 v, and the scatter in α was a factor of about 1.2 at the higher fields and about 2.0 at the lower fields. It is clear that for over two decades of α, the results follow the *empirical* law

$$\alpha=\alpha_\infty \exp(-b/E), \qquad (1)$$

where α_∞ and b are constants. It should be pointed out that the absolute values of $\alpha(E)$ for the lower fields are quite highly dependent on the manner in which M is determined from the recorder charts. In earlier work,[3,7] the M vs bias characteristic had an appreciable region in which M was equal to unity and a fairly well-defined threshold bias at which M started to increase. Such a region was generally absent with the present junctions, possibly because their breakdown voltages were considerably higher than those of the junctions in the earlier work. Higher breakdown voltages mean wider junctions and lower fields, and these in turn give greater opportunity for carriers to lose energy by collisions with optical phonons. Thus, the onset of multiplication is bound to be less clearly defined in a wide junction than in a narrow one.[7] In practice it was found that the present junctions, even at low biases (<10 v), the multiplication characteristic had a slight slope which could be at least partly explained by the above mechanism. Another possible contributing factor is an injection efficiency that increases slightly with bias because of the potential drop set up in the end-regions of the junctions by the current flow. Such an effect will also be more marked in the present junctions on account of the higher resistance of the p-type end-region. Perhaps the most important cause of the slight slope, though, is the increase in junction width with bias, thereby increasing the carrier collection efficiency. The diffusion length in the p-type side was estimated to be of the order of 10^{-2}, cm and the junction width increased by about 4×10^{-5} cm in going from 1- to 10-v reverse bias. Thus, over this range, the collection efficiency increases by about 0.4% from this cause alone. There will be a smaller contribution, also, from a similar mechanism operative in the n-type side of the junction.

Curve *A* of Fig. 1 was obtained by using a sloping base-line to the multiplication curve, the base line being taken as an extrapolation of the multiplication curve over the bias range 0–10 v. It should be emphasized that the slope of the base-line was relatively slight (see Fig. 8 of the previous paper) though it causes some quantitative uncertainty in the $\ln\alpha$ vs E^{-1} curves. By using a level base line, corresponding to $M=1$ at very small biases, the data for the four junctions lead to curve *B*. It will be seen that the form of the dependence of α on E is preserved but the constants, α_∞ and b, are different. In view of the above discussion, however, it is felt that curve *A* is to be preferred to curve *B*. It should be noted that as curves *A* and *B* both apply to the same junction and, therefore, the same breakdown

[7] A. G. Chynoweth and K. G. McKay, Phys. Rev. **108**, 29 (1957).

field, they must eventually cross in order to satisfy the breakdown condition

$$\alpha(E_B)\cdot W_B=1/m,$$

where E_B is the breakdown field and W_B is the junction width at breakdown. This apparent ambiguity can be resolved, however, by slight adjustment of the factor m.

DISCUSSION

Whatever the absolute values of $\alpha(E)$, it is clear that α obeys the *empirical* law of Eq. (1) very closely, at least over the range of field strength used. (The deviations in the curves at the highest fields are very likely caused either by field distortions forming in the space-charge region close to breakdown or by secondary effects, such as internal field and photoelectric emission.) Thus, the *form* of the dependence of α on E appears to be the same for junctions either with or without microplasma-inducing defects. In particular, Eq. (1) is obeyed by junctions which are free from dislocations and therefore free from the associated band-gap distortions. As noted in the introduction, it had been previously proposed[5] that such distortions could lead to the observed $\exp(-b/E)$ type of law if they served to make the carrier flow more unidimensional than spherically symmetric. However, by this argument one would expect that the uniform junctions would exhibit a more spherically symmetric velocity distribution, and as Wolff showed theoretically,[4] this leads to a law of a form which can be expressed approximately by $\exp(-b'/E^2)$. Thus, these latest experiments show even more conclusively that for some reason not yet fully understood, the actual field dependence of the ionization rate is different from that predicted by Wolff.

It is clear from Fig. 1 that the curves derived from the present studies lie considerably below the older curves, even when all possible allowances have been made for uncertainties in the measurements of M and in the choice of m. This is consistent with the higher breakdown voltages of the present junctions.[6] Unfortunately, it is not obvious whether the old and new data should be scaled to fit each other by scaling the ordinates or the abscissas (or both). If the linear portions of curve A and the older curves are extrapolated back to $E^{-1}=0$, they yield the following values for α_∞: 5.5 (curve A), 17 (electrons[3]), 21 (McKay's data,[2] which follow the same law quite closely over the limited field range), and 34 (holes[3]), all times 10^5 cm^{-1}. We note also that the present data should be compared with the earlier *electron* data as in the uniform junctions, the geometry is such that virtually all the carriers are being injected from the p-type side. At the lower fields, curve A and the electron curve differ by nearly two orders of magnitude whereas they are quite comparable at $E=\infty$. This is slight evidence that the scaling should be done on the E^{-1} axis only, and that any persisting small discrepancies at $E=\infty$ could be compensated for by adjusting the value of m for the uniform junctions. However, it is equally obvious that apart from extrapolation considerations, the data could be fitted to each other to within experimental error by a factor of about 40 applied to the values of α. These two scaling methods will be considered next.

Scaling the field axis alone implies that the $\ln\alpha$ vs E^{-1} curves converge to the same value for α_∞. For the electron curve and curve A, the geometric mean of their respective α_∞ values is about 10^6 cm^{-1}. As α_∞ is the ionization rate in an infinite field, we have $\lambda_\infty=\alpha_\infty^{-1}$, where λ_∞ is the mean free path of an energetic electron before it produces a secondary electron by collision. Thus, $\lambda_\infty\simeq 100$ A. This is higher by a factor of about 3 than a recent estimate based on the analysis of hot-electron-emission data[8] and is also somewhat higher than a simple theoretical estimate.[4] However, the disagreement is not too serious, considering the quantitative uncertainties and gross extrapolations involved. It might be noted also that the slopes of the curves yield an average value for b of about 2×10^6 v cm^{-1}. As the most obvious interpretation of Eq. 1 is that the exponential factor represents the probability that an electron has the threshold energy for pair production, ϵ_T, in a field E, we can put $b=\epsilon_T/e\lambda$, where e is the electron charge and λ is a mean free path. From the above value of b, and putting[7] $\epsilon_T=2.3$ ev, we obtain $\lambda\approx 100$ A, which is comparable to the value for the mean free path between inelastic collisions involving optical phonons.[4,7]

The scaling factor f, required on the E^{-1} axis to bring about the best fit between the new and the old data, is 1.55 ± 0.10. It is not clear, however, what physical justification there may be for applying such a factor to the old values of the field for a given ionization rate. It is gratifying, though, that a factor of 1.55 is consistent also with the observations on the bumpy junction reported[6] in paper I. According to capacitance data, the field at breakdown at 44 v was 5.9×10^5 v cm^{-1}. Applying the factor f yields a value of 3.8×10^5 v cm^{-1} for the breakdown field that would correspond to the old data, while the fields corresponding to the biases at which the two microplasmas formed were actually 3.7×10^5 and 3.9×10^5 v cm^{-1}, respectively. It thus seems reasonable to associate the factor 1.55 with the presence of defects, possibly dislocations, in the junction; i.e., the presence of a defect *effectively* enhances the field by a factor of 1.55 over that deduced from capacitance measurements. This implies that f should be applied over the whole range of biases and not just near breakdown. In other words, even at low biases most of the carriers pass through the junction in the immediate neighborhoods of the defects. (It is known that they do so at breakdown from the light-

[8] B. Senitzky, Phys. Rev. 116, 874 (1959).

emission studies.[5,6,9,10] A possible mechanism for this effect has been proposed before; the carriers may be quickly "sucked in" and channeled by the band-gap distortions caused by edge dislocations.[5] Alternatively, once appreciable current flow in and near a dislocation has been established, the potential distribution set up by the spreading resistance in the end regions will tend to steer further carriers the same way. This mechanism will be operative during multiplication measurements and will apply to all carriers liberated at a distance from the space charge region whose *diffusion* time is greater than the time taken to drift the interdislocation distance under the influence of the deformation potential. Within a few angstroms of a dislocation the latter may give rise to fields of several hundred v cm^{-1} though the field drops off as the inverse square of the distance from the dislocation. However, in materials with reasonably dense dislocation arrays, such capture effects are probably significant, and much of the carrier flow may be by way of dislocations.

While it appears that most of the current flow through the defect junctions is in the neighborhood of the defects, it is still necessary to account for the factor f. First, it does not seem possible to account for f as a *field* factor produced by the distorted energy-band structure alone. A more obvious hypothesis is that it arises through impurity concentrations at the defects, thereby imparting different field geometries. One possible result is that the field will be enhanced somewhat around a defect because of the local departures of the equipotential surfaces from planes. Though this seems the most likely explanation of the factor f, it is not obvious that a variety of defect junctions (grown, alloyed, and diffused) would exhibit roughly equal values for f. (This seems to be the case since, for example, McKay's data were obtained using a variety of grown and alloyed junctions with widely different breakdown voltages, yet they all yielded ionization rates which tended to lie along a single, smooth curve.) It would clearly be desirable to obtain other measurements of f using smooth junctions with widely different breakdown voltages.

It is clear that the impurity segregations required to produce the field distortions of the previous paragraph are rather critical, unless they can impart local step junction behavior amidst basically linear gradient junctions. In this way, similar conditions could result in a variety of junctions. Such local step junctions would result in a field factor of 1.33, which is only slightly lower than necessary. However, this hypothesis is also untenable, since data obtained on defect junctions of both types, linear gradient and step, both fit the same α vs E curve when their appropriate capacitance laws are used.[2] Furthermore, the remarkably straight lines for $\ln\alpha$ vs E^{-1} in Chynoweth's older data,[3] obtained for ostensibly linear gradient junctions, could hardly have resulted if the actual current paths went through miniature step junctions.

The factor f does not have to apply to the field. With b of the form $\epsilon_T/e\lambda$, the same empirical result would obtain if ϵ_T were increased to $f\epsilon_T$ or if λ were decreased to λ/f for the uniform junction. The former would imply that all previous estimates of ϵ_T from multiplication studies in junctions[7] and photoconduction quantum yield measurements[11] represented the threshold energies at defects rather than in undistorted silicon in which it should be $f\epsilon_T = 3.4$ ev. The interpretation of the light-emission spectrum at breakdown would also be in question.[9] This notion is untenable, particularly as the average energy required to produce an electron-hole pair by α-particle bombardment is known to be only 3.6 ev[1].

This leaves λ the mean free path between inelastic scattering. It is not known at present how, or if, λ is affected by band-gap distortions so that this possibility must be left open.

Briefly, the implications of scaling the ordinate should be considered. For a given field, the enhanced ionization rate of a defect junction could come about by an enhanced high-energy tail to the carrier velocity distribution. A possible mechanism for this would be through electron-electron interactions, an effect which would become more and more important as the bias (and therefore current) increased. These electron-electron interactions would be expected to be more important in the defect junctions where, as discussed above, the current densities in the space charge region are likely to be higher than in the uniform junctions for all significant values of the bias. But it seems unlikely that this effect can account for the different ionization rates, as it would cause the difference to increase very rapidly with the field.

CONCLUSIONS

For a given applied field the ionization rates for the uniform junctions are considerably lower than those of junctions with dislocations. However, the ionization rate has the same sort of field dependence, namely,

$$\alpha = \alpha_\infty \exp(-b/E),$$

over most of the field range covered in these junctions. Therefore, dislocations with their associated band-gap distortions are not necessary to account for this law. Thus, the cause of the discrepancy between experiment and Wolff's theory for the field dependence of α has not been discovered. It should be emphasized, however, that the foregoing law is an empirical one but one which has been shown to fit experimental data remarkably well over the somewhat limited range of fields used.

The new ionization-rate data can be brought into

[9] A. G. Chynoweth and K. G. McKay, Phys. Rev. **102**, 369 (1956).

[10] A. G. Chynoweth and K. G. McKay, J. Appl. Phys. **30**, 1811 (1959).

[11] V. S. Vavilov, J. Phys. Chem. Solids **8**, 223 (1959).

reasonable agreement with the old simply by making a factoral correction to the magnitude of the field. (The same correction also brings into agreement the breakdown fields for uniform junctions and ones with dislocations). Alternatively, this factoral correction could be applied to any other quantities represented by b, namely, the pair production threshold energy, ϵ_T, or the mean free path between inelastic collisions, λ. As discussed above, one is inclined to believe that it is actually the local field that differs in the uniform and distorted junctions, and that it is not likely to be ϵ_T, although it is not known at present whether such a difference in λ is possible. Clearly, it would be helpful to obtain further measurements of the factoral correction from junctions with widely different characteristics. The possibility that electron-electron interactions become important, since, as discussed above, the current density through junctions with dislocations is likely to be much greater than in uniform junctions for all significant values of the applied bias, does not seem enough to account for the different ionization rates.

From the experimental data it is estimated that both λ_∞ and λ are of the order of 100 A. This value seems to be about three times too high for λ_∞, the mean free path between ionizing collisions in an infinite electric field, but is very reasonable for λ. The value of λ_∞ is obtained, however, by a rather extreme extrapotion which may put too great a reliance on the empirical law for the field dependence of the ionization rate.

JOURNAL OF APPLIED PHYSICS VOLUME 31, NUMBER 7 JULY, 1960

Propagation Mechanism of Germanium Dendrites

D. R. HAMILTON AND R. G. SEIDENSTICKER*
Westinghouse Research Laboratories, Pittsburgh 35, Pennsylvania
(Received January 5, 1960; and in final form February 23, 1960)

The role of the twin planes in the rapid dendritic propagation of germanium crystals is examined on the basis of corner nucleation. A model is proposed, and it is shown that at least two twin planes must be present for continued easy propagation in ⟨211⟩ directions, in good agreement with experimental observations. The absence of the dendrite with only one twin is explained.

I. INTRODUCTION

BILLIG and Holmes,[1] Billig[2] and more recently Bennett and Longini,[3] have reported the growth of relatively long lathlike dendrites of germanium from undercooled melts. The more interesting features of these crystals are the presence of a (111) twinned structure,[3,4] the appearance of well developed {111} habit faces and the unlimited propagation of the lattice in a ⟨211⟩ direction. The tendency for branching in other coplanar ⟨211⟩ directions is also pronounced.

Billig[5] postulated that this habit might arise from growth at a pair of screw dislocations of opposite hand which would propagate the lamellar core of the dendrite, whisker fashion. He ascribed the generation of the twinned structure as an effect promoted by impurities rejected during solidification of the core. Bennett and Longini considered a single twin plane as necessary and sufficient for growth, and examined its polar growth properties on an atomic scale. New experimental information will be presented which shows that neither the screw dislocations required by the former model nor the dendrite with a single twin plane predicted by the latter have ever been observed.[6]

In the following sections, we advance a model for the propagation of germanium dendrites, a model which requires a minimum of two twin planes. We postulate that growth starts only at the reentrant corners which are formed by the intersection of habit faces on either side of the twin planes. The growth steps from corners at either twin plane cooperate so that the steps on the tip of the advancing solid-liquid interface may follow a spiral course. Although this "flow" resembles the growth at a screw dislocation, there are no unique screw dislocations present. The idea that a twin plane may influence growth has been considered in the literature,[7–9] and corner growth, mentioned by Stranski,[7] has been used by Dawson[9] to explain the behavior of dendritic n-hectane, which contains a single twin plane and a reentrant corner. The application of corner growth to a crystal with two twin planes is new. Our model for germanium dendrite explains the absence of the dendrite with only one twin, and the indefinite forward

* This research was supported by the U. S. Air Force through the Air Force Office of Scientific Research, (ARDC), Wright Air Development Center.

[1] E. Billig and P. J. Holmes, Acta. Cryst. **8**, 353 (1955).
[2] E. Billig, Proc. Roy. Soc. (London) **A229**, 346 (1955).
[3] A. I. Bennett and R. L. Longini, Phys. Rev. **116**, 53, (1959).
[4] E. Billig and P. J. Holmes, Acta Met. **5**, 53, (1957).
[5] E. Billig, Acta Met. **5**, 54, (1957).
[6] J. W. Faust, Jr., and H. F. John (to be published).
[7] I. N. Stranski, Disc. Faraday Soc. **5**, 69 (1949). I. N. Stranski, Naturwiss, **37**, 289 (1950).
[8] P. Hartman, Z. Krist. **107**, 225 (1956). F. C. Frank, Disc. Faraday Soc. **5**, 48 (1949).
[9] I. M. Dawson, Proc. Roy. Soc. (London) **A214**, 72 (1952).

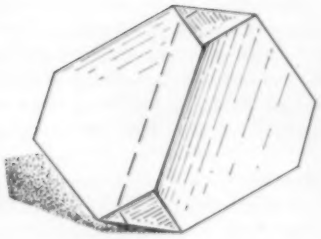

FIG. 1. The equilibrium form of germanium, an octahedron bounded by {111} surfaces. The solid is to be twinned about plane indicated by the dotted line.

propagation and the preferred coplanar ⟨211⟩ directions of branching and growth of those with two twins. New experimental information in support of the model is cited.

II. REENTRANT CORNER AND SYMMETRY RELATIONSHIPS IN GERMANIUM

The equilibrium habit of germanium is an octahedron bounded by eight {111} planes, the planes of closest packing and of lowest free energy in the diamond lattice (Fig. 1). Suppose a twinning operation is performed by removing a portion of the octahedron and reflecting the remaining solid across the twin composition plane (Fig. 2). The twin plane in the germanium bicrystal so obtained has a hexagonal periphery, outlined by the six lines of intersection of pairs of {111} planes. The external angle between these bounding planes is alternately 141° and 219°. The former is a reentrant corner, the latter a ridge structure.

Suppose that such a crystal were immersed in liquid germanium so supercooled that nucleation events are likely in the reentrant corners but improbable elsewhere. Each nucleation event in a reentrant corner is followed by growth on the two adjacent {111} planes. The reentrant corner is, at least initially, perpetuated. Thus the bicrystal has three directions in which the initial growth rate is rapid. These are $[2\bar{1}\bar{1}]$, $[\bar{1}2\bar{1}]$ and $[\bar{1}\bar{1}2]$. At orientations (in the same plane) 60° from each of these are directions in which the nucleation rate, and hence growth, is at a minimum.

If the corners are allowed to continue growing, a trigonal solid is obtained (Fig. 3) that is entirely bounded by three ridge structures and the parallel side faces. The corners are not capable of indefinite propagation, and cease to play any role in promotion of easy nucleation and growth. This is to be contrasted with the behavior of Dawson's paraffin dendrites, in which the corner cannot grow out, a corner which is indeed self-perpetuating. The two situations differ in the lower symmetry of the orthorhombic paraffin lattice, and the fact that the latter is twinned about a face diagonal rather than a prism diagonal.

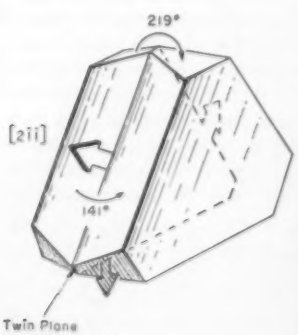

FIG. 2. A twinned crystal, derived from the equilibrium form by reflection across the twin composition plane. The twin plane emerges from the solid in three reentrant corners, ∠141°, which alternate with ridge structures, ∠219°. Ease of nucleation at the former preferred sites leads at once to three easy growth directions.

III. CRYSTALS WITH MORE THAN ONE TWIN

If a second twin is added to the solid of Fig. 2 the configuration shown in Fig. 4 is obtained. The new twofold symmetry axis, ⟨110⟩, operating on the three preferred growth directions of the bicrystal, generates

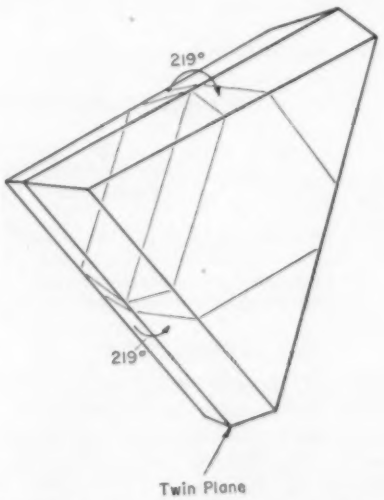

FIG. 3. The trigonal solid that is formed if the three-reentrant corner sites in the bicrystal are allowed to grow. The reentrant corners have vanished, and rapid growth has ceased.

six reentrant corners with resultant sixfold symmetry of the preferred growth directions. In Fig. 5, nucleation events (*I*) are shown schematically in two of the six corners, and, growing from them, new growth layers. In these, and in all the drawings, the highly faceted solids are bounded by {111} planes. No attempt has been made to show surface roughness, or kinks and jogs[10] in advancing growth steps, although an effort has been made to relate the shape of the steps to the events they are intended to represent.

It can be seen from Fig. 4 that growth from the two original sites has resulted in the generation of a new pair of reentrant corners, marked II, formed by two {111} planes 109½° apart. Further growth down the

[10] W. K. Burton and N. Cabrerra, Disc. Faraday Soc. **5**, 33,40 (1949). K. A. Jackson, *Growth and Perfection of Crystals* (John Wiley and Sons, Inc., New York, 1958), p. 319.

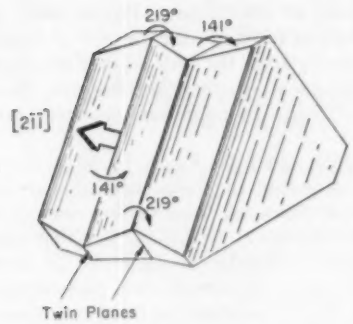

FIG. 4. A crystal containing two twin planes is found to have six of the favored reentrant sites, 60° apart, located alternatively first at one twin plane and then the other. These lead to six equivalent ⟨211⟩ preferred growth directions.

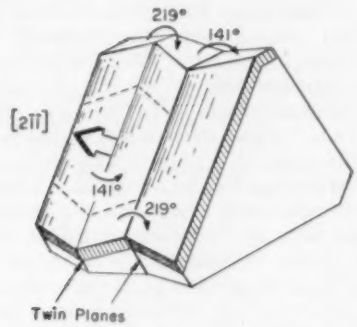

FIG. 6. The growth cycle initiated in Fig. 5 at the original reentrant corners (I) is completed by growth from the new reentrant corners (II). The solid is back to its original shape, but has increased in thickness in the directions in which growth was allowed.

sides of the ridges will require nucleation at these sites. But for the presence of a twin plane along one of the bounding faces, the geometry of these corners is identical with that which might occur in monocrystalline germanium. Furthermore, the twin plane does not bisect the nucleus. This second type of nucleation should certainly not be more difficult to accomplish than the first, and may be somewhat easier because of the more favorable geometry. The creation of new reentrant corners of type II is absolutely essential for the continuous propagation of the solid, for they relieve the nucleation problem across any ridges that may appear.

Figure 6 shows a later stage in the growth sequence. It can be seen that although the solid has the original configuration of Fig. 4, it has increased in size by one layer thickness in the two ⟨211⟩ directions that were allowed to grow. The reentrant corners supporting nucleation events of the type I, which "grew out" (Fig. 3) in the solid containing one twin, are regenerated by the activity at the second twin plane. In other words, it is no longer possible to entirely bound a solid containing *two* twins with unfavorable ridge structures across which nucleation is difficult. Our model of the bicrystal, with its *single* twin, does not have this property. The crystal with two twins possesses self-perpetuating corners or steps which permit continued growth from favored sites. This crystal has a strong tendency to exhibit sixfold ⟨211⟩ propagation and branching, in agreement with experiment.

More twins may be added to the system without removing this essential feature. For example, if a third twin is introduced, three more reentrant corners are created and added to the six corners of the two twinned crystal. The details of growth are now considerably more complex, but the reentrancies are still perpetuated.

IV. DISCUSSION

Figure 7 shows an attempt to depict in a more realistic way the extreme tip of the solid-liquid interface of a ⟨211⟩ dendrite. This figure has been derived by allowing an increase in nucleation rate, relative to lateral growth rate, in the three type I reentrant corners. The plane side faces are retained in order to

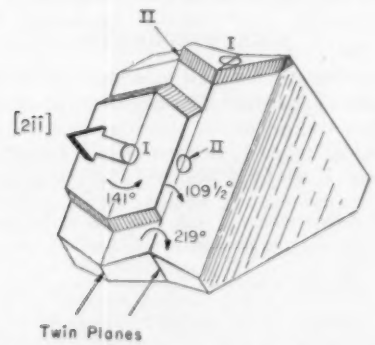

FIG. 5. Nucleation events (I) at two of the six reentrant corners of Figure 4 have been allowed to occur. Growth from these has resulted in the development of new corners ∠109½°, marked II. These straddle ridge sites across which nucleation was previously difficult.

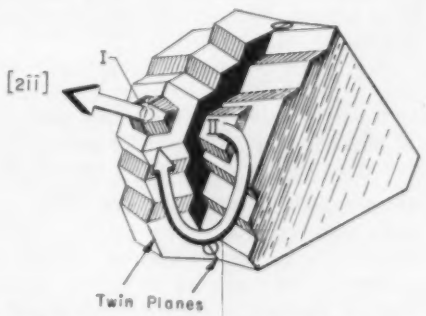

FIG. 7. By allowing an increased nucleation rate, a solid is obtained in which many steps are growing at once. It is seen that a curved interface could result from these circumstances. The "flow" of growth steps about the interface is suggested in part of the figure, showing how the reentrant corners are maintained by a growth step that "spirals back" on itself.

simplify the drawing. Many steps (shaded portions) are actively growing from various sites at the twin planes. Although the figure is still bounded on an atomic scale by steps and edges of the sort shown in earlier figures, the macroscopic surface could be curved. A possible "flow" of growth steps is indicated in one portion of the figure by an arrow. They follow a spiral course over the various portions of the interface, reminiscent of the behavior of a growth step about a screw dislocation, although there are no unique screw dislocations present. We note that the twin plane has been described by Hornstra[11] as a planar network of screws, so, in a restricted sense, one might consider the growth as the result of activity at these. However, the spiral step arises from the unusual geometry generated by the two twins, and is not the result of the activity of any unique screw or single network of screws.

It is fairly well established that the solid-liquid interface occurring in dendritic solidification of metals is highly curved because of thermal limitations. The question arises as to whether a highly faceted model, such as we have advanced, can be reconciled with a requirement that the actual interface be curved, as shown in Fig. 7. The specific requirements of the growth mechanism are that the reentrant corners be of sufficient size to ensure the requisite nucleations, and that cooperation between the various sites be maintained. There does not appear to be any reason why other regions, between the corners, should not be thermally limited (Fig. 7) and hence curved. However, if thermal conditions become so severe that the corners themselves are reduced below the minimum size, then growth by the proposed mechanism will surely cease altogether.

The actual extent of the corners will depend upon the nucleation rate relative to the velocity of the growth of the layers so initiated. If the rate is low with respect to the growth velocity, the corners will be large and the interface faceted. The nucleation rate is, of course, strongly temperature dependent, but contains a term involving the twin energy as well as the surface free energy. These are not well known, so it would not be possible to calculate the rate even if the actual temperature distribution could be defined.

By using optical interference techniques, we have been able to detect reentrant corners at places on the sides of dendrites where the twin planes intersect surfaces of high curvature. The samples themselves were prepared at rather low supercooling; the corners were of the order of 1000 A deep. Furthermore, Billig has reported slight faceting near the tips of dendrites, decanted rapidly from the melt so that transient growth would not obscure the interface features. These observations, although by no means conclusive, are at least suggestive.

H. F. John and J. W. Faust, Jr., have, over a period of time, examined the twin structures of very large numbers of dendrites from various sources prepared under a wide range of conditions. They have found that all dendrites invariably contain two or more twins. Dendrites containing a single twin plane have not been observed. We are indebted to these colleagues for permitting us to utilize this information prior to its publication elsewhere as part of a comprehensive paper describing the complex processes involved in the later stages of dendritic growth. As mentioned earlier, Billig and Holmes reported the presence of two twin planes in all the samples examined. Thus, the behavior expected on the basis of the formal model with two twins is in accord with all the available experimental evidence. To be capable of continuous propagation, dendrites of this habit must contain at least two twin planes.[12]

V. CONCLUSIONS

It has been shown that the reported directionality of growth of pure germanium dendrites can be accounted for by a simple model involving the introduction of two twin planes into the equilibrium habit. Nucleation events are allowed to take place at the reentrant corners so formed. Growth from these leads to preferred directions of continuous propagation and of branching, in agreement with reports in the literature. The reentrancies themselves have been observed on dendrites. Furthermore, the model leads to the conclusion that two twin planes are a prerequisite for continued rapid propagation of the dendrite, in contrast with previous results, but in complete agreement with the extensive experimental evidence of J. W. Faust and H. F. John, and with the original observations of Billig.

ACKNOWLEDGMENTS

The authors are indebted to members of the staff of Westinghouse Research Laboratories for stimulating discussions concerning the characteristics of dendrites, in particular to A. I. Bennett, R. L. Longini, J. W. Faust, and H. F. John.

[11] J. Hornstra, J. Phys. Chem. Solids 5, 129 (1958).

[12] R. G. Seidensticker and D. R. Hamilton (to be published).

Monte Carlo Calculation of Molecular Flow Rates through a Cylindrical Elbow and Pipes of Other Shapes*

D. H. Davis
Lawrence Radiation Laboratory, University of California, Livermore, California
(Received February 23, 1960; and in final form March 4, 1960)

A method is devised for the calculation of molecular flow rates through pipes where the mean free path for intermolecular collisions is large compared to the dimensions of the pipes. Results of the calculation are given for a straight cylindrical pipe, a cylindrical elbow, the annulus between two concentric cylinders, a straight cylindrical pipe with restricted openings, and a straight cylindrical pipe with restricted openings and a plate to block the direct beam between the openings.

INTRODUCTION

THE problem[1] of this paper is the calculation of molecular flow rates through isolated parts of vacuum systems, for example, the calculation of flow rates from a vacuum tank through a connector to a pump. The problem is one of classical kinetic theory, general analysis of which was developed by H. A. Lorentz[2] and P. Clausing.[3] An excellent account of the historical development of the problem is given by L. B. Loeb.[4]

The purpose of this paper is to describe a method of calculating flow rates in complicated connectors in vacuum systems, which is not beset by the difficulties of evaluating complicated integrals in the usual ways. The method is illustrated through the example of the cylindrical elbow. Although only the calculation of the cylindrical elbow is described in detail, the results for pipes of several other shapes are given. A calculation for a short cylindrical pipe was made for comparison with results by P. Clausing.[2]

The formulation of the problem consists in using three general assumptions. These assumptions are needed to isolate from the problem of flow through the pipe a geometric part which is independent of flow in other parts of the system. The assumptions are:

(1) The flow is steady.

(2) The distribution of the position and angle at which molecules enter the pipe at an opening is independent of the flow in other parts of the system.

(3) The molecules in the pipe move independently of each other, i.e., there are no intermolecular collisions in the pipe.

From assumption (1) (steady flow) and the conservation of molecules, an equation can be written for the flow rate through a pipe with two openings:

$$F_i = K_i P_{i\to j} - K_j P_{j\to i} \quad i, j = 1, 2, \quad i \neq j \tag{1}$$

where F_i is the net number of molecules per unit time that flow through opening i, K_i is the number of molecules that enter the pipe per unit time through opening i, and $P_{i\to j}$ is the probability that a molecule entering opening i will leave by opening j. The extension of Eq. (1) to a pipe with several openings is

$$F_i = \sum_{\substack{j=1 \\ i\neq j}}^{M} \left[K_i P_{i\to j} - K_j P_{j\to i}\right] \tag{2}$$

$$i, j = 1, 2, \cdots, M.$$

From assumptions (2) and (3), the probabilities $P_{i\to j}$ are independent of the flow in the rest of the system. These probabilities depend only on the distribution of the position and angle at which the molecules enter the pipe at an opening, and the mechanics of a single molecule in the pipe. The effect on the flow rate of such quantities as the pressure and temperature of the gas is contained in the factors K_i. The geometrical dependence of the flow rate is contained in the factors $P_{i\to j}$.

The purpose of this paper is to illustrate how the factors $P_{i\to j}$ can be calculated and to give values for several cases. Before this can be done, however, the distributions of the position and angle at which the molecules enter the pipe at the openings, and the mechanics of molecules in the pipe need to be specified. For their specification additional assumptions are necessary.

The distribution of the position and angle is based on the assumption that the openings are connected to large containers in which the gas is Maxwellian. From this assumption, the probability that a molecule enters an elementary area of an opening is proportional to this area; the probability that a molecule enters in an elementary solid angle is proportional to the cosine of the angle with respect to the normal to the surface (cosine law).

The mechanics of the molecules in the pipe is based

* This work was performed under the auspices of the U. S. Atomic Energy Commission.

[1] The problem was introduced to the author by Norman Milleron of the Lawrence Radiation Laboratory in a request to calculate flow rates in a cylindrical elbow connecting a large vacuum tank to a pump.

[2] H. A. Lorentz, *Lectures on Theoretical Physics* (Macmillan and Co., Ltd., London, 1927), Vol. 1, Chap. III.

[3] P. Clausing, Ann. Physik **12**, 404 (1932), p. 961.

[4] L. B. Loeb, *Kinetic Theory of Gases* (McGraw-Hill Book Company, Inc., New York, 1934), Chap. VII.

on an assumption of H. A. Lorentz. This assumption is that the walls of the container are "molecularly rough." Molecular roughness implies that molecules striking the walls are reflected according to the cosine law and the reflection direction is independent of the incident direction.

An important consideration to the formulation of the problem is that no net flow occurs through a pipe between two tanks at equal pressure and temperature, i.e.,

$$K_i P_{i\to j} = K_j P_{j\to i} \quad i, j = 1, 2. \tag{3}$$

Under the conditions of equal pressure and temperature,

$$K_i/K_j = A_i/A_j, \tag{4}$$

where A_i and A_j are the areas of the openings; then

$$A_i P_{i\to j} = A_j P_{j\to i}. \tag{5}$$

That the assumptions as stated are sufficient for condition (5) is shown by the following argument.

Consider a pipe of arbitrary shape with two openings. The probability that a molecule will enter an elementary area ds_1 and leave by an elementary area ds_m, with successive wall collisions in elementary areas ds_2, ds_3, $\cdots$, ds_{m-1}, is

$$\frac{ds_1}{A_1}\frac{\cos\theta_{12}}{2\pi}\frac{\cos\theta_{21}ds_2}{r_{12}^2}\frac{\cos\theta_{23}}{2\pi}\frac{\cos\theta_{32}ds_3}{r_{23}^2}\cdots \times\frac{\cos\theta_{m-1,m}\cos\theta_{m,m-1}ds_m}{2\pi r_{m-1,m}^2}. \tag{6}$$

The probability that a molecule will enter ds_m and leave by ds_1, with successive wall collisions in elementary areas ds_{m-1}, ds_{m-2}, $\cdots$, ds_2, is

$$\frac{ds_m}{A_2}\frac{\cos\theta_{mm-1}}{2\pi}\frac{\cos\theta_{m-1m}ds_{m-1}}{r_{m-1,m}^2}\cdots \times\frac{\cos_{22}\cos_{22}ds_2}{2\pi r_{22}^2}\frac{\cos\theta_{21}\cos\theta_{12}ds_1}{2\pi r_{12}^2}. \tag{7}$$

The probability for a molecule entering opening 1 and leaving by opening 2 is obtained from (6) by integration and summation; the probability for a molecule entering by opening 2 and leaving by opening 1 is obtained from (7) by the same integration and summation. The only difference between the two probabilities are the factors $1/A_1$ and $1/A_2$. Therefore, A_1P_{12} is equal to A_2P_{21}.

A corollary to Eq. (5) is

$$\sum_{i=1}^{M} A_i P_{i\to j} = A_j, \tag{8}$$

where M is the number of openings. This implies that if the molecules enter uniformly over all the openings, they will leave uniformly over all the openings. Also, it can easily be shown that if the molecules enter uniformly, following a cosine law, they will exit uniformly, following a cosine law.

It should be noticed that the conditions as stated are sufficient for Eq. (5) but are not necessary. For example, the "molecularly rough" wall-collision condition can be changed to a specular-reflection condition.

CALCULATION OF $P_{i\to j}$

The calculation is a standard application of the Monte Carlo method. The method consists of generating a sequence of molecule histories from a set of random numbers. The sequence of histories is then used to obtain an estimate of the $P_{i\to j}$ values.

The generation of the histories consists of the following processes. First, the space coordinates of a molecule at an opening are generated. Then the direction cosines of the velocity vector of the molecule are generated. With the space coordinates and the direction cosines, it is determined whether the molecule has a collision with the wall or hits an opening. If the molecule hits a wall, the coordinates of the collision point are calculated and new direction cosines are generated. It is again determined whether the molecule has a collision with the wall or hits an opening. The molecule is thus followed from wall collision to wall collision until it hits an opening. If the molecule hits an opening, the history is terminated, and the coordinates of a new molecule are generated. The calculation is terminated when enough histories have been generated for the accuracy required in the estimates of the $P_{i\to j}$ values. The estimates of the $P_{i\to j}$ values are

$$\hat{P}_{i\to j} = N_{i\to j}/N_i, \tag{9}$$

where N_i is the number of molecules starting from opening i and $N_{i\to j}$ is the number that start from opening i and leave by opening j. The standard deviation of $\hat{P}_{i\to j}$ from $P_{i\to j}$ is given by

$$\sigma P_{i\to j} = [P_{i\to j}(1-P_{i\to j})/N_i]^{\frac{1}{2}}. \tag{10}$$

DETAILS OF THE CALCULATION

The details of the calculation are illustrated by the example of the cylindrical elbow (Fig. 1). The calculation depends on two parameters, A/R and B/R, where A and B are the lengths of the pipe sections and R is the common radius. For conveniences in the calculation R is set equal to one.

The openings A and B are subdivided into equal area openings as shown in Fig. 2. The subscripts on the quantities $P_{i\to j}$ refer to the areas, as indicated. For example, $P_{3\to 7}$ is the probability for a molecule to enter opening 3 and leave by opening 7. The purpose of the subdivision is to permit a check of the calculation using Eq. (8) and to show the asymmetry of the flow.

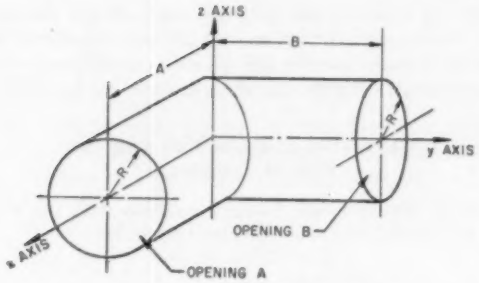

FIG. 1. Diagram of the cylindrical elbow.

Starting Coordinates

The molecules are started on the surface A, uniformly distributed over the surface with a direction distribution that is proportional to the cosine of the angle with the normal.

The starting-position coordinates are

$$\begin{aligned} x&=A \\ y&=2U_1-1 \\ z&=2U_2-1. \end{aligned} \tag{11}$$

If $y^2+z^2\geqslant 1$, two new random numbers[5] U_1 and U_2 are selected and new values of y and z computed.

The starting-direction cosines are

$$\begin{aligned} \alpha&=-\mu_3 \\ \beta&=\mu_2 \\ \gamma&=\mu_1 \end{aligned} \tag{12}$$

$$\begin{aligned} \mu_1&=\cos\varphi\,\sin\theta \\ \mu_2&=\sin\varphi\,\sin\theta, \\ \mu_3&=\cos\theta \end{aligned} \tag{13}$$

where

$$\sin\varphi=[2(2U_1-1)U_2]/[(2U_1-1)^2+U_2^2]$$
$$\cos\varphi=[(2U_1-1)^2-U_2^2]/[(2U_1-1)^2+U_2^2].$$

If $(2U_1-1)^2+U_2^2\geqslant 1$, two new random numbers are selected:

$$\begin{aligned} \cos\theta&=U_3 \quad \text{if} \quad U_3\geqslant U_4 \\ \sin\theta&=(1-\cos^2\theta)^{\frac{1}{2}}. \end{aligned} \tag{14}$$

If $U_3<U_4$, two new random numbers are selected.

Equations (13) and (14) give random-direction cosines that obey the cosine law with respect to the z axis. Equation (12) rotates the z axis into the negative x axis.

The index number i in $P_{i\to j}$ is calculated from the coordinates x, y, z using Eq. (32).

[5] Throughout the report, U, U_1, U_2, $\cdots$ denote random variables independently and uniformly distributed in the interval (0,1).

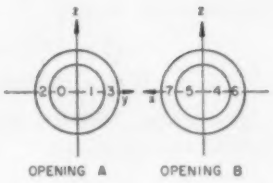

FIG. 2. Subdivision of the openings A and B.

First-Distance Calculations

The next calculation is to find whether the molecule has a collision with the wall of cylinder A or crosses into cylinder B. The plane $x=y$ separates the two cylinders. To find which of the two cases occurs, the distances to cylinder A and to the plane are calculated and compared. The shorter distance determines which of the two cases has occurred:

$$S_1=-Q/P+[(Q/P)^2-R/P]^{\frac{1}{2}}, \tag{15}$$

where

$$\begin{aligned} P&=\beta^2+\gamma^2 \\ Q&=\beta y+\gamma z \\ R&=y^2+z^2-1. \end{aligned}$$

The distance S_2 to the plane is

$$S_2=\begin{cases} (x-y)/(\beta-\alpha) & \text{if positive} \\ S_m & \text{if negative.}[6] \end{cases} \tag{16}$$

If $S_1\leqslant S_2$, then a wall collision with cylinder A occurs and the distance to the collision is

$$S=S_1. \tag{17}$$

If $S_2<S_1$, the molecule crosses into cylinder B.

If the molecule has a collision with the wall, the coordinates of the collision point are calculated. These are

$$\begin{aligned} x_1&=x_0+\alpha S \\ y_1&=y_0+\beta S \\ z_1&=z_0+\gamma S. \end{aligned} \tag{18}$$

Distance Calculation When a Molecule Goes from One Cylinder to the Other Cylinder

If the molecule is in cylinder A and crosses to cylinder B, the distance S_3 to cylinder B and the distance S_4 to opening B are calculated and compared. If the molecule is in cylinder B and crosses to cylinder A, the distance S_1 to cylinder A and the distance S_0 to opening A are calculated and compared. The smaller of the two distances determines which event occurs.

The cylinder in which the molecule is located is

[6] If any of the distances is negative, it is set equal to a number S_m, where S_m is a distance larger than any dimension of the pipe. Since the least distance determines which event occurs, this device is justified.

determined by the test:

$$\begin{aligned} &\text{If } x \gtrless y, \text{ the molecule is in } A. \\ &\text{If } x < y, \text{ the molecule is in } B. \end{aligned} \tag{19}$$

The distances when a molecule crosses from one cylinder to another are:

$$S_0 = \begin{cases} (A-x)/\alpha & \text{if positive} \\ S_m & \text{if negative,} \end{cases} \tag{20}$$

$$S_1 = -Q/P + [(Q/P)^2 - R/P]^{\frac{1}{2}}, \tag{21}$$

where

$$\begin{aligned} P &= \beta^2 + \gamma^2 \\ Q &= \beta y + \gamma z \\ R &= y^2 + z^2 - 1, \\ S_2 &= -Q/P + [(Q/P)^2 - R/P]^{\frac{1}{2}}, \end{aligned} \tag{22}$$

where

$$\begin{aligned} P &= \alpha^2 + \gamma^2 \\ Q &= \alpha x + \gamma z \\ R &= x^2 + y^2 - 1, \end{aligned}$$

and

$$S_4 = \begin{cases} (B-y)/\beta & \text{if positive} \\ S_m & \text{if negative.} \end{cases} \tag{23}$$

If the distance to an opening is less than the distance to the cylinder, the molecule escapes through the opening. The statistics calculation is made. If the distance to the cylinder is less, a wall-collision calculation is made. In both cases the new position coordinates on the plane or the cylinder wall are calculated by Eq. (18).

Calculation at a Collision with the Wall of Cylinder *A*

When the molecule makes a collision with the wall of cylinder A, the new direction cosines are

$$\begin{aligned} \alpha &= -\mu_2 \\ \beta &= (-z\mu_1 - y\mu_3)/(y^2+z^2)^{\frac{1}{2}} \\ \gamma &= (y\mu_1 - z\mu_3)/(y^2+z^2)^{\frac{1}{2}}, \end{aligned} \tag{24}$$

where μ_1, μ_2, μ_3 are given by Eqs. (13) and (14), and y, z are the coordinates of the collision point.

The next calculation is to determine whether the molecule has another collision with the wall, hits opening A, or enters cylinder B. This decision is made by comparing the distances S_0, S_1, and S_2 as before.

These distances are

$$S_0 = \begin{cases} (A-x)/\alpha & \text{if positive} \\ S_m & \text{if negative,} \end{cases} \tag{25}$$

$$S_1 = -2Q/P, \tag{26}$$

where

$$\begin{aligned} P &= \beta^2 + \gamma^2 \\ Q &= \beta y + \gamma z, \end{aligned}$$

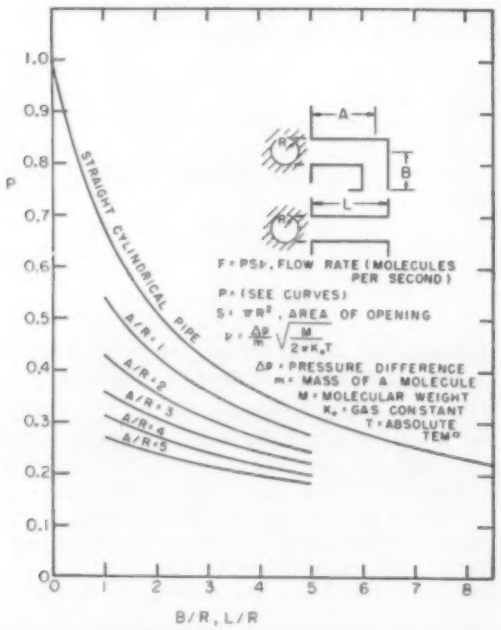

FIG. 3. Molecular flow rate in a 90° cylindrical elbow calculated by the Monte Carlo method, and in a straight cylindrical pipe calculated by Clausing.[2]

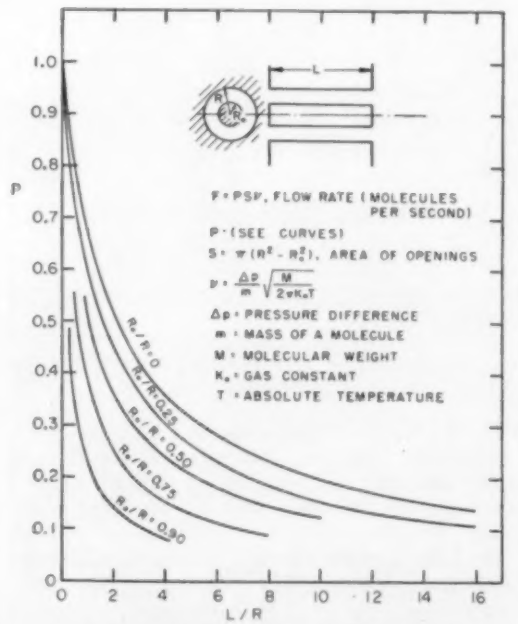

FIG. 4. Molecular flow rate in a cylindrical annulus.

and

$$S_2=\begin{cases}(x-y)/(\beta-\alpha) & \text{if positive}\\ S_m & \text{if negative.}\end{cases} \tag{27}$$

If S_0 or S_1 is least, the new position coordinates are calculated by Eq. (18). If S_2 is least, the calculation for crossing from one cylinder to the other is made.

Calculation at a Collision with the Wall of Cylinder *B*

When the molecule makes a collision with the wall of cylinder B, the new direction cosines are

$$\begin{aligned}\alpha&=(-z\mu_1-x\mu_3)/(x^2+z^2)^{\frac{1}{2}}\\ \beta&=\mu_2\\ \gamma&=(x\mu_1-z\mu_3)/(x^2+z^2)^{\frac{1}{2}},\end{aligned} \tag{28}$$

where μ_1, μ_2, μ_3, are given by Eqs. (13) and (14), and x, z are coordinates of the collision point.

As before, the next calculation is to determine whether the molecule has another collision with the wall, hits the opening B, or enters cylinder A. This decision is made by comparing the distances S_2, S_3, and S_4. These distances are

$$S_2=\begin{cases}(x-y)/(\beta-\alpha) & \text{if positive}\\ S_m & \text{if negative,}\end{cases} \tag{29}$$

$$S_3=-2Q/P, \tag{30}$$

where

$$P=\alpha^2+\gamma^2$$

$$Q=\alpha x+\gamma z,$$

$$S_4=\begin{cases}(B-y)/\beta & \text{if positive}\\ S_m & \text{if negative.}\end{cases} \tag{31}$$

If S_2 or S_4 is least, the new position coordinates are calculated by Eq. (18). If S_2 is least, the calculation for crossing from one cylinder to the other is made.

Statistics Calculation

The statistics calculation is made when an opening is reached.

The first calculation to be made is the calculation of the index j for $P_{i\to j}$ (see Fig. 2). If the opening is A, i.e., $x>y$, then

$$j=2L+m, \tag{32}$$

where

$$m=\begin{cases}0 & \text{if } y\leqslant 0\\ 1 & \text{if } y>0\end{cases}$$

If the opening is B, i.e., $y>x$, then

$$j=4+2L+m, \tag{33}$$

where

$$m=\begin{cases}0 & \text{if } x\leqslant 0\\ 1 & \text{if } x>0\end{cases}$$

L = greatest integer less than $2(x^2+z^2)$.

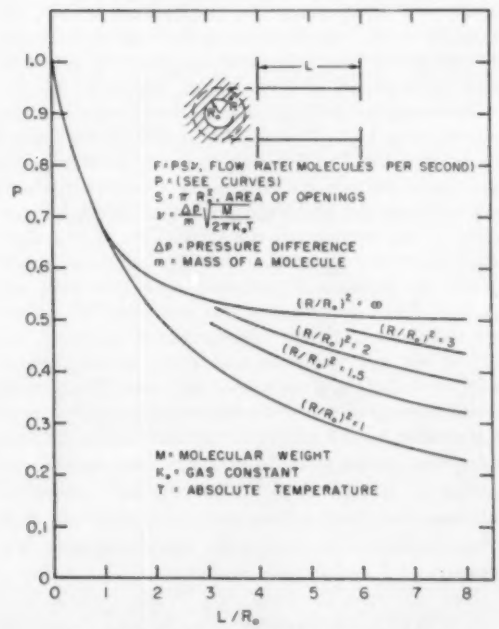

FIG. 5. Molecular flow rate in a cylindrical pipe with restricted openings.

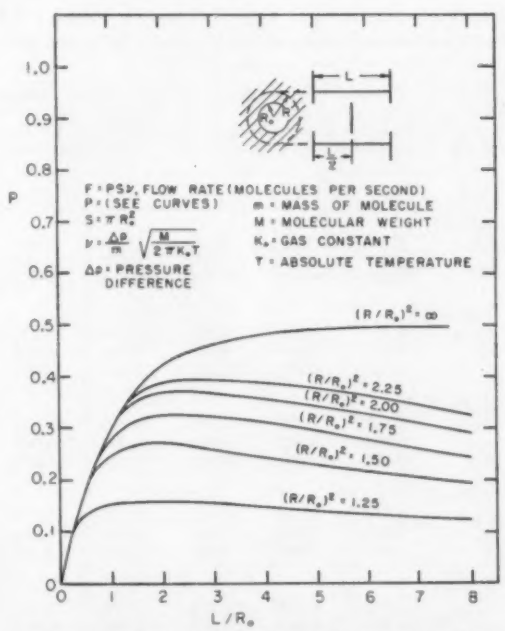

FIG. 6. Molecular flow rate in a cylindrical pipe with restricted openings and a central blocking plate.

TABLE I. Values of P for cylindrical pipes. P_c are values of P calculated by Clausing[3]; P_M are Monte Carlo estimates; L is the length of the cylinder; R is the radius; σ_{P_M} is the standard deviation of P_M; N is the sample size.

L/R	P_c	P_M	σ_{P_M}	N	L/R	P_c	P_M	σ_{P_M}	N	L/R	P_c
0.0	1.0000				1.8	0.5384				9	0.2131
0.1	0.9524				1.9	0.5256				10	0.1973
0.2	0.9092				2.0	0.5136	0.522	0.005	12001	12	0.1719
0.3	0.8699				2.2	0.4914				14	0.1523
0.4	0.8341				2.4	0.4711				16	0.1367
0.5	0.8013	0.804	0.009	2000	2.5		0.460	0.011	2000	18	0.1240
0.6	0.7711				2.6	0.4527				20	0.1135
0.7	0.7434				2.8	0.4359				30	0.0797
0.8	0.7177				3.0	0.4205	0.425	0.005	10001	40	0.0613
0.9	0.6940				3.2	0.4062				50	0.0499
1.0	0.6720	0.678	0.004	11975	3.4	0.3931				60	0.0420
1.1	0.6514				3.6	0.3809				70	0.0363
1.2	0.6320				3.8	0.3695				80	0.0319
1.3	0.6139				4.0	0.3589	0.361	0.005	10001	90	0.0285
1.4	0.5970				5.0	0.3146	0.315	0.005	10001	100	0.0258
1.5	0.5810	0.571	0.011	2000	6.0	0.2807				1000	0.002658
1.6	0.5659				7.0	0.2537					$8R/3L$
1.7	0.5518				8.0	0.2316					

One is added to the counts N_i and $N_{i\to j}$. Another molecule is generated if the total number of molecules generated is less than a preassigned number. Otherwise, the estimates in Eqs. (9) and (10) are made and the calculation concluded.

In the actual calculations where values of $P_{i\to j}$ for several values of B are wanted, the calculation is continued with a new and larger value of B. In this way several problems are computed simultaneously.

RESULTS

The results of the calculations for pipes of various shapes are presented in Figs. 3–6 and in Tables I–VI. In each figure a drawing of the pipe with the dimensions pertinent to the flow rate through the pipe is given. Also given in each figure is the equation for the flow rate in terms of the probability P for a molecule to enter one opening and to leave by the other. The flow-rate equations are appropriate where the pipe is a connector between two large tanks containing a Maxwellian gas with a pressure difference Δp between the tanks, and the highest pressure in either of the tanks is sufficiently low so that the effect of intermolecular collisions in the pipe can be neglected. The graphs in the figures present P vs one of the geometrical parameters of the pipe.

TABLE II. Values of P for a cylindrical elbow. R is the common radius; A is the length of the cylinder on the source side of the elbow; B is the length of the cylinder on the sink side of the elbow (see Fig. 1); σ_p is the standard deviation of P; N is the sample size.

B/R	1	2	3	4	5
$A/R=1$					
$P_{A\to B}$	0.541	0.429	0.359	0.308	0.275
σ_p	0.005	0.005	0.005	0.005	0.004
N	10 001	10 001	10 001	10 001	10 001
$A/R=2$					
$P_{A\to B}$	0.427	0.357	0.305	0.272	0.240
σ_p	0.005	0.005	0.005	0.004	0.004
N	10 001	10 001	10 001	10 001	10 001
$A/R=3$					
$P_{A\to B}$	0.360	0.308	0.272	0.245	0.222
σ_p	0.005	0.005	0.004	0.004	0.004
N	10 001	10 001	10 001	10 001	10 001
$A/R=4$					
$P_{A\to B}$	0.314	0.273	0.241	0.271	0.197
σ_p	0.005	0.005	0.005	0.004	0.004
N	8397	8397	8397	8397	8397
$A/R=5$					
$P_{A\to B}$	0.271	0.239	0.215	0.197	0.183
σ_p	0.005	0.005	0.005	0.004	0.004
N	7837	7837	7837	7837	7837

The tables contain the Monte Carlo estimates of the values of P from which the graphs were drawn. The standard deviations of the estimates and sample sizes are also given. The errors in the estimates P are of the order of magnitude of the standard deviations σ_p.

The estimates of P and the standard deviations were calculated by Eqs. (9) and (10), except for the cases in which the radius R of the outer cylinder was infinite. For these cases, the assumption was made that after several wall collisions the probability of a molecule leaving by either of the openings is the same. The Monte Carlo molecule-history generation was the same as before, except the number of collisions with the walls was counted. After six or seven wall collisions the history was terminated. Every odd-numbered molecule was allowed six wall collisions and every even-numbered molecule was allowed seven wall collisions. The alternation of number of collisions was made because after an even number of wall collisions, the molecule has to make at least one more wall collision before it can leave by the opening it started from. After an odd number of collisions, the molecule has to make at least one more collision before it can leave by the opposite opening. The estimates of P and σ_p were made by

$$P=(0.5N_T+N_{1\to 2})/N \tag{34}$$

$$\sigma_p=\{[(0.25N_T/N)+(N_{1\to 2}/N)-P^2]/N\}^{\frac{1}{2}}, \tag{35}$$

TABLE III. Values of P for a cylindrical annulus. R is the radius of outer cylinder; R_0 is the radius of the inner cylinder; L is the length of the cylinders; σ_p is the standard deviation of P; N is the sample size.

$R_0/R=0.25$											
L/R	1.0	2.0	3.0	4.0	5.0	6.0	7.0	8.0	10.0	12.0	14.0	16.0
P	0.605	0.449	0.362	0.304	0.260	0.233	0.205	0.185	0.154	0.134	0.118	0.101
σ_p	0.007	0.007	0.007	0.006	0.006	0.006	0.006	0.006	0.010	0.010	0.009	0.008
N	5000	5000	5000	5000	5000	5000	5000	5000	1268	1268	1268	1268

$R_0/R=0.50$										
L/R	1.0	2.0	3.0	4.0	5.0	6.0	7.0	8.0	9.0	10.0
P	0.524	0.360	0.289	0.238	0.203	0.177	0.162	0.146	0.136	0.124
σ_p	0.007	0.007	0.006	0.006	0.006	0.012	0.011	0.011	0.010	0.010
N	5000	5000	5000	5000	5000	1070	1070	1070	1070	1070

$R_0/R=0.75$										
L/R	0.5	1.0	1.5	2.0	2.5	3.0	4.0	5.0	6.0	8.0
P	0.541	0.388	0.305	0.252	0.217	0.193	0.145	0.128	0.115	0.086
σ_p	0.007	0.007	0.007	0.006	0.006	0.006	0.011	0.010	0.010	0.009
N	5000	5000	5000	5000	5000	5000	1029	1029	1029	1029

$R_0/R=0.90$											
L/R	0.25	0.50	0.75	1.00	1.25	1.50	2.00	2.50	3.00	3.50	4.00
P	0.488	0.351	0.279	0.230	0.197	0.173	0.144	0.123	0.102	0.094	0.083
σ_p	0.007	0.007	0.006	0.006	0.006	0.005	0.008	0.008	0.007	0.007	0.006
N	5000	5000	5000	5000	5000	5000	1879	1879	1879	1879	1879

where N_T/N is the fraction of molecules that do not reach either of the openings, $N_{1\to 2}/N$ is the fraction that start at one opening and reach the other, and N is the total number of molecule histories.

Table VI illustrates the asymmetry in the flow through the cylindrical elbow. This table gives the values of the probabilities $P_{i\to j}$ for a molecule entering the ith opening to leave by the jth opening. The numbering of the openings and their relationship to the elbow are given in Figs. 1 and 2. All the openings have equal area.

The $P_{i\to j}$ table provides a check for the calculation. If the pressure at both ends of the elbow is the same, then the probability of a molecule entering any one of

TABLE IV. Values of P for a cylindrical pipe with the openings at both ends restricted. The openings are circular and coaxial with the cylinder. R is the radius of the cylinder; R_0 is the radius of both openings; L is the length of the cylinder; σ_p is the standard deviation of P; N is the sample size.

$(R/R_0)^2=1.5$			
L/R_0	4	6	8
P	0.449	0.369	0.324
σ_p	0.007	0.007	0.007
N	5000	5000	5000

$(R/R_0)^2=2.0$			
L/R_0	4	6	8
P	0.491	0.426	0.377
σ_p	0.007	0.007	0.007
N	5000	5000	5000

$(R/R_0)^2=3.0$			
L/R_0		6	8
P		0.478	0.437
σ_p		0.008	0.009
N		3889	3182

$(R/R_0)^2=\infty$				
L/R_0	1	2	4	6
P	0.667	0.575	0.521	0.510
σ_p	0.005	0.004	0.002	0.0015
N	5000	5000	4983	5000

TABLE V. Values of P for a cylindrical pipe with the openings at both ends restricted and with a central plate to block the direct beam between openings. R is the radius of the cylinder; R_0 is the radius of both openings and the blocking plate; L is the length of the cylinder. The openings, the blocking plate, and the cylinder are coaxial; σ_p is the standard deviation; N is the sample size.

$(R/R_0)^2$ \ L/R_0		1.0	2.0	3.0	4.0	6.0	8.0
1.25	P	0.153	0.160	0.157	0.147	0.134	0.125
	σ_p	0.005	0.005	0.005	0.005	0.005	0.005
	N	5000	5000	5000	5000	5000	5000
1.50	P	0.247	0.273	0.256	0.235	0.220	0.195
	σ_p	0.006	0.006	0.006	0.006	0.006	0.006
	N	5000	5000	5000	5000	5000	4323
1.75	P	0.277	0.326	0.320	0.314	0.278	0.245
	σ_p	0.006	0.007	0.007	0.007	0.006	0.006
	N	5000	5000	5000	5000	5000	5000
2.00	P	0.300	0.370	0.366	0.357	0.336	0.289
	σ_p	0.006	0.007	0.007	0.007	0.008	0.007
	N	5000	5000	5000	5000	3355	4152
2.25	P	···	0.388	0.393	0.385	0.363	0.322
	σ_p	···	0.007	0.007	0.011	0.007	0.008
	N	···	5000	5000	2043	5000	3079
∞	P	0.294	0.423	···	0.483	0.4945	···
	σ_p	0.004	0.003	···	0.002	0.0009	···
	N	5000	5000	···	5000	5000	···

TABLE VI. Values of $P_{i\to j}$ for subdivisions (see Fig. 2) of the openings of the cylindrical elbow to illustrate the asymmetry of the flow. The subdivisions have equal area. $A/R=1$; $B/R=2$. $\sigma_{P_{i\to j}}$ are standard deviations.

$P_{i\to j}$ i \ j	1	2	3	4	5	6	7	8	$\sum_i P_{i\to j}$
1	0.155	0.140	0.154	0.131	0.120	0.110	0.100	0.099	1.01
2	0.130	0.138	0.127	0.137	0.127	0.132	0.115	0.103	1.01
3	0.150	0.111	0.237	0.112	0.093	0.102	0.091	0.093	0.99
4	0.122	0.141	0.109	0.191	0.121	0.107	0.101	0.095	0.99
5	0.114	0.137	0.100	0.118	0.143	0.132	0.144	0.112	1.00
6	0.121	0.117	0.107	0.116	0.141	0.157	0.113	0.159	1.03
7	0.109	0.118	0.088	0.111	0.136	0.114	0.217	0.106	1.00
8	0.099	0.098	0.078	0.084	0.119	0.146	0.119	0.233	0.98

$\sigma_{P_{i\to j}}$ i \ j	1	2	3	4	5	6	7	8	
1	0.008	0.007	0.008	0.007	0.007	0.006	0.006	0.006	0.02
2	0.007	0.007	0.007	0.007	0.007	0.007	0.007	0.006	0.02
3	0.008	0.007	0.009	0.007	0.006	0.006	0.006	0.006	0.02
4	0.007	0.007	0.006	0.009	0.007	0.006	0.006	0.006	0.02
5	0.007	0.007	0.006	0.007	0.007	0.007	0.007	0.007	0.02
6	0.007	0.007	0.006	0.007	0.007	0.008	0.007	0.008	0.02
7	0.006	0.007	0.006	0.007	0.007	0.007	0.009	0.006	0.02
8	0.006	0.006	0.006	0.006	0.007	0.007	0.007	0.009	0.02

the openings is proportional to the area of the opening. Also, the probability of a molecule leaving by an opening is proportional to the area of the opening. Therefore,

$$\sum_{i=1}^{8} A_i P_{i\to j} = A_j, \tag{36}$$

and because $A_i = A_j$,

$$\sum_{i=1}^{8} P_{i\to j} = 1.00. \tag{37}$$

The sums $\sum_{i=1} P_{i\to j}$ are given in the last column of Table VI. The values are equal to 1.00, within the accuracy of the calculation.

ACKNOWLEDGMENTS

I would like to thank Mark Z. Brown, who did all the coding on the IBM 709 for the problem, and Donald Reeves, who helped with the checking of the code. I would also like to thank Norman Milleron, Lenard Levenson, and Ray E. Kidder for their assistance and encouragement.

JOURNAL OF APPLIED PHYSICS VOLUME 31, NUMBER 7 JULY, 1960

Transport Equation for the Spectral Density of a Multiple-Scattered Electromagnetic Field*

DIMITRI S. BUGNOLO

Department of Electrical Engineering, Columbia University, New York 27, New York

(Received October 16, 1959; and in final form February 11, 1960)

The use of a first Born approximation is open to question when the path length is greater than a mean free path in the scattering region. It is therefore of interest to develop a transport equation capable of predicting the spectral density for such cases. The general theory presented in this paper is applied to the case of multiple scattering by dielectric noise. It is independent of models for the dielectric fluctuations. A method of solution is developed for the case of forward scattering. The particular case of a monochromatic plane wave incident of a half space is discussed in detail. The results are applied to a numerical example in the troposphere.

1. INTRODUCTION

THE propagation of electromagnetic waves in regions containing dielectric noise has received considerable attention in the past decade. Bergmann in 1946[1] noted that "the most important non-solid media of propagation, the atmosphere and the ocean, are known to possess a rapidly changing random structure." He proceeded to find the solution for the mean squared field on the assumption that the high-frequency (WBKJ) approximation was applicable.

The accumulation of a great deal of experimental data and its publication in 1948 caused K. A. Norton to postulate the existence of a tropospheric field due to scattering by small variations in the refractive index of the atmosphere.[2] The early theoretical work due to Bergmann[1] was then followed in 1950 by Booker and Gordon's theory of scattering by the troposphere.[3] For a detailed historical summary of the problem to date the reader is referred to the paper by Bullington[4] and a recent paper by Staras and Wheelon[5] and another by Wheelon.[6]

Some recent experimental studies of tropospheric

* This research was supported in whole or in part by a United States Air Force contract, monitored by the Air Force Office of Scientific Research of the Air Research and Development Command. Publication was assisted by the Marcellus Hartley Fund.

[1] P. G. Bergmann, Phys. Rev. **10**, 486 (1946).

[2] K. A. Norton, Advances in Electronics, **1**, 391 (1948).

[3] H. G. Booker and W. E. Gordon, Proc. Inst. Radio Engrs. **38**, 401 (1950).

[4] K. Bullington, Proc. Instr. Radio Engrs. **43**, 1175 (1955).

[5] H. Staras and A. D. Wheelon, IRE Trans. on Antennas and Propagation, **AP-7**, 80 (1959).

[6] A. D. Wheelon, J. Research Nat. Bur. Standards, **63-D**, No. 2, 205 (1959).

scatter links indicate that the stochastic process involved is not stationary.[7] This was previously suspected by Bolgiano who sought to explain the possible causes by constructing a new model for atmospheric turbulence.[8] In a recent paper Norton concluded that the basic transmission loss is a statistically stationary random process.[9]

The majority of theoretical efforts to date[3,5,7–15] have been restricted to a solution for the scattered field in the special case of a monochromatic source. In a recent paper[16] the writer has shown that a first approximation for the Fourier transformation is tacitly assumed. It was also shown that this approximation can be used to characterize the field problem by a time variable transfer tensor. This analogy permitted an extension to the more general case of arbitrary sources.

All theoretical efforts reduce, in effect, to the solution of a vector wave equation with time variable coefficients. As in the case of the Schroedinger equation,[17] the vector equation is reduced to an integral equation for scattering. The usual iteration—perturbation solution can then be used. Unfortunately the complexity of the result has limited considerations to the first Born approximation. This assumes that every part of the scattering region "sees" the unperturbed incident wave, or in other words, that any ray of the incident field is scattered at most once.

The scattering cross section as given by the first Born approximation and the resulting mean free path can be used as a measure of reliability for the "single scatter" results. For example, it will be shown that the mean free path in the troposphere at a frequency of 1 kmc is on the order of 5 000 km under normal conditions while it can be as small as we please in the ionosphere.[18] It can also be shown that the mean free path in the troposphere will decrease as the square of frequency in the radio spectrum. From this it is evident that multiple scattering effects should be of importance at very high frequencies in the troposphere and in the vicinity of critical frequency in the ionosphere. This has also been noted by Feshbach in a letter to Wheelon.[5]

It is well known that the mean squared value of a multiple scattered field can be obtained as a solution of the transport equation for the photon distribution function.[17] This has been applied to the special case of scattering by dielectric noise.[18] This paper is concerned with the derivation and solution of a spectral transport equation. Such an equation can be used to study the effects of multiple scattering on the spectral density of an electromagnetic field given the spectral density of the source.

The particular case of a monochromatic plane wave incident on a turbulent half space is discussed in detail. We would expect the spectrum to spread more and more as the field penetrates further into the scattering region. It will be shown that the spectral distribution is Gaussian to a first approximation with standard deviation

$$\sigma_\omega(x,\omega_0)=(x)^{\frac{1}{2}}\int d\Omega\sigma(\theta)(\mathbf{K}\cdot\mathbf{V})^2, \tag{1.1}$$

where X is the distance of penetration in meters, $\sigma(\theta)$, the cross section per unit solid angle per unit volume for scattering, and $(\mathbf{K}\cdot\mathbf{V})$ a scalar related to the mean wind $\mathbf{V}$ and the direction of scattering. The above result is independent of any particular model for the scattering media with the constraint that the scattering be primarily forward. It should be noted that the single scatter theory predicts no such change with distance.

2. TRANSPORT EQUATION FOR THE SPECTRAL DENSITY

It is well known that the total energy density of the electromagnetic field U can be related to N_ω, the number of photons per unit volume in a frequency band $(\omega, \omega+d\omega)$, by the integral

$$U=\int U_\omega d\omega=\hbar\int\omega N_\omega d\omega, \tag{2.1}$$

where $\hbar$ = Plancks constant. It is also possible to define a probability density function for the photon distribution in positional velocity space such that expectation of N_ω

$$\langle N_\omega(\mathbf{r})\rangle=\int f_\omega(\mathbf{r},\mathbf{v})dV_v, \tag{2.2}$$

where $\mathbf{v}$ is the velocity vector and dV_v signifies integration over all velocity space. By substituting for N_ω in (2.1) we have for the total energy density of the field,

$$\langle U(\mathbf{r})\rangle=\left\langle\int U_\omega d\omega\right\rangle=\hbar\int d\omega\int\omega f_\omega dV_v. \tag{2.3}$$

From this it is evident that the spectrum of the energy

[7] R. G. Finney, Proc. I.R.E. **47**, 84 (1959).
[8] R. Bolgiamo, Jr., Cornell University Research Report EE 385, (1958).
[9] Kenneth A. Norton, Memorandum Report PM-83-21, National Bureau of Standards.
[10] "Scatter Propagation Issue," Proc. I.R.E. **43**, (1955).
[11] Osamu Trikizi, IRE Trans. on Antennas and Propagation, **AP-5**, 130 (1957).
[12] Martin Balser, IRE Trans. on Antennas and Propagation **AP-5**, pp. 383 (1957).
[13] David Paul, IRE Trans. on Antennas and Propagation, **AP-6**, 61 (1950).
[14] S. Steiñ, IRE Trans. on Antennas and Propagation, **AP-6**, p. 299 (1958).
[15] Richard Silverman, Proc. Cambridge Phil. Soc. **54**, Part 4, 530 (1958).
[16] D. S. Bugnolo, IRE Trans. on Antennas and Propagation, **AP-7**, 137 (1959).
[17] P. M. Morse and H. Feshbach, *Methods of Theoretical Physics*, (McGraw-Hill Book Company, Inc., 1953).
[18] D. S. Bugnolo, "Multiple Scattering of E. M. Waves and the Transport Equation for Photon Diffusion," Joint Meeting URSI-IRE, April, 1958, Washington, D. C.

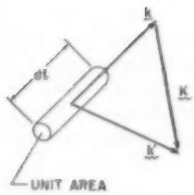

FIG. 1. Differential volume, $\mathbf{k}$-wave number of the incident field, $\mathbf{k}'$-wave number of the scattered field.

density $\mathfrak{v}_\omega$ is given by

$$\langle U_\omega(\mathbf{r})\rangle=\hbar\int\omega f_\omega dV_v. \tag{2.4}$$

It is convenient at this point to define a spectral density function $S(\mathbf{r},\mathbf{v},\omega)$ such that

$$S(\mathbf{r},\mathbf{v},\omega)=\omega f_\omega(\mathbf{r},\mathbf{v}). \tag{2.5}$$

The remainder of this section will be devoted to the construction of a transport equation for this spectral density function.

On substituting the above definition into (2.3) it follows that

$$\langle U(\mathbf{r})\rangle=\hbar\int d\omega\int dV_v S. \tag{2.6}$$

Accordingly, Poynting's vector can also be related to the spectral density function S by

$$\langle\mathbf{P}(\mathbf{r})\rangle=\hbar\int d\omega\int\mathbf{v}S dV_v. \tag{2.7}$$

Consider an element of volume of unit area and length dl as illustrated by Fig. 1. In the absence of scattering or absorption, Maxwell's equations yield

$$\nabla\cdot\mathbf{P}dV=-(\partial U/\partial t)dV. \tag{2.8}$$

From this equation, under the condition that the electromagnetic field constitutes a strictly stationary random process, one obtains

$$\langle\nabla\cdot\mathbf{P}\rangle=-\langle\partial U/\partial t\rangle,$$

where $\langle\partial U/\partial t\rangle=\langle\partial/\partial t\rangle\langle U\rangle=0$. Consequently, $\langle\nabla\cdot\mathbf{P}\rangle=0$. Furthermore, since $\langle\nabla\cdot\mathbf{P}\rangle=\nabla\cdot\langle\mathbf{P}\rangle$, it follows from (2.7) that

$$\nabla\cdot\int d\omega\int dV_v\mathbf{v}S=\int d\omega\int dV_v\mathbf{v}\cdot\nabla S=0.$$

Since the integrand is positive definite, we have

$$v\cdot\nabla S=0. \tag{2.9}$$

From the definition of the gradient this implies that the maximum rate of change of the spectral density is normal to the direction of propagation of the electromagnetic field in the absence of scattering. In the presence of scattering the above result must be modified. Let $\Gamma(\omega,\omega'|\mathbf{v},\mathbf{v}')d\omega dV_v\equiv$ the probability that a photon located at ω', v' is scattered into the range $(\omega+d\omega)$, $(\mathbf{v}+d\mathbf{v})$ per unit volume. It therefore follows that (2.9) must be modified by

$$\hat{v}\cdot\nabla S=\int\Gamma(\omega,\omega'|\mathbf{v},\mathbf{v}')S(\mathbf{r},\omega',\mathbf{v}')d\omega' dV_v'. \tag{2.10}$$

Some of the photons will also be scattered *out* of the position $(\omega,\mathbf{v})$. This must be subtracted, yielding a transport equation for the spectral density.

$$\hat{v}\cdot\nabla S=\int\Gamma(\omega,\omega'|\mathbf{v},\mathbf{v}')S(\mathbf{r},\omega',\mathbf{v}')d\omega' dV_v'-\int Q_T S(\mathbf{r},\omega')d\omega', \tag{2.11}$$

where

$$Q_T\equiv\frac{1}{2\pi}\int\exp[-j(\omega-\omega')\tau]d\tau\int d\Omega\sigma(\mathbf{K},0).$$

The probability function Γ can be related to the usual cross section per unit volume per unit solid angle as obtained by the first Born approximation for the scattered field. From[6] we have

$$\sigma(\mathbf{K},\tau)=\frac{\pi^2}{\lambda^4}\sin^2\gamma\int\exp[-j\mathbf{K}\cdot\mathbf{r}]R(\mathbf{r},\tau)d\mathbf{r}, \tag{2.12}$$

where $R(\mathbf{r},\tau)$ is the space-time correlation function for the dielectric noise. And where $\mathbf{K}=\mathbf{k}-\mathbf{k}'$ as illustrated by Fig. 1. Let

$$\Gamma(\omega,\omega'|\mathbf{v},\mathbf{v}')\equiv\frac{1}{2\pi}\int\sigma(\mathbf{K},\tau)\exp[-j(\omega-\omega')\tau]d\tau. \tag{2.13}$$

[This should be divided by the cross section $\sigma(\theta)$ if normalization is required. See (3.2)]. The change in notation follows directly since $\mathbf{v}$ and $\mathbf{k}$ are codirected. Let $\hat{k}$ be a unit vector in the k direction. Then,

$$\mathbf{v}=\hat{k}v;\quad\mathbf{k}=\hat{k}\omega/v.$$

It should be noted that the above results are quite general in that they only assume a strictly stationary electromagnetic field. An extension to the nonstationary case is possible and will be considered at a later date.

3. SOLUTION OF THE SPECTRAL TRANSPORT EQUATION IN DIELECTRIC NOISE

In general, the method of solution will depend on the form of the spectral cross section. In the troposphere and ionosphere, the usual form is, predominantly, small angle. This is in contrast to the *Milne problem*, which assumes isotropic scattering. The *spectral density* for the *Milne problem* will be discussed at a later date.

In the case of small angle scattering, it is possible to reduce the transport equation to a partial differential equation.

Let us consider the case of a source radiating into a semi-infinite half space characterized by the spectral cross section Γ. (See Fig. 2). It is evident that the spectral density as measured by an observer within the half space will depend on the distance of penetration X and the directional angle θ. The spectral transport equation (2.12) reduces to

$$\mu\frac{\partial S}{\partial x}=\int d\Omega' d\omega' \Gamma(\omega,\omega'|\theta,\theta')S(x,\theta',\omega')-\int Q_T S d\omega'. \quad (3.1)$$

From the definition of the spectral cross section as given by Eq. (2.13) and the relationship between the cross section and the time space correlation function (2.11), it follows that

$$\Gamma=\frac{1}{2\pi}\int_{-\infty}^{\infty}\sigma(\theta')\exp[j(\mathbf{K}'\cdot\mathbf{V})\tau]\times\exp[-j(\omega-\omega')\tau]d\tau; \quad (3.2)$$

$$\therefore \Gamma=\sigma(\theta')\delta[\omega-\omega'-\mathbf{K}'\cdot\mathbf{V}],$$

when the motion of the dielectric noise is due to a drift with the mean wind $\mathbf{V}$ alone. On substituting (3.2) into (3.1), the integration in ω' yields

$$\int_{-\infty}^{\infty}d\omega'\Gamma S=\sigma(\theta')S(x,\theta',\omega-\mathbf{K}'\cdot\mathbf{V}).$$

Consequently, the transport equation reduces to

$$\mu\frac{\partial S}{\partial x}=\int d\Omega'\sigma(\theta')S(x,\theta',\omega-\mathbf{K}'\cdot\mathbf{V})-\int Q_T S d\omega'. \quad (3.3)$$

The final integral on the R.H.S. of (3.3) is of the form

$$\int d\omega'\frac{1}{2\pi}\int d\Omega\int_{-\infty}^{\infty}\exp[-j(\omega-\omega')\tau]\sigma(\mathbf{K},0)d\tau.$$

By using the definition for the cross section per unit volume per unit solid angle this reduces to

$$\int Q_T S d\omega'=\int d\omega' S(x,\omega')\int d\Omega\sigma(\theta)\delta(\omega-\omega'), \quad (3.4)$$

$$\int Q_T S d\omega'=Q_S S(x,\theta,\omega),$$

$$Q_S=\int\sigma(\theta)d\Omega.$$

In order to reduce this to a partial differential equation it is convenient to expand the spectral density in a

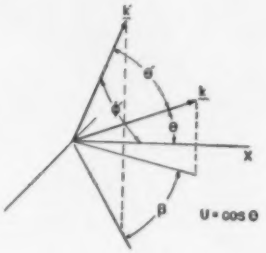

FIG. 2. Geometry for scattering.

Taylor series about the point ω

$$S(\omega-\mathbf{K}'\cdot\mathbf{V})=S(\omega)-\mathbf{K}'\cdot\mathbf{V}\frac{\partial S}{\partial\omega}+\frac{(\mathbf{K}'\cdot\mathbf{V})^2}{2}\frac{\partial^2 S}{\partial\omega^2}+\cdots\frac{(-\mathbf{K}\cdot\mathbf{V})^n}{n!}\frac{\partial^n S}{\partial\omega^n}. \quad (3.4)$$

This is necessary since $\mathbf{K}$ will in general be a function of the variable of integration Ω'. In a similar manner $S(\theta')$ can be expanded in a Taylor series about the point θ.

$$S(\theta')=S(\theta)+(\theta'-\theta)\frac{\partial S}{\partial\theta'}\bigg|_{\theta'=\theta}+\tfrac{1}{2}(\theta'-\theta)^2\frac{\partial^2 S}{\partial\theta'^2}\bigg|_{\theta'=\theta}+\cdots.$$

The notion of expanding in θ was introduced by Morse and Feshbach[17] in the solution of the transport equation of diffusion.[19] Using the condition of small angle scattering, $\theta'\ll 1$, it follows from Fig. 2 that

$$\mu'-\mu=\mu(\cos\theta'-1)-\sin\theta'(1-\mu^2)^{\frac{1}{2}}\cos\beta$$

or

$$\mu'-\mu\cong-\mu(\theta'^2/2)-\theta'(1-\mu^2)^{\frac{1}{2}}\cos\beta. \quad (3.6)$$

On substituting (3.4), (3.5), and (3.6) into (3.3) we have for the spectral density,

$$\frac{\partial S}{\partial\xi}\cong\sum_{n=1}^{N}(-1)\gamma_{2n}^2\frac{\partial^{2n}S}{\partial\omega^{2n}}+\sum_{m=0}^{M}(-1)\frac{\alpha_{2m}^2}{4}\times\left\{\frac{\partial^{2m+2}}{\partial\theta^2\partial\omega^{2m}}+\frac{1}{\theta}\frac{\partial^{2m+1}}{\partial\theta\partial\omega^{2m}}\right\}S. \quad (3.7)$$

Here θ, the distance as measured in mean free paths, is

$$\xi\equiv Q_S X=X\int d\Omega\sigma(\theta),$$

$$\alpha_{2m}^2\equiv\frac{2}{Q_S}\int d\Omega'\sigma(\theta')(1-\cos\theta')\frac{(\mathbf{K}'\cdot\mathbf{V})^{2m}}{(2m)!}, \quad (3.8)$$

$$\gamma_{2n}^2\equiv\frac{1}{Q_S}\int d\Omega'\sigma(\theta')\frac{(\mathbf{K}'\cdot\mathbf{V})^{2n}}{(2n)!}. \quad (3.9)$$

[19] See problem 12.14, pp. 1750, footnote reference 17.

A partial differential equation of this type is best solved by successive use of a Laplace, Hankel, and Fourier transformation for the ξ, θ, and ω dependence, respectively. The mechanics are left to the reader. The solution is given by

$$S(\xi,\theta,\omega)=\frac{1}{2\pi}\int_{-\infty}^{\infty}e^{j\omega s}ds\int_{0}^{\infty}J_0(g\theta)\exp\left\{\sum_{n=1}^{N}(-j)^{2n}\gamma_{2n}{}^2s^2+\sum_{m=0}^{M}(-j)^{2m}\frac{\alpha_{2m}{}^2}{4}s^{2m}g^2\right\}\xi\cdot\Psi(g,s)gdg, \quad (3.10)$$

where

$$\Psi(g,s)=\int_{-\infty}^{\infty}e^{-j\omega s}d\omega\int_{-\infty}^{\infty}s(\beta,\omega)J_0(g,\beta)\beta d\beta$$

is related to the source $s(\beta,\omega)$. This result is a complete solution of the spectral transport equation for the case of small angle scattering and band-limited inputs. In other words, the result will be reasonable if $\theta\ll 1$ and if the majority of the energy is contained within a band 2Δ such that $2\Delta\ll\omega_0$, the mean frequency.

First-Order Approximation for a Monochromatic Source

As a first order approximation of the result given by (3.10) consider the case where $n=1$, $m=0$. The integral equation reduces to:

$$S(\xi,\theta,\omega)=\frac{1}{2\pi}\int_{-\infty}^{\infty}e^{j\omega s}\exp[-\gamma_2{}^2\xi s^2]ds\int_{0}^{\infty}J_0(g\theta)\times\exp[-\alpha_0{}^2g^2\xi/4]\Psi(g,s)gdg. \quad (3.11)$$

This is a reasonable approximation since it can be shown that the ratio of [20]

$$[\alpha_{2(m+1)}{}^2/\alpha_{2m}]\cong(v/l_0)^2$$

in the troposphere when the dielectric noise is characterized by a Norton space correlation function.[9] This is noted in Sec. 4 of this paper. The same is true of γ_{2n}.

Let us further assume that the incident plane wave source is normally incident on the turbulent space. Then,

$$s(\beta,\omega)=s(\beta)/\beta\{\delta(\omega-\omega_0)+\delta(\omega+\omega_0)\}.$$

On using (3.10) it follows that

$$\Psi(g,s)=e^{-j\omega_0 s}+e^{j\omega_0 s}.$$

On substituting this into (3.11) we have for the spectral density,

$$S(\xi,\theta,\omega)=(\alpha_0{}^2\xi)^{-1}(\pi\gamma_2{}^2\theta)^{-1}\exp[-\theta^2/\alpha_0{}^2\xi]\times\exp[-(\omega-\omega_0)^2/4\gamma_2{}^2\xi], \quad (3.12)$$

for $\omega>0$. A similar expression will result for negative frequencies. It is of interest to note that the first approximation implies that the distribution in θ and ω are statistically independent. This would not be the case if the α_2 term must be included.

From (3.12) it is evident that the spectral density is normally distributed in ω with standard deviation

$$\sigma_\omega\cong(2\gamma_2{}^2\xi)^{\frac{1}{2}}=(x)^{\frac{1}{2}}\int d\Omega\sigma(\theta)(\mathbf{K}\cdot\mathbf{V})^2, \quad (3.13)$$

with the mean, $m=\omega_0$.

Note that the deviation of the spectrum increases with the depth of penetration.

Comparison to the Solution of the Transport Equation of Diffusion.

As a check of the previous results, it is convenient to compare the photon probability density function so obtained to the usual solution of the transport equation for the photon distribution function. This transport equation is considered in detail by Morse and Feshbach.[21] This is defined such that

$$\langle\mathbf{P}(\mathbf{r})\rangle=\hbar\int\mathbf{v}f_M(\mathbf{r},\mathbf{v})dV_v$$

A comparison of this to Eq. (2.7) yields

$$f_M(\mathbf{r},\mathbf{v})=\int d\omega S(\mathbf{r},\mathbf{v},\omega).$$

On substituting for the spectral density from Eq. (3.12), we have

$$f_M(\mathbf{r},\theta)=2/\alpha_0{}^2\xi\exp[-\theta^2/\alpha_0{}^2\xi].$$

This is indeed the solution given by Morse and Feshbach as can be verified by taking $K=1$ (no absorption) and $\phi=0$, (normal incidence) in the result given by problem 12.14 of this reference.

As a further and final check, it should be noted that the integration of the spectral transport equation (2.11) over ω yields the transport equation for the density function as given by Morse and Feshbach.

4. APPLICATION TO SCATTERING IN THE TROPOSPHERE

The application of the multiple scatter theory to the troposphere requires a model for the dielectric noise. This paper will be limited to a class of best possible models as noted by Norton.[9]

$$R(\mathbf{r})=2^{(1-\mu)}/\Gamma(\mu)(r/l_0)^\mu K_\mu(r/l_0), \quad (4.1)$$

where K_μ is a modified Hankel Function.

It should be noted that the usual exponential space correlation function is a special case of (4.1) for $\mu=\frac{1}{2}$.

[20] l_0 is mean blob size.

[21] See p. 180 and problem 21.14 on p. 1750, footnote reference 17.

A. Cross Section Per Unit Volume Per Unit Solid Angle

This can be obtained by direct integration using Eq. (2.12) or by substitution into the well-known result for the space-wise spectrum, S. Under the assumption of a homogeneous isotropic space correlation model moving with the mean wind V we have[22,23]

$$\sigma(\mathbf{K},\tau)=(\pi^2/\lambda^4)S\{(4\pi/\lambda\sin\theta\tfrac{1}{2}\}\exp j(\mathbf{K}\cdot\mathbf{V})\tau. \quad (4.2)$$

The appropriate space-wise spectrum can be found in the literature.[9] Hence,

$$\sigma(\mathbf{K},0)=\frac{\sqrt{\pi}/\lambda(2\pi l_0/\lambda)^3[\Gamma(\mu+\frac{3}{2})/\Gamma(\mu)]\langle\Delta\epsilon^2\rangle}{\{1+4(2\pi l_0/\lambda)^2\sin^2\tfrac{1}{2}\theta\}^{\mu+\frac{1}{2}}}, \quad (4.3)$$

where

$$K=(4\pi/\lambda)\sin\tfrac{1}{2}\theta.$$

B. Total Cross Section for Scattering

As noted in Sec. 3, the total cross section for scattering is defined by

$$Q_S=\int d\Omega\sigma(\mathbf{K},0). \quad (4.4)$$

Under the very reasonable assumptions that $2\pi l_0/\lambda>10$, it can be shown that

$$Q_S\cong 2\pi^{\frac{1}{2}}/(2\mu+1)[\Gamma(\mu+\tfrac{3}{2})/\Gamma(\mu)]2\pi l_0/\lambda^2\langle\Delta\epsilon^2\rangle. \quad (4.5)$$

C. Moments of the Distribution

The moments of the distribution for the spectral density equation were defined in Sec. 3 as

$$\alpha_{2m}{}^2=\frac{2}{Q_S}\int d\Omega'\sigma(\theta')(1-\cos\theta')\frac{(\mathbf{K}'\cdot\mathbf{V})^{2m}}{(2m)!}, \quad (4.6)$$

$$\gamma_{2n}{}^2=\frac{1}{Q_S}\int d\Omega'\sigma(\theta')\frac{(\mathbf{K}'\cdot\mathbf{V})^{2n}}{(2n)!}. \quad (4.7)$$

The first approximation to the spectral density as discussed in Sec. 3 was restricted to the first two moments α_0 and γ_2. From equation (4.3), we have after some integration:

$$\begin{aligned}&\alpha_0{}^2\cong(\ln 4a^2-1)/a^2, \quad \text{for} \quad \mu=\tfrac{1}{2};\\ &\alpha_0{}^2\cong[2/(2\mu-1)]a^{-2}, \quad \text{for} \quad \mu>\tfrac{1}{2};\end{aligned} \quad (4.8)$$

where $a=2\pi l_0/\lambda$ and

$$\begin{aligned}&\gamma_2{}^2\cong 1/2(V/l_0)^2(\ln 4a^2-1), \quad \text{for} \quad \mu=\tfrac{1}{2};\\ &\gamma_2{}^2\cong 1/(2\mu-1)(V/l_0)^2, \quad \text{for} \quad \mu>\tfrac{1}{2}.\end{aligned} \quad (4.9)$$

The ratio of higher order moments can be found by a similar calculation. It can be shown that

$$\frac{\alpha_{2(m+1)}{}^2}{\alpha_{2m}{}^2}\cong\left(\frac{V}{l_0}\right)^2\frac{2m}{2m-1}\frac{2m+1}{2m+2}\frac{m+2}{m+1}\frac{1}{\mu-m+\frac{3}{2}} \quad (4.10)$$

for $a>10$, and $m>0$ and $\mu\neq\frac{3}{2}$. For $m=0$, this reduces to

$$\frac{\alpha_2{}^2}{\alpha_0{}^2}\cong\frac{1}{\mu-\frac{3}{2}}\left(\frac{V}{l_0}\right)^2; \quad \mu\neq\tfrac{3}{2}.$$

A similar result holds true for the γ moments. In the above analysis l_0 is the scale length or *average* size of the blobs in the troposphere. Since this is of the order of 100[24] it follows that the first approximation is a good one.

D. The Spectrum of a Monochromatic Source

In Sec. 3 it was shown that the first approximation for the spectral density is given by (3.12).

$$S(\xi,\theta,\omega)\cong(\alpha_0{}^2\xi)^{-1}\exp[-\theta^2/\alpha_0{}^2\xi](\pi\gamma_2{}^2\xi)^{-\frac{1}{2}}\times\exp[-(\omega-\omega_0)^2/4\gamma_2{}^2\xi]. \quad (4.11)$$

A similar expression exists for negative frequencies.

It was also noted that the spectrum was normally distributed in ω with standard deviation

$$\sigma_\omega=(2\gamma_2{}^2\xi)^{-\frac{1}{2}},$$

and mean, $m=\omega_0$. On substituting for γ_2 from (4.9) we have for the standard deviation

$$\begin{aligned}&\sigma_{\omega_0}{}^2(\xi)\cong(V/l_0)^2(\ln 4a^2-1)\xi, \quad \mu=\tfrac{1}{2};\\ &\sigma_{\omega_0}{}^2(\xi)\cong[2/(2\mu-1)](V/l_0)^2\xi, \quad \mu>\tfrac{1}{2},\end{aligned} \quad (4.12)$$

where $a=2\pi l_0/\lambda_0$ and ξ is the distance in mean free paths: $\xi=Q_sX$, mean free path$=1/Q_s$. There is one difference of great significance between these results and the corresponding spectrum under single scattering assumptions. (The single scatter spectrum has been considered in detail for the special case of a monochromatic input by Muchmore and Wheelon.)[25] For the Gaussian space correlation function the distribution in the single scatter approximation is also normal with standard deviation

$$\sigma_\omega{}^2\cong 2(V/l_0)^2.$$

Single scatter theory in all cases predicts a spectrum with a distance independent standard deviation. It is evident from the above results (4.12) that the standard deviation will increase as the square root of distance. A change with distance has recently been observed over long paths.[26]

For the convenience of future experimental in-

[22] Albert D. Wheelon, J. Appl. Phys. **28**, 684 (1957).
[23] Richard Silverman, J. Appl. Phys. **28**, 506 (1957).
[24] p. 208, footnote reference 6.
[25] R. B. Muchmore and A. D. Wheelon, Proc. I.R.E. **43**, 1437 (1950).
[26] Norman R. Ortwein, U. S. N. Electronics Research Laboratory, San Diego, California (private communication).

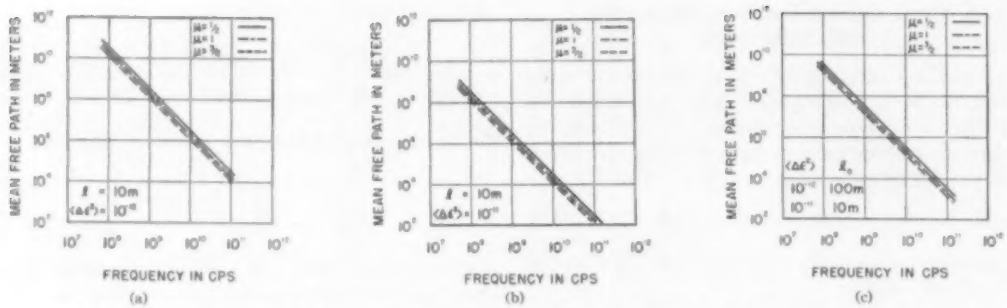

FIG. 3. Mean free path vs frequency in kilomegacycles. Based on the mean blob size in the troposphere.

vestigations the mean free path has been calculated and plotted as a function of frequency for $\langle\Delta\xi^2\rangle=10^{-12}$, 10^{-11} and $l_0=10$, and 100 m (mean blob size) in Fig. 3.

Any practical application of the theoretical result for the spectral density as given by (4.11) must consider the characteristics of the receiving antenna. As a simple example, let us consider the special case of a matched isotropic antenna of unity gain. The observed spectral density is then given by

$$S(\xi,\omega)=\int_0^{\pi} S(\xi,\theta,\omega)\sin\theta d\theta. \tag{4.13}$$

A straightforward integration yields

$$S(\xi,\omega)=-\tfrac{1}{2}j\left(\frac{\pi}{\alpha_0^2\xi}\right)^{\frac{1}{2}}\exp[-\alpha_0^2\xi/4]\times\mathrm{Erf}[\tfrac{1}{2}j(\alpha_0^2\xi)^{\frac{1}{2}}]\frac{\exp[-(\omega-\omega_0)^2/4\gamma_2^2\xi]}{(\pi\gamma_2^2\xi)^{-\frac{1}{2}}},$$

under the assumption that

$$\alpha_0^2\xi=2/(2\mu-1)(\xi/a^2)\ll 1.$$

This reduces to

$$S(\xi,\omega)\cong 1/2(\pi\gamma_0^2\xi)^{-\frac{1}{2}}\exp[-(\omega-\omega_0)^2/4\gamma_0^2\xi].$$

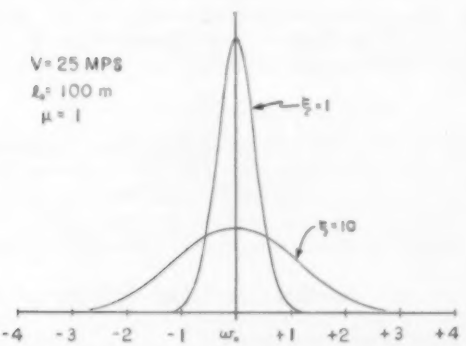

FIG. 4. Spectral density of a monochromatic wave in the troposphere at 1 and 10 M.F.P.

Or in terms of the standard deviation as defined by (4.12), we have

$$S(\xi,\omega)\cong 1/2(2\pi)^{-\frac{1}{2}}(\sigma\omega_0)^{-1}\times\exp[-(\omega-\omega_0)^2/2\sigma^2\omega_0]. \tag{4.14}$$

A similar expression exists for negative frequencies. It should be noted that the integration of $S(\xi,\omega)$ over ω yields unity as expected. The above result for the case when $l_0=100$ m, $V=25$ m/sec has been sketched in Fig. 4. The parameter μ has been taken equal to unity.

5. CONCLUSIONS

Let us briefly review the problem and the progress we have made towards its solution. A transport equation has been developed for the spectral density of a multiply scattered electromagnetic field (2.11). A solution has been developed in detail for the case of scattering by dielectric noise (3.10). This is predominantely a forward scatter problem. The resulting equation has been applied to the scattering of very high frequency waves in the troposphere for the special case of a monochromatic source (3.12).

Numerical results have been presented for the case of a normal troposphere. Application of the results to any particular long line-of-sight or scatter propagation link would follow directly and is consequently left to the interested reader.

However, the subject is not closed. There remains an interesting application in the ionosphere under conditions of nonequatorial spread F. The Milne problem is also of interest. There is also the question of a band limited source and the resulting bounds on the information capacity as a result of dielectric noise. Such a bound should be compared to that obtained from single scatter results.[16] These latter problems will be discussed in future publications by the author.

It should also be noted that the spectral transport equation as presented in this paper is quite general and could be applied to other problems in physics.

JOURNAL OF APPLIED PHYSICS VOLUME 31, NUMBER 7 JULY, 1960

Small Angle Scattering Investigation of Ludox Mixtures

ROBERT H. BRAGG, IRENE CORVIN, AND JOHN W. BUTTREY
Armour Research Foundation, Chicago 16, Illinois

(Received November 23, 1959; and in final form March 14, 1960)

Small angle scattering measurements have been made on distributions of particles prepared by mixing two silica sols of about 90A and 190A mean particle diameter in varying proportions. The scattering at small angles arises predominantly from the larger particles, whereas the smaller ones control the scattering at large angles, as predicted by theory. Attempts to determine the size distribution by the graphical method of Jellinek *et al.* were unsuccessful, but Porod's result relating the scattering at large angles to the total surface area was verified. Bounds for the largest and smallest sizes were estimated from the experimental data by means of simple calculations based on the properties of the scattering function.

I. INTRODUCTION

SMALL angle x-ray scattering experiments are usually interpreted in terms of a "particle size" or "radius of gyration" characteristic of the material under investigation. The radius of gyration can usually be determined from experiment since the scattering at sufficiently small angles conforms to the Guinier approximation.[1] In some instances, such as for monodisperse systems of spherical particles, this parameter suffices to characterize the system completely. However, monodisperse systems are rare; most systems have a distribution of particle sizes and for such systems the significance of a single parameter becomes less clear.

Techniques for determining the size distribution from small angle scattering data have been described and applied to a variety of systems.[2–5] It appears that where indirect confirmatory data are available the calculated size distribution sometimes leads to good agreement with experiment. For example, one verification is afforded by comparing the specific surface area calculation from the particle size distribution with the specific surface area determined by gas adsorption. Another commonly used method is to compare the calculated distribution with that observed in electron micrographs of the material. However, when confirmation from other sources is not available the evidence from small angle scattering alone has not been particularly convincing because of the belief that very large or very small particles are not detected.

There has been no direct verification of a particle size distribution using known systems synthesized from known size fractions. The purpose of the work reported herein was to study the properties of the simplest possible distribution consisting of mixtures of two monodisperse systems of spherical particles of uniform electron density. The materials used in the present work, two different silica sols, did not fulfill these stringent requirements. However, the results demonstrate how small angle scattering can be used to reveal polydispersity and distinguish systems of different size distributions. In particular the work shows how use of the data at large scattering angles[6] leads to a more complete characterization of a material than is obtained by the conventional Guinier analysis alone.

II. EXPERIMENTAL

Apparatus and Measurements

A Norelco Geiger counter diffractometer, converted for small angle scattering by adding a long two-slit collimator between the sample and the detector tube, was used for all the x-ray measurements.[7] With this modification, accurate intensity data can be obtained down to 10 minutes of the direct beam. The x-ray beam was partially monochromatized by use of a Ni filter, and further monochromatization was achieved by carefully adjusting the sample thickness to $1/\mu$, where μ is the linear absorption coefficient. All measurements were made in transmission with the sample held in a cell, consisting of a metal plate with a hole punched in it, having windows of Scotch tape. Optimum sample absorption was obtained by adjusting the sample cell thickness according to the attenuation by the sample. This was determined by placing the sample directly in front of the detector in the path of x rays previously scattered by a sample of carbon black.[8] Intensity data were obtained by manual fixed count measurements in the region from 0.15 to 2.00° 2θ. With the x-ray tube operated at 40 kv and 20 ma, measurements on a typical sample required about one hour.

Description of Samples

Three series of samples were employed: Series *A* was derived from a silica sol designated Ludox SM having an average particle diameter stated to be 70A. As

[1] A. Guinier and G. Fournet, *Small Angle Scattering of X-Rays* (John Wiley & Sons, Inc., New York, 1955), pp. 25, 67.
[2] M. H. Jellinek, E. Solomon, and I. Fankuchen, Ind. Eng. Chem. Anal. Ed. **18**, 172 (1946); M. H. Jellinek and I. Fankuchen, Ind. Eng. Chem., **41**, 2259 (1949).
[3] C. G. Shull and L. C. Roess, J. Appl. Phys., **18**, 295 (1947).
[4] R. Hoseman, Kolloid Z. **117**, 13 (1950).
[5] J. Riseman, Acta Cryst. **5**, 193 (1952).
[6] G. Porod, Kolloid Z., **124**, 83 (1951); **125**, 51 (1952).
[7] L. E. Copeland and R. H. Bragg, Fourteenth Annual Pittsburgh Diffraction Conference, October, 1956.
[8] Auxiliary measurements, wherein the absorption of this radiation by both Al and Ni foils was determined, showed that the scattered radiation is highly monochromatic.

received it had a concentration of 17% by weight. Dilutions of this material down to 1% were used. Similar remarks apply to series *B*, which was derived from Ludox HS, a special experimental sol having a stated mean particle diameter of 130A. The concentration of this material before dilution was 22% by weight and dilutions down to 1% were studied in this material also. Series *C* was obtained by mixing the dilutions of series *A* and series *B* in different proportions.

The average particle diameters given above were supplied by the manufacturer, and were probably derived from surface area measurements. An attempt was made to obtain electron microscope photographs of the *A* material, but much of this material was found to be smaller than the resolution of the microscope used, about 50A. No micrographs of the *B* material were obtained.

Corrections to Experimental Data

In all instances, a background correction was subtracted for the scattering contributed by the solution in which the sols were dispersed. Data for this correction were obtained by measuring the scattering from a sample of alkaline solution of appropriate pH containing no sol but having optimum thickness. Corrections were applied for coincidence losses[9] before the background was subtracted, but no further corrections, such as for slit height, were made.

Analysis of Data

The data were analyzed for the radius of gyration, R, according to the method of Guinier.[1] Here use is made of the fact that at sufficiently small angles the scattered intensity, $I(h)$ (in electron units) by a collection of N identical particles of uniform electron density is

$$I(h)=Nn^2\exp(-h^2R^2/3) \qquad (1)$$

where h is $4\pi\sin\theta/\lambda$, 2θ is the usual Bragg angle, and λ is the wavelength of the x rays. The difference between the number of electrons per particle and the number in an equal volume of material having the mean electron density of the scattering medium is n. The radius of gyration is defined by using electron density as the analog of mass. In using Eq. (1), valid for $hR\leq 1$, the slope of the limiting linear portion of a curve of ln $I(h)$ vs h^2 is used to determine R.

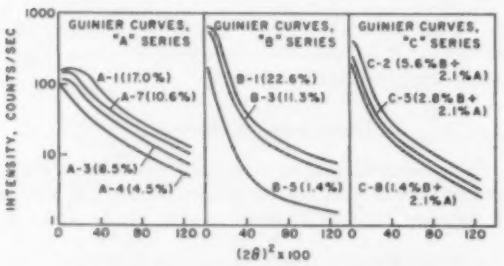

FIG. 1. Typical curves showing effect of dilution in *A* and *B* Series. (*C*) curves are for mixtures of *A* and *B*. Note: 2θ is expressed in degrees.

[9] R. H. Bragg, Rev. Sci. Instr. **28**, 839 (1957).

TABLE I. Parameters of original sols and mixtures.

Sample	Composition, percent by weight	Observed diameter from radius of gyration, *A*	Total surface area, cm^2/cm^3, calculated using Eq. (4)	Diameter calculated from specific surface area, *A*
A-1	17.0	···	6.6×10^8	96
A-2	12.7	···	5.4	88
A-3	8.5	···	3.7	86
A-4	4.2	142	1.7	92
B-2	17.0	212	3.1	206
B-3	11.3	212	2.2	192
B-4	5.6	204	1.3	162
C-1	5.6*B*+4.2*A*	184	2.9	126
C-2	5.6*B*+2.1*A*	192	2.1	138
C-3	5.6*B*+1.0*A*	194	1.7	146
C-4	2.8*B*+4.2*A*	178	3.1	84
C-5	2.8*B*+2.1*A*	184	1.9	96
C-6	2.8*B*+1.0*A*	190	1.2	122

For a polydisperse system of spherical particles containing a distribution of sizes such that $N(R_0)$ is the mass fraction of particles of radius R_0 Eq. (1) is replaced by[2]

$$I(h)=K\textstyle\sum_{R_0}V(R_0)R_0^3\exp(-h^2R_0^2/5). \qquad (2)$$

The method of Jellinek, Solomon, and Fankuchen[2] is based on Eq. (2). It is clear that the method is also applicable only in that region of h for which $hR\leq 1$ for all the particles of the system. The data were analyzed using Eq. 2 and assuming two well defined size groups.

At sufficiently large angles the theoretical intensity function falls off as

$$I(h)=2\pi\rho^2S/h^4, \qquad (3)$$

where ρ is the mean electron density and S is the total surface area of the irradiated volume.[6] The quantity h^4 is replaced by h^3 when the collimating system has wide slits. Evidently a curve of ln $I(h)$ vs ln h should be a straight line in this region of h. Theory further shows that

$$S=4c(1-c)\lim h^3I(h)/\int_{-\infty}^{\infty}hI(h)dh, \qquad (4)$$

where c is the volume fraction of particles in the medium, cm^3/cm^3, and S is in cm^2/cm^3. Values of S, and S/c, the specific surface area were calculated from the observed data.

III. RESULTS

Guinier Analysis

Typical curves used to obtain a radius of gyration are shown in Figs. 1(a)–1(c). The influence of interparticle interference is clearly evident in the curves for the concentrated samples, particularly in the *A* series. There the effect persists down to a concentration of about 5% for which the corresponding volume fraction is about 12%. Similar remarks pertain to the *B* series except that

in this instance the intercepts at $h=0$ are larger for a given concentration, and the curves fall off more rapidly with h.

In the C series some mixtures, not shown, which contained concentrations of solids up to 20% did not cause prominent interparticle effects. In all cases, as the concentration was decreased, a limit was reached below which the intensity at all angles was proportional to the concentration, i.e., the effect of interparticle interference became negligible.

In some instances, e.g., in the more concentrated samples of the A series [Fig. 1(a)], it was not possible to determine the radius of gyration, because data could not be obtained at sufficiently small angles. However, most of the curves were susceptible to the Guinier analysis, and usually the curves appeared to have two definite slopes suggesting two well defined sizes. This is particularly apparent in the curves of Figs. 1(b) and 1(c). Data obtained using the Guinier method are tabulated in Table I.

The value of the radius obtained for the A series was 71A, whereas both the B and C series gave values not very different from 100A irrespective of composition. That is, the value of R or R_0 estimated from the limiting slope at $h=0$ is strongly biased toward the larger particles, and is relatively unaffected by the presence of appreciable amounts of small particles.

Porod Analysis

Figures 2(a)–2(c) show typical curves plotted so as to demonstrate the asymptotic $1/h^3$ relationship. This limiting behavior was always attained at sufficiently large angles, but the minimum angle at which it begins depends upon the composition of the sample. It was found that whenever a limiting straight line was not obtained on this logarithmic graph, some error in measurement or correction had been made. Similar results have been reported by Van Nordstrand and his coworkers on a variety of gels, blacks, and clays.[10]

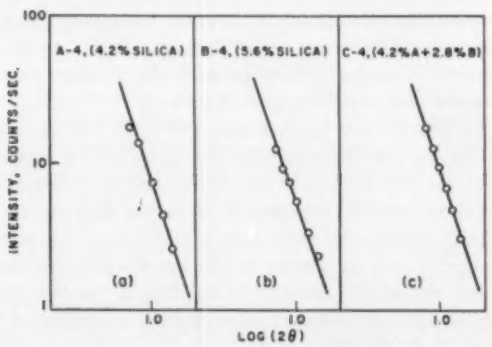

FIG. 2. Curves showing asymptotic $(2\theta)^{-3}$ behavior at large angles for typical samples.

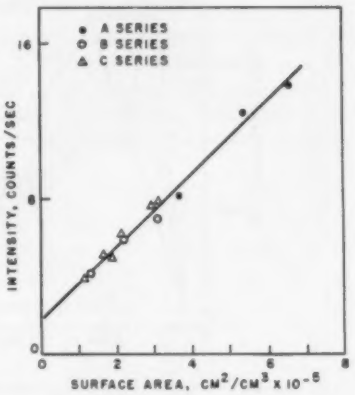

FIG. 3. Showing the relationship between the scattering at 1.0° 2θ and total surface area.

According to Eq. (3) the intensity for a fixed value of h is proportional to the total surface area, S. The total intensity at 1.0° 2θ was selected for convenience and a curve of the scattered intensity at 1.0° 2θ vs the value of S as determined using Eq. (4) is shown in Fig. 3. It can be seen that surface area is the correct basis for comparison, a rather good straight line being obtained on this basis. The residual scattering at vanishing surface area is thus far unexplained. It may be due to a systematic error in measurements, or an improper background correction, but all known sources of error were checked to no avail.

It is well known that for a monodisperse system of N spherical particles, the radius, R_0, of the particles is

$$R_0=3V/S=[3(\tfrac{4}{3}\pi R_0^3N)]/(4\pi R_0^2N). \qquad (5)$$

For a polydisperse system the *surface averaged particle radius* is defined in a similar way by analogy. This parameter is essentially a volume-to-surface ratio. Thus the observed values of S can be used to obtain an estimate of R_0. Values of $2R_0$ obtained using Eq. (5) are also given in Table I. It can be seen that the data for the A series group around 90 A, and the B series group around 190 A, but the C series ranges from 84 to 146A with the smaller radii corresponding to those mixtures containing a large proportion of A material. Thus, in this instance the calculated radius favors those particles which make the largest contribution to the surface area.

IV. DISCUSSION

In general the results are as expected from theory. The data demonstrate that the radius of gyration is strongly weighted toward the larger particles. Equation (2) shows that these weights are in the ratio of the cubes of the radii. In the instance of equal quantities of material of radii R_0 and $2R_0$, the contribution of the larger

[10] R. A. Van Nordstrand and K. M. Hach, Catalysis Club, Chicago, May, 1953; R. A. Van Nordstrand and M.F.L. Johnson, Pittsburgh Conference, X-Ray Electron Diffraction and ACA No. 23. November, 1954.

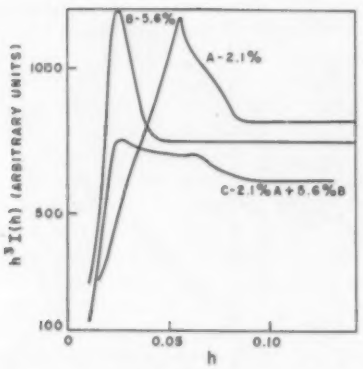

FIG. 4. Curves of $h^3I(h)$ from experimental data. Note correspondence of maxima in the three curves.

particles is 8 times that of the smaller at $h=0$. The present results show (column 3, Table I) that although the ratio of A to B material changes by a factor of 3:1 to 1:5, the B material clearly dominates at the small angles.

It is tempting to interpret the two slopes which seem to be apparent in Fig. 1, particularly from the B and C series, as indicating the presence of two well defined size fractions. This is especially true for the C material, where it is already known that two sols have been mixed. However, a two-slope analysis according to Eq. (2) gave very similar indications, i.e., well defined particle diameters of 90A and 200A, for both the B and C series, whereas the chemical history suggested that the B material was very uniform in size. It was finally concluded that the two slope analysis was not applicable to the data at hand. More accurately, the method was not applicable because the original assumption, $hR \leq 1$, was not satisfied in the region where the second slope seems to dominate the curves of Fig. 1. In fact the second apparent slope begins in the region where the asymptotic $1/h^3$ behavior has already begun to hold. The importance of strictly observing the region of applicability of Eq. (2) has recently been re-emphasized by the results of Kuroda.[11]

Whereas the radius of gyration is strongly weighted toward the larger particles, the radius estimated from the surface area is more nearly a mean based on the relative volumes of different sizes present. In the instance of the B material the two estimates are not very different, further evidence that this material was nearly monodisperse. Since it is well known that the Guinier analysis gives good agreement with the size of known monodisperse systems[12] it follows that the absolute value of the surface area determined according to Eq. 4 is also correct. On the other hand the same comparison shows that the A and C materials consist of mixtures of sizes. The minimum diameter obtained for the C mixtures, 84A, shows that the surface area estimate closely approximates the smallest size present in the sample when an appreciable proportion of the material is present in the smaller size fraction. The corresponding radius of gyration also underestimates the largest size by a considerable margin.

It was not possible to make precise intercomparisons between the samples because the surface area data, and the particle sizes estimated from them, are only accurate to about 20%. In general, however, the value obtained from the radius of gyration was less than the largest size, and the surface area radius was greater than the smallest. The two parameters will coincide only for a monodisperse system of particles. The extent to which the two estimates differ is an indication of the range of sizes present in the sytem. Evidently the use of surface area determined as indicated above provides a convenient and powerful tool for the analysis of small angle scattering data. In view of the simplicity of the calculation and the check it affords on the radius of gyration, it seems almost mandatory to determine this parameter *and* the radius of gyration whenever sufficient data are available.

The results obtained in the present experiment do not pertain to a strictly bimodal distribution. Nevertheless, it is clear that the Guinier and Porod parameters provide approximate, but easily calculated upper and lower bounds of the sizes in distributions of arbitrary character. It is not necessary to resort to extensive analytical treatments, and it is natural to speculate whether other parameters of the distribution could not also be determined by relatively simple calculations. Other analytical treatments of the data, suggest that much more information can be obtained in this way.

The general direction that the analysis should take was indicated by the presence of several maxima in the curve of $h^3I(h)$ vs h for the C material, as shown in Fig. 4. This figure shows that the curve for the B material has only one maximum, but the A curve has a sharp maximum superimposed upon a broad one. It can be seen that the positions of the maxima in the C curve correspond to those of the A and B curves.

Evidently these maxima also correspond to maxima in the size distributions, and this supports the conclusion that the B material was essentially monodisperse, but the A material contained a mixture of sizes. Because of the properties of the function $h^3I(h)$ a maximum *must* occur for each maximum in the size distribution and should correspond roughly to maxima in the function $h^3\sum_{R_0} \exp(-h^2R_0^2/5)$, where each R_0 is the radius of a mode of the distribution.

The theoretical basis for this explanation will be developed in detail in a later publication. Meanwhile the treatment just mentioned, when added to Guinier and

[11] H. Kuroda, J. Colloid Sci. **12**, 496 (1957).
[12] K. Yudowitch, J. Appl. Phys. **20**, 174 (1949).

Porod analyses, provides estimates of the peak and two different moments or rough upper and lower bounds of the size distribution. This suffices to characterize triangular or rectangular distributions rather fully, and gives considerable information about more complicated cases.

V. ACKNOWLEDGMENTS

It is a pleasure to acknowledge the help of Bernadine Tooper in making calculations and in obtaining some of the experimental data. Douglas Wilson and Jack Howard of the DuPont Chemical Company, East Chicago, Indiana, kindly provided the Ludox samples.

JOURNAL OF APPLIED PHYSICS VOLUME 31, NUMBER 7 JULY, 1960

Charged-Particle Orbits in Varying Magnetic Fields

E. I. GORDON
Bell Telephone Laboratories, Inc., Murray Hill, New Jersey
(Received March 1, 1960)

A solution for the paraxial orbits of charged particles in varying magnetic fields is given. The magnetic field is assumed to be azimuthally symmetric but is allowed to vary arbitrarily with time or axial distance. The instantaneous guiding center and radius vector of the orbit are given in terms of the initial guiding center and radius vector and two parameters which are determined from the solution of a first-order differential equation containing the magnetic-field variation. One exact and two approximate constants of the motion are evaluated and discussed.

INTRODUCTION

OVER the years there has been a general interest in the motion of charged particles in time- and space-varying magnetic fields, particularly in the field of astrophysics.[1] More recently, the necessity to control charged-particle orbits in thermonuclear fusion machines, in particle accelerators, and in electron-beam tubes has heightened interest in the subject.

A large amount of effort has been devoted to the examination of certain invariants or constants of the motion. For example, it is known that for slow changes in the magnetic-field strength, the ratio of the energy associated with the rotational motion to the magnetic-field strength is approximately constant. To the extent that the magnetic field must vary slowly, the ratio is known as an adiabatic invariant.[1-4]

Analytical and numerical solutions of the equation of motion for special cases have yielded exact particle orbits, but these are not in a form amenable to ready interpretation. They must be plotted point-by-point to yield the trajectory, or they yield the envelope of a collection of particles.[5,6] A particularly useful representation is one in which the particle orbit is described by the motion and location of a guiding center plus the position of the particle on an approximately circular orbit about the guiding center. To the author's knowledge, no exact solutions in this form have been given although approximate solutions are easily obtained.

In this paper a general solution in the guiding center representation will be given. It will be seen that the instantaneous guiding center and radius vectors are expressible as a linear combination of the original quantities. The time-dependent coefficients are determined by solution of a first-order differential equation and the evaluation of an integral containing the magnetic-field variation. The coefficients will be shown to be related in a simple way. The invariants of the motion can then be expressed and discussed most naturally in terms of the guiding center, the radius of the circular motion and one parameter. Finally, an exact solution for the coefficients will be determined for a particular magnetic-field variation.

MOTION OF AN ELECTRON IN VARYING MAGNETIC FIELDS

We will assume that there are no scalar potentials and that the existing azimuthally symmetric electromagnetic fields can be derived from a vector potential $\mathbf{A}$ with rectangular components $[-\frac{1}{2}yH(z,t), \frac{1}{2}xH(z,t), 0]$. This leads to an electric field $\mathbf{E}=-c^{-1}\partial\mathbf{A}/\partial t$ with components $(\frac{1}{2}c^{-1}y\partial H/\partial t, -\frac{1}{2}c^{-1}x\partial H/\partial t, 0)$ in the form of circles concentric about the z-axis and a magnetic field $\mathbf{H}=\text{curl}\mathbf{A}$ with components $[-\frac{1}{2}x\partial H/\partial z, -\frac{1}{2}y\partial H/\partial z, H]$. The function $H(z,t)$ is arbitrary, consequently the vector potential as given does not satisfy the wave equation $\nabla^2\mathbf{A}-c^{-2}\partial^2\mathbf{A}/\partial t^2=0$ in general, although it satisfies the gauge condition $\text{div}\mathbf{A}=0$. However, it represents an accurate approximation

[1] H. Alfven, *Cosmical Electrodynamics* (Clarendon Press, Oxford, 1950), p. 120.
[2] F. Hertweck and A. Schlüter, Z. Naturforsch. **A12**, 844 (1957).
[3] R. Kulsrud, Phys. Rev. **106**, 205 (1957).
[4] R. K. M. Landshoff *The Plasma in a Magnetic Field* (Stanford University Press, Stanford, California, 1958), p. 3.
[5] C. S. Gardner, "Particle trajectories in homogeneous magnetic field with linear time dependence," University of California, Lawrence Radiation Laboratory, Berkeley, California, Rept. 4563 (August, 1955).
[6] J. R. Anderson, IRE Trans. on Electron Devices **ED-6**, 101 (1959). (This reference contains a bibliography of earlier works on periodic focusing.)

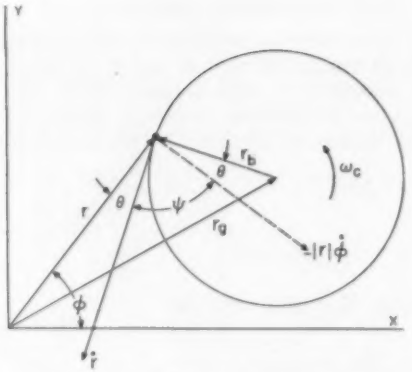

FIG. 1. Definition of guiding center coordinates.

when x and y are confined to small values. The assumed vector potential thus represents a paraxial approximation. For example, for the case in which H is a function of t, we are neglecting terms of the order $(x^2+y^2)c^{-2}H^{-1}\partial^2H/\partial^2t$ compared to one.

The equations of motion in rectangular coordinates for a particle of charge e and mass m for the fields given above become

$$\begin{aligned} mx'' &= +(e/c)[\tfrac{1}{2}y(\partial H/\partial t+z'\partial H/\partial z)+y'H] \\ my'' &= -(e/c)[\tfrac{1}{2}x(\partial H/\partial t+z'\partial H/\partial z)+x'H] \\ mz'' &= -\tfrac{1}{2}(e/c)[x'y-y'x]\partial H/\partial z, \end{aligned} \tag{1}$$

in which the prime represents the total time derivative. We recognize also that we may write $\partial H/\partial t+z'\partial H/\partial z = H'$. Multiplying the second equation by $i=(-1)^{\frac{1}{2}}$, adding the first two and defining $\mathbf{r}=x+iy$ yields

$$\mathbf{r}''-i[\omega_c\mathbf{r}'+\tfrac{1}{2}\omega_c'\mathbf{r}]=0, \tag{2}$$

in which $\omega_c(z,t)=-eH(z,t)/mc$ is the local cyclotron frequency. The minus sign is appropriate, since ω_c is positive, i.e., the rotation is clockwise looking along the direction of the magnetic field, for a negative charge. The quantity $\mathbf{r}$ is a vector representing the position of the particle in the xy plane. The third equation in Eq. (1) can be written

$$z''=\tfrac{1}{2}\ \mathrm{Im}\ (\mathbf{r}\mathbf{r}'^*)\partial\omega_c/\partial z. \tag{3}$$

We see from Eq. (2) that the motion of a particle in the transverse plane is the same for a given variation in ω_c whether the change takes place because ω_c varies with time or with distance. On the other hand, from Eq. (3) we see that the drift velocity z' does not change if ω_c varies with time, but does change when ω_c varies with z. The difference arises because in the time-varying case the particle may exchange energy with the electromagnetic field, whereas in the case of the static magnetic field the associated radial components of field deflect the particle, and energy is exchanged between the rotational and drift motion. As a consequence, the z-coordinate of the particle is influenced by the transverse motion when the field varies with z.

Neglecting this difficulty and assuming for the moment that the time dependence of the z-coordinate may be specified, the solution for Eq. (2) may be written

$$\mathbf{r}=AG(t)+BG(t)^*\exp i\varphi(t), \tag{4}$$

in which

$$\varphi(t)=\int_{t_0}^{t}\omega_c(\tau)d\tau, \tag{5}$$

and

$$G(t)=\exp -i\int_{t_0}^{t}\omega_c(\tau)X(\tau)/[1-X(\tau)]d\tau, \tag{6}$$

subject to the condition that the function $X(t)$ satisfy the differential equation

$$X'-i\omega_cX+\tfrac{1}{2}\omega_c'(1-X^2)/\omega_c=0. \tag{7}$$

We will determine the constants A and B by specifying the guiding center and radius vector of the particle at time t_0 and taking $X(t_0)=0$.

An alternate form for the function $G(t)$ follows by substituting Eq. (7) and writing

$$\begin{aligned} G=\exp -\int_{t_0}^{t}\{[X'/(1-X)]+[\tfrac{1}{2}\omega_c(1+X)/\omega_c]\}d\tau \\ =[1-X(t)][\omega_{c0}/\omega_c(t)]^{\frac{1}{2}}F(t), \end{aligned} \tag{8}$$

in which $\omega_{c0}=\omega_c(t_0)$ and

$$F(t)=\exp -\frac{1}{2}\int_{t_0}^{t}[\omega_c'X/\omega_c]d\tau. \tag{9}$$

The instantaneous radius vector $\mathbf{r}_b$ and guiding center $\mathbf{r}_g$ are defined as

$$\begin{aligned} \mathbf{r}_b &= \mathbf{r}'/i\omega_c \\ \mathbf{r}_g &= \mathbf{r}-\mathbf{r}_b, \end{aligned} \tag{10}$$

as can be seen from Fig. 1. Thus, using Eq. (4) we have

$$\begin{aligned} \mathbf{r}_b &= AG'/i\omega_c+B[G-G'/i\omega_c]^*\exp i\varphi \\ \mathbf{r}_g &= A[G-G'/i\omega_c]+B[G'/i\omega_c]^*\exp i\varphi. \end{aligned} \tag{11}$$

From Eqs. (6) and (8) we have $G'/i\omega_c=-XF(\omega_{c0}/\omega_c)^{\frac{1}{2}}$ and $G-G'/i\omega_c=F[\omega_{c0}/\omega_c]^{\frac{1}{2}}$. On writing $\mathbf{r}_{b0}=\mathbf{r}_b(t_0)$ and $\mathbf{r}_{g0}=\mathbf{r}_g(t_0)$ and remembering that $X(t_0)=0$ and $G(t_0)=F(t_0)=1$, we identify $A=\mathbf{r}_{g0}$ and $B=\mathbf{r}_{b0}$ from Eq. (11). Thus, we have, finally,

$$\begin{aligned} \mathbf{r}_b &= (\omega_{c0}/\omega_c)^{\frac{1}{2}}[\mathbf{r}_{b0}F^*\exp i\varphi-\mathbf{r}_{g0}XF] \\ \mathbf{r}_g &= (\omega_{c0}/\omega_c)^{\frac{1}{2}}[-\mathbf{r}_{b0}(XF)^*\exp i\varphi+\mathbf{r}_{g0}F]. \end{aligned} \tag{12}$$

In the limit of constant magnetic field, $X=0$ and $F=1$, and $\mathbf{r}_b$ and $\mathbf{r}_g$ are unchanged. In general, X is not zero and there is coupling between the guiding center and radius of rotation. The origin of the coupling can be understood from the following considerations.

The charged particle moving in a changing magnetic

field experiences, in addition to the axial field causing the rotational motion, a circular field of force that increases in magnitude with increasing distance from the axis. The force arises from the induced electric field, associated with a time-varying magnetic field, or the radial magnetic field, associated with spatial variations, acting on the drift velocity. Thus, a particle with no initial rotational motion $\mathbf{r}_{b0}=0$ must gain rotational motion proportional to its distance from the axis $\mathbf{r}_{g0}$. Likewise, the original circular motion causes the particle to walk across the field lines in the crossed longitudinal magnetic field and transverse force field even when $\mathbf{r}_{g0}$ is initially zero.

A simple and useful relationship exists between the quantities X and F and can be demonstrated in the following way. Multiplying Eq. (7) by X^* and the complex conjugate equation by X and adding the resulting equations yields

$$(d/dt)|X|^2+\tfrac{1}{2}(X+X^*)(1-|X|^2)\omega_c'/\omega_c=0. \quad (13)$$

Integrating, we obtain

$$|F|^2(1-|X|^2)=1, \quad (14)$$

in which we have used Eq. (9) and the initial condition $X(t_0)=0$, $F(t_0)=1$. One immediate conclusion we may reach is that the maximum value of X, and the minimum value of F, is unity. We are now in a position to discuss the invariants of the motion.

INVARIANTS OF THE MOTION

There is one absolute invariant associated with the particle motion. The invariant follows directly from Eqs. (12) and (14) and can be written[7]

$$\omega_c(r_b^2-r_g^2)=\omega_{c0}(r_{b0}^2-r_{g0}^2). \quad (15)$$

This particular invariant also follows easily from the fact that the assumed vector potential, when written in cylindrical coordinates (r,φ,z), has only an azimuthal component given by $A_\varphi=rH(z,t)/2$. The particle Hamiltonian is thus independent of φ, and the conjugate momentum $p_\varphi=mr^2\varphi'+erA_\varphi/c=mr^2(\varphi'-\omega_c/2)$ is a constant of the motions. It is shown in an appendix that $2r^2[\varphi'-\omega_c/2]\equiv\omega_c[r_b^2-r_g^2]$ and consequently Eq. (15) follows. Note that this simple form follows only as a result of the paraxial approximation.

Equation (15) implies that the relative magnitudes of $\mathbf{r}_g$ and $\mathbf{r}_b$ are preserved.[8] For example, orbits which do not include the origin $r_g>r_b$ never will. Likewise, an orbit which passes through the origin $r_g=r_b$ always will. Thus an increasing radius of rotation is always accompanied by an increase in the magnitude of the guiding center. The reverse is also true.

The quantities $\omega_c r_g^2$ and $\omega_c r_b^2$ are approximate constants of the motions for adiabatic variations in the magnetic field strength. From Eqs. (12) and (14) we may write

$$\omega_c r_b^2=\omega_{c0}r_{b0}^2[1-|X|^2]^{-1}\times|1-(\mathbf{r}_{g0}/\mathbf{r}_{b0})X\exp i(2\,\mathrm{Arg}F-\varphi)|^2$$
$$\omega_c r_g^2=\omega_{c0}r_{g0}^2[1-|X|^2]^{-1}\times|1-(\mathbf{r}_{b0}/\mathbf{r}_{g0})X^*\exp i(\varphi-2\,\mathrm{Arg}F)|^2. \quad (16)$$

The invariant $\omega_c r_b^2$ is better known and is often written r'^2/ω_c. The deviation from exact invariance is expressed by the fact that X is not zero. For slowly varying fields, $X\ll1$ and the deviation from invariance is of order X unless either $\mathbf{r}_{g0}/\mathbf{r}_{b0}$ or its inverse is very small. Under this circumstance only one of the invariants can be good, the deviation being of order X^2, the other will not be good at all. The linear term will also disappear when one considers the average motion of a swarm of particles, if the average over the initial phases is zero. In this circumstance both invariants will be good.

The particular advantage of the formulation given here is that the form of the expression is correct within the limits of the paraxial approximation for any magnetic-field variation. The limitations of the invariants can be determined by inspection, and the parameter X can be determined to any desired accuracy by appropriate approximate solutions of Eq. (7). In particular a complete separation of the guiding center and rotational motion has been achieved. For any problem of interest one need only solve the first-order equation for $X(t)$. Some solutions of interest will be discussed in the following section.

When ω_c is a function of z only, the independent variable for the particle motion is more conveniently taken to be the z-coordinate of the particle. Solution of Eq. (7) in this case requires knowledge of the functional dependence of the drift velocity. When the drift energy is sufficiently large compared to the change in rotational energy, the effect of the magnetic-field variations on the drift velocity is negligible. When this condition is not satisfied, iterative procedures must be used.

ANALYTICAL SOLUTION FOR X

A monotonically changing magnetic field is a case of practical interest. We take for the magnetic field variation

$$\omega_c(t)=\omega_{c0}/(1+\mathcal{K}\omega_{c0}t), \quad (17)$$

in which the parameter $\mathcal{K}$ is a positive or negative constant which measures the rate of change of the field. Its value is given by $\mathcal{K}=-\omega_c'/\omega_c^2$. Under this circumstance the differential equation for X,

$$X'-\omega_c[iX+\tfrac{1}{2}\mathcal{K}(1-X^2)]=0,$$

is separable. Using the initial condition $X(0)=0$, the solution for X can be shown to be

$$X(t)=i\mathcal{K}/[1+i(1-\mathcal{K}^2)^{\frac{1}{2}}\cot\theta(t)] \quad (18)$$

in which $\theta(t)=\frac{1}{2}[(1-\mathcal{K}^2)^{\frac{1}{2}}/\mathcal{K}]\ln(1+\mathcal{K}\omega_{c0}t)$.

[7] This particular form of the invariant was first brought to the author's attention by W. P. Allis.

[8] We assume that ω_c never passes through zero, otherwise the paraxial approximation breaks down.

For $|\mathcal{K}|<1$ the magnitude of X returns to zero whenever θ is a multiple of π. The maximum value of X equals $i\mathcal{K}$ and occurs whenever θ is an odd multiple of $\frac{1}{2}\pi$. The closer $|\mathcal{K}|$ is to the value one the longer is the time interval between zeros of X. In the adiabatic limit, $|\mathcal{K}|\ll 1$, $\theta\simeq\frac{1}{2}\omega_{c0}t$ and X returns to zero approximately once each cyclotron orbit.

When $|\mathcal{K}|>1$, Eq. (18) can be written

$$X(t)=i\mathcal{K}/[1+i(\mathcal{K}^2-1)^{\frac{1}{2}}\coth|\theta|] \tag{19}$$

In this case the magnitude of X increases monotonically from zero to the value one. In the limit $\mathcal{K}=\pm 1$, the solution for X can be written

$$X(t)=[\mp i+2/\ln(1\pm\omega_{c0}t)]^{-1} \tag{20}$$

and has the same behavior.

The parameter $F(t)$ can be written

$$F(t)=\exp\tfrac{1}{2}\mathcal{K}\int_0^t\omega_c(\tau)X(\tau)d\tau \tag{21}$$

Defining $y=i\cot\theta(\tau)$, Eq. (21) becomes

$$F(t)=\exp\mathcal{K}^2(1-\mathcal{K}^2)^{-\frac{1}{2}}\int_{i\cot\varphi}^{i\infty}dy/[1-y^2]$$
$$\times[1+(1-\mathcal{K}^2)^{\frac{1}{2}}y] \tag{22}$$

which we can write as

$$F(t)=\mathcal{K}(1-\mathcal{K}^2)^{-\frac{1}{2}}X(t)^{-1}\sin(\theta(t)$$
$$\times\exp i\theta(t)/(1-\mathcal{K}^2)^{\frac{1}{2}}. \tag{23}$$

It can be seen that Eq. (14) is satisfied by this result. When $\mathcal{K}<1$ and θ is a multiple of π, $F=\exp i[(1-\mathcal{K}^2)^{-\frac{1}{2}}-1]\theta$ and we may conclude that $\mathbf{r}_g$ and r_b periodically return to their initial magnitudes although their phase is changed. Thus, the guiding center walks in the azimuthal direction at an average rate equal to $\theta'[(1-\mathcal{K}^2)^{-\frac{1}{2}}-1]=\frac{1}{2}\omega_c(t)[1-(1-\mathcal{K}^2)^{\frac{1}{2}}]$.

When the magnetic field has a sinusoidal component which varies at a frequency, $\omega=m\omega_{c0}$, X increases asymptotically toward the value one when m is an integer. The fastest rate of increase occurs for $m=1$ and corresponds to cyclotron resonance; $m=2$ corresponds to a magnetic dipole interaction. When m is not an integer, X returns periodically to zero, with periodicity corresponding to the smallest difference frequency. This corresponds, of course, to periodic focusing.

CONCLUSION

A solution for the orbits of charged particles in varying azimuthally symmetric magnetic fields has been given in the guiding-center representation which separates the guiding center and rotational motion. It has been shown that the motion in a particular magnetic field can be determined by the solution of a first-order differential equation that determines the necessary parameters. The invariants of the system have been discussed, and in the case of slow magnetic field variations it has been shown that the corrections to the adiabatic invariants are of the first order for a single particle. Averages over the initial conditions eliminate the first-order term so that the invariant is truly adiabatic only for a swarm of particles. When particles start with their guiding centers on the axis or with no rotational energy, the correction term for the appropriate invariant is also of the second order.

The formalism given here has been particularly useful in understanding the properties of transverse waves on electron beams in changing magnetic fields. A future paper will treat this topic.

ACKNOWLEDGMENT

The author gratefully acknowledges the interest of and discussion provided by S. J. Buchsbaum.

APPENDIX

Demonstration that $2r^2(\varphi'-\omega_c/2)=\omega_c(r_b^2-r_g^2)$

Referring to Fig. 1, we define the instantaneous radius vector and guiding center in terms of the instantaneous position and velocity of the particle and the instantaneous cyclotron frequency $\mathbf{r}_b=\mathbf{r}'/i\omega_c$ and $\mathbf{r}_g=\mathbf{r}-\mathbf{r}_b$. Thus we can write $r\varphi'=-\omega_c r_b\cos\psi$, $r^2(\varphi'-\omega_c/2)=-\omega_c(2rr_b\cos\psi+r^2)/2$, and $r_g^2=r_b^2+r^2-2rr_b\cos(2\theta+\psi)$. Since $\theta=\frac{1}{2}\pi-\psi$, it follows that $2r^2(\varphi'-\omega_c/2)=\omega_c(r_b^2-r_g^2)$.

On the Kinetics and Mechanism of the Precipitation of Lithium from Germanium†

J. R. CARTER, JR.,* AND R. A. SWALIN
Department of Metallurgy, University of Minnesota, Minneapolis, Minnesota
(Received January 11, 1960; and in final form March 17, 1960)

The kinetics of precipitation of lithium from germanium have been investigated and the following variables have been studied: (a) crystal source; (b) preannealing treatments prior to the introduction of lithium; (c) the effect of selective impurity additions, namely, oxygen and copper. The precipitation process can be described as following the law given below:

$$\log C/C_0 = \exp[-(t/\tau)^n].$$

Upon saturation at elevated temperatures, (about 425°C), n is found to be $\frac{3}{2}$ for the first part of the process and 1 for the later part of the process. Upon saturation at low temperatures, however, n is found to be $\frac{1}{2}$. It is suggested that this results from the nonuniform distribution of lithium in the crystal prior to precipitation.

Nucleus number densities varying by orders of magnitude were obtained from different crystals. It was found that a preannealing treatment at 900°C was sufficient to increase the nuclei number densities for all crystals and the differences tend to disappear upon the preannealing treatment.

Doping with oxygen tended to increase very markedly the number density of nuclei whereas doping with small amounts of copper (several orders of magnitude less than lithium present) decreased the number density of nuclei by about an order of magnitude. Interpretation of these results suggests that an impurity, consisting either of particles or oxygen-vacancy pairs, is catalyzing the precipitation process.

I. INTRODUCTION

THIS paper represents the first part of a series dealing with precipitation phenomena in semiconducting elements. The general aims of the program are (a) to test some recent theories of growth kinetics of precipitate particles as a function of particle shape and size, (b) to determine, if possible, the mechanism of nucleation of precipitate particles, and (c) for those cases where impurities are shown to be important in the nucleation reaction to learn something concerning the distribution of the impurities in the lattice. With regard to the last point, kinetic studies can be thought of as an additional tool for the study of the form and concentration of defects in a lattice.

Considerable theoretical work has been performed concerning the kinetics of competitive growth of precipitate particles in a supersaturated solution.[1–9] In general, consideration has only been given to spherical particles. Wert[1] and Zener[2] also considered the growth kinetics of particles shaped as rods and disks and deduced that the exponent n in the following equation:

$$\log C/C_0 = [t/\tau]^n \qquad (1)$$

was characteristic of the particle shape for diffusion-limited growth, being $\frac{3}{2}$, 2, and $\frac{5}{2}$ for spheres, rods, and disks, respectively. In Eq. (1), C is the concentration of the precipitating species at time t, C_0 is the concentration at $t=0$, and τ is the characteristic time. Ham,[8,9] using a variational method, calculates that n is $\frac{3}{2}$ for the first 50% of the process regardless of particle shape and becomes equal to 1 for the last half of the process. In the limiting case of a rodlike particle capturing solute only near the ends, n is 1 for the whole process. For disks growing only in radius, n is 2 for the initial part of the process. It would be most desirable to examine the correctness of these ideas by examining the kinetics of growth of a variety of differently shaped particles.

Semiconductor base materials are useful for precipitation research because of the reliability of electrical techniques for following the progress of precipitation and the feasibility of obtaining supersaturation ratios of solute concentration covering a wide range of values. These points are discussed more fully elsewhere.[10]

Morin and Reiss[6] made the initial study of precipitation in the germanium-lithium system and from their results postulated that the critically sized nucleus for growth was a substitutional lithium atom formed through the following reaction:

$$\mathrm{Li}_i^+ + V^- = \mathrm{Li}_s \qquad (2)$$

where V^- denotes a negatively charged vacancy and the subscripts i and s refer to interstitial and substitutional, respectively. Their theory is unique in that it is the first time that evidence has been obtained that point defects can act as catalysts for precipitation reactions. Because of this it seemed advisable to make additional studies in order to test this viewpoint. As a consequence, it was decided in the present investigation to investigate the following points: (a) precipitation rates in crystals supplied from various sources; (b) effect of thermal history prior to introduction of lithium; and (c) the influence of selective impurity additions on the kinetics of the precipitation of lithium.

* Now with Pacific Semiconductors, Culver City, California.
† Research supported by Office of Naval Research.
[1] C. Wert, J. Appl. Phys. **20**, 943 (1949).
[2] C. Zener, J. Appl. Phys. **20**, 950 (1949).
[3] C. Wert and C. Zener, J. Appl. Phys. **21**, 5 (1950).
[4] H. Reiss and V. K. La Mer, J. Chem. Phys. **18**, 1 (1950).
[5] H. L. Frisch and F. C. Collins, J. Chem. Phys. **20**, 1797 (1952).
[6] F. Morin and H. Reiss, J. Phys. Chem. Solids **3**, 196 (1957).
[7] T. R. Waite, Phys. Rev. **107**, 463 (1957).
[8] F. Ham, J. Phys. Chem. Solids **6**, 335 (1958).
[9] F. Ham, J. Appl. Phys. **30**, 1518 (1959).
[10] R. A. Swalin in *Kinetics of High Temperature Processes*, edited by W. O. Kingery (John Wiley & Sons, Inc. and Massachusetts Institute of Technology Press, New York, 1959).

II. EXPERIMENTAL TECHNIQUE AND MATERIALS

A. Materials

The basic technique involved the saturation of a sample of germanium with lithium at a high temperature and the subsequent quenching to a lower temperature where precipitation of the lithium occurred. The progress of precipitation was followed using electrical resistivity techniques as discussed later in more detail.

Crystals of nearly intrinsic germanium were obtained from several sources.[11] In Table I are listed the specifications of the crystals used for the main part of the study.

The lithium was obtained from the Lithium Corporation of America and had been prepared as a 30% dispersion of lithium metal powder in petrolatum.

B. Sample Preparation

The as-received germanium crystals were sliced parallel to a {111} plane into wafers 0.150 cm thick. These wafers were cut into rectangular blocks 1 cm long and 0.3 cm wide. The samples were lapped with No. 600 carborundum and etched in CP-4 to remove any damaged or contaminated surface material. The samples were rinsed in KCN solution to remove any copper and rinsed again in triply distilled water after which lithium dispersion coating was applied to the sample. The samples were gently heated in an evacuated Pyrex tube to vaporize the petrolatum. Care was taken not to overheat or carbonize the petrolatum. When the sample was dry, the tube was flushed several times with helium and the sample was sealed under ½ atm of helium.

C. Saturation and Precipitation

A sample coated with lithium was suspended in a vertical tube furnace, and saturated for the desired time at the desired temperature. Saturation times always exceeded the theoretical saturation times calculated from the diffusion data of Fuller and Severiens.[12] When the saturation program was completed, the sample was dropped into a cold water quench bath whereupon the capsule fractured as a result of thermal shock. The sample was rapidly cleaned with No. 600 carborundum, rinsed in distilled water and placed in the resistivity measuring jig. It was possible to determine resistivity within 5 min after quenching. The resistivity of the sample was measured as a function of time at the precipitation temperature without disturbing its position in the jig. Measurements were made at appropriate intervals through the experiments. Zero time was assumed to be the instant of quenching.

TABLE I. Various data regarding germanium crystals.

Source	No.	Resistivity (Ω cm)	Type	Dislocation density (pits/cm²)	Crystal orientation
Sylvania	1	25–40	*N*	6.8×10^3 to 1.3×10^4	{111}
Sylvania	2	42–50	*N*	2.1×10^3 to 3.55×10^4	{111}
Minneapolis-Honeywell	1	45–49	*N*	1.39×10^3 to 3.76×10^3	{111}
Minneapolis-Honeywell	2	34–40	*N*	Undetermined	Undetermined
Bell	1	42.5	*P*	800	{111}

[11] The authors are indebted to the Minneapolis-Honeywell Research Center and Dr. F. Morin of Bell Telephone Laboratory for providing two of the crystals.

[12] C. S. Fuller and J. C. Severiens, Phys. Rev. **95**, 21 (1954).

D. Measurements of Electrical Resistivity

A schematic diagram of the resistivity measuring apparatus is shown in Fig. 1. For the electrical measurements, an L&N type K-3 potentiometer was used in conjunction with the Poggendorf or two-point probe technique of measurement.

The current through the sample was supplied by a variable-voltage power supply. A jig applied two spring-loaded current contacts to the ends of the germanium sample and two spring-loaded emf probes to the sample surface. A known current of less than 10 ma was passed through the sample and the emf between the two probes was measured. The emf across the standard 0.1-ohm resistor accurately determined the current for the sample. With this current and the emf across the probes the resistance of the sample is determined by Ohm's law. From the dimensions of the sample and the probe spacing the resistivities were calculated. The procedure was repeated several times for each reading and the average resistivity value was computed.

E. Conversion of Electrical Resistivity Data to Lithium Concentration

As is well known, the electrical resistivity for an *n*-type semiconductor is given by the following equation:

$$1/\rho = ne\mu \qquad (3)$$

where n is the effective concentration of charge carriers, e is the unit of electric charge, and μ is the carrier mobility. For the case in point here, lithium is known to exist as a singly ionized donor at an above room tem-

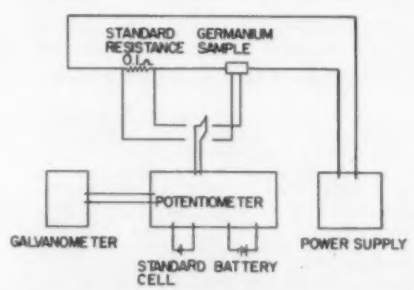

FIG. 1. Schematic diagram of resistivity measurement apparatus.

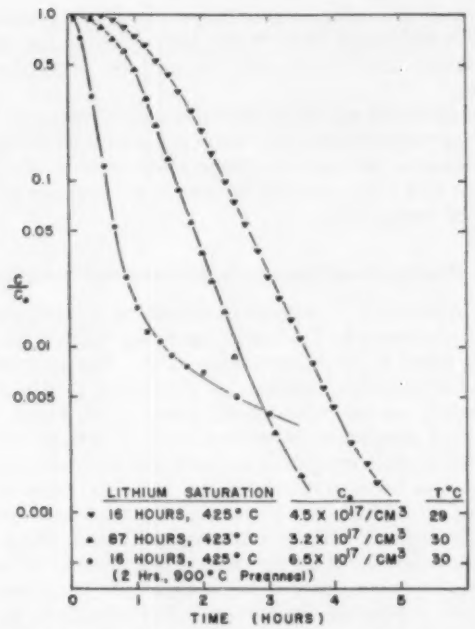

FIG. 2. Precipitation of lithium in germanium; log of remaining solute fraction vs time for several experiments with varied thermal programs. Germanium from Minneapolis-Honeywell No. 2 crystal.

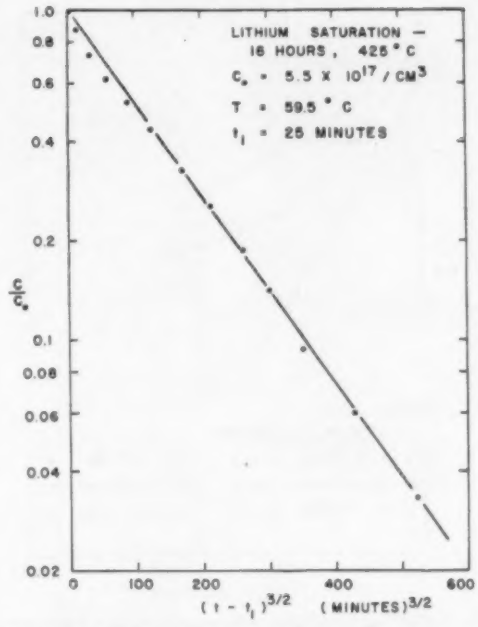

FIG. 3. Precipitation of lithium in germanium; log of remaining solute fraction vs time minus incubation time, the quantity raised to the $\frac{3}{2}$ power for an experiment exhibiting an incubation time. Germanium from Bell No. 1 crystal.

perature.[13] Since the concentration of impurity acceptor ions is several orders of magnitude smaller than the added concentration of lithium ions $[Li^+]$, n in Eq. (3) is simply equivalent to $[Li^+]$. In order to obtain $[Li^+]$, the mobility as a function of donor concentration has to be known. The data of Debye and Conwell[13] and Fritzsche[14] were used for this purpose. From these considerations and by using Eq. (3), we obtained $[Li^+]$ as a function of precipitation time by assuming that a dissolved lithium ion loses its charge upon attaching to a precipitate particle.

III. RESULTS

A. Growth Law of Precipitate Particles

For purpose of analysis, the data are generally plotted as $\log C/C_0$ vs t. Two general types of curves were found. A series of one type is shown in Fig. 2. No direct observations of particle shape have been made in this system but one might expect them to be essentially platelike since considerable lattice straining occurs during precipitation.[15] It is to be noted that one of the curves on this figure shows about a 30-min incubation time during which no precipitation occurred. This phenomenon occurred commonly in the experiments. In Fig. 3 are shown the data for this curve plotted vs $(t-t_i)^{\frac{3}{2}}$ where t_i is the incubation time. The data yield a straight line in general agreement with Ham's theory[8] for spheroidal particles and Wert and Zener[3] and Morin and Reiss[6] for spherical particles. The straight-line relationship is generally found to hold for about the first 95% of the process as compared to Ham's prediction that it should only hold for the first 50%, however.

A series of curves of the second type is shown in Fig. 4, plotted as $\log C/C_0$ vs time. The curves exhibit significant transient effects for the first 30% of the process. The data shown in Fig. 4 show the following relationship: $\log C/C_0 \sim t^{\frac{1}{2}}$ as shown in Fig. 5. Data following the $t^{\frac{1}{2}}$ relationship were obtained when the lithium saturation temperature was low (below 325°C) and data following the $t^{\frac{1}{2}}$ relationship were obtained for high saturation temperatures. This phenomenon will be discussed more fully in a later section.

B. Method of Presentation of Kinetic Data

Regardless of the exact nature of the growth law followed by the precipitate process in the early state, the latter stage of the precipitation process is characterized by simple exponential-decay-type kinetics according to all theories. As a result a characteristic time, τ

[13] W. Shockley, *Electrons and Holes in Semiconductors* (D. Van Nostrand Company, Inc., Princeton, New Jersey, 1950).
[14] H. Fritzsche, J. Phys. Chem. Solids **6**, 69 (1958); P. Debye and E. M. Conwell, Phys. Rev. **93**, 693 (1954).
[15] B. W. Batterman, J. Appl. Phys. **30**, 508 (1959).

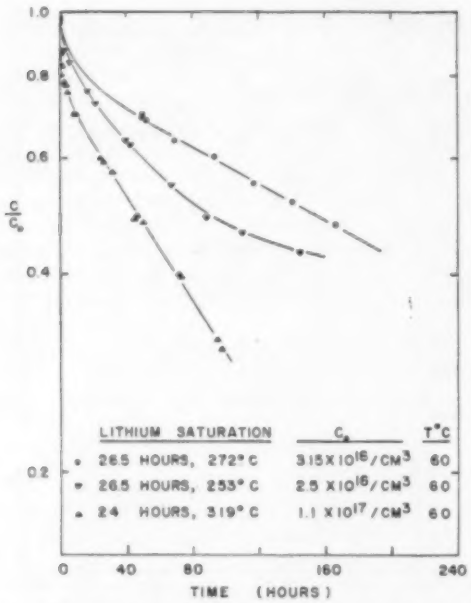

FIG. 4. Precipitation of lithium in germanium; log of remaining solute fraction vs time for several experiments showing transient precipitation. Germanium from Sylvania No. 1 crystal.

can readily be obtained since

$$\frac{C-C_f}{C_0-C_f}=G\exp\left[-\frac{t}{\tau}\right], \tag{4}$$

where G is a constant and C_f is the equilibrium lithium concentration as $t\rightarrow\infty$. C_f can usually be neglected since C is generally an order of magnitude larger in the concentration region where the τ values are obtained.

Because of the fact that τ depends on C_0 and temperature, this quantity is not the most useful for comparison purposes. A more desirable quantity is N_p, the number density of precipitate particles. Following Morin and Reiss,[6] for ease of calculation, it will be assumed that the particles are spherical in shape. If the particles are not spherical, N_p will be different but for purposes of comparison of one set of data with another the relationship of apparent N_p values will be approximately independent of shape. Thus, it is useful to think of N_p values not in an absolute sense but as a useful quantity for comparison purposes. Values of N_p can be obtained using the following equation,[6,8] applicable to diffusion-controlled precipitation

$$1/\tau\cong 3D(C_0v)^{\frac{1}{3}}(4\pi)/3^{\frac{1}{3}}(N_p)^{\frac{1}{3}} \tag{5}$$

of spherical particles where D is the diffusion coefficient of lithium in germanium[4] and v is the *effective* volume of a lithium atom in the precipitate phase. In using the above equation, it is assumed that all particles are present at $t=0$. The quantity v is not known experimentally so a value equal to the volume of a germanium lattice position, 2.2×10^{-23} cm³, will be used in the calculations. This value was also used by Morin and Reiss.[6]

In Table II are listed the experimental values of τ for each experiment along with the initial lithium concentrations, precipitation temperature, and calculated value of N_p. The essential features of the data are presented below.

C. Precipitation Kinetics in As-Received Samples

The values of N_p depended markedly on the temperature of saturation. The higher saturation temperatures were found to yield larger values of N_p. The apparent number density of nuclei was also found to depend markedly on the crystal being investigated. Figure 6 shows a comparison of nucleus number densities obtained in three crystals. The curve labeled Morin and Reiss was taken from Morin and Reiss[6] hereafter referred to as Bell. All germanium crystals used were nearly intrinsic initially as shown in Table I. The intrinsic resistivity of the crystal gave no indication of the nucleus number densities to be expected. The lowest nucleus density was found in the Bell crystal. In this crystal a lithium saturation time of 16 hr at 425°C produced 10^{12} nuclei/cm³. An identical saturation treatment of the Sylvania No. 1 crystal, on the other hand, was found to yield about 3×10^{13} nuclei/cm³. As shown

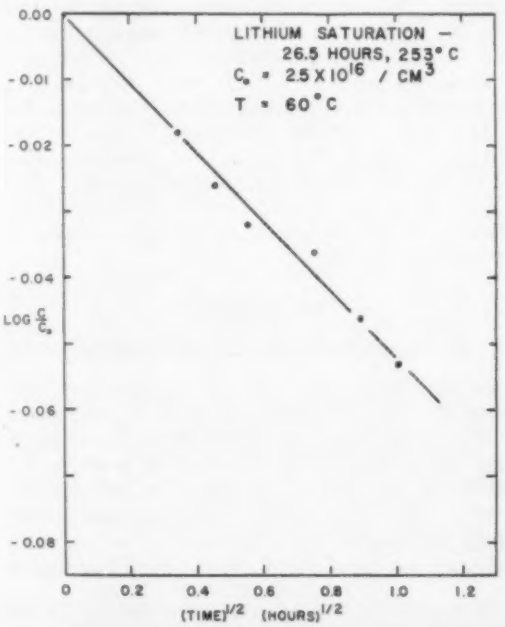

FIG. 5. Precipitation of lithium in germanium; log of remaining solute fraction vs time to the one-half power during transient precipitation. Germanium from Sylvania No. 1 crystal.

TABLE II. Experimental results.

Saturation time	Saturation temperature	$C_0\times10^{-17}$/cm³	$C_f\times10^{-15}$/cm³	τ linear (min)	Precip. T (°C)	N_p/cm³	Remarks
			Sylvania No. 1 crystal				
26 hr	253°C	0.23	···	Nonlinear	60	···	Plotted in Fig. 4.
26	272	0.31	···	2×10^{4}	60	2×10^{9}	Plotted in Fig. 4.
24	319	1.0	···	6×10^{3}	60	7×10^{9}	Plotted in Fig. 4.
17	325	0.75	2.5	60	60	5×10^{11}	
24	376	2.2	2.5	41	60	9×10^{12}	
16	425	4.0	2.0	19	25	2×10^{13}	
19	425	6.2	5.0	16	26	2×10^{13}	
16	425	7.5	3.5	10	29	5×10^{13}	Sample from surface of crystal
16	425	7.7	4.9	14	27	2×10^{13}	
16	425	4.7	4.2	14	26	3×10^{13}	
16	425	6.0	5.5	15	27	3×10^{13}	
94	425	3.2	2.5	5	27	2×10^{13}	
16	425	6.7	0.5	5	27	1×10^{14}	Preannealed at 900°C, water quench
16	425	5.8	2.2	6	25	1×10^{14}	Preannealed at 900°C, air cooled
16	425	7.0	6.5	5	27	1×10^{14}	Preannealed at 900°C, furnace cooled
			Sylvania No. 2 crystal				
16	425	0.14	3.5	524	27	8×10^{11}	
16	425	9.2	3.0	20	27	1×10^{13}	
			Bell crystal				
16	425	5.5	···	15	60	1×10^{12}	Plotted in Fig. 3.
16	425	5.0	···	7	30	9×10^{13}	Preannealed at 900°C, water quench
			Honeywell No. 1 crystal				
16	425	7.1	0.9	5	60	6×10^{13}	
16	425	2.1	0.7	28	27	2×10^{13}	
16	325	1.5	···	1.8×10^{3}	30	4×10^{10}	
64	325	0.9	···	1.9×10^{3}	27	4×10^{10}	
16	425	4.5	···	30	29	1×10^{13}	Plotted in Figs. 2 and 7
87	425	3.2	···	21	30	2×10^{13}	Plotted in Fig. 2
16	425	2.2	···	77	61, 31	4×10^{13}	Plotted in Fig. 9
16	425	4.9	···	21	30	2×10^{13}	Preannealed 600°C, water quench
16	425	7.5	···	21	30	1×10^{13}	Preannealed 760°C, water quench
16	425	6.5	···	12	30	3×10^{13}	Preannealed 900°C, water quench, Fig. 2
16	425	4.0	···	112	30	1×10^{13}	Saturated with Cu at 425°C, Fig. 7
16	425	2.4	···	40	28	9×10^{12}	Saturated with Cu, 425°C prior to Li introduction, evaporated
16	425	2.1	···	270	30	6×10^{11}	Saturated with Cu, 425°C, Fig. 8
16	425	1.0	···	···	30	···	Saturated with Cu, quenched to −78°C, Fig. 8
16	425	4.5	···	15	30	3×10^{13}	Preannealed at 900°C, saturated with Cu
			Philips crystal				
18	425	Precipitation too fast	22	<5	25	···	Grown in N_2+2 mm O_2 pressure
16	425	Precipitation too fast	19	<5	26	···	Grown in N_2+2 mm O_2 pressure
16	425	Precipitation too fast	37	<5	26	···	Grown in N_2+10 mm O_2 pressure
16	425	Precipitation too fast	15	<5	26	···	Grown in N_2+10 mm O_2 pressure
18	425	Precipitation too fast	46	<5	26	···	Grown in N_2 doped with GeO_2

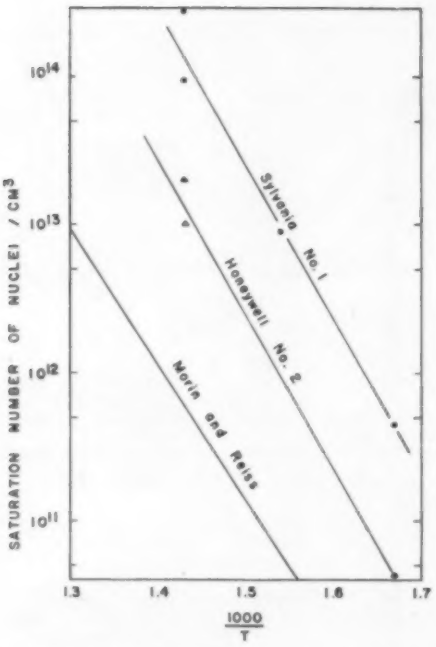

FIG. 6. Precipitation of lithium in germanium; log of saturation number density of nuclei vs the reciprocal of the absolute temperature times 1000 for various crystals.

in Fig. 6, however, the temperature dependence of N_p is approximately the same for the various crystals.

Another prominent difference between crystal precipitation characteristics is the final concentration of lithium in apparent equilibrium with a new second phase. The solubility of lithium in germanium at room temperature, the usual precipitation temperature, is about 10^{14}/cm^3.[16] When precipitation of lithium in the Sylvania crystals was complete, about 3×10^{15} lithium atoms/cm^3 remained in solution. As seen in Table II these final equilibrium lithium values vary from one run to another. The Sylvania and Honeywell No. 1 crystals, however, all have C_f values well above the equilibrium solubility of lithium reported in the literature. The Honeywell No. 2 and Bell crystals precipitated until C_f approached the room-temperature equilibrium solubility of lithium. To a crude approximation, crystals with high values of C_f were those which had the highest nucleus number densities.

D. Precipitation Kinetics in Preannealed Samples

Preannealing the germanium wafers prior to saturation with the lithium *in vacuo* was found to have a profound effect on the kinetics of subsequent precipitation of lithium. In Fig. 2 is shown the effect of a 2-hr preanneal at 900°C on the rate of precipitation. It is to be observed that the precipitation rate is much faster in the preannealed crystal than in the as-received crystals. In fact, a 900° preanneal was found to increase the number density of nuclei by one to two orders of magnitude, the amount of increase depending on the particular crystal being investigated. Experiments were performed to study the effect of cooling time from the preanneal temperature on the subsequent kinetics of precipitation of lithium. Two cooling rates were investigated, namely, a furnace cool at 25°/hr from 900°C to room temperature, and water quenching from 900°C to room temperature. It was found that the method of cooling to room temperature from the 900°C preanneal had virtually no effect on the precipitation kinetics. The influence of preannealing temperature was also investigated and it was found that very little influence of preannealing temperature was found below 900°C. The data in Table II indicate also that the differences between individual crystals as discussed in the last section tend to disappear upon preannealing. The values of N_p obtained by preannealing at 900°C were found to approach 10^{14} nuclei/cm^3 regardless of the crystal.

E. Influence of Selective Impurities on the Kinetics of Precipitation

In order to determine the effect of specific contaminants on the nucleation of lithium, two types of impurities were investigated, namely, copper and oxygen. These will be discussed in turn.

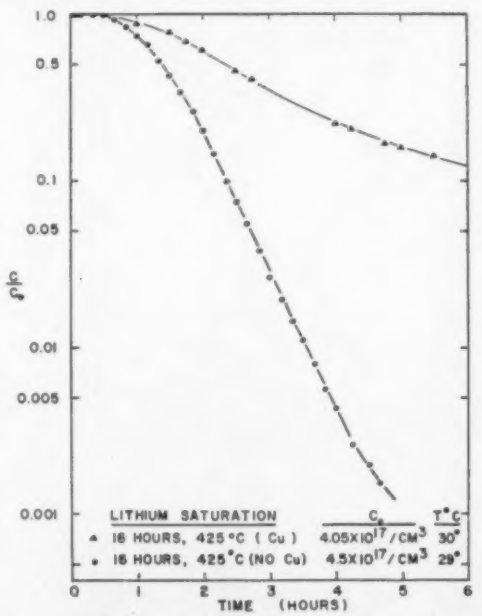

FIG. 7. Precipitation of lithium in germanium; log of remaining solute fraction vs time for experiments with and without copper contamination during lithium saturation. Germanium from Minneapolis-Honeywell No. 2 crystal.

[16] E. M. Pell, J. Phys. Chem. Solids **3**, 74 (1957).

Several wafers were coated with cupric nitrate concurrent with the application of the lithium dispersion. The wafers were then treated in an identical fashion to those discussed previously. The copper was found to have a marked influence upon the precipitation kinetics of lithium as shown in Fig. 7. The data shown in this figure indicate that the copper retards the precipitation kinetics of lithium by about an order of magnitude. These data indicate that the number density of nuclei is about 1.5×10^{12} particles/cm³ in the contaminated sample as compared with 10^{13} particles/cm³ in the uncontaminated sample. To further clarify this effect, two samples were simultaneously saturated with copper and lithium in the manner just discussed. Upon quenching from 425°C one sample was precipitated at room temperature immediately. The other sample was stored at dry-ice temperature. After more than two days at −78°C this sample was returned to room temperature at which temperature the precipitation kinetics were followed. No noticeable precipitation had occurred at −78°C. The data from this experiment are shown in Fig. 8. It can be seen from Fig. 8 that the sample which received the low-temperature treatment precipitates at a much slower rate once brought back to room temperature than did the sample which did not have this interrupted treatment.

Another experiment was performed in order to combine the effect of copper contamination and preannealing treatment with regard to the precipitation kinetics of lithium. A sample was preannealed for 7 hr at 900°C, quenched in water, and saturated with lithium and copper for 16 hr at 425°C. Upon precipitation at room temperature a value of N_p equal to 2.7×10^{13} particles/cm³ was obtained. This was a much larger value than obtained by copper contamination of an as-received sample. It was also much smaller than the value of N_p found from studies of preannealed uncontaminated germanium.

The copper contamination phenomenon will be discussed in more detail in the Discussion section but perhaps it might be well to point out at this time that the amount of copper in the crystal is several orders of magnitude less than the initial lithium concentration put in the sample based on solubility determination by various investigators. Woodbury and Tyler,[17] on the basis of electrical measurements, determined that the solubility of copper in germanium at 500°C is equal to 8×10^{12}/cm³. Penning[18] determined the solubility at 500°C by plating a germanium sample with radioactive Cu^{64} and analyzing for the total amount of copper in the sample. The concentration they obtained was 4×10^{13} copper atoms/cm³. The difference in the two results presumably is related to the fact that Woodbury and Tyler's measurements only counted the electrically active atoms whereas Penning's measurements counted both the electrically active and inactive copper atoms. On the basis of these data, therefore, we can conclude that the total copper content at 425°C in the sample probably does not exceed 10^{13}/cm³ whereas the initial lithium content is of the order of 10^{17}/cm³.

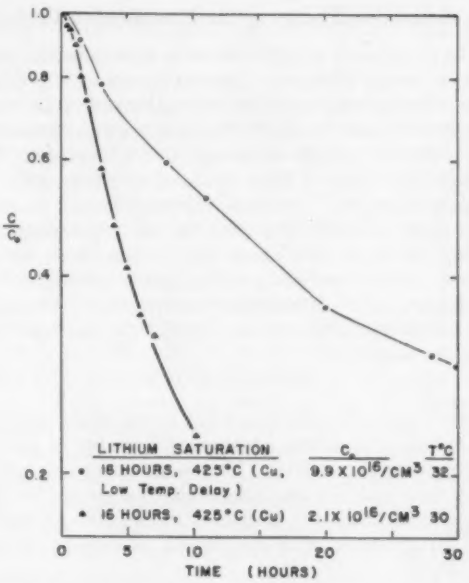

FIG. 8. Precipitation of lithium in germanium; log of remaining solute fraction vs time for experiments with copper contamination, but with and without a low-temperature delay following the quench. Germanium from Minneapolis-Honeywell No. 2 crystal.

Because of the important role which oxygen appears to play in silicon[19] as a catalyzing agent it seemed desirable to investigate the effect of oxygen in germanium. Several samples which had been grown under differing oxygen partial pressures were obtained from P. Penning of the Philips Research Laboratory. Infrared studies by Bloem, Haas, and Penning[20] indicate that the oxygen content ranged from 5×10^{16}/ to about 6×10^{17}/cm³. These wafers were saturated with lithium at 425°C and treated in the same way as the samples discussed previously. It was found that the precipitation kinetics of lithium proceeded so rapidly at room temperature that 90% had precipitated before measurements could be made. This clearly indicates that oxygen plays a very active role in the nucleation process of lithium in germanium. The lithium concentration at long times did not approach the equilibrium lithium content of 10^{14}/cm³. Rather, a plateau was reached which was about equal to the oxygen content of the samples. This particular phenomenon has been reported by Tyler.[21]

[17] H. H. Woodbury and W. W. Tyler, Phys. Rev. **105**, 84 (1957).
[18] P. Penning, Philips Research Repts. **13**, 17 (1958).
[19] E. M. Pell (to be published).
[20] J. Bloem, C. Haas, and P. Penning (to be published).
[21] W. W. Tyler, Bull. Am. Phys. Soc. Ser. II, 4, 145 (1959).

F. Activation Energy of the Precipitation Process

An experiment was conducted to determine the activation energy of the precipitation process. A precipitation anneal was begun at 61°C after saturation with lithium for 16 hr at 425°C. The process was allowed to enter the linear stage on a $\log C/C_0$ vs time plot. The sample was removed from the furnace at this time and rapidly cooled to 31°C where the precipitation kinetics was again followed. The data for this experiment are shown in Fig. 9. The characteristic times were determined for the two parts of the curve and since $1/\tau$ is proportional to the diffusion coefficient for a diffusion-controlled process as indicated by Eq. (5), the following relation holds:

$$1/\tau = Ae^{[-Q/RT]} \tag{6}$$

where Q represents the activation energy of the process. From this relationship an activation energy of 12 950 cal/mole was calculated. This is in reasonably good agreement with the published activation energy for the diffusion of lithium in germanium of 11 800 cal/mole[12] and in agreement with conclusions reached by Morin and Reiss.[6]

IV. DISCUSSION

Listed below is a summary of the experimental findings of this paper.

(a) The precipitation kinetic data follow qualitatively the theory of Ham for spheroidal particles and Wert, Zener, Morin, and Reiss for spherical particles if the lithium is introduced at a high temperature, in that the $\log C/C_0$ is proportional to $t^{\frac{1}{2}}$ for the first part of the process and becomes proportional to t for the last stage of the process. If the lithium is introduced at a low temperature, however, the growth kinetics are drastically altered and $\log C/C_0$ becomes proportional to $t^{\frac{1}{2}}$ in the initial stage.

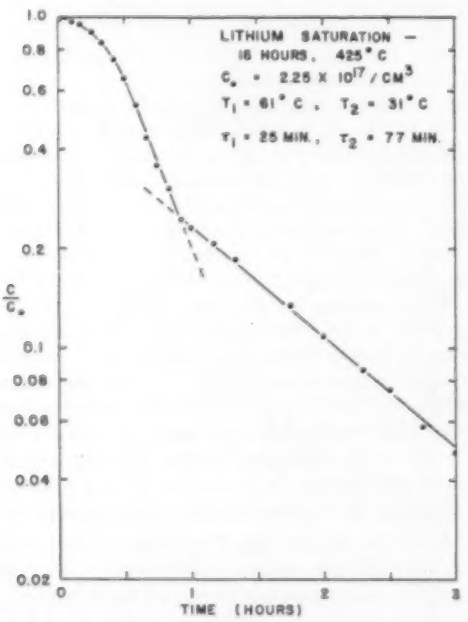

FIG. 9. Precipitation of lithium in germanium; log of remaining solute fraction vs time for a precipitation conducted at two temperatures. Germanium from Honeywell No. 2 crystal.

(b) Crystals obtained from different sources yielded drastically differing values of the apparent number density of nuclei N_p. Variation of an order of magnitude were observed.

(c) Thermal treatment of the germanium wafers prior to saturation with lithium had a profound effect on the subsequent precipitation kinetics of lithium. A 2-hr 900° anneal was sufficient to increase the number of nuclei for all samples markedly. It is significant that the variations between crystals tend to disappear when given the 900° preanneal treatment. Annealing at lower temperatures had very little effect on the subsequent kinetics. The rate of cooling 900°C to the precipitation temperature also had no influence.

(d) If a small amount of copper is introduced into the sample in a concentration several orders of magnitude less than the lithium concentration the apparent number of nuclei decreases by about a factor of 10. Furthermore, if a sample which is saturated at 425° is quenched to dry-ice temperature and held for a period of time, and then subsequently precipitated at room temperature, the apparent number of nuclei decreases even further.

(e) Oxygen is found to catalyze the precipitation process markedly. This implies that oxygen can act as a nucleating agent for lithium.

A. Interpretation of the Kinetic Data

A detailed interpretation of the kinetic data cannot be made until information is provided concerning the detailed shapes and sizes of the nuclei, but some comments can be made regarding the change in the nature of the kinetics upon changing the saturation temperature from a high temperature to a low temperature. It is apparent from this observation that one must proceed cautiously in attempting to interpret kinetic data, particularly with regard to interpretation concerning the morphology of the growth particles. Waite[7,22] has considered in some detail the theory of bimolecular reaction rates in solids on the basis of probability theory. Waite has shown that, in certain cases, if the initial distribution of the precipitating species is not uniform, a significant transient can be associated with the process. Furthermore, it is calculated that during this transient period the precipitation kinetics process does indeed follow the $t^{\frac{1}{2}}$ power. Thus, the data obtained in this paper suggest, by analogy, that the peculiar kinetics involving the $t^{\frac{1}{2}}$ power kinetics might be due to a nonuniform distribution of lithium around the precipitation centers. At 425°C where this peculiarity is

[22] T. R. Waite, Phys. Rev. **107**, 471 (1957).

not found it would be suggested that the distribution is essentially uniform. At low temperature attractive forces between the precipitation centers and lithium ions could become important and result in a clustering of dissolved lithium ions about these centers. Since about 30% of the atoms are involved in this transient period at lower temperatures, significant long-range forces would have to come into play to account for this clustering. Such forces could be Coulombic in nature if it is postulated that the precipitating centers are negatively charged. Since the solubility of lithium is of the order of $5\times10^{16}/cm^3$ and the number of precipitate particles is of the order of $10^{13}/cm^3$, about 10^3 lithium ions would have to be associated with each precipitate ion center. This indicates that the precipitating center would have to have a large size in order not to be screened by the first few solute atoms that arrive in the vicinity. This would tend to eliminate point defects from consideration since it has been shown by Reiss, Fuller, and Morin[23] that ion pairing is favorable in semiconductors. It seems possible, however, that if precipitation centers are being generated in the vicinity of dislocations and if lithium ions are attracted to dislocations a nonuniform distribution could result. This would tend to be aggravated at low temperatures. Since it is known that dislocations have an effective negative charge[24] conditions are favorable for a preferential distribution of lithium about a dislocation at low temperatures. Regardless of the exact nature of the precipitation catalyst, it might be expected that vacancies play a role either in the growth of the catalysts to the critical size or as catalysts themselves. Since dislocations can act as sources for vacancies it might be expected that at low temperature the vacancies would be preferentially grouped around the dislocations and hence the precipitation catalyst also.

B. Nature of the Nucleating Site

Certain general comments can be made about the nature of the precipitate particles on the basis of the kinetic data. For example, the process appears to be controlled by the diffusion rate of lithium. Since the diffusivity of germanium is several orders of magnitude less than that of lithium, the process of particle growth must not involve the long-range diffusion of germanium atoms away from the particle. The germanium atoms therefore probably basically remain on their equilibrium lattice sites with the lithium ions ordering themselves in interstitial sites. Furthermore, since in some cases the equilibrium solubility of lithium in contact with the precipitate particles approaches the room temperature solubility of lithium this suggests that the precipitating phase is thermodynamically very similar to the equilibrium phase Ge_4Li as shown in the phase diagram[25] but not necessarily identical to it.

The data also indicate that the precipitation centers themselves form at the temperature of precipitation and not at the saturation temperature or during the quench. This seems to be true because, as mentioned in the last section, an incubation time during which no precipitation occurs is frequencly observed. This would suggest that a redistribution is occuring during this period after which precipitation can begin. This is in contrast with Morin and Reiss' suggestion that the precipitate centers form at the saturation temperature.[6]

The results presented in Sec. III relating to the nucleus number densities obtained in various crystals shed interesting light on the nature of the nuclei. The curve labeled Morin and Reiss on Fig. 6 supposedly represents the maximum number of nuclei obtained at various equilibration temperatures on the basis of the vacancy nucleation mechanism. If one had saturated for a time insufficient to generate enough vacancies, according to their theory, one would obtain fewer nuclei than represented by this curve in Fig. 6. It can be seen, however, that the other crystals generally were found to yield an order of magnitude larger number of nuclei. Furthermore, as mentioned before, a preanneal treatment at 900°C increased the concentration of nuclei even further. These features coupled with the fact that the crystals which yielded the highest number density of nuclei generally had a high plateau as t approaches infinity suggests that an impurity of some type is catalyzing the precipitation reaction. The tail of the curve is significant since this high quasi-equilibrium value probably represents a reaction of the following type:

$$Li^+ + X = Li^+X,$$

where X represents a neutral impurity atom. Through this reaction lithium has paired with an immobile ion in the lattice and has thus become immobilized itself and cannot diffuse to the precipitate particles. The fact that the rate of quenching from the 900°C preanneal temperature had little to do with the number density of nuclei produced after equilibration with lithium at 425°C during subsequent precipitation at room temperature indicates that the nuclei are produced irreversibly as a result of the high-temperature treatment.

The interpretation of these observations must be correlated with the work of Morin and Reiss[6] in which vacancies are shown to be important. The pertinent experimental observations in their paper are that the precipitation reaction was accelerated upon gamma-ray bombardment which produces lattice vacancies and the rate of nucleus generation was proportional to the dislocation content of the samples. Since lithium diffuses interstitially, the vacancy content should have no influence on the diffusion coefficient of lithium.

Since it is shown in this work that samples doped

[23] H. Reiss, C. A. Fuller, and F. Morin, Bell System Tech. J. **35**, 535 (1956).
[24] C. J. Gallagher, Phys. Rev. **88**, 721 (1952).
[25] E. M. Pell, J. Phys. Chem. Solids **3**, 77 (1957).

with oxygen yield very large number densities of nuclei, it is postulated here that oxygen is playing a key role with regard to nucleation catalysis. The difference in nuclei densities between the crystals studied is believed due to the difference in oxygen content of the crystals. Two possibilities exist concerning the nature of the nucleation catalyst. One possibility is that stable oxygen-vacancy complexes are acting as nucleation catalysts. The increase in the nucleus number density upon high-temperature annealing would be interpreted as resulting from the increasing opportunity for pairing between vacancies and oxygen atoms because of the increased diffusivities and concentrations of defects at higher temperatures. There is some evidence that, at high temperatures, oxygen tends to exist in the monatomic form as opposed to grouping in clusters of oxygen atoms.[20] Another possibility is that precipitation occurs in GeO_2 particles. In this case the role of vacancies could be to facilitate the diffusion of oxygen to the clusters. For this mechanism to be valid, oxygen would have to exist and diffuse substitutionally in the germanium lattice. No certain information as to the nature of dissolved oxygen in germanium is available although available evidence (particularly the low diffusivity) indicates that oxygen dissolves substitutionally in silicon.[26,27]

With regard to this mechanism, the role of the high-temperature treatment would be to facilitate the formation of GeO_2 particles. Evidence exists for the precipitation of oxygen in germanium at elevated temperatures.[28] Before the nature of the catalyst can be described with any certainty, however, considerably more information concerning the state of oxygen in germanium is needed.

The role of copper in lowering the nucleus density can be interpreted satisfactorily on the basis of either mechanism. The diffusion coefficient of copper in germanium is several orders of magnitude larger than that of lithium in germanium.[29] This means that when the sample is cooled from the lithium saturation temperature to the precipitation temperature, the copper which is also supersaturated can seek out preferentially the precipitation catalyst. The copper can block the precipitation of lithium by forming a screen of copper around the catalyst. This point of view is further confirmed by the experiment in which the sample was quenched from the saturation temperature to liquid-nitrogen temperature and held for a couple of days whereupon it was brought back to room temperature and precipitation commenced. At liquid-nitrogen temperatures copper is still presumably very mobile whereas lithium is in an immobile state having a very low diffusion constant. This means that the copper has more time to seek out the precipitate centers and form an atmosphere about them. In agreement with experiment the number density of nuclei resulting from this treatment was substantially less than the experiment in which the sample was cooled directly to the precipitation temperature.

[20] A. Smakula and J. Kalnajs, J. Phys. Chem. Solids **6**, 46 (1958).
[27] Pearson, Read, and Feldman, Acta Met. **5**, 181 (1957).
[28] W. Kaiser, H. J. Hrostowski, and C. D. Thurmond, Bull. Am. Phys. Soc. **5**, 61 (1960).
[29] C. S. Fuller, J. D. Struthers, J. A. Ditzenberger, and K. B. Wolfstirn, Phys. Rev. **93**, 1182 (1954).

V. CONCLUSIONS

The results of this investigation indicate that the type of growth kinetics one obtains for the precipitation process depends markedly on the temperature of saturation with the solute atoms. It is suggested that low-temperature saturation treatments may be influenced by a nonuniform distribution of solute atoms due to an attraction between the precipitation centers and solute. Since very little concentration dependence of τ is observed, it is suggested that the precipitation process occurs by heterogeneous nucleation. Further, it is suggested that an impurity, probably oxygen, is responsible for the nucleation catalysis. The role of vacancies as suggested by Morin and Reiss should perhaps be modified in the sense that vacancies are important for obtaining the particular distribution of impurity necessary to catalyze precipitation but do not act as nucleation catalysts themselves. It is suggested that GeO_2 clusters or stable oxygen-vacancy pairs act as the nucleation catalysts. Surprisingly enough, extremely minute amounts of copper can markedly influence the kinetics of the process and in fact can decrease the rate by about a factor of 10 compared with the case where there is no copper.

The results of current research with semiconductor materials in the highly purified state indicate that impurities are probably important regardless of the concentration level. This observation suggests that it is difficult for homogeneous nucleation to occur.

ACKNOWLEDGMENTS

The authors wish to express their thanks to J. W. Ferman and W. C. Olander for assistance with the experimental aspect of the program.

Beam Refrigeration by Means of Large Magnetic Fields

ROBERT ADLER
Research Department, Zenith Radio Corporation, Chicago 39, Illinois

AND

GLEN WADE†
Electronics Research Laboratory, Stanford University, Stanford, California

(Received February 18, 1960; and in final form March 14, 1960)

The resistive loading which an electron beam produces in an adjacent structure can be made to exhibit a very low noise temperature. This is achieved by coupling to the fast cyclotron wave in a large magnetic field; the noise temperature at a given signal frequency is shown to be equal to the cathode temperature times the ratio of signal frequency to cyclotron frequency.

An experiment is described in which this ratio is $\frac{1}{4}$. The coupling structure interacts with the fast cyclotron wave but rejects the slow cyclotron wave. A noise temperature of 186°K is measured.

In conclusion, it is shown that the large magnetic field required for beam cooling need not extend throughout the tube.

INTRODUCTION

A METHOD for cooling an electron beam by using a large magnetic field has been verified experimentally. The cooling refers to a decrease in the noise power associated with the fast cyclotron wave of a beam which is immersed in a uniform magnetic field. How the cooling is accomplished is seen from the following expression giving the noise power propagating in the fast wave[1]:

$$P_{\text{noise}}=k(f/f_c)T_c\Delta f, \tag{1}$$

where f=the frequency of interest, f_c=the cyclotron resonant frequency $(\eta B/2\pi)$, k=Boltzmann's constant, T_c=cathode temperature, Δf=noise bandwidth. The noise temperature is taken to be the coefficient of $k\Delta f$ in Eq. (1), i.e., $(f/f_c)T_c$.

Obviously we can cool this wave by increasing the magnetic field B which increases the cyclotron resonant frequency f_c. In principle, the wave can be cooled indefinitely by increasing B indefinitely. Hence, the fast wave of such an electron beam can serve as a refrigerated load in principle approaching zero-degrees absolute temperature.

This paper describes how Eq. (1) can be derived and reports preliminary experiments in which the measured noise temperature of the beam was more than 100° below room temperature.

DERIVATION OF NOISE POWER

The power carried by the fast cyclotron wave is given by[1,2]

$$P=(I_0/2\eta)(f/f_c)v_t^2, \tag{2}$$

where I_0=dc beam current, η=magnitude of ratio of charge to mass for an electron, and v_t=component of the transverse velocity of the electrons corresponding to the fast wave. For the fast wave, P can be interpreted in several ways including the following:

(1) In a beam containing only fast-wave modulation at frequency f, all electrons have the same transverse velocity v_t. P is the amount of power extractable by coupling to such a beam.

(2) In a beam containing both fast- and slow-wave modulation at frequency f, a certain component v_t of the transverse velocity is assignable to the fast wave. By coupling to the fast wave only, an amount of power P can be extracted.

(3) If we feed into the fast wave of an initially unmodulated beam an amount of power P at frequency f, each electron of the beam will acquire a transverse velocity v_t.

That Eq. (2) can be interpretated as described in the preceding paragraph is readily demonstrated by using Eqs. (9), (12), and (18) of Wade *et al.*[3] For example, consider a filamentary beam which is unmodulated before it reached a particular transverse plane containing the x and the y axes. The beam axis and the magnetic field are both in the z direction. Assume that the beam is transverse-velocity modulated at frequency f in the y direction as it passes through the x, y plane. Upon emerging from the plane the beam will contain both fast- and slow-wave modulation in equal amounts. This is apparent from Eqs. (9) of Wade *et al.*[3] (Modulation on the intermediate-velocity waves will also be established but these waves as well as the slow wave need not concern us further since we assume that our output coupler couples only to the fast wave.) From Eqs. (9) of Wade *et al.*,[3] we see that

$$v_t=\tfrac{1}{2}\dot{y}_{pk}, \tag{3}$$

† Now at Spencer Laboratory, Raytheon Company, Burlington, Massachusetts.

[1] The same expression with a minus sign appended gives the slow-wave power. Since our experiments have dealt only with the fast wave, we shall not discuss slow-wave cooling, although it will be obvious that both the slow and the fast waves are cooled by the same technique.

[2] Equation (2) has been derived by a number of workers; for example, A. E. Siegman, J. Appl. Phys. **31**, 17 (1960).

[3] G. Wade, K. Amo, and D. A. Watkins, J. Appl. Phys. **25**, 1514 (1954).

where $\dot{y}_{pk}$ is the peak value of the impressed velocity modulation. Equations (12) and (18) of Siegman[2] can be used to show that if at a position beyond the x,y plane we place an output coupler capable of completely demodulating the fast wave without coupling to any other wave, we can extract an amount of power given by (2) where v_t is expressed in (3).

Let us now assume that rather than modulating the beam in the y direction, we modulate it in the x direction as it passes through the x, y plane. For this modulation we obtain

$$v_t=\tfrac{1}{2}\dot{x}_{pk}, \tag{4}$$

and the power extracted by our fast wave coupler is given by (2) and (4).

A filamentary beam emerging from a point cathode is modulated by two uncorrelated sources of noise at the cathode plane: The noise arising from fluctuations in the y component of the electron emission velocity and the noise arising from fluctuations in the x component of this velocity. If for each source we know the corresponding v_t we can use (2) to calculate the noise power extracted by our coupler. Note that v_t is a transverse velocity component associated with the motion of *each electron* rather than with the motion of the electron pattern. A broad spectrum of noise in cyclotron waves results because electrons come out of the cathode having a distribution of transverse velocities randomly oriented. This distribution of velocities is a function only of the cathode temperature. In calculating the effect of the velocity distribution we replace the actual velocities by the mean-square transverse velocity. This is the standard procedure for calculating noise in space-charge waves as well as in cyclotron waves. Since the velocity distribution and hence the mean-square velocity of the electrons is a function of cathode temperature only (and not a function of frequency), P as given by (2) must continue to be a function of f/f_c even in the case of beam noise. From Eqs. (28), (29), and (31) of Siegman[2] we have for the noise fluctuation

$$\tfrac{1}{2}\dot{y}_{pk}^2=\tfrac{1}{2}\dot{x}_{pk}^2=\langle\dot{y}^2\rangle_{av}=\langle\dot{x}^2\rangle_{av}=(2\eta/I_0)kT_c\Delta f. \tag{5}$$

On combining (2)–(5), we derive Eq. (1).

DESCRIPTION OF EXPERIMENT

According to Eq. (1), the signal frequency f should be quite small compared to the cyclotron frequency f_c to obtain substantial refrigeration. To understand the reasons for the tube construction used in this experiment, consider the well-known equation for the wave number $1/\lambda$ of fast and slow cyclotron waves:

$$1/\lambda_{f,s}=|(\pm f-f_c)/u_0|, \tag{6}$$

where u_0 is the velocity of electron travel. (The $+$ sign corresponds to the fast wave.) When $f\ll f_c$, the magnitudes of $1/\lambda$ for the fast and slow wave are not very different. To separate the two waves cleanly, the interdigital coupler shown schematically in Fig. 1(A) was used. The electron beam travels between two fencelike arrays of flat fingers alternately connected to the two terminals. Fingers which face each other across the beam are of opposite polarity. This is a standing-wave structure; maximum interaction with the beam occurs when the wavelength on the beam corresponds to the distance λ_f shown in Fig. 1(B).

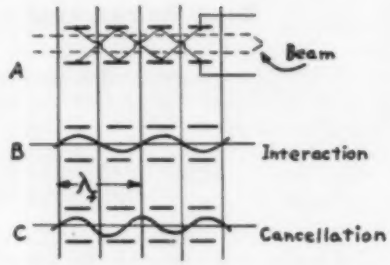

FIG. 1. Connections and operation of interdigital coupler.

For certain wavelengths, coupling to the beam is zero. This property of the structure is utilized to suppress coupling to the slow wave. With a ratio $f/f_c=\frac{1}{9}$, eight fast wavelengths equal ten slow wavelengths. The coupler structure in the tube contains 16 pairs of fingers, corresponding to eight fast wavelengths; cancellation of slow-wave coupling occurs in each quarter of this structure as illustrated in Fig. 1(C).

Figure 2 shows the complete experimental setup. The tube contains a pencil-beam electron gun A, a Cuccia coupler[4] B, the interdigital coupler C, and a collector. The Cuccia coupler is tuned by a built-in parallel coil to the cyclotron frequency $f_c=810$ Mc, and is included only for measurement of the unrefrigerated beam temperature. The interdigital coupler is tuned by means of two built-in series coils D to the signal frequency $f=90$ Mc. Across terminals E the interdigital coupler appears as a series resonant circuit loaded by the electron beam; this circuit constitutes the refrigerated resistance.

The impedance across E is transformed by a fixed matching network F to a nominal value of 50 ohms across terminals G. The resistive and reactive components of the impedance observed at G may be adjusted by varying beam current and beam velocity, respectively. A bridge circuit H, operating at the signal frequency f, makes it possible to adjust the impedance at G to $R=50$ ohms, $X=0$ ohms, with an accuracy of ± 1 ohm.

After the adjustment is completed, terminals G are switched to the input of a 90-Mc low-noise receiver K. By means of a second switch the noise output of the 50-ohm reference resistor J (at room temperature) may be compared with the noise output from the interdigital coupler.

[4] C. L. Cuccia, R C A Rev. **10**, 270–303 (1949).

Receiver K has a noise figure of about 2.5 db. Once the excess noise temperature of the receiver and the power calibration of the output meter are known, the noise temperature of any 50-ohm resistance connected to the receiver input may be determined directly from the output meter reading.

The noise temperature of the beam at the cyclotron frequency f_c is measured for comparison by means of receiver L, tuned to 810 Mc and connected to Cuccia coupler B. This is found to be about 1100°K.

The lowest noise temperature observed at 90 Mc across terminals G is 186°K. Figure 3 shows how the apparent noise temperature increases when the magnetic field is varied so that the cyclotron frequency departs from $f_c=9f$. This increase is attributed to imperfect slow-wave cancellation.

Measurements were made with a beam current of 52 μA, a dc potential of 17 v on the interdigital coupler and a magnetic field of 290 gauss. Losses in the coupler circuit were equivalent to about one-fifth of the loading by the beam. The tuning coils D inside the tube were at an estimated temperature of 360°K. The theoretical noise temperature of the beam at $f=\frac{1}{9}f_c$ should be about 122°K. Because the circuit losses with a noise temperature of 360°K make up one-sixth of the total source resistance, one-sixth of the temperature difference between 360° and 122°K must be added to the theoretical beam temperature. This gives 122°K+40°K = 162°K, which compares rather well with the measured value of 186°K.

CONCLUSIONS

It has thus been shown that a refrigerated load resistance can be produced by means of an electron beam by employing a high ratio between cyclotron and signal frequencies. Equation (1) also applies to slow waves; it is evidently possible to build conventional slow-wave amplifiers, e.g., transverse-field traveling-wave tubes, with very low noise figures (assuming circuit losses can be kept low) by raising f_c sufficiently.[5]

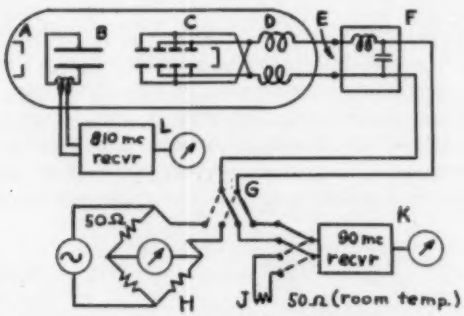

FIG. 2. Measurement of effective beam noise temperature at two frequencies.

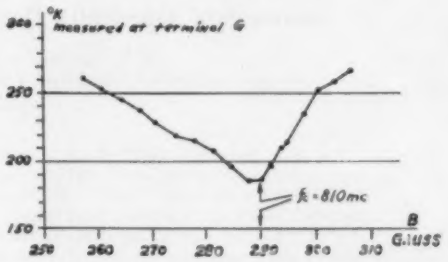

FIG. 3. Beam noise temperature at $f=90$ Mc plotted against magnetic field.

A further interesting conclusion can be drawn for the case of a beam in a nonuniform magnetic field. If the change of field intensity with position along the beam occurs gradually enough to permit application of the principle of adiabatic invariance to the electron orbits, it is easy to show that at any signal frequency the available noise power remains the same anywhere along the beam, even though the local field varies.

In other words, the f_c to be used in Eq. (1) corresponds to the field *prevailing at the cathode, not at the coupler*. This immediately suggests that beams with low noise content for fast-wave amplifiers, conventional amplifiers, or refrigerated loads could be produced by providing a high magnetic field merely in the immediate vicinity of the cathode. One could, for instance, utilize a pole piece positioned right behind the cathode for this purpose.

When a beam travels in a divergent magnetic field, its cross section increases. Cutler[6] has shown that, generally, the product of transverse noise temperature and cross section remains constant for a given beam. The noise reduction just derived is thus in accordance with Cutler's theorem.

[5] This can also be seen from Eq. (35) of footnote reference 3 which, for the condition of coupling to the slow wave only, reduces to $F=1+[(T_c/T)(f/f_c)]$.

[6] C. C. Cutler and M. E. Hines, Proc. I.R.E. 43, 307–315 (1955).

Growth of Atomically Flat Surfaces on Germanium Dendrites

R. L. Longini, A. I. Bennett, and W. J. Smith*
Westinghouse Research Laboratories, Beulah Road, Churchill Boro, Pittsburgh 35, Pennsylvania
(Received March 2, 1960)

This note presents a theory of the formation of extended flat surfaces on germanium dendrites. It is suggested that part of the liquid-solid interface is a supercooled {111} surface, on which new atomic planes are occasionally nucleated. Thermal limitations on the nucleation and propagation of these monolayers are discussed. When such a growing layer reaches the melt surface it creates a step on the solid. It is proposed that the meniscus momentarily sticks to the corner of this step. Subsequent planes nucleated during this sticking period result in a step several atomic layers high, in accord with experiment. Elementary estimates of corner energy and amount of meniscus sticking yield results consistent with experiment.

INTRODUCTION

IT has been shown by Billig,[1] and by Bennett and Longini,[2] that crystals of germanium grown by a dendritic mechanism can have a ribbon like shape. The wide faces are seen to have very shallow steps; the surfaces between steps appear to be atomic planes. The steps, in fact, are relatively far apart so that the variation of thickness of the sample can be very small over considerable length. The previously given mechanism of growth of the dendritic ribbon did not explain the formation of the flat surfaces between steps. A theory is herewith presented which explains the conditions under which the dendritic mechanism of growth will produce the ribbon like shape.

ASSUMPTIONS OF THE THEORY

Growth by the dendritic mechanism takes place in a supercooled liquid. It is assumed that the dendrite grows at a rate limited either by its ability to dissipate the latent heat of fusion or by the rate of nucleation of new planes. Bennett and Longini[2] explained the importance of the twin plane on which the dendrite grows.[3] The propagation of additional layers on the faces is relatively easily accomplished if these added layers are extensions of the seed crystal, because no nucleation process is necessary.

As the dendrite grows, the latest heat of fusion is given off. Since growth takes place in a supercooled liquid, the heat flow is directed into the liquid. Recent experimental evidence indicates[4] that the shape of the liquid-solid interface is essentially as sketched in Fig. 1, where the interface comprises a plane or nearly plane region A and a curved region B. The interface region B of the dendrite has a shape determined by both thermal and crystallographic considerations. The rate at which heat can be given off depends upon the curvature of the interface in the region of generation, larger curvature resulting in greater ease of latent-heat dissapation.

INTERFACIAL TEMPERATURE DISTRIBUTION

If, during growth, a new plane is nucleated on region A, its rate of growth is limited by the rapidity with which the latent heat can be dissipated. In germanium dendrites the growth planes are (111) and are parallel to a central twin structure. If the rate of nucleation of new planes is low, the crystal may grow rapidly enough so that, although the shape of the end of the crystal, region B is controlled by thermal dissipation considerations, the flat surfaces of region A are regions of negligible growth and therefore will not give off any appreciable latent heat. The temperature distribution along these flat side regions will be determined entirely by the heat flow with each side acting as a passive element of volume. Except for the latent heat evolved by the occasional nucleation of new layers on A, the only heat source within the melt is the latent heat of crystallization evolved over the interfacial region B, which must be at (or perhaps slightly below) the melting temperature; furthermore, the melt far from the growing tip is supercooled. As a result the region A will be supercooled. The area of this supercooled liquid-solid interface is appreciable and occasionally nucleation of new layers will take place. These layers will spread rapidly over the entire plane since the heat

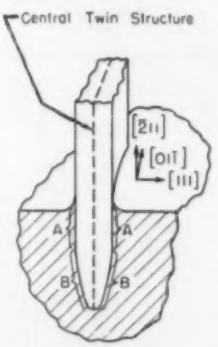

FIG. 1. Assumed shape of dendrite interface.

* This research was supported by the U. S. Air Force through the Air Force Office of Scientific Research and Wright Air Development Division.
[1] E. Billig, Proc. Roy. Soc. (London) **A229**, 346 (1955).
[2] A. I. Bennett and R. L. Longini, Phys. Rev. **116**, 53 (1959).
[3] For discussion of twin structure see D. R. Hamilton and R. G. Seidensticker, this issue J. Appl. Phys. **31**, 1165 (1960).
[4] A. I. Bennett and S. O'Hara, paper presented at American Physical Society, March, 1960.

of fusion for this spreading can be dissipated extremely rapidly both into the supercooled melt and into the solid. The layer grows until it reaches (a) the meniscus of the liquid, where the growth is terminated merely because no more liquid exists to be converted to the solid, and (b) the edge of region B where growth is limited by ability to give off the latent heat.

VELOCITY OF PROPAGATION OF ADDED MONOLAYERS

A thermal limit to the velocity of propagation of a monatomic layer nucleated on the supercooled interface A can be estimated as follows.

Consider the edge of the advancing interface to be a cylindrical heat source, whose radius a we shall take as 1.6 A units, approximately half the thickness of a monolayer in the germanium lattice. Suppose this to be advancing to the right at uniform velocity v, as in Fig. 2. Assuming the thermal conductivity and specific heat of solid and liquid to be equal, the problem of the distribution of temperature around the moving cylinder becomes the two-dimensional case of a cylindrical heat source moving through a uniform fluid at constant velocity. The solution is given by, among others, Jakob[b]; it is

$$T(r)-T(\infty)=(q/2\pi k)e^{-[(v/2\alpha)\xi]}K_0(vr/2\alpha) \qquad (1)$$

where r is the distance from the center of the moving source to the point in question, and ξ is the component of this distance parallel to v; k is the thermal conductivity of the fluid, q is the quantity of heat produced by the source per unit length and per unit time, α is the "thermal diffusivity" $k/\rho c_p$ (ρ=density, c_p=specific heat), and K_0 is the modified Bessel function of second kind and zero order. In turn, the evolved heat q is proportional to the velocity v; specifically, $q=bv$ where $b=2\times10^{-5}$ cal/cm^2, the latent heat of solidification of a monolayer per unit area. We will assume the layer propagates at a velocity which brings the temperature at the surface of the cylinder, where $r=a$, to the melting point. Thus, letting $r=\xi=a$, we have

$$\Delta T=(bv/2\pi k)e^{-(va/2\alpha)}K_0(va/2\alpha), \qquad (2)$$

where ΔT is the supercooling at the surface prior to the formation of the new layer. Letting $x=va/2\alpha$, we obtain

$$xe^{-x}K_0(x)=(\pi ka/b\alpha)\Delta T=1.1\times10^{-3}\Delta T \qquad (3)$$

on insertion of numerical values. This transcendental equation can readily be solved approximately for x by noting that for $\Delta T\sim5$°C, x is of the order of 10^{-3}; thus $e^{-x}\approx1$ and $K_0(x)\approx-\ln x$. Iteration then rapidly yields $x=7.7\times10^{-4}=1.5\times10^{-4}\Delta T$ at $\Delta T=5$°C. A change of a factor of ten in x will change $K_0(x)$ by about 35% and change e^{-x} negligibly, so that for supercoolings of several degrees, the approximation $x=1.5\times10^{-4}\Delta T$ is satisfactory. From this the velocity v is

$$v=2\alpha x/a=(2\pi k/b)[\Delta T/e^{-x}K_0(x)]\approx0.9(k/b)\Delta T$$
$$=2.3\times10^3\Delta T, \qquad (4)$$

where v is in cm sec^{-1} and ΔT, in °C. Note that to the accuracy of this approximation the velocity is independent of the radius a of the assumed heat source. This lack of dependence is important in that the value selected for "a" should perhaps be as large as a phonon mean free path—of the order of several atomic spacings. The supercooling ΔT is that at the surface of region A prior to the growth of the new layer, and does not necessarily equal the supercooling at a point in the melt far from the interface. Experimentally it appears that ΔT may be in the neighborhood of 5°C; for this value, $v=10^4$ cm/sec.

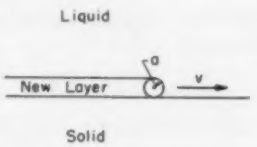

FIG. 2. Edge of advancing layer.

THERMAL INTERACTION OF LAYERS

Layers may interact thermally in two ways. As a layer propagates across the plane region A, the evolving latent heat is assumed to reduce the local supercooling to zero. Further layers cannot be nucleated until this latent heat has been sufficiently dissipated to reestablish the necessary supercooling. Thus a certain minimum time will be required between nucleation of adjacent layers. The order of magnitude of this time can be estimated by considering how rapidly the latent heat of formation of a layer is dissipated after passage of the layer.

According to Eq. (1), the thermal distribution produced by the advancing layer is constant in time when referred to a set of axes fixed in the advancing cylindrical source; the edge of the layer may be thought of as dragging a rigid thermal configuration through the liquid and solid as it progresses. Accordingly, the time decay of the temperature may be obtained from the spatial decay of the distribution behind the source. To this end we substitute $q=vb$, with our previous approximation $v\approx(k/b)\Delta T$, into Eq. (1). This yields

$$T_r-T_\infty=(\Delta T/2\pi)e^{-(v\xi/2\alpha)}K_0(vr/2\alpha). \qquad (5)$$

We now inquire at what distance c behind the advancing layer edge this temperature difference has been reduced by a factor 2π, i.e., for what distance $c=r=-\xi$ does $T_r-T_\infty=\Delta T/2\pi$? Letting $vc/2\alpha=y$, this requires $e^yK_0(y)=1$. The only solution to this equation is readily shown by numerical inspection to be very nearly $y=1$. It follows that

$$c=2\alpha/v\approx2\alpha b/k\Delta T=10^{-4}/\Delta T \text{ cm}. \qquad (6)$$

[b] M. Jakob, *Heat Transfer* (John Wiley & Sons, Inc., New York, 1949), Vol. I, p. 349.

The time required for the layer to advance a distance c is then

$$\tau = c/v = 2\alpha/v^2 \approx 2ab^2/k^2(\Delta T)^2 = 0.05/(\Delta T)^2\ \mu\text{sec} \quad (7)$$

For the previously assumed value of $\Delta T = 5°C$, the time lag between nucleation of successive planes thus cannot be less than about 2×10^{-9} sec.

The layers might interact thermally in a second way. If the edge of an advancing layer should be followed by the more rapidly advancing edge of the succeeding layer, the latent heat evolved by the first layer edge will decrease the velocity of the following edge of the next layer when the distance between the two edges becomes sufficiently small. This interaction distance is just the c of Eq. (6), and for $\Delta T = 5°C$ is 0.2 μ.

The total vertical extent of region A is of the order of a centimeter. From the pull rate and observed step height of 500 A or less, it follows that the average time between nucleation of successive layers is 10^{-3} sec or more. From this it is evident that the rate of nucleation of new layers is not limited by the time required for dissipation of the latent heat of previous layers, and further that a layer, once nucleated, entirely covers the area A long before the next layer is nucleated, so that the hypothetical overtaking of a slow edge by a faster one does not in fact occur.

CORNERS AND STEP FORMATION

When the newly nucleated layer has spread to the meniscus it of course stops growing. The liquid is now in contact with a corner of the solid rather than a plane surface of the solid. Prior to the formation of this step, the meniscus could remain stationary as the growing dendrite was withdrawn as in Fig. 3(a). However, when the step is formed in Fig. 3(b), the meniscus will no longer remain stationary, for this would result in the immediate emergence of the step from the liquid, forming the configuration of Fig. 3(c). It is likely that the surface energy of the configuration (c) is considerably higher than that of (a) or (b); for in (c) the row of atoms along the convex corner of the step will be only doubly-bonded to the adjacent solid, while in (a) all surface atoms are triply-bonded and in (b) the doubly-bonded corner atoms are also bound to the liquid. As a consequence, the edge of the meniscus will momentarily move upward along with the step. Naively speaking, the extra unsatisfied bonds of the corner atoms lift the neighboring liquid to a height where the increased vertical component of the liquid surface tension is sufficient to break these bonds. When this breaking occurs the meniscus will drop past the equilibrium position, and it may "stick" there by a new corner formation.

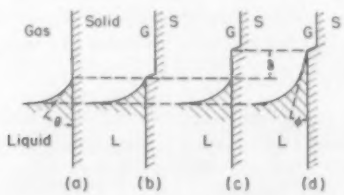

FIG. 3. Corners and step formation.

It is instructive to make an elementary calculation of the energies involved in step formation. The height to which the meniscus rises in the case of Fig. 3(a), where no corner formation is involved, will be governed by the relative values of surface energy of the liquid-gas, liquid-solid, and solid-gas interfaces. If these are denoted by λ, κ, and σ, respectively, the angle θ is determined by the minimum-energy relation $\lambda\cos\theta = \sigma - \kappa$. Although λ has been measured,[6] no reliable values, either experimental or theoretical, are known for σ or κ; there is thus no basis for a direct calculation of θ.

In Fig. 3(d), where a step has raised the meniscus, one might roughly reason that since the corner atoms are in general only doubly-bonded to the solid and thus have twice as many unsatisfied bonds as the atoms of the plane surface in Fig. 3(a), the vertical component of surface tension required to tear the meniscus away from the corner will be twice the equilibrium value in Fig. 3(a), or $\cos\varphi \approx 2\cos\theta$. This reasoning is meant only to be suggestive of the idea that there is a line energy associated with the edge of the step, analogous to the surface energy of the interfaces. No numerical significance is meant to be implied by this argument, other than that this corner energy should result in a momentary lifting of the meniscus and that $\cos\varphi$ should appreciably exceed $\cos\theta$. The experimentally observed meniscus lifting actually indicates a ratio of the order of two.

The time required for the meniscus to break away from a corner by this process will be the time required to pull the dendrite a distance equal to the height difference δ between (a) and (d) of Fig. 2. During this time new planes will be nucleating on region A at random times. Depending on pull rate, area of supercooled interface A, degree of supercooling, and perhaps other things as impurity concentrations, a moderate number of planes may be nucleated during the "sticking" period. Because of their rapid growth they will arrive at the surface increasing the step height. This explains the observed formation of steps a large number of lattice constants high.

It has been observed for some time that in ordinary crystal growth meniscus sticking occurred at the interface between the growing crystals and the melts from which they are drawn. It is also observed on most of these crystals that there are very small flats on the side, which, under microscopic examination, are seen to be steps. It may be these steps that cause the sticking of the meniscus just as steps do in dendritic growth.

[6] P. H. Keck and W. Van Horn, Phys. Rev. **91**, 512 (1953).

EXPERIMENTAL VERIFICATION

According to the theory the flats are grown in a supercooled liquid and therefore there is no possibility of any meltback occurring. As a result one would expect that the dendrite would become continuously thicker with time.

An estimated 12 000 steps have been observed using a two-beam interference microscope. It was ascertained that the steps were smaller than 500 A (using white light). All of these steps were of the type to increase the thickness with growth. This does not preclude the possibility that negative "steps" might be "spread" out, being more ramps than steps. When long dendrites have been grown it has been found that they grow continuously thicker with time. The rate of growing thicker does not appear to be inconsistent with a dependence upon the width of area on which nucleation could occur as well as on the degree of supercooling of the liquid. Since we have grown dendrites on which observable adjacent steps are several centimeters apart, it appears possible to adjust conditions so that the probability of nucleation of new planes on region A is quite small. This indicates either small area of region A, little supercooling on A, or both.

Since the central twin structure is not always uniform, or even present, across the entire width of the dendrite,[7] and since no obvious growth pattern differences are observed between such varying cases, it follows that the mechanism of lateral growth must be different from that of downward growth, in which a twin structure is required.

As the dendrite grows thicker more heat is given off at its edge. Giving off heat there becomes more and more difficult and, as a result, the dendrite becomes narrower as it grows thicker.

[7] H. F. John and J. W. Faust, Westinghouse Research Laboratories, Bull. Am. Phys. Soc. 5, 165 (1960).

JOURNAL OF APPLIED PHYSICS VOLUME 31, NUMBER 7 JULY, 1960

Parametric Diode Figure of Merit and Optimization

K. E. MORTENSON
General Electric Research Laboratory, Schenectady, New York
(Received February 8, 1960; and in final form March 28, 1960)

The noise figure and gain expressions for the diode parametric amplifier are presented and discussed which include the effects of diode losses. From these relationships, a new diode figure of merit is defined as follows: $f_D = a_n/4\pi a_0^2 C_0 R_D$, where a_n is the normalized Fourier coefficient of the time dependent (pumped) capacitance; C_0, the diode capacitance at the operating bias point; and R_D, the equivalent series diode resistance. It is shown that this figure of merit is directly applicable in comparing diodes of various types as well as in optimizing their respective design for low-noise amplifier use. Further, it is indicated how this figure of merit can be directly employed by the circuit designer to predict an amplifiers' noise figure performance including the effects of choice of bias, pump swing, and signal and idle frequency for a given diode.

A complete evaluation of the proposed figure of merit is made for the abrupt junction diode by expressing f_D in terms of device design parameters and examining as a function of bias and base doping. It is concluded, if no constraints are considered, that the maximum value of f_D is obtained for a bias approximately equal to half the breakdown voltage with full pump swing and that $f_D(\max)$ increases with decreasing base doping from 10^{18} to $3\cdot10^{15}$ atoms/cc. It is further concluded that the maximum possible value of a_1/a_0^2 for the inverse square root of voltage capacitance law is approximately 0.557 such that the greatest value $f_D(\max)$ can attain is 20% of f_c, the diode cutoff frequency. Some possible limitations on this evaluation are discussed including the effects of diode deviation from model, pump power or diode dissipation restrictions, nonsinusoidal pumping waveform, and ambient temperature.

I. INTRODUCTION

FOR some time since the advent of the low-noise parametric amplifier, there has been a need for a true parametric diode figure of merit. As the primary reason for the use of the parametric amplifier lies in its low-noise amplifying ability, any figure of merit for the capacitor diode employed should be based on the amplifier noise performance. Further, the resultant diode figure of merit should be directly usable by the circuit designer by indicating the minimum possible noise figure obtainable with a given diode as well as providing information for obtaining the actual operating noise figure. The figure of merit must also lend itself to evaluation and optimization by the device designer for any form of voltage dependent capacitor.

One of the first diode capacitor figures of merit to be put forth was that proposed by Uhlir,[1] namely, the diode "cutoff" frequency, $f_c = 1/2\pi C_{\min} R_D$ or the frequency at which the maximum diode Q becomes unity. Although this figure of merit embraces an extremely important aspect of the diode and is useful in establishing the best diode of a given type, it, by itself, cannot be used to compare the merit of diodes of different type for it lacks a measure of the "pumped" diode's ability to produce gain. As a measure of a

[1] A. Uhlir, Jr., Proc. I. R. E. 46, 1099 (1958).

diode's ability to yield gain is contained in its possible capacitance swing, this author[2] proposed a diode figure of merit F_D which, in essence, was the product of f_c and a capacitance ratio C_{max}/C_{min}, where C_{max} was arbitrarily specified at zero bias and C_{min}, of course, at breakdown. Although this figure of merit is useful in indicating possible design directions, it was based on a somewhat intuitive argument and lacks direct usefulness to the circuit designer. Other similar figures of merit have also been proposed, generally based on small signal pumping conditions which have similar or other faults.

It is thus the purpose of this paper to present a new figure of merit which is based directly on optimized amplifier noise figure and gain considerations. As a result, this diode figure of merit should prove to be both more definitive and more useful than earlier ones.

This paper will first indicate the derivation of the expression for the diode figure of merit utilizing noise figure and gain relationships and, in turn, the evaluation of the expression for the abrupt junction diode, both as a function of bias and doping. A discussion of some of the limitations in this evaluation is then presented followed by appropriate conclusions.

II. DERIVATION OF DIODE FIGURE OF MERIT

A. Amplifier Noise Figure and Gain

If one utilizes the parallel equivalent circuit of the diode capacitor; i.e., C_D (diode capacitance) paralleled with G_D (equivalent diode conductance), in series with a signal and idle circuit and equivalent pump voltage source, then the following expression for the noise figure of a parametric amplifier can be obtained provided the diode Q employed is greater than four at signal or idle frequency:

$$F \cong 1+(G_1/G_g)+[G(\omega_1)/G_g](\omega_1/\omega_2)+(G_{D1}/G_g), \quad (1)$$

where G_1 = the unloaded conductance of the signal tank, G_g = the source conductance in shunt with the signal tank, $G(\omega_1)$ = the negative conductance produced in shunt with the signal tank, G_{D1} = the diode conductance at the signal frequency under pumped conditions, ω_1 = signal angular frequency, ω_2 = idle angular frequency. It can be seen that this expression is nearly the same as that derived by Heffner and Wade[3] for the lossless diode case ($G_{D1}=0$) except for the last term, G_{D1}/G_g, part of the excess diode noise. The result of including a diode conductance in their derivation can readily be deduced by recognizing that the diode conductance evaluated at the signal frequency G_{D1} in effect appears across the signal tank (adding to G_1), while that evaluated at the idle frequency G_{D2} in effect appears across the idle tank (adding to G_2). The effect of G_{D2} on the noise figure expression is its reduction of $G(\omega_1)$ as can be seen from the following expression for $G(\omega_1)$:

$$G(\omega_1)=(C_n^2\omega_1\omega_2/4G_{T2})=(a_nC_0)^2\omega_1\omega_2/4G_{T2}, \quad (2)$$

where C_n = the appropriate harmonic time-dependent capacitance, and G_{T2} = the total conductance in shunt with the idle tank = G_2+G_{D2} under pumped conditions. C_n can be expressed in terms of the product of the normalized capacitance coefficient a_n and C_0, the value of junction capacitance at the chosen bias point, as indicated in Eq. (2). The value of a_n for any harmonic n of the pump can be determined for any C-V law by Fourier analysis or the following expression for cosinusoidal pumping:

$$a_n=\frac{2}{\pi}\int_0^{\pi}\frac{\cos n\theta d\theta}{[1+\gamma\cos\theta]^m}, \quad n=1, 2, 3, \cdots, \quad (3)$$

where γ = the relative capacitance voltage swing $= V_m/V_0'$, V_m = applied pump voltage amplitude, V_0' = sum of reverse bias V_0 and internal junction voltage φ_0, m = exponent of C-V law; e.g., $m=\frac{1}{2}$ for abrupt junction, $\frac{1}{3}$ for graded junction, and even greater than one for hyper-abrupt junctions; θ = integration factor. Note that this capacitance coefficient depends only upon the *relative* voltage swing (not on the absolute values of V_0' or V_m) and the C-V law exponent m. As an example, see Fig. 1 when $m=\frac{1}{2}$ (abrupt junction).[4]

Having examined the general noise figure expression for the parametric amplifier and the effect the equivalent diode conductance has on it, the influence of gain considerations on the noise figure will next be determined. It can be shown that the power gain is given by the following relationship[3]:

$$\text{power gain}=4G_gG_L/[G_{T1}-G(\omega_1)]^2, \quad (4)$$

where G_L = the load conductance in shunt with the signal tank, G_{T1} = the total conductance in shunt with the signal tank = $G_1+G_g+G_L+G_{D1}$ if no circulator is employed. To make the over-all system noise figure approach that of the parametric amplifier, the parametric amplifier gain must be made high such that any post-amplifier noise becomes insignificant. Therefore, without regard to the precise gain required or stability consideration, it can be concluded that G_{T1} must be approximately equal to the negative conductance $G(\omega_1)$. Furthermore, from both over-all noise figure and gain considerations, $G_g \gg G_1+G_{D1}+G_L$ (assuming no circulator) such that $G_g \cong G_{T1} \cong G(\omega_1)$. Thus, the need for high parametric amplifier gain imposes the condition that $G_g \cong G(\omega_1)$ in the general noise figure expression. Making this substitution in Eq. (1) and utilizing the expression for $G(\omega_1)$ Eq. (2) with the added assumption that $G_{D2} \gg G_2$ (generally true at least for the narrow to moderate bandwidth idle circuit as can be approxi-

[2] K. E. Mortenson, J. Appl. Phys. **30**, 1542 (1959).
[3] H. Heffner and G. Wade, J. Appl. Phys. **29**, 1321 (1958).
[4] K. E. Mortenson, "An analysis of sub-harmonic pumping of parametric amplifiers," International Solid-State Circuits Conference, February 10–12, 1960.

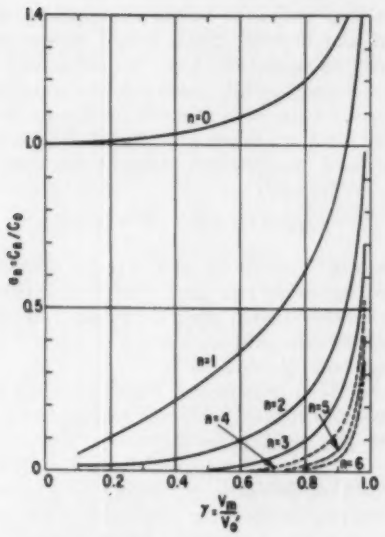

FIG. 1. Plot of the normalized Fourier coefficients of the time-dependent (pumped) capacitance as a function of the relative pump voltage swing.

mately seen from the relative Q's involved), the following noise figure expression results:

$$F = 1 + (G_1/G_g) + [(f_1/f_2) + (4G_{D1}G_{D2}/a_n^2 C_0^2 \omega_1 \omega_2)]. \quad (5)$$

The noise contribution of G_1, although normally very small by choice of G_g, has been kept in this high gain noise figure expression as it still can contribute to very small amplifier noise figures.

B. Diode Figure of Merit

From the high gain expression for noise figure, Eq. (5), after substituting $\omega_1 a_0^2 C_0 R_D$ for $G_{D1}/\omega_1 C_0$ and $\omega_2 a_0^2 C_0 R_D$ for $G_{D2}/\omega_2 C_0$ where R_D is the average diode series resistance, a quantity which involves only the diode parameters can be specified such that the noise figure can be expressed as follows:

$$F = 1 + (G_1/G_g) + [(f_1/f_2) + (f_1 f_2/f_D^2)], \quad (6)$$

where

$$f_D \equiv a_n/4\pi a_0^2 C_0 R_D \quad (7)$$

and is termed the diode figure of merit and has the units of frequency. This expression for the high gain amplifier noise figure is restricted in the sense that f_2 must be chosen to exceed a certain fraction of f_D if amplification is to exist and oscillations are not to exist. This restriction results from the fact that as a_n/a_0^2 is increased to increase f_D and lower the noise figure, G_g must be increased to prevent oscillations (also improves noise figure). There is, however, a limit to increasing G_g if any amplification is to exist; namely,

$$B_1/G_{T1} \geq 1,$$

where $G_{T1} \cong G_g \cong G(\omega_1)$ and $B_1 \cong w_1 a_0 C_0$ or $f_2 \geq (a_n/2a_0) f_D$ using Eqs. (2) and (7). As an example, if various values of γ are chosen, the following conditions on f_2 must be met for fundamental pumping (using a_1):

If $\gamma = 0.7$, then	$f_2 \geq 0.21\, f_D$
0.8	$0.26\, f_D$
0.9	$0.33\, f_D$
1.0	$0.50\, f_D$.

Should f_2 be chosen less than this limiting fraction of f_D, then γ, the relative pump swing, must be reduced to reduce a_1/a_0 (which also reduces f_D) such that the condition is satisfied and a state of amplification as opposed to oscillation exists. Under these conditions, however, the full potential of a given diode is not utilized, and a poorer noise figure than possible will exist.

A minimum noise figure expression for a chosen signal frequency can be immediately obtained from Eq. (6) by recognizing that the minimum value for the quantity within the brackets is obtained when $f_2 = f_D$. Thus,

$$F_{\min} = 1 + (G_1/G_g) + (2f_1/f_D) \quad (8)$$

with the idle frequency chosen to be equal to the diode figure of merit.

It can be noted here that, since f_D can be evaluated for any voltage dependent capacitor (knowing its C-V law, series resistance, and the choice of bias and relative swing), this choice of diode figure of merit should be directly useful in comparing capacitors of various types as well as optimizing their respective designs. Furthermore, since this figure of merit is directly involved in the choice of idle frequency, and in conjunction with the choice of signal and idle frequencies, it determines the amplifier noise figure. Such a figure of merit should prove very useful to the amplifier circuit designer.

III. EVALUATION OF f_D FOR ABRUPT JUNCTIONS

A. Expressing f_D in Device Design Parameters

The following expressions for junction capacitance and base or diode resistance (as discussed in the authors' earlier paper[5]) can be substituted into the figure of merit expression.

$$C_0 = [\epsilon A_J^2 e N_d/2(\varphi_0 + V_0)]^{\frac{1}{2}} \text{ in farads}, \quad (9)$$

where ϵ = the dielectric constant, e = the electronic charge, N_d = the base doping concentration (donors—n type base), A_J = the junction area, and

$$R_D \cong t/e\mu_n N_d \alpha A_J \text{ in ohms}, \quad (10)$$

where t = the base thickness, μ_n = the electron mobility, α = the ratio of the effective base cross-sectional area to the junction area. On substituting (9) and (10) into Eq. (7) the following relationship for the figure of

merit in terms of device design parameters is obtained:

f_D (abrupt junction)

$$=\frac{\sqrt{2}}{4\pi}\left(\frac{e}{\epsilon}\right)^{\frac{1}{2}}\frac{\alpha}{l}\mu_n N_d^{\frac{1}{2}}(\varphi_0+V_0)^{\frac{1}{2}}\frac{a_n(\gamma)}{a_0^2(\gamma)}. \quad (11a)$$

Equation (11a) can be further reduced for the particular case when germanium is employed:

f_D (abrupt junction, Ge)

$$=40.8(\alpha/l)N_d^{0.335}(\varphi_0+V_0)^{\frac{1}{2}}a_n(\gamma)/a_0^2(\gamma), \quad (11b)$$

where

$$\mu_n\cong 1.08\cdot 10^6\, N_d^{-0.165} \text{ in cm}^2/\text{v-sec} \quad (12)$$

(within $\pm 15\%$ of most recent data[5] on μ_n vs N_d within the range 10^{15} to 10^{18} atoms/cc, and

$\varphi_0\equiv E_f(n)-E_f(p^+)$ or difference in Fermi levels,

$E_f(p^+)=E_v$ (edge of the valence band) as the p^+ region is degenerate $N_a\cong 10^{19}$ to 10^{20} atoms/cc,

$E_f(n)\cong E_c-0.025\ \ln 1.03\cdot 10^{19}/N_d$, E_c (edge of conduction band),[6]

$E_c-E_v=E_g=0.67$ ev for Ge,

$$\varphi_0\cong 0.67-0.025\ \ln 1.03\cdot 10^{19}/N_d \text{ in volts.} \quad (13)$$

B. f_D as a Function of Bias and Doping

From an examination of Eq. (11b), it can be seen that f_D depends upon doping, bias, and relative pump swing. For the purpose of detailed examination, the variation of f_D with choice of V_0 using the maximum permissible swing (γ) for various values of doping has been plotted in Fig. 2. The maximum permissible swing is determined by the ratio $V_m/(\varphi_0+V_0)$, where V_m (pump voltage amplitude) is limited by the choice of V_0, the breakdown voltage V_{BD}, and/or the maximum forward bias voltage V_{FWD}. V_{FWD} is the maximum forward bias permitted before shot noise becomes significant and depends upon several factors including frequency of operation, base thickness, and doping. For the purposes of this evaluation, however, a constant value of 0.1 v has been assumed for V_{FWD}. The values of a_n/a_0^2 used are taken from Fig. 1. The breakdown voltage used was obtained from the following expression:[7]

$$V_{BD}\cong 1.03\cdot 10^{13}N_d^{-0.725} \text{ in volts.} \quad (14)$$

From Fig. 2, it can be seen that for each choice of base doping, as the bias (and thus also the pump voltage) is increased from zero, the diode figure of merit rapidly increases until a maximum value is reached at a voltage corresponding to $\frac{1}{2}(|V_{BD}|-|V_{FWD}|)$. If the bias is still further increased, the value of the figure of merit rapidly drops off, becoming zero at the breakdown voltage. The explanation for these "saw-tooth" like curves can be readily gained from Eq. (11b), for, assuming fixed geometry and doping, f_D is proportional to the relative pump swing and the bias voltage. Thus near zero bias both V_0 and γ (and thus a_n/a_0^2) are small; at $\frac{1}{2}(|V_{BD}|-|V_{FWD}|)$, V_0 is approximately half its maximum value while γ (and a_n/a_0^2) is at a maximum and dominates; near breakdown, V_0 is maximum but γ (and a_n/a_0^2) is approaching zero and again dominates.

From the dependency of f_D upon bias, it was concluded that to obtain the maximum possible figure of merit the bias must be set at $\frac{1}{2}(|V_{BD}|-|V_{FWD}|)$. A plot of f_D(max) vs doping is presented in Fig. 3, both for the case of direct pumping $n=1$, and subharmonic pumping $n=2$ and $n=3$ (no resonant mode at two or three times the pump frequency). It is observed that for all three conditions of pumping, f_D(max) can be increased by reducing the doping (at least over the range $N_d=3\cdot 10^{15}-10^{18}$ atoms/cc). The reason for the more rapid increase in f_D(max) with $n=2$ and 3 is that in all cases the dependency upon doping is almost entirely through γ and a_n/a_0^2, and a_2/a_0^3 and a_2/a_0^2 are faster functions of γ than a_1/a_0^2 (see Fig. 1). The dependency of f_D(max) upon a_n/a_0^2 can most readily

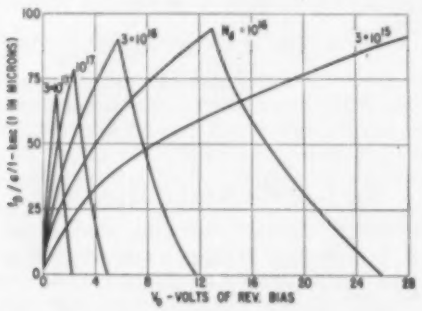

FIG. 2. Plot of diode figure of merit as a function of bias voltage (with full pump swing) for several values of base doping.

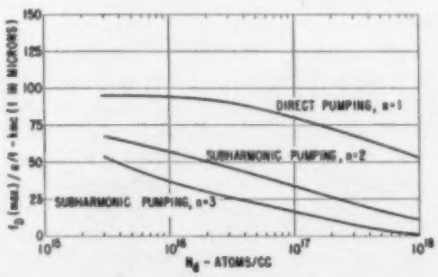

FIG. 3. Plot of maximum (with respect to bias) diode figure of merit as a function of base doping.

[5] W. W. Tyler and T. J. Soltys, G. E. Research Laboratory (private communication).

[6] N. B. Hannay, *Semiconductors* (Reinhold Publishing Corporation, New York, 1959), pp. 331, 362.

[7] S. L. Miller, Phys. Rev. **99**, 1234 (1955).

be seen by letting

$(\varphi_0+V_0)^{\frac{1}{2}}\cong(\frac{1}{2}V_{BD})^{\frac{1}{2}}$ in Eq. (11b)

or $\cong 2.27\cdot 10^6\, N_d^{-0.3625}$ using Eq. (14).

Thus,

$$f_D(\max)\cong 9.26\cdot 10^7(\alpha/t)N_d^{-0.0775}a_n(\gamma)/a_0^2(\gamma)$$
$$\cong 3.4\cdot 10^7(\alpha/t)a_n(\gamma)/a_0^2(\gamma) \quad (15)$$

within the doping range 10^{15} to 10^{18} atoms/cc and is approximately independent of doping except through γ. It should be noted here that, if V_{FWD} had not been assumed constant at 0.1 v, but had been assumed to increase somewhat with doping, then the maximum relative swing and therefore a_n/a_0^2 and $f_D(\max)$ would be higher than that shown for heavier doping. However, in general, $f_D(\max)$ would still be decreased by increasing the base doping.

It is interesting at this point to compare $f_D(\max)$ to the earlier figures of merit (as discussed previously), namely, the diode cutoff frequency f_c and the over-all device figure of merit F_D, involving the product of f_c and C_{max}/C_{min}. The comparison of $f_D(\max)$ with f_c for the abrupt junction can be readily gained by recognizing that, for $f_D(\max)$, C_0 is approximately specified at $V_{BD}/2$ or is equal to $\sqrt{2}C_{min}$. Making this substitution into Eq. (7),

$$f_D(\max)\cong 0.354\, a_n/a_0^2 f_c \text{ (for abrupt junction)}, \quad (16a)$$
$$\cong 0.397\, a_n/a_0^2 f_c \text{ (for graded junction)}. \quad (16b)$$

For a doping such that $\gamma_{max}=0.9$, $a_1/a_0^2\cong 0.50$ (abrupt junction), $a_1/a_0^2\cong 0.38$ (graded junction), $f_D(\max)\cong 0.18\, f_c$ for the abrupt junction and $0.15\, f_c$ for the graded junction. At best, the maximum ratio of a_1/a_0^2 for the abrupt junction using sinusoidal pumping is 0.557 (occurring for $\gamma=0.992$) such that the greatest value of $f_D(\max)$ is $0.20\, f_c$ (abrupt junction, $m=\frac{1}{2}$). The greatest value for the graded junction ($m=\frac{1}{3}$) is approximately $0.17\, f_c$. Thus, it can be concluded that $f_D(\max)$ can range up to 20% of the diode "cutoff" frequency depending on the maximum relative permissible swing and the diode type. A comparison of $f_D(\max)$ (using $n=1$) with the authors' earlier figure of merit F_D[2] indicates that the present figure of merit possesses the same general trend with respect to doping, but with a considerably different scale factor in that F_D by definition is greater than f_c, not less, and that the degree of dependency upon doping is significantly less than that originally indicated for F_D.

C. Examples of the Evaluation and Use of f_D

To illustrate the use of the diode figure of merit f_D and this evaluation, consider a direct pumped ($n=1$) amplifier whose signal frequency f_1 is chosen to be 6 kMc and the minimum possible amplifier noise figure is required. Assume that two different abrupt junction diodes are available, both with $\alpha=1$, and $t_0=5$ microns (t at zero bias), but one with $N_d=3\cdot 10^{17}$ atoms/cc ($t\cong t_0$), the other with $N_d=10^{16}$ atoms/cc ($t\cong 4\mu$). From Fig. 3, it can be immediately calculated that $f_D(\max)=13.6$ kMc and 23.5 kMc corresponding to $f_c=170$ kMc and 240 kMc (using $\bar{R}_D$ or $\bar{t}$), respectively. On using the expression for minimum noise figure, Eq. (8), and assuming the term G_1/G_g to be negligible, the amplifier employing the heavier doped diode would have a minimum noise figure of 2.74 db ($T_A=264°K$) with $f_2(\text{optimum})=13.6$ kMc; whereas, the one employing the lighter doped diode would have a minimum noise figure of 1.79 db (153°K) with $f_2(\text{optimum})=23.5$ kMc. If $f_2(\text{optimum})$ were not used in the latter case but rather the same f_2 (13.6 kMc) used with the heavier doped diode case, the noise figure would certainly increase but would still be the lower, being 2.01 db (177°K) as calculated from Eq. (6). Thus it can be seen that superior amplifier noise performance can be achieved with diodes of greater f_D but of approximately the same cutoff frequency (or at least the same t_0). It should be recognized that in this instance, at least, the superior noise performance is achieved at the expense of greater required pump *voltage* (13.45 v as compared to 2.71 v).

D. Limitations of This Evaluation

As this evaluation of the diode figure of merit is by no means all inclusive, the following specific limitations are pointed out.

1. Deviations of the Actual Diode from the Model Assumed

(*a*) Diodes, particularly of the double-alloyed type, which have a small base thickness t and are lightly doped will have a base thickness which is voltage dependent (depletion layer comparable to base thickness) and thus, a voltage dependent base or diode resistance R_D. This factor, then, would have to be accounted for in studying the variation of f_D with bias as well as with doping.

(*b*) With the actual diodes required for microwave operation possessing very small junction diameters, surface effects can be quite significant. Surface effects cause additional resistive and capacitive elements to appear in shunt with the body junction thus yielding equivalent series diode parameters which are frequency dependent.[5] Therefore, in actual practice, it may be necessary to specify f_D as a function of frequency.

(*c*) Diodes obviously require mounting or packaging and therefore possess parastic elements such as package capacitance, inductance, or in general, an impedance transforming network. Ideally, any diode transforma-

[5] D. E. Sawyer, J. Appl. Phys. **30**, 1689 (1959).

tion introduced by the packaging can be undone by an appropriate inverse impedance transforming network. In practice, however, to design such inverse transforming networks which are effective over appreciable bandwidths at both the signal and idle frequencies can be quite difficult. It is for this reason that it is imperative to minimize all package parasitics such that the full active junction parameters can be utilized even at high frequencies.

2. *Pump Power and Diode Dissipation Limitations*

In some instances, particularly at very high frequencies, adequate pump power to provide the maximum permissible capacitance swing may not be available or the diode swing may be restricted by dissipation limitations. In the event that either condition existed for a given diode, then the evaluation of f_D would be constrained and $f_D(\max)$ would not be obtainable. To examine the factors which influence the amount of pump power dissipated by the diode (which is approximately equal to the pump power required by the amplifier), the following relationship for diode power dissipation (derived for the condition of negligible amplifier circuit impedance at pump harmonics)[4] can be considered.

$$P_D=[(V_0')^2/4Q_0X_0]\gamma^2 f(\gamma), \tag{17a}$$

where Q_0 and X_0 are the diode parameters at the bias point and at the pump frequency f_p and $\gamma^2 f(\gamma)$ is a function of γ (the maximum relative voltage swing consistent with V_0) which is nearly an exponential function of γ (0.3 to 0.9, abrupt junction diode).

If in Eq. (17a) device parameters are substituted,

$$P_D=[\tfrac{1}{2}\pi^2(\epsilon/\mu_n)(t/\alpha)]A_J f_p^2 V_0'\gamma^2 f(\gamma), \tag{17b}$$

where all the quantities have been previously defined. Examination of (17b) immediately reveals that the only device parameter which can be used to reduce P_D without altering f_D is the junction area A_J. Thus A_J should always be kept as small as possible commensurate with amplifier impedance levels and fabrication technology. The quantity t/α should be kept to a minimum both for minimizing P_D and maximizing f_D. Reducing f_p will rapidly decrease P_D, but this may force f_2 to be chosen less than $f_2(\text{optimum})=f_D$ resulting in obtaining a noise figure greater than the minimum value. Certainly reducing V_0' or γ to reduce P_D will decrease f_D as can be seen from Eq. (11a). Thus, if pump powder availability or diode dissipation becomes a constraint and the junction area has been reduced to its limit, it may become necessary to compromise f_D and the amplifier noise figure. Such a compromise would establish the limit in lightening the base doping to achieve higher values of f_D.

3. *Effects of Nonsinusoidal Pump Voltage*

If appreciable impedance exists in the amplifier circuit at harmonics of the pump or the pump source does not appear as a voltage source to the diode (at pump frequency), then the voltage waveform producing the time-dependent capacitance will not be sinusoidal. Under such conditions a_n as a function of γ would differ from the values used here and would, therefore, have to be reevaluated for the appropriate waveform. It might be noted here that other waveforms such as a square wave could yield higher values of f_D for the same diode provided such waveforms could be impressed.

4. *Effects of Different Ambient Temperatures*

The evaluation of f_D for the abrupt junction diode as described is valid only for room temperature and would have to be reevaluated for other diode temperatures. In addition, all the noise terms in the amplifier noise figure expressions [(1), (5), (6), and (8)] would have to be multiplied by the appropriate temperature ratio (i.e., actual to reference temperature).

IV. CONCLUSIONS

A parametric diode figure of merit based directly on the high gain amplifier noise figure expression has been derived. With appropriate evaluation, this figure of merit will permit a direct comparison of diodes, even of different type, as well as lead to their respective optimization and ultimate limitations. Further, if the amplifier circuit designer is given the value of this figure of merit as a function of bias, frequency, and possibly temperature, he can determine the prospective amplifier noise figure under various operating conditions as well as knowing the optimum choice of conditions such as that of $f_2(\text{optimum})=f_D=(f_{D1}f_{D2})^{\frac{1}{2}}$ (if frequency dependent).

On using the derived figure of merit, an evaluation carried out for the abrupt junction diode, such as the double-alloyed units, has indicated that, without constraints, the diode swing should be as great as possible (up to $\gamma=0.992$, $m=\frac{1}{2}$) resulting in a choice of bias point as being nearly equal to one-half the breakdown voltage of the diode. Further, such a maximum (with respect to bias) figure of merit can be increased by reducing the base doping. Limitations on these results such as might be imposed by deviations in the diode model, pump power or diode dissipation restrictions, and other constraints, can be accounted for or incorporated in the evaluation to yield the more restricted results.

V. ACKNOWLEDGMENT

The author wishes to express his gratitude to W. N. Coffey for many helpful discussions, particularly concerning the effects of diode losses on the amplifier gain and noise figure expressions.

Use of the Omegatron in the Determination of Parameters Affecting Limiting Pressures in Vacuum Devices

DAVID LICHTMAN
Sperry Gyroscope Company, Great Neck, New York
(Received February 9, 1960; and in final form March 18, 1960)

The omegatron mass spectrometer has been used to determine residual gases in vacuum systems, including ion pump systems. The predominant residual gas in ion pumps was found to be methane, while the gases found in oil diffusion pump systems include water vapor and carbon monoxide. Analysis has been performed to determine the residual gases in vacuum tubes which are difficult to outgas, and conditions that lead to considerable hydrogen content are described. Examples of the use of the omegatron mass spectrometer as a tool in aiding solution of outgassing problems are given.

INTRODUCTION

THE purpose of this paper is to point out that the identification of gases within a vacuum system is as important as the measurement of the total pressure that they cause. These gases, even at pressures as low as 10^{-9} mm of Hg, can be identified by a suitable mass spectrometer.

The vacuum systems of concern to us can be grouped into two categories. One category is that of the pump station and all components utilized in the production of vacuum. The other category includes the components to be evacuated and eventually sealed off from the system. In our work, these latter components are microwave tubes of the traveling-wave tube and klystron types.

The limitations of vacuum pumping systems may be determined by the use of the omegatron mass spectrometer, with which it is possible to identify the residual gases that make the achievement of exceedingly low ultimate pressures difficult. Simple procedures can eliminate such offenders as alcohol or acetone; however, tenacious gases such as water vapor and carbon monoxide will require more elaborate elimination techniques.

The components to be evacuated present a more difficult problem. But fortunately, identification of the gases evolved during tube processing makes the prior elimination of these gaseous contaminations possible. For this reason, the information obtained with the aid of the mass spectrometer can be used to help eliminate unwanted gases or prevent their occurence in other vacuum systems.

Thus, this type of program can lead to the evolvement of better pump systems and components. It can be used to aid the improvement of the construction of microwave tubes and the processing techniques used on them.

EXPERIMENTAL FACILITIES

A major problem in tubes is one of achieving and maintaining a desired degree of vacuum. To pursue this problem effectively, an experimental system was constructed that would enable the analysis of gases under all desired conditions. The heart of this system is the mass spectrometer tube. Of the various mass spectrometers available, it was decided to use an omegatron type because this type is small, portable, and can be attached simply to almost any vacuum system. Also, it can be completely baked and outgassed, enabling measurements to be made at very low pressures (e.g., 10^{-9} mm of Hg).[1,2]

In a mass spectrometer, the two parameters of interest are the sensitivity and the resolution. The resolution of the omegatron mass spectrometer has a theoretical maximum given by[3]

$$\rho = M/\Delta M = (RH^2/2E_0)(e/M), \tag{1}$$

where R is the distance of the collector from the point of formation of ions, H is the magnetic field strength, E_0 is the peak rf field, and e/M is the charge-to-mass ratio of the ion under study.

If one works with a reasonable-size magnet of about 2500 gauss and an rf field of 0.5 v/cm maximum, the maximum resolution becomes (for $R=1$ cm)

$$\rho \cong 600/M, \tag{2}$$

where M is the mass number of the ion.

The maximum sensitivity can be calculated from the known cross section for ionization using 50-ev electrons. The sensivity S is defined by

$$S = i^+/(i^- P), \tag{3}$$

(ion current/electron current/unit pressure). The ion current is given by

$$i^+ = i^- \sigma N L, \tag{4}$$

where i^+ is the ion current, i^- is the electron current, σ is the cross section for ionization, N is the gas density, and L is the reaction length.

Now, $\sigma \cong 3\times10^{-15}$ cm^2 for a typical gas (e.g., nitrogen), and $N = N_0 P/1.86\times10^7$, where N_0 (Avogadro's number) $= 6\times10^{23}$, and P is the pressure in mm of Hg, assuming a temperature of 300° K. Then the sensitivity becomes

$$S = i^+/(i^- P) = \sigma L N_0/1.86\times10^7. \tag{5}$$

[1] D. Alpert and R. S. Buritz, J. Appl. Phys. **25**, 202 (1954).
[2] J. S. Wagener and P. T. Marth, J. Appl. Phys. **28**, 1027 (1957).
[3] H. Sommer, H. A. Thomas, and J. A. Hipple, Phys. Rev. **82**, 697 (1951).

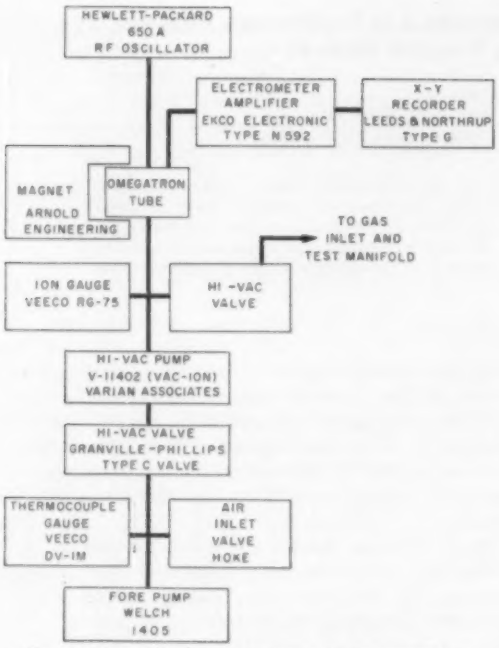

FIG. 1. Schematic of mass spectrometer vacuum system.

And for $L=2$ cm (the actual dimension in the omegatron),

$$S=[(3\times10^{-15})(2)(6\times10^{22})]/(1.86\times10^{7})$$
$$=20 \text{ amp} i^{+}/\text{amp} i^{-}/mm \quad \text{of} \quad \text{Hg}.$$

For example, $i^{+}=20\times10^{-12}$ amp, for $i^{-}=1$ μa and $P=10^{-6}$ mm of Hg.

The first experimental system was arranged as shown in Fig. 1. There are three basic components of the system: the mass spectrometer, the pumping system, and the manifold, where reactions to be studied may take place. The use of knife-edge seals permits the construction of a versatile system capable of simple modification and rearrangement when desired. The construction of the knife-edge seal used is shown schematically in Fig. 2. These seals are tight enough to allow the use

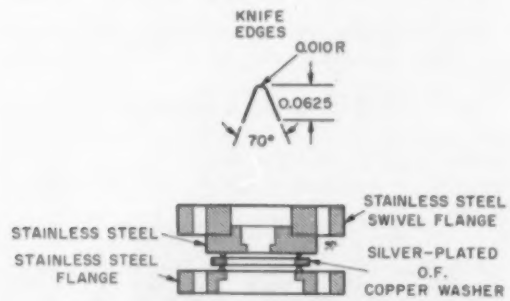

FIG. 2. Knife-edge seal.

TABLE I. Omegatron sensitivity data. Sensivitity in amp (i^{+}) per amp (i^{-}) per mm Hg.[a]

Gas	Sensitivity
Argon	4.8
CO_2	20.0
Argon (rerun)	5.0
Nitrogen	16.0

[a] Electron voltage 50 v, trapping voltage 0.0 v, collector voltage 50 v, rf peak field 0.56 v/cm.

of at least ten of them in a system which can be easily pumped down to 2×10^{-9} mm of Hg by a 5 liter/sec pump. The system also contains metal ultra-high-vacuum valves that permit complete control of gas flow and allow the achievement of very low pressures. The system was first operated with no addition to the manifold to test the performance of the omegatron tube.[4]

The resolution was measured utilizing the values of magnetic field and electric field as indicated in the above section. The value obtained was a resolution of 25 at mass 20. This value is very close to the theoretical maximum value and indicates good performance of the omegatron tube.

The sensitivity of the omegatron tube was measured for several gases, and the data are shown in Table I. This data can be compared to the theoretical maximum values derived, indicating a fairly high collection efficiency in the tube. The relative sensitivities for the different gases are about as expected for 50-ev electrons. It is interesting to note the relative secondary peaks obtained, since these values are useful for differentiating carbon monoxide and nitrogen, as well as helping in accurate determinations when many gases are present simultaneously. The data are shown in Table II. The sensitivity obtained permits the measurement of partial pressures of 10^{-9} mm of Hg with an electrometer capable of reading 10^{-14} amp. The leakage resistance in the spectrometer tube is high enough to permit the measurement of these low currents. There are several elec-

TABLE II. Intensity of ion fragments referred to the principal mass (100) for several gases.

Gas	Mass number	Relative peak height	Gas ion
Argon	40	100.0	A^{+}
	20	7.5	A^{++}
CO_2	44	100.0	CO_2^{+}
	32	1.35	O_2^{+}
	28	29.5	CO^{+}
	22	0.68	CO_2^{++}
	16	7.7	O^{+}
	14	1.35	CO^{++}
	12	2.7	C^{+}
Nitrogen	28	100.0	N_2^{+}
	14	4.5	(N_2^{++},N^{+})

[4] The first tubes used were purchased from Leybold, Cologne, Germany, through N.R.C. Equipment Corporation, Newton, Massachusetts.

TABLE III. Residual runs in glass oil diffusion pump system.

Mass numbers 1–150 checked			
Mass number	Gas ion	Relative peak height	
28	N_2^+	1.	Pressure =
18	H_2O^+	1.3	5×10^{-7} mm Hg
17	OH^+	0.6	
16	O^+	Trace	Ionization
14	N^+	Trace	gauge off
2	H_2^+	0.6	
28	N_2^+	1.7	Pressure =
18	H_2O^+	1.4	5×10^{-7} mm Hg
17	OH^+	0.6	
14	N^+	Trace	
14	N^+	Trace	Ionization
2	H_2^+	0.8	gauge on

trometers commercially available which are useful in this range. Thus, the omegatron tube was operating as close to theoretical limits as could be expected, and further experiments were set up.

TEST DATA

Vacuum Systems

Analyses were performed on various vacuum systems to determine the residual gases under specific conditions. The great interest in ion pumps led to numerous tests on ion pump systems. For comparison, some experiments were performed on a diffusion pump vacuum system. The data obtained on a conventional oil diffusion pump vacuum system, made of glass and using liquid nitrogen trapping, are shown in Table III. The data indicate the existence of three main peaks, namely, water vapor, hydrogen, and probably the nitrogen and carbon monoxide that make up the value at mass 28. Because the sensitivity during this run was inadequate to determine the secondary peaks of nitrogen and carbon monoxide, it is not possible from the data available to distinguish between the two gases.

It is interesting to note that no peaks were found up to mass 150, indicating that there are no detectable oil fractions up to that point. This system is apparently well trapped, since at the time of the test it had been operating for many days since its last bakeout.

TOTAL PRESSURE = 5×10^{-9} mm Hg

MASS NUMBER	GAS ION	RELATIVE PEAK HEIGHT
18	H_2O^+	0.5
41		7.5
56	ALCOHOL	8.8
71	FRACTIONS	6.3

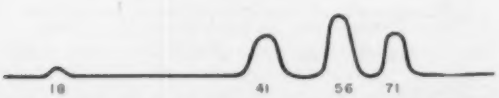

FIG. 3. Residual gases in ion pump system.

TOTAL PRESSURE = 5×10^{-9} mm Hg

MASS NUMBER	GAS ION	RELATIVE PEAK HEIGHT
17	OH^+	1.6
18	H_2O^+	3.8

FIG. 4. Residual gases in ion pump system.

Considerable work is presently being performed on ion pump systems. In the ion pump, a glow discharge mechanism is maintained at low pressures by the use of a combined electric and magnetic field. The cathode structure is made of titanium and accomplishes the pumping by reacting with the ionized gases driven into it by the electric field. Sputtering of the cathode also contributes to the pumping process. These vacuum systems are being used for both experimental work as well as tube processing. Since ion pumps contain no oil or other material of potential high vapor pressure, vacuum systems utilizing these pumps should be capable of achieving exceedingly low ultimate pressures. In addition, the desire to understand the basic operation of ion pumps makes it necessary to know the residual gases under various operating conditions.

Measurements made on an ion pump system are shown in Figs. 3–6. Several interesting features are ap-

MASS NUMBER	GAS ION	RELATIVE PEAK HEIGHT
2	H_2^+	61.1
12	C^+	0.3
13	CH^+	6.0
14	CH_2^+	15.6
15	CH_3^+	61.2
16	CH_4^+	69.0
17	OH^+	0.8
18	H_2O^+	0.2
20	A^{++}	0.7
27	$C_2H_3^+$	6.2
28	$C_2H_4^+$	26.7
29	$C_2H_5^+$	6.5
40	A^+	36.0

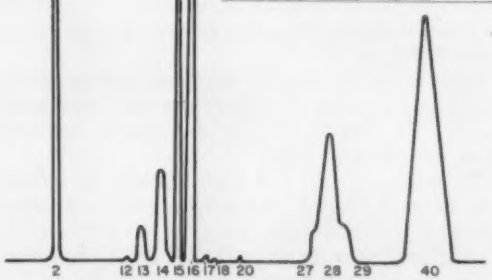

FIG. 5. Build-up of gases in ion pump system after pump has been off five minutes.

MASS NUMBER	GAS ION	RELATIVE PEAK HEIGHT
12	C^+	0.6
13	CH^+	2.3
14	CH_2^+, N^+	11.2
15	CH_3^+	41.3
16	CH_4^+, O^+	50.2
17	OH^+	1.3
18	H_2O^+	5.0
20	A^{++}	—
28	$CO^+, N_2^+, C_2H_4^+$	—
32	O_2^+	15.0
40	A^+	—
44	CO_2^+	—

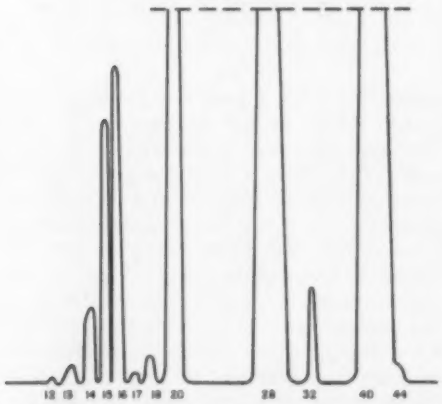

FIG. 6. Typical run showing the ability to readily identify masses in the range of 12 to 44.

parent from these curves. Figure 3 indicates the existence of alcohol fractions as the predominant residual gas. The alcohol had been introduced during previous experiments and the portions still remained since the system had not been thoroughly rebaked.

Figure 4 indicates the residual gases when the total pressure was 5×10^{-9} mm of Hg. The only gas found at this pressure was water vapor. All other components were below the sensitivity level of the omegatron tube.

Since ion pumps are basically electronic devices that can be turned on and off instantaneously, the problem of oil cooling, trapping, etc. does not affect the system. The system is completely closed, and the pump action can be started and stopped at will. To determine which gases exist in the system when the ion pump is turned off, an analysis was made on the closed system when the ion pump had been off for five minutes. The results are shown in Fig. 5.

It was surprising to see the very large peaks at masses 12 and 13, indicating the existence of methane. The residual gases consist primarily of hydrogen, methane, argon, and probably C_2H_4.

The results, which have been reported by others,[5] seem to be a property of titanium getter-ion pumps regardless of their design.

Many analyses were made on the gases in the system when the ion pump was turned off. The results always follow the typical spectrum shown in Fig. 5. For example, another spectrum is shown in Fig. 6. Here, the spectrum due to the residual build-up is similar to that shown in Fig. 5, as far as the methane peaks are concerned. However, a peak appears at mass 32, and exceptionally large peaks appear at mass 28 and 40. These peaks were determined to be due to a small air leak.

The spectrum in Fig. 6 does indicate the general usefulness of the omegatron in the range of masses from 12 to 44. (This is the range of masses in which most gases of interest in vacuum tube work lie.) It is interesting to note the resolution and the sensitivity capability of the omegatron for peaks such as those at 12 and 17 which are considerably less than 1% of the major peaks at 28 and 40.

Gas Evolution from Microwave Tubes

Identification of the residual gases in microwave tubes is usually necessary before they can be eliminated or at least reduced. The omegatron mass spectrometer makes this analysis possible as well as practical. Analysis of the gases evolved at various steps of operation will aid in determining optimum processing procedures and in pin-pointing the sources of difficulty in obtaining the desired degree of vacuum. A typical problem will be described indicating how the omegatron pointed to the source of difficulty. To determine what the residual gas was in a high-power klystron tube, a diode structure was fabricated using standard production techniques but including a Ceralloy[6] getter coating on a heat shield adjacent to the cathode. This diode was processed through bakeout and cathode conversion. A high-vacuum valve in the tubulation was closed. The diode was removed from the processing station by disconnecting a knife-edge seal and was then placed on the omegatron station Thus, the tube was maintained under vacuum. When the pressure in the omegatron vacuum system (utilizing an ion pump) was reduced to less than 5×10^{-9} mm of Hg, the valve to the tube was opened. The heater was brought up to normal operating tem-

TOTAL PRESSURE = 3×10^{-7} mm Hg

MASS NUMBER	GAS ION	RELATIVE PEAK HEIGHT
2	H_2^+	12.0
14	CO^{++}, N^+	0.2
16	O^+	0.3
18	HOH^+	1.7
28	CO^+, N_2^+	10.65
41	} ALCOHOL FRACTIONS	1.35
56		1.10
71		0.50
88		0.45

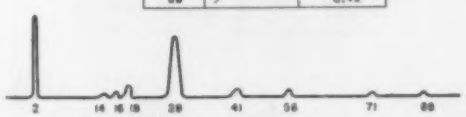

FIG. 7. Gas analysis-high-power klystron diode on ion pump station with tube heater on.

[5] G. Reich and H. G. Nöller, *Production of Very Low Pressures with Getter-Ion Pumps* (E. Leybold, Cologne, Germany).

[6] "Ceralloy-400 continuous getter," Ceralloy Bull. No. 2 (New Process Metals, Inc., Newark, New Jersey).

perature and the spectrum taken. The data are shown in Fig. 7, and indicate the existence of hydrogen and carbon monoxide with a small amount of water vapor and some alcohol fractions.

After the tube had operated long enough to become completely warmed up, another spectrum was taken. The results are shown in Fig. 8, where it is noted that the hydrogen peak is dominant, with carbon monoxide as the secondary gas. Smaller quantities of water vapor and alcohol still exist.

The existence of large hydrogen peaks verifies the results of work done previously and reported at the A.S.T.M. Conference on Cleaning of Electronic Device Components and Materials (1958).[7] It was found that the brazing operations used in assembling the tube, which are performed in a hydrogen atmosphere, cause the tube parts to absorb a very large quantity of hydrogen gas. This hydrogen is re-evolved when the gun structure is operated at full power, and causes considerable gas evolution over a long period of time, i.e., up to one hundred hours.

To determine the other reactions taking place within the tube structure, the ion pump was turned off, leaving the tube in the sealed system. Analyses were made at intervals of time, and the rate of gas increase for the major components is shown in Fig. 9. The argon pressure shows a steady linear increase with time and is useful as a reference.

Of great interest is the very rapid rise of hydrogen when the heater is turned off at point *A*. Normally, this result would seem strange, since the hydrogen evolvement rate should be proportional to the temperature of the gun structure and should gradually decrease when the heater is turned off. However, the Ceralloy was placed in such a position as to reach a temperature of about 250°C when the heater was at full power. Experiments performed on the reactions of Ceralloy-400 and hydrogen at this laboratory indicated an optimum pumping speed of Ceralloy for hydrogen at about 250°C.

MASS NUMBER	GAS ION	RELATIVE PEAK HEIGHT
2	H_2^+	23.0
12	C^+	0.1
14	CO^{++}, N^+	0.45
18	HOH^+	3.0
28	CO^+, N_2^+	12.9
41	ALCOHOL	1.50
56	FRACTIONS	0.90

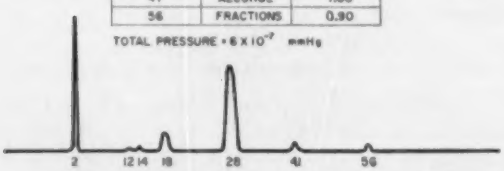

FIG. 8. High-power klystron on ion pump system-tube heater on for extended period.

[7] D. Lichtman, "Hydrogen absorption by tube parts due to various processing procedures," *Proceedings of the* A.S.T.M. *Conference on Cleaning of Electronic Device Components and Materials*, 1958.

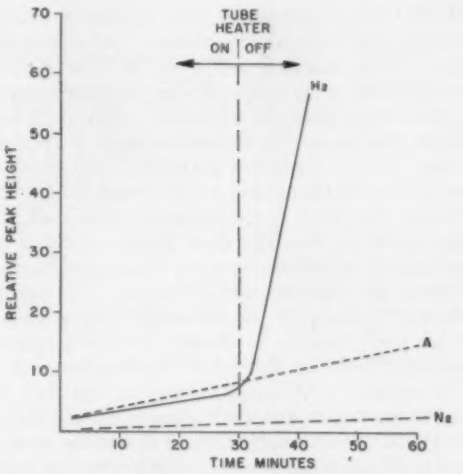

FIG. 9. Gas build-up in system with klystron diode on system and ion pump turned off.

Thus, hydrogen was evolved from the tube structure at a very rapid rate. The Ceralloy was gettering this hydrogen and maintaining a moderately low hydrogen pressure. When the heater was turned off, the Ceralloy cooled quickly while the rest of the tube structure (weighing about 30 lb) remained at a moderately high temperature due to its large thermal capacity.

Under these conditions, the tube structure continued to evolve hydrogen, while the Ceralloy, when cooled, ceased to absorb it. To further evaluate this process, other analyses were made at various time intervals, leaving the ion pump off. The results are shown in Fig. 10. The heater is on and the ion pump off during the time interval *A* to *B*. In this region we have a slowly

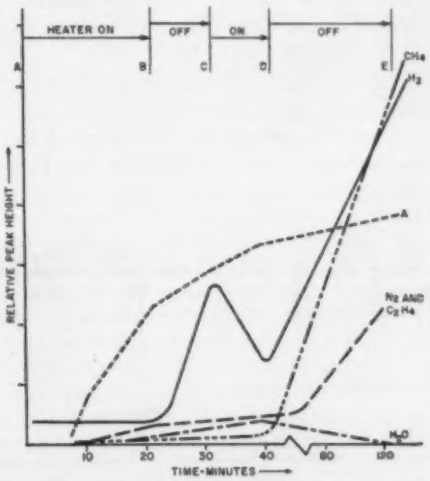

FIG. 10. Analysis with high-power klystron on ion pump system-ion pump off.

increasing argon pressure, a slow increase of nitrogen and water vapor, and a fairly constant level of hydrogen. At point *B* the heater is turned off. All other gas pressures continue to rise uniformly, but the hydrogen pressure rises very rapidly, as was found before. After a few minutes, the heater was turned on again, as indicated at point *C*; the hydrogen pressure decreases as the Ceralloy reaches the optimum temperature for gettering hydrogen. At point *D*, the heater is turned off for a longer period of time. The argon pressure increase continues unaffected. The hydrogen pressure climbs rapidly following the same pattern as before. The methane peaks start to show up, as was found on the analysis of the ion pump station itself when the ion pump was turned off. However, the rate of methane pressure rise in the region *D* to *E* is considerably greater than that found in the region *A* to *D*. The ion pump has been off throughout the entire period *A* to *E*, but the methane pressure increases much more rapidly when the heater is off than when the heater is on. This result seems to indicate that there may be a reaction between the methane and the Ceralloy somewhat similar to that occurring between the hydrogen and Ceralloy. Further tests will be performed on the reactions of Ceralloy and methane to evaluate this process in greater detail.

The tube remained on the system with the heater at full power and data were taken at intervals of time. The hydrogen pressure slowly decreased until it completely disappeared after about 100 hours of operation. At this time, the total pressure in the system was 2×10^{-8} mm of Hg. A residual analysis is shown in Fig. 11. There remains essentially some nitrogen and a small amount of water vapor. It has been shown that the nitrogen is evolving from the tube structure and is not leaking or permeating through the envelope. The rate of nitrogen evolution in this particular tube structure is about 5×10^{-6} μ liters/sec and is consistent with measurements made on similar structures run on a cycloidal mass spectrometer system.

It is found that this nitrogen evolution decreases with time much more slowly than the hydrogen evolution. The tube must be pumped for many hours before the nitrogen evolution rate is sufficiently low to permit pinch-off.

MASS NUMBER	GAS ION	RELATIVE PEAK HEIGHT
14	N^+	1
18	H_2O^+	2
28	N_2^+	5

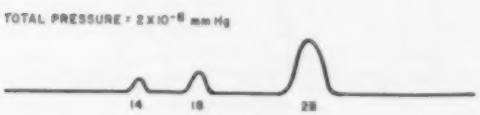

FIG. 11. Residual gas in high-power klystron diode after 100-hr operation.

The results of the hydrogen and nitrogen evolution rates are consistent with the known ratios of hydrogen and nitrogen diffusion rates in metals; for example, the ratio of the diffusion rates of hydrogen in nickel to nitrogen in nickel (at a temperature of 200°C) is about 10^{5}.[8]

Specific Problems

A vacuum system containing an omegatron mass spectrometer enables one to determine and understand many aspects which would be masked by consideration of only total pressure. Several interesting mechanisms were observed during the research work, and much of the information found helps explain why one occasionally has difficulty in pumping-down a vacuum system.

During one series of tests it was found that the pressure in the system remained fairly high. An analysis of the residual gas resulted in the data presented in Fig. 12 representing a type of spectrum not previously observed. It was determined that this spectrum indicates the presence of acetone, which has the following chemical formulation:

MASS NUMBER	GAS ION	RELATIVE PEAK HEIGHT
2	H_2^+	0.2
12	C^+	1.1
14	CO^{++}	2.1
15	CH_3^+	11.4
16	O^+	0.3
18	HOH^+	1.3
21.5	$(CH_3CO)^{++}$	8.7
27	$(C_2H_3)^+$	4.8
28	$(C_2H_4)^+$,$(CO)^+$	15.3
29	$(COH)^+$	3.0
43	$(CH_3CO)^+$	60.0
58	$(CH_3)_2CO^+$	20.7

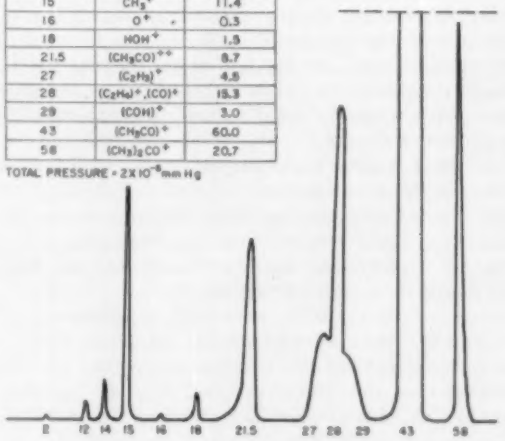

FIG. 12. System containing acetone vapors.

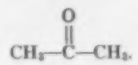

This molecule has a total mass number of 58 and predominant fractions at 43 and 15 (when the CH_3 radical is broken off by an electron beam). The general form of the spectrum agrees well with published data for the spectrum of acetone. It was determined that the acetone found its way into the system through a valve (Fig. 1)

[8] S. Dushman, *Vacuum Techniques* (John Wiley & Sons, New York, 1949), pp. 610–611.

that had been leak-checked with acetone four days before the time of the analysis. The large acetone pressure was found when attempts were made to open the valve to introduce calibrating gas. It had often been assumed that acetone evaporates comparatively quickly, leaving no residue, but in this experiment, sufficient acetone remained after four days to provide a considerable gas pressure. At room-temperature operation, the acetone pressure decreased very slowly. Thus the valve was heated to about 150°C for 30 minutes. After this processing, the acetone pressure decreased to a few per cent of the original value, and additional heating removed it completely.

To further evaluate this problem, some iso-amyl alcohol was introduced on the gas-inlet side of the high-vacuum valve (shown in Fig. 1) while the valve was closed tight. The chemical formulation of iso-amyl alcohol is

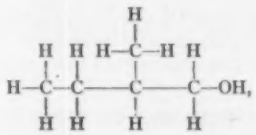

which has a total mass number of 88. After several hours, the valve was partially cracked open. An analysis

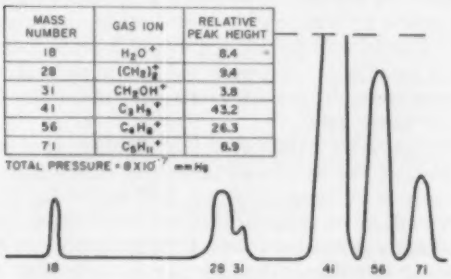

FIG. 13. System containing iso-amyl alcohol vapors.

of the gases in the system produced the results shown in Fig. 13, in which several fractional components of the alcohol are seen. The 71 peak corresponds to the radical $C_5H_{11}^+$ after the OH has been dissociated. Further dissociation of the CH_2 groups leads to the mass peaks of 56 and 41. The mass peak at 31 is probably CH_2OH^+, while that at 28 is due to CO^+, $(CH_2)_2^+$, $C_4H_5^{++}$, etc. This alcohol was present in the system for a considerable time, as was reported in the previous section. Baking to several hundred degrees centigrade was required to remove traces of the alcohol.

Another interesting application was found during the investigation of the cause of a high equilibrium pressure of 2×10^{-7} mm of Hg. This pressure was considered questionable since the system normally operates at 10^{-9} mm of Hg. An analysis of the residual gases at this time is shown in Fig. 14. The existence of the 32 peak is

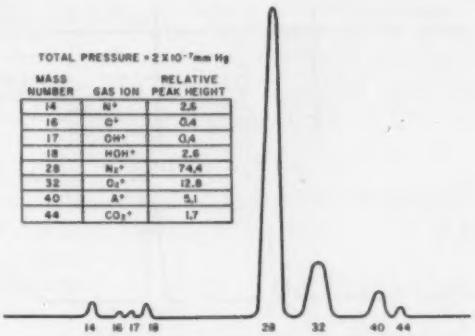

FIG. 14. Ion pump system with air leak.

striking since it is very rarely found in gas analyses of vacuum systems. It has been shown that oxygen is very difficult to contain in a vacuum system since it will react very rapidly with any heated filament.[9] An analysis of the spectrum indicates the major gas components to be nitrogen, oxygen, argon, and some water vapor, in the percentages which would indicate the existence of an air leak. The relatively high argon peak would be due to the slow pumping speed of the ion pump for argon. Thus, the omegatron indicates immediately that the equilibrium pressure of 2×10^{-7} mm of Hg in this case is caused by an air leak and is not due to internal outgassing or pump limitations. The omegatron was then tuned to helium, and the system was probed with helium gas, utilizing the omegatron as a leak detector. The leak was readily found by this means and was repaired. Before the leak was repaired, many spectra were taken. The spectrum shown in Fig. 14 is a typical example of the gases existing in the ion pump vacuum system due to a minute air leak.

The ion pump is capable of determining its own pressure since the current in the pump is directly proportional to the pressure in the system. A conventional ion gauge normally is not used in our ion pump systems. It is known that many reactions take place in an ionization gauge and the gauge itself can contribute to the gas content of the vacuum system. An Alpert (Veeco model RG-75) type ion gauge was attached to the system (as shown in Fig. 1), and measurements were made with this gauge in operation. It was generally found that the pressure in the system was slightly higher when the gauge was operating than when it was off. Analyses of the gases in the system with the gauge on at a gauge pressure of 6×10^{-8} mm of Hg are shown in Fig. 15. The existence of carbon monoxide, water vapor, and some acetone is observed. The water vapor and acetone peaks increase as the temperature of the glass walls of the ion gauge increases. Thus, it is seen that these two gases are being desorbed from the glass walls of the gauge.

[9] J. R. Young, "On the interaction of oxygen with incandescent filaments," 19th Annual Conference on Physical Electronics at M.I.T., March, 1959.

MASS NUMBER	GAS ION	RELATIVE PEAK HEIGHT
2	H_2^+	1.0
17	OH^+	1.5
18	H_2O^+	7.0
28	CO^+, N_2^+	8.0
43	ACETONE	2.0

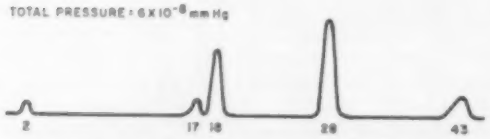

FIG. 15. Gas analysis in ion pump system with ionization gauge in operation.

The gauge was turned on and off while the hydrogen and carbon monoxide peaks were monitored. It was found that when the filament was turned off, the hydrogen peak increased and the carbon monoxide peak decreased. When the filament was turned on, the hydrogen peak decreased rapidly and the carbon monoxide pressure increased rapidly. Thus, the filament of the ion gauge (which in this case is thoria-coated platinum iridium) acts as a getter for hydrogen and as a source of carbon monoxide when hot. The reactions with hydrogen agree with data obtained in a separate series of experiments on specific gauge reactions. It had been found in this laboratory that this type of filament (when hot) absorbs hydrogen at a very rapid rate and that it has a high capacity for hydrogen gas. The evolution of carbon monoxide from the hot filament has been observed in many instances.

TOTAL PRESSURE = 2 X 10⁻⁶ mm Hg

MASS NUMBER	GAS ION	RELATIVE PEAK HEIGHT
12	C^+	4.0
14	CO^{++}, N^+	0.5
15	CH_3^+	2.0
16	O^+	5.0
17	OH^+	5.0
18	NOH^+	16.0
28	CO^+	120.0
40	A^+	30.0
43	ACETONE	40.0
58	ACETONE	4.0

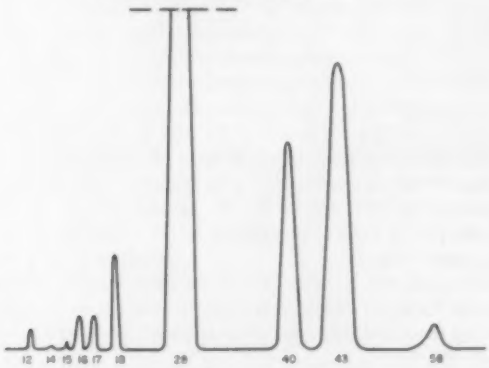

FIG. 16. Gas analysis in ion pump system with grid of ion gauge being outgassed.

The grid of the ion gauge was then outgassed. At this time, ac current is sent through the grid windings so that the grid (made of moly) heats up to a temperature of about 1000°C. After a few minutes, the pressure leveled at a value of 2×10^{-6} mm of Hg. Analysis of the gas at this time is shown in Fig. 16. The major component is seen to be carbon monoxide. A considerable quantity of acetone and water vapor is indicated and results from the increased evolution rate due to the considerably higher wall temperature. Considerable evolution of argon is also noted and is probably due to argon being driven out of the glass wall at the higher temperatures. The rate of argon evolution is too great to be accounted for by permeation through the glass walls of the gauge. (Considerable argon can be accumulated in the walls, because the ionization gauge pumps during its operation. The 1% argon component in the air as well as the argon used for calibration provide a considerable quantity of this gas.)

DISCUSSION OF RESULTS

The limiting factor in glass-oil diffusion systems seems to be the amount of water vapor and carbon monoxide that evolve from the ion gauge. Adequate trapping devices can prevent oil fractions from contaminating the system for a reasonable period of time, i.e., several days. Careful construction and thorough bakeout of the entire vacuum system permit the achievement of very low pressures, the limiting factor being determined by the ion gauge itself.

The use of ion pumps allows the elimination of glass ion gauges. The ion pumps permit the achievement of pressures in the range of 10^{-9} to 10^{-10} mm of Hg. However, methane becomes the predominant limiting factor to an otherwise clean, compact pumping system. The methane is probably formed on the surface of the titanium from either the hydrogen and carbon that exist in the titanium itself, or from the hydrides and carbides formed during the pumping operation. It would be interesting to fabricate ion pumps utilizing vacuum-cast titanium to determine if this form of titanium would reduce the formation of methane. Additional experiments will be necessary to determine the exact source of the methane gas. Water vapor seems to be a tenacious component of the residual gases in all kinds of vacuum systems, and thorough baking is required to reduce its presence adequately.

The evolution of hydrogen from large tube structures can probably be traced to the brazing operations performed in hydrogen-atmoshpere furnaces.

Solvents, such as acetone and alcohol, must be used with proper precautions. The assumption that these solvents evaporate completely at room temperature has been shown to be completely erroneous. When not used properly, these solvents can lead to considerable gas

evolution within the system and can cause high equilibrium pressures to exist for long periods of time.

The gases of general concern are hydrogen, water vapor, nitrogen, carbon monoxide, and methane. The system in question determines the specific gas problems. The reactions of Ceralloy getter material with many of the gases discussed make it an interesting material for use in vacuum systems.

CONCLUSIONS

The omegatron mass spectrometer has proved itself an excellent tool in analyzing vacuum systems and gas-solid reactions under vacuum conditions. It enables one to determine the source of gas causing high equilibrium pressures. During the specific experiments, many incidental results were observed which add considerably to the sum total of knowledge of what occurs in a vacuum system.

ACKNOWLEDGMENTS

The author wishes to acknowledge the considerable aid of Vincent Voss and Audrey Hebling in the experimental program.

Appreciation is also due to J. E. McLinden for his continuing encouragement.

JOURNAL OF APPLIED PHYSICS VOLUME 31, NUMBER 7 JULY, 1960

Low-Temperature Transport Properties of Commercial Metals and Alloys. IV. Reactor Grade Be, Mo, and W†

ROBERT L. POWELL, JAMES L. HARDEN, AND EDWARD F. GIBSON
Cryogenic Engineering Laboratory, National Bureau of Standards, Boulder, Colorado

(Received February 8, 1960; and in final form March 21, 1960)

The thermal conductivity, electrical resistivity, Lorenz ratio, and thermoelectric power are given in the temperature range 4°–120° K for four reactor grade metals: beryllium with sample axis parallel to the pressing axis, beryllium with sample axis perpendicular to the pressing axis, molybdenum, and tungsten, the latter two doped with ThO_2. Within the given temperature range the molybdenum and tungsten show slight maxima in thermal conductivity, the beryllium does not. The various components of the electronic and lattice thermal conductivities and resistivities are resolved. The residual electrical resistivities are, respectively, 0.64, 1.01, 0.57, and 0.16×10^{-6} ohm-cm.

The Lorenz ratios for molybdenum and tungsten show both maxima and minima and are always below the Sommerfeld value. The ratios for the beryllium samples have broad maxima and generally are above the Sommerfeld value. The thermoelectric powers of the samples with respect to pure copper are negative for the higher temperatures and positive for the lower temperatures.

I. INTRODUCTION

DEVELOPMENTAL research on nuclear powered rockets is being carried out at the Los Alamos Scientific Laboratory under the sponsorship of the U. S. Atomic Energy Commission.[1] One of the many problems encountered is the lack of knowledge of the macroscopic physical properties of the reactor materials over a very wide range of temperatures. For that reason, a cooperative research program is under way at the Cryogenic Engineering Laboratory to study the low-temperature mechanical and transport properties of several reactor materials. This paper reports work on the transport properties of beryllium, molybdenum, and tungsten, all of reactor grade or doped for reactor use.

The thermal conductivities of each of the three metals have been determined at low temperatures before[2] (although not for the same purity or composition): beryllium by White and Woods,[2] Rosenberg,[4] and others[2]; molybdenum by Rosenberg[4] and others[2]; and tungsten by Rosenberg[4], de Nobel,[5] and others.[2] The thermal conductivity of beryllium was intensively studied at room temperatures and above by Powell.[6] He also included a critical review of earlier work on the electrical and thermal conductivities of beryllium. Each of the foregoing[3–6] also gave values for the electrical resistivities; none included information on the thermoelectric power. The electrical resistivity and thermoelectric power of molybdenum and the thermoelectric power of tungsten were measured by Potter.[7]

Discussions of the basic conduction apparatus and techniques have been published previously.[8] Recent

† The research was supported by the U. S. Atomic Energy Commission and was under the technical direction of Dr. E. F. Hammel of the Los Alamos Scientific Laboratory.

[1] See the general discussion by J. J. Newgard and M. Levoy, Sci. American **200**, 46 (1959).

[2] See the compilation, R. L. Powell and W. A. Blanpied, Natl. Bur. Standards Circ. No. 556.

[2] G. K. White and S. B. Woods, Can. J. Phys. **33**, 58 (1955).

[4] H. M. Rosenberg, Trans. Roy. Soc. (London) **A247**, 441 (1955).

[5] J. de Nobel, Physica **23**, 261 (1957); **23**, 349 (1957).

[6] R. W. Powell, Phil. Mag. **44**, 645 (1953).

[7] H. H. Potter, Proc. Phys. Soc. (London) **53**, 695 (1941).

[8] R. L. Powell, W. M. Rogers, and D. O. Coffin, J. Research Natl. Bur. Standards **59**, 349 (1957).

modifications in the apparatus were described in paper II of this series.[9] The corrections for thermal contraction of the samples were taken from a preliminary compilation being prepared at this Laboratory.[10] The specific values were based mainly on the work of Erfling[11] for beryllium, Erfling[11] and Nix and MacNair[12] for molybdenum, and Nix and MacNair[12] for tungsten.

II. SAMPLES

Four reactor-grade metals were investigated: beryllium with the sample axis parallel to the pressing axis, beryllium with the axes perpendicular, molybdenum doped with ThO_2, and tungsten doped with ThO_2. All four samples were ground down to a rod with 3.67-mm diam, 13 cm long, and were not annealed or heat-treated after machining. The sample rods were furnished by Paul Wagner of the Los Alamos Scientific Laboratory. He also supplied the spectrochemical analysis for the Mo and W rods. The Be analyses were certified by S. Washkewicz of the Quality Control Division of the Brush Beryllium Company. The chemical analyses (in mole percentages) are as follows:

(1) Be (parallel): 98.7 Be; 1.2 BeO; 0.056 Al; 0.035 Si; 0.016 Ni; 0.010 Mn; and traces less than one part-per-million of B and Li.

(2) Be (perpendicular): 98.7 Be; 1.18 BeO; 0.044 Al; 0.014 Ni; 0.009 Mn; and traces less than one part-per-million of B and Li.

(3) Mo: 1–2 (by volume), ThO_2; 0.01–0.1 Fe, Si; 0.001–0.01 Al, Cb, Cu; less than 0.001 Ca, Cr, Mg.

(4) W: 1–2 (by volume), ThO_2; 0.01–0.1 Si; 0.001–0.01 Cb, Fe; less than 0.001 Al, Cr, Cu, Mg, Mn, Mo.

III. EXPERIMENTAL RESULTS AND DISCUSSION

A. Thermal Conductivity

The total thermal conductivities of the samples are given in Fig. 1. For each, the total conductivity consists of two additive terms, the electronic conductivity λ_e and the lattice conductivity λ_g. The electronic thermal conductivity is predominant for all four metals. There are two processes that limit this electronic conductivity, the electron-phonon scattering and the electron-imperfection scattering. The total electronic thermal resistivity W_e is approximately the sum of the electron-phonon resistivity W_L and the electron-imperfection resistivity W_0; that is,

$$1/\lambda_e \equiv W_e \approx W_L + W_0 \approx AT^n + B/T; (n \approx 2.5, \quad \text{for} \quad T < 60°\text{K}). \quad (1)$$

Above 60°K the W_L gradually levels off and approaches a constant value labeled W_∞. The electron-imperfection resistivity dominates in most of the temperature range for all four samples.

The lattice thermal conductivity λ_g is also measureable in these metals, and it similarly is limited by three main processes: phonon-dislocation scattering W_D; phonon-electron scattering W_E; and phonon-point defect scattering W_P. Again, the total thermal resistivity is approximately the sum of the separate terms:

$$1/\lambda_g \equiv W_g \approx W_D + W_E + W_P \approx DT^{-2} + ET^{-2} + PT. \quad (2)$$

The phonon-dislocation resistivity dominates the total lattice thermal resistivity in these reactor-grade metals. A more complete discussion of the separate components and the method of analysis was given paper II of this series.[9]

The beryllium and molybdenum samples have low conductivity at low temperatures, indicating strong electron-imperfection scattering of the predominant electronic component of the thermal conductivity. This scattering is undoubtably caused by crystal imperfections in the beryllium samples and metallic impurities in the molybdenum sample. The results of Powell[6] on various pure beryllium samples gave values from 1 to 2 w/cm °K at room temperature with decreasing values at higher temperatures. Therefore, the commercial beryllium samples used in this report should show broad maxima somewhere between 120°K and room temperatures. Results on two beryllium samples of the same conductivity by White and Woods[3] show such maxima at 120°K, just at the temperature where our experiments on thermal conductivity stop. Our curve for the beryllium perpendicular sample lies exactly on theirs for the entire temperature range up to 120°K. The beryllium sample used by Rosenberg[4] had a thermal conductivity about four times lower than our beryllium perpendicular one for temperatures up to 40°K, the upper limit for his curve. Rosenberg[4] did not have available information on the exact purity of his sample.

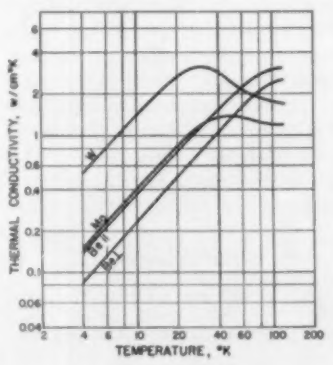

FIG. 1. Total thermal conductivity of several reactor metals.

[9] R. L. Powell, W. J. Hall, and H. M. Roder, J. Appl. Phys. **31**, 496 (1960).

[10] *A compilation of thermophysical properties of cryogenic materials*, V. J. Johnson, Editor (Natl. Bur. Standards, Boulder, Colorado, 1960), unpublished.

[11] H. D. Erfling, Ann. Physik **34**, 136 (1939).

[12] F. C. Nix and D. MacNair, Phys. Rev. **61**, 74 (1942).

White and Woods[3] tested two samples, one of which was more pure than ours, one less pure. The molybdenum sample investigated by Rosenberg[4] was much more pure than ours (it was not doped for reactor use) and, correspondingly, its thermal conductivity was considerably higher at low temperatures.

Even though the thermal conductivity of the tungsten rod is the highest for the metals discussed in this report, it is still quite small compared to values for a pure tungsten sample.[5] De Nobel[5] reported about 50 w/cm °K at 20°K, approximately 20 times larger than the value for our sample. His specimens were single crystals of very high purity. Rosenberg[4] quoted values just slightly higher than ours in spite of the fact that his sample was supposed to be 99.99% pure.

An accurate estimate of the electron-phonon scattering resistivity W_L could not be made for any of the samples. Therefore, above about 40°K the total electronic component W_e was somewhat uncertain and, consequently, accurate values for the various lattice conductivity terms could not be obtained. In particular, the phonon-point defect resistivity W_P could not be determined at all for the molybdenum or tungsten samples. The constants of Eqs. (1) and (2) for the samples are given in Table I. The relatively large values of B indicate strong electron-imperfection scattering; the large values of $(D+E)$ for the beryllium samples indicate strong phonon-dislocation scattering; and the small values for P for the beryllium samples indicate relatively minor phonon-point defect scattering. The resolved lattice conductivities are given in Fig. 2. The curves are given only in the temperature ranges where consistent values for the lattice conductivity could be obtained. It should be noted that the *lattice* thermal conductivity component is larger for the beryllium perpendicular sample than it is for the beryllium parallel one, though the reverse is true for the *total* thermal conductivity.

Because of the uncertainties in determining the lattice conductivity component, comparisons to the experimental work of others is somewhat difficult. The values of lattice conductivity given by White and Woods[3] for their beryllium sample fall on the same curve as those for our beryllium parallel sample. This again is a reverse from the total thermal conductivity curves. Rosenberg[4] did not determine the lattice conductivity for his molybdenum, tungsten, or beryllium samples. De Nobel[5] determined the lattice thermal conductivity of his tungsten samples by a method utilizing high magnetic fields. At 20°K he obtains values approximately three times larger than ours. This would correspond to the probable lack of a large number of dislocations in his single crystals. His values below 20°K do not show the T^2 dependence that we observed, and that is expected theoretically.

TABLE I. Transport properties constants of several reactor metals. See Eqs. (1) and (2) of the text. The units for B, $(D+E)$, and P are those that give the total thermal resistivity in cm °K/w.

	Be ∥	Be ⊥	Mo	W
B				
Electron-imperfection $(D+E)\times10^{-3}$	30	50	27	7.8
Phonon-dislocation and phonon-electron	5	4	2.5	0.1
P				
Phonon-point imperfection	0.02	0.01	···	···
ρ_0 ($\mu\Omega$-cm)				
Residual electrical	0.64	1.01	0.57	0.16
ρ_{273}/ρ_4				
Residual ratio	6.01	4.22	9.7	···

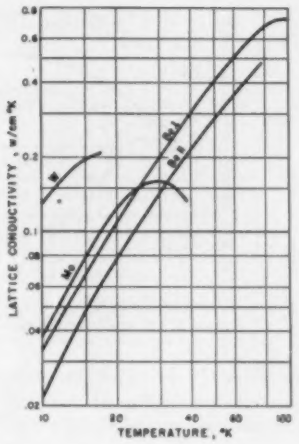

FIG. 2. Lattice thermal conductivity of several reactor metals.

B. Electrical Resistivity and Thermoelectric Properties

The total electrical resistivities of the samples are given in Fig. 3; the residual resistivities and ratios are given in Table I. The total electrical resistivity ρ is ap-

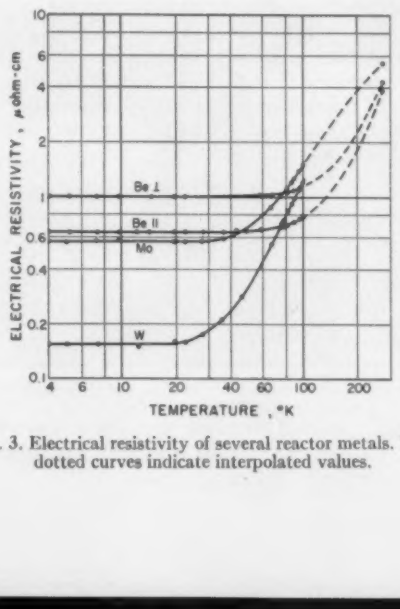

FIG. 3. Electrical resistivity of several reactor metals. The dotted curves indicate interpolated values.

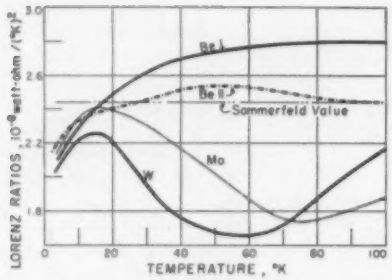

FIG. 4. Lorenz ratios of several reactor metals. The Sommerfeld value for the electronic components is 2.44×10^{-8}.

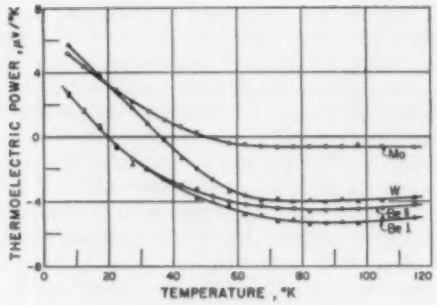

FIG. 5. Thermoelectric power of several reactor metals with respect to pure copper.

proximately the sum of two separate terms, the electron-phonon resistivity ρ_L and the residual or electron-imperfection resistivity ρ_0; that is,

$$\rho\approx\rho_L+\rho_0$$
$$\approx\alpha T^n+\beta(n\approx4 \text{ to } 5, \quad T<80°\text{K}). \tag{3}$$

Above 80°K the ρ_L approaches a linear temperature variation. The electron-imperfection term dominates the total resistivity for all four samples. The temperature exponent n between 20° and 50°K was found to be 5.0 ± 0.4 for molybdenum and 3.6 ± 0.2 for tungsten. The latter is in good agreement with the value 3.5 found by de Nobel.[5] The electron-phonon term could not be accurately separated from the total resistivity for the two beryllium samples because of their large residual resistivities.

The electrical resistivity of the beryllium perpendicular sample was approximately the same as the resistivities of the two samples reported by White and Woods.[3] Rosenberg[4] gave values for the residual resistivity of his molybdenum sample that were about three times lower than ours, the same ratio that held for the total thermal resistivities at low temperatures. Potter[7] included only values of resistance ratios, not the actual resistivities. His residual resistance ratio (ρ_{273}/ρ_0) for molybdenum was 8.6, less than our 9.7, indicating that his sample was effectively slightly less pure. The residual resistivity of our tungsten sample was approximately 40 times higher than those values reported by de Nobel,[5] again indicating the extreme purity and perfection of his samples.

The Lorenz ratios L defined by

$$\rho=LWT, \tag{4}$$

where W is the total thermal resistivity, are given in Fig. 4 for each of the samples. A maximum or curve above the Sommerfeld value (2.44×10^{-8}) indicates a significant lattice contribution λ_v to the total thermal conductivity.

The thermoelectric powers of each of the samples with respect to pure copper[13] are given in Fig. 5. We cannot give any significant interpretation of the qualitative or quantitative behavior of the results. Our results on molybdenum and tungsten are somewhat similar in behavior to those reported by Potter.[7] Both sets of curves show a positive power of several microvolts per degree at the lowest temperatures, a smooth decrease to a minimum, and then a rise as the temperature increases further. Our curves are consistently one or two microvolts per degree lower than his and the minima occur at lower temperatures. His minima were at approximately 100°K.

IV. ACKNOWLEDGMENTS

We would like to thank Paul Wagner of the Los Alamos Scientific Laboratory for supplying the fabricated samples; M. D. Bunch for assistance on some of the experimental runs; and W. J. Hall for advice and assistance on computation problems.

[13] R. L. Powell, H. M. Roder, and W. J. Hall, Phys. Rev. 115, 314 (1959).

Ultra-High-Speed Photographs Refuting "Cohesion in Plasma"*

W. C. Davis and A. W. Campbell
University of California, Los Alamos Scientific Laboratory, Los Alamos, New Mexico
(Received February 17, 1960; and in final form March 25, 1960)

In a recent issue of this journal [M. A. Cook and W. S. McEwan, J. Appl. Phys. **29**, 1612 (1958)] and in a recent book [Melvin A. Cook, *The Science of High Explosives* (Rheinhold Publishing Corporation, New York, 1958), 1st ed., pp. 158, 420–426], a sequence of framing camera pictures was presented, and the sequence was interpreted as evidence that, as the result of the detonation of a quantity of explosive, a plasma was ejected into the atmosphere, and that the plasma exhibited a strong cohesive force. This paper presents pictures of an essentially identical subject, taken at three exposure times: the same exposure time used for the sequence in the references (4 μsec); 1/20th of that time; and 1/400th of that time. These pictures show that the phenomena are those of a shock wave, and that no new assumption of cohesive force is necessary to interpret the pictures. A simple analysis of the shock wave interpretation using the usual theory is presented to show that the interpretation is consistent with the known properties of air and the explosive used.

IN a recent issue of this journal,[1] as well as in a recently published book,[2] a sequence of framing camera photographs was presented and the sequence was interpreted as evidence that, as the result of the detonation of a quantity of explosive, a plasma was injected into the ambient atmosphere, and that the plasma exhibited a strong cohesive force. This interpretation is in error, possibly because the authors did not understand how space and time are confused in framing camera photographs. Pictures are presented here of an essentially identical subject, taken at three exposure times: the same exposure time used for the sequence in the references; 1/20th of that time; and 1/400th of that time. We wish to point out that records similar to those of footnote references 1 and 2 are commonly obtained in the photography of explosive phenomena, that the luminosity is that of a shock wave, and that the assumption of cohesive force is unnecessary to explain the observations.

In order to illustrate the error of interpretation, it was first necessary to duplicate the photographs shown in the references. Sufficient details of the charge used were given in neither reference, but a study of the photographs suggested a charge consisting of detonator, a cylindrical composition B booster measuring 2 in.×2 in., a ¼-in. glass plate as shock attenuator, and a tall-form, 600-ml beaker containing about 300 ml of dithekite-13.[1] Figure 1 shows four frames from a framing camera record of such a charge, each with an exposure time of 4 μsec, which reproduce the chief features of frames 2 and 4–6 of footnote reference 1. Figure 2 shows a velocity record obtained with a rotating-mirror smear camera, with the slit arranged along the axis of a similar charge. From this record, the velocity of detonation of dithekite-13 was found to be 6800 m/sec, and the air shock velocity was 6900 m/sec near the top of the beaker.

The explanation of these records is easily available from the well-known phenomena of shock waves; no introduction of new theories is needed. The detonation products expand upward, cooling adiabatically from the detonation temperature,[3] which our measurements of

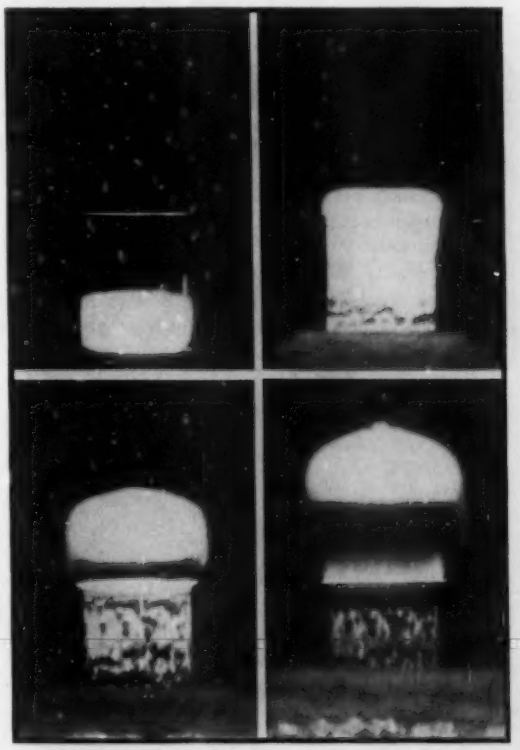

FIG. 1. Frames 1, 4, 6, and 8 of a sequence showing the air shock wave above a beaker half full of the liquid explosive dithekite-13. Exposure time: 4 μsec; framing interval: 5 μsec.

* Work done under the auspices of the U. S. Atomic Energy Commission.

[1] M. A. Cook and W. S. McEwan, J. Appl. Phys. **29**, 1612 (1958). The framing sequence was used as the cover photograph of that issue.

[2] Melvin A. Cook, *The Science of High Explosives* (Reinhold Publishing Corporation, New York, 1958), 1st ed., pp. 158, 420–426.

[3] See footnote reference 2, p. 38.

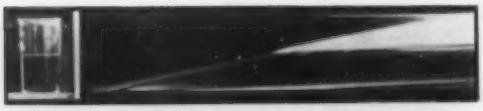

FIG. 2. Smear camera photograph giving velocities of the explosive detonation and of the air shock driven by the expanding products. The air shock is very heavily overexposed.

brightness indicate is about 3400°K. The expanding products drive an air shock wave at Mach 21. Hochstim,[4] in his report on the Hugoniot of air, gives the temperature of the shock as about 9700°K. The photographic brightnesses of blackbodies at the two temperatures are different by a factor of more than 300, so that it is impossible for a photograph properly exposed for the air shock, even though it is not as bright as a blackbody, to record the self-luminosity of the expanding products, cooled to less than 1000°K by expansion, and nearly completely transparent. In Fig. 2 it can be seen that the exposure is proper for recording the light from the detonating explosive, but that the region of the air shock is greatly overexposed, so that no detail is visible. The luminosity seen in the pictures shown in footnote references 1 and 2 is produced entirely by the air shock.

To be sure that the interpretation is correct it can be checked against calculations made using the usual theory. Calculations of the equation of state of this explosive have been made by C. L. Mader, using a generalized version of the scheme described by Fickett and Cowan.[5] Taking the initial density as 1.39 g/cm³, and the detonation velocity as 6800 m/sec, he finds the Chapman-Jouguet pressure to be 174 kb, and $\gamma=2.70$ for the constant-γ isentrope; $PV_\gamma=$constant. The isentrope intersects the experimental $\rho_0 D=890$ g/cm² sec line for the air shock in the pressure vs particle-velocity plane[6] at about 600 bars. The air Hugoniot curve calculated by Hochstim[4] passes very close to the intersection of the two curves. If theory and experiments were perfect, the three curves should intersect in one point. The agreement is entirely satisfactory. There seems to be no contradictory evidence, and we are convinced that our interpretation is the correct one.

Figure 3 shows a framing sequence from an experiment which was in all details like the one photographed in Fig. 1, except that the subject was back-lit and that the framing time was reduced to 0.20 μsec. The air shock is now distinguishable from the expanding detonation products. The distortion evident in Fig. 1 by contrast with Fig. 3 is due both to the fact that in the framing-time interval the luminous shock front moves a distance (ca 28 mm) which is comparable with the dimensions of the subject, and to the fact that the subject is not uniformly bright and thus does not record uniformly during the opening and closing of the shuttering aperture.

That Fig. 3 also has suffered loss of detail by image motion during the exposure is evident from Fig. 4. This is a back-lit single frame taken at an exposure time of 0.01 μsec. The irregularity of the shock front at the top, due to instability,[7] is evident. The shock wave is in propane in this case, and is opaque. Figure 5 is a similar photograph taken with the shot surrounded by helium, and the lip of the beaker cut away. Helium, with its very high ionization potential, was used to be certain that the surrounding gas did not interfere with, or quench, the plasma postulated by Cook and McEwan. No plasma can be seen. The shock waves in helium are all transparent, and can be seen only by shadow or schlieren lighting. The leading helium shock wave has been retouched for reproduction. The fact that the grid

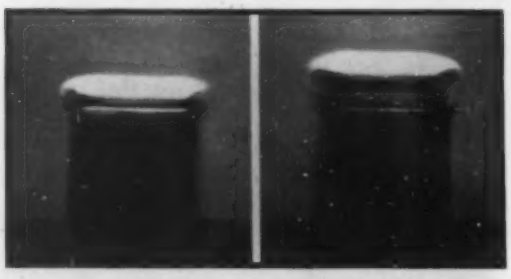

FIG. 3. Frames 2 and 14 of a sequence taken of a subject identical to that of Fig. 1 with the exposure time reduced by 20 times. Weak back-lighting has been added. Exposure time: 0.20 μsec; framing interval: 0.25 μsec.

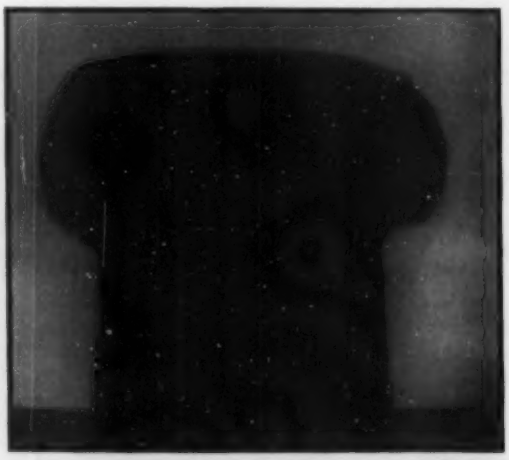

FIG. 4. Silhouette photograph taken of a subject identical to that of Fig. 1 in a butane atmosphere with the exposure time reduced by 400 times. Exposure time: 0.01 μsec. The line at the right side indicates the position of the top of the beaker.

[4] Adolf R. Hochstim, Convair Report ZPh(GP)-002 (January 30, 1957), Convair, San Diego 12, California.
[5] R. Cowan and W. Fickett, J. Chem. Phys. **24**, 932 (1956).
[6] J. M. Walsh *et al.*, Phys. Rev. **108**, 196 (1957), Part I, Sec. B.
[7] G. I. Taylor, Proc. Roy. Soc. (London) **A201**, 192 (1950).

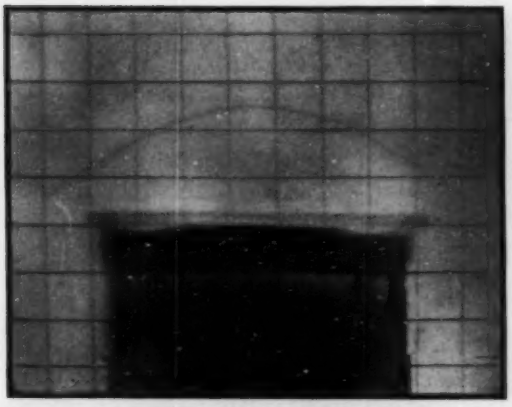

FIG. 5. Silhouette photograph taken of a subject identical to that of Fig. 1 in a helium atmosphere with exposure time reduced by 400 times. Exposure time: 0.01 μsec. The grid is ½-in. squares. The line at the right indicates the position of the top of the beaker. The lip of the beaker has been cut off. This photograph has been retouched.

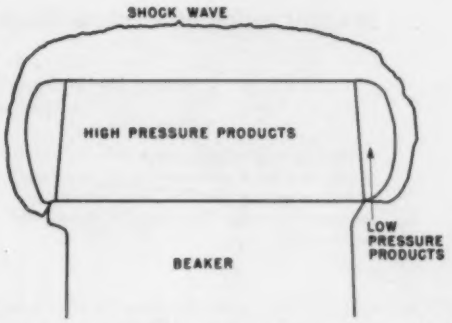

FIG. 6. Diagram of Fig. 4 showing the structure of the shock waves and products produced by detonation of explosive in a beaker.

over the light source shows through the products in this picture shows that the products are transparent, as one would expect for this explosive. Their temperature is low (less than 1000°K) and they are composed principally of H_2O, CO_2, CO, and N_2. The structure seen within the high-pressure boundary of the products is caused by refraction of the light. The apparent edge of the products is the position of the strong rarefaction proceeding back into the products as the pressure is relieved. The expanded products, at very low pressure, are transparent, and do not show in this picture. Figure 3 shows the weak air shock to the sides.

The structure of the system is summarized diagrammatically in Fig. 6. This has been drawn as a tracing of Fig. 4, which shows the outline nicely because all the shock waves, even the weak ones, are opaque. The lines marking boundaries have been sketched in without accurate knowledge of their positions. The instability of the shock wave seen in the photograph indicates that other instabilities may exist, but no attempt has been made to indicate them. The products have expanded behind the gas shock wave as they proceeded up the beaker, but side rarefactions were prevented or lessened by the beaker. After reaching the top of the beaker, the products expanded again, driving a weak shock wave to the sides. The high-pressure products have a pressure of a few hundred bars, and the low-pressure products less than 100 bars. The line between the two marks a rarefaction, which is, of course, not a discontinuity but a continuous transition.

ACKNOWLEDGMENTS

We are indebted to Dr. C. W. Mautz, Dr. W. Fickett, and Dr. R. G. Shreffler for helpful discussions of the phenomena discussed.

Magnetization of a Dilute Suspension of a Multidomain Ferromagnetic

C. P. Bean and I. S. Jacobs
General Electric Research Laboratory, Schenectady, New York
(Received March 8, 1960)

The observed magnetization curve of a dilute suspension of carbonyl iron powder, type E, is shown to be closely that one would derive from consideration of a dilute assembly of randomly oriented, single-crystal, multidomain spheres. The deviations are in the directions expected from the effects of stress and nonspherical clumping. The effects of packing and the applicability of various laws of approach to saturation are discussed.

FERROMAGNETIC particles may be divided into three size categories with differing characteristic properties. The first category consists of those particles that are so large that they contain many domains, and in which the initial stage of magnetization is accomplished by the motion of domain walls that are relatively unimpeded by imperfections. The second category includes those particles that are so small that, in addition to their containing but one domain, the thermal energy at the temperature of experiment is sufficient to equilibrate the magnetization of an assembly in a time short compared with that of the experiment.[1] The third category contains particles that are single domain in all fields and accomplish their magnetization by coherent rotation of the magnetic moments against anisotropies present in the particles. This class may not always exist, since the first two classes may overlap at some temperatures. This note is concerned with a description of the magnetization process of a dilute suspension of particles of the first category. A discussion of the magnetization process for particles of the third category has recently been presented by Giron and Pauthenet.[2]

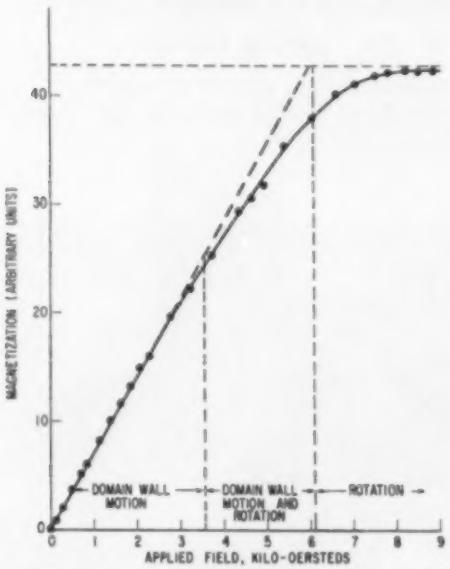

FIG. 1. Magnetization curve of dilute suspension of carbonyl iron (three percent by volume), showing the general divisions of the magnetization process as predicted in Table I.

Carbonyl iron powder of type E consists of spherical polycrystalline particles about 6μ in diam, which is about 300 times the limiting diameter of particles which are single domain in zero field.[3] Their structure and typical impurity content have been discussed by Taylor.[4] As their coercive force is less than 5 oe, they are nearly ideal multidomain spheres.

A small amount of carbonyl E iron powder was thoroughly mixed with a nonmagnetic plastic clay and the whole shaped into a small prolate ellipsoid of about 5:1 axial ratio. The volume concentration of ferromagnetic material was about three percent. The sample ellipsoid was frozen into place in an L-shaped glass tube ("golf stick") with a little alcohol. All measurements were made at 77°K. The technique of measurement was a common one,[5] that of noting the deflection of a Grassot-type fluxmeter when the sample is withdrawn from an attached test coil placed in a uniform magnetic field.

The magnetization was measured as a function of applied field from 0 to 11 000 oe. The magnetization curve was completely reversible within the errors of measurement. The low-field portion of these data is plotted in Fig. 1. The initial part is linear to $I/I_s \approx 0.5$ and extrapolates to an intersection with the line $I/I_s = 1.00$ at a field of 6000 ± 200 oe. The high-field portion of these data, constituting the approach to saturation, is plotted in Figs. 2 and 3. The first of these curves shows the approach to saturation as a function of $1/H$, while the second curve employs $1/H^2$ as the abscissa. It is evident that the apparent saturation magnetization and apparent laws of approach depend on the method of extrapolation and the field strengths employed. This is discussed later. The saturation induction was estimated to be $19.0 \pm 1.0 \times 10^3$ gauss from the impurity content.

[1] L. Néel, Compt. rend. **228**, 664 (1949); C. P. Bean and J. D. Livingston, J. Appl. Phys. **30**, 120S (1959).

[2] V. Giron and R. Pauthenet, Compt. rend. **248**, 943 (1959).

[3] C. Kittel, Revs. Modern Phys. **21**, 541 (1949).

[4] A. Taylor, in *Soft Magnetic Materials for Telecommunications*, edited by C. E. Richards and A. C. Lynch, (Pergamon Press, New York, 1953), p. 202.

[5] See, e.g., L. F. Bates, *Modern Magnetism*, (Cambridge University Press, 1951), 3rd ed., p. 287.

The basic features of the magnetization curve of a dilute suspension of spherical, multidomain ferromagnetic particles are easy to derive. We shall assume that the field necessary to move the domain walls is zero and further that the easy directions are sixfold, i.e., along the cube edges in the iron lattice. The initial magnetization takes place by motion of the domain walls. For a spherical particle, the demagnetizing field is $-4\pi I/3$, where I is the magnetization of the particle. Since no field is required to move the domain walls, the total field in the particle must be zero:

$$H-4\pi I/3=0. \tag{1}$$

The constant permeability implied by the previous equation will obtain until the magnetization reaches such a value that the magnetic moments must rotate

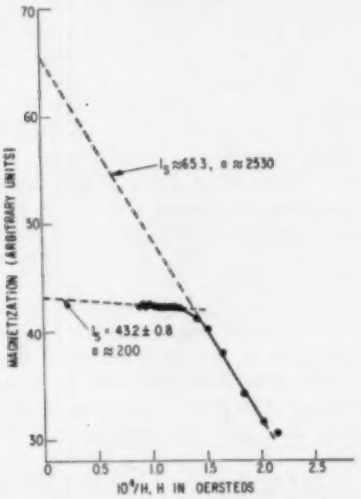

FIG. 2. The approach to saturation as a function of $1/H$, for a dilute suspension of carbonyl iron. The straight lines imply the law of approach $I/I_s=1-(a/H)$.

in some crystals to continue the linear increase of magnetization. This happens first in those crystals whose <111> directions coincide with the magnetic field and occurs when the magnetization has the value $I_s/\sqrt{3}$. From Eq. (1), the field at this point is $4\pi I_s/3\sqrt{3}$. From this value of magnetization until the field $4\pi I_s/3$ is reached, domain wall motion, in the main, is taking place in those crystals whose <100> directions lie close to the direction of the applied field and, in the main, rotation in those crystals whose <111> directions lie close to the field direction. At the field $4\pi I_s/3$ those crystals whose <100> directions coincide with the field direction have become fully magnetized, and the rest of the magnetization is accomplished by rotation of the magnetization of the crystals whose <100> directions do not lie along the field direction. It is only above this field that all the crystals are

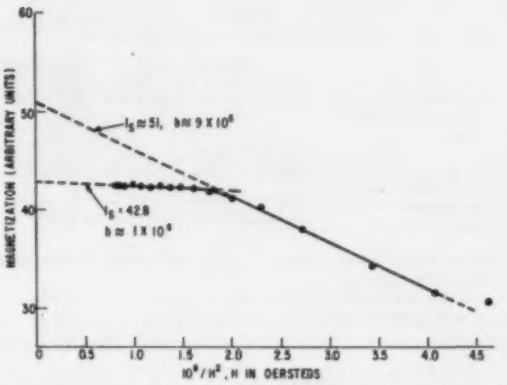

FIG. 3. The approach to saturation as a function of $1/H^2$, for a dilute suspension of carbonyl iron. The straight lines imply the law of approach $I/I_s=1-(b/H^2)$.

single domains and may be treated as such in deriving their approach to saturation.

Having established the general divisions of the magnetization process for an infinitely dilute specimen, we shall examine the effects of packing upon these divisions. The field in one sphere, in addition to containing the external field and the demagnetizing field, will have a field due to the other particles. In the Lorentz approximation,[6] this field is $4\pi If/3$, where f is the volume fraction of ferromagnetic material. Equation (1) then becomes

$$H-4\pi I/3+4\pi If/3=0, \tag{2}$$

and correspondingly the deviation from linearity occurs at the field, $H=4\pi I_s(1-f)/3\sqrt{3}$. The point at which domain wall motion ceases is less easily specified but lies between $4\pi I_s(1-0.83f)/3$ and $4\pi I_s(1-f)/3$. The difficulty lies in the fact that the magnetization is no longer linear in this region. The use of the Lorentz field approximation implies a uniform distribution of particles. Franklin[7] has pointed out that if this condition does not obtain, the nonspherical clumps of spherical particles will act as gross nonspherical particles with a consequent higher initial susceptibility, lower field at which departure from linearity appears, and a higher field at which domain wall motion is complete.

The carbonyl iron particles employed, while approximately spherical, differ from the theoretical model in that they are composed of many crystallites under large stresses.[4] To estimate the effects of having many crystallites, consider an aggregate of spherical single-domain crystals that has a spherical shape. The field in any single crystal is composed of three parts: the external field, the demagnetizing field within the crystal owing to its boundaries, and the fields from neighboring crystals. Again using the approximation of the Lorentz field, we construct a spherical shell about the crystal

[6] H. A. Lorentz, *Theory of Electrons*, (Teubner, Verlags gesellschaft Leipzig, 1916), 2nd ed., p. 138.

[7] A. D. Franklin (private communication).

TABLE I.

	Theoretical	Experimental
Saturation field extrapolated from initial slope	$4\pi I_s(1-f)/3$ 6150±300	6000±200 oe
Field at which departure from linearity first appears in initial magnetization	$4\pi I_s(1-f)/3\sqrt{3}$ 3550±150	2600±500 oe
Field at which departure from linearity appears in the approach to saturation	$4\pi I_s(1-f)/3$ 6150±300	7200±200 oe

in question and consider the region between this shell and the outer surface of the aggregate to be filled with uniformly magnetized matter. The interaction field is identically zero, since the fields associated with the divergence of the magnetization at the inner and outer surfaces exactly cancel one another. It is pushing the Lorentz theory beyond its domain of validity to extend this result to a packing factor of unity, but its results are certainly correct to a first approximation. The results previously derived for spherical single crystals hold true to this approximation for spherical aggregates of many crystals. The stress, by x-ray line broadening,[4] is estimated to be about 1.5×10^{10} d/cm^2. The anisotropy induced by this stress is given approximately by

$$K_{\text{stress}}=\tfrac{3}{2}\lambda\sigma,$$

where σ is the stress, assumed uniaxial, and λ the magnetostriction, assumed isotropic. Assuming a magnetostriction[5] for iron of -7×10^{-6}, the stress induced anisotropy is 1.6×10^5 ergs/cm^3. The first-order crystal anisotropy constant for iron at 77°K is approximately 5.5×10^5 ergs/cm^3. Since the stress-induced anisotropy is only one-third of the crystal anisotropy, the initial assumption of six easy directions is closely correct, though there will be some preference among easy directions. This preference will cause the magnetization to fall below the initial linear portion somewhat before the predicted field of $4\pi I_s(1-f)/3\sqrt{3}$.

A comparison between theory and experiment for the divisions of the magnetization curve is shown in Table I.

The approach to saturation as plotted in Fig. 2 implies the applicability of the law $I/I_s=1-(a/H)$, while that in Fig. 3 implies the law $I/I_s=1-(b/H^2)$. Inspection of each of these curves reveals a sharp change in slope at a field of about 7000 oersteds ($10^4/H\approx1.4$, $10^8/H^2\approx1.9$). In each case there is a large difference in the apparent value of saturation magnetization and of the slope coefficient a or b, depending on whether the behavior is based on data above or below 7000 oe. From an experimental viewpoint, it is clear that little or no significance can be attached to parameters of the approach laws derived from data at fields below 7000 oe. The experimental errors in the present work and the limited range of $1/H$ or $1/H^2$ available above 7000 oe prevent a very accurate determination of the saturation parameters. Only an approximate upper limit can be set to the slope coefficient, while the relative saturation magnetization can be determined within an error of one or two percent. The values of the slope coefficient, determined above 7000 oe, are $a\lesssim340$ oe, $b\lesssim1.0\times10^8$ oe^2.

The law of approach in $1/H$ has a long history, and its use for samples having nonmagnetic fractions has been discussed by Néel[6] and by Franklin and Berkowitz.[9] As described by Néel, it is not valid as an approach to saturation until all magnetization by domain wall motion has ceased. It was shown previously that this requires a field of 6000–7000 oe. This accounts for the sharp change in slope at this field region in each of the curves, Figs. 2 and 3. The region of validity of the $1/H$ law was chosen by Néel to be $0.4\leq4\pi I_s f/H\leq4$. Franklin and Berkowitz prefer the region $1\leq4\pi I_s f/H\leq5$. For the present sample, $f=0.03$, so that at $H\approx7000$ oe the function $4\pi I_s f/H\approx0.1$, which is its largest possible value in the field range where domain wall motion is completed. This is precisely the region where Néel's theoretical approach goes over toward a $1/H^2$ law. The work of Akulov,[10] and that of Gans,[11] has theoretically established the law of approach in $1/H^2$ for an assembly of noninteracting particles magnetizing by rotation processes alone. Their neglect of interactions, as pointed out by Holstein and Primakoff,[12] as well as by Néel,[6] is negligible in the present case of a very dilute suspension. An estimate of the theoretical value of the slope coefficient b falls by a factor of 100 below the upper limit for b obtained in the experiment. This is not disturbing, since the conditions and errors in this experiment prevent an accurate determination of a low value of b. Nonspherical clumps, as pointed out by Franklin,[7] will give rise to a large value of b because of the shape anisotropy of the clumps. This can mask the effect of crystal anisotropy.

The preceding discussion accounts for the principal features of the curves of approach to saturation. It is clear that the appropriate method of extrapolation to obtain a value of the saturation magnetization of very dilute ferromagnetic suspensions is that in $1/H^2$. In addition, the fields must be high enough to insure completion of domain wall motion in the magnetization process.

In summary, the magnetization curve of a dilute suspension of carbonyl iron powder, type E, is close to what one would derive from consideration of a dilute assembly of randomly oriented, single-crystal, multidomain spheres. The deviations are in the directions expected from the effects of stress and nonspherical clumping.

[6] L. Néel, J. Phys. radium **9**, 184, 193 (1948).
[9] A. D. Franklin and A. E. Berkowitz, Phys. Rev. **89**, 1171 (1953).
[10] N. Akulov, Z. Physik **69**, 822 (1931).
[11] R. Gans, Ann. Physik [5] **15**, 28 (1932).
[12] T. Holstein and H. Primakoff, Phys. Rev. **59**, 388 (1941).

Thermionic Properties of UC

GEORGE A. HAAS AND JOHN T. JENSEN, JR.
Naval Research Laboratory, Washington, D. C.
(Received January 25, 1960)

Thermionic emission measurements using pulse techniques have been obtained from UC-coated W filaments in the temperature range of 1200°–2100°K. From the slope and intercept of the Richardson plot, a value of $\phi = 2.94$ ev and $A = 33$ amp/cm^2 deg^2 was indicated. There is evidence that the energy required for electrons to escape at low fields might be several tenths ev higher than the 2.94 ev value.

INTRODUCTION

RECENT progress in the field of thermionic energy conversion has focused attention to several new types of thermionic emitters. Among these uranium monocarbide, UC is of particular interest because it not only is a copious electron source, but also can be fission heated in a neutron flux. Preliminary thermionic data on this emitter have been obtained at Los Alamos[1] from UC formed by arc-melting uranium metal and graphite in an inert atmosphere. Thermionic measurements were then carried out using a planar-diode geometry in a demountable, metal vacuum system which was necessitated by further cesium-plasma-diode experiments.

The experiments described here were not limited by this application, and consequently permitted the use of a sealed-off glass system using cataphoretically coated UC filaments in a cylindrical geometry. This aided in proceeding to much higher fields and higher temperatures.

TUBE CONSTRUCTION

Since UC is pyrophoric as well as radioactive, the complete cathode-coating procedure and tube assembly was carried out in a dry box under an argon atmosphere. The cathodes used for the thermionic emission studies were 5-mil diam UC-coated W filaments prepared from a cataphoretic bath consisting of 400-mesh UC powder[2] in a solution of absolute ethyl alcohol and nitrocellulose binder. The filaments, with their attached tension springs, were then mounted in a cylindrical anode-guard-ring geometry consisting of three Mo cylinders, 0.75 in. in diam, mounted on sapphire rods. Because of these rods, the entire anode-guard-ring structure could be hydrogen-fired as a unit just prior to the insertion of the filament.

The assembled tube (Fig. 1) was then enclosed, using a matched butt-seal while argon was flowing from *A* to *B*. After the enclosure, stopcock *A* was sealed off and the tube was leak-checked through stopcock *B*, after which it too was sealed off leaving the tube under vacuum. In this condition, the tube was sealed onto a vacuum system at point *C*. After the system was exhausted, the glass bubble was broken by means of the iron slug, and tube processing began. This consisted of alternately baking and rf heating the metal parts until no appreciable rise in pressure was obtained by flashing the filament or by glowing the Mo cylinders.

The highest temperature used in flashing the filament was approximately 2000°C since it was observed that an irreversible "poisoning" effect takes place above this temperature. The tube was sealed off at point *D* and then pumped to its ultimate pressure by means of the Alpert gauge. The final pressure in all tubes was consistently in the low 10^{-10} mm of Hg range. Getters were not used, in order to avoid possible contamination of the tube with extraneous, low-work-function agents (e.g., Ba).

EMISSION MEASUREMENTS

The temperature of the filaments was measured with an optical pyrometer and then corrected for the spectral emissivity of UC. This latter property was obtained from tubes containing UC coated Ta sleeves having a number of small drilled holes through which blackbody measurements were made. Comparison of the surface

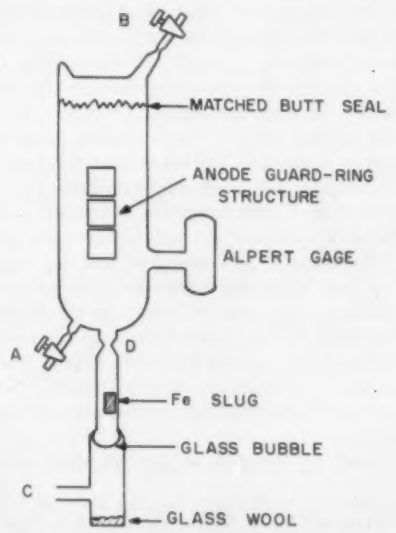

FIG. 1. Design of experimental diode used for emission studies.

[1] R. W. Pidd, G. M. Grover, D. J. Roehling, E. W. Salmi, J. D. Farr, N. H. Krikorian, and W. G. Witteman, J. Appl. Phys. 30, 1575 (1959).
[2] Prepared at the Argonne National Laboratories.

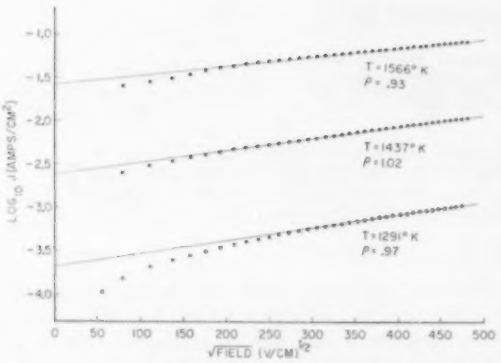

FIG. 2. Typical Schottky plots obtained for UC-coated filaments. The value ρ is the ratio of the experimental to theoretical Schottky slope.

to hole temperature in the region of 1100°K to 2000°K, yielded a 0.65 μ spectral emissivity of 0.9 ± 0.05, with a tendency to favor the lower limit at the higher temperatures. This value agrees very well with that obtained from metallic samples described in footnote reference 1.

The current-voltage characteristics were obtained by microsecond pulse techniques, in order to minimize anode dissipation effects. The pulse system, which is described in greater detail elsewhere,[3] permitted, in a matter of seconds, the recording of Schottky plots for fields as high as 230 000 v/cm with better than one percent accuracy. Monitoring the pressure during this time indicated that only at the high temperature did the pressure increase to the 10^{-9} mm of Hg range.

An example of several Schottky plots is shown in Fig. 2. It was observed, especially at the lower temperatures, that the current rose quite rapidly for the lower field values. This anomalous rise in current is common in varying degrees to nearly all thermionic emitters and is explained by the nonuniformity in the work function of the emitting surface, or patch effect.[4] The resulting surface fields of these patches cause the electron barrier in front of the lower work function regions to be decreased by weak applied fields much more rapidly than the simple mirror-image barrier, as dictated from Schottky theory.[5] At the higher fields (Fig. 2), a linear dependence was observed, and the slopes were found to agree generally within 10% of the theoretical Schottky slope of $1.912/T$. This agreement indicates that the effect of the patch fields is overshadowed by the much-stronger applied fields and that in this region the application of Schottky theory is valid. It was only for these conditions that the extrapolation to zero field was made.

The resultii. Richardson plot obtained from such extrapolated values for two tubes (UC-3, UC-4) is shown in Fig. 3. These data were quite reproducible and indicated a stable state of emission. The slope and intercept of the Richardson plot gave a value of $\phi=2.94$ ev and $A=33$ amp/cm² deg². This work function and A value is considerably lower than the values obtained by Pidd *et al.*[1] ($\phi=4.57$, $A=7.3\cdot10^5$), which are also shown in Fig. 3. Possible reasons for this are given in the following section.

Because of the pronounced patch effects observed (ranging in field up to $\sim10^5$ v/cm) an attempt was also made to measure the work function at zero-field.[6] While such results are strongly affected by varying patch structures, depending on method of fabrication, etc., they are still significant, especially for low-field applications such as thermionic energy converters. The measurements were obtained from the knee of the emission curve in going from the retarding to the accelerating region. However, because of the difficulty in separating retarding field and space-charge effects from such a patchy surface, the value thus obtained, $\phi\simeq3.14$ ev, $A\simeq50$ amp/cm² deg², can be considered only as approximate.

DISCUSSION OF RESULTS

The interpretation of the apparent work function (slopes of Richardson plots) obtained by the extrapolated high-field and zero-field methods has been discussed by Herring and Nichols.[4] They show that for a surface containing n patches, with individual work functions ϕ_i,

$$\phi_{\text{high fields}}\simeq\sum_{i=1}^{i=n}\omega_i\phi_i \qquad (1)$$

and

$$\phi_{\text{zero field}}\simeq\sum_{i=1}^{i=n}\theta_i\phi_i, \qquad (2)$$

where ω_i is the fraction of the total strong field emission that comes from the ith patch and θ_i is the fraction of the total area that is occupied by this patch. If it is assumed that the emitting surface is essentially a two-patch emitter covered in part with regions of low work function surfaces, i.e., patches of UC, and the remainder covered with regions of high work function, then Eq. (1) or the strong-field method gives a fairly accurate determination of the work function of UC, while the high work function component can be estimated from Eq. (2), giving

$$\phi_{\text{high work function}}\simeq(\phi_{\text{zero field}}-\theta_{UC}\phi_{UC})/(1-\theta_{UC}), \qquad (3)$$

where ϕ_{UC} is the value for the UC-covered patches and θ_{UC} is the fraction of the total area covered by these patches. From this it is seen that for patches of high

[3] G. A. Haas and F. H. Harris, Rev. Sci. Instr. **30**, 623 (1959).
[4] C. Herring and M. H. Nichols, Revs. Modern Phys. **21**, 185 (1949).
[5] W. Schottky, Physik. Z. **15**, 872 (1914).
[6] This is not to be confused with extrapolation from the patch region, which can give erroneous results, owing to excessive slopes in this range of fields.[4]

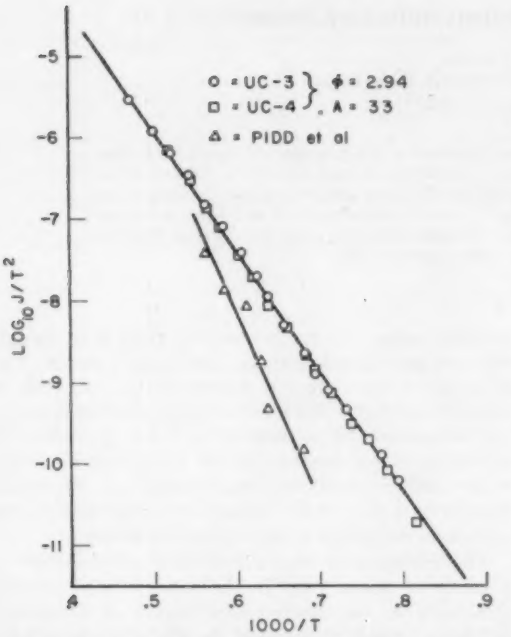

FIG. 3. Richardson plot obtained from extrapolated Schottky plots for two different tubes (UC-3, UC-4). Also shown are the results of Pidd *et al.*, ($\phi = 4.57$, $A = 7.3 \cdot 10^5$), which were taken from Fig. 2 of footnote reference 1.

work-function surface having an average diameter one-half that of the UC patches, the ϕ value for the high work function component is ~ 4 ev. If the ratio is one-third, then this value is ~ 5 ev.

In summary then, it appears that the work function of UC prepared in the manner described here is very nearly 2.94 ev with an A value of 33 amp/cm^2 deg^2. However, because of the presence of high work function patches, a strong retarding field exists outside the UC-covered patches, so that the barrier for electron emission from these near zero field has been increased by several tenths ev.[7] Furthermore, it is not unreasonable to assume that the value of the high work function component is 4 to 5 ev, which might explain why similar type surfaces[8] have been able to employ Cs (ionization potential 3.8 v) to suppress space charge effects.

The reason for the difference between these results and those of Pidd *et al.*[1] may be ascribed in part to the difference in vacuum conditions and the use of dc techniques, in addition, the solid UC might have properties unlike those of the UC powder used here. A further possibility lies in the limited field which could be employed in the Los Alamos geometry ($\sim 3 \cdot 10^3$ v/cm). This appears to be in the patch region (Fig. 2),[9] and it was found that analyzing our results from extrapolated values taken in this field range could cause both ϕ and A to appear appreciably higher even than those obtained by the zero-field method.

The authors are indebted to Dr. F. E. Jamerson of the General Motors Research Laboratories for suggesting this problem and supplying the UC powder.

[7] There is also a possible contribution of the order of a tenth ev arising from the temperature coefficient of the work function as estimated from the observed A value.

[8] G. M. Grover, Nucleonics **17**, 54 (1959).

[9] Thermionic emission data taken at the General Motors Research Laboratories (private communication) under conditions similar to Los Alamos techniques substantially agreed with Los Alamos data, whereas the ratio of the experimental to theoretical Schottky slope was of the order of five.

Criteria for the Choice of a Superconducting Bolometer*

BOGOLJUB LALEVIC
The Franklin Institute, Philadelphia 3, Pennsylvania
(Received March 7, 1960)

The usefulness of the superconducting bolometer was recognized a long time ago. All experimental data obtained up to now are far below the calculated value for a sensitivity of such a bolometer, because of the presence of the noise in the transition region of a superconductor. We have presented the correlation between the noise and the value of the surface boundary energy (interface between normal and superconducting laminas) and given on this basis the criteria for the choice of a superconducting bolometer. Attempt has been made to evaluate the noise on the basis of the Thomas-Fermi approximation.

IT was calculated[1] that it is possible to measure extremely low rf and microwave power down to $\sim 10^{-15}$ w by using a superconducting bolometer and having the helium bath temperature controlled to within 10^{-5} deg.

The existence of the random variation of the resistance, i.e., the noise in the transition region of a superconductor, can be a serious limitation of its sensitivity as a bolometer despite all other qualities, such as large temperature coefficient of resistance and disappearance of the thermal noises.

The source of noise in superconductors was not known. We will present the correlation between the noise and the value of the surface boundary energy (interface between normal and superconducting laminas), i.e., the number of domains in a superconductor. On this basis we will give the criteria for the choice of a superconducting bolometer and its minimum dimensions.

Weber[2] was first to observe the fluctuation of the resistance of the long tantalum wire in the transition region. The maximum fluctuation was about 5% of the total resistance in that region.

Andrews[3] has observed the noise of about 5×10^{-10} w using CbN as a bolometer for infrared radiation. The noise persisted even when there was no current flowing through the bolometer. Love[4] observed low resistance levels with an indium specimen of 50 μ diam while decreasing magnetic field in the transition region. Kaplan and Daunt[5] have observed a large current noise in a tantalum specimen in the transition region, but none in a partially superconducting, leaded-phosphor-bronze specimen. Kaplan[6] studied a noise increasing as $\sim i^2$ when specimens were in a magnetic field. Finally, Baird[7] has undertaken a systematic investigation of the resistance noise in tantalum. He has established the existence of definite resistance levels in the intermediate region. The levels can cover from $\frac{1}{10}$ to the full value of the resistance in the intermediate region. The resistance levels were well defined for the specimen of about 2-cm length. The use of a longer specimen adds to the resistance states available and has the effect of averaging over a large number of states, with the result that smaller resistance fluctuations are obtained. Baird's data for a long specimen passing through the transition region are similar to that of Weber's.[2]

The existence of the well-defined levels within a distance of about 2 cm indicates very large domain structures in the intermediate region of tantalum. Schawlow[8] has demonstrated, by the niobium powder method, that these domains are considerably larger in hard superconductors such as vanadium, tantalum, and niobium than in soft superconductors, such as tin, for the same thickness. According to Landau's theory[9] the width of a domain depends on the surface (interface between normal and superconducting laminas) boundary energy and the dimensions of the specimens.

On the basis of the niobium powder pattern of the domains in tantalum, Schawlow[8] estimated the interface energy in tantalum as at least a thousand times greater than in tin. This value is well beyond any possible explanation on the basis of Landau's or any other existing theory. Moreover, Schawlow has observed the instability, i.e., the abrupt change of the boundaries, with the change of the field. One can assume that these abrupt changes of the boundaries indicate the destruction of the equilibrium on the normal-superconducting interface, between the electromagnetic-kinetic stresses, pointing toward the interior of the superconducting phase, and the Meissner pressure.

If the boundary is displaced by the volume element δV, then the change of the internal free energy is given by

$$\delta F = \pm (f_n - f_s)\delta V$$
$$\pm \partial F/\partial V = f_n - f_s,$$

where f_n and f_s represent the internal free energies of the two phases.

* Supported by U. S. Signal Corp.

[1] D. Birx, M. Hirsch, and B. Lalevic, First Quarterly Engineering Report, written under contract to the U. S. Signal Corps.
[2] R. Weber, Phys. Rev. **72**, 1241 (1947).
[3] D. H. Andrews, R. M. Milton, W. DeSorbo, J. Opt. Soc. Am. **36**, 520 (1946).
[4] W. Love, Phys. Rev. **85**, 715 (1952).
[5] B. Kaplan, and J. G. Daunt Phys. Rev. **89**, 907 (1953).
[6] B. Kaplan, thesis, Ohio State University (1954).
[7] D. Baird, Can. J. Phys. **37**, 120 (1959).
[8] A. Schawlow, Phys. Rev. **101**, 573 (1956).
[9] L. Landau, Phys. Z. Sowjet **11**, 129 (1937).

TABLE I. Values of $\varphi(\eta)$.

η	$\varphi(\eta)$	η	$\varphi(\eta)$
0.1	0.0055	0.6	0.0182
0.2	0.0136	0.7	0.0128
0.3	0.0195	0.8	0.0065
0.4	0.0224	0.9	0.0020
0.5	0.0221		

TABLE II.

Metal	λ_0 cm$\times 10^{-6}$	H_0 gauss	S_0
Al	4.9	106	0.039
Hg	4.5	415	0.125
In	6.4	270	0.17
Pb	3.9	800	0.19
Sn	5.0	305	0.115

The equilibrium condition is given by[10]

$$f_n - f_s = (2\pi\lambda^2/c^2) j_{s11}^2,$$
$$f_n - f_s = H_{11}^2/8\pi,$$

where

$$j_{s11} = (c/4\pi\lambda)|H_{11}|.$$

The boundary of a superconducting region is, therefore characterized by a critical magnetic field or, better, by the density of the supercurrent. This conclusion we will use in evaluating the magnitude of the fluctuation in a intermediate region. It is reasonable to conclude that in the case of a hard superconductor or a soft superconductor of small dimensions, i.e., when the phase boundary effects become important, one can expect the observed resistance fluctuations. Therefore the criteria for the choice of a superconducting bolometer will be the element with (a) a small interface energy, and (b) a large number of domains, so the aforementioned averaging effect would smooth out the variation of the resistance-vs-temperature curve. These criteria explain why Andrews,[2] using a hard superconductor of small dimensions, was limited by the noise of 5×10^{-10} w, and Jones[11] has succeeded in measuring infrared radiation up to 3×10^{-12} w by using tin wire. Jones was limited in attempts to attain higher sensitivity only by the fluctuation of the temperature in the helium bath.

The values for the interface energy and the number of states can be obtained from the Landau theory, i.e., from the equations he has derived for the case of a plate oriented normal to the magnetic field.

According to Landau, the total free energy per unit area of a plate surface is given by

$$F = (2L\Delta/a)(H_c^2/8\pi) + 2a\varphi(\eta)(H_c^2/8\pi). \quad (1)$$

The first term on the right side of Eq. (1) gives interface boundary energy and the second term magnetic energy. a = total thickness of two neighboring laminas, L = width of the plate, H_c = critical field for a given specimen, $\eta = H/H_c$, and the limiting expressions for $\varphi(\eta)$ are, for small η,

$$\varphi(\eta) = (\eta^2/\pi)\log(1/2\eta) \quad \eta \ll 1,$$

and, for large η,

$$\varphi(\eta) = \log(2/\pi)(1-\eta)^2 \quad 1-\eta \ll 1.$$

A numerical evaluation calculated by Lifshitz[12] is given in Table I. Δ is a surface energy parameter and has the dimensions of length.

In Landau's theory Δ is given by

$$\Delta = \lambda g(s)/S, \quad (2)$$

where λ is field penetration depth and varies with temperature as

$$\lambda = \lambda_0/[1-(T/T_c)^4]^{\frac{1}{2}}, \quad (3)$$

in which λ_0 = penetration depth at $T = 0°$K, T_c = critical temperature;

$$S = eH_c\lambda^2/\hbar c$$

and varies with temperature as

$$S = S_0/[1+(T/T_c)^2], \quad (4)$$

and $g(s)$ is given by an approximate expression

$$g(S) = (1.1-1.6S)$$

The values for λ_0, H_0, and S_0 for different metals are given in Table II. The value of "a" is determined by the condition that the total free energy F should be a minimum. Differentiating (1) with respect to "a" gives

$$a = (L\Delta/\varphi(\eta))^{\frac{1}{2}}. \quad (5)$$

We see by using Eqs. (5) and (1) that the surface energy contribution will be negligible when $l > \Delta/\varphi(\eta)$, where l is the smaller dimension of the specimen. This gives us a criterion for a dimension to be used for a soft superconducting bolometer. The number of domains per cm^2 is therefore

$$n^2 = \varphi(\eta)/L\Delta \quad (6)$$

and the total free energy F

$$F = (H_c^2/2\pi)(\varphi(\eta)L\Delta)^{\frac{1}{2}}. \quad (7)$$

Eliminating hard superconductors as possible bolometers, because of the noise problem and because they do not conform to Eq. (6) and (7), we will concern ourselves only with the soft superconductors. The critical parameters for soft superconductors may be calculated from Eq. (6) and (7). We will use $\eta = \frac{1}{2}$ because this value gives the largest number of domains per cm. Also we will use T quite close to T_c, because, following Schawlow's[8] work, this region yields the

[10] F. London, *Superfluids* (John Wiley & Sons, Inc., New York, 1950), Part I.

[11] G. Jones and J. Hulbert, Proc. Phys. Soc. (London) **A69**, 801 (1956).

[12] E. Lifshitz and Y. V. Shazvin, Dokl. Akad. Nauk. U. S. S. R. **79**, 783 (1951).

TABLE III.

Metal	$\lambda\times10^{-5}$ cm	$S\times10^{-2}$	$g(s)$	$\Delta\times10^{-4}$ cm	n^3	$F\times10^{-4}$ H_c	Recommended smallest dimension $l\times10^{-2}$ cm
Sn	1.798	5.866	1.00615	3.084	71.66	4.15	>1.4
In	2.30	8.67	0.961	2.55	86.66	3.78	>1.15
Al	1.76	1.99	1.0682	9.447	23.6–1	7.27	>4.5
Pb	1.403	9.69	0.945	1.368	161.5–5	2.77	>0.62
Hg	1.62	6.37	0.998	2.54	87	3.75	>1.14

closet fit between experimental determination of Δ and the theoretical prediction.

On using the values from the Tables I and II and using Eqs. (2)–(4), (6), and (7), we obtain the data given in Table III. As can be seen from Table III, lead best satisfies our conditions because it has the largest number of states per cm^2 and the smallest interface energy, which is in agreement with Schawlow[8] experimental observations. The disadvantage of using lead is that it is not as easy to maintain the temperature of the bath with the required accuracy of 10^{-5} degrees as with the case of In and Sn.

As we have pointed out previously, the boundary of the superconducting region is characterized by the density of the supercurrent. Therefore, the fluctuation of the supercurrent density will influence the equilibrium on the normal-superconducting interface. In order to calculate the fluctuations, we will start with a rather rough approximation for our case, i.e., we will use the Thomas-Fermi approximation.

The electron-density fluctuations $\rho_k=eN$ have a part $\delta\rho_k$, which represents a response to the ionic vibrations, and a part $\rho_k{}^0$, which fluctuates randomly with respect to the phonon coorbinates q_k.

In the Thomas-Fermi approximation the electron density ρ is proprotional to

$$\rho\sim(E_F-V)^{\frac{1}{2}}, \tag{8}$$

where E_F is Fermi energy and V the combined potential from electron and ion motion.

Differentiating (8),

$$\delta\rho=-\tfrac{3}{2}(n/E_F)\delta V, \tag{8a}$$

where $n=ZN$ and Z is the ionic valence.

The Fourier component[13] of (8a) is

$$\delta\rho_k=\tfrac{3}{2}(n/E_F)V_k, \tag{9}$$

where V_k is the interaction potential and it is a sum of $V_k{}^i$ owing to the motion of ions and V_k, owing to the motion of electrons.

$$V_k=V_k{}^i+V_k{}^e. \tag{10}$$

The Poisson equation gives the relation

$$-k^2\delta V_k{}^e=4\pi e^2\delta\rho_k, \tag{11}$$

where K is a wave vector in the first Brillouin zone. On using (11)–(9), we obtain

$$V_k=\{k^2/[k^2+(6\pi ne^2/E_F)]\}V_k{}^i. \tag{12}$$

In the free electron approximation

$$V_k{}^i=-4\pi iZe^2(N/M)^{\frac{1}{2}}\cdot1/|k|. \tag{13}$$

Finally, using (13), (12), and (9), we obtain in long-wave approximation

$$|\delta\rho_k|\sim Z(N/M)^{\frac{1}{2}}$$

and for the fractional fluctuation $\sim Z/(NM)^{\frac{1}{2}}$. As we can see, lead is from this standpoint also the best choice for a superconducting bolometer.

ACKNOWLEDGMENTS

I am indebted to Professor K. R. Atkins and Dr. F. Donahoe for reading the manuscript and several useful discussions.

[13] J. Bardeen and D. Pines, Phys. Rev. **99**, 1140 (1955).

JOURNAL OF APPLIED PHYSICS VOLUME 31, NUMBER 7 JULY, 1960

Response of a Loaded Idealized Piezoelectric Plate to an Electric Signal*

LEO LEVI†
New York, New York
(Received January 5, 1960)

The response of piezoelectric plates and rods are generally treated in the form of "equivalent" electric circuits. When the actual mechanical displacements and strains are of interest, such equivalent circuit treatment may be inconvenient. In the present paper the response of a loaded piezoelectric plate to an arbitrary electric input signal is derived on the basis of certain idealizations which are closely approximated by practical systems.

A. INTRODUCTION

THE present exposition is an attempt to analyze the response of a piezoelectric plate to any applied field, when this plate is in contact with other acoustic media. A rigorous solution of this problem is, of course, too complex to attempt here. But it seems that by introducing a degree of idealization, the situation may be reduced to a very simple one-dimensional boundary value problem, whose solution will not differ greatly from the results to be expected in an actual system for a wide variety of practical conditions. As a result of this simplification the solution will, with minor modifications, be applicable also to other electromechanical transducers.

A survey of the literature shows considerable work on loaded piezoelectric crystals such as done primarily by Langevin and Biquard[1] and by Mason.[2] Compare also May.[3] But the former work was strictly on sinusoidal signals and all the later work seems to have been by the use of "equivalent electric circuits," which are highly appropriate when only the electrical characteristics are of interest, but are less readily applicable when the mechanical effects are being investigated. It is therefore hoped that the results presented here will serve a useful purpose.

The following simplifying assumptions will be made:

1. We are dealing with a transducer plate whose lateral dimensions far exceed its thickness, so that fields, strains, and stresses may all be considered plane.[4]

2. The shearing stress introduced by a compressional strain and the compressional stress introduced by a shearing strain will be negligible compared to the corresponding compressional and shearing stresses, respectively.[5]

3. The losses within the transducer are negligible compared to the energy radiated into the surrounding media.

4. The transducer is surrounded by homogeneous acoustic media, extending to infinity.

5. The displacements are maintained low enough, so that the transducer does not separate from the medium during any part of the cycle and that the elastic and electromechanical effects may be considered to be linear.

Although the foregoing conditions may seem rather ideal and will never be fully realized in a practical situation, the deviation will be negligible in many practical applications. In particular, the results will be applicable to many systems where high-frequency acoustic energy is used for information purposes, as in ultrasonic delay lines and ultrasonic light modulators. They are further justified by the fact that they make these situations readily amenable to an analysis which would otherwise probably be not practical.

Since the above conditions reduce the problem to a one-dimensional one, only the following parameters need be considered:

1. The compressional and shear strains ($2d$) introduced by a unit signal under static conditions with the transducer clamped laterally.

2. The restoring stress introduced by a unit compressional or shear strain, both in the transducer and in the media, i.e., the appropriate moduli of elasticity.

3. The densities (ρ) of the transducer material and the media.

4. The thickness ($2D$) of the transducer.

In the following, the ratio of the elastic modulus to the density is written as v^2, since it equals the square of the velocity with which a local disturbance would be propagated.

As a result of the above simplifying assumptions, a single differential equation results for each medium, namely $(\partial^2 a/\partial t^2)-v^2(\partial^2 a/\partial x^2)=0$, where a is the displacement in the particular medium.

This set of differential equations will be solved for a unit-step input, since for this case the boundary conditions are most obvious physically. Differentiating the result with respect to time, yields the impulse response.

* Work done for Fairchild Camera and Instrument Company, Syosett, New York, and sponsored by the Johns Hopkins University, Applied Physics Laboratory, Silver Springs, Maryland.
† Consulting Physicist, New York, New York.
[1] P. Biquard, Rev. d'Acoustique **3**, 104 (1934).
[2] W. P. Mason, *Electromechanical Transducers and Wave Filters* (D. Van Nostrand Company, Inc., Princeton, New Jersey, 1942), 2nd ed., p. 230.
[3] J. G. May, Jr., J. Acoust. Soc. Am. **26**, 347 (1954).
[4] In order for this assumption to apply rigorously the results must be limited to time intervals short with respect to the lateral dimension divided by the velocity of strain propagation in the transducer.
[5] This is rigorously true, certainly for homogeneous magnetostrictive transducers, but also for the most common piezoelectric transducers, such as the x-cut quartz crystal where c_{15} and c_{16} vanish.

The convolution of this with any arbitrary input signal, will yield the corresponding response.

One set of boundary conditions is due to the fact that the displacement must be continuous across a boundary, as must be the stress (which equals $\rho v^2 \partial a/\partial x$). The system will be considered to be at rest with a negative unit potential applied across the crystal electrodes producing strain, d. The electrodes are then short circuited at time $t=0$. The resulting vibrations will then be strictly elastic ones, since the mechanical effects of the locally created electric polarization are included in the moduli of elasticity, ρv^2. Thus the initial unit strain is assumed to be $-d/D$ in the transducer and vanishing elsewhere. The displacement at all finite times vanishes for infinite $|x|$ (or, in view of our boundary conditions at $t=0$, this displacement remains at d).

B. DERIVATION OF IMPULSE AND STEP-FUNCTION RESPONSES

Our system consists of three media, limited in the x direction and infinite in the yz plane. Let the magnitude of vibration in these media be a, b, c, where a refers to the piezoelectric transducer; ρ and v, with the appropriate subscripts, refer respectively to the density of the medium and to the velocity of the disturbance for the three regions. Let $2D$ be the transducer thickness and $2d$ the initial total strain.

We have then the following equations and boundary conditions:

$-\infty < x < -D$:

$$(\partial^2 b/\partial x^2) - (1/v_b^2)(\partial^2 b/\partial t^2) = 0; \tag{1}$$

$$b(0,x) = +d; \tag{2}$$

$$\dot{b}(0,x) = 0; \tag{3}$$

$$b(t,-\infty) = d; \tag{4}$$

$-D < x < D$:

$$(\partial^2 a/\partial x^2) - (1/v_a^2)(\partial^2 a/\partial t^2) = 0; \tag{5}$$

$$a(0,x) = -xd/D; \tag{6}$$

$$\dot{a}(0,x) = 0; \tag{7}$$

$D < x < \infty$:

$$(\partial^2 c/\partial x^2) - (1/v_c)(\partial^2 c/\partial) t^2 = 0; \tag{8}$$

$$c(0,x) = -d; \tag{9}$$

$$\dot{c}(0,x) = 0; \tag{10}$$

$$c(t,\infty) = -d; \tag{11}$$

$x = -D$:

$$a(t,-D) = b(t,-D); \tag{12}$$

$$\rho_a v_a^2 [\partial a(t,-D)/\partial x] = \rho_b v_b^2 [\partial b(t,-D)/\partial x]; \tag{13}$$

$x = D$:

$$a(t,D) = c(t,D); \tag{14}$$

$$\rho_a v_a^2 [\partial a(t,D)/\partial x] = \rho_c v_c^2 [\partial c(t,D)/\partial x]. \tag{15}$$

Note that the Laplace transforms are

$$\mathfrak{L}(\partial^2 a/\partial t^2) = s^2 A - sa(0,x) - \dot{a}(0,x);$$
$$\mathfrak{L}(\partial^2 a/\partial x^2) = \partial^2 A/\partial x^2.$$

Thus Eqs. (1), (5), and (8) become, respectively,

$$\partial^2 B/\partial x^2 - (s^2 B - sd)/v_b^2 = 0, \tag{16}$$

$$\partial^2 A/\partial x^2 - (s^2 A + sxd/D)/v_a^2 = 0, \tag{17}$$

$$\partial^2 C/\partial x^2 - (s^2 C + sd)/v_c^2 = 0. \tag{18}$$

The solutions are, respectively, of the form

$$B = \beta_1 e^{sx/v_b} + \beta_2 e^{-sx/v_b} + d/s, \tag{19}$$

$$A = \alpha_1 e^{sx/v_a} + \alpha_2 e^{-sx/v_a} - xd/sD, \tag{20}$$

$$C = \gamma_1 e^{sx/v_c} + \gamma_2 e^{-sx/v_c} - d/s, \tag{21}$$

where the α, β, γ represent functions of s determined by the boundary conditions. From conditions (4) and (11) it is apparent that $\beta_2 = \gamma_1 = 0$. From Eqs. (12) and (14), by substituting Eqs. (19)–(21), we find

$$\alpha_1 e^{-sD/v_a} + \alpha_2 e^{sD/v_a} + (d/s) = \beta e^{-sD/v_b} + (d/s),$$

or

$$\beta = [\alpha_1 e^{-sD/v_a} + \alpha_2 e^{sD/v_a}] e^{sD/v_b}. \tag{22}$$

Similarly,

$$\alpha_1 e^{sD/v_a} + \alpha_2 e^{-sD/v_a} - (d/s) = \gamma e^{-sD/v_a} - (d/s),$$

or

$$\gamma = [\alpha_1 e^{sD/v_a} + \alpha_2 e^{-sD/v_a}] e^{sD/v_c}, \tag{23}$$

where we have set $\beta_1 = \beta$ and $\gamma_2 = \gamma$. Again, from Eqs. (13) and (15), substituting Eqs. (19)–(21), we find

$$\rho_a v_a^2 [(s/v_a)\alpha_1 e^{-sD/v_a} - (s/v_a)\alpha_2 e^{sD/v_a} - (d/sD)]$$
$$= \rho_b v_b^2 [(s/v_b)\beta e^{-sD/v_b}]$$

or, letting

$$\rho_a v_a / \rho_b v_b = m_1, \tag{24}$$

$$\beta = m_1 [\alpha_1 e^{-sD/v_a} - \alpha_2 e^{sD/v_a} - (v_a d/s^2 D)] e^{sD/v_b}. \tag{25}$$

Similarly,

$$\rho_a v_a^2 [(s/v_a)\alpha_1 e^{sD/v_a} - (s/v_a)\alpha_2 e^{-sD/v_a} - (d/sD)]$$
$$= \rho_c v_c^2 [-(s/v_c)\gamma e^{-sD/v_c}]$$

or, letting

$$\rho_a v_a / \rho_c v_c = m_2, \tag{26}$$

$$\gamma = m_2 [-\alpha_1 e^{sD/v_a} + \alpha_2 e^{-sD/v_a} + (v_a d/s^2 D)] e^{sD/v_c}. \tag{27}$$

Equations (22), (23), (25), and (27) involve four unknown functions of s: α_1, α_2, β, γ. Solving for these functions we obtain, after some straightforward but

tedious manipulations, letting $\tau \equiv D/v_a$,

$$\alpha_1 = \frac{2d}{s^2\tau}\left[\frac{m_1(1-m_2)+m_2(1+m_1)e^{s\tau}}{-(1-m_1)(1-m_2)+(1+m_1)(1+m_2)e^{2s\tau}}\right]e^{\frac{1}{2}s\tau}, \tag{28}$$

$$\alpha_2 = \frac{-2d}{s^2\tau}\left[\frac{m_2(1-m_1)+m_1(1+m_2)e^{s\tau}}{-(1-m_1)(1-m_2)+(1+m_1)(1+m_2)e^{2s\tau}}\right]e^{\frac{1}{2}s\tau}, \tag{29}$$

$$\beta = \frac{2dm_1}{s^2\tau}\left[\frac{(1-m_2)+2m_2e^{s\tau}-(1+m_2)e^{2s\tau}}{-(1-m_1)(1-m_2)+(1+m_1)(1+m_2)e^{2s\tau}}\right]e^{sD/v_b}, \tag{30}$$

$$\gamma = \frac{2dm_2}{s^2\tau}\left[\frac{-(1-m_1)-2m_1e^{s\tau}+(1+m_1)e^{2s\tau}}{-(1-m_1)(1-m_2)+(1+m_1)(1+m_2)e^{2s\tau}}\right]e^{sD/v_c}. \tag{31}$$

After introducing the following simplifying definitions, involving only constants of the transducer and the media

$$K = 2d/\tau(1+m_1)(1+m_2),$$
$$k = (1-m_1)(1-m_2)/(1+m_1)(1+m_2), \tag{32}$$

we may write

$$A = \frac{Ke^{s\tau/2}}{s^2(e^{2s\tau}-k)}\{[m_1(1-m_2)+m_2(1+m_1)e^{s\tau}]e^{sx/v_a} + [m_2(1-m_1)+m_1(1+m_2)e^{s\tau}]e^{-sx/v_a}\} - \frac{xd}{sD}, \tag{33}$$

$$B = \frac{m_1Ke^{sD/v_b}}{s^2(e^{s\tau}-k)}[(1-m_2)+2m_2e^{s\tau}-(1+m_2)e^{2s\tau}]e^{sx/v_b} + \frac{d}{s}, \tag{34}$$

$$C = \frac{m_2Ke^{sD/v_c}}{s^2(e^{s\tau}-k)}[-(1-m_1)-2m_1e^{s\tau}+(1+m_1)e^{2s\tau}] \times e^{-sx/v_c} - \frac{d}{s}. \tag{35}$$

These expressions represent the Laplace transform of the displacement of any part of the system at any time after a negative unit potential has been removed from the transducer. By subtracting the initial displacement, the response to a unit step is obtained. By multiplying these expressions by s, the Laplace transform of the system response to a unit impulse is obtained. The Laplace transform of the system response to any signal in time is obtained simply by multiplying the Laplace transform of the signal with sA, sB, or sC.

In considering the response of the medium we note that a change in the x coordinate Δx introduces only a time shift $\Delta t = \Delta x/v$. This is, of course, due to the fact that absorption losses in the medium have been neglected. For an analysis of the medium response it will therefore suffice to limit the discussion to Eq. (35) with $x = D$. Under these conditions, the impulse response of the system will be given by the inverse Laplace transform of

$$C_0' = sC_0 = s^{-1}[m_2K/(e^{s\tau}-k)] \times [(m_1+1)e^{2s\tau}-2m_1e^{s\tau}+(m_1-1)].$$

Since an expansion of

$$(e^{s\tau}-k)^{-1} = \sum_{n=1}^{\infty} k^{n-1}e^{-2ns\tau},$$

we may write

$$C_0' = \frac{m_2K}{s}[(m_1+1)e^{2s\tau}-2m_1e^{s\tau}+(m_1-1)]\sum_{n=1}^{\infty} k^{n-1}e^{-2ns\tau}.$$

By multiplying out and combining terms with equal exponents, we obtain

$$C_0' = \frac{m_2K}{s}\{[k(m_1+1)+(m_1-1)]\sum_{n=1}^{\infty} k^{n-1}e^{-2ns\tau} - 2m_1\sum_{n=1}^{\infty} k^{n-1}e^{-(2n-1)s\tau}+m_1+1\}. \tag{36}$$

The impulse response of the system at any time, that is the inverse Laplace transform of this expression, may readily be obtained by noting that Ke^{-sT}/s transforms into a step of height K at time T.

Consequently, in order to obtain the magnitude of the response at any time T, it is necessary only to sum the coefficients of those exponentials with exponents less than T in Eq. (36). Thus, for instance, for $2r\tau < t < (2r+1)\tau$ the displacement at the transducer face (on the positive side m_2) will be

$$c = m_2K(m_1+1)k^r.$$

For

$$(2r+1)\tau < t < 2(r+1)\tau, \quad C = -m_2K(m_1-1)k^r. \tag{37}$$

The following special cases may be of interest:

1. The transducer is loaded on one side only. This condition corresponds to $\rho_b = 0$ and therefore $m_1 = \infty$.

Consequently,

$$K=2d/[\tau m_1(1+m_2)]\equiv K'/m_1,$$
$$k=[(m_2-1)/(m_2+1)]\equiv k_a. \tag{38}$$

The resulting expression for the Laplace transform of the impulse response is

$$C_0'=\frac{m_2K'}{s}[(k_a+1)\sum k_a^{n-1}e^{-2n s\tau} - 2\sum_{n=1}^{\infty} k_a^{n-1}e^{(2n-1)s\tau}+1], \tag{39}$$

and for $2r\tau<t<(2r+1)\tau$,

$$c=m_2K'k_a^r.$$

For

$$(2r+1)\tau<t<2(r+1)\tau, \quad c=-m_2K'k_a^r. \tag{40}$$

2. The transducer is loaded equally on both sides. Then

$$K=2d/[\tau(1+m)^2]$$

and

$$k_d=[(1-m)/(1+m)]^2=k_a^2. \tag{41}$$

$$C_0'=\frac{mK}{s}\{[(m+1)k_a^2+m-1]\sum_{n=1}^{\infty} k_a^{2(n-1)}e^{-2n s\tau} - 2m\sum_{n=1}^{\infty} k_a^{2(n-1)}e^{-(2n-1)s\tau}+m+1\}$$
$$=\frac{mK}{s}\{2m[k_a\sum k_a^{2(n-1)}e^{-2n s\tau} - \sum k_a^{2(n-1)}e^{-(2n-1)s\tau}]+m+1\}, \tag{42}$$

is the impulse response Laplace transform. Thus for $2r\tau<t<(2r+1)\tau$,

$$c=m(m+1)Kk_a^{2r}.$$

For

$$(2r+1)\tau<\tau<2(r+1)\tau, \quad c=-m(m-1)Kk_a^{2r}. \tag{43}$$

3. The transducer is completely unloaded. In this case the relations are the same as in the preceding case with m approaching infinity. Thus

$$K=2d/\tau m^2, \quad k=1, \tag{44}$$

$$C_0'=\frac{2d}{\tau ms}[2m\sum e^{-2n s\tau}-2m\sum e^{-(2n-1)s\tau}+m] =\frac{4d}{\tau s}[\sum e^{-2n s\tau}-\sum e^{-(2n-1)s\tau}+\tfrac{1}{2}]. \tag{45}$$

The impulse response is thus a square wave with double amplitude $4d/\tau$ and period 2τ. This result is due to the fact that the above results have been derived for a lossless transducer.

A graphic presentation of the displacement of the transducer face, as a function of time, is shown in Fig. 1. Figure 1(a) represents the response to a step-function and Fig. 1(b) the response to an impulse. For normalization purposes, the coefficient m_1m_2K is assumed equal to unity and $m_1\gg1$.

In the case of the step-function input we might have expected a net displacement d at $t=\infty$. The fact that displacement vanishes at $t=\infty$ is due to the fact that our assumption of $m_1\gg1$ corresponds to a transducer effectively unloaded on the rear surface so that the difference between initial and steady state strain will appear at the rear of the crystal.

In the case of $m_1=m_2$, the integral of the impulse response from $t=0$ to $t=\infty$ equals d, half the steady state total strain, as would be expected from symmetry considerations. This result can be obtained by summing Eqs. (43) for $r=0$ to $r=\infty$ and multiplying by τ, corresponding to integration from $t=0$ to $t=\infty$.

In some instances the state of strain of the media may be of interest. For instance, the change of refractive index of the medium may be considered, to a first approximation, proportional to the strain.

The strain of the medium is equal to the rate of change of the displacement (with respect to the direction of propagation). Thus the Laplace transforms of the strains resulting from a step-function are, using Eqs. (33), (34) and (35):

$$A^*=\frac{\partial A}{\partial x}=\frac{Ke^{s\tau/2}}{sv_a(e^{2s\tau}-k)} \times\{[m_1(1-m_2)+m_2(1+m_1)e^{s\tau}]e^{sx/v_a} -[m_2(1-m_1)+m_1(1+m_2)e^{s\tau}]e^{-sx/v_a}\}-\frac{d}{sD}, \tag{46}$$

$$B^*=\frac{\partial B}{\partial x}=\frac{m_1Ke^{sD/v_b}}{sv_b(e^{2s\tau}-k)} \times[(1-m_2)+2m_2e^{s\tau}-(1+m_2)e^{2s\tau}]e^{sx/v_b}, \tag{47}$$

$$C^*=\frac{\partial C}{\partial x}=\frac{m_2Ke^{sD/v_c}}{sv_c(e^{s\tau}-k)} \times[(1-m_1)+2m_1e^{s\tau}-(1+m_1)e^{2s\tau}]e^{-sx/v_c}. \tag{48}$$

The corresponding expressions for an impulse input are obtained from the above simply by multiplying by s. Corresponding to Eq. (36), the expressions at the transducer face are for a step-function input and impulse input, respectively,

$$C_0^*=-\frac{m_2K}{v_cs}\{[k(m_1+1)+(m_1-1)]\sum_{n=1}^{\infty} k^{n-1}e^{-2n s\tau} - 2m_1\sum_{n=1}^{\infty} k^{n-1}e^{-(2n-1)s\tau}+m_1+1\}, \tag{49}$$

$$C_0'^*=-\frac{m_2K}{v_c}\{[k(m_1+1)+(m_1-1)]\sum_{n=1}^{\infty} k^{n-1}e^{-2n s\tau} - 2m_1\sum_{n=1}^{\infty} k^{n-1}e^{-(2n-1)s\tau}+m_1+1\}. \tag{50}$$

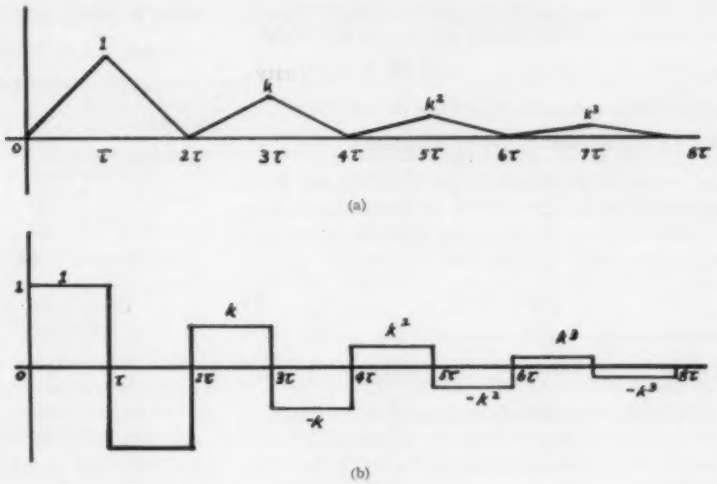

FIG. 1. Graphic presentation of the displacement of the transducer face, as a function of time. Part (a) represents the response to a step-function and part (b) is the response to an impulse.

The former is, within a factor $(-v_c)$, equal to the Laplace transform of the displacement due to an impulse and the latter represents a series of impulses of alternating polarity—the time derivative of the step-function represented by the former.

C. RESPONSE TO A SINUSOIDAL INPUT

The steady-state response to a sinusoidal signal both in amplitude and phase angle is readily obtained from the impulse response, simply by substituting (iw) for (s) in the latter, where w is the radian frequency of the applied signal.

In the case where $w=\pi/\tau$, this results in particularly simple expressions, which are listed below for reference. This condition corresponds, of course, to the case where the fundamental resonance frequency of the transducer is applied to its electrodes.

In the case of the non-symmetrically loaded transducer, the amplitude of the resulting displacement variations are for a signal $V=\sin\pi t/\tau$:

$$c_p = (4m_1m_2d)/\pi(m_1+m_2). \tag{51}$$

When one side only is loaded, the response is

$$c_p = 4md/\pi. \tag{52}$$

When both sides are loaded equally

$$c_p = 2md/\pi. \tag{53}$$

The corresponding expressions for the unit strain are

$$c_p^* = (4m_1m_2d)/v_c\tau(m_1+m_2), \tag{54}$$

$$c_p^* = 4md/v_c\tau, \tag{55}$$

$$c_p^* = 2md/v_c\tau. \tag{56}$$

D. NUMERICAL EXAMPLE

If the transducer is an air-backed, x-cut quartz crystal, with resonant frequency 15 Mc, in contact with water, and if a square pulse (duration $T=0.11\,\mu$sec, magnitude 1000 volts) is applied, we write the following equation for the strain at the transducer face as a function of time, referring to Eq. (49) and applying the simplifications incorporated in Eq. (39):

$$\mathfrak{L}[S(t)] = \frac{2dm}{s\tau v_c(1+m)}\Big[(k_s+1)\sum_{n=1}^{\infty} k_s^{n-1}e^{-2ns\tau} - 2\sum_{n=1}^{\infty} k_s^{n-1}e^{-(2n-1)s\tau}+1\Big](1-e^{sT}). \tag{57}$$

The factor $(1-e^{-Ts})$ takes into account that the applied signal may be viewed as resulting from the superposition of two step functions, equal magnitude but opposite sense, one being delayed with respect to the other by a time equal to the pulse duration T.

It can be seen that $S(t)$ represents the superposition of two "staircase" functions. One of these takes on the following values:

$$-\frac{2dm}{\tau v_c(m+1)}k_s^r, \quad 2r<t<2r+1;$$
$$\frac{2dm}{\tau v_c(m+1)}k_s^r, \quad 2r+1<t<2r+2. \tag{58}$$

While the other one takes on the negative of these values T seconds later. Thus, setting

$$2dm/[\tau v_c(m+1)] = K_1, \tag{59}$$

the values of the first function during successive intervals τ are

$$-K_1, +K_1, -k_sK_1, k_sK_1, -k_s^2K_1, +k_s^2K_1, -k_s^3K_1, +k_s^3K_1, \cdots.$$

To determine the numerical values involved, the following constants of the quartz crystal are required:

modulus of elasticity: $c_{11}=86\times10^{10}$ d/cm^2,[6]

piezoelectric constant: $e_{11}=5.2\times10^4$ cm$^{-\frac{1}{2}}$ g$^{\frac{1}{2}}$ s^{-1},[7]

density of the quartz: $\rho a=2.65$ g/cm^3.

The strain d, produced in an x-cut quartz plate, whose lateral dimensions exceed its thickness considerably, is different under static and dynamic conditions. Under static conditions it is

$$d_s=Vd_{11}, \tag{60}$$

whereas under dynamic conditions it is

$$d=V(e_{11}/c_{11})=V[d_{11}-d_{11}(c_{12}/c_{11})+d_{14}(c_{14}/c_{11})], \tag{61}$$

where d_{11} is the piezoelectric modulus in the x direction and V is the applied voltage in electrostatic units (1 e.s.u.$=$300 v). The difference is due to the fact that under static conditions the crystal will be strained laterally by the applied field whereas under dynamic conditions it must be considered clamped in those directions.[8] In our case, therefore,

$$d=(1000/300)(5.2\times10^4/86\times10^{10})=0.2\times10^{-6}\text{ cm}.$$

For water, $\rho_e=1$ g/cm^3, $v_e=1.5\times10^5$ cm/sec. For quartz, under the applicable conditions, $v=(c_{11}/\rho)^{\frac{1}{2}}$. Therefore

$$m=(\rho_a v_a/\rho_e v_e)=(2.65/1.5\times10^5)[86\times10^{10}/2.65]^{\frac{1}{2}}=10,$$

$$\tau=(2f_0)^{-1}=0.033\times10^{-6}\text{ sec}.$$

Therefore

$K_1=7.3\times10^{-5}$,

$k_s=0.82$,

$k_s^n=0.82,\ 0.67,\ 0.55,\ 0.45,\ 0.37,\ 0.30,\ 0.25,\ 0.20,\ 0.17,\ 0.14,\ 0.11,\ 0.09,\ 0.08,\ 0.06,\ 0.05,\ 0.04,\ 0.03,\ 0.03,\ 0.02,\ 0.02,$

for $n=1,\ 2,\ 3,\ \cdots,\ 20$.

The net result due to the total pulse is obtained by adding the values of the positive step-function to those of the negative step-function, delayed by 0.11 μsec.

If this pulse is repeated at 1.18 Mc, new step-functions must be added to every 0.85 μsec.

Comparing the amplitude of the initial pulse, K_1 Eq. (59), to the amplitude of strain variations due to a sinusoidal signal, Eq. (55), we find that the latter exceeds the former by a factor of $2(m+1)$ which equals 22 in our example.

The maximum pulse in our example occurs at the termination of the input pulse ($t=-0.11$ μsec) at which time the amplitude due to the start of the pulse is (-0.82) so that the net value at that time is -1.82. This, then, corresponds to the amplitude due to a *sinusoidal* signal of

$$(1000/22)\times1.82/\sqrt{2}=58.5\text{ v rms}.$$

[6] W. P. Mason, *Piezoelectric Crystals* (Van Nostrand Company, New York, 1950), p. 84.

[7] W. G. Cady, *Piezoelectricity* (McGraw-Hill Book Company, New York, 1946).

[8] L. F. Epstein, W. A. M. Anderson, and L. R. Harden, J. Acoust. Soc. Am. **19**, 248 (1947), Appendix.

Electrostatic Acceleration of Microparticles to Hypervelocities*

H. Shelton, C. D. Hendricks, Jr.,† and R. F. Wuerker
Research Laboratory, Ramo-Wooldridge Division of Thompson Ramo-Wooldridge, Inc., Los Angeles, California
(Received March 14, 1960)

By electrostatic methods, μ-diam spheres of iron have been accelerated to hypervelocities. Techniques have been developed to give single impacts in vacuum of measured incident velocity, mass, and position.

RECENT interest in hypervelocity impact phenomena has resulted in a critical examination of the methods of obtaining impacts from single hypervelocity particles. One of the most promising methods of accelerating particles whose radius is in the micron range uses electrostatic fields.

I. ELEMENTARY THEORY

If a particle of mass m, kilograms, and radius r, meters, is given a surface charge q, coulombs, and is accelerated through a potential drop V, volts, the velocity of the particle will be

$$v=(2Vq/m)^{\frac{1}{2}} \text{ m/sec.} \quad (1)$$

In terms of the electrostatic field E, v/m, at the surface of a spherical particle

$$q=4\pi r^2\epsilon_0 E \text{ coul,} \quad (2)$$

where ϵ_0 is the permittivity of free space $(1/36\pi)\times10^{-9}$ farads/m. The particles used are spheres so that

$$m=\tfrac{4}{3}\pi r^3\rho \text{ kg,} \quad (3)$$

where ρ is the particle material density in kg/m³. Thus,

$$v=(6VE\epsilon_0/r\rho)^{\frac{1}{2}} \text{ m/sec.} \quad (4)$$

Equation (4) indicates that for a particle of given radius, material, and for a fixed accelerating potential V, the velocity is dependent on the square root of the field strength at the particle surface. For this reason, one is concerned with the maximum surface field strength it is possible to obtain both theoretically and in practice. The maximum field strength at the surface of a negatively charged particle is determined by the electron field emission limit. Electron-field emission occurs at about 10^9 v/m. If a particle is charged positively, the maximum surface field intensity is determined by the forces binding the atoms to their lattice sites. For iron the maximum positive surface field strength is about 2×10^{10} v/m.[1,2] An iron sphere whose radius is 0.25 μ with a surface electric-field strength of 2×10^{10} v/m can be accelerated to a velocity of 2.3×10^4 m/sec by a potential of one-million v. The same particle would be accelerated to a velocity of 8.2×10^3 m/sec if the surface field strength were 2.5×10^9 v/m. Figure 1 shows velocity as a function of particle radius for iron spheres with a surface field strength of 2.5×10^9 v/m and various accelerating potentials. These curves are computed from Eq. (4). For particles with radii less than a few μ, the electrostatic acceleration method appears to have advantages over other ballistic acceleration techniques.[3]

II. PARTICLE CHARGING AND DETECTING TECHNIQUES

A. Particle Charging

Since the velocity obtained by a particle in an electrostatic field is dependent on the charge-to-mass ratio q/m, it is desirable to have the charge q as large as possible. Particle charging experiments have been performed using x-ray, electron, and ion beams[4,5] and by

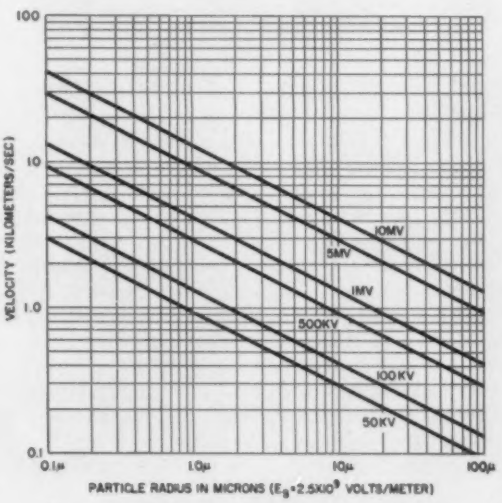

FIG. 1. Theoretical performance for the electrostatic acceleration of iron spheres.

* This work was done under contract to the U. S. Air Force and a Ramo-Wooldridge General Research contract.

† University of Illinois, Consultant to the Ramo-Wooldridge Division of Thompson Ramo Wooldridge, Inc.

[1] E. W. Müller, Phys. Rev. **102** (618) 1955.

[2] R. H. Good, Jr., and E. W. Müller *Handbuch der Physik* (Springer-Verlag, Berlin, Vienna, 1956), Vol. 21, p. 174.

[3] C. D. Hendricks, Jr., "Macroscopic particle accelerators," ERL-LM-154, Electronic Research Laboratory, The Ramo-Wooldridge Corporation, Los Angeles 45, California.

[4] R. F. Wuerker, H. Shelton, and R. V. Langmuir, J. Appl. Phys. **30**, 342 (1959).

[5] R. F. Wuerker, H. M. Goldenberg, and R. V. Langmuir, J. Appl. Phys. **30**, 444 (1959).

contact with highly charged surfaces. Only the latter method has resulted in particle charge-to-mass ratios high enough to be useful for present acceleration purposes.

In order for particles to be charged by contact, they are dropped or projected onto a spherical electrode maintained at a high potential. The charging electrode is a sphere of tungsten 100 μ or less in diam formed on the end of a tungsten wire tapered from 250-μ diam to about 5-μ diam. If a sphere of radius r is placed in contact with a sphere of radius R, where $R>r$ and both are raised to a potential V, the charge on the small sphere will be

$$q=2\pi^3\epsilon_0 R r^2 V/3(r+R)^2 \text{ coul.} \quad (5)$$

If R is much larger than r, the surface field strength on the small sphere after separation of the two spheres will be

$$E=\pi^2 V/6R \text{ v/m.} \quad (6)$$

While the two spheres are in contact the potential V may be raised until the field at the surface of the small sphere reaches the limiting value for the initiation of field emission. The maximum field at the surface of the small sphere will be higher by a factor of approximately 4.2 than the field on the large sphere while they are in contact. The field strength on the surface of the large sphere will be V/R. If the small sphere is iron, the maximum potential V_{max} that can be used on the charging electrode will be

$$V_{max}=E_{lim}R/4.2 \text{ v} \quad (7a)$$

$$V_{max}=[(2\times10^{10})/4.2]R \text{ v.} \quad (7b)$$

By substituting the value of V_{max} found in (7b) into Eq. (6), a value of 7.8×10^9 v/m for the maximum surface field strength on an iron particle is obtained. In practice, the charging electrode is maintained at a potential V_{max}, and the small spheres of iron are projected onto the electrode. The iron spheres are charged by contact at the surface of the charging electrode and are repelled by the electric field. The charging electrode is at the end of a thin shaft, as has been mentioned, and thus has its surface fields modified by a factor K_1 that depends on the ratio of shaft diameter to sphere diameter. Further, the fields on the electrode are modified by the geometric arrangement of surrounding ground surfaces. These geometric effects can be included by another constant K_2, so that the field which may actually be obtained on a small, spherical iron particle is

$$E=(\pi^2/6)K_1K_2(V_{app}/R) \text{ v/m.}$$

By making the supporting shaft of the charging electrode as small as possible and by suitably arranging the system geometry, it has been possible to obtain a value of $K_1K_2=0.91$. It has also been found that the charging process is not limited, as the theory would indicate, by the field strength at the particle surface. The value of V_{max} that has been found has been 45 kv. At higher voltages destruction of the charging electrode occurs. The maximum particle-surface field strengths which have been obtained with safety to the charging electrode are about 2.5×10^9 v/m. The charging electrode used to obtain these values is 12 μ in radius and is maintained at a positive potential of 20 kv.

Figure 2 is a diagram of the charging system which also acts as an injector to introduce the charged particles into the accelerator. Iron powder[6] is placed in the cup A which is normally at a high positive potential, as is the perforated cylindrical cover B. The charging electrode is mounted on the cover B and projects as shown into a hemispherical cavity in the ground surface C. A small opening is made from the cavity through the ground surface through which the charged particles can leave the charging system and enter the accelerator. To inject charged particles into the accelerator, a negative pulse is applied to the cup A. This produces an electric field between covers B and A, much as in a charged capacitor. The particles on the surface of the iron powder in A are charged and are accelerated across the gap between A and B. At B the particles exchange charge and also have a semielastic collision with the surface. After accelerating back and forth between A and B several times, the particles will gain energy from the electric field until the energy loss at each collision is just equal to that gained in the transit across the gap. There will be many particles in motion and some will escape into the space between B and C where an action similar to that occuring between A and B will occur. Some particles will collide with the charging electrode E, and of these a few will have the proper trajectories to escape through the hole in C and into the accelerator which is external to C (see Fig. 6).

B. Electronic Detection of Charged Dust Particles

The presence of charge on the accelerated particles has led to the development of electronic detectors for

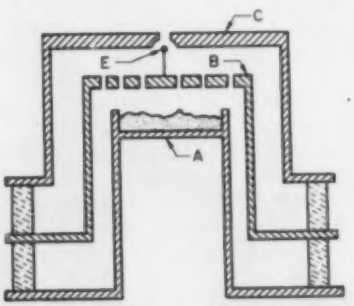

FIG. 2. Particle charging and injection system.

[6] Carbonyl iron powder consists of pure iron spheres whose radii are the order of a few microns or less. This material is manufactured by General Aniline and Film Corporation, Dyestuff and Chemical Division, Linden, New Jersey.

the measurement of particle velocity, charge, and mass. Figure 3 shows, schematically, a detector which consists of an insulated drift tube mounted coaxially within a grounded shield with grids on either end. The passage of a charged particle through the detector will induce on the detector a voltage proportional to the charge on the particle and inversely proportional to the capacity of the system. The duration of this induced signal is equal to the time of flight through the detector. The sensing drift tube is connected to the grid of a cathode-follower amplifier through a short length of shielded cable. The signal from the output of the amplifier is then displayed on an oscilloscope. Knowing the measured velocity and charge of one of these particles and measuring the voltage through which it has been accelerated, one can then compute the mass of the particle from Eq. (1). With the present simple techniques, the mass is calculated to an accuracy of about 20%. The size of the particle can then be found from the measured mass and known density.

A detector which measures both position and velocity is shown in Fig. 4, together with a photograph of an oscilloscope trace taken using this detector. The device consists of a shielded arrangement of two cylinders, between which are situated two mutually orthogonal pairs of parallel plates. The inner tubes and one each of the parallel plates are connected together to the input of the amplifier. The other plates are connected to the shield. The operation of this system is exactly the same as that of the simpler one described in the previous paragraph. However, instead of one pulse the signal will consist of four pulses. The first and last pulses are equal in amplitude, and the time measured from the beginning of the first to the end of the last gives the velocity of the particle. The second and third pulses give the position of the particle in the plane perpendicular to the direction of flight, since their magnitudes are directly proportional to the distance of the particle from the grounded plates. Through the use of one of these detectors the impact site of the particle on the target can be specified to about 0.2 mm by present techniques.

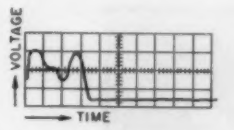

DETECTOR OUTPUT SIGNAL

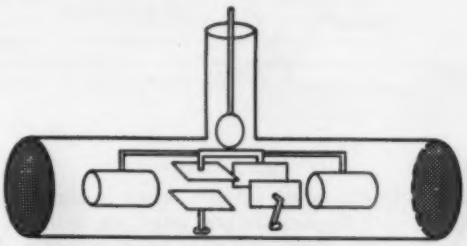
FIG. 4. Detector for measuring particle velocity, charge, and position (with reproduction of oscilloscope trace).

III. ELECTRICAL ACCELERATION OF MICRON-SIZED PARTICLES

Figure 5 is a diagram of the accelerator which is mounted on a vacuum system. The operation of the accelerator is as follows: The charging and injecting system was described in Sec. II. A. Upon leaving the injector the charged particles enter a region of high accelerating field established by an external 100 kv dc source. The accelerated particles pass through an aperature in the high voltage electrode, through a charge-velocity-position detector (described in Sec. II.B), and

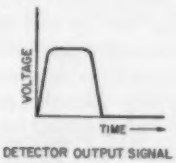

DETECTOR OUTPUT SIGNAL

FIG. 3. Detector for measuring particle velocity and charge.

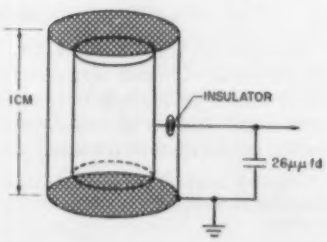

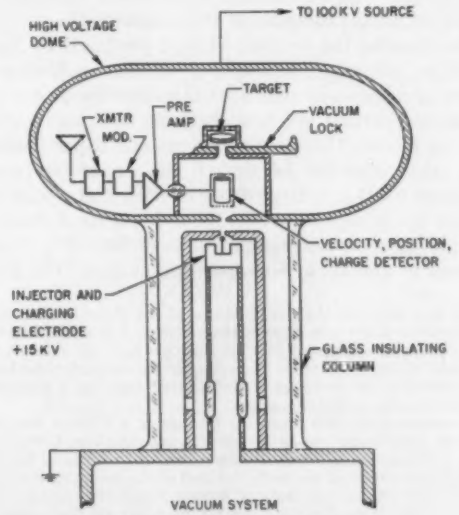

FIG. 5. Electrostatic accelerator.

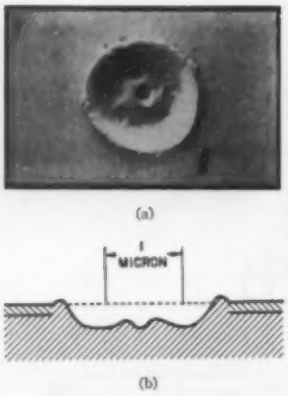

FIG. 6. Electron micrograph of a nitrocellulose replica of a crater in a thin aluminum film on glass with a reconstructed cross section of the crater.

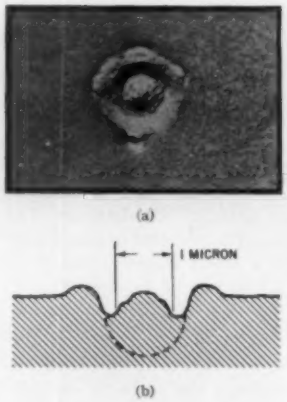

FIG. 7. Electron micrograph of a nitrocellulose replica of a crater in polished copper with a reconstruction cross section of the crater.

impact onto the target surface, which is also in the vacuum. Since the detector and target are mounted in the high-voltage dome, the information from the detector is telemetered for display on an oscilloscope located at a safe distance from the high voltage. The detector information and the measured value of the accelerating potential make possible the computation of the mass and velocity of the impacting particle and the location of the crater in the target. With this system, controlled impacts in the 1–3 km/sec velocity range have been obtained.

Impact damage has been produced in targets of metallic films on glass microscope slides (i.e., evaporated films of aluminum, silver, copper, and gold), metallic films on plastics, and solid micropolished targets of copper. The opaque metallic films on glass or plastic were used exclusively in the earlier work, since the projectiles punctured the metallic films, making it possible to locate the impact sites with optical microscopes. The film targets were also helpful in the visual examination of the focusing properties of the accelerator.[7]

To examine the detailed damage produced by these particles, one must necessarily go to more sophisticated forms of microscopy than optical microscopes, since the impacting-particle size is of the same order as their resolving power. The electron microscope is particularly well adapted to this job since it has a resolving power of about 0.002 μ, a large depth of field, and a magnification up to approximately 100 000. Figure 6 shows a sample electron micrograph[8] of a replica of a crater formed in aluminum films on glass targets. The films were estimated to be about 0.1 micron thick.[9] Figure 7 shows an electron micrograph of a replica of a crater formed in a solid piece of micropolished copper. For these micrographs, the incident velocity and mass of the bombarding particles were not measured, since these particular craters were made before the perfection of techniques for measuring individual impacts of known incident velocity and mass. Cross-sectional views of the craters, as shown in Figs. 6 and 7, can be reconstructed knowing the angle of shadowing of the replica.

IV. CONCLUSION

This research demonstrated the merits of the electrostatic system as a practical means of accelerating micron-sized particles to hypervelocities. In comparison to other ballistic methods, the electrostatic system has four outstanding features:

(1) The entire experiment is conducted in high vacuum, providing an excellent simulation of free space environment and freedom from extraneous effects of propellants or shock waves.

(2) The point of impact can be localized by electrical measurements, thus greatly facilitating the location of the very small craters which are the object of study.

(3) The velocity and mass of each particle can be directly measured just before impact.

(4) The attainable particle velocity is limited only by the total accelerating potential available; a possible source of high potential for the electrostatic accelerator might be a Van de Graaff generator.

ACKNOWLEDGMENTS

The authors wish to thank Dr. David B. Langmuir for his initial direction and encouragement; Joseph F. Friichtenicht for his help in the operation of the acceleration and analysis of data; and Miss Beverly Bieritz for the preparation of the manuscript.

[7] It is to be noted that the behavior of any electrostatic lens is independent of the q/m ratio of the particles. The initial focus of the accelerator was tested by substituting a hair pin filament for the point charging electrode, reversing the accelerating potentials, and observing the terminus of the electron beam on a phosphor screen mounted before the target.

[8] Arrangements were made for the use of a Phillips EM-100 electron microscope owned by the Harvey Machine Company, Inc., of Torrance, California. The members of the Artificial Meteor Project want to thank the technical staff of this company for their helpful cooperation; particularly Robert Simonson, engineer, for operating the microscope and also for many helpful discussions.

[9] A simple multiple-beam interferometer was constructed for measuring to within 0.003 μ the thickness of the evaporated films on glass.

Impact Crater Formation in Rock

WILLIAM C. MAURER AND JOHN S. RINEHART
Mining Research Laboratory, Mining Engineering Department, Colorado School of Mines, Golden, Colorado
(Received February 1, 1960)

Craters were produced by firing spherical steel projectiles of $\frac{3}{16}$- and $\frac{9}{32}$-in. diam into sandstone and granite at velocities ranging from 300 to 6000 ft/sec. Impact angles of 30, 60, and 90 deg were used for the sandstone and 90 deg for the granite. The craters are formed by two mechanisms: (a) crushing of material in front of the projectile and (b) fracturing which takes place as fractures are initiated by a constant impulse in steplike fashion in front of the projectile and propagated along logarithmic spirals of maximum shear to the free surface of the rock. The volume of the material removed by crushing varies as the first power of the impact velocity and the volume removed by fracturing, as the second power of the impact velocity. Penetration varies linearly with the impact velocity and is inversely proportional to the specific acoustic resistance of the target material, the proportionality constant being dependent upon the shape of the projectile.

I. INTRODUCTION

THE purpose of this study was to develop a better understanding of the mechanics of impact crater formation in rock, information which is relevant to percussive drilling and impact crushing. Although the impact velocities used are considerably higher than those normally encountered in percussive drilling and impact crushing, the mechanics of crater formation at these high velocities is probably not significantly different from that at low velocities since in both cases the impacts are nonhydrodynamic and the projectile does not deform or break up.

Sandstone and granite were chosen as target materials both because of their great differences in strength characteristics and because one is a sedimentary and the other an igneous rock. The sandstone used was a poorly cemented, argillaceous, feldspathic sandstone ranging from thinly bedded to massive structure; the granite was a holocrystalline, coarse-grained, inequigranular, quartz-biotite granite.

This paper describes the shapes of the craters obtained, the mechanisms involved in the formation of the crater, and the physical rock characteristics that are involved in crater formation.

II. EXPERIMENTAL PROCEDURE

The projectiles were $\frac{3}{16}$-in. diam, 0.442-g and $\frac{9}{32}$-in. diam, 1.503-g steel balls which were accelerated by firing them from guns having calibers of 0.22- and 0.30 in., respectively. The projectiles were placed in the cartridge on top of the powder and a tissue-paper wad. Tests showed that the wadding was broken up as it hit the air and, therefore, did not affect the measurement of the projectile velocity. Impact angles of 30, 60, and 90 deg were used for the sandstone and 90 deg for the granite, the angles being measured from the surface of the rock. Impact velocities ranging from 300 to 6000 ft/sec were used. These velocities were measured using a ballistic pendulum upon which the rock specimens were mounted.

III. TYPICAL CRATERS

The typical crater produced in sandstone by a projectile fired at an impact angle of 90 deg is shown in Fig. 1. (See also Figs. 2 and 3 for impact angles of 60 and 30 deg, respectively.) As the projectile penetrates the sandstone, it crushes the material in front of it, forcing the crushed material aside and forming a long cylindrical hole or burrow of the same diameter as the projectile, surrounded by a zone of compressed crushed target material. The upper part of the crater, formed as material is broken and the chips and debris blown from the face of the rock, has a cup shape.

Below this cup, but not below the base of the burrow, a set of fractures occur with the several fractures of each set (of equal length and an equal distance apart)

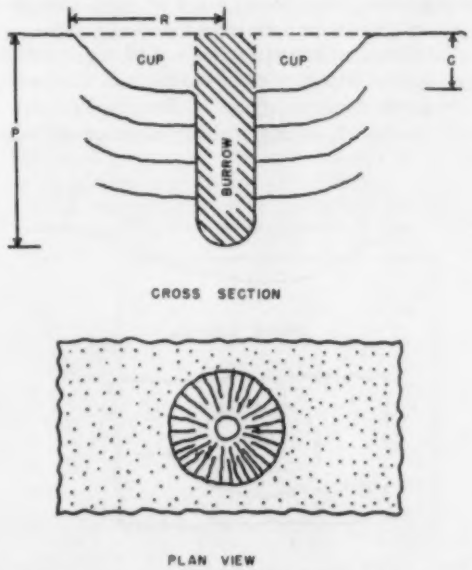

FIG. 1. Typical crater produced by a small steel sphere impacting sandstone at an angle of 90° with the surface. P is the penetration; R, the radius of the crater; and C, the cup depth.

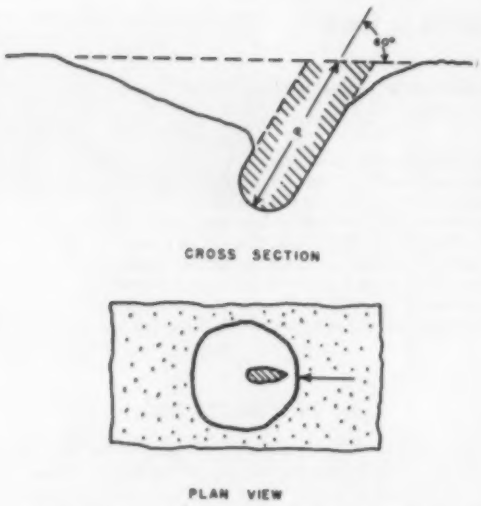

FIG. 2. Typical crater produced by a small steel sphere impacting sandstone at an angle of 60° with the surface. P is the penetration.

being parallel to the base of the cup. These unexpected fractures provide the key needed to formulate an adequate description of crater formation.

In granite, at an impact angle of 90 deg, the crater has gentle sloping sides and no evidence of a burrow exists, the total crater being composed of the cup. The projectiles ricocheted at impact angles of 30 and 60 deg in the granite.

In plan view, the craters formed by impact angles of 90 deg are circular in both sandstone and granite.

In sandstone, at an impact angle of 60 deg, the crater has a steeply sloping surface on the side from which the projectile impacted (Fig. 2). The opposite side is greatly elongated, having a much more gentle slope, similar to craters in plaster of Paris, previously reported.[1] In plan view this crater is elliptical.

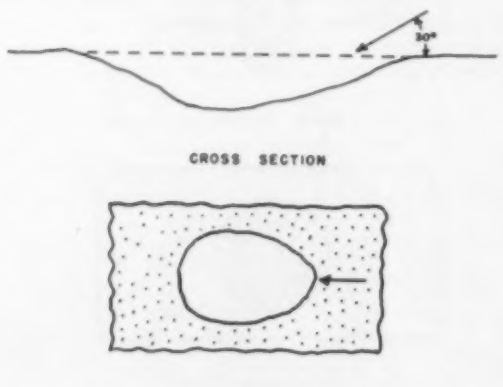

FIG. 3. Typical crater produced by a small steel sphere impacting sandstone at an angle of 30° with the surface.

At a 30-deg impact angle in sandstone the projectile ricocheted. The crater formed (Fig. 3) is greatly elongated and relatively shallow. The side of the crater from which the projectile impacted usually has more gentle slope than the opposite side. In plan view, this crater is eggshaped with the narrow end of the egg pointed in the direction from which the projectile impacted.

IV. MEASUREMENTS

The physical attributes of the craters which were measured were penetration, the distance from the original surface of the rock to the deepest point in the burrow; cup depth, the distance from the original surface of the rock to the intersection of the bottom of the cup and the burrow; the radius of the crater at the original surface of the rock; and the total volume of material that was removed from the crater.

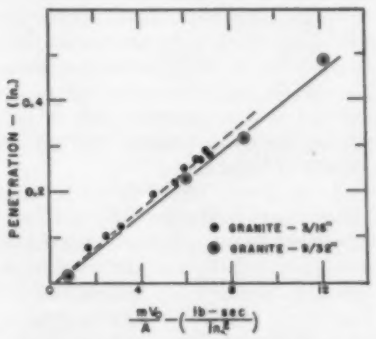

FIG. 4. Penetration vs the parameter Mv_0/A for craters produced by steel spheres of two different sizes impacting granite at an angle of 90° with the surface.

The volume was measured by first removing all loose and broken fragments lying on the surface of the cup and in the burrow and then filling the crater level with graded Ottawa sand, subsequently measured in a graduated cylinder. For the purpose of preserving the small fractures which occurred below the base of the cup, sand was used rather than some coherent material such as wax, so that these fractures could be filled, thereby including their volume in the measurements. If wax had been used, the fractures would have been destroyed because of their delicate nature. An attempt was made to keep the compaction in the graduated cylinder equal to the compaction in the crater. Two tests (one using wax as the determinant and the other using sand) comparing the volume showed that the error caused by compaction was negligible.

The velocity of sound was measured in each rock, the velocity of propagation of the longitudinal wave

[1] J. S. Rinehart, Popular Astronomy **58**, 458 (1950).

being determined by measuring the time required for a mechanical pulse to traverse a core of given length. A pulse generator supplied an electrical pulse (having an intensity of approximately 70 volts and a duration of 1–10 μsec) to a barium titanate transmitter crystal which was placed in intimate contact with the core; the transmitter crystal imparted a mechanical pulse to the rock which was picked up and converted into an electrical pulse by a barium titanate receiver crystal.

V. PENETRATION

Penetration P (Figs. 4 and 5) is well represented by the relationship normally applicable to materials having low strength[2]:

$$P=K_1(M/A)(v_0-v_c), \tag{1}$$

where K_1 is a constant characteristic of the target material; M, the mass of the projectile; A, its projected cross-sectional area; v_0, its impact velocity; and

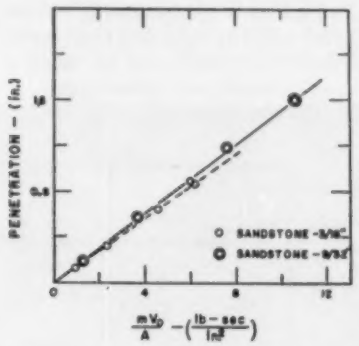

FIG. 5. Penetration vs the parameter Mv_0/A for craters produced by steel spheres of two different sizes impacting sandstone at an angle of 90° with the surface.

v_c, the minimum velocity at which cratering takes place.

In Figs. 4 and 5 the slopes of the lines are the material constant K_1. It can be seen that K_1 is the same for the different sized projectiles. The slight variations are due to small differences in the physical properties of the rocks used in the different tests.

Equation (1) implies that

$$Mdv/dt=-C_1v, \tag{2}$$

where v is the instantaneous velocity of the projectile and C_1 a constant. The following relationships are then deduced:

$$F=(A/K_1)v \tag{3}$$

$$\sigma=v/K_1, \tag{4}$$

where F is the instantaneous force resisting the projectile and σ is the instantaneous force per unit projected area.

[2] J. S. Rinehart and John Pearson, *Behavior of Metals Under Impulsive Loads* (American Society for Metals, Cleveland, Ohio, 1954), p. 204.

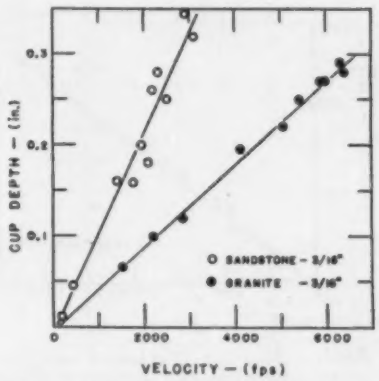

FIG. 6. Cup depth vs impact velocity for craters produced by steel spheres impacting sandstone and granite at an angle of 90° with the surface.

VI. CUP DEPTH AND RADIUS OF CRATER

The cup depth in both sandstone and granite is a linear function of the impact velocity (Fig. 6). In granite, cup depth and penetration are equal, since no burrow is present in the crater.

The square of the radius of the crater varies linearly with the impact velocity (Figs. 7 and 8) in both sandstone and granite.

The surface area of the cup was determined by plotting the contour of the base of the cup, dividing this curved line into small increments and mathematically rotating these increments around the central axis of the crater. The area of the base of the cup was found to vary linearly with the impact velocity in both sandstone and granite (Fig. 9).

The impact force per unit surface area of cup was found to remain independent of the impact velocity in both sandstone and granite (Fig. 10). The impact force

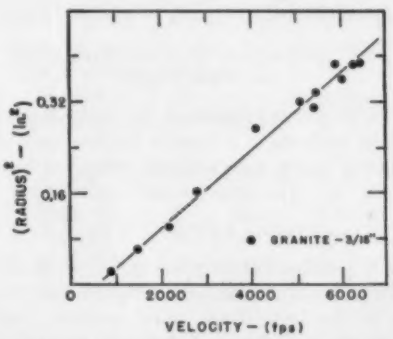

FIG. 7. Radius of crater squared vs impact velocity for craters produced by steel spheres impacting granite at an angle of 90° with the surface.

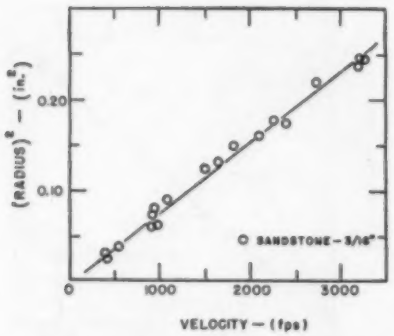

FIG. 8. Radius of crater squared vs impact velocity for craters produced by steel spheres impacting sandstone at an angle of 90° with the surface.

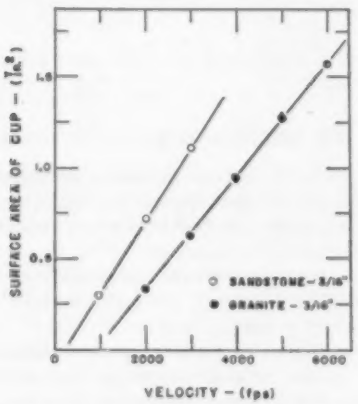

FIG. 9. Surface area of crater cup vs impact velocity for craters produced by steel spheres impacting sandstone and granite at an angle of 90° with the surface.

F_i was taken as

$$F_i = (A/K_1)(v_0 - v_c), \tag{5}$$

where

$$(A/K_1)v_c \tag{6}$$

is the threshold force required to initiate failure.

VII. INITIATION AND PROPAGATION OF FRACTURES

As the projectile penetrates the rock, fractures appear to be initiated in a steplike fashion, each fracture propagating along a logarithmic spiral[3] of maximum shear (Fig. 11). The equation of these spirals is

$$r = r_0 \exp[\pm\theta \tan(45° + \tfrac{1}{2}\varphi)], \tag{7}$$

where r is a radius vector of the spiral; r_0, the distance from the point of application of the load to the intersection of the logarithmic spiral and the horizontal boundary; θ, the polar angle from the nearest surface; and φ, the angle of internal friction. In elastic media, the angle of internal friction is zero and, therefore, the logarithmic spirals are equivalent to the trajectories of maximum shear.

The angles of internal friction were determined from specimens that had failed under static compressive loads and were approximately zero degrees for sandstone and 30 degrees for granite. Since granite has a much larger angle of internal friction than sandstone, the granite craters have sides of much more gentle slope.

The point of application of the force changes continuously, always being located at the projectile so that the stress field is likewise continuously changing; new sets of trajectories, similar in configuration to the original set are continuously forming. Moreover, there is at all times a concentration of stress trajectories in the center of the crater, which because of the large cross-sectional area of the projectile is obliterated by the projectile as it penetrates.

Central peaks are often obtained in craters in brittle materials such as lucite subjected to hypervelocity impacts.[4] These central peaks arise by virtue of the fact that the cross-sectional area of the particle is not large enough to obliterate the peak.

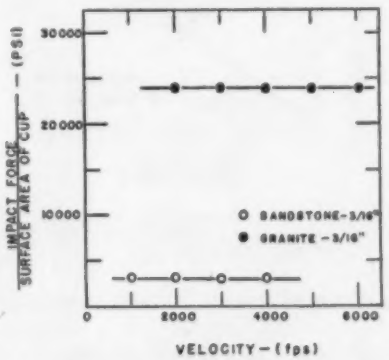

FIG. 10. Impact force per unit of surface area of crater cup for craters produced by steel spheres impacting sandstone and granite at an angle of 90° with the surface.

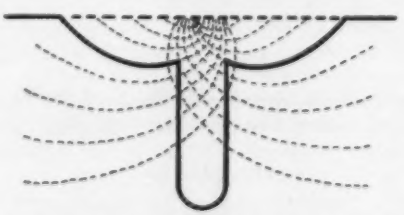

FIG. 11. Typical crater produced by a steel sphere impacting sandstone at an angle of 90° with the surface is superimposed upon a set of maximum shear trajectories.

[3] D. P. Krynine, *Soil Mechanics* (McGraw-Hill Book Company, Inc., New York, 1947), 2nd ed., p. 141.

[4] W. W. Adkins, Naval Research Laboratory, has been kind enough to show us several Lucite specimens of this type.

Figure 12 shows the cross section of an actual sandstone crater with a set of maximum shear trajectories superimposed upon it.

The uniformity of spacing of the lateral fractures implies that a constant impulse is required to initiate each successive fracture. Let the distance between two fractures be Δs. The time Δt that the projectile acts on a portion of the burrow of length Δs is

$$\Delta t = \Delta s / v. \tag{8}$$

The force F is given by Eq. (3). The impulse I being given by

$$I = F\Delta t = (A/K_1)\Delta s \tag{9}$$

is thus constant.

VIII. VOLUME

The volume of the cup was found to vary as the square of the impact velocity and the volume of the burrow as the first power of the impact velocity. Since the crater in granite consists of only the cup, the total volume is proportional to the square of the impact velocity as shown in Fig. 13. In granite, the energy required to remove a unit volume of material remains constant, independent of the impact velocity of the projectile (Fig. 14).

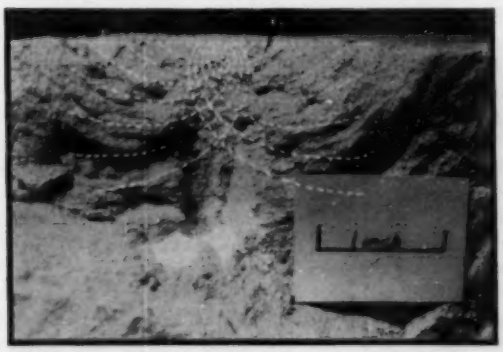

FIG. 12. Photograph of cross section of crater produced by a steel sphere impacting sandstone at an angle of 90° with the surface, having a set of maximum shear trajectories superimposed upon it.

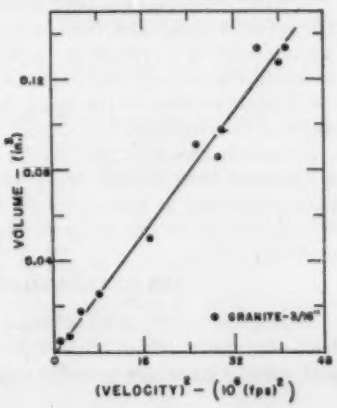

FIG. 13. Volume vs impact velocity squared for craters produced by steel spheres impacting granite at an angle of 90° with the surface.

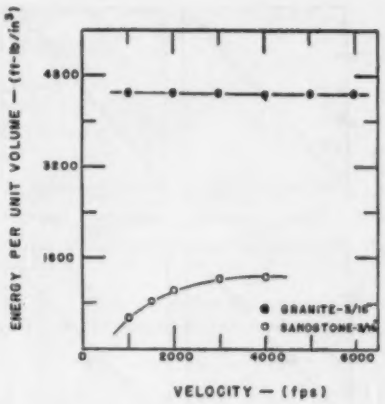

FIG. 14. Energy per unit volume vs impact velocity for craters produced by steel spheres impacting sandstone and granite at an angle of 90° with the surface.

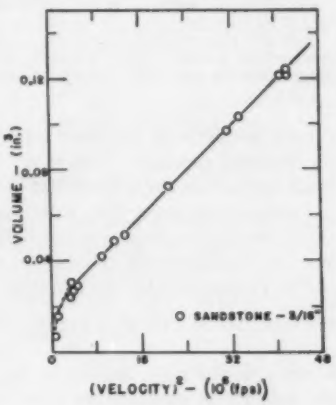

FIG. 15. Volume vs impact velocity squared for craters produced by steel spheres impacting sandstone at an angle of 90° with the surface.

The sandstone crater consists of both a cup and a burrow; thus, the total volume is a function of both the first and second power of the impact velocity, consistent with Fig. 15. The energy required to remove a unit volume of material from the sandstone increases as the impact velocity increases, the increase occurring because the volume of the burrow has a greater relative size at lower velocities (Fig. 14).

IX. MATERIAL CONSTANT

An attempt was made to relate the material constant K_1 of Eq. (1) to some measurable physical property of the rock. For this purpose two additional rocks, potash and volcanic tuff, were employed in the study.

The different strengths of the rocks have been plotted against the reciprocal of the material constant in Fig. 16. From Fig. 16 it can be seen that there is a good

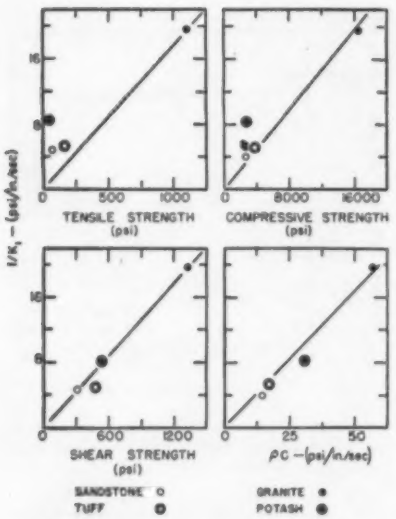

FIG. 16. The material parameter $1/K_1$ vs tensile strength, compressive strength, shear strength, and specific acoustic resistance for the four target materials used.

correlation between the shear strength of the rock and its material constant. This is an important fact and lends support to the theory that the rock fails in shear.

Furthermore, from Fig. 16 it appears that the material constant is inversely proportional to the specific acoustic resistance of the target material and hence can be represented by the equation

$$K_1 = 1/K_2\rho_t c, \tag{10}$$

where ρ_t is the mass density of the target material; c, the velocity of propagation of a longitudinal wave in the target material; and K_2, the shape factor for the projectile represented by

$$v_p = K_2 v. \tag{11}$$

Here v_p is the average velocity of the particles in front of the projectile, and v is the instantaneous velocity of the projectile.

Table I shows the values of the shape factor K_2 for a spherical projectile in the four rocks tested. For a projectile of given shape, the shape factor should be independent of the target material. The variations of K_2 listed in the table are attributed to an accumulation of small errors in the many measurements which are included in this constant caused by variations in the physical properties due to inhomogeneities in the rock. From the values of K_2 listed in Table I it appears that the shape factor for a spherical projectile is approximately 0.3 which means that the average velocity of the particles in front of the projectile is 30% of the instantaneous velocity of the projectile.

TABLE I. Comparison of the material constants and the shape factors of the rocks tested.

Material	Mass density	Longitudinal velocity	K_1	K_2
	lb-sec^2×10^{-3}/in.^{3}-ft	ft/sec	in.^{3}/lb-sec	
Potash	2.27	13 850	0.12	0.27
Granite	3.06	19 050	0.05	0.34
Sandstone	2.68	4 850	0.23	0.33
Tuff	2.19	7 350	0.19	0.33

On combining Eqs. (4) and (10) the following relationship is obtained:

$$\sigma = K_2\rho_t c v. \tag{12}$$

This equation is usually used in connection with stress waves. This is a significant and logical result: The reaction to the force retarding the projectile imparts appropriate momentum to the target in the same manner that the momentum of a stress wave moves forward.

X. SUMMARY

The craters formed in sandstone consist of two parts: the burrow, which is a long cylindrical hole formed as the material is forced aside in front of the projectile; and the cup, the blown-out part of the crater, formed as a series of fractures, each initiated by a constant impulse propagate along logarithmic spirals to the surface of the rock. In granite, no burrow is formed.

The volume of the burrow varies as the first power of the impact velocity and the volume of the cup varies as the second power of the impact velocity. The energy required to remove a unit volume of material remains constant for the granite; for the sandstone it increases as the impact velocity increases.

The penetration of the projectile is directly proportional to its mass, to a material constant for the target material, and to the difference between the impact velocity and the minimum velocity at which cratering takes place. Penetration is inversely proportional to the projected cross-sectional area of the projectile.

A close correlation has been found between the shear strengths of rocks and their material constants. The material constant appears to be inversely proportional to the specific acoustic resistance of the target material, the proportionality factor being dependent upon the shape of the projectile.

The mechanics of impact crater formation in rocks as outlined here should apply to other brittle materials subjected to impact velocities below the critical velocity at which the projectile begins to deform or break up.

ACKNOWLEDGMENTS

Assistance of the Ideal Cement Company for the fellowship under which a large part of this work was performed is gratefully acknowledged.

Equation of State for Nineteen Metallic Elements from Shock-Wave Measurements to Two Megabars*

R. G. McQUEEN AND S. P. MARSH
Los Alamos Scientific Laboratory, Los Alamos, New Mexico
(Received October 12, 1959; and in final form December 23, 1959)

Plane-wave explosive systems were used to accelerate thin metal plates to high velocities. Shock pressures resulting from the collision of these driver plates with a stationary target plate are approximately three times greater than the original shock pressure in the driver plate. The photographic flash-gap technique was used to record velocities associated with the shock waves. The new experimental data extend the Hugoniot loci into the one-to two-megabar region for 19 metallic elements: Ag, Au, Cd, Co, Cr, Cu, Mo, Ni, Pb, Sn, Th, Ti, Tl, V, W, Zn, Bi, Fe, Sb.

The Hugoniot P, V, E data have been extended to a more complete P, V, E, T equation of state by use of the Mie-Grüneisen theory. The thermodynamic variable, $\gamma = V(\partial P/\partial E)_v$, necessary for this extension, was obtained by solving the Dugdale-MacDonald relation.

INTRODUCTION

WORK by Schreffler and Deal[1] demonstrated that considerably higher local energies could be obtained from an explosive system if the explosive was used to accelerate a thin metal plate over a distance of several centimeters. Such plates, moving at velocities of several mm/μsec, were used as driver plates to produce strong shock waves in stationary brass target plates. The equation of state for the brass, used here as a standard, was determined separately through shock-wave velocity and free-surface velocity measurements. For the other materials, small test specimens were mounted on the free surface of the brass target plate, and in each experiment the shock-wave velocity for each specimen and the shock strength in the brass were measured. These data and the impedance-match method[2,3] determine the P, V, E state behind the shock wave in each specimen. A typical shot system is illustrated in Fig. 1, and details of the target plate assembly are shown in Fig. 2.

The experimental data, including previously published shock-wave results[2,3] and initial compressibilities from papers by Professor Bridgman,[4–6] have been fitted over the entire pressure range by a linear relation between the shock-wave velocity and shock-particle velocity. Bi, Fe, and Sb, for which transitions[7–12] at low pressures obviate fitting the data to zero pressure, are exceptions. The Rankine-Hugoniot equations were used to transform these fits to P, V, E loci, which were extended to a more complete P, V, E, T thermodynamic description by calculations based upon the Mie-Grüneisen theory and zero-pressure data.

More detailed descriptions of the photographic flash-gap technique and of the equation-of-state calculations are to be found in footnote references 2, 3, and 13.

EXPERIMENTATION

Since the experimentation was done for materials of relatively high shock impedance ($\rho_0 U_s$), a new standard (brass) was determined that would give impedance-match solutions to two megabars with minimum dependence on the extension of the equation

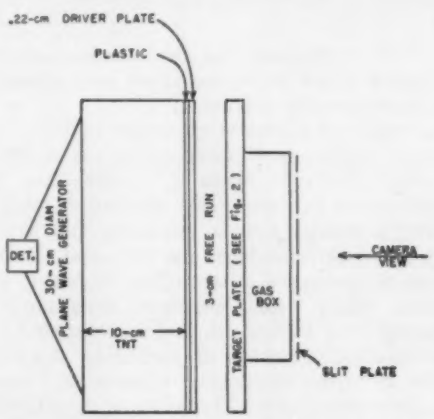

FIG. 1. Profile of a typical shot assembly. A range of pressures can be obtained by varying the dimensions and materials; for example, the system in the figure using steel or nickel driver plates gives a pressure of 1.0 megabar in the brass target, which can be increased to 1.5 megabars by exchanging the 10-cm TNT charge for a 15-cm 7-5/25 Cyclotol charge.

* Work done under the auspices of the U. S. Atomic Energy Commission.

[1] R. G. Shreffler and W. E. Deal, J. Appl. Phys. **24**, 44 (1953).
[2] J. M. Walsh, M. H. Rice, R. G. McQueen, and F. L. Yarger, Phys. Rev. **108**, 196 (1957).
[3] M. H. Rice, R. G. McQueen, and J. M. Walsh, *Solid State Physics, Advances in Research and Applications* (Academic Press, Inc., New York, 1958), Vol. 6, p. 1.
[4] P. W. Bridgman, Proc. Am. Acad. Arts Sci. **77**, 189 (1949).
[5] P. W. Bridgman, Proc. Am. Acad. Arts Sci. **76**, 9 (1945).
[6] P. W. Bridgman, Proc. Am. Acad. Arts Sci. **76**, 55 (1948).
[7] P. W. Bridgman, Phys. Rev. **48**, 893 (1935).
[8] P. W. Bridgman, Phys. Rev. **60**, 351 (1941).
[9] P. W. Bridgman, Proc. Am. Acad. Arts Sci. **74**, 425 (1942).
[10] R. E. Duff and F. S. Minshall, Phys. Rev. **108**, 1207 (1957).
[11] D. Bancroft, E. L. Peterson, and S. Minshall, J. Appl. Phys. **27**, 291 (1956).
[12] S. Katz, D. G. Doran, and D. R. Curran, J. Appl. Phys. **30**, 568 (1959).
[13] J. M. Walsh and R. H. Christian, Phys. Rev. **97**, 1544 (1955).

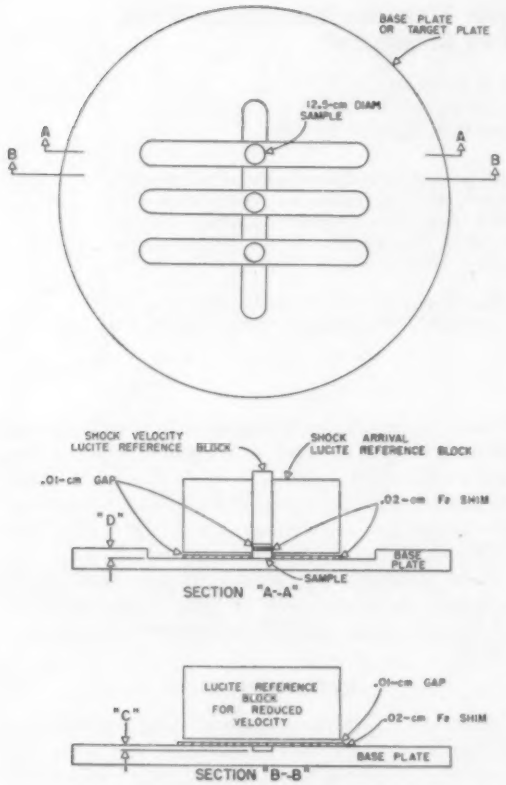

FIG. 2. Scale drawing of target plate. Section *A-A* shows details for shock-velocity determination. Section *B-B* shows details for measuring the reduced velocity,[14] i.e., a combined shock and free-surface velocity. *Note.* Dimension $D=2C=0.5$ cm.

of state off the Hugoniot. The dural standard previously established[2] could be extended to only about one megabar by present techniques.

The brass used in present experimentation was of the following weight-percent composition: Cu/Zn/Pb/Fe: 61.5/36.0/2.5/<0.05. While it would have been desirable to use an element as a standard, the only one apparently suitable from a machining and handling standpoint was iron. Iron was not used, however, because it undergoes a transition[11] at about 0.130 megabar, which could introduce uncertainties in evaluating it as a standard. Experimentation for the brass standard consisted of measuring shock-wave velocity and either the associated free-surface velocity or the reduced velocity.[14] The results of these measurements are given in the first two columns of Table I. The remaining columns in Table I define the brass Hugoniot deduced from this data in a manner outlined later in this paper. Shock-wave data for the various other materials are listed in Table II.

[14] J. M. Walsh and M. H. Rice, J. Chem. Phys. **26**, 815 (1957).

Three conditions must be met in the design of these free-run experiments to avoid systematic errors. First, the driver plate must be at essentially uniform pressure when it strikes the brass target plate. This is necessary in order to assure that the shock wave in the target plate and specimens is not overtaken by small compression or rarefaction waves. As can be seen from the results of Shreffler and Deal,[1] a thin plate driven by explosive is subjected to a series of accelerations of decreasing magnitude. These accelerations become quite small for a $\frac{1}{2}$-cm plate driven by a 10-cm-thick explosive charge after a run of several centimeters, which assures uniform zero-pressure distribution.

The second condition necessary to avoid consistent errors is that the driver plate must be sufficiently thick so that the initial shock wave into the target plate and specimens is not overtaken by the large rarefaction wave originating at the explosive-driver plate interface. The condition for the maximum ratio R of target thickness (including the specimens) to driver plate thickness is

$$R=[U_s^{-1}+(\rho_0/\rho C)]_d/[U_s^{-1}-(\rho_0/\rho C)]_t, \qquad (1)$$

where C is the sound velocity behind the shock wave, ρ_0/ρ is the ratio of densities across the shock front, and U_s is the shock-wave velocity. The subscripts d and t refer to the driver and target plates, respectively.

TABLE I. Experimental data for the brass standard and the computed Hugoniot. The quantities U_s and U_{fs} are the average shock-wave and free-surface velocities for a given shot. W (the weighting factor for subsequent least-square analysis) is proportional to the number of shock velocity measurements made on each shot. The shock-particle velocity U_p was determined from these quantities by calculation outlined in the text. The pressure P and relative volume V/V_0 were determined by using the appropriate Rankine-Hugoniot equations.

U_{fs} cm/μsec	U_s cm/μsec	U_p cm/μsec	P megabar	V/V_0	W
0.090	0.438	0.045	0.167	0.897	4
0.090	0.441	0.045	0.168	0.898	4
0.101	0.450	0.050	0.192	0.888	4
0.100	0.451	0.050	0.191	0.889	5
0.112	0.454	0.056	0.214	0.877	3
0.119	0.456	0.059	0.229	0.869	3
0.140	0.477	0.070	0.282	0.853	4
0.141	0.479	0.070	0.284	0.853	3
0.182	0.510	0.091	0.391	0.822	4
0.180	0.514	0.090	0.389	0.826	5
0.192	0.515	0.096	0.415	0.814	6
0.182	0.515	0.091	0.394	0.824	5
0.189	0.517	0.094	0.411	0.818	6
0.189	0.519	0.094	0.412	0.819	6
0.350	0.622	0.172	0.906	0.723	3
0.363	0.629	0.178	0.947	0.717	3
0.372	0.639	0.182	0.985	0.715	4
0.407	0.659	0.199	1.108	0.698	3
0.461	0.692	0.224	1.308	0.677	2
0.471	0.697	0.228	1.342	0.673	2
0.468	0.704	0.226	1.348	0.679	3
0.474	0.705	0.229	1.365	0.675	3
0.485	0.717	0.234	1.420	0.674	3
0.557	0.754	0.266	1.694	0.648	2
0.557	0.757	0.266	1.702	0.649	2
0.564	0.777	0.269	1.764	0.654	1

The relation is easily derived by using the straight-line characteristics of the simple centered wave for one-dimensional flow in Lagrangian coordinates.[15] If the driver and target were made from brass, the ratio R would vary with pressure in the following manner:

P (megabars)	0.5	1.0	1.5	2.0
R	7.7	5.7	5.0	4.5.

As can be seen, the higher the pressure the thicker must be the driver plate. The indicated requirements on driver-plate thickness, when combined with precision considerations concerning specimen size, serve to limit the maximum usable pressures associated with a given charge size. In principle, the use of very large explosive charges, relative to the driver-plate thickness, should lead to plate velocities approaching the explosive escape velocity, approximately 0.8 cm/μsec for composition B.[16] The associated brass shock pressure could be as high as four megabars. Practical considerations on charge size and precision requirements limit the present data to about two megabars.

The third shot-design criterion is that the specimens on the brass plate must have a sufficiently large width-to-thickness ratio to assure that side rarefactions do not affect the entire shock front. An analysis of the flow leads to the following expression for the minimum possible specimen width to thickness ratio:

$$w/l = 2[(C\rho/\rho_0 U_s)^2 - 1]^{\frac{1}{2}}. \quad (2)$$

In the experiments reported here, a width to thickness ratio of 2.5 was used. The shock parameter listing of

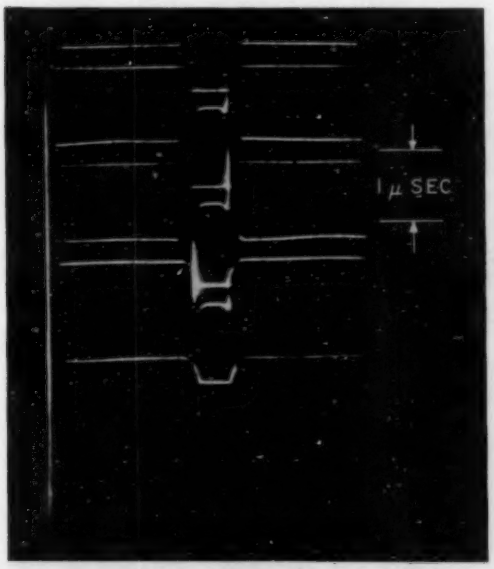

FIG. 3. Experimental record. Time increases downward. The long lines on either side of center are reference lines. Reference lines 1, 3, and 5, counted from the top, are the shock arrival times at the base of the shock velocity reference blocks (see Fig. 2). The corresponding shock arrival times at the top of the specimens are indicated by the central time offsets numbers 2, 4, and 6. The remaining traces are the reduced velocity references and offsets.

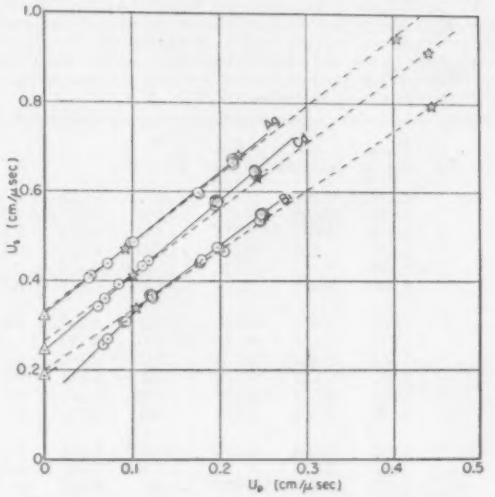

FIG. 4. U_s vs U_p curves for Ag, Bi, and Cd. The experimental U_s vs U_p data for Walsh *et al.*, and the present authors are shown as circles. The solid lines are the linear least-squares fits of that data. Bridgman's data are shown as triangles. The data presented by Al'tshuler *et al.*, are shown as stars and their fits are the dashed lines. The iron and brass points represent the average of several determinations made on a particular shot.

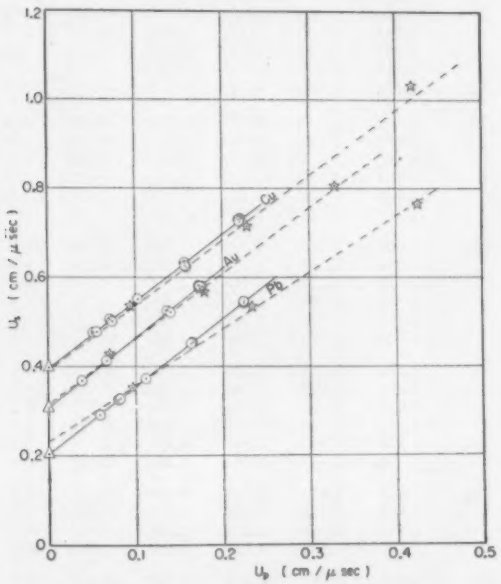

FIG. 5. U_s vs U_p curves for Au, Cu, and Pb.

[15] R. Courant and K. O. Friedricks, *Supersonic Flow and Shock Waves* (Interscience Publishers, Inc., New York, 1948), p. 31.
[16] W. E. Deal, Phys. Fluids **1**, 523 (1958).

TABLE II. Experimental data and Hugoniot values. Previously unpublished experimental shock-wave data are given. Unless otherwise noted, the pressure listed in column two refers to the shock pressure in the brass standard obtained by measuring shock velocity and free-surface or reduced velocity. Shock velocities listed in column three come from the straightforward interpretation of the measured shock transit times and known sample thicknesses. Particle velocities in column four and pressures in column five are the result of the impedance-match interface solution (see footnote reference 3). Application of the Rankine-Hugoniot equation for conservation of mass gives the relative specific volumes V/V_0.

Material	P_{brass} megabar	U_s cm/μsec	U_p cm/μsec	P megabar	V/V_0	W
Ag	1.027	0.598	0.177	1.107	0.705	0.5
	1.034	0.596	0.178	1.109	0.702	0.5
	1.378	0.673	0.214	1.512	0.681	0.5
	1.388	0.663	0.217	1.509	0.673	0.5
	1.393	0.668	0.216	1.510	0.677	0.5
	1.399	0.672	0.217	1.530	0.677	0.5
Au	1.002	0.525	0.137	1.387	0.739	0.5
	1.025	0.521	0.141	1.410	0.730	0.5
	1.384	0.580	0.173	1.932	0.702	0.5
	1.387	0.578	0.174	1.931	0.700	0.5
	1.398	0.578	0.174	1.936	0.699	0.5
	1.399	0.579	0.174	1.942	0.699	0.5
Cd	1.022	0.566	0.196	0.957	0.654	0.5
	1.031	0.578	0.196	0.976	0.662	0.5
	1.034	0.577	0.196	0.980	0.663	0.5
	1.043	0.577	0.197	0.982	0.658	0.5
	1.045	0.645	0.198	0.986	0.657	0.5
	1.403	0.648	0.240	1.339	0.628	0.5
	1.406	0.648	0.240	1.345	0.629	0.5
	1.410	0.639	0.243	1.339	0.620	0.5
	1.421	0.643	0.243	1.351	0.622	0.5
Co	1.038	0.715	0.179	1.121	0.750	0.5
	1.050	0.715	0.180	1.137	0.748	0.5
	1.064	0.712	0.183	1.148	0.743	0.5
	1.267	0.750	0.206	1.362	0.726	0.5
	1.267	0.745	0.207	1.358	0.723	0.5
	1.267	0.743	0.207	1.357	0.721	0.5
	1.478	0.781	0.230	1.584	0.706	0.5
	1.478	0.779	0.230	1.581	0.705	0.5
	1.478	0.777	0.230	1.577	0.703	0.5
	1.497	0.788	0.231	1.608	0.707	0.5
	1.497	0.783	0.232	1.603	0.703	0.5
Cr	0.914	0.763	0.171	0.924	0.777	0.5
	0.914	0.759	0.171	0.922	0.775	0.5
	1.363	0.844	0.225	1.347	0.734	0.5
	1.369	0.857	0.227	1.382	0.735	0.5
	1.358	0.863	0.225	1.379	0.739	0.5
Cu	0.842	0.633	0.157	0.883	0.752	0.5
	0.842	0.623	0.158	0.875	0.746	0.5
	0.842	0.626	0.157	0.877	0.749	0.5
	1.362	0.726	0.220	1.424	0.697	0.5
	1.366	0.729	0.221	1.430	0.698	0.5
	1.378	0.732	0.222	1.444	0.697	0.5
Mo	1.064	0.729	0.169	1.256	0.769	0.5
	1.064	0.720	0.170	1.245	0.764	0.5
	1.058	0.729	0.168	1.250	0.770	0.5
	1.380	0.765	0.206	1.604	0.731	0.5
	1.387	0.771	0.206	1.618	0.733	0.5
	1.399	0.775	0.207	1.633	0.733	0.5
Ni	0.931	0.695	0.164	1.009	0.764	0.5
	0.931	0.699	0.164	1.014	0.766	0.5
	0.931	0.711	0.162	1.022	0.772	0.5
	1.359	0.778	0.215	1.478	0.724	0.5
	1.373	0.776	0.217	1.491	0.721	0.5
	1.368	0.780	0.216	1.490	0.723	0.5
Pb	0.842	0.452	0.164	0.838	0.638	0.5
	0.842	0.452	0.164	0.837	0.638	0.5
	1.354	0.544	0.225	1.388	0.587	0.5
	1.352	0.542	0.225	1.383	0.585	0.5
Sn	0.931	0.559	0.194	0.792	0.652	0.5
	0.931	0.555	0.195	0.788	0.648	0.5
Sn	0.931	0.557	0.195	0.790	0.651	0.5
	1.586	0.671	0.280	1.364	0.583	0.5
	1.587	0.680	0.278	1.377	0.591	0.5
	1.599	0.675	0.281	1.378	0.584	0.5
Th	1.028	0.451	0.190	1.003	0.578	0.5
	1.022	0.453	0.194	1.026	0.572	0.5
	1.403	0.516	0.232	1.400	0.550	0.5
	1.385	0.511	0.231	1.378	0.548	0.5
	1.396	0.509	0.233	1.384	0.543	0.5
	1.414	0.510	0.236	1.405	0.538	0.5
Ti	1.043	0.735	0.230	0.762	0.687	0.5
	1.040	0.740	0.229	0.764	0.691	0.5
	1.038	0.734	0.229	0.758	0.689	0.5
	1.497	0.794	0.297	1.063	0.626	0.5
	1.497	0.792	0.297	1.060	0.625	0.5
Tl	0.860	0.442	0.165	0.864	0.627	0.5
	0.860	0.441	0.165	0.862	0.626	0.5
	0.860	0.441	0.165	0.862	0.626	0.5
	1.276	0.513	0.215	1.306	0.581	0.5
	1.478	0.539	0.237	1.515	0.560	0.5
	1.478	0.540	0.237	1.516	0.561	0.5
	1.478	0.540	0.237	1.517	0.561	0.5
V	0.149[a]	0.578	0.058	0.204	0.900	1.0
	0.149[a]	0.573	0.058	0.203	0.898	1.0
	0.218[a]	0.616	0.080	0.301	0.870	1.0
	0.218[a]	0.607	0.081	0.301	0.866	1.0
	0.218[a]	0.608	0.081	0.302	0.866	1.0
	0.220[a]	0.605	0.082	0.301	0.865	1.0
	0.220[a]	0.608	0.081	0.301	0.866	1.0
	0.320[a]	0.649	0.112	0.441	0.828	1.0
	0.320[a]	0.650	0.111	0.441	0.829	1.0
	0.320[a]	0.646	0.112	0.441	0.827	1.0
	0.914	0.729	0.186	0.825	0.746	0.5
	0.914	0.728	0.186	0.825	0.745	0.5
	0.914	0.732	0.185	0.828	0.747	0.5
	0.914	0.734	0.185	0.829	0.748	0.5
	1.378	0.820	0.259	1.244	0.697	0.5
	1.388	0.817	0.249	1.241	0.695	0.5
W	0.218[a]	0.456	0.045	0.395	0.901	1.0
	0.218[a]	0.455	0.045	0.394	0.901	1.0
	0.320[a]	0.478	0.064	0.587	0.866	1.0
	0.320[a]	0.482	0.064	0.590	0.868	1.0
	0.853	0.547	0.117	1.225	0.786	0.5
	0.853	0.549	0.117	1.227	0.788	0.5
	1.430	0.621	0.173	2.061	0.721	0.5
	1.427	0.619	0.173	2.054	0.721	0.5
	1.426	0.624	0.173	2.074	0.723	0.5
Zn	0.853	0.581	0.180	0.745	0.690	0.5
	0.853	0.582	0.180	0.747	0.691	0.5
	0.853	0.578	0.180	0.743	0.688	0.5
	1.563	0.722	0.271	1.394	0.625	0.5
	1.573	0.734	0.271	1.416	0.631	0.5
	1.560	0.730	0.269	1.403	0.631	0.5
Bi	0.339[a]	0.367	0.123	0.444	0.665	1.0
	0.339[a]	0.364	0.123	0.443	0.661	1.0
	0.882	0.444	0.180	0.786	0.596	0.5
	0.867	0.442	0.179	0.781	0.594	0.5
	0.869	0.446	0.179	0.787	0.599	0.5
	1.008	0.475	0.197	0.923	0.585	0.5
	1.050	0.466	0.206	0.945	0.558	0.5
	1.020	0.473	0.200	0.931	0.577	0.5
	1.410	0.533	0.247	1.299	0.536	0.5

TABLE II.—*Continued.*

Material	P_{brass} megabar	U_s cm/μsec	U_p cm/μsec	P megabar	V/V_0	W
Bi	1.410	0.536	0.247	1.303	0.540	0.5
	1.453	0.551	0.251	1.360	0.545	0.5
	1.436	0.549	0.248	1.344	0.548	0.5
	1.423	0.549	0.247	1.335	0.551	0.5
Fe	0.339[a]	0.557	0.109	0.477	0.804	2.0
	0.847	0.654	0.164	0.843	0.749	1.0
	0.860	0.657	0.166	0.857	0.748	1.5
	0.917	0.665	0.174	0.911	0.738	0.5
	0.950	0.671	0.179	0.943	0.733	0.5
	0.988	0.663	0.186	0.968	0.720	1.0
	1.030	0.689	0.189	1.024	0.726	1.0
	1.034	0.695	0.189	1.033	0.728	1.5
	1.267	0.742	0.217	1.267	0.707	1.5
	1.276	0.742	0.219	1.276	0.705	1.5
	1.391	0.766	0.232	1.397	0.697	1.0
	1.400	0.758	0.234	1.393	0.692	1.5
	1.619	0.800	0.257	1.618	0.679	0.5
	1.724	0.822	0.268	1.728	0.675	1.0
	1.728	0.820	0.268	1.730	0.673	1.0
Sb	0.220[a]	0.361	0.103	0.248	0.716	1.0
	0.220[a]	0.359	0.103	0.248	0.713	1.0
	0.220[a]	0.363	0.102	0.249	0.720	1.0
	0.339[a]	0.430	0.139	0.400	0.678	1.0
	0.339[a]	0.433	0.138	0.401	0.681	1.0
	0.869	0.512	0.196	0.673	0.617	0.5
	0.819	0.506	0.188	0.637	0.629	0.5
	1.040	0.564	0.219	0.828	0.611	0.5
	1.042	0.572	0.219	0.838	0.618	0.5
	1.051	0.571	0.220	0.843	0.614	0.5
	1.422	0.631	0.270	1.142	0.572	0.5
	1.442	0.634	0.273	1.158	0.569	0.5
	1.452	0.643	0.273	1.175	0.576	0.5

[a] Dural standard was used for this data. The entry is the pressure in dural.

Table IV may be used to verify that this ratio is sufficiently large to satisfy this criterion. Moreover, since at high pressure the shock velocity is greater than the sound speed, it is necessary to consider only the compression for a minimum safety criterion. Using this approximation, the value $w/t=2.5$ is sufficient for making shock-wave measurements for compressions with ρ/ρ_0 as great as 1.6.

A final remark is in order concerning the explosive-driver-plate geometry. In order to perform the shock-time arrival interpolations, necessary for data analysis, a smooth plane shock wave has been found to be highly desirable. This is apparent by inspection of a photo-

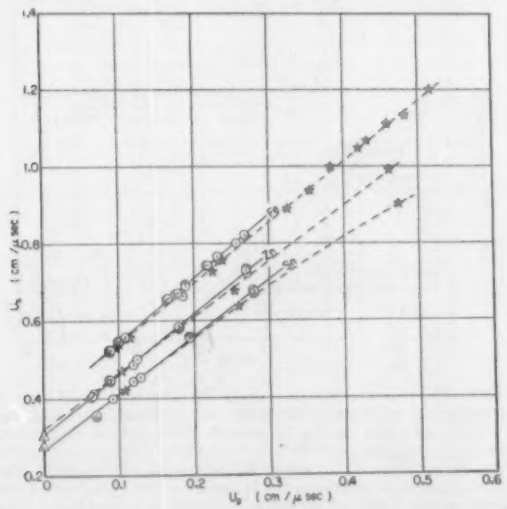

FIG. 6. U_s vs U_p curves for Fe, Sn, and Zn.

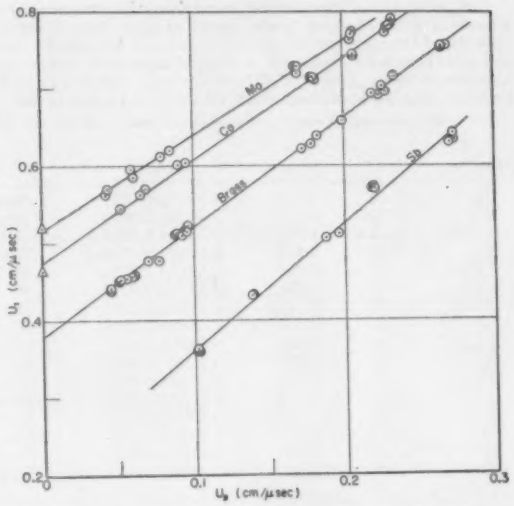

FIG. 7. U_s vs U_p curves for brass, Co, Mo, and Sb.

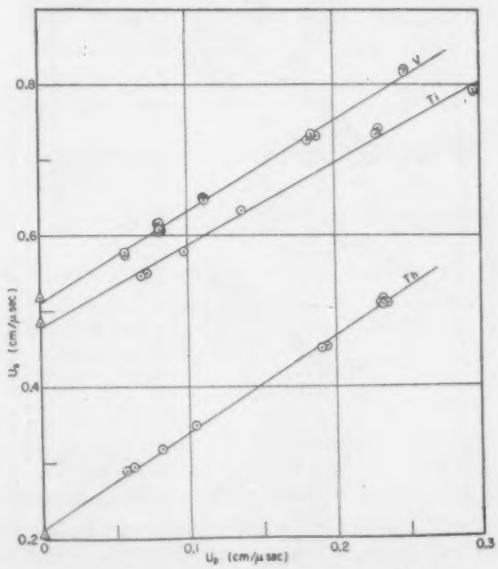

FIG. 8. U_s vs U_p curves for Th, Ti, and V.

TABLE III. Fits of the data and comparison with zero-pressure data. The results of the least-square fits of the U_s vs U_p data are given. Under C_B is the adiabatic "sound speed" obtained from Bridgman's static measurements. The columns C and S give the coefficients in cgs units of the equation $U_s = C + SU_p$. C_B and C are directly comparable. The quantity $(\partial E/\partial V)_{p=0} = C_p/V_0\alpha$, where C_p is specific heat and α is the volume coefficient of thermal expansion, was computed from quantities obtained from references listed in the text. The Grüneisen's ratios, $\gamma_T = C^2/V_0(\partial E/\partial V)_{p=0}$ and $\gamma_D = 2S-1$ (at $p=0$), are described in the text. The heading % *P.E.* is the percent probable error of the average shock velocity determined by the experimental data and the linear least-squares fit of the U_s vs U_p data.

Material	ρ_0 g/cm³	C_B cm/μsec	C cm/μsec	S	$(\partial E/\partial V)_{p=0}$ ergs/g/cm³	γ_T	γ_D	γ_T/γ_D	% *P.E.*
Ag	10.49	0.319	0.3243±0.0017	1.586±0.013	0.43×10^{12}	2.55	2.17	1.17	0.55
Au	19.24	0.305	0.3075±0.0010	1.560±0.009	0.58	3.29	2.12	1.55	0.30
Cd	8.64	0.241	0.2443±0.0018	1.671±0.012	0.22	2.32	2.34	0.99	0.58
Co	8.82	0.463	0.4748±0.0018	1.330±0.011	1.00	1.97	1.66	1.19	0.46
Cr	7.10	0.515	0.5217±0.0024	1.465±0.020	1.65	1.19	1.93	0.62	0.63
Cu	8.90	0.398	0.3958±0.0015	1.497±0.012	0.70	2.00	1.99	1.01	0.42
Mo	10.20	0.519	0.5157±0.0015	1.238±0.013	1.78	1.52	1.48	1.03	0.41
Ni	8.86	0.463	0.4646±0.0018	1.445±0.015	1.04	1.83	1.89	0.97	0.48
Pb	11.34	0.202	0.2028±0.0003	1.517±0.003	0.17	2.77	2.03	1.36	0.11
Sn	7.28	0.276	0.2640±0.0030	1.476±0.019	0.24	2.11	1.95	1.08	0.94
Th	11.68	0.205	0.2132±0.0018	1.278±0.012	0.42	1.26	1.56	0.81	0.74
Ti	4.51	0.484	0.4779±0.0029	1.089±0.018	0.93	1.09	1.18	0.93	0.74
Tl	11.84	0.183	0.1859±0.0013	1.515±0.010	0.18	2.25	2.03	1.11	0.63
V	6.1	0.518	0.5108±0.0017	1.210±0.014	1.24	1.29	1.42	0.91	0.49
W	19.17	0.405	0.4005±0.0011	1.268±0.011	1.99	1.54	1.54	1.00	0.32
Zn	7.14	0.303	0.3050±0.0011	1.559±0.009	0.27	2.45	2.12	1.16	0.45

graphic record, Fig. 3, where a 0.1-mm plate irregularity corresponds to a time perturbation of 0.02–0.04 μsec.

Nearly simultaneous shock arrival is obtained at a given level by using an explosive charge and driver plate which are flat and of uniform thickness. Large explosive diameter relative to free run distance, as indicated in Fig. 1, is required to obtain useful plane wave area. Moreover, for thin driver plates it was found necessary to place a sheet of plastic about 0.1 cm thick between the explosive charge and the driver plate to prevent plate breakup during the free run. Recovery experiments demonstrated that these driver systems were free from spalling.

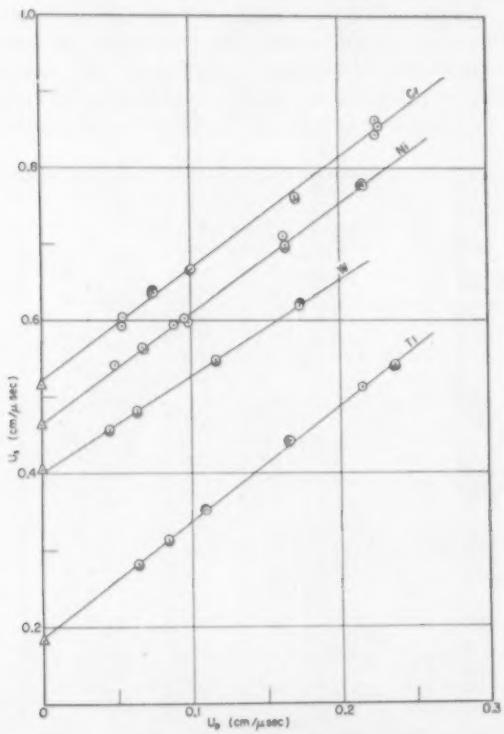

FIG. 9. U_s vs U_p curves for Cr, Ni, Tl, and W.

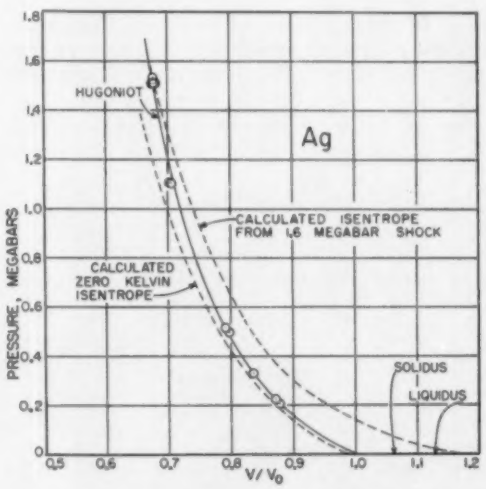

FIG. 10. Pressure-volume curves for Ag. The solid curves represent the experimental Hugoniot loci obtained from the linear U_s vs U_p least-squares fits. In general, the indicated data points below 0.5 megabar are from previous work.[3] The dashed curves show the location of two calculated isentropes in this plane. The curve on the right intersects the Hugoniot at the upper end of the experimental range or at lower pressure if vaporization was encountered.

TRANSFORMATION OF EXPERIMENTAL RESULTS TO HUGONIOT LOCI

The P, V, E equation of state for the brass was obtained by an iterative calculation which resolved the free-surface velocity U_{fs} into two components

$$U_{fs}=U_p+U_r, \tag{3}$$

where U_p is the particle velocity associated with the shock wave and

$$U_r=\int_{P_0}^{P_H}\left(-\frac{\partial V}{\partial P}\right)_s^{\frac{1}{2}}dP \tag{4}$$

is the material velocity due to the rarefaction wave.[3] On starting with the approximation $U_p=\frac{1}{2}U_{fs}$, the experimental U_s vs U_{fs} curve was transformed to the corresponding pressure-volume (Hugoniot) curve by straightforward application of the Rankine-Hugoniot equations. Several isentropes were then calculated by

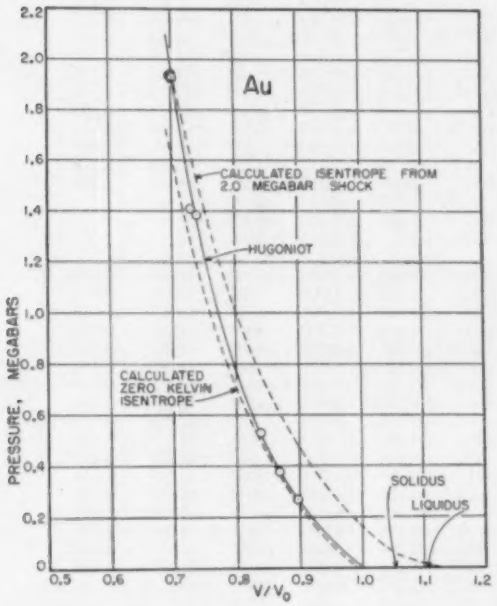

FIG. 11. Pressure-volume curves for Au (see caption to Fig. 10).

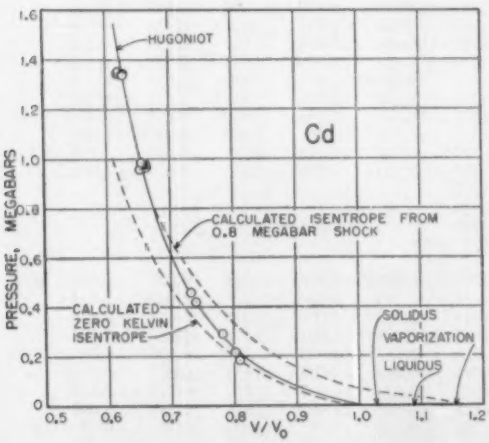

FIG. 12. Pressure-volume curves for Cd (see caption to Fig. 10).

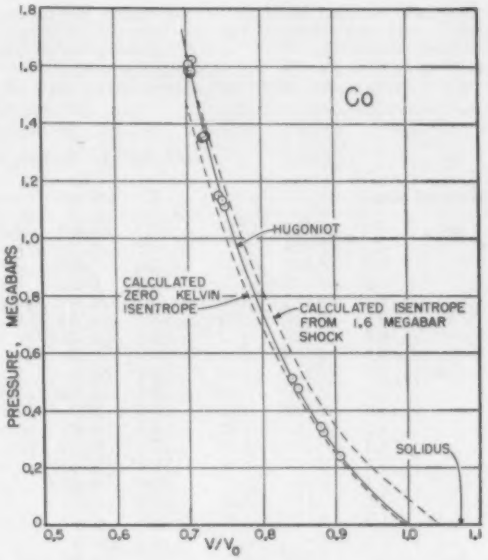

FIG. 13. Pressure-volume curves for Co (see caption to Fig. 10).

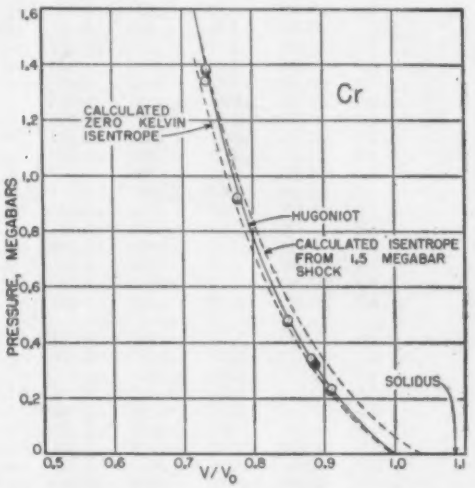

FIG. 14. Pressure-volume curves for Cr (see caption to Fig. 10).

TABLE IV. Summary of calculations and results. The columns headed "shock-wave parameters" refer to equation-of-state or hydrodynamic quantities associated with the various shock pressures listed in the second column. Previous undefined quantities are: $C_H = (\partial P/\partial \rho)_s^{\frac{1}{2}}$ on the Hugoniot; T_H is the temperature on the Hugoniot; $T_{p=0}$ is the temperature of the material relieved isentropically to zero pressure from P_H. The last two entries are the relative volume and internal energy for the zero-degree-Kelvin isentrope. The pressure P in the second column now refers to the corresponding pressure for these parameters.

		Shock-wave parameters						Isentropic release-wave parameters at $P=0$			Zero-Kelvin parameters	
Material	P megabar	V/V_0	γ	T_H °K	C_H cm/μsec	U_s cm/μsec	U_p cm/μsec	U_{fs} cm/μsec	V/V_0	T °K	V/V_0	E ergs/g
Ag	0.0	1.000	2.55	293	0.324	0.324	0.000	0.000	1.000	293	0.987	0.000×10¹⁰
	0.1	0.929	1.97	358	0.377	0.366	0.026	0.052	1.001	303	0.918	0.030
	0.2	0.881	1.74	452	0.418	0.400	0.048	0.096	1.003	344	0.872	0.096
	0.3	0.845	1.73	593	0.452	0.430	0.067	0.134	1.007	416	0.836	0.185
	0.4	0.817	1.76	783	0.480	0.457	0.083	0.169	1.013	511	0.806	0.287
	0.5	0.794	1.81	1021	0.505	0.481	0.099	0.201	1.020	622	0.781	0.395
	0.6	0.775	1.84	1302	0.526	0.504	0.113	0.230	1.028	743	0.760	0.505
	0.7	0.759	1.84	1621	0.546	0.526	0.127	0.259	1.036	869	0.742	0.617
	0.8	0.744	1.84	1974	0.565	0.546	0.140	0.286	1.046	998	0.725	0.740
	0.9	0.731	1.83	2356	0.582	0.565	0.152	0.312	1.056	1126	0.711	0.855
	1.0	0.720	1.82	2733	0.599	0.583	0.163	0.337	1.068	1233	0.698	0.955
	1.1	0.710	1.81	2955	0.615	0.601	0.175	0.362	1.090	1233	0.686	1.085
	1.2	0.700	1.79	3176	0.630	0.618	0.185	0.387	1.112	1233	0.674	1.220
	1.3	0.692	1.78	3471	0.644	0.634	0.195	0.410	1.131	1265	0.664	1.340
	1.4	0.684	1.77	3998	0.657	0.650	0.205	0.433	1.144	1390		
	1.5	0.677	1.76	4558	0.671	0.665	0.215	0.454	1.157	1514		
	1.6	0.670	1.75	5148	0.683	0.680	0.224	0.476	1.171	1637		
Au	0.0	1.000	3.29	293	0.308	0.308	0.000	0.000	1.000	293	0.989	0.000×10¹⁰
	0.1	0.953	3.14	347	0.339	0.332	0.016	0.031	1.000	297	0.943	0.011
	0.2	0.917	3.02	419	0.363	0.353	0.029	0.059	1.001	317	0.907	0.042
	0.3	0.888	2.92	519	0.384	0.373	0.042	0.084	1.003	355	0.878	0.080
	0.4	0.864	2.84	651	0.402	0.391	0.053	0.107	1.005	409	0.852	0.125
	0.5	0.843	2.78	816	0.418	0.407	0.064	0.129	1.008	474	0.831	0.174
	0.6	0.825	2.72	1014	0.432	0.423	0.074	0.149	1.011	550	0.812	0.227
	0.7	0.810	2.67	1243	0.445	0.437	0.083	0.168	1.015	632	0.795	0.284
	0.8	0.796	2.62	1503	0.457	0.451	0.092	0.187	1.019	720	0.778	0.349
	0.9	0.783	2.58	1791	0.468	0.465	0.101	0.205	1.024	812	0.764	0.415
	1.0	0.772	2.54	2107	0.479	0.477	0.109	0.222	1.029	905	0.750	0.482
	1.1	0.762	2.51	2448	0.489	0.490	0.117	0.239	1.034	1000	0.738	0.549
	1.2	0.752	2.48	2812	0.499	0.502	0.124	0.255	1.039	1094	0.727	0.617
	1.3	0.743	2.45	3199	0.508	0.513	0.132	0.270	1.044	1188	0.716	0.685
	1.4	0.735	2.42	3607	0.516	0.524	0.139	0.286	1.050	1280	0.706	0.758
	1.5	0.728	2.39	3966	0.524	0.535	0.146	0.301	1.058	1336	0.697	0.829
	1.6	0.720	2.37	4224	0.532	0.545	0.153	0.316	1.070	1336	0.687	0.899
	1.7	0.714	2.35	4489	0.540	0.556	0.159	0.331	1.082	1336		
	1.8	0.708	2.33	4760	0.547	0.566	0.165	0.346	1.093	1336		
	1.9	0.702	2.31	5037	0.554	0.575	0.172	0.360	1.105	1336		
	2.0	0.696	2.29	5530	0.561	0.585	0.178	0.374	1.113	1404		
Cd	0.0	1.000	2.32	293	0.244	0.244	0.000	0.000	1.000	293	0.978	0.000×10¹⁰
	0.1	0.877	1.99	434	0.324	0.307	0.038	0.076	1.003	328	0.862	0.060
	0.2	0.815	2.02	674	0.375	0.354	0.065	0.132	1.012	430	0.798	0.170
	0.3	0.774	2.03	995	0.413	0.392	0.089	0.179	1.024	556	0.755	0.293
	0.4	0.745	2.01	1253	0.446	0.426	0.109	0.223	1.059	594	0.722	0.425
	0.5	0.722	1.98	1612	0.474	0.456	0.127	0.264	1.096	650	0.694	0.570
	0.6	0.704	1.96	2247	0.500	0.484	0.144	0.301	1.120	806	0.672	0.705
	0.7	0.688	1.94	2983	0.523	0.510	0.159	0.335	1.143	960	0.654	0.840
	0.8	0.675	1.92	3808	0.545	0.534	0.173	0.367	1.166	1109	0.637	0.985
	0.9	0.664	1.90	4704	0.564	0.557	0.187	0.398	1.188	1252	0.623	1.125
	1.0	0.654	1.89	5656	0.583	0.579	0.200	0.428	0.209	1390	0.611	1.260
	1.1	0.646	1.87	6652	0.601	0.599	0.212					
	1.2	0.638	1.86	7681	0.617	0.619	0.224					
	1.3	0.631	1.85	8726	0.633	0.638	0.236					
	1.4	0.624	1.84	9776	0.648	0.657	0.247					
Co	0.0	1.000	1.97	293	0.475	0.475	0.000	0.000	1.000	293	0.993	0.000×10¹⁰
	0.1	0.956	1.65	321	0.510	0.505	0.022	0.045	1.000	295	0.950	0.023
	0.2	0.920	1.42	354	0.541	0.532	0.043	0.085	1.000	307	0.915	0.078
	0.3	0.890	1.35	400	0.567	0.556	0.061	0.122	1.001	331	0.886	0.163
	0.4	0.865	1.36	463	0.591	0.579	0.078	0.157	1.003	367	0.860	0.269
	0.5	0.843	1.41	543	0.611	0.600	0.094	0.190	1.005	414	0.837	0.390
	0.6	0.823	1.45	641	0.630	0.621	0.110	0.220	1.007	471	0.817	0.513
	0.7	0.806	1.47	754	0.647	0.640	0.124	0.250	1.009	535	0.798	0.665
	0.8	0.791	1.48	882	0.662	0.658	0.138	0.278	1.012	604	0.782	0.790
	0.9	0.776	1.48	1022	0.677	0.676	0.151	0.304	1.015	677	0.766	0.943

TABLE IV.—*Continued.*

	Shock-wave parameters							Isentropic release-wave parameters at $P=0$			Zero-Kelvin parameters	
Material	P megabar	V/V_0	γ	T_H °K	C_H cm/μsec	U_s cm/μsec	U_p cm/μsec	U_{fs} cm/μsec	V/V_0	T °K	V/V_0	E ergs/g
	1.0	0.764	1.46	1173	0.691	0.693	0.164	0.330	1.019	753	0.753	1.105×10^{10}
	1.1	0.752	1.45	1332	0.705	0.709	0.176	0.356	1.022	830	0.740	1.235
	1.2	0.741	1.43	1498	0.718	0.724	0.188	0.380	1.026	908	0.728	1.395
	1.3	0.731	1.41	1669	0.730	0.740	0.199	0.404	1.030	984	0.717	1.540
	1.4	0.721	1.40	1844	0.742	0.755	0.210	0.427	1.034	1059	0.706	1.714
	1.5	0.712	1.39	2021	0.754	0.769	0.221	0.449	1.038	1133		
	1.6	0.704	1.37	2199	0.764	0.783	0.232	0.471	1.042	1203		
Cr	0.0	1.000	1.29	293	0.522	0.522	0.000	0.000	1.000	293	0.996	0.000×10^{10}
	0.1	0.955	1.24	314	0.568	0.585	0.025	0.050	1.000	296	0.933	0.032
	0.2	0.920	1.19	346	0.608	0.591	0.047	0.095	1.000	312	0.890	0.102
	0.3	0.891	1.15	396	0.644	0.621	0.068	0.136	1.001	344	0.856	0.196
	0.4	0.867	1.12	467	0.675	0.648	0.086	0.173	1.002	392	0.827	0.313
	0.5	0.846	1.09	558	0.704	0.674	0.104	0.208	1.004	455	0.803	0.433
	0.6	0.827	1.07	669	0.731	0.698	0.120	0.241	1.005	531	0.782	0.563
	0.7	0.811	1.05	796	0.756	0.721	0.136	0.273	1.007	618	0.764	0.698
	0.8	0.797	1.03	939	0.780	0.743	0.151	0.303	1.010	712	0.748	0.832
	0.9	0.784	1.01	1093	0.803	0.764	0.165	0.332	1.013	812	0.734	0.967
	1.0	0.772	1.00	1256	0.824	0.784	0.179	0.360	1.016	916	0.720	1.118
	1.1	0.761	0.98	1424	0.845	0.803	0.192	0.387	1.020	1019		
	1.2	0.751	0.97	1592	0.865	0.822	0.205	0.413	1.024	1119		
	1.3	0.742	0.96	1755	0.884	0.840	0.217	0.438	1.028	1211		
	1.4	0.733	0.95	1914	0.902	0.857	0.229	0.463	1.033	1297		
Cu	0.0	1.000	2.00	293	0.396	0.396	0.000	0.000	1.000	293	0.990	0.000×10^{10}
	0.1	0.940	1.80	334	0.445	0.434	0.026	0.052	1.000	298	0.933	0.032
	0.2	0.897	1.74	391	0.484	0.468	0.048	0.096	1.001	319	0.890	0.102
	0.3	0.864	1.73	472	0.516	0.497	0.068	0.136	1.003	360	0.856	0.196
	0.4	0.836	1.74	582	0.544	0.524	0.086	0.172	1.006	417	0.827	0.313
	0.5	0.814	1.74	719	0.569	0.549	0.102	0.206	1.010	487	0.803	0.433
	0.6	0.794	1.72	881	0.591	0.572	0.118	0.238	1.015	568	0.782	0.563
	0.7	0.777	1.70	1068	0.612	0.594	0.132	0.268	1.019	656	0.764	0.698
	0.8	0.762	1.68	1277	0.631	0.615	0.146	0.296	1.025	751	0.748	0.832
	0.9	0.749	1.67	1506	0.649	0.634	0.159	0.323	1.031	849	0.734	0.967
	1.0	0.737	1.65	1755	0.666	0.653	0.172	0.350	1.037	950	0.720	1.118
	1.1	0.726	1.63	2020	0.683	0.671	0.184	0.375	1.044	1053	0.708	1.253
	1.2	0.716	1.62	2301	0.698	0.689	0.196	0.400	1.051	1156	0.696	1.410
	1.3	0.707	1.61	2596	0.713	0.706	0.207	0.424	1.058	1257	0.686	1.550
	1.4	0.698	1.60	2902	0.727	0.722	0.218	0.447	1.066	1356		
	1.5	0.690	1.59	3042	0.740	0.738	0.228	0.471	1.079	1356		
Mo	0.0	1.000	1.58	293	0.516	0.516	0.000	0.000	1.000	293	0.997	0.000×10^{10}
	0.1	0.966	1.43	310	0.542	0.538	0.018	0.036	1.000	295	0.962	0.019
	0.2	0.937	1.31	335	0.565	0.559	0.035	0.070	1.000	305	0.934	0.067
	0.3	0.912	1.26	372	0.585	0.579	0.051	0.102	1.000	327	0.910	0.118
	0.4	0.890	1.26	426	0.604	0.597	0.066	0.132	1.001	363	0.887	0.198
	0.5	0.870	1.27	499	0.620	0.614	0.080	0.160	1.002	412	0.866	0.290
	0.6	0.852	1.28	591	0.636	0.631	0.093	0.187	1.003	475	0.849	0.383
	0.7	0.836	1.29	702	0.650	0.647	0.106	0.213	1.004	549	0.832	0.493
	0.8	0.821	1.28	832	0.664	0.662	0.118	0.238	1.005	635	0.817	0.600
	0.9	0.807	1.27	980	0.677	0.677	0.130	0.262	1.007	730	0.803	0.717
	1.0	0.795	1.25	1144	0.689	0.691	0.142	0.285	1.008	833	0.788	0.858
	1.1	0.783	1.23	1324	0.700	0.705	0.153	0.308	1.011	943	0.776	0.982
	1.2	0.772	1.21	1517	0.711	0.718	0.164	0.330	1.013	1059	0.764	1.107
	1.3	0.762	1.20	1722	0.722	0.731	0.174	0.351	1.016	1178	0.754	1.245
	1.4	0.752	1.18	1938	0.732	0.744	0.184	0.372	1.018	1300	0.744	1.380
	1.5	0.743	1.17	2161	0.742	0.756	0.194	0.392	1.021	1422	0.734	1.520
	1.6	0.734	1.16	2389	0.752	0.768	0.204	0.413	1.024	1543		
	1.7	0.726	1.15	2620	0.761	0.780	0.214	0.432	1.028	1660		
Ni	0.0	1.000	1.83	293	0.465	0.465	0.000	0.000	1.000	293	0.993	0.000×10^{10}
	0.1	0.954	1.71	321	0.506	0.497	0.023	0.045	1.000	295	0.948	0.023
	0.2	0.919	1.69	356	0.540	0.526	0.043	0.086	1.000	307	0.912	0.085
	0.3	0.889	1.70	405	0.570	0.553	0.061	0.123	1.000	330	0.882	0.172
	0.4	0.865	1.70	471	0.595	0.578	0.078	0.157	1.003	365	0.858	0.267
	0.5	0.843	1.70	554	0.619	0.600	0.094	0.189	1.005	410	0.836	0.378
	0.6	0.825	1.68	654	0.640	0.622	0.109	0.219	1.007	464	0.816	0.504
	0.7	0.808	1.65	768	0.660	0.642	0.123	0.247	1.010	525	0.799	0.628
	0.8	0.794	1.62	897	0.679	0.662	0.136	0.275	1.013	592	0.784	0.757
	0.9	0.780	1.60	1040	0.696	0.680	0.149	0.301	1.016	664	0.770	0.892
	1.0	0.768	1.58	1195	0.713	0.698	0.162	0.326	1.019	739	0.757	1.030

TABLE IV.—*Continued.*

Material	P megabar	V/V_0	γ	Shock-wave parameters: T_H °K	C_H cm/μsec	U_s cm/μsec	U_p cm/μsec	Isentropic release-wave parameters at $P=0$: U_{fs} cm/μsec	V/V_0	T °K	Zero-Kelvin parameters: V/V_0	E ergs/g
	1.1	0.757	1.56	1360	0.729	0.715	0.173	0.351	1.023	817	0.745	1.173×10^{10}
	1.2	0.747	1.54	1536	0.744	0.732	0.185	0.375	1.027	896	0.734	1.315
	1.3	0.738	1.53	1720	0.758	0.748	0.196	0.398	1.031	976	0.724	1.455
	1.4	0.729	1.52	1913	0.772	0.764	0.207	0.420	1.036	1057	0.714	1.606
	1.5	0.721	1.51	2111	0.785	0.779	0.217	0.442	1.040	1137		
Pb	0.0	1.000	2.77	293	0.203	0.203	0.000	0.000	1.000	293	0.977	0.000×10^{10}
	0.1	0.865	2.39	504	0.263	0.255	0.034	0.069	1.004	342	0.849	0.050
	0.2	0.796	2.20	901	0.300	0.294	0.060	0.121	1.018	487	0.776	0.142
	0.3	0.751	2.08	1343	0.328	0.326	0.081	0.166	1.042	600	0.726	0.251
	0.4	0.718	1.99	1862	0.351	0.354	0.100	0.206	1.071	702	0.689	0.367
	0.5	0.693	1.92	2722	0.372	0.379	0.116	0.242	1.095	897	0.660	0.484
	0.6	0.673	1.86	3739	0.390	0.402	0.131	0.276	1.118	1091	0.635	0.601
	0.7	0.656	1.82	4904	0.407	0.424	0.146	0.307	1.141	1280	0.615	0.717
	0.8	0.642	1.78	6210	0.423	0.444	0.159	0.337	1.164	1465	0.597	0.833
	0.9	0.630	1.74	7651	0.437	0.463	0.171	0.366	1.185	1642	0.582	0.947
	1.0	0.619	1.71	9218	0.451	0.481	0.183	0.393	1.206	1813		
	1.1	0.609	1.69	10910	0.464	0.498	0.195	0.419	1.226	1976		
	1.2	0.600	1.66	12720	0.476	0.515	0.206					
	1.3	0.593	1.64	14640	0.488	0.531	0.216					
	1.4	0.586	1.62	16670	0.500	0.546	0.226					
Sn	0.0	1.000	2.11	293	0.264	0.264	0.000	0.000	1.000	293	0.986	0.000×10^{10}
	0.1	0.871	1.62	435	0.338	0.326	0.042	0.084	1.003	336	0.861	0.077
	0.2	0.802	1.59	709	0.386	0.373	0.074	0.149	1.013	471	0.792	0.214
	0.3	0.757	1.61	871	0.422	0.412	0.100	0.203	1.032	505	0.742	0.383
	0.4	0.724	1.61	1197	0.451	0.446	0.123	0.252	1.054	614	0.704	0.565
	0.5	0.698	1.58	1829	0.477	0.477	0.144	0.297	1.077	838	0.674	0.750
	0.6	0.677	1.56	2585	0.500	0.505	0.163	0.339	1.100	1068	0.650	0.931
	0.7	0.659	1.54	3455	0.522	0.531	0.181	0.378	1.123	1298	0.629	1.118
	0.8	0.644	1.52	4442	0.541	0.556	0.198	0.415	1.146	1525	0.611	1.304
	0.9	0.631	1.51	5455	0.559	0.579	0.213	0.450	1.169	1749	0.595	1.495
	1.0	0.620	1.49	6630	0.576	0.601	0.228	0.484	1.191	1970	0.580	1.682
	1.1	0.610	1.48	7910	0.592	0.622	0.243	0.517	1.218	2194		
	1.2	0.601	1.47	9290	0.606	0.643	0.256	0.548	1.235	2420		
	1.3	0.593	1.46	10760	0.621	0.662	0.270					
	1.4	0.585	1.45	12320	0.635	0.681	0.282					
Th	0.0	1.000	1.26	293	0.213	0.213	0.000	0.000	1.000	293	0.992	0.000×10^{10}
	0.1	0.870	1.09	402	0.260	0.256	0.033	0.067	1.001	340	0.863	0.049
	0.2	0.795	1.00	667	0.292	0.289	0.059	0.118	1.007	511	0.787	0.142
	0.3	0.744	0.94	1074	0.317	0.316	0.081	0.162	1.016	764	0.735	0.253
	0.4	0.707	0.89	1577	0.339	0.341	0.100	0.202	1.027	1054	0.697	0.373
	0.5	0.677	0.85	2122	0.358	0.363	0.117	0.237	1.039	1352	0.665	0.493
	0.6	0.652	0.82	2708	0.375	0.384	0.133	0.270	1.052	1639	0.639	0.615
	0.7	0.632	0.79	3282	0.391	0.403	0.148	0.301	1.065	1905	0.616	0.737
	0.8	0.614	0.77	3659	0.406	0.421	0.162	0.331	1.086	2023	0.597	0.858
	0.9	0.599	0.75	4128	0.420	0.437	0.175	0.360	1.111	2168	0.581	0.978
	1.0	0.585	0.74	5091	0.434	0.454	0.188	0.388	1.133	2558	0.566	1.095
	1.1	0.573	0.72	6129	0.446	0.469	0.200	0.414	1.155	2950	0.554	1.212
	1.2	0.562	0.71	7239	0.458	0.484	0.212	0.440	1.177	3344		
	1.3	0.553	0.69	8418	0.470	0.498	0.223	0.465	1.199	3737		
	1.4	0.544	0.68	9666	0.481	0.512	0.233	0.489	1.221	4128		
	1.5	0.535	0.67	10980	0.492	0.525	0.244	0.512	1.242	4516		
Ti	0.0	1.000	1.10	293	0.478	0.478	0.000	0.000	1.000	293	0.995	0.000×10^{10}
	0.1	0.919	1.05	303	0.524	0.524	0.042	0.085	1.000	302	0.914	0.087
	0.2	0.860	1.10	406	0.558	0.564	0.079	0.157	1.001	346	0.855	0.284
	0.3	0.814	1.09	535	0.586	0.599	0.111	0.222	1.004	427	0.809	0.536
	0.4	0.777	1.02	714	0.610	0.631	0.141	0.282	1.007	541	0.771	0.835
	0.5	0.746	0.96	937	0.631	0.661	0.168	0.337	1.011	679	0.738	1.150
	0.6	0.719	0.93	1199	0.649	0.688	0.193	0.388	1.015	834	0.710	1.504
	0.7	0.696	0.91	1490	0.666	0.714	0.217	0.437	1.021	1000	0.686	1.850
	0.8	0.675	0.89	1776	0.681	0.739	0.240	0.484	1.029	1150	0.664	2.217
	0.9	0.657	0.88	1994	0.694	0.763	0.262	0.531	1.049	1230	0.644	2.590
	1.0	0.640	0.87	2388	0.707	0.785	0.282	0.574	1.056	1427	0.626	2.970
	1.1	0.625	0.86	2823	0.718	0.807	0.302	0.615	1.064	1636		
Tl	0.0	1.000	2.25	293	0.186	0.186	0.000	0.000	1.000	293	0.978	0.000×10^{10}
	0.1	0.853	1.76	484	0.249	0.239	0.035	0.071	1.005	351	0.838	0.054

TABLE IV.—*Continued.*

Material	Shock-wave parameters							Isentropic release-wave parameters at $P=0$			Zero-Kelvin parameters	
	P megabar	V/V_0	γ	T_H °K	C_H cm/μsec	U_s cm/μsec	U_p cm/μsec	U_{fs} cm/μsec	V/V_0	T °K	V/V_0	E ergs/g
	0.2	0.781	1.75	860	0.287	0.278	0.061	0.123	1.020	518	0.764	0.147×10^{10}
	0.3	0.736	1.76	1130	0.315	0.310	0.082	0.167	1.046	576	0.714	0.250
	0.4	0.703	1.74	1781	0.339	0.337	0.100	0.207	1.079	775	0.678	0.306
	0.5	0.678	1.71	2647	0.359	0.362	0.116	0.243	1.114	996	0.648	0.470
	0.6	0.658	1.69	3685	0.376	0.385	0.132	0.277	1.148	1213	0.624	0.582
	0.7	0.642	1.67	4887	0.392	0.406	0.145	0.309	1.181	1421	0.603	0.700
	0.8	0.628	1.66	6261	0.407	0.426	0.159	0.338	1.211	1618	0.586	0.808
	0.9	0.616	1.64	7825	0.421	0.445	0.171				0.570	0.920
	1.0	0.605	1.63	9613	0.433	0.462	0.183				0.586	0.808
	1.1	0.596	1.62	11690	0.445	0.479	0.194					
	1.2	0.587	1.61	14170	0.456	0.496	0.204					
	1.3	0.580	1.60	17330	0.467	0.511	0.215					
	1.4	0.573	1.59	21880	0.477	0.526	0.225					
	1.5	0.567	1.58	30900	0.486	0.541	0.234					
V	0.0	1.000	1.29	293	0.511	0.511	0.000	0.000	1.000	293	0.995	0.000×10^{10}
	0.1	0.945	1.23	318	0.551	0.547	0.030	0.060	1.000	297	0.940	0.045
	0.2	0.902	1.26	360	0.584	0.579	0.057	0.113	1.000	317	0.898	0.148
	0.3	0.867	1.29	428	0.612	0.609	0.081	0.162	1.002	357	0.862	0.295
	0.4	0.838	1.27	524	0.636	0.636	0.103	0.207	1.003	417	0.831	0.475
	0.5	0.812	1.22	647	0.658	0.661	0.124	0.249	1.005	495	0.806	0.663
	0.6	0.790	1.17	796	0.679	0.685	0.144	0.288	1.008	587	0.783	0.872
	0.7	0.770	1.14	970	0.697	0.707	0.162	0.326	1.011	692	0.763	1.087
	0.8	0.753	1.11	1165	0.715	0.729	0.180	0.362	1.014	806	0.744	1.313
	0.9	0.737	1.09	1379	0.731	0.749	0.197	0.397	1.018	928	0.727	1.555
	1.0	0.723	1.08	1611	0.746	0.769	0.213	0.430	1.022	1056	0.712	1.785
	1.1	0.709	1.06	1857	0.760	0.788	0.229	0.462	1.026	1186	0.698	2.037
	1.2	0.697	1.05	2114	0.773	0.806	0.244	0.493	1.030	1319	0.684	2.293
	1.3	0.686	1.05	2382	0.786	0.824	0.259	0.523	1.035	1451		
W	0.0	1.000	1.54	293	0.400	0.400	0.000	0.000	1.000	293	0.997	0.000×10^{10}
	0.1	0.970	1.46	308	0.419	0.416	0.012	0.025	1.000	294	0.967	0.007
	0.2	0.944	1.41	329	0.436	0.431	0.024	0.048	1.000	303	0.942	0.027
	0.3	0.921	1.39	362	0.451	0.445	0.035	0.070	1.000	321	0.918	0.058
	0.4	0.901	1.37	409	0.464	0.458	0.045	0.091	1.000	352	0.898	0.093
	0.5	0.882	1.37	472	0.477	0.471	0.055	0.111	1.001	394	0.879	0.138
	0.6	0.866	1.36	552	0.489	0.483	0.065	0.130	1.002	449	0.862	0.190
	0.7	0.851	1.35	648	0.500	0.494	0.074	0.148	1.003	514	0.847	0.242
	0.8	0.836	1.33	761	0.510	0.505	0.083	0.166	1.004	589	0.832	0.300
	0.9	0.824	1.31	890	0.519	0.516	0.091	0.182	1.005	674	0.819	0.355
	1.0	0.812	1.30	1034	0.529	0.526	0.099	0.199	1.006	767	0.807	0.417
	1.1	0.800	1.28	1193	0.538	0.536	0.107	0.215	1.008	867	0.795	0.480
	1.2	0.790	1.27	1365	0.546	0.546	0.115	0.230	1.009	973	0.784	0.548
	1.3	0.780	1.26	1550	0.554	0.555	0.122	0.245	1.011	1085	0.774	0.615
	1.4	0.771	1.25	1747	0.562	0.564	0.129	0.260	1.013	1201	0.764	0.683
	1.5	0.762	1.24	1954	0.569	0.573	0.136	0.275	1.014	1321	0.754	0.757
	1.6	0.754	1.23	2171	0.577	0.582	0.143	0.289	1.016	1443	0.746	0.825
	1.7	0.746	1.22	2396	0.583	0.591	0.150	0.302	1.018	1568	0.738	0.895
	1.8	0.738	1.21	2629	0.590	0.599	0.157	0.316	1.020	1694	0.729	0.977
	1.9	0.731	1.21	2869	0.597	0.607	0.163	0.329	1.021	1820	0.721	1.053
	2.0	0.725	1.20	3114	0.603	0.615	0.170	0.342	1.025	1947		
	2.1	0.718	1.20	3363	0.609	0.623	0.176	0.355	1.027	2073		
Zn	0.0	1.000	2.45	293	0.305	0.305	0.000	0.000	1.000	293	0.998	0.000×10^{10}
	0.1	0.895	1.84	395	0.379	0.365	0.038	0.077	1.002	311	0.880	0.064
	0.2	0.834	1.68	547	0.431	0.411	0.068	0.137	1.008	374	0.821	0.185
	0.3	0.793	1.68	768	0.472	0.450	0.093	0.189	1.019	470	0.777	0.338
	0.4	0.762	1.71	1053	0.505	0.485	0.116	0.235	1.032	583	0.743	0.504
	0.5	0.737	1.73	1375	0.533	0.516	0.136	0.278	1.048	692	0.715	0.680
	0.6	0.717	1.73	1496	0.558	0.545	0.154	0.317	1.063	692	0.692	0.863
	0.7	0.700	1.73	1636	0.582	0.572	0.171	0.354	1.078	699	0.672	1.040
	0.8	0.686	1.72	2083	0.603	0.597	0.188	0.390	1.099	817	0.656	1.215
	0.9	0.673	1.71	2578	0.623	0.621	0.203	0.424	1.120	933	0.640	1.406
	1.0	0.662	1.70	3119	0.642	0.644	0.218	0.457	1.140	1047	0.626	1.593
	1.1	0.652	1.69	3704	0.659	0.666	0.231	0.489	1.160	1158	0.614	1.773
	1.2	0.643	1.68	4333	0.676	0.687	0.245					
	1.3	0.635	1.67	5007	0.692	0.707	0.258					
	1.4	0.628	1.66	5727	0.707	0.726	0.270					
	1.5	0.621	1.65	6498	0.722	0.705	0.282					

TABLE V. Temperature estimates along the Hugoniots for Bi, Fe, Sb.

P	Bi		Fe		Sb	
megabar	V/V_0	T °K	V/V_0	T °K	V/V_0	T °K
0.00	1.000	293	1.000	293	1.000	293
0.25	0.710	···	0.867	500	0.723	850
0.50	0.651	2800	0.801	800	0.651	2100
0.75	0.606	6300	0.759	1300	0.615	5000
1.00	0.576	10900	0.729	1750	0.590	8700
1.25	0.556	16600	0.706	2200	0.573	13100
1.50	0.538	23100	0.688	2650		
1.75			0.673	3400		

methods outlined in the equation-of-state section, and values of U_r were obtained from Eq. (4). The trial values of U_p and the calculated values of U_r are used to form a correction curve of U_{fs} vs U_{fs}/U_p used for the subsequent trial. This procedure was repeated until the correction curve no longer changed. At each stage of this iteration the experimental shock velocities and the associated trial particle velocities were fitted by least squares. This calculation yields the required hydrodynamical variables (pressure and particle velocity) needed for an impedance-match-solution[2,3] standard.

The Hugoniot locus thus determined is subject to errors due to uncertainties existing in the zero-pressure data (specific internal energy versus volume) and the volume dependence of the Grüneisen ratio. It is estimated that these effects cause uncertainties of about 0.2% at one megabar, increasing to 0.4% at two megabars, in the shock velocity at a given particle velocity.

Data for the other materials consist of a shock-wave velocity measurement and a simultaneous measurement of the shock strength in the brass standard. The impedance-match method[2,3] was then used to determine U_p, or the pressure P from which the relative volumes V/V_0 were obtained. These results are listed in Table II. Since all the materials investigated have shock-wave impedances comparable to the brass standard, any errors involved in determining its Hugoniot will be transmitted to the Hugoniots of the other materials; however, any other errors which can be assigned to

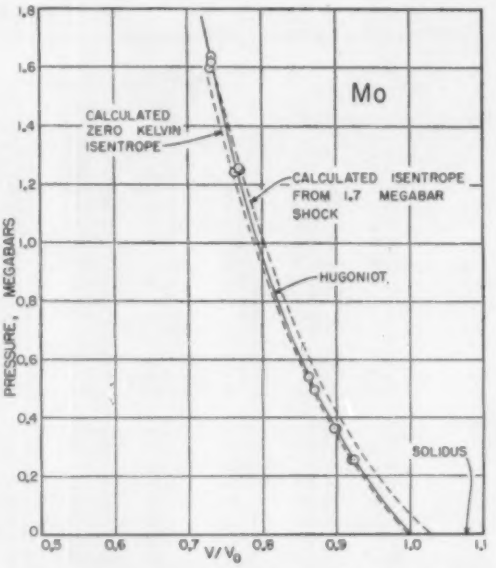

FIG. 16. Pressure-volume curves for Mo (see caption to Fig. 10).

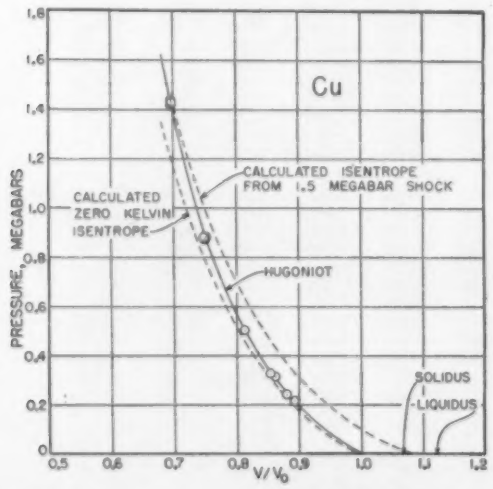

FIG. 15. Pressure-volume curves for Cu (see caption to Fig. 10).

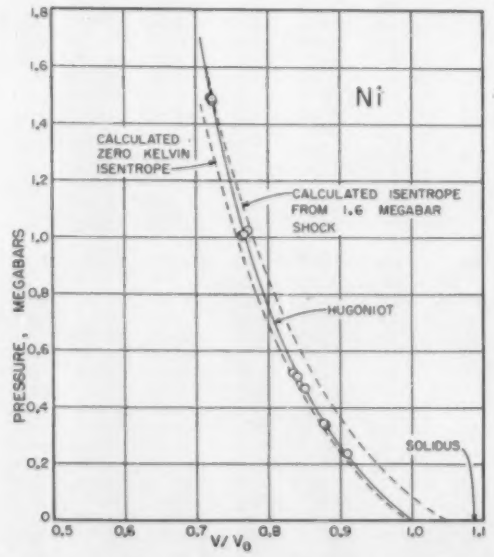

FIG. 17. Pressure-volume curves for Ni. (see caption to Fig. 10).

determining the pressure-velocity loci for the impedance-match solution have only a very slight effect on the Hugoniots of the other materials.

FITTING THE DATA

The U_s vs U_p data were fitted by the method of least squares to the relations

$$U_s = C + SU_p \tag{5}$$

and

$$U_s = C + SU_p + KU_p^2. \tag{6}$$

These fits include all the data recorded by Walsh *et al.*,[3] each point of which is given a weighting factor of one. The present high-pressure data points are given a weight of ½ due to the relatively thinner samples, higher shock velocities, and the somewhat larger uncertainties in estimating shock arrival times caused by the increased curvature of the traces. Professor Bridgman's

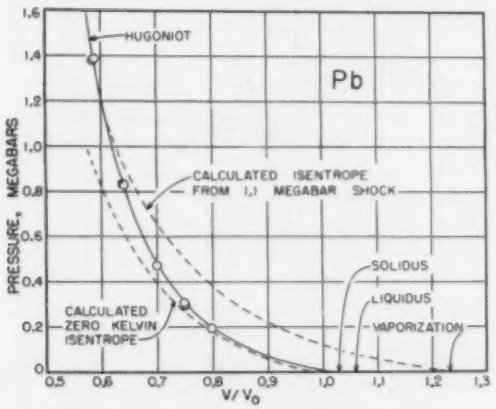

FIG. 18. Pressure-volume curves for Pb (see caption to Fig. 10).

initial isothermal compressibilities have been converted to adiabatic "sound speeds," $C_B = V[-(\partial P/\partial V)_s]^{\frac{1}{2}}$, to give a value of the shock velocity at zero particle velocity. These data have been given a weighting factor of one. Since the computed probable error of the data was generally smaller for the linear relation than for the quadratic relation, and because the quadratic coefficients were quite small, the linear functions were chosen to describe the Hugoniot loci and were used in the equation-of-state calculations. Moreover, since the quadratic coefficients are positive for seven materials and negative for nine, there is apparently no trend for these materials to become either relatively stiffer or softer at high pressures. It is interesting that these new quadratic coefficients are on the average a factor of 5.5 smaller than those obtained from the low-pressure data reported previously.[3] The quality of the linear fits can be seen in Figs. 4 thru 9. The results of the foregoing least-square analysis are given in Table III.

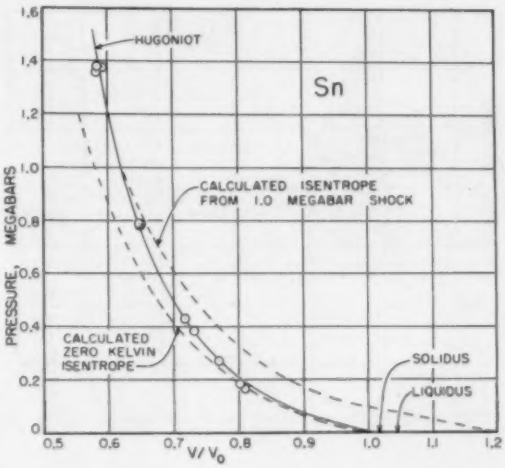

FIG. 19. Pressure-volume curves for Sn (see caption to Fig. 10).

The average probable error in the coefficients C and S are 0.5% and 0.9%, respectively. The average probable error in the measured shock velocity at a given particle velocity as determined from the linear fits is 0.5%.

COMPARISON WITH RECENT WORK BY AL'TSHULER *ET AL.*

Two papers were recently published in the Soviet literature, reporting an extensive investigation of iron[17] to shock pressures of about five megabars, and less extensive work on Ag, Au, Bi, Cd, Cu, Pb, Sn, and Zn, also measured to shock pressures of four or five megabars.[18] These data are shown with the present results

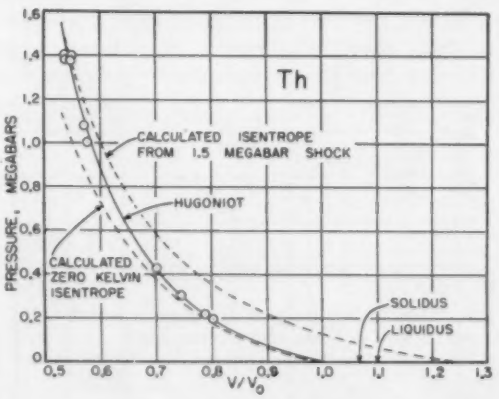

FIG. 20. Pressure-volume curves for Th (see caption to Fig. 10).

[17] L. V. Al'tshuler, K. K. Krupnikov, B. N. Ledenev, V. I. Zhuchikhin, and M. I. Brazhnik, J. Exptl. Theoret. Phys. (U.S.S.R.) **34**, 874 (1958); Soviet Phys. JETP **34**, 606 (1958).

[18] L. V. Al'tshuler, K. K. Krupnikov, and M. I. Brazhnik, J. Exptl. Theoret. Phys. (U.S.S.R.) **34**, 886 (1958); Soviet Phys. JETP **34**, 614 (1958).

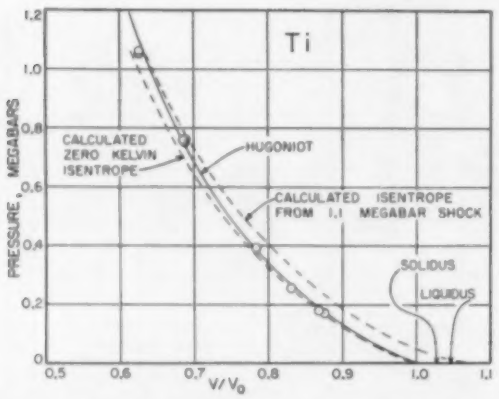

FIG. 21. Pressure-volume curves for Ti (see caption to Fig. 10).

in Figs. 4–6. For all of the materials, the U_s vs U_p slope reported by Al'tshuler *et al.* is smaller than that found in the present work. The ratio of these slopes to ours for the various elements are as follows: 1.03, Ag; 1.06, Au; 1.13, Bi; 1.13, Cd; 1.02, Cu; 1.04, Fe; 1.20, Pb; and 1.07, Zn. The Al'tshuler data for Sn were not fitted by a straight line, but also appear to show the same trend as the other materials.

For the relatively incompressible materials, Au, Ag, and Cu the differences are attributable to the different results for iron, which was used as a standard in the Soviet experiments. This suggests a consistent error in either their work on the iron standard or in our work determining the brass standard. Our efforts to find such an error have so far been unsuccessful. For the compressible materials Bi, Cd, Pb, and Zn, the relatively larger disagreement is possibly due to an unfavorable w/t ratio of two used in the Soviet experiments. Considerations given before suggest that this ratio is not sufficiently large for the high-pressure point on these materials to prevent serious shock-wave attenuation by side rarefactions.

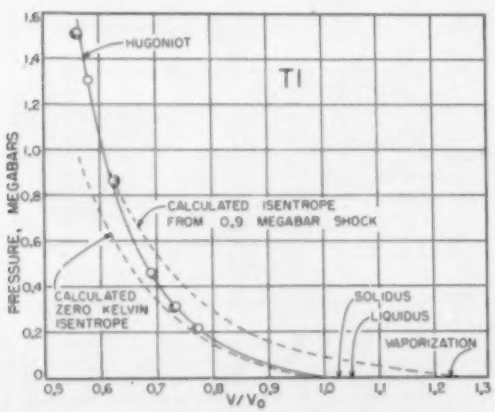

FIG. 22. Pressure-volume curves for Tl (see caption to Fig. 10).

EQUATION OF STATE

The data fitted by the equation $U_s=C+SU_p$ can be transformed by the Rankine-Hugoniot equations to give the experimental results in terms of pressure and energy vs volume. These are

$$P_H=C^2(V_0-V)/[V_0-S(V_0-V)]^2 \qquad (7)$$

and

$$E_H=E_0+\tfrac{1}{2}\{C(V_0-V)/[V_0-S(V_0-V)]\}^2, \qquad (8)$$

where P_H is the pressure and E_H is the specific internal energy on the Hugoniot. These two relations are a direct consequence of the experimental data fits and do not depend upon theoretical estimates of the

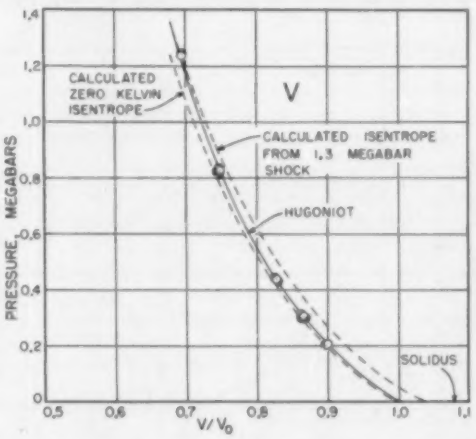

FIG. 23. Pressure-volume curves for V (see caption to Fig. 10).

Grüneisen's function. The foregoing relations coupled with the Mie-Grüneisen equation of state[2] form the basis for calculating a more complete thermal description of the materials. Since Grüneisen's ratio γ is assumed to be a function of volume only, the equation

$$\gamma(V)=V(P_H-P_I)/(E_H-E_I) \qquad (9)$$

relates pressure and energy on any isentrope (I) to the corresponding quantities on the Hugoniot (H) at the specific volume V. For most materials the Grüneisen's ratio used in Eq. (9) was obtained by solving the Dugdale-MacDonald relationship,

$$\gamma_D(V)=-\frac{V}{2}\frac{d^2(PV^3)/dV^2}{d(PV^3)/dV}-\frac{1}{3} \qquad (10)$$

(assumed valid along the zero-degree-Kelvin isentrope). The initial γ used for this integration was obtained

from the thermodynamic gamma γ_T, given by

$$\gamma_T = V(\partial P/\partial E)_v = C^2/V_0(\partial E/\partial V)_p, \quad P=0, \quad T=293°\text{K} \quad (11)$$

and the volume derivative of γ_D

$$d\gamma_D/dV = (1/V_0)[S^2 - \tfrac{1}{3}S + (5/9)], \quad P=0, \quad T=293°\text{K}. \quad (12)$$

Necessary values of the initial internal energy E_0 at the foot of the Hugoniot (relative to an arbitrary zero internal energy at $P=0$, $T=0°$K) were obtained by integrating a normalized Debye specific-heat curve using Debye temperatures listed by de Launay.[19] The foregoing conditions together with the known Hugoniot

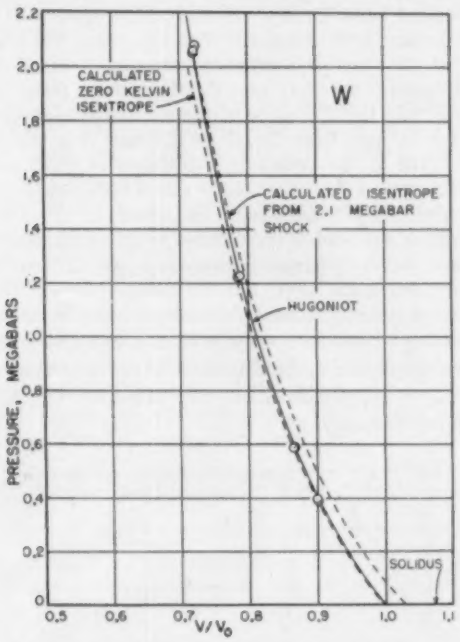

FIG. 24. Pressure-volume curves for W (see caption to Fig. 10).

loci and the assumption that $d\gamma_D/dV$ is constant over the small volume increment between 293°K and 0°K then determine the zero-degree-Kelvin pressure-volume isentrope and $\gamma(V)$.

Equation (10) simplifies[3] at zero pressure to

$$\gamma_D = 2S - 1, \quad P=0, \quad (13)$$

which is compared with the γ_T, Eq. (11), obtained from known thermodynamic variables in Table III. For several materials (Au, Th, Pb) the disagreement was so large that the γ_D's obtained from Eq. (10) could not

[19] J. de Launay, *Solid State Physics, Advances in Research and Applications* (Academic Press, Inc., New York, 1956), Vol. 2, p. 233.

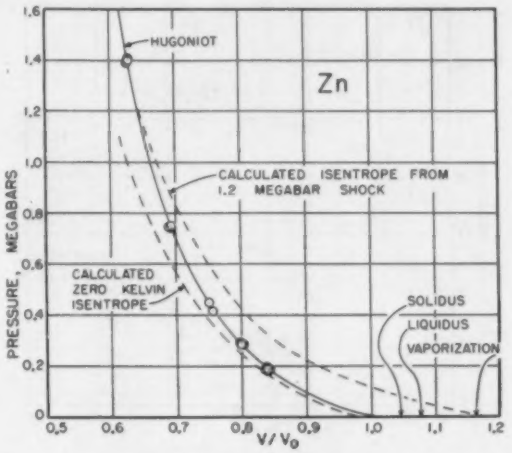

FIG. 25. Pressure-volume curves for Zn (see caption to Fig. 10).

be used. $\gamma(V)$ was then determined by assuming $(\partial E/\partial P)_v$ was constant [see Eq. (11)]. The Grüneisen's ratio computed from Eq. (10) for $V>V_0$ can be subjected to a simple test contingent on the assumed linearity of the U_s vs U_p and the Mie-Grüneisen

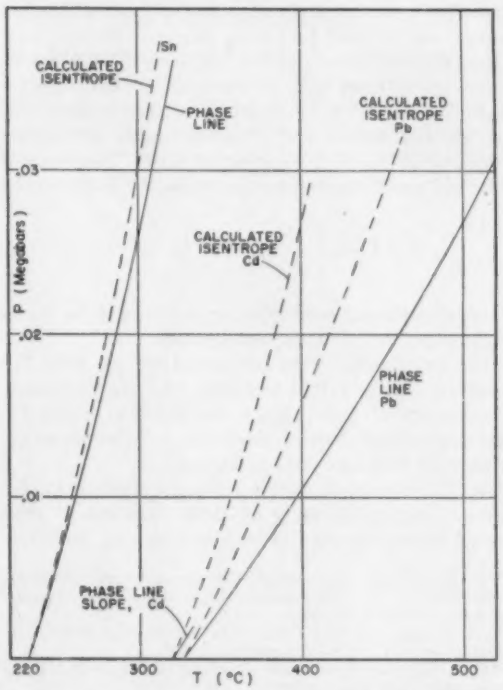

FIG. 26. Comparison of melting phase line data and calculated isentropes. Melting phase line data[21] and calculated isentropes are compared for Pb and Sn. The initial slope of the Cd phase line is also compared with the appropriate isentrope.

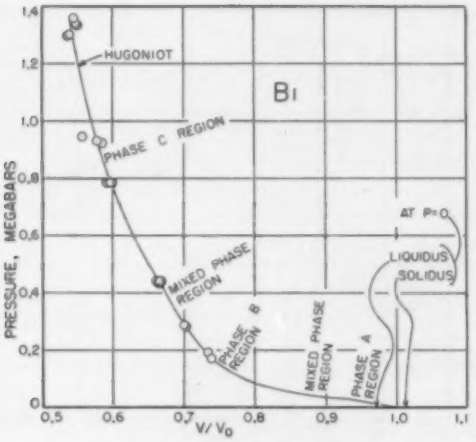

FIG. 27. Hugoniot curve for Bi.

theory. The Hugoniot extrapolated to negative pressures and the known E vs V data at zero pressure give two equations-of-state loci from which an average gamma $\bar{\gamma}$ can be found from the equation

$$\bar{\gamma}=VP_H/(E_H-E_{P=0}). \tag{14}$$

When the two room-temperature γ's agreed [Eqs. (11) and (13)], then the γ's obtained at higher temperatures (large volume) from Eqs. (10) and (14) would also agree. E and T were fitted as functions of V for $V>V_0$, along $P=0$ from specific heat data[20] and thermal expansion data.[21–23] These initial data, combined with Eq. (9) and known $\gamma(V)$, then suffice to determine a complete P, V, E, S equation of state. Temperatures were calculated on various isentropes by the equation

$$T=T_i\exp\left[\int_{v_i}^{v}(\gamma/V)dV\right], \quad dS=0, \tag{15}$$

where the starting conditions are given by T_i vs V_i fits of the experimental zero pressure data.

The calculations were performed on an IBM 704 computer using a 0.01-megabar pressure increment. A summary of these results are listed in Table IV. Pressure-volume plots of two calculated isentropes are given with Hugoniot data in Figs. 10–25.

On the rarefaction release wave the residual specific internal energy of many of these elements is great enough to cause partial or complete melting. Sufficient thermodynamic data do not exist, however, to permit a complete description of the melting phenomenon at high pressure. The assumption used in these calculations that the Grüneisen γ is a function of volume only necessarily falsifies the detailed description of phase boundaries; however, since the over-all energy (from the Hugoniot locus to $P=0$) is conserved it is felt that the high-pressure thermal description in Table IV is substantially correct. The Riemann integrals U_r, in particular, are primarily dependent upon the P, V, E end points.[13]

Although several metals have enough internal energy to melt after the shock wave is released to zero pressure, it is not possible to state whether melting has actually occurred behind the shock wave. As an aid in answering this question the slopes dP/dT at the melting phase line, computed from known thermodynamic quantities at $P=0$, have been compared with the slopes $(\partial P/\partial T)_s$ of our calculated isentropes (at the same temperature and volume). In every case the slope of the phase line is less than the P-T slope of the calculated isentropes. As can be seen from the phase diagram (Fig. 26) the curvature of the computed isentropes is quite comparable to the curvature of the phase lines determined experimentally.[24] Extrapolations based on the above considerations lead to the conclusion that materials not melted on the pressure-release wave are not melted behind the shock wave. For the group of low-melting-point materials it appears that shock-induced melting should occur behind the shock front somewhere in the experimental region. Similar remarks could be made in regard to the vaporization transformation but with even less certainty.

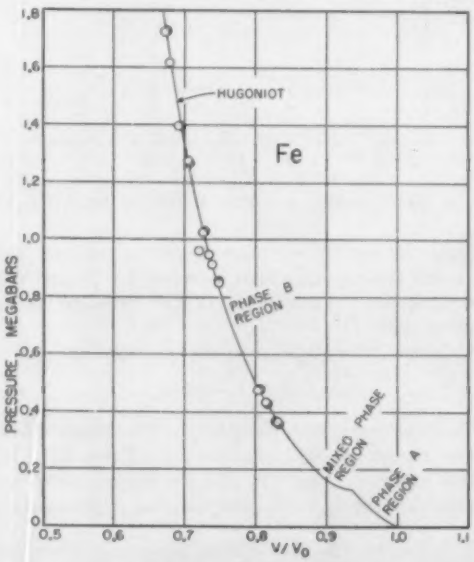

FIG. 28. Hugoniot curve for Fe.

[20] D. R. Stull and G. C. Sinke, *The Thermodynamic Properties of the Elements in Their Standard States* (The Dow Chemical Company, Midland, Michigan, 1955).
[21] *Smithsonian Physical Tables* (The Smithsonian Institution, Washington, D. C., 1956), 9th rev. ed., p. 145.
[22] C. A. Hampel, *Rare Metals Handbook* (Reinhold Publishing Corporation, New York, 1954).
[23] *Metals Handbook* (The American Society for Metals, Cleveland, Ohio, 1948).
[24] V. P. Butuzov and M. G. Gonikberg, Doklady Acad. Nauk S.S.S.R. **91**, 1083 (1953).

Less extensive results are reported for Bi, Fe, and Sb (see Figs. 27–29) because of complications arising from phase changes.[7–12] At low shock pressures these transitions are manifested by a multi-wave structure[3] in the shock front. Although the Hugoniot data are correct this type of transition implies that isentropic-rarefaction waves will become rarefaction shocks,[25,26] which invalidates our calculated free-surface velocities and associated quantities. Temperatures listed in Table V are less reliable because of larger uncertainties in thermodynamic variables needed for the calculations.

It appears from the data (see Fig. 4) that Bi, at a particle velocity of about 0.15 cm/μsec, undergoes a transition to a new state or perhaps back to one of the phases previously discovered.[7] Since Tl melts on relatively weak shocks and because the 40-Kb transition[8,9] is quite small, it has been neglected in the calculations.

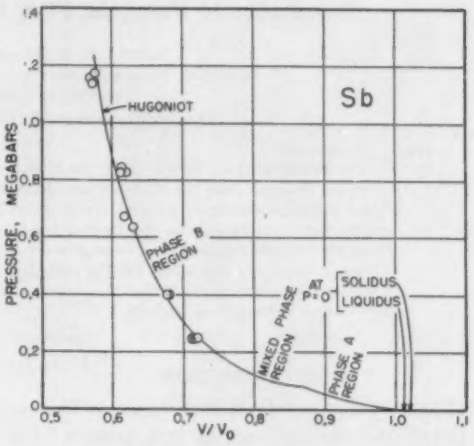

FIG. 29. Hugoniot curve for Sb.

CONCLUSIONS

The accuracy with which the linear relationship $U_s=C+SU_p$ fits the experimental data is quite good. Since the data can be described so simply some credulity can be given to various zero-pressure quantities determined from the coefficients of these fits. The adiabatic compressibility, given by

$$V_0(\partial P/\partial V)_s=-C^2/V_0, \tag{16}$$

can be compared with Professor Bridgman's work (assuming the initial densities are the same) by taking the squares of the coefficients listed in Table III. The dynamic and static values of the zero-pressure "sound speeds" agreed on the average to 1.5% with $C<C_B$ nine times and $C>C_B$ seven times, so that the two types of experimentation appear to be equivalent. Comparable probable errors are found for the two computed Grüneisen's ratios, Eqs. (11) and (13). As shown before,[3] the agreement between these ratios lends support to the Dugdale-MacDonald relationship, used here to generalize the experimental Hugoniot curves to a more complete thermodynamic description.

[25] R. E. Duff (private communication).
[26] W. E. Drummond, J. Appl. Phys. 28, 998 (1957).

ACKNOWLEDGMENTS

In addition to the cooperation of a very large number of people in this Laboratory, the authors wish to acknowledge their gratitude to Felix DePaula, Austin Bonner, and John Chavez, who were in charge of various technical aspects of the experimentation, and especially to John M. Walsh whose aid and encouragement were invaluable.

Resistance to Potential Flow through a Cubical Array of Spheres*

ROBERT E. MEREDITH† AND CHARLES W. TOBIAS
Lawrence Radiation Laboratory, and Department of Chemical Engineering, University of California, Berkeley, California

(Received November 12, 1959; and in final form March 14, 1960)

Precise conductivity measurements on models sectioned out from a cubic lattice of spheres in a continuous medium indicate that the effective conductance of such a system deviates from the values predicted by Lord Rayleigh's analytic solution of this potential distribution problem. Deviations become particularly significant when the spheres approach close packing, and when the conductance of spheres is much greater than that of the continuum. By use of a different function for potential, and by consideration of higher terms in the series expression for the potential in the continuous phase, Rayleigh's results are modified, yielding an analytical expression that represents effective conductance satisfactorily in the concentration region approaching close packing.

INTRODUCTION

INTEREST in the classical problem of evaluating the effective conductance k_m in a uniform medium of conductance k_c that is interrupted by discrete regions of known shape characteristics and of conductance k_d has been renewed in recent years.[1–5] Paralleling Maxwell's treatment,[6] which is valid for very dilute dispersions of spheres, Fricke[7] developed correct relations for the cases when the dispersed phase consists of spheroids.

When the obstacles are no longer very small in comparison to the distance between them, the effects of fields around each particle on each other must further be taken into account. Lord Rayleigh[8] considered the case of a cubic array of uniform size spheres, and analyzed the effect on the potential in the neighborhood of a sphere by 248 of its closest neighbors (lying within the first 15 shells around a central sphere). In essence, Rayleigh solved the Laplace equation for the potential inside and about a sphere by using the principle of superposition to take into account the effects of surrounding spheres on the field in the neighborhood of the central sphere.

The resulting final equation, expressing the conductivity of the mixture in terms of the conductivities of the two phases and the volume fraction is[9]

$$K_m=\frac{[(2+K_d)/(1-K_d)]-2f-0.525[(3-3K_d)/(4+3K_d)]f^{10/3}}{[(2+K_d)/(1-K_d)]+f-0.525[(3-3K_d)/(4+3K_d)]f^{10/3}}, \quad (1)$$

where $K_d=k_d/k_c$, $K_m=k_m/k_c$, and f is the volume fraction of the dispersed phase. Inspection of Eq. (1) reveals that it reduces to Maxwell's relation when $f\rightarrow 0$:

$$K_m=[K_d+2-2f(1-K_d)]/[K_d+2+f(1-K_d)], \quad (2)$$

indicating that at this lower limit the solution becomes exact. With increasing f and also with K_d, the discrepancy between the Maxwell relation and the Rayleigh expression becomes increasingly significant. Of particular interest is the region of volume concentrations when the spherical particles in the cubic lattice nearly touch each other. At $f=0.5236$ the spheres are in point contact and, for $K_d\rightarrow\infty$ therefore, the effective conductance should also approach infinity. Obviously, this condition is approached asymptotically as the volume fraction of the dispersed phase nears this limit in volume fraction.

These qualitative conditions, however, are not satisfied by Rayleigh's equation, neither has Rayleigh elaborated on this point in his definitive work on the subject. To obtain information about this critical region of volume concentrations, an experimental investigation was undertaken, and the steps involved in the mathematical development by Rayleigh were reevaluated.

EXPERIMENTAL

Experimental studies on ordered arrangements of spheres were previously performed by Slawinski,[10] Pearce,[11] and Mashovets.[12] Findings of these authors on identical models are not in good agreement. The

* Work done under the auspices of the U. S. Atomic Energy Commission.

† Present address: Oregon State College, Corvallis, Oregon.

[1] D. Cornell and D. L. Katz, Ind. Eng. Chem. **45**, 2145 (1953).
[2] R. H. Wang and J. G. Knudsen, Ind. Eng. Chem. **50**, 1667 (1958).
[3] R. M. De La Rue and C. W. Tobias, J. Electrochem. Soc. **106**, 827 (1959).
[4] L. Topper, Ind. Eng. Chem. **47**, 1377 (1955).
[5] D. A. deVries, Ind. Eng. Chem. **49**, 1936 (1957).
[6] J. C. Maxwell, *A Treatise on Electricity and Magnetism*, (Clarendon Press, Oxford, 1881), 2nd ed., Vol. 1, p. 435.
[7] H. Fricke, Phys. Rev. **24**, 575 (1924).
[8] Lord Rayleigh, Phys. Mag. **34**, 481 (1892).
[9] This equation includes a numerical correction introduced by I. Runge [Z. Tech. Physik **6**, 61 (1925)]; the coefficient 0.525 replaces 1.65 in the denominator, correcting for the omission of a factor of $1/\pi$ in Rayleigh's derivation.
[10] A. Slawinski, J. Chem. Phys. **23**, 710 (1926).
[11] C. A. R. Pearce, Brit. J. Appl. Phys. **6**, 113 (1955).
[12] V. P. Mashovets, J. Appl. Chem. U.S.S.R. (English Translation) **24**, 391 (1951).

experimental techniques employed and the analysis of data in all three cases point to questions left unresolved.

The conductivity cell used for this study consisted of a unit of cubical geometry defined by lucite walls and silver-plated copper electrodes. Two of these cells were used; one cell was designed to act as a reference unit and to give a measurement of the conductivity of the continuous phase or electrolyte. The overflow outlets and the electrode spacing were such that each cell had the internal dimensions of 5×5×5 in. (see Fig. 1).

Two carefully machined brass or lucite hemispheres were constructed for each run representative of a volume packing. The difference between the volumes of any pair of hemispheres was less than 0.1%. The hemispheres were locked flush against the electrodes by means of locking screws. Tap water was used as the electrolyte in this study, and prior to any measurements the water was circulated between the working cell and the reference cell and allowed to come to equilibrium at room temperature. The liquid level was in both cells carefully brought up to a standard reference mark by use of a hypodermic syringe.

The conductivity bridge used in this study contained components that were symmetrically shielded and arranged to cover from 0.1 to 100 kc with less than 1% absolute error. The results of this study are given in Figs. (3) and (4). At least four measurements were made for every data point that appears in these figures. The typical standard deviation for data taken at each volume fraction is less than 1%.

Conductance measurements obtained with a set of brass hemispheres corresponding to a volume fraction of 0.516 gave K_m values that varied from 5.7 to 7.6 as the bridge frequency was increased from 0.4 to 50 kc. No further variation in the effective conductivity was obtained above 50 kc. Such measurements indicate that polarization can continue to be a source of error up to relatively high frequencies. Pearce's data, taken on a similar model at 0.4 kc, could therefore be in error by as much as 25%.

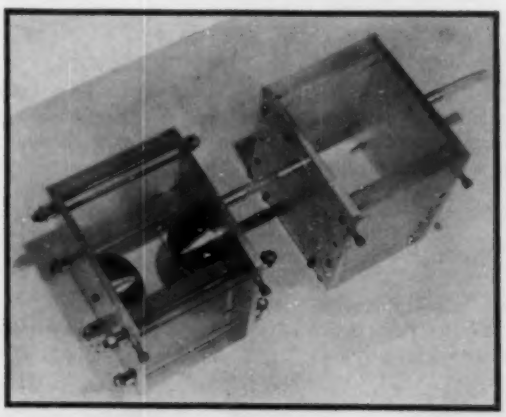

FIG. 1. A view of the cells used in measurements on the ordered arrangements of spheres.

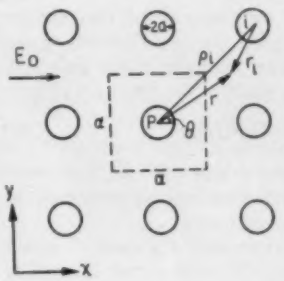

FIG. 2. Section of three-dimensional lattice of spheres.

THEORETICAL

In the original work by Rayleigh, terms higher than those involving the cube of the distance were omitted from the Legendre polynomials which were used to express the potential about the point of origin.[13] This is a perfectly reasonable and acceptable measure, one, however, which should be subjected to scrutiny in regards to limitations it may have introduced.

Rayleigh considered a cubical lattice of spheres oriented in such a manner that the field E_0 pointed in the x direction and was perpendicular to a principal plane of the lattice (Fig. 2). If the shortest distance between spheres is α, then a unit cell consists of a cube with edge length equal to α which contains a sphere of radius a in its center. Let the center of a sphere at point P be chosen as the origin for rectangular coordinates and let θ be an angle in the xy plane. Symmetry considerations require that the potential be reversed when $(\pi-\theta)$ is substituted for θ, and require also that the results be independent of angle in the yz plane. The expressions for the potential in the continuous phase around P and in the dispersed phase which includes P are thus expansions in odd Legendre polynomials P_{2n-1}:

$$V_c = A_0 + \sum_{n=1}^{n=\infty} (A_{2n-1} r^{2n-1} + B_{2n-1} r^{-2n}) P_{2n-1},^{14} \quad (3)$$

$$V_d = \sum_{n=1}^{n=\infty} (C_{2n-1} r^{-2n}) P_{2n-1}. \quad (4)$$

At the interface between the dispersed and continuous phases, the potential and the current must be continuous. Using these boundary conditions, one obtains for the constants in Eq. (3),

$$A_n = B_n \frac{K_d + [(n+1)/n]}{1 - K_d} a^{-(2n+1)}. \quad (5)$$

[13] See footnote reference 8, p. 494, Eq. (61).

[14] The expressions for the potential given in Eqs. (3) and (4) are of a different form from the relations used by Lord Rayleigh. In his work he used series expansions which result in changing the P_{2n-1} term to a Y_{2n-1}, where $P_n = [1 \cdot 3 \cdot 5 \cdots (2n-1)/n!] Y_n$.

An expression for the conductivity of the mixture may be obtained by applying Green's Theorem to the boundary of the continuous medium in the unit cell. From this application one finds

$$K_m = 1 - 4\pi B_1/E_0\alpha^3. \tag{6}$$

For further development a value for $B_1/E_0\alpha^3$ must be found. An approximate value for this term may be arrived at in the following manner:

Note that the potential around P, when P is not included, is given by Eq. (3) with terms containing B omitted. This same potential, however, may be regarded as due to the original field plus sources of potential at each of the neighboring spheres (P not included). This identity can be expressed as

$$A_0 + \sum_{n=1}^{n=\infty} (A_{2n-1} r^{2n-1}) P_{2n-1} = E_0 x + \sum_{n=1}^{n=\infty} \sum_{i=1}^{i=\infty} (B_{2n-1} r_i^{-2n}) P_{2n-1,i}. \tag{7}$$

In this latter expression, the summation in i extends over all spheres in the mixture except the sphere P which is located at the center of the coordinate system. The radius vector and the Legendre Polynomials that appear in this relation are understood to be evaluated with an origin at the ith sphere. That is, if r is a radius vector with respect to the center of the sphere at P and ξ_i, η_i, and ζ_i are the coordinates of the ith sphere with respect to P, then we have

$$x_i = x - \xi_i, \quad y_i = y - \eta_i, \quad z_i = z - \zeta_i \tag{8}$$

and

$$r_i^2 = (x-\xi_i)^2 + (y-\eta_i)^2 + (z-\zeta_i)^2. \tag{9}$$

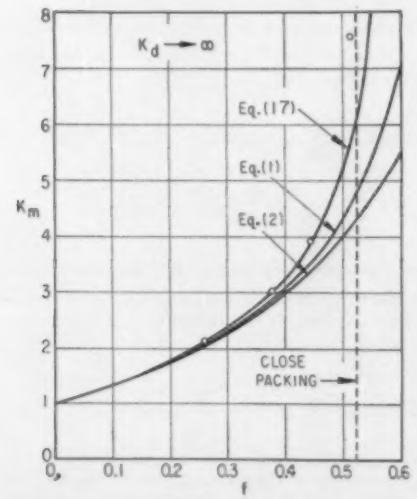

FIG. 3. Comparison of equations by Rayleigh (1), Maxwell (2), and present authors (17). Data points as circles.

For convenience let us also set

$$\rho^2 = \xi^2 + \eta^2 + \zeta^2, \tag{10}$$

so that when r is zero we have $r_i = \rho_i$ with respect to the origin centered at P.

The next step in evaluating $B_1/E_0\alpha^3$ is to take successive derivatives of Eq. (7) with respect to x and evaluate the results at the point P. In performing this latter operation we note that the point (x_i, y_i, z_i) becomes the point (ξ_i, η_i, ζ_i), and r_i is replaced by ρ_i. The Legendre polynomials, $P_{2n-1,i}$ become functions of ξ_i/ρ_i, and we find that the first five derivatives yield

$$\begin{aligned} A_1 - E_0 &= -(2n) B_{2n-1} \rho_i^{-2n-1} P_{2n,i} \\ 6A_3 &= -(2n)(2n+1)(2n+2) B_{2n-1} \rho_i^{-2n-3} P_{2n+2,i} \\ 120A_5 &= -(2n)(2n+1)(2n+2)(2n+3)(2n+4) \\ &\quad \times B_{2n-1} \rho_i^{-2n-5} P_{2n+4,i}, \end{aligned} \tag{11}$$

where summations in n and i extend from unity to infinity.

The coordinates of all spheres with respect to the sphere at P are of the form 1α, $m\alpha$, $n\alpha$, where 1, m, and n are integers. If α is chosen as a unit distance, then we may write

$$\sum_{i=1}^{i=\infty} \rho_i^{-2n-1} P_{2n,i} = \alpha^{-2n-1} S_{2n}, \tag{12}$$

where S_{2n} is now purely numerical and represents a sum over all spheres except the one at P.

Noting that the A's may be expressed in terms of the B's by use of Eq. (5), we may generate an n-by-n matrix in terms of S's and the unknown B's. Thus, by substitution of Eq. (12) into the relations given under Eq. (11), we obtain A_1, A_3, A_5, $\cdots$ in terms of S_2, S_4, S_6, $\cdots$. Rayleigh considered only A_1 and A_3 in terms of S_2 and S_4. A larger expansion yields

$$\begin{aligned} A_1 - E_0 &= -2B_1 S_2 \alpha^{-3} - 4B_3 S_4 \alpha^{-5} - 6B_5 S_6 \alpha^{-7}, \\ A_3 &= -4B_1 S_4 \alpha^{-5} - 20B_3 S_6 \alpha^{-7}, \\ A_5 &= -6B_1 S_6 \alpha^{-7}. \end{aligned} \tag{13}$$

Lord Rayleigh has evaluated S_2 and S_4 for a medium which is infinitely more extended in the direction of the field. He obtains $S_2 = 2\pi/3$ and $S_4 = 3.11$. To evaluate S_6, we use Eq. (12) and obtain

$$S_6 = \sum_{i=1}^{i=\infty} \frac{231\xi_i^6 - 315\xi_i^4\rho_i^2 + 105\xi_i^2\rho_i^4 - 5\rho_i^6}{16\rho_i^{13}}. \tag{14}$$

Numerical evaluation of this sum yields $S_6 = 0.576$.

Noting that the volume fraction of the dispersed phase is given by

$$f = (4\pi/3)(a/\alpha)^3, \tag{15}$$

we can combine the foregoing relations to yield an expression for the conductivity of the system in terms

of K_d and f, i.e.,

$$K_m=1-\left(3f\Big/\left\{\frac{2+K_d}{1-K_d}+f-\frac{1.315f^{10/3}}{[(\frac{4}{3}+K_d)/(1-K_d)]+0.409f^{7/3}}-\frac{0.016(1-K_d)}{[(6/5)+K_d]}f^{14/3}\right\}\right). \tag{16}$$

It may be shown that the last term in the denominator of Eq. (16) is negligible for all values of K_d, and for all $f<0.5236$ (the volume fraction corresponding to maximum packing.) Neglecting this term and rearranging Eq. (16), we obtain our final result in a form similar to that presented by Rayleigh:

$$K_m=\left(\frac{2+K_d}{1-K_d}-2f+0.409\frac{6+3K_d}{4+3K_d}f^{7/3}-2.133\frac{3-3K_d}{4+3K_d}f^{10/3}\right)\Big/$$

$$\left(\frac{2+K_d}{1-K_d}+f+0.409\frac{6+3K_d}{4+3K_d}f^{7/3}-0.906\frac{3-3K_d}{4+3K_d}f^{10/3}\right). \tag{17}$$

DISCUSSIONS AND CONCLUSIONS

Graphical representations of Eq. (17) are given in Figs. (3) and (4), together with the curves corresponding to Rayleigh's original equation and to Maxwell's equation. The experimental data lie very close to the "modified Rayleigh relations," except for the conductivity corresponding to $K_d\rightarrow\infty$ and $f=0.5161$, which is well above the value predicted by the new equation. This behavior is not surprising in view of the neglection of still higher terms in Eq. (11). It should be noted that the inclusion of the term involving S_6 has actually introduced a lower-order term in the volume fraction than the last one given by Rayleigh. The coefficients are such, however, that both the terms in $f^{7/3}$ and $f^{10/3}$ are of the same order of magnitude, and thus if one is used both must be used. It must further be noted that the simple elimination of the term in $f^{7/3}$ from Eq. (17) does not cause the relation to reduce to Rayleigh's equation. This is a consequence both of the steps in rearranging Eq. (16), and of the changes caused by the more rapidly converging series introduced in Eqs. (3) and (4).

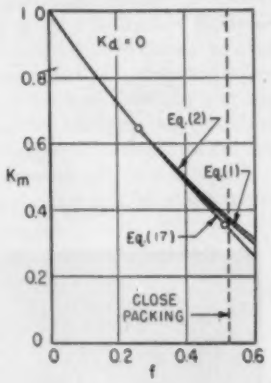

FIG. 4. Comparison of equations by Rayleigh (1), Maxwell (2), and present authors (17). Data points as circles.

In the preceding section we have presented a modified derivation of Rayleigh's equation for the conductivity of a cubic array of spheres in a continuum. The agreement with experimental data is very satisfactory. The influence of close neighboring particles on the field that exists when they are distant is much larger than predicted by the original Rayleigh equation. The degree of improvement over the original Rayleigh equation is obvious in principle, and not negligible for practical purposes.

Photographic Verification of Ultrasonic Plane Wave Scattering by Cylinders

HARMON D. NINE AND NORMAN W. SCHUBRING
Research Laboratories, General Motors Corporation, Warren, Michigan
(Received January 12, 1960; and in final form March 11, 1960)

The ability to photograph the ultrasonic field around a model may obviate the need for extensive mathematical analysis of ultrasonic or analogous field problems. In this paper a method of photographing an instantaneous field invariant in one direction is described. Through use of a parallel-beamed light pulse of very short duration photographs were made of the ultrasonic field of continuous 3-Mc traveling sound waves in water impinging perpendicularly upon the side of a cylindrical tube. Shadowgraphs thus obtained verified the wave shapes predicted by IBM 704 computation of the mathematical analysis.

INTRODUCTION

A NUMBER of investigators have treated the problem of scattering of plane ultrasonic waves from cylinders.[1–6] There has, however, not been a method reported for experimentally resolving the incident and scattered waves. Previous methods were capable of recording only the net intensity of the two waves.

Reported in this paper is a method of viewing the instantaneous wave pattern thus permitting separate identification of the incident and scattered waves that occur when a cylindrical scattering boundary is present. The use of a pulse of light that is short compared to the period of an ultrasonic wave permits the wave to be photographed.

A typical photograph of the scattering of plane ultrasonic waves by a cylinder is shown in Fig. 1. A study was made of photographs of this type. Mathematical analysis of the scattering problem was conducted and the results compared to the shadowgraphs.

EQUIPMENT AND TECHNIQUE

Figure 2 shows schematically the experimental arrangement. The equipment consists of a spark source of the coaxial barium titanate capacitor discharge type,[7] a parabolic mirror, a glass-windowed water-filled test cell, an ultrasonic generator feeding a barium titanate transducer, and a film holder.

A light pulse originating at the spark source strikes the parabolic mirror and is reflected in a parallel beam back through the test cell, forming a shadowgraph on the film. Within the test cell, a barium titanate transducer generates ultrasonic waves in a vertical direction and a cylindrical glass tube, serving as the scattering boundary, is positioned with its axis parallel to the light path and perpendicular to the ultrasonic propagation direction. Tubes of various diameters or other types of scattering boundaries may readily be inserted in the test cell. In the figures discussed, tubes of 0.103-, 0.113-, and 0.468-in. o.d. were used. The spark source employed in this experiment was capable of resolving 7-Mc waves; however, 3-Mc waves gave the best results.

ANALYSIS

The shadowgraphs show the field resulting from ultrasonic waves impinging normally upon the cylindrical surface of a glass tube. An angular reflector seen at the top of each picture serves to destroy standing wave patterns. The tubes are held in position between the two windows by wires or springs at each end which show up as apparent deviations from circular cross section in the shadowgraphs.

Figure 3 is a line drawing to aid in identifying the components of the equipment and the details of the

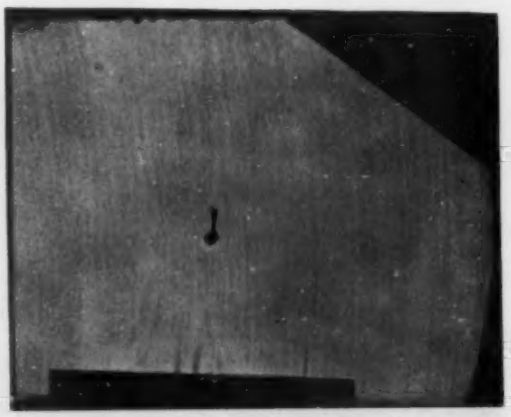

FIG. 1. Typical photograph of the field pattern resulting from 3-Mc ($\lambda=0.019$ in.) compressional ultrasonic plane waves in water incident upon a reflecting cylinder of radius $a=0.051$ in. The supporting wires are outside the field (see Fig. 2) but show as a dark vertical tail on the cylinder and as an apparent deviation from circular geometry. Incident plane waves, quasi-cylindrical reflected waves, transmitted waves and diffracted waves are evident. Note the apparent parabolic waves (discussed in Sec. 5).

[1] P. M. Morse and H. Feshbach, *Methods of Theoretical Physics* (McGraw-Hill Book Company, Inc., New York, 1953), p. 1377.
[2] P. M. Morse, *Vibration and Sound* (McGraw-Hill Book Company, Inc., New York, 1948), p. 346.
[3] L. Bauer, P. Tararkin, and R. B. Lindsay, J. Acoust. Soc. Am. **20**, 858 (1948).
[4] R. H. Cook and P. Chrzanowski, J. Acoust. Soc. Am. **17**, 315 (1946).
[5] M. Lax and H. Feshbach, J. Acoust. Soc. Am. **20**, 108 (1948).
[6] R. M. White, J. Acoust. Soc. Am. **30**, 771 (1948).
[7] J. A. Fitzpatrick, J. C. Hubbard, and W. J. Thaler, J. Appl. Phys. **21**, 1269 (1950).

field pattern which appear in the shadowgraphs. For purposes of analysis the wave pattern has been divided into five sections which are labeled in Fig. 3 and discussed herewith.

1. Plane Wave

The transducer at the bottom of each photograph produces an approximately plane wave in the region photographed. Apparent distortions in the plane waves shown in the figures are attributable in part to fluid flow caused by the high ultrasonic intensities required, and in part to interference between separate patterns.

2. Reflected Wave

The reflected wave is curved and is best seen to the sides of the plane wave beam. A mathematical analysis of the scattering of a plane wave from a cylinder was carried out and the shape of the reflected wave was calculated.

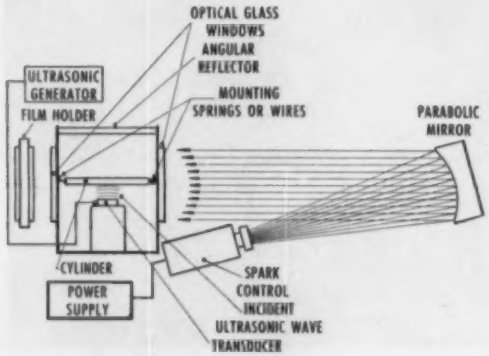

FIG. 2. Schematic drawing of the experimental arrangement for photographing ultrasonic waves.

The expression for an unattenuated plane wave may be written as,

$$\Psi_p = A \exp(ikx - i\omega t). \tag{1}$$

Cylindrical boundaries suggest a change to cylindrical coordinates with their associated Bessel functions:

$$\Psi_p = A \exp(-i\omega t) \sum_{m=0}^{\infty} \epsilon_m i^m J_m(kr) \cos m\phi, \tag{2}$$

where $\epsilon_m = 1$ for $m = 0$ and $\epsilon_m = 2$ for $m > 0$.

A general expression for an outgoing scattered wave from a cylinder is

$$\Psi_s = \exp(-i\omega t) \sum_{m=0}^{\infty} B_m H_m(kr) \cos m\phi, \tag{3}$$

where B_m is an arbitrary constant and $H_m(kr)$ denotes a Hankel function. The Neumann boundary condition, that the normal gradient is specified along the boundary, is applicable for acoustic waves. Thus, assuming the

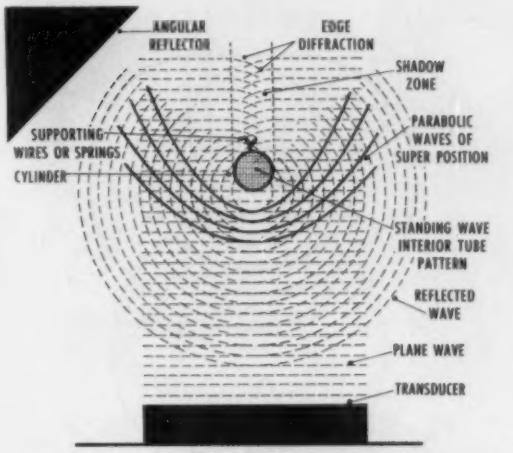

FIG. 3. Line drawing identifying the images on the shadowgraphs and showing the division of the shadowgraphs into sections to aid in analysis and discussion.

cylinder surface to be rigid, one writes

$$(d/dr)(\Psi_p + \Psi_s)|_{r=a} = 0, \tag{4}$$

where a = cylinder radius. Equation (4) yields the following expression for B_m:

$$B_m = -\epsilon_m i^m \frac{[J_{m-1}(ka) - J_{m+1}(ka)]}{\{[J_{m-1}(ka) - J_{m+1}(ka)] + i[N_{m-1}(ka) - N_{m+1}(ka)]\}}, \tag{5}$$

where $N_m(ka)$ is the Bessel function of the second kind. The expression for the scattered wave then becomes

$$\psi_s(r,\phi) = \sum_{m=0}^{\infty} \frac{-\epsilon_m i^m H_m(kr)}{1 + iN_m'(ka)/J_m'(ka)} \cos m\phi, \tag{6}$$

where $\Psi = \psi \exp(-i\omega t)$.

The method of asymptotic approximations normally employed to evaluate Eq. (6) is not valid near the cylinder, i.e., kr small. Therefore, it was necessary to use the full series for satisfactory evaluation. Equation (6) was put in the form $\alpha + i\beta$ and coded for the IBM 704 computer. Recursion formulas and the technique of interval halving were used to solve the equation. For values relatively close to the cylinder ninety-one terms were required to obtain the desired degree of accuracy.

The locus of the reflected wave front corresponds to a line of equal phase of the ψ_s function, i.e., β/α = constant. Figure 4(a) shows plots of the loci of the reflections computed for two wave fronts. Comparison of the computed wave fronts in Fig. 4(a) to the shadowgraphs of Fig. 5, 6, or 7 shows that the calculated reflected shapes agree very well with the shadowgraphs.

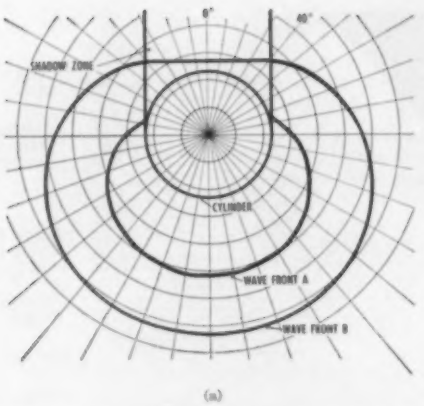

(a)

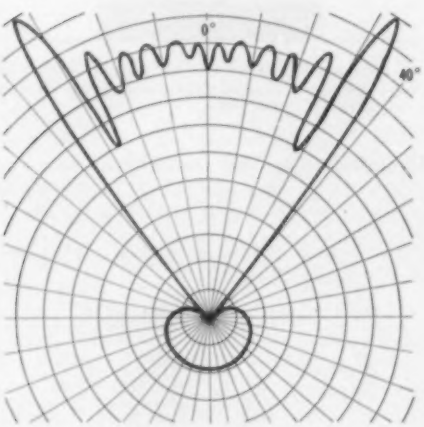

(b)

FIG. 4(a). The calculated wave shapes for waves at two different distances from the tube for the case $a=0.234$ in. For the wave front A which intercepts the tube, the ψ_s function does not converge inside the tube. Note that the solution for wave front B which crosses the shadow region yields a plane wave in the shadow region which for this wave front lies between approximately $\pm 40°$.

FIG. 4(b). Polar plot of the scattered intensity of the Fig. 4(a) case. Note that the intensity drops to zero at approximately $\pm 40°$ which, as seen in Fig. 4(a), corresponds to the edges of the shadow zone for wave front B indicating separation of the solution into a reflected wave and a shadow-forming wave.

3. Shadow Region

The intensity of wave front B for $a=0.234$-in. was also computed and is shown in Fig. 4(b). It is seen that the intensity of the wave drops to zero at about $\pm 40°$ and then goes very high in the region behind the cylinder. This is interpreted to mean that the scattered wave is divided into two parts, a reflected wave and a shadow-forming wave.[8,9] The reflected wave part gives the characteristic curved line in the shadowgraphs and the shadow-forming wave portion destructively interferes with the incident plane wave to give a shadow in the region behind the cylinder. The region directly behind the cylinder which is shielded by the cylinder from the direct path of the plane wave is by definition the shadow region. It is then seen that the ends of the plane shadow-forming wave segment intercept the defined shadow zone boundaries at approximately $\pm 40°$ which also corresponds to the position of vanishing intensity. This indicates a sharp-edged shadow which would be expected for the case of $a \gg \lambda$.

In the actual experimental case some waves appear in the shadow region due to transmission through and diffraction around the cylinder. There is a varying amount of transmission through the cylinder depending upon the wave energy and on the material in the cylinder. For a water-filled cylinder at rather high intensity, as in Fig. 5, the transmission is seen to be

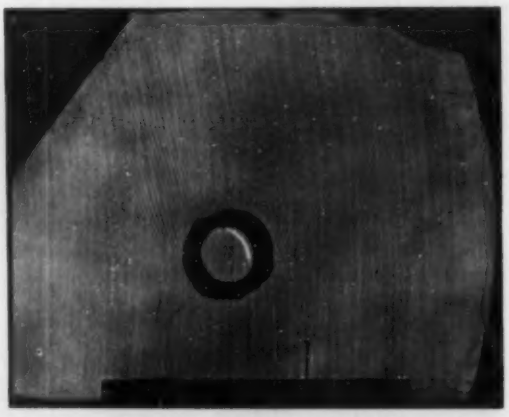

FIG. 5. Field about water-filled tube $a=0.234$ in. at relatively high intensity showing strong transmission. A symmetrical standing wave pattern is visible in the tube interior.

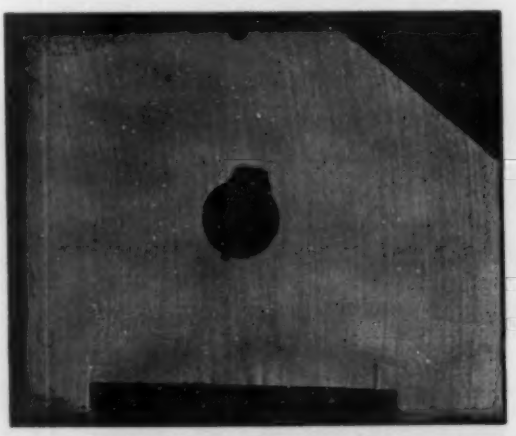

FIG. 6. Air-filled tube $a=0.234$ in. but at lower intensity than Fig. 5 to show a well defined shadow zone. Note some edge diffraction into shadow zone.

[8] See footnote reference 1, p. 1379.
[9] See footnote reference 2, p. 350.

considerable. At relatively low intensity, with an air-filled cylinder as in Fig. 6, the shadow is clearly seen.

Even when $a \gg \lambda$, diffraction of the incident plane wave into the shadow region takes place. Figure 7 shows a good example of diffraction of the plane wave by the cylinder edges into the shadow region as evidenced by the continuity of the plane wave into the curved shape in the shadow zone. The rapid fluctuation of the calculated intensity in the shadow region in Fig. 4(b) is believed to be related to diffraction phenomena.

In cases where $a \rightarrow \lambda$ diffraction plays a greater part in the scattering of the plane wave. In Fig. 8 the scattered wave shape and the intensity for $a=0.057$ in., $\lambda=0.019$ in. is plotted for a wave front relatively far from the tube. The wave shape in this case is not flat in the shadow region nor does the intensity plot show a cutoff at the edge of the shadow region. The shadowgraphs in Figs. 1 and 9, which do not have a shadow, are good examples of this. Further investigation of diffraction is being carried out.

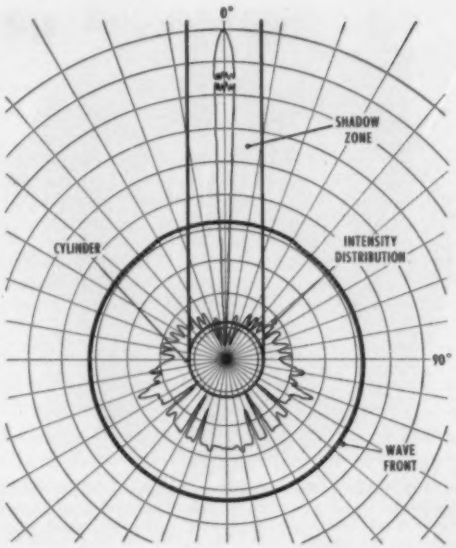

FIG. 8. Calculated wave shape and intensity for a tube of $a=0.057$ in. The non-planer wave shape in the shadow zone and irregularity of the intensity distribution indicate that diffraction becomes important as $a \rightarrow \lambda$.

4. Tube Interior

Waves are transmitted into the interior of the tubes and set up standing wave patterns. In the water-filled tube, Fig. 5, an example of a standing wave pattern can be seen. Symmetry about a vertical line can be noted.

5. Waves of Superposition

Wavelike patterns of approximately parabolic shape may be seen extending outward and upward from near the cylinders in the shadowgraphs. These are especially apparent in Fig. 1. The wave shapes are caused by superposition of the approximately circular reflected wave and the plane incident waves. A model to illustrate this situation was constructed. Figure 10 shows the moire pattern resulting from the superposition of concentric circles and straight lines of the same line spacing. The intersections of the circles and lines form the family of parabolas $x^2=2ny+n^2$, $n=1, 2, 3, \cdots,$. The shadowgraphs do not show the symmetry about a horizontal line exhibited by the model since the reflected wave pattern is not truly circular and is not concentric to the cylinder but displaced downward. Interference in the section under the cylinder due to multiple reflections masks the lower pattern although some downward opening parabolas may be seen in Fig. 9.

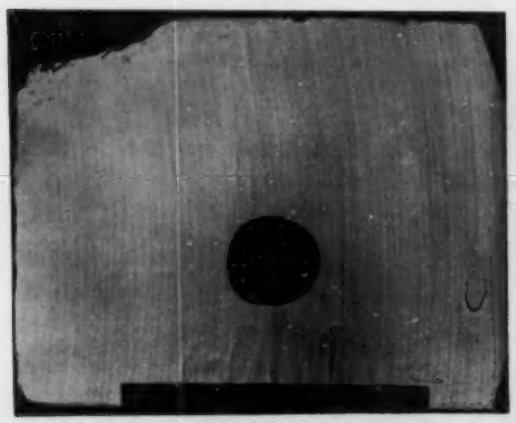

FIG. 7. Same as Fig. 6 but at intermediate intensity to show strong diffraction around the tube into the shadow region.

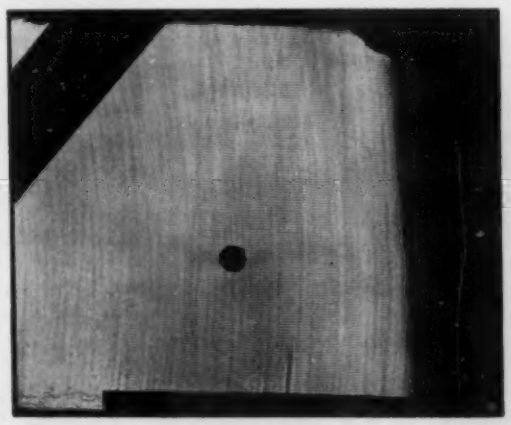

FIG. 9. Similar to Fig. 1 but glass cylinder radius $a=0.057$ in. Note a trace of a parabolic moire pattern opening downward.

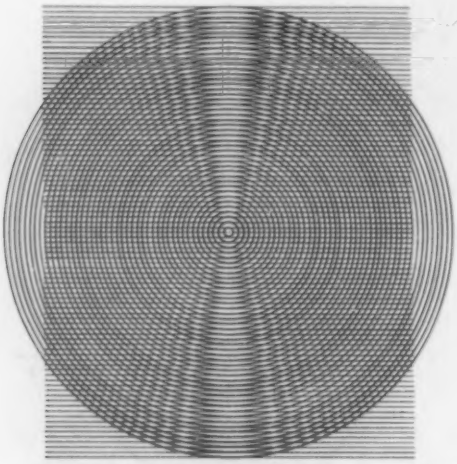

FIG. 10. Parabolic moire pattern resulting from superposition of parallel lines and concentric circles of equal line spacing. The parabolic wave fronts apparent in the shadowgraphs may be explained by this model.

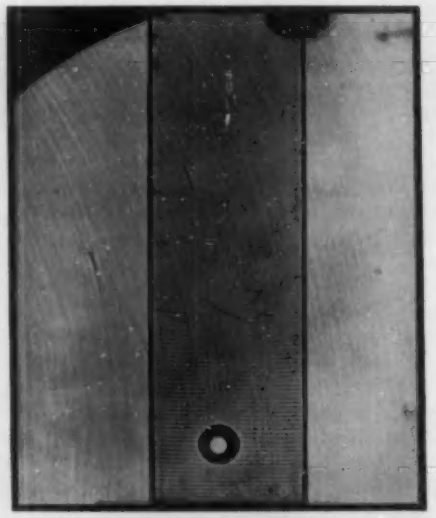

FIG. 11. Plane 3-Mc compressional waves in lucite ($\lambda = 0.038$ in.) scattered by a cylindrical hole. The dark ring around the hole is due to strain in the Lucite resulting from drilling.

CONCLUSIONS

It was found possible to correlate the results of a photographic investigation of ultrasonic wave scattering from cylinders in water with a mathematical analysis of the problem. The success of the photographic method suggests its use in studying field problems of more complex geometries. The method can even be extended to studying waves in solid transparent materials. For example, Fig. 11 shows a traveling compressional plane wave in Lucite being reflected from a drilled hole. Work in Lucite and interpretation of results are now under way.

The technique also holds promise of supplying information on electromagnetic field problems by analogy. However, careful consideration must be given to insure that the boundary conditions parallel those of the ultrasonic model.

ACKNOWLEDGMENTS

The authors are indebted to Robert N. Hollyer, Jr., of the Physics Department for use of his specially designed spark source, optical arrangement and suggestions on the technique of shadowgraph photography.

Valuable discussions with Denos C. Gazis of the Theoretical Physics Department and Lawrence D. Dyer of the Mechanical Development Department are gratefully acknowledged. Finally we wish to thank C. Richard Lewis of the Data Processing Department for his ingenuity in coding and carrying out the IBM 704 computation of the problem.

Gamma Irradiation of Silicon. I. Levels in *n*-Type Material Containing Oxygen

E. SONDER AND L. C. TEMPLETON
Solid State Division, Oak Ridge National Laboratory, Oak Ridge, Tennessee*
(Received January 29, 1960; and in final form March 17, 1960)

The resistivity and Hall coefficient of *n*-type silicon containing oxygen have been measured as a function of temperature before and after a number of successive irradiations in a Co^{60} gamma-ray source. A net acceptor level 0.17 ev below the conduction band was observed to result from the irradiation. Its rate of introduction was 7×10^{-4} traps/cm³ per photon/cm² in 50- ohm-cm material and was about twice that in more heavily doped material (~2 ohm-cm). Acceptor levels, lying deep within the forbidden gap, were also observed. Their total introduction rate was smaller than that of the 0.17-ev level by a factor of 50. A lowering of the mobility below ~100°K was also a result of the irradiations. In heavily irradiated samples this lowering of the mobility was much greater than could be explained on the basis of point-charge scattering.

I. INTRODUCTION

THE electrical properties of semiconductors are very sensitive to irradiation by energetic particles. As a result, the study of changes of these properties due to irradiation has been used extensively for investigations of radiation damage.[1] The findings have, in a general way, been consistent with the idea that irradiation-produced defects create energy levels in the forbidden gap of the semiconductor and that these can act as acceptors or donors of current carriers. In the simple model proposed by James and Lark-Horovitz[2] the irradiating particle was thought to create a number of vacancy-interstitial pairs, each member of the pair being the source of possibly two levels in the gap. Unfortunately, much of the data accumulated in recent years have indicated that additional complications exist. Different results have been obtained with different types of irradiation[3,4] and different energies of irradiation particles.[5] This in itself would not be too difficult to treat. The introduction of defects, however, seems also to be affected by the type and density of imperfections and impurities in the sample,[6] as well as by the temperature and Fermi level at the time of irradiation.[7,8] It now seems evident that the detailed structure of the damage seen at room temperature is a result not only of the irradiation but also of rearrangement processes which involve imperfections and impurities present before irradiation.

Much of the work in the past has been performed with germanium, where a profusion of energy levels has been seen.[1] Silicon has been investigated less intensively, even though it seems to be somewhat more desirable for irradiation studies because of its larger energy gap and the consequent expectation that the irradiation-produced energy levels are further apart and might, therefore, be more easily resolved.

The investigation, the first results of which are reported here, was started with the intent of investigating a relatively simple system. Cobalt-60 gamma rays were used; these create Compton electrons with energies in the range of 1 Mev or less, uniformly throughout the sample, thus creating a uniform distribution of damage sites. Since the energy of each damaging electron is relatively small, one or at most two displacements are produced at each damage site. The use of gamma rays also permits precise comparison of the introduction rate of defects or levels in different samples irradiated in the same source.

II. EXPERIMENT AND RESULTS

A total of five samples of *n*-type silicon was used in these measurements. The initial resistivities of these samples were distributed over the range 2–50 ohm-cm; the measurements covered the temperature range 50–300°K, making it possible to probe a portion of the forbidden gap between 0.05 and 0.4 ev below the conduction band. The characteristics of the samples are listed in Table I.

The Hall effect (using 7.5 kgauss) and resistivity were measured as a function of temperature before the samples were irradiated and after a number of successive room-temperature irradiations. The radiation history is also shown in Table I. The different irradiation dosages were obtained by irradiating the samples in a Co^{60} gamma-ray source for times of a few hours to a few weeks in a flux of 1.0×10^{12} photons/cm² sec. This value was obtained by use of Ceric Sulphate solution calibration capsules.

Results of Hall effect measurements on one of the samples (1019-2) are shown in Fig. 1. Very similar curves were obtained for all samples. The most obvious result of the gamma irradiation is the increase in Hall

* Oak Ridge National Laboratory is operated by the Union Carbide Corporation for the U. S. Atomic Energy Commission.

[1] For a review of radiation effects in semiconductors, see, for instance, J. H. Crawford, Jr., and J. W. Cleland, *Progress in Semiconductors* (John Wiley & Sons, Inc., New York, 1957), Vol. 2, p. 67; or J. Appl. Phys. **30**, 1117 ff. (1959), containing papers and discussions presented at the Conference on Radiation Effects in Semiconductors, Gatlinburg, Tennessee, May, 1959.

[2] H. M. James and K. Lark-Horovitz, Z. physik Chem. (Leipzig) **198**, 107 (1951).

[3] G. K. Wertheim, Phys. Rev. **111**, 1500 (1958).

[4] E. I. Blount, J. Appl. Phys. **30**, 1218 (1959).

[5] D. E. Hill, Phys. Rev. **114**, 1414 (1959).

[6] G. D. Watkins, J. W. Corbett, and R. M. Walker, J. Appl. Phys. **30**, 1198 (1959).

[7] J. W. Cleland and J. H. Crawford, Jr., J. Appl. Phys. **29**, 149 (1958).

[8] G. K. Wertheim, Phys. Rev. **115**, 568 (1959).

TABLE I. Characteristics and radiation history of samples used.

Sample designation	Resistivity (300°K) ohm-cm	Donor density[a] cm^{-3}	Acceptor density[a] cm^{-3}	Irradiation number	Irradiation dosage photons/cm^2	Total dosage at end of irradiating photons/cm^2
1019-2	2.1	2.4×10^{15}	3.6×10^{14}	1	6.0×10^{17}	6.0×10^{17}
				2	6.4×10^{17}	1.24×10^{18}
				3	4.2×10^{17}	1.66×10^{18}
				4	7.0×10^{17}	2.36×10^{18}
1123-2	11.9	4.3×10^{14}	1.0×10^{14}	1	1.10×10^{17}	1.10×10^{17}
				2	1.51×10^{17}	2.61×10^{17}
				3	5.5×10^{16}	3.16×10^{17}
1123-4	30	2.1×10^{14}	9×10^{13}	1	4.64×10^{16}	4.64×10^{16}
				2	4.49×10^{16}	9.13×10^{16}
				3	5.49×10^{16}	1.46×10^{17}
				4	2.53×10^{16}	1.71×10^{17}
				5	4.88×10^{17}	6.60×10^{17}
1123-3	53	1.4×10^{14}	6.6×10^{13}	1	2.81×10^{16}	2.81×10^{16}
				2	7.05×10^{16}	9.86×10^{16}
				3	7.2×10^{15}	1.06×10^{17}
1123-30	56	1.4×10^{14}	6.6×10^{13}	1	8.17×10^{16}	8.17×10^{16}
				2	2.56×10^{16}	1.07×10^{17}
				3	4.35×10^{16}	1.50×10^{17}
				4	2.29×10^{17}	3.80×10^{17}
				5	4.25×10^{17}	8.05×10^{17}

[a] These values were obtained using Hall effect results to determine N_D-N_A and estimates of compensation supplied by the manufacturer, Silicon Crystals, Inc., Wilmington, Delaware.

coefficient at temperatures below 250°K. If the relationship between Hall coefficient R and number of electrons n in the conduction band is

$$R=\gamma/ne, \tag{1}$$

where the mobility ratio, $\gamma=\mu_H/\mu$, is of the order of one, then it is evident that the main effect of the irradiation is the introduction of a net acceptor level in the upper half of the energy gap. The slope of the Hall effect and resistivity curves locate it roughly between 0.15 and 0.2 ev below the conduction band. A more precise analysis to determine the location of the level is performed herein. There was evidence, especially after long irradiation, of additional net acceptor levels deep (at least 0.4 ev) in the forbidden gap.[9] Measurements at room temperature indicated that these deep acceptors were introduced at a rate of about 2×10^{-5} traps/cm^3 per photon/cm^2, or a factor of 50 more slowly than the level located between 0.15 and 0.2 ev below the conduction band.

Figure 2 shows the temperature variation of the mobility of one of the samples measured. In general, for all the samples, there was little change in mobility above about 150°K. However, below that, the irradiations caused an appreciable lowering of the mobility for all specimens studied.

III. ANALYSIS AND DISCUSSION OF RESULTS

A. Introduction Rate for Acceptor Levels

If it is assumed that the radiation-produced change in Hall coefficient results from the introduction of a single electron trapping level,[10] then it is fairly simple to determine the number of such states present. In the range near 110°K ($1000/T=9$) it is evident from Fig. 1 that most of the donors are ionized, while most of the traps are filled. Thus, the number of current carriers in the conduction band should be equal to the difference between the number of electrons donated by the phosphorous atoms N and the number of traps introduced by the irradiation N_T, i.e., $n=N-N_T$, so that the number of trapping centers is given by the equation

$$N_T=N-n=\gamma/eR \text{ (unirradiated)}$$
$$-\gamma/eR \text{ (irradiated)}. \tag{2}$$

Figure 3 shows how the number of introduced traps [calculated using Eq. (2)] increases with gamma dose for the samples used in this investigation. Although the absolute calibration of the gamma flux may be somewhat in error,[11] the relative flux used in the

[9] A level 0.4 ev below the conduction band has been seen by Hill[6] and also by Wertheim (private communication). In both cases its introduction rate was about a factor of 40 smaller than the introduction rate of the 0.17-ev level.

[10] We shall refer to the irradiation-produced levels as "trapping" levels so as not to confuse them with chemical acceptor levels. They should not be confused with metastable traps usually considered in lifetime measurements.

[11] It has been suggested that the large introduction rate differences observed with gamma-produced Compton electrons and accelerator electrons are perhaps due to the fact that, in a cylindrical source of the type we use, the internal scattering produces a large low energy flux which would tend to register in the calibrating dosimeter but would cause little damage. That some such effect exists is no doubt true [see, for instance, measurements by W. Bernstein and R. H. Schuler, Nucleonics 13, 11, 110 (1955)]. However, calculations of the internal scattering of our source make it clear that this effect could cause at most an error of 30–50%, not a factor of ten. Using the calibration (1878 C; this was obtained by comparison with other Co^{60} standards which were, in turn, calibrated using coincidence counting on the 0.3-Mev electron and the 1.37-Mev gamma ray) of the 1-cm diam slugs which make up our source, it is estimated that 1.1×10^{12} photons would reach the sample if there were no scattering; and 0.8×10^{12} unscattered photons would reach it when internal absorption and scattering are taken into consideration.

various samples is much more accurate, since the same source was used and a decay correction was applied when samples were irradiated at dates differing more than a few weeks. There is a source of possible error which should be kept in mind. This is the uncertainty in the mobility ratio γ in Eq. (1). In the calculations cognizance was taken of the temperature dependence of γ.[12] However, because of a lack of accurate knowledge of the change in γ with trap introduction, the constant was assumed to remain unchanged by the irradiation. If there were a change, it would probably be in the direction of increasing γ, as one might expect a fairly large impurity contribution to the electron scattering.

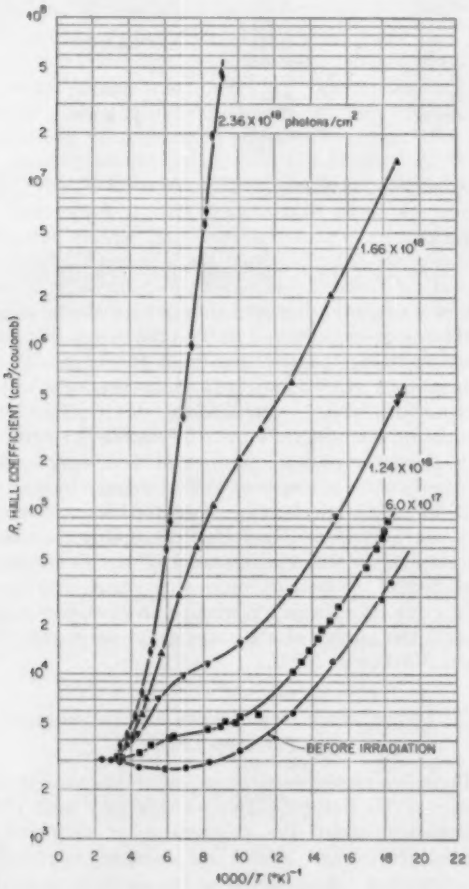

FIG. 1. Hall coefficient of sample 1019-2 as a function of temperature. The different curves were obtained after irradiating with a total gamma-ray dose as shown.

[12] The temperature variation of the mobility ratio was obtained from the variation of the pre-irradiation Hall data of the various samples in the range where the donors are ionized and where n should be independent of temperature. Our results agree with the much more careful analysis of the mobility ratio made by D. Long and J. Myers [Phys. Rev. 115, 1107 (1959)].

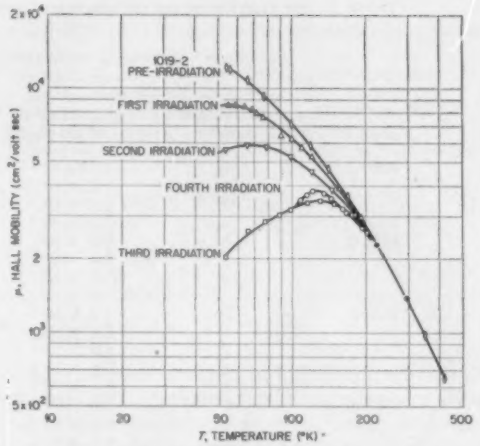

FIG. 2. The Hall mobility of sample 1019-2 as a function of temperature and irradiation.

This would tend to accentuate the slight curvature apparent in the curves of Fig. 3.

The slopes of the curves in Fig. 3 give the introduction rates, which, as can be seen, vary monotonically with the density of donors. Values are given in Table II, together with information concerning doping and Fermi level. There was no correlation between the introduction rates and the oxygen content of the samples, the latter being the same, $5\pm1\times10^{17}$ cm^{-3} (obtained by infrared absorption) in all specimens.

B. Pinning of the Fermi Level

One method of determining the position of an energy level in the forbidden gap is to observe how the Fermi

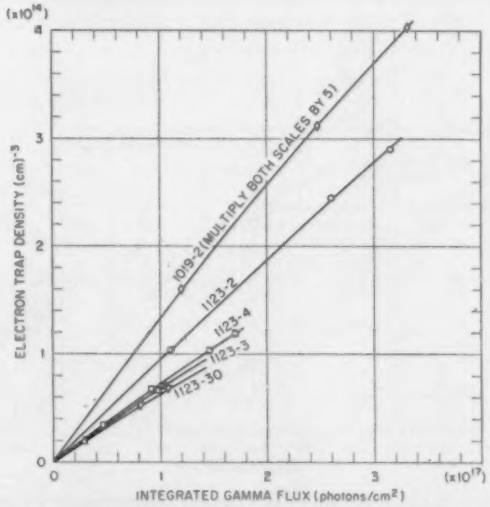

FIG. 3. The density of net acceptors introduced by Co^{60} gamma rays for various samples.

TABLE II. Introduction rate of electron traps compared with Fermi level and initial characteristics of sample.

Sample	Irradiation number	Approximate introduction rate at end of irradiation (Traps/cm³ per photon/cm²)	Measuring temperature (110°K) Fermi level (ev)	Irradiation temperature (311°K) Fermi level (ev)	Initial phosphorous content $(cm)^{-3}$
1019-2	0	1.35×10^{-3}	−0.076	−0.255	2.4×10^{15}
	1	1.25×10^{-3}	−0.082	−0.256	
	2	1.15×10^{-3}	−0.091	−0.257	
	3	1.10×10^{-3}	−0.113	−0.250	
1123-2	0	9.5×10^{4}	−0.092	−0.304	4.3×10^{14}
	1	9.4×10^{4}	−0.094	−0.304	
	2	9.2×10^{4}	−0.103	−0.305	
	3	8.8×10^{4}	−0.110	−0.305	
1123-4	0	7.5×10^{-4}	−0.102	−0.332	2.1×10^{14}
	1	7.1×10^{-4}	−0.105	−0.332	
	2	6.9×10^{-4}	−0.109	−0.332	
	3	6.6×10^{-4}	−0.118	−0.332	
	4	6.4×10^{-4}	−0.131	−0.332	
1123-3	0	7.1×10^{-4}	−0.105	−0.343	1.4×10^{14}
	1	6.8×10^{-4}	−0.108	−0.343	
	2	6.6×10^{-4}	−0.128	−0.343	
	3	6.4×10^{-4}	−0.135	−0.343	
1123-30	0	7.0×10^{-4}	−0.106	−0.344	1.4×10^{14}
	1	6.2×10^{-4}	−0.116	−0.344	
	2	6.0×10^{-4}	−0.127	−0.344	

level is affected by the introduction of this state. The temperature dependence of the Fermi level is shown for one of the samples in Fig. 4. It is quite evident in the case of the unirradiated or slightly irradiated samples that the Fermi level at low temperatures tends toward 0.05 ev, i.e., toward the position of the phosphorous donor. However, when the number of irradiation-produced traps exceeds the number of electrons donated by the phosphorous atoms, the Fermi energy levels off near 0.165 ev. The position of the trapping state can be obtained from the percentage occupancy, N/N_T, of the trap, which should be equal to the Fermi function, i.e.,

$$N/N_T=\{1+(\omega^0/\omega^-)\exp[(E_T-\xi)/kT]\}^{-1},$$

where ω^0/ω^- is the degeneracy ratio between the empty and full trapping state and $E_T-\xi$ is the energy difference between the trap and Fermi level. In the case of the two samples 1019-2 and 1123-30, the ratio, N/N_T is 0.75 and 0.8, respectively, yielding −0.176 and −0.177 ev for the quantity $[E_T-E_c+kT\ln\omega^0/\omega^-]$ at 100°K. It is of interest that the position of the energy level is nearly the same in two samples that differed by a factor of 27 in their original donor concentration.

A comment should be added concerning the above calculation. In the determination of the Fermi level, any effect of the mobility ratio, γ, was neglected. For a 50% error in γ (which is about the most one might expect) the energy of the trap would be in error by about 0.003 ev at 100°K.

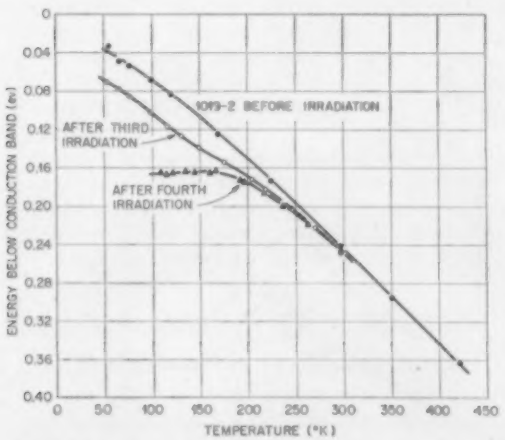

FIG. 4. The Fermi energy as a function of temperature for two samples and a number of irradiations. The ordinate in the notation of the text is $(E_c-\xi)$.

C. Temperature Dependence and Degeneracy of the Trap Level

There is a more sensitive method of determining the energy of the trapping level, which may also yield information about the degeneracy or temperature dependence of the level. This consists, essentially, of considering the ionization of the electrons from the trapping level as a chemical reaction and then plotting log equilibrium constant vs reciprocal temperature. For negatively charged traps (N_T^-/cm^3) in chemical equilibrium with empty traps (N_T^0/cm^3) and conduction electrons (n/cm^3) the equilibrium constant, K, can be written in the form

$$K=N_T^0 n/N_T^-=(\omega^0/\omega^-)AT^{\frac{3}{2}}\exp(E_T-E_c)/kT, \quad (5)$$

TABLE III. Parameters of trapping level observed in the various samples.

Specimen	Irradiation number[a]	Ratio of electrons available to number of traps (N/N_T)	Temperature independent part of trap energy $E_{T_0}-E_c$ (ev)	Temperature dependent part of trap energy (assuming $\omega^0/\omega^-=1$) (ev/deg K)	Degeneracy ratio ω^0/ω^- (assuming $\alpha=0$)
1019-2	4	1.3	−0.170	-5.3×10^{-4}	0.59
1123-30	3	1.2	−0.173	-1.1×10^{-4}	0.27
1123-30	2	0.88			
1123-3	3	0.96	∼−0.173	-1×10^{-4}	∼0.27
1123-3	2	0.91			
1019-2	3	0.98			
1123-2	3	0.88	∼−0.146	-2×10^{-4}	0.11
1123-2	2	0.74			

[a] This refers to irradiation completed before measurements were made.

where $A=12[2\pi m^*kT/h^2]^{\frac{3}{2}}=5.45\times10^{15}$ and E_T-E_c is the position of the energy level with respect to the conduction band edge. Since the total number of traps N_T equal to the sum $N_T^0+N_T^-$, can be determined (see Sec. 3.A) and since the number of electrons in the conduction band is equal to the difference between the number of net donors and the number of filled traps,[12] i.e., $n=N-N_T^-$, the equilibrium constant can be determined in the temperature range in which ionization of the trap level is taking place, namely, 110–250°K. Figure 5 shows $\log K/AT^{\frac{3}{2}}$ plotted versus reciprocal temperature for two of the samples after heavy irradiation. If it is assumed that the temperature dependence of the trap position is only of the first power, i.e., $E_T=E_{T_0}+\alpha T$, then the temperature-independent part of the activation energy (E_{T_0}) and a value for $\alpha+k\ln(\omega^0/\omega^-)$ can be obtained from the slope and intercept, respectively, of the curve. Unfortunately, it is not possible in this type of analysis to separate the effect due to degeneracy from that due to temperature dependence of the trapping level. In Table III are given values obtained from Fig. 5 for E_{T_0}, α (assuming $\omega^0/\omega^-=1$) and ω^0/ω^- (assuming $\alpha=0$).

Although the data shown in Fig. 5 indicate that the trapping level is the same for the two samples shown and that it is a discrete simple level, there is some indication from other data obtained that this may not be quite the case. Figure 6 shows results of identical analyses made for some other conditions and samples, superimposed upon one of the curves shown in Fig. 5. In the case of the purer samples (1123-3 and 1123-30) there seems to be no anomaly. However, in the case of the more heavily doped samples (1123-2 and 1019-2) when there are less traps than there are donor electrons, the trapping level appears to be somewhat closer to the conduction band. Values are given in Table III.

A rough estimate can be made of the separation between traps that would be necessary to account for trapping states as much as 0.02 ev above the 0.17 level. If an electron filled a site at a distance r from the one we are considering, then the energy level located at the site in question would be raised an amount $\Delta E=e^2/Kr$, by the electrostatic interaction. For $\Delta E=0.02$ ev and a dielectric constant K of 11.9, the separation distance r would be about 50 A. Now, if a random distribution of sites is assumed, it can be shown that about half of the

TABLE IV. Comparison of introduction rate of 0.17-ev net acceptor for electron and gamma ray irradiation.

Author(s)	Type and energy of irradiation	Resistivity of material (ohm-cm)	Temperature of irradiation (°K)	Introduction rate of traps (traps/cm³ per particle/cm²) per Co^{60} photon	per electron (assuming 0.3 ev threshold)	per electron (assuming 0.6 ev threshold)	per accelerator electron
Sonder and Templeton	Co^{60} gamma	2	311	1.35×10^{-3}	0.013	0.019	
		11	311	9.5×10^{-4}	0.009	0.013	
		50	311	7.1×10^{-4}	0.007	0.009	
Willardson[a]	Co^{60} gamma	1000	probably room temperature	$\sim1\times10^{-3}$	∼0.01	∼0.014	
Wertheim[b]	0.7 Mev electrons	0.4	333				0.35
	0.7 Mev electrons	7	333				0.16
Hill[c]	0.7 Mev electrons	0.5	273				0.22
	4.5 Mev electrons	16	273				0.1

[a] R. K. Willardson, J. Appl. Phys. 30, 1158 (1959).
[b] G. K. Wertheim, footnote references 8 and 15 and private communication.
[c] D. E. Hill, footnote reference 5.

[12] At the lower temperatures electrons will begin to freeze out at donors as well as at trap sites. Corrections for freezeout at donors were included in the calculations. These corrections were usually negligible and were, at most, a few percent.

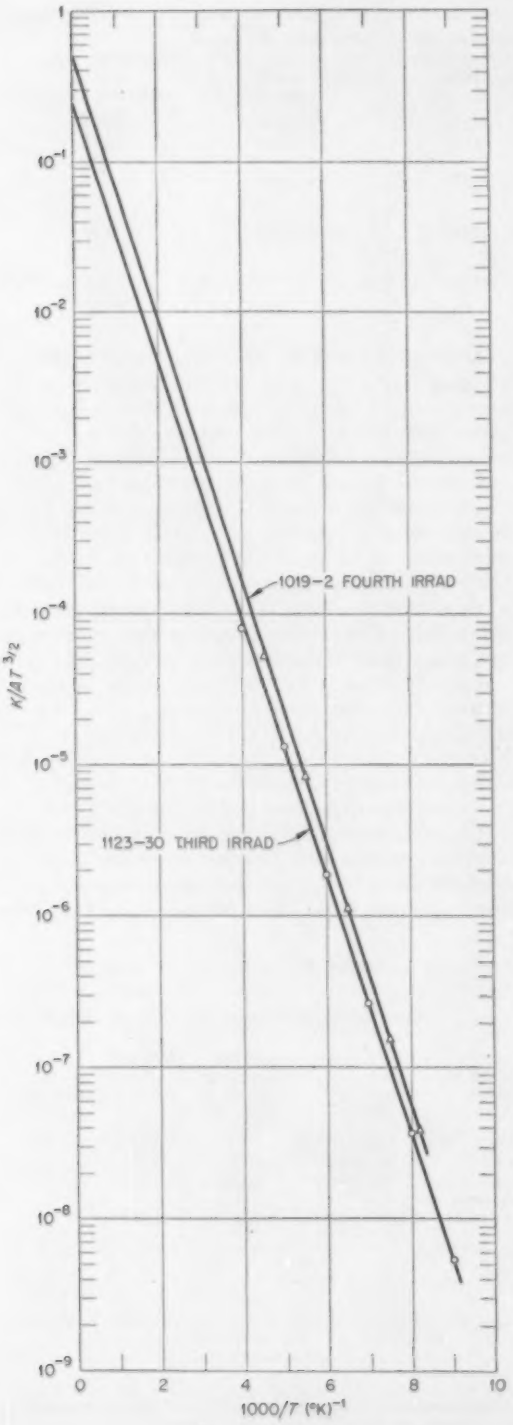

FIG. 5. Plot of $\ln K/AT^{\frac{3}{2}}$ vs reciprocal temperature for two samples containing more net acceptors than there are donor electrons. See text for discussion.

sites will be within a distance of $\frac{1}{2}N_T^{-\frac{1}{3}}$ of each other.[14] For a sample containing 10^{15} traps, this would also be at a distance of 50 A. This is of the correct order of magnitude and in the right direction to account for the apparent change in trap energy observed.

The position in the forbidden gap of the level seen in this investigation is roughly the same as that of a level seen in *n*-type silicon irradiated with 0.3-,[5] 0.7-,[5,15] 1.0-,[15] and 4.5-[5] Mev electrons. The much slower introduction of an additional deep-lying acceptor also is similar to what has been seen in the case of electron irradiation.[5] These results are not surprising, in view of the assumption that the damage in gamma-irradiated silicon is accomplished actually by the Compton electrons. A comparison of introduction rates of electron traps indicates that a 0.7-Mev electron is about a factor of 100–200 more efficient for causing damage than is a Co^{60} gamma ray. If the efficiency of creation of Compton electrons is computed, it is found that electrons produced by gamma rays produce less damage than do electrons of comparable energies from an accelerator by an order of magnitude. Values of introduction rates per photon and per electron are shown in Table IV. They have been computed assuming a uniform energy of 1.2 Mev for the photons produced in the gamma source and thresholds of 0.3 and 0.6 Mev for production of damage in the silicon by the Compton electrons. (It is evident from the table that the choice of threshold has only a small effect on the introduction rate per Compton electron with energy above the threshold.) Since the introduction rate for gamma irradiation is smaller than that for accelerator irradiation, the effect of an additional damage process in the gamma case as, for instance, contributions of photo electrons, would be in the wrong direction to explain the order-of-magnitude discrepancy. Neither could the degradation of the photon energy due to self absorption in the cobalt source explain such a large difference.[11]

D. Mobility

An attempt was made to compare observed data with estimates of changes of mobility that would result from various simple models of the irradiation-produced center. These included: (a) a simple acceptor which is negatively charged when an electron is frozen out on it and which is uncharged when empty; (b) equal numbers of donors and lower-lying acceptors, in which case the acceptors contain the charge of one electron, while the donor is uncharged when full and charged when empty; (c) similar centers which, when filled, contain charge Ze where the number of electronic

[14] E. Sonder and H. C. Schweinler, Phys. Rev. **117**, 1216 (1960).
[15] G. K. Wertheim, Phys. Rev. **110**, 1272 (1958).

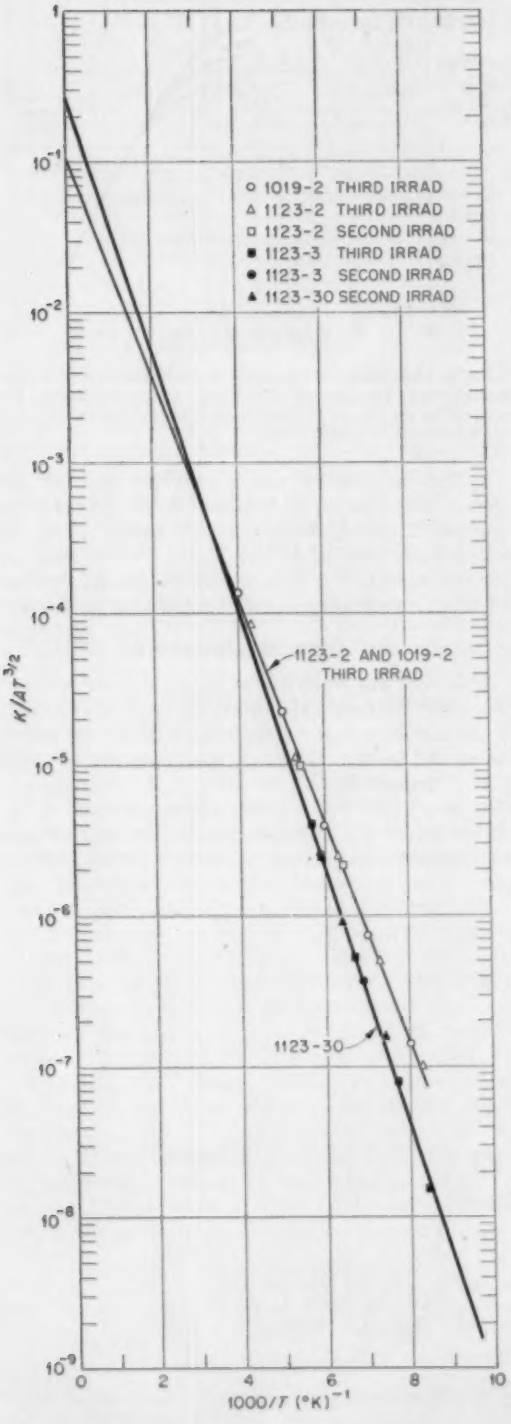

FIG. 6. Plot of $\ln K/AT^{\frac{3}{2}}$ vs reciprocal temperature for samples containing less net acceptors than there are donor electrons. The heavy curve labeled 1123-30 is reproduced from Fig. 5. The light curve is drawn to connect the open points shown.

charges Z is greater than one. The Brooks Herring[16] formula was used for the calculations.

In Fig. 7 are shown some experimental data points and curves calculated using the simple models. Since charged impurity scattering becomes important only at low temperature where all the traps are filled, models *a* and *b* will give identical curves. These are labeled $Z=1$ in Fig. 7. It is evident that these models do not account for the data. Even with high values of charge (curves for $Z=5$ are shown) agreement cannot be obtained.

Probably what is observed in this sample is not due to point-charge scattering at all but, rather, to variations in Fermi level with position within the sample. Since the irradiation has increased the resistivity of the samples used in this study by a factor of 100 or more, a gradient in the donor concentration of the original sample of only 1% would cause a variation with position of 100% after heavy irradiation. Such a variation of donor concentration would cause a high value of resistivity to be obtained. This is because the method of measuring the resistivity consists of determining the voltage drop across two probes ~ 1 cm apart, thus emphasizing the contributions of any highly resistive portions of the sample. This effect would be especially great at low temperatures when kT becomes as small as the variations in Fermi level along the sample due to inhomogeneities, thus interposing potential barriers. Since the Hall coefficient is less strongly affected by gradients of donor concentration, an anomalously high resistivity would appear as a low mobility on our graphs.

If we now limit ourselves to the data obtained under conditions where this effect of nonuniformities might be minimized, we might still be able to obtain some useful information about the charge of the scattering centers. Unfortunately, those are just the cases where the irradiation and, therefore, the mobility changes are small. The data shown in Fig. 8 for a light irradiation of one of the samples fall somewhere between curves calculated for $Z=1$ and $Z=2$.

These mobility results are roughly in agreement with electron irradiation work. Wertheim,[18] who irradiated his samples relatively lightly, found that charged impurity scattering with $Z=1$ would account for the mobility changes observed in a 0.4 ohm-cm sample. Hill,[6] who irradiated more heavily, observed, as did we, much larger changes in the Hall mobility.

IV. SUMMARY

1. The predominant effect of irradiating oxygen-containing *n*-type silicon with Co^{60} gamma rays is the

[16] F. J. Blatt, in *Solid State Physics*, edited by F. Seitz and D. Turnbull (Academic Press, Inc., New York, 1957), Vol. 4, pp. 199–366 and references therein.

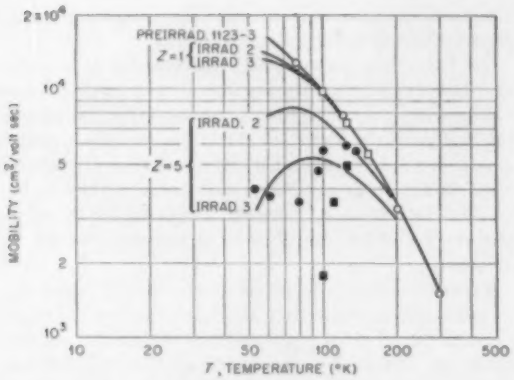

FIG. 7. Comparison of computed mobility curves with experimental results for specimen 1123-3. The experimental points are for the following conditions: ○ before irradiation, □ after first irradiation, ● after second irradiation, ■ after third irradiation.

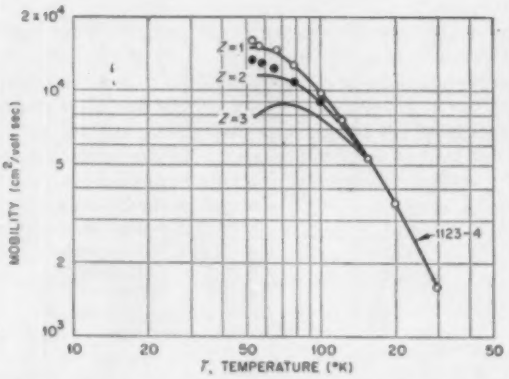

FIG. 8. Comparison of computed mobility curves with experimental results for specimen 1123-4 after a light irradiation. The open circles are the pre-irradiation data; the filled circles are data taken after the first irradiation.

production of a single discrete net acceptor level 0.17 ev below the conduction band. Additional acceptors, deep in the gap, are also produced but at a rate about a factor of 50 smaller.

2. There is some indication in the more heavily doped material ($\sim 10^{15}$ cm^{-3}) of structure in the 0.17-ev level. This may be caused by electrostatic interaction of closely situated centers.

3. The introduction rate of these centers is dependent upon the initial characteristics of the sample. It is about a factor of two higher in material containing 2×10^{15} donors/cm^3 than it is in material containing only 1×10^{14} donors/cm^3. There is also a slight decrease (10–20%) of introduction rate as irradiation proceeds in the various samples.

4. The introduction rate ($\sim 1\times10^{-3}$ trap/cm^3 per photon/cm^2) can be transformed to an introduction rate per Compton electron having energy above the displacement threshold. This value ($\sim$0.01 trap/cm^3 per electron/cm^2) is a factor of 10 smaller than the introduction rate obtained with accelerator electrons.

V. ACKNOWLEDGMENTS

This work was performed at the Solid State Division, Oak Ridge National Laboratory. Discussions with many of the members of the division have been most provocative and helpful. Especially we would like to thank J. H. Crawford, H. C. Schweinler, J. W. Cleland, O. S. Oen, and J. H. Barrett. Our thanks, also, to G. K. Wertheim, of the Bell Laboratories, for supplying us with unpublished information about his work.

Electron Microscopic Study of Thin Films of the Aluminum-Copper Eutectic Prepared by a Melting Method

NOBORU TAKAHASHI
University of Yamanashi, Kofu, Japan
(Received February 25, 1960)

Thin films of the Al-Cu eutectic (67 wt% Al, 33 wt% Cu) were prepared by the melting method previously described and examined by electron microscopy. The lamellar structure of this eutectic was revealed so clearly that the contrast of the image obtained was comparable to that obtained by a replica method, which proved that the present film represented the same structure as the massive specimen. Electron diffraction study revealed which lamella belongs to the κ or θ phase and permitted the determining of the relative crystal orientation between two types of lamellas.

INTRODUCTION

THE importance of the direct study of crystal specimens by means of electron microscopy has increased remarkably with the development of a high resolution electron microscope. Since the original study on thin aluminum films by Heidenreich[1], many workers have contributed to the development of this field.[2] Thin metallic films are ordinarily prepared by thinning by electropolishing. The author proposed a very simple method of preparation of thin metallic films and examined the structure of the Pb/Sn eutectic.[3] In order to confirm the results obtained with respect to this alloy the author has prepared thin films of the aluminum-copper eutectic in the same way and examined their crystallographic features by electron microscopy and electron diffraction.[4]

TECHNIQUES

The aluminum-copper eutectic (67 wt% Al, 33 wt% Cu) was prepared under vacuum in a crucible from the weighed masses corresponding to this relative quantity. This proportion corresponds exactly to the eutectic between the θ ($CuAl_2$) and κ (almost aluminum) phase. The thin films of this eutectic were prepared in air by dipping a small elliptical loop of iron wire 0.3 cm in diam[5] into the molten alloy and withdrawing it at a rate of about 2 cm/sec. Before the operation was begun the oxide film produced on the surface of the melt was carefully removed. A suitable area of the film was chosen under the optical microscope, cut out, and mounted on a specimen holder of the electron microscope.

The electron microscope used was a JEM-5 model, the accelerating voltage of which was of 100 kv. In general, a higher voltage, which increases the penetrating power of electrons, is desirable in order to obtain clear electron micrographs. For the present specimens, the order of 100 kv was sufficient, though the electron micrographs obtained were sometimes less clear.

RESULTS AND DISCUSSIONS

1. Electron Micrographs

Different from the case of the Pb/Sn eutectic, one phase of this eutectic is not a terminal solid solution but an intermetallic compound. We always obtained beautiful electron micrographs revealing the lamellar structure of this eutectic. Figure 1 shows an example. As in the case of the Pb/Sn eutectic, two types of lamellas are visible; one is dark and the other is light. The contrast between them is comparable to that obtained by a replica method. Interference fringes owing to Bragg reflection are produced from suitably oriented portions of the specimen. They are continuous in all the dark and all the light lamellas meaning that these two types of lamellas possess the same crystal orientation in any one colony.

It is interesting to confirm experimentally the phase that causes the lamellas to appear darker than the others in electron microscopy. It is easy to distinguish this by using the electron diffraction spot, suitably chosen, and its corresponding image in a dark field. Figure 2 shows a series of photographs that indicate clearly that the spots of diffraction owing to the θ phase are due to the dark lamellas.

The electron diffraction pattern corresponding to the structure of this eutectic is always a spot pattern, showing the monocrystalline nature of this structure; that is, all the lamellas belonging to the same phase

FIG. 1. Electron micrograph of film of 67 wt% Al—33 wt% Cu alloy.

[1] R. D. Heidenreich, J. Appl. Phys. **20**, 993 (1949).
[2] R. Castaing, Compt. rend. **237**, 1330 (1953). J. W. Menter, Proc. Roy. Soc. (London) **A 236**, 119 (1956). M. J. Whelan, P. B. Hirsch, R. W. Horne, and W. Bollman, Proc. Roy. Soc. (London) **A 240**, 524 (1957).
[3] N. Takahashi and K. Ashinuma, J. Inst. Metals **87**, 19 (1958–9).
[4] N. Takahashi and K. Ashinuma, Comp. rend. **246**, 3430 (1958).
[5] Long axis measuring about 1 cm.

FIG. 2. (a) Electron micrograph of film of 67 wt% Al—33 wt% Cu alloy. (b) Electron diffraction pattern corresponding to (a); the spots indicated by the short arrows are due to the κ phase. All the spots except these are due to the θ phase. (c) Dark-field electron micrograph corresponding to the diffraction spot $(\bar{1}10)\theta$ in (b).

have the same crystal orientation in the interior of any one colony, as mentioned earlier. The lamellas belonging to one phase seem to crystallize in the form of single crystals, as if there were no other lamellas among them. It follows, therefore, that a definite relative crystal orientation would exist between the crystals belonging to the two types of lamellas.

The origin of the contrast of the images would arise from the diffraction effects[6] due to the orientation of the two types of lamellas and their crystal structure and from the mass thickness effects between them. In the present case, the latter seems to predominate over the former, because the contrast of the images was not so influenced when we inclined the specimen in relation to the beam direction. A more detailed discussion is given later.

In spite of some ambiguity which we encounter in trying to explain the origin of the contrast of the image of Fig. 1, we can show that the films have a real lamellar structure. When we etch them by a chemical reagent, such as a dilute KOH solution, we obtain the skeleton of the θ lamellas. By comparison with the results obtained by a replica method, we could confirm that the structure shown in the present film really corresponds to that found in a massive specimen, though we must take into account the difference in the velocity of solidification between them.[7]

FIG. 3. (a) Electron micrograph and (b) corresponding diffraction pattern of film of 67 wt% Al—33 wt% Cu alloy.

2. Relative Orientation of the Two Types of Lamellas

It was comparatively unusual to obtain the electron diffraction pattern, showing the two phases κ and θ in this eutectic at the same time. In general, it was the spots owing to the θ phase that appeared frequently; the diffraction spots due to the κ phase were recognized rarely.

As a rule, the crystal structures of the two types of lamellas are quite different; one is simple and the other complicated. Their lattice constants are also different. In the present case, the crystal of the θ phase is tetragonal with $a=6.04$ A and $c=4.86$ A, and that of the κ phase is face-centered cubic with a slightly larger lattice constant than that of pure aluminum $a=4.04$ A. So, when the orientation of the lamellas in relation to the film surface is arbitrary, there is a large chance of the occurrence of the orientations producing many spots because of the more complicated crystal, especially in the case of a definite relative orientation between the two types of lamellas.

In the aforementioned discussion we assumed that the thicknesses of the two types of lamellas are equal, but in the film prepared by a melting method it is not the same, because of the coefficient-of-contraction difference between them. In general, the thickness of

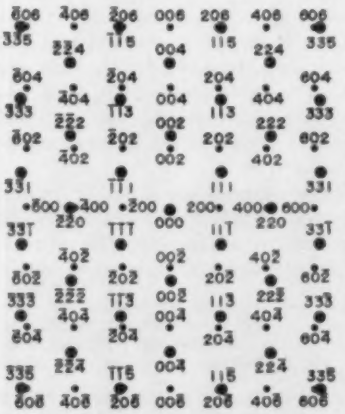

FIG. 4. Schematic diagram of Fig. 3 with corresponding Miller indices. The large circles indicate the diffraction spots of the κ phase. The small circles correspond to those of the θ phase.

[6] P. B. Hirsch, R. W. Horne, and M. J. Whelan, *Electronmicroscopy* (Proc. Stockholm Conference, September, 1956) (Almqvist & Wiksell, Stockholm, 1957) p. 312.

[7] The development of crystals would be also limited two-dimensionally in a certain measure in thin films.

the κ lamellas is smaller than that of the θ lamellas, which favors the penetration of electrons.

All these factors play a role in the appearance of electron diffraction spots, as well as the image formation from the thin films of the eutectic. Thus, in the case of the Pb/Sn eutectic, we very often obtained the spots owing to the β phase (almost Sn) and, in the present case, the spots which appeared frequently were those owing to the θ phase. In both cases, it was the spots caused by a more complicated crystal that appeared frequently, while for the pearlite structure the spots owing to the ferrite of simpler crystal form frequently appeared.[8] Therefore, in order to discuss the electron diffraction pattern of the thin films of eutectic, we must take into account all the factors mentioned earlier; it would be difficult, for the time being, to draw a general conclusion for all eutectic structures.

The relative crystal orientation of the two types of lamellas which we found by analysis of the electron diffraction pattern (Figs. 3 & 4), is as follows:

$$(001)\theta // (001)\kappa \text{ and } [100]\theta // [110]\kappa. \qquad (1)$$

When the crystal of the intermetallic compound $CuAl_2$ precipitates from the matrix, an intermediate transition structure θ' is formed with the orientation relationship shown in Fig. 5. Preston[9] demonstrated that it fitted perfectly onto the cube planes of the aluminum matrix. If the copper atoms keep the same position relative to the matrix in the course of the transformation from the θ' to θ phase, the relative orientation (1) would be obtained as a fitted one between the two crystals forming the lamellar structure, although it is not certain whether the transformation $\theta' \rightarrow \theta$ really occurs in the case of the formation of the present lamellas. Moreover, it is not yet sufficiently certain that this orientation exists in all the lamellar structure of the present eutectic, but there is no doubt that this sort of definite orientation plays an important rôle in the formation and transformation of the eutectic.

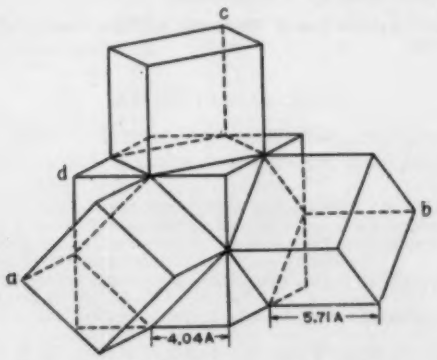

FIG. 5. Orientations of $\theta'-CuAl_2$ cells (a, b, c,) on the matrix (d) (Preston[6]). The cube d represents eight units of the Al lattice.

[8] Unpublished.
[9] G. D. Preston, Phil. mag. **26**, 855 (1938).

FIG. 6. (b) Electron micrograph of thick film of 67 wt% Al—33 wt% Cu alloy, showing two regions of different lamellar widths. Arrows indicate the grain boundary. (a) and (b) are electron diffraction patterns corresponding to the upper and lower section of (b), respectively. In (a) faint Kikuchi lines are visible, showing the perfectness of the crystal.

3. Breadth of the Lamellas

The interlamellar spacing varies according to the conditions of the film, but is usually of the order of 10^{-5} cm. Their apparent width varies according to their orientation in relation to the film surface.

Figure 6 shows very clearly the differences of width of the lamellas which appeared from the different orientations in relation to the film surface of the two regions on both sides of the grain boundary. The upper section in Fig. 6 represents almost no lamellar structure, but the lower section in it has a fine lamellar structure. Electron diffraction reveals that the former has an orientation such as $(2\bar{1}5)\kappa$ is parallel to the film surface. There appear almost no spots due to the θ phase. The latter would be too thick to be penetrated by an electron

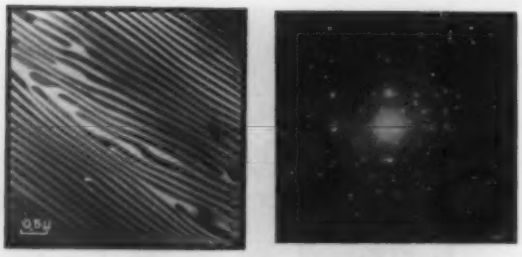

(a) (b)

FIG. 7. (a) Electron micrograph and (b) corresponding electron diffraction pattern of film of 67 wt% Al—33 wt% Cu alloy. Rings are due to the aluminum oxide $\gamma-Al_2O_3$, which generally plays the role of support for metallic films. It seems that the presence of oxide films is necessary, though thicker ones are not desirable.

beam, while the former, which appears white, is thin enough to produce some spots of diffraction.

The spots obtained from the lower section are due to the θ phase, showing that $(159)\theta$ is parallel to the film.

Though the electron micrographs obtained in the present experiment always revealed a lamellar structure, the corresponding diffraction patterns were widely different, showing that the crystal orientations found in these films are accordingly different. In Fig. 7, the orientations of the lamellas are such that $(\bar{1}12)\alpha$ and $(\bar{1}11)\theta$ are parallel to the film surface.

4. Comparison of the Present Film with the Massive Specimen

It is necessary to compare the image obtained by the present method with that obtained from the massive specimen prepared in the same physical process as the present thin film. By etching the surface of a massive specimen of the present eutectic with a dilute solution of 20% nitric acid (70°C) for several minutes, we obtained the structure shown in Fig. 8 by a replica method. The replica was collodion, backed with Etocell and shadowing with gold. The image was always the same over all the regions of the specimen. The appearance is not different from that seen in Fig. 7, but the interlamellar spacing is about three times greater for the massive specimen than for the film prepared by a melting method. This difference arises from the difference of the velocity of solidification. It is more rapid in the present film than in the massive specimen of the same alloy. Taking into account this fact, we utilize the films prepared by a melting method for metallurgical research, especially for the purpose of studying the effect due to heating[10] or cooling of the specimen after preparation.

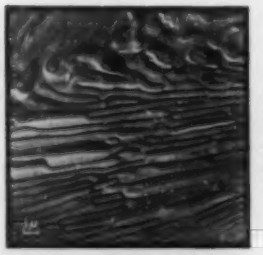

FIG. 8. Electron micrograph of the 67 wt% Al—33 wt% Cu alloy prepared by cooling on a metal surface in air from the molten state. Collodion replica, shadowed with gold.

CONCLUSION

The thin films prepared by a melting method reveal the real structure of the massive specimen of the same alloy. The simplicity of the operation will permit us to apply this method to a wide field of metallurgical research. For the time being, the possibility of preparing thin films of any metal or alloy is limited to the elements of a melting point under about 900°C, but, even to this extent, we could expect to realize numerous applications.

ACKNOWLEDGMENTS

The author wishes to offer his sincere thanks to Miss S. Oguchi for her technical aid and also to K. Ashinuma of the Japan Electron Optics Laboratory, Tokyo, for his interest in this investigation. The work was carried out with the aid of the Scientific Research Fund of the Japanese Ministry of Education.

[10] N. Takahashi and K. Ashinuma, J. Electronmicroscopy **37**, 37 (1959).

Microwave Properties of Nonstoichiometric Polycrystalline Yttrium Iron Garnet*

P. E. SEIDEN†
Research Laboratory, Lockheed Missiles and Space Division, Palo Alto, California, and Microwave Laboratory, W. W. Hansen Laboratories of Physics, Stanford University, Stanford, California

AND

C. F. KOOI AND J. M. KATZ‡
Research Laboratory, Lockheed Missiles and Space Division, Palo Alto, California

(Received December 23, 1959; and in final form March 8, 1960)

An investigation has been made of the microwave properties of nonstoichiometric yttrium iron garnet ranging from 31% iron excess through stoichiometric to 12% yttrium excess. No ion substitution in the garnet lattice is observed. All material in excess of stoichiometric proportions goes into ceramic second phases. The phases observed are perovskite ($YFeO_3$) for yttrium excess, hematite (Fe_2O_3) for iron-excess samples fired in oxidizing atmospheres, and magnetite (Fe_3O_4) for iron-excess samples fired in neutral atmospheres.

On the basis of the assumption that all excess material goes into the appropriate ceramic second phase, we may account for the behavior of the saturation magnetization, spectroscopic splitting factor, and linewidth as a function of composition.

It is found that the linewidth is strongly narrowed by the large magnetization as predicted by Geschwind and Clogston. The behavior of the dielectric constant can be explained, at least qualitatively, by a theory of Wagner and Sillars which considers particles of one dielectric material imbedded in a matrix of another. The behavior of the dielectric loss tangent is not understood and cannot be accounted for by this theory.

INTRODUCTION

IN this paper we will be interested in the behavior of the microwave properties of polycrystalline yttrium iron garnet as a function of deviations from stoichiometry. There have been a number of studies[1–4] of polycrystalline yttrium iron garnet as a function of preparation parameters (e.g., sintering time and temperature) and some information on the behavior of nonstoichiometric samples has been obtained from these investigations; however, since these investigations were not primarily designed to determine the effects of nonstoichiometry, the results were not systematic nor complete in this regard. We therefore undertook the systematic investigation of polycrystalline yttrium iron garnet as a function of yttrium to iron ratio. We were concerned with the microwave properties of these materials, and both the ferrimagnetic resonance and dielectric parameters were measured.

SAMPLE PREPARATION

A series of polycrystalline yttrium iron garnet samples were prepared of compositions ranging from strongly iron excess through stoichiometric to strongly yttrium excess. The composition was determined by the amount of yttria and iron oxide used in preparing the sample and the oxidation state by the atmosphere used during the firing process.

The procedure used for all samples was to mix Research Chemicals 99.9% pure Y_2O_3 and Columbian Carbon Mapico Red high purity Fe_2O_3 and ball mill for 72 hours and then fire at 1150°C for two hours. The material was remilled for another 72 hours and then pressed into 2- by 2-in. squares $\frac{1}{8}$-in. thick by a pressure of 50 tons/in.^{2}. For the final firing, the temperature was raised at about 100°/hr until 1425°C, where the material was fired for two hours. The cooling took place at the natural rate of the furnace without any control (some samples were made at 1370°C and 1450°C, but no systematic differences in properties were noted).

X-ray diffraction powder patterns were taken on the samples after firing. Small pieces were then polished and photomicrographs taken of both the unetched and etched surfaces. The samples for the magnetic measurements were spheres approximately one millimeter in diameter made by the tumbling method.[5] The dielectric measurements were made on surface ground rectangular prisms 0.496-in. long by 0.020-in. square.

SAMPLE COMPOSITION

It has been shown by Van Uitert *et al.*[2,3] that the method of preparation strongly effects the microwave properties. Since we are here interested in only the effects of nonstoichiometry and oxidation state we desired to be sure that all effects such as this were eliminated. A number of sets of samples were made and

* This research was supported in part by the U. S. Air Force under a contract monitored by the Air Force Office of Scientific Research of the Air Research and Development Command, and in part by Lockheed Missiles and Space Division.

† Now at the Laboratoire D'Électrostatique et de Physique du Métal, Grenoble, France.

‡ Now at Lockheed Electronics and Avionics Division, Maywood California.

[1] W. P. Wolf and G. P. Rodrigue, J. Appl. Phys. **29**, 105 (1958).

[2] L. G. Van Uitert, F. W. Swanekamp, and S. E. Haszko, J. Appl. Phys. **30**, 363 (1959).

[3] L. G. Van Uitert, F. W. Swanekamp, and S. Preziosi, J. Am. Ceram. Soc. **42**, 471 (1959).

[4] L. G. Van Uitert, R. R. Soden, and F. W. Swanekamp, J. Appl. Phys. **31**, 226S (1960).

[5] W. L. Bond, Rev. Sci. Instr. **22**, 344 (1951).

the reproducibility of the data for each sample type was found to be quite good so that one may assume that no preparation parameters were affecting the results. It has also been shown[1,4] that the microwave properties are affected by the porosity and pore distribution of the sample. Density measurements taken on the sample result in values between 97–99% of theoretical density (taking into account the amount of second phase present and its density) showing that the air-pore density was approximately constant for all samples (the effect of a 2% change in density is much to small to account for the observed effects). Also, photomicrographs have shown the samples to be quite homogeneous and the number of air pores per unit area to be constant. It was clearly seen that the distribution of air pores and second phases (which were found to occur) is quite uniform.

As will be seen in Figs. 3 and 4, the minimum linewidth obtained is about 50 oersteds, which is the right order[1] for a polycrystalline sample of yttrium iron garnet. Van Uitert *et al.*[2,3] have reported linewidths on sintered samples of as much as a factor of 10 below this; however, although their samples were sintered, the measurements were not made on polycrystalline samples. The crystallite size reported for these samples was of the order of one millimeter and the samples used for the linewidth measurements were of a smaller size. Therefore, the measurements were taken on single crystals (or perhaps a few crystals) obtained by a sintering method.

We were very careful to be sure that the crystallite size in all our samples was small compared to sample size. The photomicrographs showed that for all samples the crystallite size of the yttrium iron garnet matrix, the size of the air pores, and the crystallite size of the second phase inclusions were between 5–10 μ, which is the order of one hundredth of the sample size. Therefore, we are justified in calling our data truly representative of polycrystalline samples.

The first observation made from the x-ray diffraction patterns was that the garnet lines do not shift as a function of sample composition. This means that the lattice constant does not change and no ion substitution occurs in the lattice as the excess of either iron or yttrium increases. What is observed is that for yttrium excess samples, a second phase of perovskite ($YFeO_3$) appears. For iron excess samples fired in oxidizing atmospheres (air, O_2), hematite (Fe_2O_3) appears, and for neutral atmospheres (N_2, Ar), magnetite (Fe_3O_4)[6] appears.

An additional indication of composition comes from sample photomicrographs. On the unetched samples one can see the grains of the second phases since they reflect light differently than garnet. In addition, since Fe_2O_3 has a hexagonal crysral structure and is birefringent, extinction of light may be observed by rotation under polarized light. Extinction is only observed for iron excess samples fired in oxidizing atmospheres.

[6] Fe_3O_4 and $\gamma-Fe_2O_3$ are difficult to separate from x-ray data; however, $\gamma-Fe_2O_3$ is unstable at the temperatures used in sample preparation so that it would not be expected to appear.

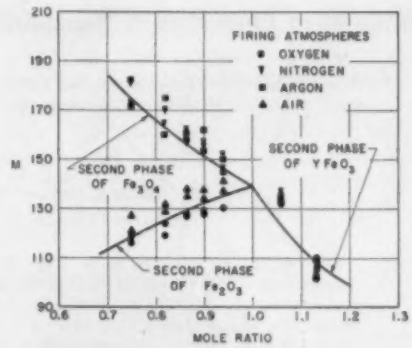

FIG. 1. Saturation magnetization as a function of mole ratio.

On the basis of this discussion, we will assume that all excess yttrium goes into the perovskite phase ($YFeO_3$), excess iron for air and oxygen fired samples goes into hematite (Fe_2O_3), and for nitrogen and argon firing atmospheres the excess iron goes into the magnetite (Fe_3O_4) phase.

SATURATION MAGNETIZATION

We must now calculate the expected saturation magnetization of our various materials based on the two phase composition determined in the preceding section. On this model the net magnetization will be given by the weighted average of the magnetizations of the two phases. That is, we correct the stoichiometric magnetization by accounting for the deviations caused by the second phase. We will take

$$M = F_G M_G + F_P M_P, \tag{1}$$

where F_G and F_P are the fractional volumes of the garnet phase and second phase, respectively, and M_G and M_P are their magnetizations. The fractional volumes are determined from the initial proportions of yttria to iron oxide used in making the samples.

The curves of Eq. (1) are shown in Fig. 1 along with the experimental magnetization measurements determined from observing the force exerted on the sample by a magnetic field gradient. The agreement between theory and experiment is seen to be good. The fact that all the data of the air fired samples lie above the data for oxygen firing may be due to some Fe_3O_4 being present in the former, since air is not as good an oxidizing atmosphere as pure oxygen.

The abscissa of all the figures in this paper are expressed in terms of the mole ratio (R) defined as the ratio of the weights of yttria and iron oxide used, divided by their respective molecular weight taken in the proportion of stiochiometric yttrium iron garnet.

That is,

$$R=\frac{\text{wt } Y_2O_3}{\text{mol. wt } 3Y_2O_3}\Big/\frac{\text{wt } Fe_2O_3}{\text{mol. wt } 5Fe_2O_3}. \quad (2)$$

The value $R=1$ corresponds to stoichiometric yttrium iron garnet.

MICROWAVE MEASUREMENTS

The microwave parameters determined at 9300 Mc were the spectroscopic splitting factor (g), linewidth (ΔH), the real part of the dielectric constant (K'), and dielectric loss tangent ($\tan\delta$). The experimental methods were similar to those described by Artman and Tannenwald.[7]

A. Spectroscopic Splitting Factor (g)

In ferrimagnetic resonance in a sphere, the resonance relation is given by

$$\omega=\gamma H_0=(e/2mc)g^*H_0, \quad (3)$$

where ω is the resonant circular frequency, γ the gyromagnetic ratio, H_0 is the applied dc magnetic field, c is the velocity of light, and e and m are the charge and mass of the electron, respectively. The effective g value of the sample is g^*. It is found experimentally that g^* determined from this equation depends on the ratio of yttrium to iron. This behavior can be explained by the same type of an assumption used by Okamura[8,9] and Kojima.[10] We take the resonance relation to be given by

$$\omega=(e/2mc)g(H_0+H_p), \quad (4)$$

where g is the g value for a stoichiometric sample, and H_p is a field in the nonstoichiometric sample caused by the second phase "pores." This field may be evaluated by considering the internal field in the sample. For the stoichiometric sample, the internal field is

$$H_I'=H_0'-(4\pi/3)M', \quad (5)$$

where the prime refers to the stoichiometric sample. For any nonstoichiometric sample we have

$$H_I=H_0-(4\pi/3)M. \quad (6)$$

This sample will be at ferrimagnetic resonance when $H_I'=H_I$, so that

$$H_p=H_0'-H_0=(4\pi/3)(M'-M). \quad (7)$$

Combining this expression with Eqs. (3) and (4), we obtain

$$g^*=g[1+(4\pi/3H_0)(M'-M)]. \quad (8)$$

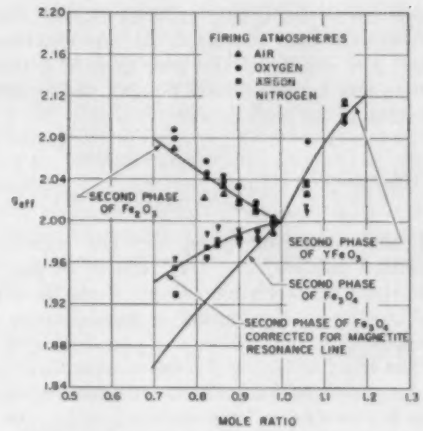

FIG. 2. Spectroscopic splitting factor as a function of mole ratio.

Equation (8) is plotted in Fig. 2 using the magnetization curves of Fig. 1 to determine M as a function of mole ratio. The agreement with experimental data is seen to be good for the nonmagnetic second phases (Fe_2O_3, $YFeO_3$), but is very bad for the magnetic second phase (Fe_3O_4). This discrepancy is an additional consequence of the magnetism of Fe_3O_4. Bickford[11] has measured the resonance parameters of magnetite and finds

$$\Delta H\approx 2000 \text{ oe}$$

$$g=2.12.$$

Therefore, we have, in the samples containing Fe_3O_4, a very broad line with a large g value superposed on the garnet line. This will result in an increase of g^*. The new effective $g(g^{**})$ can be approximated by

$$g^{**}=F_Gg^*+F_mg_m, \quad (9)$$

where F is again the fractional volume, and G and m refer to garnet and magnetite, respectively. The corrected curve for Fe_3O_4 is also shown in Fig. 2 and gives good agreement with the data.

Schlömann[12] has considered the pore problem from a different point of view. He considers a spherical pore in a spherical sample and calculates the susceptibility of the sample by means of a weighted average of the susceptibility of the nonporous material. The pore field (H_p) is then obtained in terms of the porosity of the sample as (P=volume of pores divided by total volume)

$$H_p=(4\pi M'/3)P. \quad (10)$$

Schlömann points out in a subsequent paper,[13] however,

[7] J. O. Artman and P. E. Tannenwald, J. Appl. Phys. **26**, 1124 (1955).
[8] T. Okamura, Y. Torizuka, and Y. Kojima, Phys. Rev. **88**, 1425 (1952).
[9] T. Okamura, Sci. Repts., Research Insts. Tôhoku Univ., Ser. A **6**, 89 (1954).
[10] Y. Kojima, Sci. Repts. Research Insts. Tôhoku Univ., Ser. A **6**, 614 (1954).
[11] L. R. Bickford, Jr., Phys. Rev. **78**, 449 (1950).
[12] E. Schlömann, Raytheon Research Division Tech. Rept. R-15 (September 1, 1956); also *Proceeding of the Conference on Magnetism and Magnetic Materials*, Boston, 1956 (American Institute of Electrical Engineers, New York, 1957), AIEE Spec. Publ. T-91, p. 600.
[13] E. Schlömann, J. Phys. Chem. Solids **6**, 242 (1958).

that this calculation is only valid for $H_0 \gg H_p \gg 4\pi M'$. This condition does not apply in our experiments. Snieder[14] has calculated the pore field in a manner similar to that used to obtain Eq. (8), and he obtains H_p in terms of the porosity as

$$H_p = (4\pi M'/3)P\left\{\frac{(3H_0+8\pi M')}{[3H_0+4\pi(2M'-M)]}\right\}. \quad (11)$$

Under the conditions given for the validity of Schlömann's analysis, Eq. (11) reduces to Eq. (10) since the curly bracket reduces to one. Under our experimental conditions, the bracket is approximately 1.15 and represents a 15% increase in pore field over Eq. (10). The effect of having a magnetization large compared to the pore field also affects the linewidth calculations as is shown in the next section.

B. Linewidth

The pores in the material give rise to an inhomogeneous field in the sample which will cause different parts of the sample to resonate under different external fields. Therefore, the resonance linewidth should be broadened.

Schlömann[12] has calculated an inhomogeneously broadened linewidth in the same manner as the calculation for the change in g value. The result of this calculation yields

$$\Delta H = \Delta H_0 + 1.5(4\pi M')P, \quad (12)$$

where ΔH_0 is the linewidth of the stoichiometric sample. With the help of Eq. (10), we have

$$\Delta H = \Delta H_0 + 4.5H_p. \quad (13)$$

However, as has been noted earlier, the theory used in deriving this relation cannot be assumed to be valid where $4\pi M \gg H_p$. Geschwind and Clogston[15] and Schlömann[13] have considered this case and have shown that the strong dipolar coupling arising from the large magnetization narrows[16] the resonance line from the value predicted by Eq. (13). Geschwind and Clogston give the dipole narrowed expression as

$$\Delta H = (18\pi/10)(H_I^2/4\pi M)J, \quad (14)$$

where J is a shape factor involving the saturation magnetization, dc magnetic field, and demagnetizing factors of the sample. In our experiments for a sphere of yttrium iron garnet, J is approximately 2.5. H_I will consist of two parts:

$$H_I = H' + H_p. \quad (15)$$

H' is the field due to anisotropy and air pores and is determined to be about 80 oe from the measured linewidth of a stoichiometric sample. The term H_p is again the pore field due to second phases. Figure 3 contains plots of both Eqs. (13) and (14) and data for samples fired in oxidizing atmospheres. The data for mole ratios close to one show good agreement with the dipole narrowed curve; however, as the deviations from stoichiometry become larger, the data begin to approach the inhomogeneously broadened curve. One should expect the linewidth to have this behavior, since the field H_p becomes larger as the excess increases (more second phase pores) and ceases to be small compared to $4\pi M$. For the largest excess, $H_p = 205$ oe, which is about 12% of $4\pi M$. Therefore, the line will not be as strongly narrowed by dipole forces.

The situation for the iron excess samples fired in nitrogen and argon is again different. Figure 4 shows that the experimental data for an Fe_3O_4 second phase do not follow the dipole narrowed expression, Eq. (14). This can be explained by looking into the nature of the dipole narrowing. A pore in the sample gives rise to poles on its surface that cause the total dc field in the parts of the sample near the pore to vary, causing a spread of resonant frequencies; however, if the magnetization is large, the dipole fields of the regions affected by the pore will partially overide the effect of the inhomogeneity. Now in a sample with nonmagnetic pores, the dipole coupling is provided by the sample magnetization; however, when a magnetic pore is present, the magnetization of the pore itself can cause the coupling. Magnetite has a magnetization ($4\pi M = 6100$ gauss) about 3½ times that of garnet, so that we should expect the magnetite pores to strongly narrow the resonance line. This will be true only for small porosities, otherwise we will be measuring the magnetite line itself. We may attempt to calculate this effect by modifying Eq. (14),

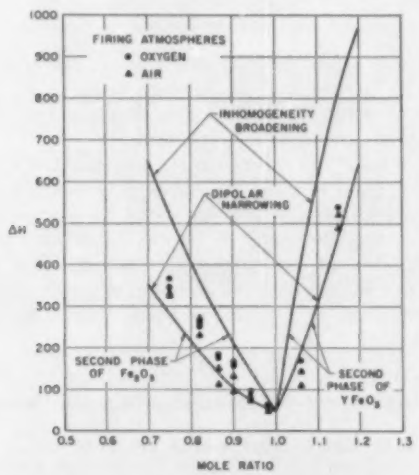

FIG. 3. Linewidth as a function of mole ratio for samples fired in oxidizing atmospheres.

[14] J. Snieder, J. Appl. Sci. Res. **36**, 301 (1957).

[15] S. Geschwind and A. M. Clogston, Phys. Rev. **108**, 49 (1957).

[16] A. M. Clogston, H. Suhl, L. R. Walker, and P. W. Anderson [J. Phys. Chem. Solids **1**, 129 (1956)] have discussed narrowing caused by the exchange field; however, since our crystallite sizes are large compared to a lattice constant, we may neglect these effects.

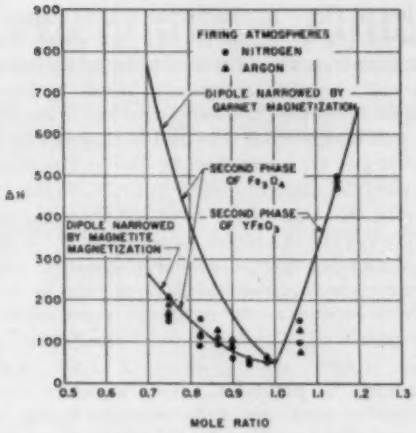

FIG. 4. Linewidth as a function of mole ratio for samples fired in neutral atmospheres.

accounting for the different magnetizations as follows:

$$H=(18\pi/10)J\{(H_I)^2/[(H'/H_I)4\pi M_G + (H_p/H_I)4\pi M_M]\}, \quad (16)$$

where M_G is the magnetization of garnet, M_M is the magnetization of magnetite, and H_p is given by Eq. (7); that is, we weight the magnetizations by the fractional fields of their respective phases. The field inhomogeneity in the stoichiometric sample is H', so that the dipole field tending to decrease the effect of this inhomogeneity results from the garnet magnetization. The factor H_p is caused by the second phase, so that for this field we should consider that the dipole narrowing is produced by the second phase magnetization. A plot of Eq. (16) is given in Fig. 4 and shows good agreement with the data. The agreement is seen to be good for even the largest values of iron excess, whereas in the case of a second phase of Fe_2O_3, deviations from the theory were observed at large iron excesses. This difference is caused by the ratio of $4\pi M$ to H_I. The factor H_I in the Fe_3O_4 case has approximately the same value as for Fe_2O_3; however, we must now use the $4\pi M$ of magnetite which is 3½ times that of yttrium iron garnet, so that the dipole narrowing theory should still apply even for large iron excesses in the case of an Fe_3O_4 second phase.

C. Dielectric Constant

The problem of small ellipsoids of dielectric constant K_2' and conductivity σ_2 imbedded in a dielectric constant K_1' and a very low conductivity has been treated by Wagner[17] and Sillars.[18] We apply their theory [Eqs. (7)–(16) of footnote reference 18] directly to our case of iron excess in a neutral atmosphere. The other cases, namely, iron excess in an oxidizing atmosphere and yttrium excess, are not treated because the dielectric constants, real and imaginary, of pure Fe_2O_3 and $YFeO_3$ are unknown;[19] however, by assuming that they are comparable to that of yttrium iron garnet, one can explain the rough constancy of K' and K'', the real and imaginary parts of the dielectric constant, as one proceeds from yttrium excess to iron excess in an oxidizing atmosphere. The only large changes in K' and K'' occur for iron excess in a reducing atmosphere. Sillars[18] has shown that the real part of the dielectric constant for prolate spheroids of medium 2 imbedded in medium 1 is given by

$$K'=K_1'(1-F_2)+F_2K_2' + K_1'\{nF_2/[1+n^2(K_1'\nu/2\sigma_2)^2]\}, \quad (17)$$

where F_2 = fractional volume of phase 2, n ≈ square of the ratio of major axis to minor axis of the prolate spheroid (for large n), ν = frequency, and K' = real part of the dielectric constant of the composite material. The subscript 1 refers to the major constituent (yttrium iron garnet) and the subscript 2 refers to the second phase. The conductivity of magnetite[20] is 5×10^3 ohm^{-1}-cm^{-1}, so that the denominator of the last term in Eq. (17) reduces to one. On assuming $K_1'=K_2'=14.5$ (measured on a stoichiometric sample), Eq. (17) reduces to

$$K'=K_1'(1+nF_2). \quad (18)$$

Equation (18) is plotted in Fig. 5 for prolate ellipsoids of magnetite with $n=13.5$. Actually, since the photo-

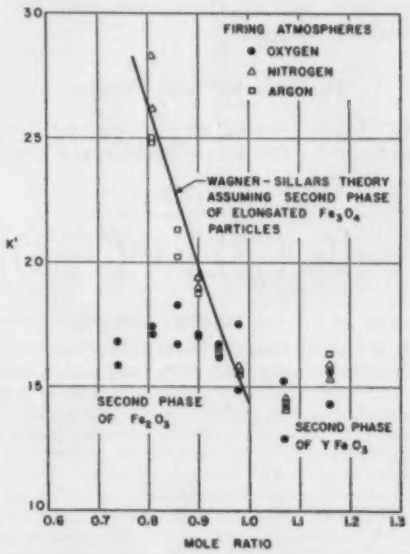

FIG. 5. Dielectric constant as a function of mole ratio.

[17] K. W. Wagner, Arch. Elektrotech. **2**, 371 (1914).
[18] R. W. Sillars, J. Inst. Elect. Engrs. (London) **80**, 378 (1937).
[19] The values of K' and K'' for polycrystalline materials are unsuitable because of the effects of grain boundaries, voids, etc., [see Koops, Phys. Rev. **83**, 121 (1951)].
[20] A. R. Von Hippel, W. B. Westphal, and P. A. Miles, WADC Tech. Rept. 55-149, 113 (1955).

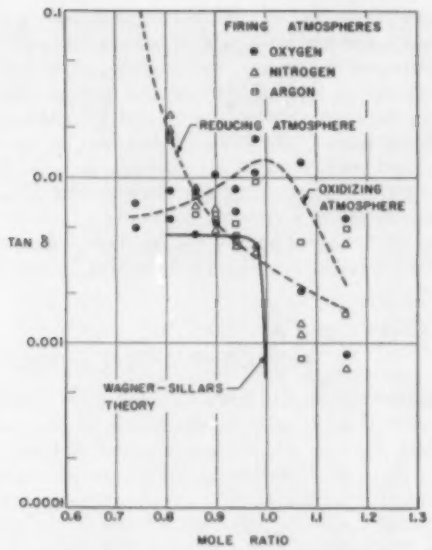

FIG. 6. Dielectric loss tangent as a function of mole ratio.

micrographs show variously shaped particles, the increase of K' is due to groups of spheroids of different eccentricity, each contributing in proportion to its population. The eccentricity of $\sqrt{13.5}$ is not unreasonable since the photomicrographs display a large number of particles whose eccentricity is of this order. Therefore, the agreement between theory and experiment is at least qualitatively good.

D. Dielectric Loss Tangent

Sillars[18] has also derived an expression for the dielectric loss tangent ($\tan\delta$) which for this case is given as

$$\tan\delta=\frac{n^2F_2(K_1'\nu/2\sigma_2)}{nF_2+\left[1+n^2\left(\frac{K_1'\nu}{2\sigma_2}\right)^2\right]\left[1+F_2\left(\frac{K_2'-K_1'}{K_1'}\right)\right]}. \quad (19)$$

In the case of the loss tangent, however, we were not able to get even qualitative agreement between the Wagner–Sillars theory [Eq. (19)] and our results. The solid line of Fig. 6 represents the nearest approach to agreement (for $n=3200$) for the iron excess neutral atmosphere case, and it is seen to be in complete disagreement with the experimental trends as indicated by the broken lines. The only behavior of the data in Fig. 6 that is expected is that the loss tangents for Fe_3O_4 second phases are larger than for Fe_2O_3. This is due to the presence of divalent iron[21,22] in Fe_3O_4. In this regard it may be that part of the increased dielectric loss for iron excess is due to a higher conductivity of the sample caused by a small amount of divalent iron in the yttrium iron garnet itself. Qualitatively, one expects the loss tangent to increase as the amount of highly conductive Fe_3O_4 increases and to be relatively unaffected by the addition of small amounts of either Fe_2O_3 (oxidizing atmosphere) or perovskite, both of which have a relatively low conductivity. By reference to Fig. 6 this is seen to be the case. Data for the case of the air atmosphere is not shown due to inaccuracies in the dielectric measurements on that series.

CONCLUSIONS

We have been successful in accounting for the saturation magnetization, g value, and linewidth of nonstoichiometric polycrystalline yttrium iron garnet by assuming all excess material over stoichiometric proportions goes into ceramic second phases, corrections for a magnetic second phase being necessary for Fe_3O_4. The linewidths agree with the dipole narrowing theory of Geschwind and Clogston[15] as long as the inhomogeneity field does not get too large compared to the saturation magnetization. The agreement of the dielectric constant data with the Wagner-Sillars[18] theory is qualitatively good for a second phase of Fe_3O_4. The behavior of the dielectric loss tangent, however, is not at all understood.

ACKNOWLEDGMENTS

We would like to thank R. W. Moss and L. Freiberg for the dielectric measurements, R. Holmquist for the photomicrographs, and M. Baldwin for the saturation magnetization measurements and assisting with the sample preparation. We would like to express our appreciation to M. A. Gilleo for very helpful discussions.

[21] A. M. Clogston, Bell System Tech. J. **34**, 739 (1955).
[22] W. A. Yager, J. K. Galt, and F. R. Merritt, Phys. Rev. **99**, 1203 (1955).

Letters to the Editor

Technique for Calculating X-Ray Intensities in the Electron Probe Microanalyzer

L. S. Birks
U. S. Naval Research Laboratory, Washington, D. C.
(Received April 14, 1960)

INTEREST in electron probe x-ray microanalysis has grown rapidly in the past two or three years with an increasing number of instruments, both commercial- and laboratory-constructed, becoming available. In the electron probe, a 1-μ diam beam of electrons excites characteristic x-rays from the chemical elements in a correspondingly small region on the specimen surface[1,2] and allows measurement of individual segregations, diffusion regions, etc.[3,4] For quantitative analysis, it is necessary to relate the observed x-ray emission intensity for each element to percent composition. A series of known composition standards may be used to prepare a calibration curve for this purpose, but they are expensive and it is not always possible to prepare them homogeneously on the micron-size scale required. On the other hand the composition may be calculated from the measured x-ray intensity by assuming some analytical relation. The simplest analytical relation was assumed by Castaing[1] for a first-order approximation; namely that the x-ray intensity was linearly related to composition. Although this is more nearly valid for the electron probe than for fluorescent x-ray spectroscopy,[5] there are many cases where it is by no means sufficient. For instance, in a 50-50 wt.% alloy of Ti-Zr, the relative TiKα x-ray intensity is only about 25% (using a 100% Ti specimen as a standard). In stainless steel, 68 wt% Fe may yield a relative FeKα intensity of only 55%. These examples point out the need for better analytical relationships. The method described below is only part of a general program for developing analytical techniques, but the preliminary curve has proved so valuable at N. R. L. that it was believed worthwhile to present it for use by others in the field.

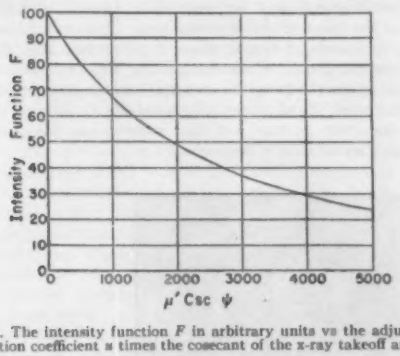

FIG. 1. The intensity function F in arbitrary units vs the adjusted absorption coefficient α times the cosecant of the x-ray takeoff angle.

In Fig. 1 an x-ray intensity variable which we shall call F is plotted against an adjusted x-ray absorption coefficient μ' times the cosecant of the x-ray takeoff angle ψ. The use of the curve is explained below; the derivation of the value of F is too lengthy to present here and will follow in a subsequent paper. Figure 1 has been tested for elements of atomic number greater than 22 (Ti) and would be expected to hold reasonably well down to 13 (Al). It is valid for any concentration and for any matrix material. Precision is about as good as the values estimated for absorption coefficients and will almost always be well within 10% of the amount present.

Only a single standard of the desired element is required and it may have any concentration. That is, it may be in the form of the pure element or as a known compound or as a homogeneous analyzed alloy. The procedure requires that the x-ray mass absorption coefficients of the specimen elements be known or estimated at the wavelength of the desired element and that weight fractions be assumed for the various elements. In other words, the expected x-ray intensity will be calculated for a *known* or *assumed* composition. Several calculated values may then be used in preparing calibration curves and will completely eliminate the need for a series of standards. It is also possible to estimate composition in a complete unknown as is described at the end of this letter but that problem occurs infrequently.

To illustrate the technique, consider the calculation of expected FeKα intensity from type 316 stainless steel of composition 68.5% Fe, 17% Cr, 12% Ni, and 2.5% Mo. The x-ray absorption coefficients at the FeKα wavelength are estimated from tabulated values to be: $\mu_{Fe}=71.2$; $\mu_{Cr}=440$; $\mu_{Ni}=89.5$; $\mu_{Mo}=275$. The adjusted absorption coefficient μ' for FeKα radiation is given by the equation

$$\mu'=\mu_{Fe}W_{Fe}+\mu_{Cr}W_{Cr}+\mu_{Ni}W_{Ni}+\mu_{Mo}W_{Mo}, \quad (1)$$

where W_{Fe}, W_{Cr}, etc., are the weight fractions of the various elements and the sum of all W's equals unity. On substituting the composition and absorption coefficients in the foregoing, $\mu'=141$. For an x-ray takeoff angle of 6°, $\mu'\csc\psi=1351$, and from Fig. 1 the corresponding value of F is $F_1=59.7$. Now suppose we are using a 100% Fe specimen as standard. For the standard $W_{Fe}=1$, and $\mu'=\mu_{Fe}\times1=71.2$; $\mu'\csc\psi=682$ and $F_2=74.6$. The expected relative intensity of FeKα is merely the fraction

$$\frac{F_1\times W_1}{F_2\times W_2}=\frac{59.7\times0.685}{74.6\times1.0}=55\%.$$

That is, the FeKα intensity from the type 316 steel should be 55% of the intensity from a 100% Fe standard.

TABLE I. Comparison of calculated and measured x-ray intensities for alloys and compounds.

Specimen	Element measured	True weight %	Relative x-ray intensity I_{meas}	Relative x-ray intensity I_{calc}	Error in % of amount present this method	Error in % of amount present linear assumption
Type 304 steel	Fe	69.5	54.8	55.0	0.4	27
Type 304 steel	Cr[a]	18.6	21.8	17.3	20.6	15
Type 304 steel	Ni	9.4	4.7	4.3	8.7	100
316 steel	Fe	65.9	50.8	52.4	3.0	30
317 steel	Fe	65.2	50.0	51.5	2.9	30
347 steel	Fe	70.2	53.6	55.4	3.3	31
347 steel	Ni	10.1	5.5	4.6	16.5	84
Timkin alloy	Fe	55.1	42.4	43.7	2.9	30
Timkin alloy	Ni	15.2	7.8	7.5	4.0	95
50-50, Ti-Zr	Ti	50.0	25	28	12.0	100
Nb_3S_8	Nb	53.8	54.0	54.7	1.3	0.4
NbNi	Ni	38.8	30.7	29.9	2.6	26
$NbFe_2$	Fe	54.6	40.5	41.2	1.7	35

[a] The measured relative intensity from chromium exceeds the calculated value appreciably because of selective fluorescent excitation of chromium by FeKα radiation from the matrix. The preliminary technique presented here is obviously not satisfactory for such selective cases but further correction curves are being prepared.

Table I shows calculated and measured relative intensities for a number of alloys and compounds. The agreement is considered very good considering that the x-ray absorption coefficients must often be extrapolated a long ways from tabulated values and even the tabulated values are sometimes in error by 5% or more. In the last two columns of the table, the difference between measured and calculated values are expressed as percent of the measured value for both this method of calculation and the linear relation which has been used frequently in the past. As may be seen, the present method usually removes more than 90% of the error and completely eliminates the need for extensive calibration standards.

For the infrequent case when the specimen is a complete unknown, the procedure outlined in the foregoing must be altered but only slightly. First a qualitative analysis must be established, and then as a first approximation, the relative measured x-ray intensity I_{meas} is substituted directly as a trial value of the weight

fraction W_i. Using the foregoing method, an expected x-ray intensity I_{calc} is obtained for comparison with the measured value. A new estimate of W_i' is obtained by assuming $W_i' = W_i \times I_{meas}/I_{calc}$ and a second value I_{calc}' found. If this does not agree with I_{meas}, a third value of W_i and I_{calc} may be found, etc., but usually two or three approximations are sufficient. Fortunately each approximation step takes only two or three minutes time.

There is one limitation to the technique at the present. In alloys or compounds where the desired element is selectively excited by the characteristic radiation of the major matrix element, its resulting intensity may be appreciably higher than the calculated value. An example is the excitation of chromium by FeKα in stainless steel; as is shown in Table I, the measured relative intensity for chromium exceeds the calculated value by more than 10% of the amount present. Curves to allow correction for selective fluorescent excitation are now being prepared.

[1] R. Castaing, Thesis, University of Paris (1951).
[2] L. S. Birks and E. J. Brooks, Rev. Sci. Instr. **28**, 709 (1957).
[3] E. J. Brooks and L. S. Birks, ASTM Special Tech. Pub. 245 (1958).
[4] J. Philibert and H. Bizouard, Les Memoires Scientific de la Revue de Metallurgie **56**, 187 (1959).
[5] L. S. Birks, *X-Ray Spectrochemical Analysis* (Interscience Publishers, Inc., New York, 1959).

Classification of Wire Explosions

WILLIAM G. CHACE AND MORTON A. LEVINE
Geophysics Research Directorate, Air Force Cambridge Research Center, Bedford, Massachusetts
(Received February 8, 1960)

THE mechanism by which wires disintegrate in an electrical wire explosion differs greatly with the energy available and with the rate at which the energy is supplied. Lack of attention to this fact has led to confusion in cases where attempts have been made to compare experiments in which different mechanisms were involved.

Some scheme of classification, therefore, seems desirable. One based on energy density (and rate of supplying this energy) is here proposed.

It is obvious that if the total energy available is insufficient, the wire material cannot vaporize completely. Nevertheless, a pseudoexplosion (popping) of the wire does occur, accompanied by ejection of particles of molten metal.[1]

When the available energy is sufficient for complete vaporization, the behavior of the wire is determined by how rapidly the energy can be supplied. If it is supplied slowly, the wire will distort in its liquid state.[2] The explosion is affected by the distortion.

If the wire is supplied with energy at a high enough rate, the distortions will be insignificant, since the cylinder of liquid is practically unchanged in shape up to the instant of transplosion.[3]

A still more rapid rate of energy supply can result in a situation where the electrical and thermal skin effect prevents penetration to a significant distance and the metal is "peeled" off as the skin depth layers are vaporized in turn. So far this has not been accomplished experimentally. David[4] states that the penetration time-constant is between 1×10^{-8} and 1×10^{-9} sec, hence it is theoretically possible for ablation of this type to occur.

Our classification, based on the foregoing analysis is as follows:

I. Melting (popping)

$$\tfrac{1}{4}CV_0^2 < W_v + \int I^2 R_0 dt;$$

II. Slow explosion

$$t_v > \psi;$$

III. Fast explosion

$$t_v < \psi;$$

IV. Explosive ablation

$$t_v < \zeta,$$

where C = capacity of storage condenser; V_0 = original potential of condenser; W_v = energy to raise wire from original temperature to vaporizing point and vaporize completely; I = current through wire; R_c = effective resistance of discharge circuit (except sample wire); t = time; t_v = time required to vaporize wire; ψ = time constant of instabilities, i.e., time required for instabilities (e.g., unduloids) in the liquid to double in magnitude; ζ = electrothermal time constant, i.e., time for temperature equal to boiling point to penetrate to a depth of r/e, where r is radius of the wire, e is base of natural logarithm.

It is our belief that exploding wire experiments within any one of these classes may be reasonably compared; those in different classes may not be compared however, since they represent different phenomena.

[1] W. Kleen, Ann. Physik **11**, 579 (1931).
[2] L. Zernow, in *Exploding Wires*, edited by W. G. Chace and H. K. Moore (Plenum Press, New York, 1959).
[3] W. G. Chace, Phys. Fluids **2**, 230 (1959).
[4] E. David, Z. Physik **150**, 162 (1958).

On the Observation of Macroscopic Spirals on Gallium Arsenide Surfaces*

WARREN J. LITTLE AND KATHRYN A. MCCARTHY
Department of Physics, Tufts University, Medford, Massachusetts
(Received April 6, 1960)

SPIRAL configurations have been observed on the (111) surfaces of several III-V compounds.[1-3] It is the purpose of this letter to suggest that such spirals result from a "mistake" in the covalent bonding which occurs naturally during growth from the (111) surfaces of gallium arsenide. Spirals have not been observed on $(\bar{1}\bar{1}\bar{1})$ surfaces; on such surfaces no mistake due to bonding exists.[4]

Lang[5] has suggested that spirals are the result of lamellar growth, and that the development of these spirals does not require the presence of a screw dislocation. The spirals may develop during the growth process whenever closely packed atomic planes are at a small angle with the advancing crystal surface; under these conditions growth occurs mainly by the attachment of atoms at the edges of the atomic planes. There is a tendency for possibly hundreds of atomic steps to congregate and thus form a macroscopic dome. A mechanism for the formation of such steps during growth from the melt has been proposed by Elbaum and Chalmers.[6] From these considerations it follows that the domes may vary in size, and that some domes may even split into a number of smaller domes.

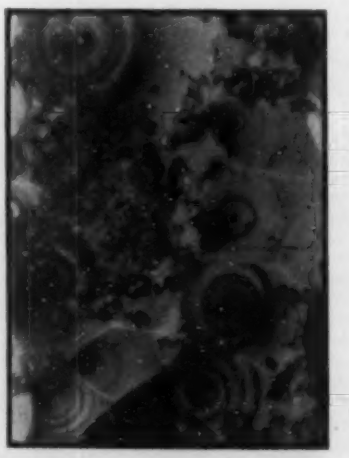

FIG. 1. Macroscopic spirals on a (111) surface of a gallium arsenide crystal, ~127×.

The process by which this dome may assume spiral form is illustrated in Fig. 1 of Lang's paper. Essentially, the lack of circular symmetry among different groups of atomic steps within the same dome causes the spiral form.

On (111) surfaces of gallium arsenide, a mistake occurs naturally which would crowd many atomic steps together. The work of Gatos, Moody, and Lavine[4] shows that when a crystal is seeded from a (111) surface, a strained configuration results because the gallium atoms which are to be added to the arsenic layer are not normally tetrahedrally bonded.

The surface of the gallium arsenide crystal shown in Fig. 1 is at an angle of ~3° with the (111) surface, as determined by the Laue back-reflection method. The surface was polished and etched for 4 min in a solution[1] of two parts HCl, one part HNO_3, and two parts H_2O. A variation in spiral size is evident; also, in lower region of Fig. 1, the splitting of spirals is shown. With this particular surface, the presence of a mistake and the consequent production of a spiral have been demonstrated.

The authors are indebted to J. R. O'Connor who kindly obtained the gallium arsenide crystals from RCA under a U. S. Air Force contract.

* Assisted by a Frederick Gardner Cottrell grant from the Research Corporation.†

[1] J. G. White and W. C. Roth, J. Appl. Phys. **30**, 946 (1959).
[2] J. W. Allen, Phil. Mag. **2**, 1475 (1957).
[3] J. L. Richards and A. J. Crocker, J. Appl. Phys. **31**, 611 (1960).
[4] H. C. Gatos, P. L. Moody, and M. C. Lavine, J. Appl. Phys. **31**, 212 (1960).
[5] A. R. Lang, J. Appl. Phys. **28**, 496 (1957).
[6] C. Elbaum and B. Chalmers, Can. J. Phys. **33**, 196 (1955).

Microscopic Study of Neutron-Irradiated Germanium

B. B. Meckel,* E. G. K. Schwarz† and R. A. Swalin‡
(Received August 3, 1959; and in final form April 11, 1960)

ALTHOUGH considerable work has been done concerning the nature of radiation damage in solids, surprisingly little has been published concerning the microscopic examination of irradiated material. A prior microscopic study of pile-irradiated germanium and silicon[1] indicated some influence of irradiation on the network-pattern revealed by a CP-4 etch applied to a (111) germanium face, however.

In the present study, a slightly modified etch of the type described by Rhodes *et al.*[2], was used, which is thought to act selectively on screw-component dislocations. Figure 1 shows the photomicrographs of three samples cut from the same germanium crystal perpendicular to the (111) direction. Figure 1(a) is the unexposed blank, while 1(b) received an integrated fast neutron flux of about 10^{10} nvt, and 1(c) of about 10^{13} nvt, respectively. Exposures were conducted in the pneumatic tube of the Convair, Ft. Worth swimming pool reactor. The temperature of the specimens never exceeded 35°C during exposure and storage. Etching revealed numerous small etch pits of random distribution in the exposed specimens; the strange pattern being superimposed on the background of the blank which is due to the screw-component dislocations ordinarily present in germanium crystals. The strange pattern etches extremely well; much faster than the background. Moreover, the small pits grow only to a well-defined extension, as opposed to the pits of the background. Thus it is possible to suppress the background by reducing the duration of etching. Figure 2 shows a high-exposure sample etched for only a small fraction of the time used in Fig. 1. The "flatness" of the field thus obtained facilitates counting of etch pit densities considerably. In 2(b) the structure of strange pits appears resolved into a triangular shape which is in register with the orientation of the background pits.

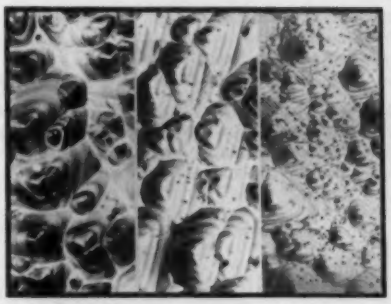

(a) (b) (c)

Fig. 1. Ge (111) surface, iodine etch fully developed: (a) unexposed blank, 270×; (b) 10^{10} nvt fast neutrons, 270×; (c) 10^{13} nvt fast neutrons, 270×.

Little is known today concerning the details of collective damage except that it should lead to disorder within well-defined closed crystal regions. Brinkman[3,4] introduced the concept of the displacement spike, and Seitz[5] invoked a somewhat different process. While one would expect part of the disorder created during spike formation to anneal out well below room temperature, another part, including the dislocation rings postulated by both theories, would exhibit activation energies sufficiently high to assure their persistence under the observed temperature limitations. The data obtained thus far are too scant as to permit any conclusions in this direction.

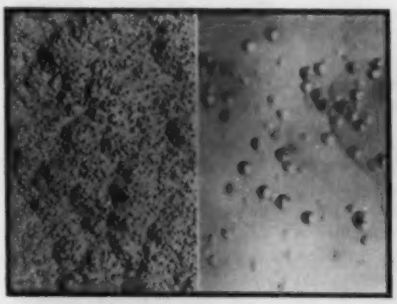

(a) (b)

Fig. 2. Ge (111) surface, iodine etch of shorter duration (a) 10^{13} nvt, 480×. (b) 10^{13} nvt, 1555×.

The observed density values agree reasonably well with estimates based on Brinkman's theory as applied to germanium. It might be added that agglomeration of distant point defects by migration can be excluded as a possible cause for the strange pits at the temperature used. Whatever the detailed mechanism of disordering may be, the etching behavior of the strange pattern indicates the presence of highly strained, well-defined regions of structural damage. Thus the authors feel that the patterns observed may represent visual evidence for spike formation in germanium crystals.

* Formerly at the University of Minnesota, Department of Metallurgy, now with Convair, San Diego, Physics Section.
† Convair, San Diego, Solid State Electronics.
‡ University of Minnesota, Department of Metallurgy.
[1] R. Chang, J. Appl. Phys. **28**, 385 (1957).
[2] R. G. Rhodes, K. O. Batsford, and D. J. Dome-Thomas, J. Electronics and Controls **3**, 403 (1957).
[3] J. A. Brinkman, J. Appl. Phys. **25**, 961 (1954).
[4] J. A. Brinkman, Am. J. Phys. **24**, 246 (1956).
[5] F. Seitz, in Solid State Physics, (Academic Press Inc., New York, 1956), Vol. 2, p. 351.

Electron Damage in Mica

T. J. SEED
University of Canterbury, Christchurch, New Zealand
(Received November 16, 1960; and in final form March 28, 1960)

DURING the operation of a soft x-ray spectrograph in which a folded-beam electron-gun[1] is used, an interesting case of electron bombardment damage to mica has been observed. The geometry of the electron gun and the mica is shown in Fig. 1.

The x-ray tube was designed to work in conjunction with a phosphor-photomultiplier detector of the soft x-radiation by means of a phase coherent demodulator, the anode current being modulated by means of a 40 cps square-wave voltage applied to grid No. 1. The three grid potentials of +500 v, +800 v, and +1000 v, respectively, and an accelerating anode potential of +6000 v results in a mean anode current of 8 ma with 30 w of heater power supplied to the tungsten filament.

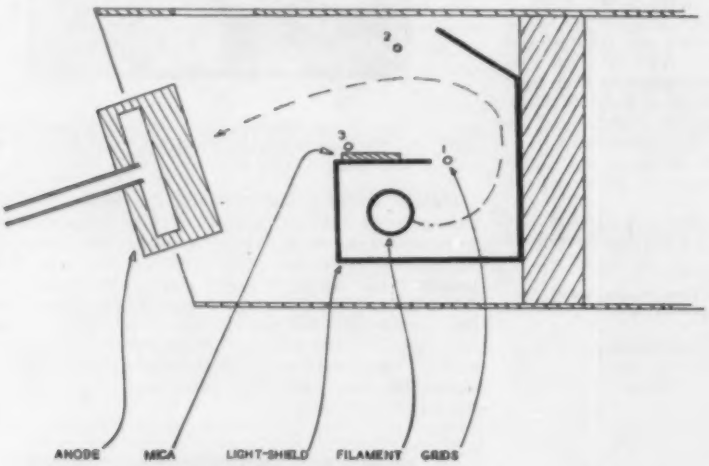

FIG. 1. Electron beam arrangement.

A piece of muscovite of dimensions approximately 20×6 mm with three tongues 3×3 mm projecting from it supports the third grid and insulates it from the nickel light shield. After having been in operation for 20 hr the tube was dismantled to replace the filament and the mica was seen to be damaged. Practically all the upper surface of the mica sustained damage which, upon closer examination with suitable lighting and a low-power binocular microscope, was found to be very systematic. The damage pattern is similar to what might be described as a casting from a laterally cut phonograph record on which a sinusoidal waveform has been cut.

The sinusoidal undulations fall into two size categories (Fig. 2): (a) the smaller and greater in number have an average pitch of 41.5 μ with standard deviation 1.2 μ; and (b) the larger which appears to be degeneration of the smaller ones, a pitch of 86.1 μ with standard deviation of 10.6 μ.

An attempt to correlate the directions of the lines of damage with the crystal axes was unsuccessful as they were 8° and 20° from the *Z*-vibration axis in the case of the coarse pitch and the degenerate undulations, while other rafts of narrow pitched undulations covering an area of a few square mm (not shown) were at 48° to 56° from the *Z* axis.

The mica insulator under the grid has been replaced on previous occasions because of damage but it had not been noticed that any symmetry was present. In this instance the lines were visible to the unaided eye as is shown in Fig. 2, where the scale graduations are of 0.5 mm spacing.

[1] A. H. McIlraith, Ph.D. Thesis, University of New Zealand, 1957.

FIG. 2. Line pattern developed on irradiated mica.

Heat Treatment Effects in Indium Arsenide

J. T. EDMOND[a] AND C. HILSUM
Services Electronics Research Laboratory, Baldock, Herts, England
(Received March 23, 1960)

WHEN specimens of InAs undergo heat treatment at temperature above 300°C, the material becomes more *n* type. If the specimens are then held at room temperature for some weeks annealing can be observed, and after 5 or 6 weeks the original Hall constant is regained. The specimen continues to anneal slowly, and after several months becomes stable, now being less *n* type than it was at first. The complete cycle is illustrated in Fig. 1. The annealing may be hastened by heating at temperatures below 200°C, and the whole annealing cycle may be observed conveniently in one week by keeping the specimens in tubes in boiling water, removing them once a day for a check of the Hall constant.

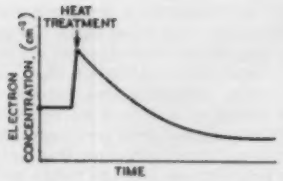

FIG. 1. Typical results for InAs heat-treated in Vitreosil.

Dixon and Enright[1] have suggested that these effects are caused by impurities which collect around dislocations; at temperatures above 300°C the impurities escape, and they may be frozen in their new position by quenching. Annealing allows them to migrate back to the dislocations. Dixon and Enright[2] also found that there was a connection between the magnitude of the effects and the amount of sulfur in the indium arsenide. Hilsum[3] showed that the effects could sometimes be reproduced by doping with copper, and his results indicated that copper was a donor in InAs. Since copper is normally an acceptor in Group IV elements and III-V compounds, and has been reported by Schillman[4] as being electrically inactive in InAs, it would be desirable to have further evidence on this point. We have therefore conducted a new series of experiments on heat treatment, designed to establish whether the effects are due to an impurity, and, if they should be, to discover the source and nature of the contamination.

In earlier experiments we had found that the changes were not markedly dependent on the prior etching treatment. The next likely source of contamination is the silica tube in which the specimen is treated. Some heat treatments were therefore carried out in Spectrosil,[5] a synthetic silica made from distilled silicon tetrachloride, which is much purer than normal silica. The specimens were held at 850°C for 17 hr, and then quenched to room temperature. Simultaneously, control experiments were made using a normal grade of silica, Vitreosil. The results for specimens treated in Vitreosil were similar to those usually found, and described above. The specimens treated in Spectrosil became more p type, and showed only a small amount of annealing afterwards. This behavior is consistent with a mechanism involving two distinct effects—a permanent change P involving a reduction in the number of ionized donors, and a temporary change N due to contamination by a donor impurity originating in the Vitreosil. These donors are rapidly diffusing, and in time migrate to dislocations, as suggested by Dixon and Enright.

Since process N is almost absent for treatments in Spectrosil, we can identify the specific impurity responsible by doping Spectrosil with it. Two small tubes of Spectrosil were therefore sealed up, one containing a few milligrams of pure sulfur, and the other a similar amount of pure copper. Both were held at 1000°C for 4 days. They were then opened, and thoroughly cleaned, together with a tube of undoped Spectrosil. Three specimens of InAs of similar electrical properties were cut from an ingot, and one was sealed in each tube. A 17-hr 850°C heat treatment was carried out simultaneously on all three specimens. The specimen treated in undoped Spectrosil had become less n type, and the other two specimens more n type. The three specimens were observed at intervals over 19 days, and $|R_H|$ for the "copper-doped" specimen decreased in just the same way as for normal heat-treated material. The other specimens showed no appreciable change. (Fig. 2). The annealing was hastened by heating at 100°C, and after several days the copper-doped specimen had become more p type than it was originally, and approached the Hall constant of the specimen treated in undoped Spectrosil.

We conclude that heat treatment on InAs in normal silica causes two changes; i.e., a permanent change, which reduces the electron concentration, and a temporary change, which increases the electron concentration. The temporary change is due to

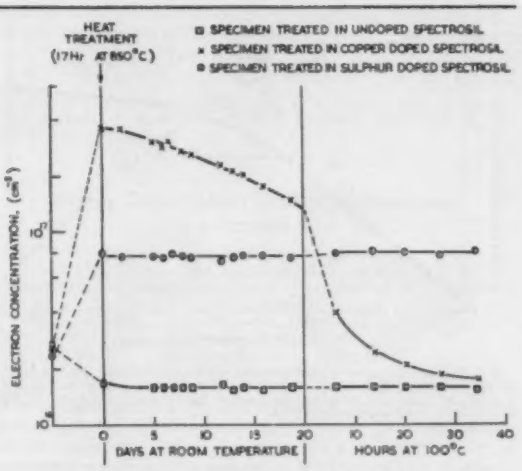
HEAT TREATMENT (17Hr AT 850°C)
□ SPECIMEN TREATED IN UNDOPED SPECTROSIL
× SPECIMEN TREATED IN COPPER DOPED SPECTROSIL
● SPECIMEN TREATED IN SULPHUR DOPED SPECTROSIL
ELECTRON CONCENTRATION, (cm⁻³)
10²
10
0 5 10 15 20 10 20 30 40
DAYS AT ROOM TEMPERATURE
HOURS AT 100°C

FIG. 2. Heat-treatment and annealing of InAs specimens.

copper contamination from the container. Copper is a rapidly diffusing donor impurity in InAs, but it has a tendency to migrate to sites where it becomes electrically inactive.

The cause of the permanent change is not established by our experiments. It is probably due to a reduction in the donor content, since the electron mobility is higher after the heat treatment. Further experimenting however is needed on this point.

We are grateful to K. E. Trezise and J. Devereux for their assistance in these measurements and to J. Goodson for making the indium arsenide.

Permission to publish has been given by the Admiralty.

* Now at Central Electricity Generating Board, Friars House, Blackfriars Road, London.
[1] J. Dixon and D. Enright, J. Appl. Phys. **30**, 753 (1959).
[2] J. Dixon and D. Enright, J. Appl. Phys. **30**, 1462 (1959).
[3] C. Hilsum, Proc. Phys. Soc. (London) **A73**, 685 (1959).
[4] E. Schillman, Z. Naturforsch **11a**, 463 (1956).
[5] Supplied by The British Thermal Syndicate.

Saturation of Photocurrent with Light Intensity

RICHARD H. BUBE
RCA Laboratories, Princeton, New Jersey
(Received April 4, 1960)

SATURATION of photocurrent with increasing voltage for fixed light intensity is a well-known phenomenon which can arise from a number of different causes, such as a primary photoeffect with blocking electrodes or photoconductivity involving both electrons and holes but only one of these replenished at the electrodes.[1] Saturation of photocurrent with increasing light intensity at fixed voltage is, by comparison, a very rare phenomenon. This letter describes the observation of such a saturation of photocurrent with light intensity in crystals of cadmium sulfide.

The crystals involved are specially prepared pure crystals of CdS, described in a previous publication.[2] These crystals are insulating and insensitive, but can be made sensitive by annealing in vacuum in a sealed tube at a low temperature with one end of the tube at room temperature. The sensitization is quite similar to that previously reported for CdSe crystals.[3] The saturation data shown in Fig. 1 are for a crystal (1.5×1.2×0.01 mm³)

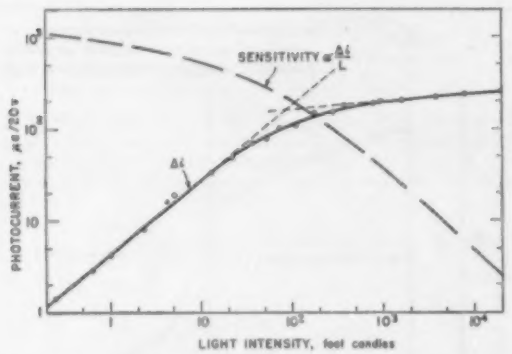

FIG. 1. The variation of photocurrent with light intensity and of sensitivity with light intensity for a crystal of pure CdS annealed in vacuum. Excitation is by an incandescent source, but spectral response of the crystal is sharply peaked at 5150 A.

annealed for 2½ hr at 325°C in this way. Ohmic indium electrodes were used. Below 10 ft-c, the variation of photocurrent with light intensity is approximately linear, but between 10^2 and 2×10^4 ft-c the photocurrent increases by only about a factor of 2. No saturation with voltage is involved; at 2×10^4 ft-c, doubling the applied voltage doubles the measured photocurrent.

The crystal for which the data of Fig. 1 are given was subjected to a series of a dozen tests over a two-week period, involving periods in the dark, periods of operation at high light levels, periods of heating to 90°C while operating, and other similar treatments. None of these tests appreciably altered the properties of the crystal. In terms of the parameters used in the paper referred to previously,[2] the crystal at low light levels was characterized by (1) a specific sensitivity of 2×10^{-1} cm²/(ohm watt), (2) a photoconductivity gain of 5×10^3, (3) a maximum gain M factor of 3, and (4) a speed of response improvement factor of 60 relative to standard CdS:Cl:Cu crystals. Traps with thermally stimulated current below −30°C were present with a density of 2×10^{14} cm^{-3}, whereas traps with thermally stimulated current between −30° and 100°C were present with a density of only 5×10^{13} cm^{-3}.

The occurrence of a saturation of photocurrent with light intensity can be interpreted as resulting from a saturation of sensitizing centers in the crystal,[1] i.e., all those centers with a large cross section for holes and a subsequent small cross section for electrons become completely occupied by holes. Additional photo-excited holes formed by increasing the light intensity further can be captured only at centers with large cross section for electrons. The saturated photocurrent can therefore be considered to be made up of current resulting from (1) electrons with long lifetime, with density equal to that of the sensitizing centers, and (2) electrons with short lifetime, produced by the absorption of photons over and above those needed to saturate the sensitizing centers.

The departure of the measured curve from complete saturation can be interpreted in terms of this additional current generated over and above that current corresponding to the holes captured at sensitizing centers. The free electron lifetime just before the beginning of saturation is 10^{-3} sec; it decreases to 8×10^{-6} sec at 2×10^4 ft-c, where the corresponding gain is 1.5. Excitation at 10^2 ft-c corresponds to the creation of about 4×10^{17} electrons/sec/cm³ (assuming 4×10^{15} photons/lumen), each with a lifetime of 10^{-3} sec. The current associated with these electrons is about equal to that associated at 2×10^4 ft-c with the creation of 8×10^{19} electrons/sec/cm³, each with a lifetime of 8×10^{-6} sec.

The photocurrent at saturation is estimated as the intersection of the straight line portions at low and high light intensities, as indicated in Fig. 1. This photocurrent corresponds to a free electron density of 3×10^{14} cm^{-3} (assuming an electron mobility of 200 cm²/v sec), and hence to a sensitizing center density of 3×10^{14} cm^{-3}. Since the crystals are highly photosensitive below the saturation range, it also indicates that the competing high-cross-section recombination centers are of the same order of magnitude in density (assuming that the hole capture cross sections of the two types of centers are comparable). Coupled with the trap density figures given previously, these results can therefore be considered as giving evidence that the density of levels throughout the forbidden gap is in the 10^{13} to 10^{14} cm^{-3} range in these special pure crystals.

[1] See R. H. Bube, *Photoconductivity of Solids* (John Wiley & Sons, Inc., New York, 1960).
[2] R. H. Bube and L. A. Barton, R C A Rev. **20**, 564 (1959).
[3] R. H. Bube and L. A. Barton, J. Chem. Phys. **29**, 128 (1958).

Damaged Layers and Crystalline Perfection in the {111} Surfaces of *III-V* Intermetallic Compounds

E. P. WARekois, M. C. LAVINE, AND H. C. GATOS
Lincoln Laboratory, Massachusetts Institute of Technology, Lexington, Massachusetts*
(Received April 15, 1960)

IT was found that the same cold-working treatment (abrasion or sandblasting) introduces an appreciably greater depth of damage in the GaAs and InSb {111} surfaces terminating with group V atoms (B surfaces) than in the {111} surfaces terminating with group III atoms (A surfaces). When no coldwork was introduced, excepting the strain that may be associated with crystal growth, it was further found that the B surfaces exhibited a somewhat greater degree of crystalline perfection than the A surfaces.

The GaAs and InSb single crystals employed in this study were grown by the Czochralski method. The parallel A and B surfaces of each sample were ground to within 1° from the (111) orientation as determined by x-ray diffraction. They were extensively etched and then subjected to the desired cold-working treatment.

Etching and x-ray diffraction techniques were employed for determining the extent of damage. In the etching technique advantage was taken of the fact that cold-work increases the surface reactivity and also alters the etch-figure patterns.[1] After the A and B surfaces were cold-worked the sample was mounted in a plastic so that only a {110} surface perpendicular to the cold-worked {111} surfaces was exposed as shown in Fig. 1. The depth of damage was determined from the portions of the exposed surface which became beveled by etching (Fig. 1). An abrupt

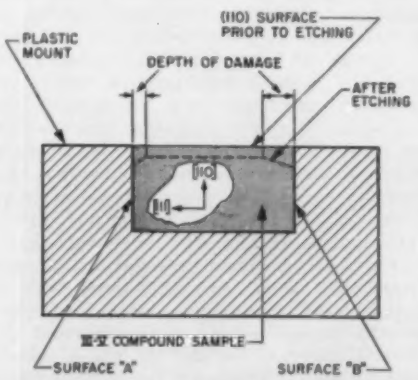

FIG. 1. Schematic illustration of the experimental arrangement for determining surface damage by etching. Surfaces A and B were given an identical cold-working treatment.

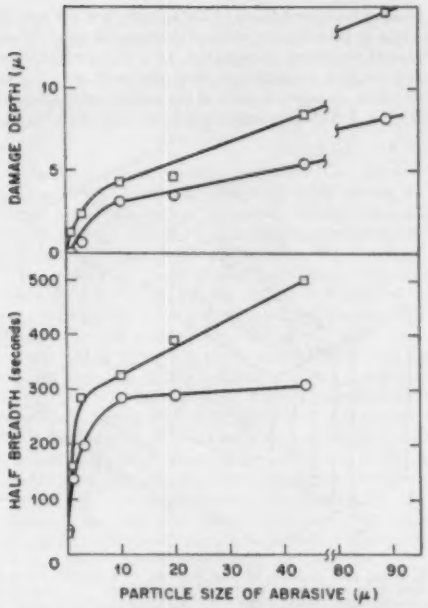

FIG. 2. Damage of the *A* and *B* surfaces of GaAs as a function of particle size or abrasive. The depth of damage in μ was determined by etching. The half-breadths correspond to the x-ray rocking curves obtained with iron radiation; □ surface *B*; ○ surface *A*.

change in the etch-figure patterns was also observed at the termination of the cold-worked area.

In addition to etching, a double crystal x-ray spectrometer was employed for determining the extent of surface damage. The rocking curves were obtained with iron radiation. A germanium single crystal served as a monochromator. The spacing of the {111} planes of germanium is nearly the same to the corresponding spacing of the compounds employed. The half-breadths of the rocking curves are taken as a measure of the surface damage without reference to specific types of damage contributing to the half-breadth of the curves.

Some typical experimental results are shown in Fig. 2. It is seen that the depth of damage increases with increasing particle size of the abrasive. For the same abrasive treatment the depth of damage is greater in the *B* surfaces than in the *A* surfaces. Similar results were obtained with InSb except the depth of damage was found to be a few microns greater than the corresponding damage in GaAs.

After the cold-work introduced during grinding was removed with chemical etching, the half-breadth (β_A) of the rocking curves of the surface *A* was found to be greater than the half-breadth (β_B) of the surface *B* for given GaAs crystal. The observed difference is outside experimental error and the calculated x-ray dispersion effect.[2] The ratios of the half-breadths measured thus far are $\beta_A/\beta_B > 1.1$, indicating that, for a given single crystal, the *B* surfaces are more perfect than the *A* surfaces. This result is consistent with the bond model proposed for the *A* and *B* surfaces of the *III-V* compounds,[1] and the finding that single crystals of InSb grown in the *B*<111> direction possess a greater degree of crystalline perfection than those grown in the *A*<111> direction.[3]

The observed differences in depth of damage between the *A* and the *B* surfaces are also believed to be closely related to the difference in the bonding characteristics of the *A* and *B* surface atoms. In order to clarify this point, further experiments are in progress employing additional *III-V* compounds, different orientations, and varying surface treatments.

[6] Operated with support from the U. S. Army, Navy, and Air Force.
[1] H. C. Gatos and M. C. Lavine, J. Electrochem. Soc. **107**, 427, 433 (1960).
[2] E. P. Warekois and P. H. Metzger, J. Appl. Phys. **30**, 960 (1959).
[3] H. C. Gatos, P. L. Moody, and M. C. Lavine, J. Appl. Phys. **31**, 212 (1960).

Direct Observation of Superdislocations in a Superlattice

M. J. MARCINKOWSKI AND R. M. FISHER
Edgar C. Bain Laboratory for Fundamental Research, United States Steel Corporation Research Center, Monroeville, Pennsylvania
AND N. BROWN
School of Metallurgical Engineering, University of Pennsylvania, Philadelphia, Pennsylvania.
(Received March 17, 1960)

KOEHLER and Seitz[1] in 1947 first proposed the concept of superdislocations in ordered alloys. In particular, they postulated that the dislocation configuration in a superlattice should consist of a pair of ordinary dislocations separated by an antiphase boundary. The separation is determined by a balance between the elastic repulsive forces of the two ordinary dislocations and the surface tension of the antiphase boundary.[2]

An original search for superdislocations in CuZn was unsuccessful. Presumably, the dislocation pairs were too closely spaced to be resolved. The first success was with vacuum melted $AuCu_3$ which was rolled into thin strips. The strips were in turn recrystallized at high temperatures to give large grains and then slowly cooled through the critical ordering temperature. Examination of specimens by x rays showed nearly perfect long-range order. The strips were electropolished to thin films and examined by transmission electron microscopy in a Siemens Elmiskop I operating at 100 kv.

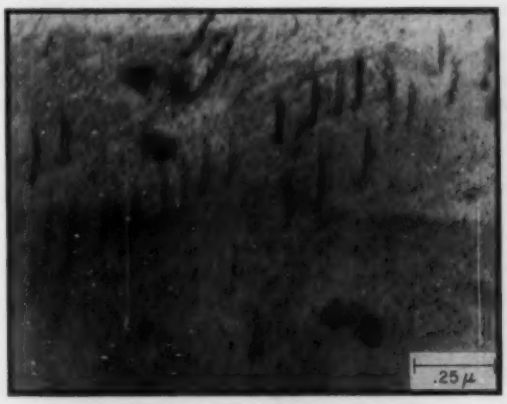

FIG. 1. Superdislocations in $AuCu_3$.

Figure 1 shows a typical dislocation array observed in the ordered alloys. All of the dislocations are arranged in pairs on parallel slip planes. Each pair is a superdislocation which was probably introduced into the specimen either by handling or from stresses introduced by heating from the electron beam. The actual width of superdislocation was found to be about 130 A. This is in good agreement with preliminary theoretical calculations that we have made.

[1] J. S. Koehler and F. Seitz, J. Appl. Mechanics **14**, A-217 (1947).
[2] For the particular case of the $AuCu_3$-type alloy, each ordinary dislocation is itself dissociated into a pair of partial dislocations separated by a stacking fault. In general, the distance between these partials is too small (<20 A) to be resolved and according to theory should be a small fraction of the total width of the superdislocation.

Fine Structure of Bloch Walls

S. Shtrikman and D. Treves*
Department of Electronics
The Weizmann Institute of Science
Rehovot, Israel

(Received April 12, 1960)

IT has been recently noted[1] that the subdivision of 180° Bloch walls into a periodic structure of right- and left-hand sections[2] is accompanied by the zigzagging of these walls. An example of this is shown in Fig. 1. The purpose of this letter is to provide a qualitative explanation of this zigzagging.

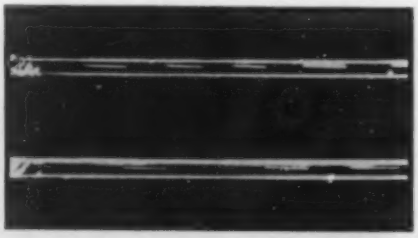

FIG. 1. Bitter patterns of a subdivided 180° domain wall in an iron whisker. The segmentation of the wall is revealed by the application of a field normal to the surface. By looking at the photograph at a grazing angle one can observe that the wall zigzags slightly. Comparison of the upper and lower photographs, which are those of the top and bottom faces of the same whisker, shows that the wall zigzags oppositely on opposite faces of the whisker; here the bottom face was photographed through a mirror.

At the first thought, zigzagging of a wall seems to increase its energy because when the wall is not parallel to the easy axis of magnetization, volume charges will appear to increase the magnetostatic energy. This will actually be the case in regions of the wall which are far from the surface of the sample. Near the surface, however, the interaction of the volume charges in the wall with the surface charges, which appear at the intersection of the wall and the surface, can cause a reduction of the magnetostatic energy[3] if the wall is tilted suitably. Figure 2 shows schematically that for a left-hand wall, the necessary tilt is a left-handed one

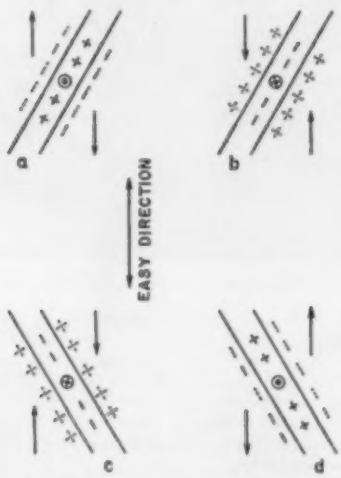

FIG. 2. Tilt in the direction of the wall that will lower its magnetostatic energy: *a*, *b* are the right-hand wall cases, and *c*, *d* are the left-hand ones. The + and − signs show the free charges. The solid ones are the surface charges at the intersection of the wall with the surface of the sample. The broken ones are the volume charges which appear in the wall because of the tilt.

when looking into the surface of the sample, and for a right-hand wall a right handed tilt is needed. Zigzagging of subdivided Bloch walls should therefore be expected. One should further expect, according to this explanation, that the wall would zigzag in opposite phase on opposite faces of the sample, as is schematically shown in Fig. 3. This conclusion is in agreement with Fig. 1, which

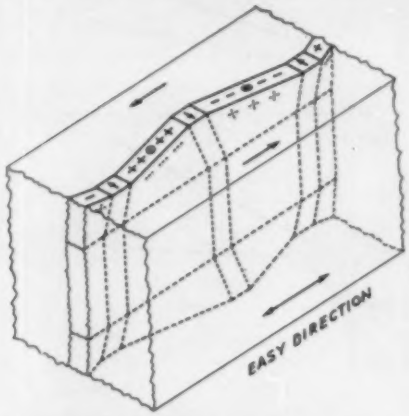

Fig. 3. Schematic drawing of the internal structure of a subdivided Bloch wall in a whisker as modified by zigzagging. (1) main domains; (2) right-hand wall; (3) left-hand wall; (4) Bloch line.

shows Bitter patterns of the top and bottom faces of an iron whisker.[4]

The authors wish to thank Dr. R. W. DeBlois and Dr. C. D. Graham for making the photographs in the letter available to them.

* Present address: Pomona College, Department of Physics, Claremont, California.
[1] R. W. DeBlois (private communication).
[2] For a theoretical discussion of the subdivision of Bloch walls into right- and left-hand sections, see S. Shtrikman and D. Treves, J. Appl. Phys. **31**, 147S (1960).
[3] Zigzagging of the wall will according to this picture occur only near the surface of the sample.
[4] See also Fig. 2 of R. W. DeBlois and C. D. Graham, J. Appl. Phys. **29**, 932 (1958). This figure should be looked at in a grazing angle.

An Experimental Test of the First Kelvin Relation

F. J. Donahoe and L. R. Testardi
The Franklin Institute Laboratories, Philadelphia, Pennsylvania

(Received March 14, 1960)

THE first Kelvin relation $\Pi = -TS$, where Π is the Peltier coefficient, S the Seebeck coefficient, and T the absolute temperature, rests on a firm theoretical foundation since the development of irreversible thermodynamics. However, data in support of the validity of this relation are scarce.[1–7] Moreover, Shtenbek and Baranskii[8] have reported a discrepancy of from 5 to 15% in a series of measurements on extrinsic germanium. The discrepancy was in the direction such that $1.05\Pi \leq -TS \leq 1.15\Pi$.

We have investigated the validity of the relation for a semiconducting alloy $Bi_2Te_{2.4}Se_{0.6}$ doped with 0.05 wt% Cu_2Br_2. The room temperature thermal conductivity of a specimen of this alloy was measured (a) by an absolute method in which the temperature gradient developed by the passage of a known amount of power was determined, and (b) by an indirect method in which the Peltier power was used to establish the temperature gradient.

For the first method an apparatus similar to that described by Satterthwaite and Ure[9] was employed. Power is supplied to a

heater at one end of the sample, the other end being in contact with a heat sink. When a steady state has been attained, the thermal conductivity κ is computed from the input power P, the temperature difference across the specimen ΔT, and the ratio of length to cross-section area L/A

$$\kappa = PL/A\Delta T. \quad (1)$$

To minimize lateral heat losses by radiation from the specimen, and radiation losses from the heater, a shield (along which a temperature gradient identical to that in the specimen is maintained by a separate heater), symmetrically surrounds the specimen. Temperature differences of 1°, 2.5°, and 10°C were impressed across the specimen. The two smaller ΔT's gave identical values for κ, while the largest ΔT gave a value which differed by 1%. Steady-state conditions were assured by repeating measurements during a 20-hr period during which the heater power was maintained at a constant value. The shield and specimen temperatures agreed to better than 1/40°C during the measurements. This difference contributes less than 0.5% error. This estimate is based on observations during which the shield was deliberately maintained at a temperature different from that of the specimen.

The second method requires the measurement of the steady-state temperature gradient established along the sample by the Peltier power liberated at one junction and absorbed at the other when a steady current flows through the specimen. When the sample is isolated from all other heat currents it is possible to describe the steady state by the equation[10]

$$\kappa = \Pi I L/A\Delta T, \quad (2)$$

where I is the electric current. If the validity of the first Kelvin relation is assumed this equation becomes

$$\kappa = -TSI\, L/A\Delta T. \quad (3)$$

The equality of the κ's computed from (1) and (3) then implies the validity of the first Kelvin relation. The results of our measurements agree to within 2%, which is within the experimental error.

Measurements using the second technique were made with ΔT's of 0.5° and 0.75°C. The values agreed to within 1%. No irreversible effects were found on reversing the direction of the electric current and temperature gradient. In a separate determination the electrical contact resistance was found to be less than 1% of the sample resistance, thereby contributing negligible error. The specimen chamber was shielded from ambient radiation with aluminum foil. The mean temperature of the sample differed by 0.1°C or less from the ambient. The radiation error depends upon the ratio of the power transferred by radiation to that conducted through the sample. After measurements were completed the specimen was cut down to one-half its original length and remeasured by the second method. For the particular geometry employed this should reduce the radiation error by approximately 70% of the original value. Since the value of κ determined on the cut specimen differed by less than 1% from that determined before cutting, the radiation error must be negligible.

Sample homogeneity was assured by zone-levelling the original ingot from which our test specimens were cut. Three specimens were cut from the center portion of the ingot. The Seebeck coefficient S and the electrical conductivity σ of each of the three specimens agreed to better than 2% among themselves. The middle section was taken for the test specimen. Since the same specimen was measured by both methods, errors in measuring L/A cannot affect the comparison of the values of κ determined by the two methods.

Thermocouples used were of selected and calibrated chromel-alumel type which were recalibrated and matched at room temperature in place. Switches and binding posts in the thermoelectric circuit were insulated from room air currents. Temperatures were measurable to 1/400°C.

TABLE I. Experimental values of the thermal conductivity determined by (a) absolute method and (b) indirect method.

T, °C	Method (a) $\kappa \times 10^6$ w/cm°K	Method (b) $\kappa \times 10^6$ w/cm°K
0.5	...	15.55
0.75	...	15.7
1	15.85	...
2.5	15.85	...
2.5	15.75	...
10	15.95	...

The results of the measurements are given in Table I. To within 2% experimental error the agreement between the κ's determined by the two different methods implies the validity of the first Kelvin relation.

The authors are indebted to the sponsors of the thermoelectric effects research program for their financial support.

[1] H. C. Barker, Phys. Rev. **31**, 321 (1910).
[2] A. E. Caswell, Phys. Rev. **33**, 379 (1911).
[3] W. Jaeger, *Handbuch der Physik* (Springer-Verlag, Berlin, 1926) Vol. 11, p. 37.
[4] G. Borelius, Ann. Physik **56**, 388 (1918).
[5] G. Borelius and A. Lindh, Ann. Physik **53**, 17 (1917).
[6] G. Borelius, Ann. Physik **52**, 398 (1917).
[7] G. Gottstein, Ann. Physik **43**, 1079 (1914).
[8] M. Shtenbek and P. I. Baranskii, Zhur. Tekh. Fiz. **26**, 683 and 1372 (1956); *ibid* **27**, 233 (1957); English translations in Soviet Phys.-Tech. Phys. **1**, 639 and 1345 (1957); *ibid.* **2**, 205 (1957).
[9] C. B. Satterthwaite and R. W. Ure, Jr., Phys. Rev. **108**, 1164 (1957).
[10] T. C. Harmon, J. H. Cahn, and M. J. Logan, J. Appl. Phys. **30**, 1351 (1959).

Errata: Books Reviewed

[J. Appl. Phys. **31**, 223 (1960)]

Bibliographical information for *Principles of Quantum Electrodynamics* and *Methods of Experimental Physics* should read as follows:

Principles of Quantum Electrodynamics. WALTER E. THIRRING, translated by J. Bernstein. Volume 3 of Pure and Applied Physics, H. S. W. Massey, consulting EDITOR. Pp. 234. Academic Press, Inc., New York, 1959. Price $8.00.

Methods of Experimental Physics. L. Marton, EDITOR IN CHIEF. Volume 6: Solid State Physics. Part A: Preparation, Structure, Mechanical and Thermal Properties. K. Lark-Horovitz and Vivian A. Johnson, EDITORS. Pp. 466. Academic Press, Inc., New York, 1959. Price $11.80.

Books Reviewed

Prompt, noncritical reviews appear in this column. Critical reviews of many of the books described here will appear in Physics Today, The Review of Scientific Instruments, *or* American Journal of Physics.

Introduction to Quantum Field Theory. F. MANDL. Pp. 189 +viii. Interscience Publishers, Inc., 1959. Price $6.00.

This introduction to the theory of quantum fields is based on the Hamiltonian formalism. A set of exercises, together with hints for their solutions are included. While some are of a routine nature, others introduce and develop important new ideas which might well have found a place in the main body of the book. The reader is assumed to possess a good knowledge of classical physics, nonrelativistic quantum mechanics, special theory of relativity, and the Dirac theory of the atom.

Physical Methods of Investigating Textiles. R. MEREDITH AND J. W. S. HEARLE, EDITORS. Pp. 386. Textile Book Publishers, Inc., New York, 1959. Price $13.00.

This book contains the following: X-ray Techniques, D. R. Holmes; Infra-red Spectroscopy, C. G. Cannon; Electron Microscopy, J. A. Chapman; etc.

Masers. GORDON TROUP. Pp. 152+xii. John Wiley & Sons, Inc., New York, and Methuen and Company, Ltd., London, 1959. Price $2.75.

A discussion of the stimulated emission process is followed by a brief outline of methods used to obtain the conditions necessary for amplification. The effects of various physical processes upon amplifier efficiency, and upon the effective frequency response of a molecular transition used to amplify are described. The book goes on to give derivations of the gain, bandwidth, and noise factor of the traveling-wave line type of stimulated emission amplifier and of the resonant cavity type of amplifier. A review of the experimental work on "masers" is given together with a comprehensive bibliography.

Sector-Focused Cyclotrons. Proceedings of an Informal Conference, Sea Island, Georgia, February 2–4, 1959. F. T. HOWARD, EDITOR. Nuclear Science Series, Report No. 26. Publication 656. Pp. 294. National Research Council, National Academy of Sciences, Washington, D. C., 1959. Price $2.50.

The National Academy of Sciences has recently published the proceedings of a conference on Sector-Focused Cyclotrons which was held in February, 1959 by the Subcommittee on Instruments and Techniques of its Committee on Nuclear Science. F. T. Howard of the Oak Ridge National Laboratory served as editor. The 49 papers presented cover the design, construction, and testing of sector-focused cyclotrons. They include discussion of ion orbit theories, calculation of complex magnetic field configuration, and factors affecting beam quality and control as well as problems encountered in the operation of fixed frequency cyclotrons. In addition to the text of the papers, the informal discussion of these topics by the members of the conference is given. A tabulation of the characteristics of 15 sector-focused cyclotrons which are either in operation or under construction is presented in an appendix.

Ionization Phenomena in Gases. GORDON FRANCIS. Pp. 280 +xii. Academic Press, Inc., New York, 1960. Price $10.50.

This book is intended to be complementary to the several excellent textbooks on ionized gases published in recent years. For this reason the author has avoided repeating accounts of the more well-known discharges—the arc, spark, and glow, for example—and has treated instead those branches of the subject which are closely linked with other branches of physics, and which cannot be studied except by intensive searching through the literature. A brief chapter on fundamental processes is included to provide a general background for the reader who is not very familiar with the subject. The book is written mainly for those finishing their degrees or about to begin research, in the hope that they may see a broader picture than is often revealed by specialized and sharply divided curricula.

Soap Films. Studies on Their Thinning and a Bibliography. KAROL J. MYSELS, KOZO SHINODA, AND STANLEY FRANKEL. Pp. 110. Pergamon Press, New York, 1959. Price $7.50.

This book presents an account of investigations into the process by which a film of soap solution or the like comes to be thin. The authors have presented this work in the form of a monograph, rather than as a number of separate succinct articles, and in it describe a number of experiments, calculations, and speculations in a discursive connected form. A bibliography which should guide the reader to the work of others and on further aspects of the subject is included. In the body of the text use has been made of many well-known relations from various branches of physics and physical chemistry. Although most of these will be familiar to each reader, elementary explanations have been included to facilitate the reading of this book without frequent reference to standard texts.

Physics in Your High School. A handbook for the improvement of physics courses. Prepared by the American Institute of Physics. Pp. 106+xxvi. McGraw-Hill Book Company, Inc., New York, 1960. Price $1.50.

The booklet begins with a discussion of the organization and activities of a school science committee. Physics programs are considered: levels of difficulty, courses and special assignments for superior students, the relation between work in mathematics and work in physics, time allotments for teaching physics, grades, some critera for the selection of content, textbooks, syllabuses, and new physics programs including the physics course of the Physical Science Study Committee and the Harvey White film-television course. The objectives and requirements of laboratory work and teacher demonstrations, the use of books and films in physics courses, and the allotment of space and the design of physics classrooms and laboratories are then discussed. The final chapter deals with the characteristics of high-quality instruction in high-school physics: what distinguishes superior teaching from routine teaching.

Appendices to the booklet contain information about the various study opportunities afforded teachers by the programs of the National Science Foundation, lists of laboratory and demonstration apparatus for physics courses at three different levels, and a list of books, periodicals, and films. The booklet was written to be as specific as possible: if full information is not included in the booklet, names and addresses of sources of further information are given.

The text for the booklet was written by T. D. Miner, Instructor of Physics at Garden City (New York) High School, and W. C. Kelly, AIP Director of Education Projects.

Mechanical Properties of Intermetallic Compounds. J. H. WESTBROOK, EDITOR. Based on a symposium held in Philadelphia in May, 1959, sponsored by the Electrothermics and Metallurgy Division of the Electrochemical Society, Inc. Pp. 404. John Wiley & Sons, Inc., New York, 1960. Price $9.50.

This book is the first explicit treatment of the mechanical properties of intermetallic compounds. It contains the proceedings of a special symposium held in Philadelphia in May, 1959, sponsored by the Electrothermics and Metallurgy Division of the Electrochemical Society, Inc. Broad coverage of the subject includes:

Phenomenology of the mechanical behavior of intermetallics
Theoretical and experimental investigations of particular properties
Experimental techniques for the preparation and study of intermetallics
An extensive review of the literature.

Fast Neutron Physics. Part I: Techniques. Part II: Experiments and Theory. Vol. IV. J. B. MARION AND J. L. FOWLER, EDITORS. Pp. 960. Interscience Publishers, Inc., New York, 1960. Price $29.00.

The upper limit of the range of neutron energy considered here is about the threshold for nonelastic nucleon-nucleon collisions—that is, several hundred Mev—although most of the material pertains to the energy region below about 40 Mev.

The emphasis of this work is on monoenergetic neutrons and their interactions with nuclei; nevertheless, polyenergetic sources are also discussed. *Fast Neutron Physics* is meant to be a reference work. Enough detail is included to make this book of interest and of use not only to research scientists, but also to reactor engineers, health physicists, and in fact to all those whom the field of nuclear energy brings in contact with neutrons. Although these two volumes are meant primarily for experimentalists, theorists will find collected here, in some instances for the first time, the theoretical material which pertains to the interpretation of the interaction of neutrons with nuclei.

Growth of Crystals. Vol. 2. A. V. SHUBNIKOV AND N. N. SHEFTAL, EDITORS. Pp. 178. Consultants Bureau, Inc., Publishers, New York, 1960. Price $16.00.

This second volume contains 24 papers on crystal growth, in addition to the major contribution by the late S. K. Popov on "Growth and uses of gem-grade corundum crystals."

These papers report on the work by leading Soviet crystallographers since the first conference on crystal growth (1956).

The symposium papers are conveniently organized into three sections:

1. Theoretical and Experimental Studies
2. Growing Monocrystals; Apparatus, Methods, and Accessory Operations
3. Reviews and Discussion Papers.

Radiation Biology. Proceedings of the Second Australasian Conference on Radiation Biology held at the University, Melbourne, December 15–18, 1958, by The Australian Radiation Society. J. H. MARTIN, EDITOR. Pp. 304. Academic Press, Inc., New York, 1959. Price $11.00.

The Proceedings of the Second Australasian Conference on Radiation Biology is a collection of papers plus some discussion dealing primarily with radiation aspects of lukemia, biological response, immunology, action on organic compounds, fall-out, protective mechanisms, and mechanisms at the cellular level. A goodly portion of the material is contributed by two eminent scientists (L. H. Gray and J. F. Loutit) of the United Kingdom, and the status of work in their own country is ably reviewed. Otherwise, the primary coverage is of Australian work. The papers are generally very well written and the volume should be of value as a status summary to anyone interested in the field of radiation biology.

Similarity and Dimensional Methods in Mechanics. L. I. SEDOV, translation by Morris Friedman. Pp. 353+iv. Academic Press, Inc., New York, 1960. Price $14.00.

In this remarkable volume are brought together an impressive number (about 40) of more-or-less unrelated topics, ranging from the motion of a simple pendulum to shock wave decay and a theory of novae and supernovae. These diverse subjects, many of them falling within the broad realm of modern fluid mechanics, have in common that they can profitably be attacked by similarity techniques and/or dimensional considerations. Here the details of this attack are presented and then the mathematical solution is carried through to the presentation of graphical results and physical interpretation. The author is recognized as one of the great engineer-scientists of our times, and it is clear that he is a master of these powerful techniques and of applied mathematics in a very broad sense.

Physics for Students of Science and Engineering. Part I. R. RESNICK AND D. HALLIDAY. Pp. 554+xxviii. John Wiley & Sons, Inc., New York, 1960. Price $6.00.

This book is the first part of a two-part textbook and is mainly concerned with mechanics, wave motion, and heat. The approach is changed from the highly deductive treatment which emphasizes engineering application by way of illustration of principles to one which is somewhat more inductive, stressing the relation between theory and experiment and illustrating the principles by application to areas of contemporary physics. A concurrent course in calculus is assumed.

Physics of Meteor Flight in the Atmosphere. ERNST J. OPIK. Pp. 155+xi. Interscience Publishers, Inc., New York, 1958. Paper bound: $1.95; hard bound: $3.85.

The booklet has originated from a series of lectures on "The Physics of Meteors and their Cosmic Relationships," delivered in the spring term of 1957 at the Department of Physics of the University of Maryland, during the author's stay there as Visiting Professor. The present scope is somewhat narrower and covers chiefly the phenomena occurring during the flight of the meteor through the terrestrial atmosphere. The intention is to provide a basis for further research.

An Introduction to Statistical Communication Theory. DAVID MIDDLETON. Pp. 1102+vii. McGraw-Hill Book Company, Inc., New York, 1960. Price $25.00.

In this new work the author is concerned with the rapidly evolving field of statistical communication theory, which may broadly be described as the application of modern statistical methods to the random phenomena (messages, signals, and noise), that influence and control the design, operation, and evaluation of communication systems. Although the specific treatment in this book is directed toward electronic and electrical systems, such as radio, radar, etc., the general methods and philosophy described herein are applicable in other areas of communication science as well. The book is also suitable as a text for first- and second-year graduate students, by appropriate selection of material, with 300 problems and a bibliography of 500 selected references.

Tables of Physical and Chemical Constants. G. W. C. KAYE AND T. H. LABY. 12th ed. Pp. 224. Longman's, Green and Company, Inc., New York, 1959. Price $5.50.

In this new edition the most extensive changes have been made in the Chemistry section: roughly 20 pages of tables dealing with Chemical Thermodynamics and Electro-Chemistry have been reshaped to bring them into line with modern usage. In the General Physics section the main revisions have been under the headings Time, Elasticities, Full Radiation. In Atomic Physics the table of Radioactive and Stable Isotopes has been greatly expanded and a more thorough introduction has been provided for the table of General Atomic Constants, which have been entirely recalculated. The preparation of the twelfth edition has been undertaken by the same editorial board as compiled the eleventh.

Proceedings of 9th Symposium in Applied Mathematics. Vol. IX. *Orbit Theory.* G. BIRKHOFF AND R. E. LANGER, EDITORS. Held at New York University in 1957. American Mathematical Society, Rhode Island, 1959. Price $7.20.

The book contains the following:

"Orbit stability in particle accelerators," by E. D. Courant.

"Motion of cosmic-ray particles in galactic magnetic fields," by S. Olbert.

"Stormer orbits," by W. H. Bennett.

"General theory of oblateness perturbations," by Paul Herget.

"Fundamental problems in predicting positions of artificial satellites," by F. L. Whipple.

"Cislunar orbits," by K. A. Ehricke.

"Satellite launching vehicle trajectories," by J. W. Siry.

"Numerical determination of precise orbits," by W. J. Eckert.

"Comments on general theories of planetary orbits," by Dirk Brouwer.

"Orbits in Birkhoff's central field," by C. G. Fernandez.

The Study of Elementary Particles by the Photographic Method. C. F. POWELL, P. H. FOWLER, AND D. H. PERKINS. Pp. 669+xvi. Pergamon Press, New York, 1959. Price $40.00.

This book had its beginning as an atlas of photomicrographs of tracks of high energy particles in nuclear emulsions. As it developed, explanatory material was added, both on the methods of measurement and analysis, and on the properties of elementary particles. As published, the book contains a fairly complete summary of experimental knowledge about the particles and their high energy behavior, including information drawn from other experimental sources besides the emulsion tracks. Most remarkable are the 190 large, well selected, and beautifully printed plates. The text is on an appropriate level for reference use by graduate or senior honor students, as an introduction to experimental research on high energy particles. It is rather specialized, large, and expensive for general use as a textbook.

Property Measurements at High Temperatures. W. D. KINGERY. Pp. 416. John Wiley & Sons, Inc., New York, 1959. Price $16.50.

A very useful introduction to techniques for the measurement and interpretation of data on condensed systems at temperatures above 1400°C. (Kingery defines this as the lower temperature limit associated with high temperature phenomena.) The utility of data on solids and liquids and their measurement and reliability are surveyed. The book is directed to the first year graduate student and is essentially a collection of pertinent information with a discussion of principles of characteristic properties and behavior of liquids and solids at high temperatures.

Three unique features of the book are its critical consideration of the validity of a wide variety of data, introductory sections to almost every topic covered, and a comprehensive bibliography at the end of each section. The author has scarcely overlooked a single important topic in the field and has not hesitated to dig into each topic in terms of both general principles and specific applications. The book is not an exhaustive treatment but it does provide a convenient and well-arranged collection of useful information on techniques and data relating to solids and liquids at elevated temperatures.

The Scattering and Diffraction of Waves. Harvard Monographs in Applied Science No. 7. RONOLD W. P. KING AND TAI TSUN WU. Pp. 204+ix. Harvard University Press, Cambridge, Massachusetts, 1959. Price $6.00.

This monograph provides a summary of those aspects of diffraction and scattering that fall under the broad heading of reflections from surfaces of complex shape. Attention is directed primarily toward the electromagnetic phases of these phenomena, but whenever appropriate, reference is made to parallel problems in acoustics. The book begins with a general discussion of theory and experiment as applied to a practical problem in electromagnetic scattering and diffraction. This is followed by a treatment of diffraction and scattering by circular cylinders, spheres, elliptic cylinders, disks or strips, and other obstacles, and transmission through apertures. The work concludes with discussions of methods of measuring the back-scattering cross sections and the diffracted fields of obstacles of various shapes. Solutions of many of the problems discussed are illustrated by means of graphs.

Finite Markov Chains. JOHN G. KEMENY AND J. LAURIE SNELL. Pp. 206+iv. D. Van Nostrand Company, Inc., Princeton, New Jersey, 1960. Price $5.00.

For the first time in English, this book explores the basic ideas of finite Markov chains, one of the most modern branches of probability theory. Only recently have mathematicians realized the full significance of Markov chain theory for pure mathematics and for the physical, biological, and social sciences. The authors concentrate exclusively on finite chains to develop the subject with a minimum of mathematical prerequisites. The treatment is therefore suitable both as an undergraduate textbook in probability and as a reference volume for workers in fields outside of mathematics. Applications to games, sociology, psychology, physics, economics, and genetics demonstrate the full power of a probability model. This new approach makes no use of the theory of characteristic values. In each case, the expressions in matrix form are simpler than the corresponding expressions in characteristic values, presumably because the fundamental matrices, unlike the characteristic values, have direct probabilistic interpretations.

Books Received

Evaporation and Droplet Growth in Gaseous Media. N. A. FUCHS, translated from the Russian by J. M. Pratt. R. S. BRADLEY, EDITOR. Pp. 70. Pergamon Press, New York, 1959. Price $5.50.

Electronic Computers. Principles and Applications. 2nd ed. T. E. Ivall. Pp. 259. Philosophical Library, Inc., New York, 1960. Price $15.00.

Servomechanism Fundamentals. 2nd ed. HENRI LAUER, ROBERT LESNICK, AND LESLIE E. MATSON. Pp. 485. McGraw-Hill Book Company, Inc., New York, 1960. Price $8.50.

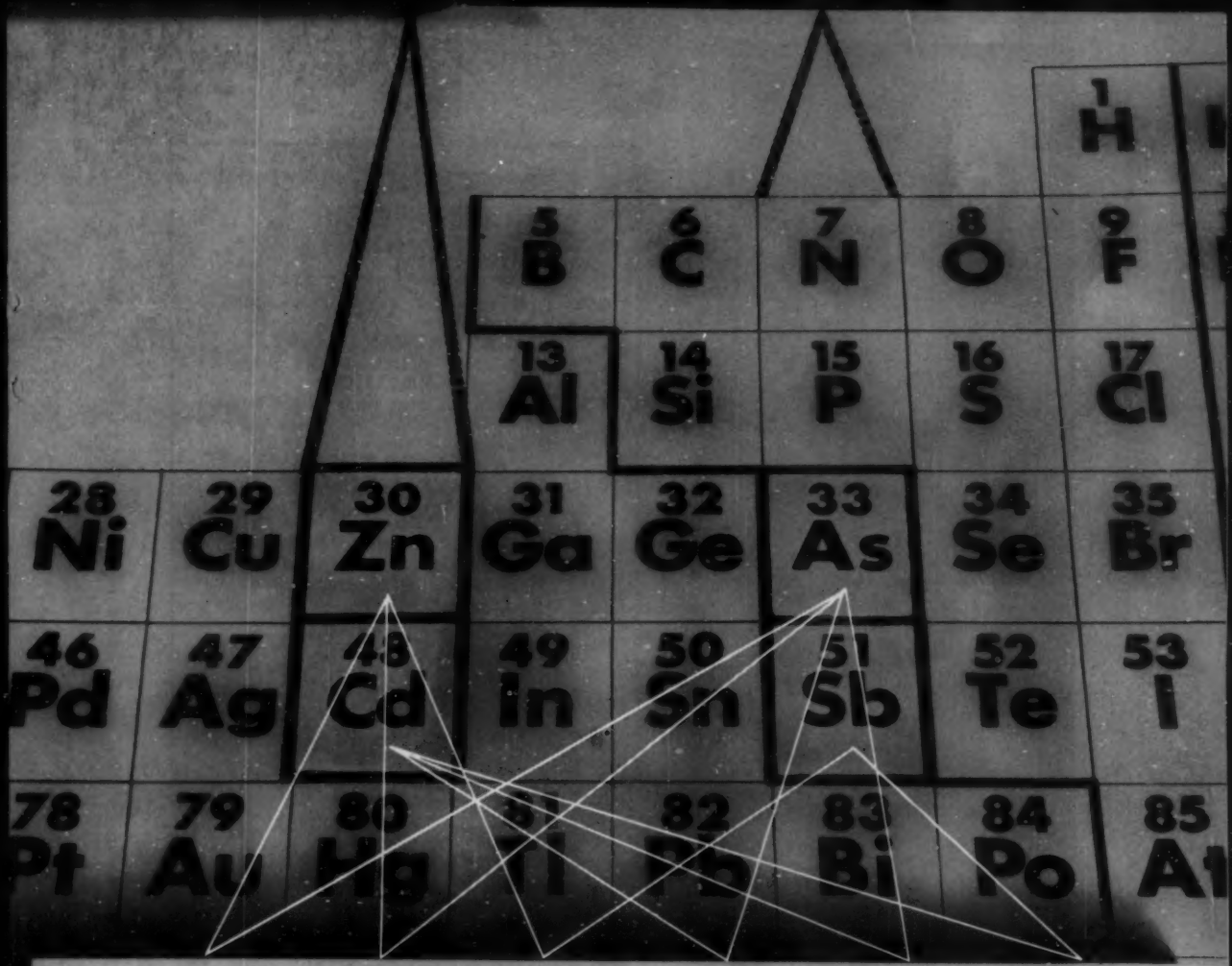

The study of these non-cubic compounds provides new insights into semiconductor physics.

Pure Physics Through "Pure" Chemistry

To obtain meaningful physical data, pure compounds are needed—compounds whose purity cannot be measured by conventional analytical means.

At IBM Research, chemists have been preparing single crystals of non-cubic Group II-V semiconductors by several methods and studying the physical chemistry, purification, and crystal growth of these compounds.

Another group, solid-state physicists, working in cooperation with the chemists, has been determining the electrical, optical, thermal, and resonance properties of these compounds. Significant in this research has been the observation of the effect of crystalline anisotropy on these fundamental properties.

From this close association of physicists and chemists have come advances in the fundamental knowledge of solid-state science. For example, out of the observations came the prediction that in one of these compounds, $CdAs_2$, cyclotron resonance might be detected. It was. In subsequent studies, cyclotron resonance was also detected in CdSb and ZnSb. Through this work, the number of semiconductors that exhibit cyclotron resonance has been doubled—because the compounds needed to make the observations were made available by IBM Research scientists. Furthermore, the interpretation of the electrical and optical measurements makes it possible to determine quantitatively how changes in preparation affect the quality of the compounds.

Our scientists are continuing to investigate the chemical and physical properties of these compounds to gain a better understanding of the fundamental nature of semiconductors.

IBM.RESEARCH

Investigate the many career opportunities available in exciting new fields at IBM.
International Business Machines Corporation, Dept. 579S, 590 Madison Avenue, New York 22, New York.

a vacuum pump as dynamically balanced as . . .

Engineered to give you years of vibration-free, superior operation, Stokes Series H Microvac pumps are the most advanced in their class. Exceptionally compact, Stokes pumps take up 50% less floor space than conventional vacuum pumps.

Learn all the reasons why Stokes offers you more pumping performance per dollar. Simply write: Vacuum Equipment Division, F. J. STOKES CORPORATION, 5500 TABOR ROAD, PHILA. 20, PA.

STOKES

SEND TODAY
for your free
Vacuum Slide Calculator!

SCIENTISTS
ENGINEERS
CALIFORNIA

offers you and your family

- **A world center of the electronics-missile-space industries for CAREER ADVANCEMENT**
- **The High Sierra and the Pacific Ocean for RECREATION**
- **And for your children some of the nation's FINEST PUBLIC SCHOOLS**
- **World Famous Universities for ADVANCED STUDY**
- **MAJOR CULTURAL CENTERS**

while living in such places as

Exciting San Francisco
Fabulous Southern California
Cultural Palo Alto

Companies pay interview, relocation and agency expenses

Submit resume in confidence to:

PROFESSIONAL and TECHNICAL RECRUITING ASSOCIATES
(a Division of the Permanent Employment Agency)
Suite A
825 San Antonio Road
Palo Alto, Calif.

To demonstrate transistor functions . . .

NEW CENCO
TRANSISTOR ANALYZER

Graphically demonstrates three basic transistor configurations—common emitter, base and collector. May also be used for simple circuit experiments and plotting response curves. Utilizes any general purpose transistor. Mounted on "Lucite".

No. 80390
$37.50

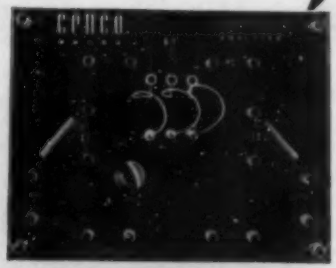

Ask for Booklet 811

cenco®
Serving education since 1899.

CENTRAL SCIENTIFIC CO.
A Subsidiary of Cenco Instruments Corporation
1718-A Irving Park Road • Chicago 13, Illinois
Branches and Warehouses—Mountainside, N. J. Boston • Birmingham • Santa Clara • Los Angeles • Tulsa Houston • Toronto • Montreal • Vancouver • Ottawa

ARMA ARMA ARMA ARMA ARMA

senior solid state scientist

ARMA has immediate need for a Senior Solid State Scientist to participate in an advanced and challenging research program.

The man selected will have a strong background in theory and application of solid state physics, with emphasis on molecular phenomena. He probably will have experience in molecular theory of gases and liquids.

His assignment: He will conduct independent investigations in thin film and surface physics and will explore several new modes of energy propagation within various media.

Most important, he will be a creative—perhaps presently stifled—physicist with wide scientific interests and a desire to advance the frontiers of research.

Salary is open.

If you fit the above description, phone Mr. E. C. Lester at PIoneer 2-2000 in Garden City, L. I. Or send your résumé in confidence to Mr. Lester, professional placement supervisor, address below.

ARMA DIVISION
AMERICAN BOSCH ARMA CORPORATION
ROOSEVELT FIELD, GARDEN CITY, LONG ISLAND, N. Y.

7848

ARMA ARMA ARMA ARMA ARMA

ACF ELECTRONICS DIVISION

ELECTRO-PHYSICS LABORATORIES

Responsible assignments in furthering the state-of-the-art of Ionospheric Physics, combining competitive salaries and unusual growth potential, are offered to men who can contribute. Our present needs are for:

Physicists

FOR RESEARCH PROGRAMS IN

IONOSPHERIC PROPAGATION & HF COMMUNICATIONS

SENIOR IONOSPHERIC PHYSICISTS

Ph.D. preferred, with several years' experience in the study of Ionospheric phenomena. Should be familiar with present knowledge of upper atmosphere physics and possess an understanding of current programs using rockets and satellites for studies in F-region and beyond. Qualified individuals with supervisory abilities will have an exceptional opportunity to assume project leadership duties on HF projects already under way involving F-layer propagation studies backed by a substantial experimental program.

The Electro-Physics Laboratories are located in the suburban Washington, D.C. area, where post-graduate study is available in several nearby universities. Housing is plentiful in attractive, well-established neighborhoods. Our relocation allowance is liberal.

All inquiries will be held in strictest confidence and answered promptly.

Please send resume to:

PROFESSIONAL EMPLOYMENT DEPARTMENT

ACF ELECTRONICS DIVISION

acf

Industries, Incorporated

Riverdale, Maryland

NOW! 2 MODELS

Provides a wide range of sensitivity, stability, and linear response particularly at extreme low-light levels. Choice of interchangeable photomultiplier tubes for optimum response in selected spectral regions. This compact, easy-to-operate instrument is now available in two models: battery power supply or transformer for line operation. Either model can be supplied with a galvanometer or with a highly sensitive microammeter.

Farrand Electron Multiplier PHOTOMETER

Technical data available on request. Specify Bulletin No. 804AP

FARRAND OPTICAL CO., INC.
BRONX BLVD. AND EAST 238th STREET • NEW YORK 70, N. Y.

3-Question Quiz for Senior Physicists who want to make original contributions in

SURFACE MECHANICS
SPUTTERING OF MATERIALS
SOLID STATE INVESTIGATIONS
SURFACE ELECTRON MICROSCOPY

1 **Do you enjoy the full measure of creative freedom to which experienced physicists are entitled?**

2 **Do you have a high degree of respect for your top management's technical competence?**

3 **What about the projects you're working on —are they stimulating enough to fully challenge your talents?**

At General Mills Mechanical Division Research Laboratories in Minneapolis, physicists answer an enthusiastic "yes" to all these questions. Approximately fifty percent of the scientists in our Physics and Electronics Laboratory work on a long-range, basic research program under the general heading of "Advanced Research on Materials and Surfaces." This company-sponsored project is now six years old and includes the development of a surface electron microscope, erosion studies on metals and semiconductors, semiconductor grain boundary work, and surface treatment and surface noise investigations. In our Materials and Mechanics Laboratories we are deeply engrossed in basic investigations in such fields as metal cutting, boundary friction, lubrication, fluid flow and rheology.

Today we have several basic research opportunities open to men with the true pioneering spirit. Perhaps you are one of the men we seek. Ideally, you have a graduate degree and 5 to 8 years pertinent research experience. In any event, if you are a man with your own ideas and have an unusual sense of curiosity, we are genuinely interested in you. And you should be interested in us, because we promise you an uninhibited environment in which you can quickly achieve the full measure of professional and personal recognition that your finest talents demand.

You'd like living in Minneapolis—some of the nation's most beautiful fishing, hunting and camping sites are just an hour's drive away. We enjoy a friendly, neighborly way of life and, at the same time, have all the advantages a major cosmopolitan center can offer. Our people spend long evenings with their families because travel to and from work is easy, uncongested. Children grow strong and healthy in this wholesome vacation-land. And they're educated in fine, trouble-free schools.

Send today for more information.

MR. G. P. LAMBERT
Manager, Professional Personnel
MECHAN.CAL DIVISION
2003 East Hennepin Avenue, Dept. AP7
Minneapolis 13, Minnesota

General Mills

GOODYEAR ATOMIC CORPORATION

Has Opening For Specialists In:

- Solid State Physics
- Physical Chemistry

and/or

- Electron Microscopy

and

- Electron Diffraction

To work on research and development projects in the fields of thin films, crystal perfection and corrosion.

SUBMIT RESUME AND SALARY REQUIREMENTS TO:

EMPLOYMENT DEPARTMENT
GOODYEAR ATOMIC CORPORATION
P.O. Box 628
Portsmouth, Ohio

MS-9 SERIES PACKAGED Helium Mass Spectrometer LEAK DETECTORS

Finds leaks in hermetically sealed components

WITH/WITHOUT AUTOMATIC ROUGHING STATION, BACKFILL CONSOLE

This is the most accurate, trouble-free

LEAK DETECTOR

you can buy

fast...simple...safe

- **Quick and Easy to Operate**

Flip a switch and the built-in automatic station does the work for you, electrically (no air supply required) ...lets you make up to 120 tests per hour...safety interlocks eliminate operator error, permits use of non-technical personnel.

- **Guaranteed Accurate and Safe**

Constant 10^{-10} cc/sec accuracy guaranteed by the patented VEECO VEETUBE®...it cleans itself...uses safe, inert helium as tracer gas.

- **Thoroughly Tested**

Each MS-9 undergoes a full week (168 hrs) of test run and inspection before shipment.

FREE MS-9 BROCHURE contains full details on performance, specifications, operation and advantages. There is an MS-9 series Leak Detector to fill your exact need. Write Department A-1435.

Veeco **VEECO VACUUM CORP.**
86 J Denton Avenue, New Hyde Park
Long Island, New York
HIGH VACUUM & LEAK DETECTION EQUIPMENT

Nuclear Scientists,
Engineers & Mathematicians:

"A man's mind stretched by a new idea can never go back to its original dimensions."

...OLIVER WENDELL HOLMES

The collective "mind" of The Knolls Atomic Power Laboratory has been stretched to new dimensions frequently by such milestone achievements in reactor technology as the *Triton* twin-reactor propulsion system, the sodium-cooled reactor system for *Seawolf* and the development of a number of unique critical assemblies for applied research and experimental programs.

Exploratory work, now underway, again calls for reactor engineers and scientists to reach beyond the conventional bounds of nuclear technology — to apply their broadest knowledge to the problems of achieving major breakthroughs in reactor simplification.

That imaginative thinking may be unobstructed by material barriers, KAPL maintains a full complement of experimental and test facilities, many of them unique, ranking with the finest in the free world.

A limited number of vacancies are available to physicists, nuclear engineers and mathematicians of demonstrated calibre. *U. S. citizenship and appropriate engineering or scientific degree required.* Address inquiries in confidence to Mr. A. J. Scipione, Dept. 37-MG.

Knolls Atomic Power Laboratory
OPERATED FOR A E C BY
GENERAL ELECTRIC
Schenectady, New York

"KAPL Review," a publication describing the Laboratory's current activities, facilities, and recent achievements is available on request to interested engineers and scientists.

Compelling Opportunities

For original BASIC thought!

Which is tailored to your career goals?

1. PULSE DOPPLER RADAR ENGINEER

THE CHALLENGE: generation of system specifications, initial design, and development of all facets of radio frequency circuitry for pulse doppler radars.

BS/EE degree + graduate work in math and electrical networks; + minimum 3 years' experience in design of radio frequency "front ends" for pulse doppler radars. Specific development experience necessary in at least 2 of these: highly stable, high frequency oscillators; high power, fast recovery duplexers; master oscillator-power amplifier (MOPA) tube chains at microwave frequencies. Desirable: familiarity with high power travelling wave tubes, backward wave amplifiers and backward wave oscillators.

2. ANTENNA ENGINEER

THE CHALLENGE: leading initial antenna research and design + conceiving satisfactory theoretical solutions to radiation and scanning problems with only fragmentary information.

Advanced degree in physics or communications engineering, with emphasis on electromagnetic theory and advanced math. Also 2 years' or more experience beyond school in fundamental design and formal math analysis of microwave antennas. Major importance: design exp. with flush mounted antennas, two dimensional arrays, electronically scanned antennas, and dielectric lenses. Experience in monopulse antennas and microwave phase shifting techniques desirable.

3. IR SYSTEM ENGINEER

THE CHALLENGE: working with top-level staff associates in the solution of a variety of intriguing IR problems involving detection, tracking and guidance systems.

Your background includes substantial formal training + experience in the application of fundamental infrared theory and technique to these systems. This opening offers unusual professional freedom + wide diversification.

For more information about these and/or other challenging openings—and about the unusual advantages at Emerson, write A. L. Depke, giving a complete resume of education and experience. All correspondence held in strict confidence.

Research, design, development and manufacturing in... avionics, electronics, consumer and industrial products.

EMERSON ELECTRIC

8100 W. Florissant—Dept. 497C—St. Louis 36, Mo.

PHYSICIST

Tech/Ops is a medium-sized research and development firm doing advanced work in the physical sciences, operations research, and computer technology. Research in the physical sciences is carried on at Tech/Ops Central Laboratory adjacent to Metropolitan Boston.

Continued expansion of Tech-Ops research activities in physics has created two positions for physicists on the Ph. D. level (or with equivalent experience). They will contribute to existing experimental and theoretical programs in atmospheric physics, spectroscopy, and dynamics of rarefied gases, applications of kilojoule discharge circuits, and shielding and scattering phenomena. Experience in atmospheric physics is particularly desirable.

Our interests are in scientists who can contribute unique solutions to non-routine problems in a variety of fields of physics and who like to work in an informal environment, with exposure to varied scientific disciplines. Our Company offers the usual benefit plan, including a profit-sharing program.

MR. ROBERT L. KOLLER

TECHNICAL OPERATIONS

INCORPORATED

South Ave., Burlington · VOlunteer 2-8500

13 Noted Scientists Present
A SPACE AGE SYMPOSIUM

Robert Jastrow
Fred L. Whipple
Thomas Gold
Eugene Parker
James A. Van Allen
N. C. Christofilos
Homer E. Newell
Gerard P. Kuiper
Harold C. Urey
G. de Vaucouleurs
Herbert Friedman
Leo Goldberg
J. W. Townsend, Jr.

THE EXPLORATION OF SPACE
edited by Robert Jastrow
illustrated, $5.50

Van Allen discusses the geomagnetically trapped corpuscular radiation; Christofilos reports on "The Argus Experiment;" de Vaucouleurs, on Mars and Venus; Goldberg, on astronomy from satellites and space vehicles; Whipple, on solid particles in the solar system. Other vital topics include rocket astronomy, plasma and magnetic fields in the solar system, the U. S. space-exploration program, and the U.S.S.R. report of an active volcano on the moon.

Order Today From Your Nearest Bookstore Or Write Dept. JAP-1.

The Macmillan Company
60 FIFTH AVENUE, NEW YORK 11, N. Y.

Engineers

SUPERVISOR
SPACE SYSTEMS
ANALYSIS

A long established California research organization has an immediate opening for a supervisor of a staff of analysts skilled in engineering, physics and mathematics and conducting mission-oriented lunar and interplanetary system and studies involving trajectories, error sensitivities, maneuvering requirements and guidance equations. The position also affords opportunity for individual research.

Advanced degree and related experience required.

Send resume today to Box 760-A, Journal of Applied Physics, 335 East 45th St., New York 17, N. Y.

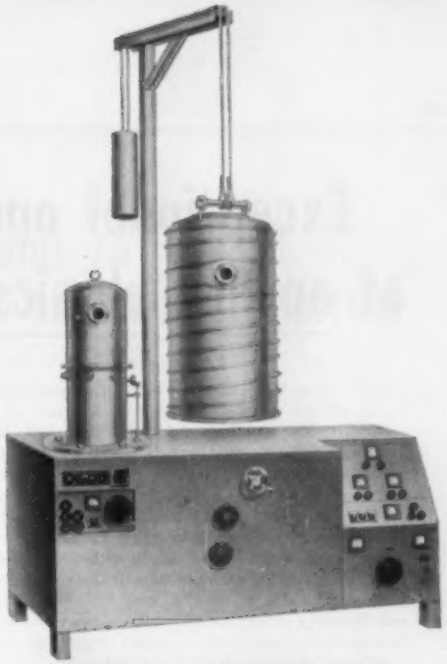

WHAT HAPPENS AT 1,200,000 FEET UP?

You can have the answer NOW . . . and leave theory and the educated guess to others. KINNEY offers fully developed working tools which provide pressures of better than 1 x 10^{-9} mm Hg . . . ready to work in areas heretofore closed to physicist and researcher.

Kinney®

TWO NEW DEVELOPMENTS IN ULTRA HIGH VACUUM

The KINNEY UH-9A Ultra High Vacuum System, (illustrated above) employing the principle of differential pumping, consistently produces Vacuum in the order of 1 x 10^{-9} mm Hg in the work chamber. KINNEY also offers a new Ionic High Vacuum System which develops pressures even lower than the $^{-9}$ scale. This system features the Ultek® Ion Pump for which KINNEY is exclusive distributor.

The facts about these significant developments in Vacuum technology are yours for the asking. **Write for KINNEY bulletins 4150, 4160 and 4450 today!**

KINNEY VACUUM DIVISION
THE NEW YORK AIR BRAKE COMPANY
35560 WASHINGTON STREET • BOSTON 30 • MASS.

Please send me copies of Bulletins 4150, 4160 and 4450 describing KINNEY Ultra High Vacuum Systems.

Name_____

Company_____

Address_____

City_____ Zone____ State_____

Exceptional opening for manager of applied physics at RCA Moorestown

This is a singular opportunity to head up a new activity specifically formed to advance the state of the radar art. The candidate selected will manage three groups of engineers and leaders working full-time on advanced technique development in the most challenging radar areas.

To qualify, you should have a strong physics background with a Ph.D. degree in either Physics or Engineering . . . the ability to stimulate and direct original thinking . . . and at least ten years' experience in optics or electro-mechanical physics as applied to radar technology, with a working acquaintance—including a knowledge of hardware techniques—in these fields. Salary will be commensurate with experience. You will enjoy outstanding professional, living, educational and recreational advantages.

For a confidential interview, please send a résumé to:

Mr. W. J. Henry, Box V-37-G
RCA, Moorestown, New Jersey
(20 minutes from Philadelphia)

EQUAL FOR All Qualified Applicants OPPORTUNITY

RCA

RADIO CORPORATION of AMERICA

Moorestown Missile and Surface Radar Division

NEW VACUUM METALLIZER

- For research or small scale deposition of metals and salts on metals, glass, plastics, ceramics, etc.
- Permits multiple source evaporations and close control of filament voltage from 0 – 40 V.
- Power, high voltage, thermocouple, work positioning, etc. feed-throughs are easily relocated at any of 17 points.

Packaged 35″ x 48″ x 112″ unit is easy to install, operate, and maintain. Geared hoist takes work out of raising 18″ shielded Pyrex or 24″ O.D. mild or stainless 30″ high bell jar. Vibration-isolated, 6″ pumping system with optical baffle cold trap gives fast, "clean" pump-down to 10^{-6} mm. Hg. Write today for details on NRC Model 3144.

NRC
EQUIPMENT CORPORATION

A subsidiary of National Research Corporation
Dept. P-7, 160 Charlemont St., Newton 61, Massachusetts • DEcatur 2-5800

Soviet Physics—SOLID STATE

Monthly. A cover to cover translation of the USSR Academy of Sciences journal, "Fizika Tverdogo Tela."

Soviet Physics—TECHNICAL PHYSICS

Monthly. A cover to cover translation of the USSR Academy of Sciences journal, "Zhurnal Tekhnicheskoi Fiziki."

Soviet Physics—CRYSTALLOGRAPHY

Bimonthly. A cover to cover translation of the USSR Academy of Sciences journal, "Kristallografiya."

Please address orders and inquiries to the publisher:

AMERICAN INSTITUTE OF PHYSICS
335 East 45th Street, New York 17, N. Y.

Off-Press In September . . .

RETRIEVAL GUIDE TO THERMOPHYSICAL PROPERTIES RESEARCH LITERATURE

Edited by Y. S. Touloukian

Thermophysical Properties Research Center

Purdue University

Ten thousand scientific and technical research papers have been coded as to property, substance, subject, language, physical state, etc. and the information stored on magnetic tapes of a computer at Purdue University. The thermophysical properties of 14,500 substances are reported. This work represents the print out of a special computer program and will provide the engineer, scientist, or reference librarian with quick access to the world literature on the following seven thermophysical properties: thermal conductivity, thermal diffusivity, diffusion coefficient, specific heat, viscosity, emissivity and Prandtl number.

Volume I, *The Three Book Set* (10,000 bibliographic references), $120.00

McGRAW-HILL BOOK COMPANY, INC.

330 West 42nd Street **New York 36, N. Y.**

EPLAB

Thermopiles

For many years the thermopile has been the accepted instrument for measuring Radiant Heat from Radiant Heaters at the American Gas Association Testing Laboratory in Cleveland, Ohio. Since 1930, when Vandaveer first described his work in this field,* an Eppley thermopile has been used for this purpose in hundreds of tests and the results have been consistent and accurate to within 1 per cent.

This is but one of the many applications in the field of radiant energy measurements for which Eppley Thermopiles are ideally suited. They may be obtained with windows of different materials, and various types of black are available for receiver coatings.

All Eppley Thermopiles are supplied with a certificate of calibration, this calibration being made against a Standard Lamp from the National Bureau of Standards.

If you have a problem involving the measurement of radiant energy we invite you to write us, describing your problem in as much detail as possible. We will be glad to make recommendations and there will be no obligation.

**Vandaveer, Industrial & Engineering Chemistry, Vol. 22, page 596, June 1930.*

BULLETIN NO. 3 ON REQUEST

ADDRESS: 6 SHEFFIELD AVE., NEWPORT, R. I.

THE EPPLEY LABORATORY, INC.

SCIENTIFIC INSTRUMENTS

NEWPORT, RHODE ISLAND, U. S. A.

INDEX TO ADVERTISERS

Name	*Page*
A.C.F. INDUSTRIES, INC.	xxi
ARMA DIVISION, AMERICAN BOSCH ARMA CORP.	xxi
ARNOLD ENGINEERING CO.	iii
BELL TELEPHONE LABS.	v
CENTRAL RESEARCH LABS.	viii
CENTRAL SCIENTIFIC CO.	xx
CORNELL-DUBILIER ELECTRIC CORP.	xiv
EASTMAN KODAK CO.	ix
EMERSON ELECTRIC MFG. CO.	xxiv
EPPLEY LAB., INC.	xxvii
FARRAND OPTICAL CO.	xxii
GENERAL ELECTRIC, KNOLLS ATOMIC POWER LAB.	xxiii
GENERAL MILLS	xxii
GENERAL RADIO CO.	Cover 4
GOODYEAR ATOMIC CORP.	xxiii
HARSHAW CHEMICAL CO.	Cover 2
IBM CORPORATION	xix
KEITHLEY INSTRUMENTS	xiii
KINNEY VACUUM DIVISION, N. Y. AIR BRAKE CO.	xxv
LOS ALAMOS SCIENTIFIC LAB.	xi
McGRAW-HILL BOOK CO., INC.	xii, xxvii
MACMILLAN CO.	xxv
N.R.C. EQUIPMENT CORP.	xxvi
PACIFIC SEMICONDUCTORS	xv
PERMANENT EMPLOYMENT AGENCY	xx
PHILIPS ELECTRONICS	vi, vii
RADIO CORP. OF AMERICA	xvii, xxvi
SPACE TECHNOLOGY LABS.	Cover 3
STOKES CORP., F. J.	xx
SYLVANIA ELECTRONIC SYSTEMS, WALTHAM LABS.	x
TECHNICAL OPERATIONS, INC.	xxiv
VARIAN ASSOCIATES	iv
VEECO VACUUM CORP.	xxiii
WELCH SCIENTIFIC CO., W. M.	xviii

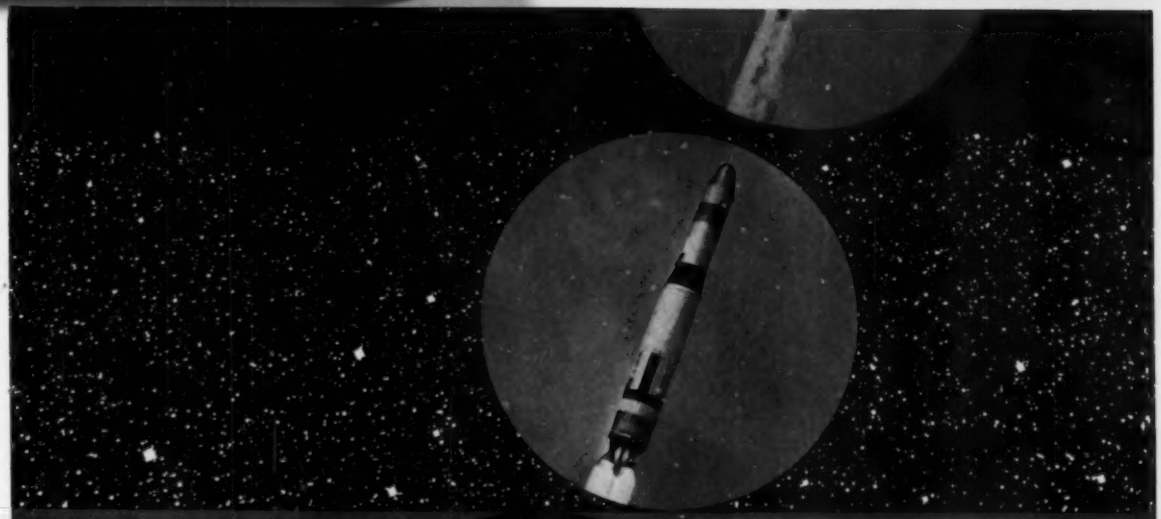

Building Strength Upon Strength... the USAF Ballistic Missile Program

The strength and prestige of this nation depends upon many things . . . important among these are the successes of the Air Force Ballistic Missile Program and related advanced space projects.

In turn, these programs depend upon the continuing flow of new ideas and inventions. All of these are part of a common pool of knowledge and know-how which are drawn upon for today's capability and tomorrow's advances.

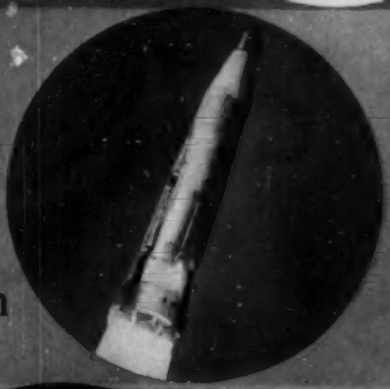

In building strength upon strength in the race for space technology leadership, the knowledge and experience gained from Atlas, Thor, and Titan ballistic missile systems development is being applied to advance Minuteman. For these programs, under the management of the Air Force Ballistic Missile Division, Space Technology Laboratories has had the direct responsibility for over-all systems engineering and technical direction. As these ballistic missile and related space programs go forward, STL continues to contribute technical leadership and scientific direction.

In this capacity STL offers unusual opportunities for creative work in the science and technology of space systems. To those scientists and engineers with capabilities in propulsion, electronics, thermodynamics, aerodynamics, structures, astrophysics, computer technology and other related fields and disciplines, STL now offers immediate opportunities. Please address your inquiries and/or resumes to:

SPACE TECHNOLOGY LABORATORIES, INC.

P. O. Box 95004, Los Angeles 45, California

Los Angeles • Santa Maria • Cape Canaveral • Washington, D. C.
Manchester, England • Singapore • Hawaii

How to Control
TIME, FREQUENCY and SPACE

A radio-guidance system, built by Space Technology Laboratories, Inc., played an important role in the successful launching of Pioneer V. This new ground-controlled guidance system, based on doppler-shift techniques, obtains and uses velocity and position data to control the missile.

The system relies on an accurately-controlled, stable, primary frequency — instability, f-m noise, or harmonic interference in the primary frequency could impair system performance. The G-R 1112-A Standard-Frequency Multiplier was picked by STL to help generate this frequency. It serves in an important in-line role as an element of the frequency synthesizer for this radio-guidance system. STL also uses the Frequency Multiplier in its world-wide network of tracking stations.

Telemetering, missile tracking, spectroscopy and atomic-resonance investigations, radar, and navigation-systems applications are but a few of the other areas where the 1112-A and its companion frequency multiplier, the 1112-B, find use.

U.S. Sun Orbiter Right on Beam

WASHINGTON, March 12 (AP) — Pioneer V hurtled through space today toward its destined place as a tiny new sister planet between earth and Venus in a giant orbit about the sun.

Good Operation

Pioneer V was speeding away at 6,487 m.p.h. This carried it to an estimated 213,140 miles out from earth at noon.

All equipment was reported operating perfectly. Giant radios, triggered from earth approximately once an hour, sent back loud and clear signals from which scientists computed speeds and distances.

Later today the instru- packed space vehicle unge into its giant five- orbit around the sun. t orbit will be a 514,- 00-mile circle through between the orbits of earth and the planet s.

the orbit Pioneer V will ach to about 74,967,000 of the sun, compared the

Type 1112-A Standard-Frequency Multiplier . . . $1450

1-Mc, 10-Mc, and 100-Mc output frequencies are generated by separate crystal oscillators that are phase locked to the input frequency to insure extremely low f-m noise levels.

INPUT: 1-volt, 100-kc sine wave from G-R 1100-A Frequency Standard or equivalent. Can be driven by 1-Mc, 2.5-Mc, or 5-Mc standard frequency as well.

OUTPUT: 1-Mc, 10-Mc, and 100-Mc sine-wave signals; output level of each independently adjustable with maximum of 20 mw into 50 ohms.

STABILITY: Long-term stability dependent only upon driving source.

F-M NOISE: Less than 1 part in 10^9.

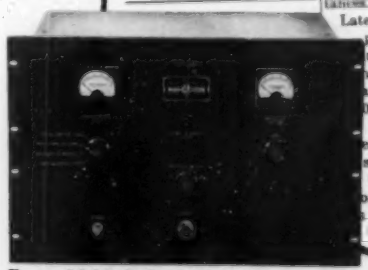

Type 1112-B Standard-Frequency Multiplier . . . $1360

1000-Mc output is generated directly by a klystron oscillator that is phase-locked to the 100-Mc input. Phase stability of the output is comparable to that of the input signal.

INPUT: 20-mw, 100-Mc sine wave from 1112-A or equivalent.

OUTPUT: 1000-Mc sine wave; at least 50 mw into a 50-ohm load.

STABILITY and F-M NOISE: Same as 1112-A.

Write For Complete Information

GENERAL RADIO COMPANY

WEST CONCORD, MASSACHUSETTS

our 45th year in Electronics

NEW YORK, WOrth 4-2722	CHICAGO	PHILADELPHIA	WASHINGTON, D.C.	SAN FRANCISCO	LOS ANGELES	IN CANADA
District Office in Ridgefield, N. J. WHitney 3-3140	Oak Park Village 8-9400	Abington HAncock 4-7419	Silver Spring JUniper 5-1088	Los Altos WHitecliff 8-8233	Los Angeles HOllywood 9-6201	Toronto CHerry 6-2171